Lecture Notes in Mechanical Engineering

D. K. Maiti · P. Jana · C. S. Mistry · R. Ghoshal · M. S. Afzal · P. K. Patra · D. Maity *Editors*

Recent Advances in Computational and Experimental Mechanics, Vol II

Select Proceedings of ICRACEM 2020

Springer

Lecture Notes in Mechanical Engineering

Lecture Notes in Mechanical Engineering (LNME) publishes the latest developments in Mechanical Engineering—quickly, informally and with high quality. Original research reported in proceedings and post-proceedings represents the core of LNME. Volumes published in LNME embrace all aspects, subfields and new challenges of mechanical engineering. Topics in the series include:

- Engineering Design
- Machinery and Machine Elements
- Mechanical Structures and Stress Analysis
- Automotive Engineering
- Engine Technology
- Aerospace Technology and Astronautics
- Nanotechnology and Microengineering
- Control, Robotics, Mechatronics
- MEMS
- Theoretical and Applied Mechanics
- Dynamical Systems, Control
- Fluid Mechanics
- Engineering Thermodynamics, Heat and Mass Transfer
- Manufacturing
- Precision Engineering, Instrumentation, Measurement
- Materials Engineering
- Tribology and Surface Technology

To submit a proposal or request further information, please contact the Springer Editor of your location:

China: Ms. Ella Zhang at ella.zhang@springer.com
India: Priya Vyas at priya.vyas@springer.com
Rest of Asia, Australia, New Zealand: Swati Meherishi at swati.meherishi@springer.com
All other countries: Dr. Leontina Di Cecco at Leontina.dicecco@springer.com

To submit a proposal for a monograph, please check our Springer Tracts in Mechanical Engineering at https://link.springer.com/bookseries/11693 or contact Leontina.dicecco@springer.com

Indexed by SCOPUS. All books published in the series are submitted for consideration in Web of Science.

More information about this series at https://link.springer.com/bookseries/11236

D. K. Maiti · P. Jana · C. S. Mistry · R. Ghoshal ·
M. S. Afzal · P. K. Patra · D. Maity
Editors

Recent Advances in Computational and Experimental Mechanics, Vol II

Select Proceedings of ICRACEM 2020

Springer

Editors
D. K. Maiti
Department of Aerospace Engineering
Indian Institute of Technology Kharagpur
Kharagpur, West Bengal, India

P. Jana
Department of Aerospace Engineering
Indian Institute of Technology Kharagpur
Kharagpur, West Bengal, India

C. S. Mistry
Department of Aerospace Engineering
Indian Institute of Technology Kharagpur
Kharagpur, West Bengal, India

R. Ghoshal
Ocean Engineering and Naval Architecture
Indian Institute of Technology Kharagpur
Kharagpur, West Bengal, India

M. S. Afzal
Department of Civil Engineering
Indian Institute of Technology Kharagpur
Kharagpur, West Bengal, India

P. K. Patra
Department of Civil Engineering
Indian Institute of Technology Kharagpur
Kharagpur, West Bengal, India

D. Maity
Department of Civil Engineering
Indian Institute of Technology Kharagpur
Kharagpur, West Bengal, India

ISSN 2195-4356 ISSN 2195-4364 (electronic)
Lecture Notes in Mechanical Engineering
ISBN 978-981-16-6489-2 ISBN 978-981-16-6490-8 (eBook)
https://doi.org/10.1007/978-981-16-6490-8

This Springer imprint is published by the registered company Springer Nature Singapore Pte Ltd.
The registered company address is: 152 Beach Road, #21-01/04 Gateway East, Singapore 189721, Singapore

Contents

About the Editors

D. K. Maiti is Professor and Former Head, Department of Aerospace Engineering at IIT Kharagpur, prior to which he has worked at ADA Bangalore as Scientist/Engineer and Department of Aerospace Engineering, IIT Bombay as Senior Research Engineer. He has published over 80 international journal papers, over 70 national and international conference papers, over 60 project reports, handled several research projects sponsored by ARDB, ADA, DST, ISRO, etc. of worth a few crores. So far, 10 research students have obtained their Ph.D. degree under his supervision. Currently, 13 research students are pursuing their doctoral research work under his supervision. He has guided over 70 M.Tech students for their Master's Projects and over 50 B.Tech students for their B.Tech Projects. His primary research areas are analysis of composite structures under static and dynamic loadings employing various higher-order shear deformation theories, damage modelling of isotropic and composite materials, smart structures, aeroelasticity/aeroservoelasticity, structural health monitoring, etc.

Dr. P. Jana is an Assistant Professor in the Department of Aerospace Engineering, IIT Kharagpur. He has worked with Indian Space Research Organization and General Electric, for a total of five years, in the area of design and analysis of composite structures. He has also worked as an Assistant Professor in IIT Mandi and IIT Dhanbad. His research interests lie primarily in the use of computational mechanics to address some underlying questions of material modelling and structural design. Presently, he is working on the broad areas of aerospace structures, composites and functionally graded materials, vibration damping, and stability of structures.

Dr. C. S. Mistry is Assistant Professor, Department of Aerospace Engineering, IIT Kharagpur. He has 19 years' experience in teaching and research. He has done his graduation in Mechanical Engineering from REC, Surat (Presently NIT-Surat); Master of Engineering in Turbo Machinery from Mechanical Engineering Department of NIT, Surat; Ph.D. From IIT Bombay. His Ph.D. thesis on "Experimental Investigation on the Performance of a Contra Rotating Fan Stage under Clean and Distorted Inflow Conditions" awarded with an "Award for Excellence in Thesis

Work", IIT Bombay in 2014. He is also recipient of "ASME-IGTI-Young Engineer Travel Award" in the year 2013. His area of research are Design and performance augmentation strategies for turbomachines, Experimental and CFD study of turbomachines, Contra rotating axial flow turbomachines aerodynamics, Electric propulsion as well as fluid mechanics & heat transfer, and experimental aerodynamics.

Dr. R. Ghoshal is an Assistant Professor Department of Ocean Engineering and Naval Architecture Indian Institute of Technology, Kharagpur. He was a postdoctoral Research Fellow in the Department of Mechanical Engineering, National University of Singapore (NUS). He worked in Keppel-NUS Corporate Laboratory to develop a new methodology for designing economic station-keeping systems for Arctic Floaters in harsh environments. During his doctoral research he worked on developing mitigation strategies of explosion induced shock loading on structures using marine grade sandwich panels. His research works have been presented in various international conferences and published in leading peer-reviewed journals and conference proceedings.

M. S. Afzal is an assistant professor in the Department of Civil engineering, Indian Institute of Technology, Kharagpur. He is a young and dynamic researcher in the field of Hydraulics and water resources. His research area focuses on Computational Fluid Dynamics, Hydraulics of sediment transport, Coastal Engineering and machine learning and artificial intelligence in Hydraulics. He is an alumnus of IIT Kanpur, TU Delft and Norwegian university of science and Technology (NTNU). He is famous for his numerical analysis technique in the field of hydraulics and sediment transport. He is very famous for his work on Three-dimensional streaming in seabed boundary layer.

Dr. P. K. Patra is an Assistant Professor in the Department of Civil Engineering, IIT Kharagpur. Prior to this, he worked as a postdoctoral research scholar in the Department of Biomedical Engineering and Mechanics, Virginia Polytechnic Institute and State University. His research interests include non-equilibrium statistical mechanics, thermodynamics, molecular dynamics simulations and thermal transport characteristics in low dimensional systems. He holds a Ph.D. degree in Mechanics from IIT Kharagpur and a B.Tech. (H) degree in Civil Engineering also from IIT Kharagpur.

Dr. D. Maity is Professor in the Department of Civil Engineering, Indian Institute of Technology, Kharagpur. He has more than 150 research publications in journals and conference proceedings of national and international repute. His research area of interest includes computation mechanics, structural health monitoring, fluid-structure interaction. He has received two best paper awards from The Institution of Engineers (India). Prof. Maity is author of a book titled, "Computer Analysis

of Framed Structures" published by I. K. International Pvt. Ltd. He has served as scientific/advisory board member of several international conferences. He served as secretary for The Indian Society of Theoretical and Applied Mechanics for three consecutive years. Prof. Maity has developed a video course on "Design of Steel Structures" and a web course on "Finite Element Analysis" under NPTEL, MHRD.

Free Vibration Study of Laminated Composite Shell with Varying Cut-Outs

Soumen Roy, Sandipan Nath Thakur, C. Ajeesh, and Chaitali Ray

1 Introduction

The fiber-reinforced layered composite shell structures are very common in recent engineering applications, e.g., spacecraft, aircraft, submarine, wind turbine blade, defence industry, etc., due to their specific stiffness, lightweight, and other advantageous properties. Shell structures have advantages over plates due to their curvature effect in carrying loads and moments. Cut-outs are the integral parts of most laminated shell structures, although the provisions of cut-outs are unavoidable in most of the engineering structures. The presence of a cut-out makes a structure weak due to the occurrence of stress concentration near the opening. These cut-out structures often initiate failure at comparatively lower stress and sometimes due to resonance. Therefore, the effect of cut-out on the dynamic behavior of laminated shells is to be dealt with carefully.

An HSDT was developed by Reddy and Liu [1] for the bending and vibration analysis of laminated shells with simply supported boundary conditions. Chakraborty et al. [2] presented the vibration behavior of laminated shells with cut-outs using the 8-node isoparametric finite element formulations. Hota and Chakravorty [3] analyzed free vibration characteristics of a conoidal stiffened shell structure with cut-outs using eight-noded curved shell elements. Nanda and Bandyopadhyay [4] presented the nonlinear analysis of undamped vibration of laminated shells with cut-outs using finite element model considering an 8-noded isoparametric element. The solution of semi-analytical analysis for free vibration behavior of laminated shells with cut-out for different geometric configurations was presented by Poore et al.

S. Roy · S. N. Thakur
University Institute of Technology, The University of Burdwan, Burdwan, West Bengal, India

C. Ajeesh · C. Ray (✉)
Indian Institute of Engineering Science and Technology, Shibpur, West Bengal, India
e-mail: chaitali@civil.iiests.ac.in

D. K. Maiti et al. (eds.), *Recent Advances in Computational and Experimental Mechanics, Vol II*, Lecture Notes in Mechanical Engineering,
https://doi.org/10.1007/978-981-16-6490-8_1

[5]. Malekzadeh et al. [6] performed free vibration of homogenous and functionally graded (FG) cylindrical shell panels with cut-out with thermal effect using the 3-D Chebyshev–Ritz method. Hu et al. [7] studied the vibration characteristics of laminated composite shell panels with circular cut-outs at the center and subjected them to axial compressive force using ABAQUS software. Biswas and Ray [8] investigated the free vibration behavior of glass fiber reinforced laminates and hybrid laminates experimentally and numerically. Mandal et al. [9] carried out fundamental natural frequencies of laminated skew plates with cut-outs and without cut-outs. Using third-order shear deformation theory, Chaubey and Kumar [10] studied free vibration behavior of spherical, cylindrical, saddle, elliptical and hyper shells with cut-outs. Mandal et al. [11] also investigated the dynamic behavior of laminated shells with and without cut-outs numerically and experimentally.

In the present work, vibration analysis of six-layered glass fiber laminated composite shell (GFRP) with cut-out has been presented using ANSYS software. The effectiveness of the present model has been verified by validating the solutions with experimental results obtained from Mandal et al. [11] and theoretical results obtained from Chakravorty et al. [2]. Also, a convergence study is carried out to decide the actual mesh size for obtaining a consistent value of natural frequency by comparing with the result taken from Reddy and Liu [1]. Several new results have been obtained using HSDT to check the effect of curvature, thickness ratio, lamination scheme, and boundary condition on the natural frequency with varying cut-out percentages of the shell.

2 Finite Element Formulation

A laminated composite cylindrical shell with cut-outs has been modeled and analyzed using ANSYS software. Triangular element SHELL281 with 6 DOFs per node (u, v, w, θ_x, θ_y, θ_z) is used for the present formulation. Modeling is done by specifying the thickness, material, orientation with a number of integration points through the thickness of the laminates.

Element stiffness matrix $[\mathbf{K_e}]$ and the element mass matrix $[\mathbf{M_e}]$ for an element is expressed as

$$[\mathbf{K_e}] = \iint [\mathbf{B}]^T[\mathbf{D}][\mathbf{B}]\mathrm{d}s\,\mathrm{d}r = \int_{-1}^{1}\int_{-1}^{1} [\mathbf{B}]^T[\mathbf{D}][\mathbf{B}]|\mathbf{J}|\mathrm{d}\xi\,\mathrm{d}\eta$$

$$[\mathbf{M_e}] = \iint [\mathbf{N}]^T[\rho][\mathbf{N}]\mathrm{d}s\,\mathrm{d}r = \int_{-1}^{1}\int_{-1}^{1} [\mathbf{N}]^T\left[\bar{\mathbf{I}}\right][\mathbf{N}]|\mathbf{J}|\mathrm{d}\xi\,\mathrm{d}\eta$$

where $[\rho]$ is the inertia matrix and $|\mathbf{J}|$ is the determinate of the Jacobian matrix.

Applying the equation of motion for undamped structure, the natural frequencies can be calculated, which is,

$$\omega^2[\mathbf{M}]\{\phi\} = [\mathbf{K}]\{\phi\}$$

where $\{\phi\}$ represent the mode shapes and ω is the natural frequency and the non-dimensional form of the frequency can be expressed as

$$\overline{\omega} = \left(\frac{\omega a^2}{h}\right)\sqrt{\frac{\rho}{E_2}}$$

The free vibration equation is analyzed and modeled using ANSYS 16.0 software package.

3 Results and Discussions

A convergence study is performed to decide the actual mesh size ($\overline{n} \times \overline{n}$) for obtaining a consistent value of the natural frequency of laminated composite shell using ANSYS 16.0 software. A simply supported anti-symmetric cross-ply (0°/90°) laminated composite shell is chosen for this study. The radius to lateral dimension ratio (R/a) is considered as 5 and thickness to lateral dimension ratio (h/a) is taken as 0.1. The results in terms of the non-dimensional fundamental frequency are presented in Table 1 and it may be observed from Table 1 that the numerical value of non-dimensional fundamental frequency converges approximately at $\overline{n} = 16$. Thus, a mesh division of 16 × 16 is considered for the subsequent comparison studies and parametric studies of laminated composite shells.

Example 1. Free vibration study of laminated shells with cut-outs is carried out in the present study. Six layers of bidirectional symmetric cross-ply glass fabrics of average thickness 0.5 mm each layer is used for the laminates. The composite laminated cylindrical shells of projected plan area 250 × 250 mm and radius of curvature 145 mm have been analyzed. Two straight edges of the shell model are simply supported (only θ_y is free) and the other two curved edges are kept free. The fundamental natural frequencies with varying cut-out sizes are determined using the SHELL281 element available in ANSYS. The numerical results of modal analysis obtained from the ANSYS software package have been compared with the experimental results in Table 2 and the comparison shows good agreement with each other.

Table 1 Convergence study of non-dimensional frequency parameter ($\overline{\omega}$) of simply supported cross ply (0°/90°) cylindrical shells (R/a = 5, h/a = 0.1)

Mesh size	Present formulation	Reddy and Liu [1]
12 × 12	8.88	8.9
14 × 14	8.88	8.9
16 × 16	8.89	8.9
18 × 18	8.89	8.9
20 × 20	8.89	8.9

Table 2 Fundamental natural frequencies of a glass fiber laminated shell having straight edges simply supported (only θ_y is free) and curved edges free with varying cut-out sizes

Cut-out (%) (X-direction)	Cut-out (%) (Y-direction)	Fundamental natural frequency		Deviation percentage (ANSYS-experiment)/experiment
		Experimental frequency [11] (Hz)	Frequency using ANSYS (Hz)	
0.2a	0.2b	271.58	280.98	3.46
0.4a	0.4b	255.34	267.14	4.62
0.2a	0.4b	272.29	279.54	2.66

Table 3 Non-dimensional fundamental frequency $\omega a^2/h\sqrt{(\rho/E_2)}$ for a cross-ply $(0°/90°)_4$ laminated cylindrical shell ($h/R_x = 1/300$, $R_x = R$, $a = b$, $a/h = 100$)

Cut-out (%) (Y-direction)	Cut-out (%) (Y-direction)	Fundamental natural frequency		Deviation percentage (ANSYS-theory)/theory (%)
		Frequency using ANSYS (Hz)	Chakravorty et al. [2]	
0.1a	0.1b	27.138	27.042	0.355
0.3a	0.3b	28.161	27.913	0.888
0.5a	0.5b	29.858	29.472	1.309

Example 2. A laminated cylindrical shell having a thickness ratio, a/h = 100, with a cut-out at the center with simply supported boundary condition has been investigated here. The material properties are taken as $E_1 = 25E_2$, $G_{12} = G_{13} = 0.5E_2$, $G_{23} = 0.2E_2$, $\gamma_{12} = 0.25$ (Chakravorty et al. [2]). The vibration results in terms of fundamental frequencies calculated using the present model are shown in Table 3. The results show good agreement with those results published by Chakravorty et al. [2]. Furthermore, we can observe that the fundamental frequency increases with the increase of cut-out size due to the reduction of mass.

4 Parametric Study

Several parametric studies have been presented in this section to check the effect of curvature, thickness ratio, lamination scheme, and boundary condition on non-dimensional frequency with varying cut-out percentage of the shell. The material properties used for the entire parametric study presented in Tables 4, 5, 6 and 7 are as follows: $E_1 = 25E_2$, $G_{12} = G_{13} = 0.5E_2$, $G_{23} = 0.2E_2$, $\gamma_{12} = 0.25$ and the cut-out percentage varies from 0 to 0.6. The effects of curvature, thickness ratio, and boundary condition have been studied for the symmetric lamination scheme

Table 4 Effect of curvature on the non-dimensional frequency of cross-ply symmetric lamination schemes $(0°/90°)_{2\,s}$ and (a/b = 1 and a/h = 100) shells with varying cut-out percentages

R/a	Cut-out ratio	Mode 1	Mode 2	Mode 3	Mode 4	Mode 5
0.5	0	10.044	21.312	22.067	36.36	40.812
	0.2	10.018	21.5	22.09	36.088	39.657
	0.4	9.9147	21.963	23.191	31.034	38.633
	0.6	10.222	16.542	20.213	21.949	38.223
1	0	30.27	53.564	54.794	56.517	84.129
	0.2	29.546	49.237	55.767	56.522	82.501
	0.4	28.024	35.168	48.349	56.613	61.356
	0.6	32.567	33.35	48.564	53.629	55.385
1.5	0	32.7	45.342	56.927	58.764	72.227
	0.2	31.706	43.152	57.94	58.666	70.707
	0.4	29.953	35.792	47.628	57.649	58.966
	0.6	34.954	35.918	52.322	55.936	57.399
2	0	33.42	41.83	55.293	57.075	62.605
	0.2	32.469	40.395	56.526	57.167	60.851
	0.4	30.963	36.059	47.178	52.483	57.559
	0.6	35.63	36.7	53.352	56.273	56.51

$(0°/90°)_{2\,s}$. Figure 1 shows a schematic view of the shell with a cut-out at the center and coordinate system (Fig. 2, 3, 4 and 5). Figures 6, 7, 8, 9 and 10 show the mode shapes with square and rectangular cut-outs.

4.1 Curvature Effect

The curvature effect on the fundamental frequencies of cylindrical laminated shells is studied with simply supported boundary conditions (straight edges simply supported and curved edges are free) with (a/b = 1, a/h = 100) and presented in Table 4 as well as Fig. 2. The value of R/a is varied from 0.5 to 2. For cylindrical laminated shells with R/a = 1, 1.5, and 2, the value of non-dimensional frequency initially starts decreasing with an increase in the cut-out percentage and gets reversed after reaching the cut-out percent of 0.4. The cylindrical shells with R/a = 0.5 have no significant change in the non-dimensional frequency as the cut-out percent increases. It can be observed that for the same cut-out percentage, the non-dimensional frequency value increases with an increase value of R/a. The increase is generally due to the reduction of curvature of the shell which will result in the increase of vibration of the shell.

Table 5 Effect of a/h on the non-dimensional natural frequency of cross-ply symmetric lamination schemes $(0°/90°)_{2\,s}$ and (a/b = 1, and R/a = 0.5) shells with varying cut-out percentage

a/h ratio	Cut-out ratio	Mode 1	Mode 2	Mode 3	Mode 4	Mode 5
a/h = 5	0	74.184	106.2	133.44	134.32	182.73
	0.2	74.032	109	131.9	136.38	183.63
	0.4	75.363	112.74	113.53	138.51	180.47
	0.6	82.974	93.407	115.19	125.21	140.22
a/h = 10	0	61.777	96.704	115.26	121.33	169.66
	0.2	61.461	98.597	116.07	119.63	171.59
	0.4	61.393	99.16	102.28	119.7	165.11
	0.6	66.221	78.021	103.93	105.24	126.46
a/h = 25	0	35.39	66.971	73.028	93.501	128.09
	0.2	35.136	67.608	72.973	92.016	123.33
	0.4	34.395	69.268	70.701	75.876	119.32
	0.6	36.015	47.346	64.017	69.621	91.272
a/h = 50	0	19.4	39.86	41.938	64.284	76.41
	0.2	19.301	40.17	41.876	63.533	73.804
	0.4	18.933	41.049	43.774	49.366	71.679
	0.6	19.581	28.501	37.183	40.919	63.532
a/h = 100	0	10.044	21.312	22.067	36.36	40.812
	0.2	10.018	21.5	22.09	36.088	39.657
	0.4	9.9147	21.963	23.191	31.034	38.633
	0.6	10.222	16.542	20.213	21.949	38.223

4.2 Effect of Thickness Ratio

The effect of the a/h ratio on natural frequency is observed for the cylindrical shell (a/b = 1, R/a = 0.5) and shown in Table 5 as well as in Fig. 3. The support condition used for the study is straight edges simply supported and curved edges are free. The results are obtained with different a/h ratios and different cut-out percentages. The a/h ratio varies from 5 to 100, and it can be observed that the value of the non-dimensional frequency increases with a decrease in a/h value. This is because of the phenomenon that as a/h ratio increases the thickness of the panel decreases and the frequency value decreases for a thin structural element. It is observed from Fig. 2, that with the increase of cut-out percent above 0.4 the non-dimensional fundamental natural frequency is subjected to a significant increase for a/h ratio 5 and 10 of the cylindrical shells when compared with the a/h ratios (25, 50, and 100).

Table 6 The effect of lamination schemes on the non-dimensional natural frequency on cylindrical shells (a/b = 1, a/h = 100 and R/a = 0.5) with varying cut-out percentages

Lamination schemes	Cut-out ratio	Orientations	Mode 1	Mode 2	Mode 3	Mode 4	Mode 5
Symmetric	0.2	0°/90°/90°/0°	8.8157	19.582	19.837	33.312	35.61
		30°/−30°/−30°/30°	7.3722	16.54	17.733	29.209	30.166
		45°/−45°/−45°/45°	8.01	16.973	18.244	28.93	31.729
	0.4	0°/90°/90°/0°	8.8808	20.204	20.931	29.572	34.975
		30°/−30°/−30°/30°	7.4081	17.153	18.062	26.433	29.35
		45°/−45°/−45°/45°	7.8077	17.311	18.398	25.197	30.115
	0.6	0°/90°/90°/0°	9.1409	15.788	18.477	20.121	35.861
		30°/−30°/−30°/30°	7.4861	14.946	15.985	17.965	29.57
		45°/−45°/−45°/45°	7.7429	14.208	15.782	17.752	28.738
Anti-symmetric	0.2	0°/90°/0°/90°	9.8106	20.711	21.447	34.418	38.361
		30°/−30°/30°/−30°	8.3396	18.855	20.03	33.253	33.733
		45°/−45°/45°/−45°	9.0472	19.632	19.784	32.485	35.13
	0.4	0°/90°/0°/90°	9.6242	21.082	22.417	29.1	37.375
		30°/−30°/30°/−30°	8.3446	19.493	20.418	29.81	33.04
		45°/−45°/45°/−45°	8.7424	19.792	20.203	28.01	33.823
	0.6	0°/90°/0°/90°	9.9546	15.624	19.533	21.156	36.271
		30°/−30°/30°/−30°	8.4417	16.78	18.015	20.308	33.432
		45°/−45°/45°/−45°	8.771	15.64	17.682	19.471	32.596

4.3 Effect of Lamination Scheme

The lamination scheme effects on the non-dimensional frequency are observed for cylindrical shells (a/b = 1, a/h = 100, R/a = 0.5) with support condition straight edges simply supported and curved edges are free used for the study are shown in Table 6 as well as Fig. 4**.** The lamination schemes used are symmetric [(0°/90°/90°/0°), (30°/−30°/−30°/30°) and (45°/−45°/−45°/45°)] and anti-symmetric [(0°/90°/0°/90°), (30°/−30°/30°/−30°) and (45°/−45°/45°/−45°)], respectively. It can be seen that the anti-symmetric laminates are having higher frequencies when compared with symmetric laminates. It also shows that the (0°/90°/0°/90°) laminate have higher non-dimensional frequencies when compared with the other schemes. For cylindrical angle-ply [(45°/−45°/−45°/−45°), (45°/−45°/45°/−45°)] shells, the non-dimensional natural frequency decreases with increase in cut-out size, whereas it is reverse trends for cross-ply [(0°/90°/90°/0°), (0°/90°/90°/0°)] schemes of cylindrical shells. The increase is less significant for the angle-ply ply [(30°/−30°/−30°/30°), (30°/−30°/30°/−30°)] symmetric and anti-symmetric laminated shells.

Table 7 Effect of support conditions on the non-dimensional frequency of cross-ply symmetric lamination schemes $(0°/90°)_{2\,s}$ and (a/b = 1, a/h = 100, and R/a = 2) shells with varying cut-out percentages

Boundary condition	Cut-out ratio	Mode 1	Mode 2	Mode 3	Mode 4	Mode 5
CCCC	0	49.038	63.601	76.24	79.695	97.278
	0.2	46.568	66.249	68.497	77.701	79.789
	0.4	41.031	48.867	61.935	76.923	78.055
	0.6	54.466	56.268	76.041	79.356	89.854
SSSS	0	48.093	63.235	73.782	78.827	97.004
	0.2	45.741	65.639	66.514	77.007	79.658
	0.4	40.559	48.82	59.725	75.93	77.153
	0.6	54.236	56.035	72.683	77.888	83.438
CFCF	0	33.438	41.843	55.309	57.089	62.612
	0.2	32.485	40.409	56.543	57.181	60.856
	0.4	30.98	36.076	47.191	52.492	57.574
	0.6	35.649	36.72	53.391	56.315	56.527
SFSF	0	33.42	41.83	55.293	57.075	62.605
	0.2	32.469	40.395	56.526	57.167	60.851
	0.4	30.963	36.059	47.178	52.483	57.559
	0.6	35.63	36.7	53.352	56.273	56.51

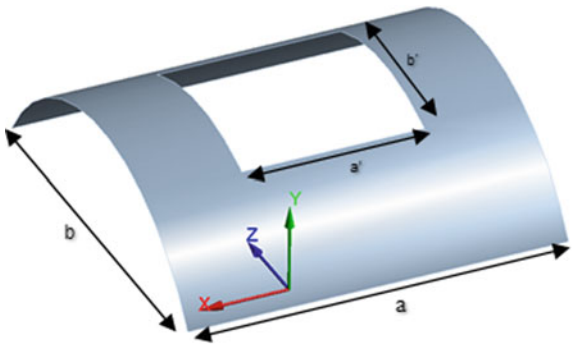

Fig. 1 Schematic view of the shell along with the cutout and coordinate system

4.4 Effect of Support Conditions

The effect of support conditions on the non-dimensional frequencies of cylindrical shells are studied for cross-ply lamination with (a/b = 1, a/h = 100, and R/a = 2) and with varying boundary conditions and different cut-out sizes are shown in Table 7 as well as Fig. 5. The support conditions used for the study are CCCC, SSSS, CFCF, and SFSF, respectively. The non-dimensional frequency of the CCCC composite laminated composite shell is highest for its highest stiffness, and SFSF

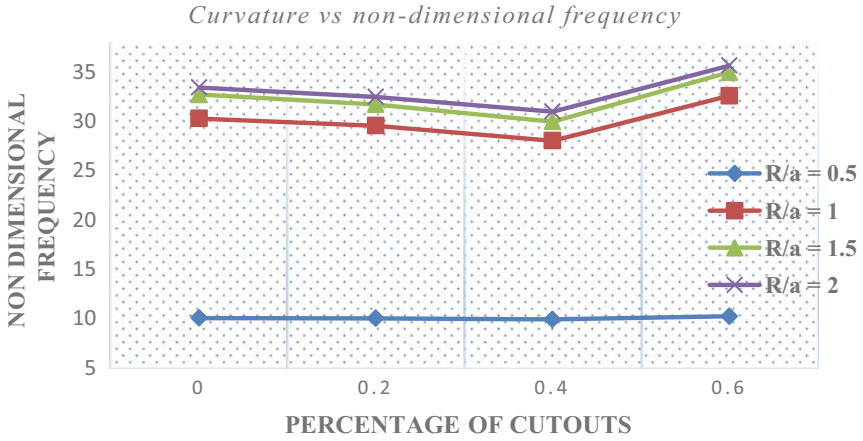

Fig. 2 Curvature effect on the non-dimensional frequency of cross-ply symmetric lamination schemes $(0°/90°)_{2\,s}$ and (a/b = 1 and a/h = 100) shells with varying cut-out percentages

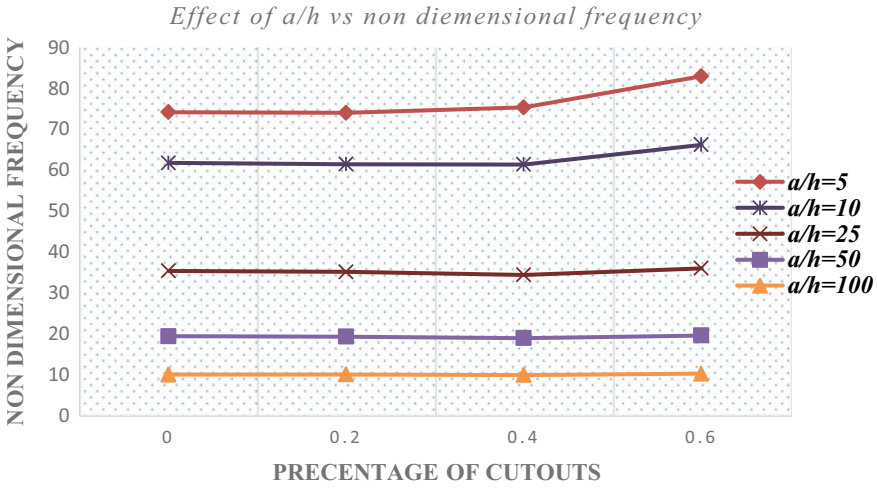

Fig. 3 Effect of a/h on the non-dimensional frequency of cross-ply symmetric lamination schemes $(0°/90°)_{2\,s}$ and (a/b = 1, and R/a = 0.5) shells with varying cut-out percentage

is the lowest. The CFCF and SFSF boundary conditions have almost the same non-dimensional frequency with varying cut-out percentages. It can be noticed that the fundamental natural frequency starts decreasing for all the boundary conditions until the percentage of cut-out reaches 0.4 and then starts increasing. This is due to the effect of mass and stiffness reduction due to cut-outs. For the cut-out percentage of 0.6, the value of natural frequency is highest.

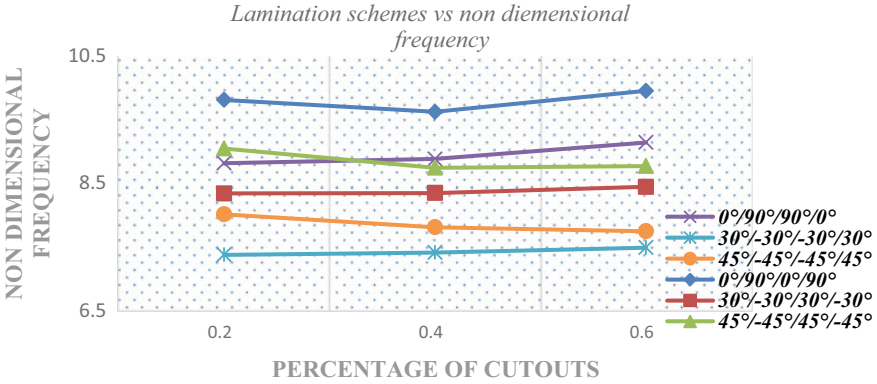

Fig. 4 The effect of lamination schemes on the non-dimensional natural frequency on cylindrical shells (a/b = 1, a/h = 100, and R/a = 0.5) with varying cut-out percentages

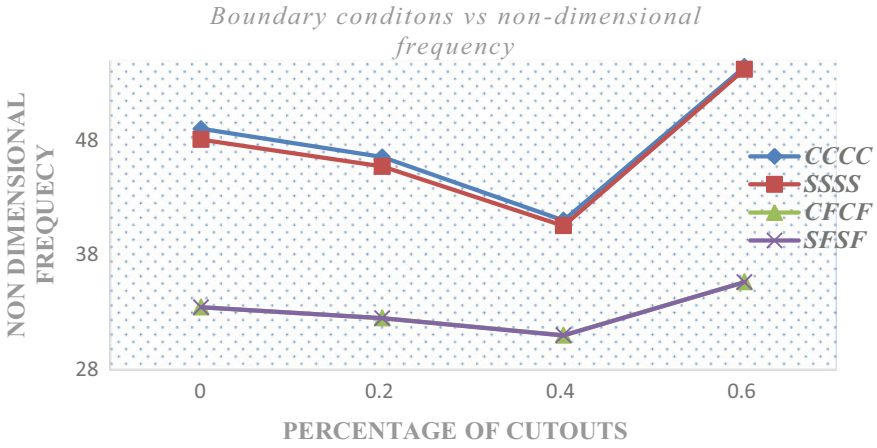

Fig. 5 Effect of support conditions on the non-dimensional frequency of cross-ply symmetric lamination schemes $(0°/90°)_{2\,s}$ and (a/b = 1, a/h = 100, and R/a = 2) shells with varying cut-out percentage

4.5 Mode Shapes

The first three mode shapes of the laminated shell with varying cutouts are obtained by using ANSYS software. Mode shapes with square cutouts (with 0.2, 0.4, and 0.6 cut-out ratios) are shown in Figs. 6, 7 and 8 and rectangular cut-outs are shown in Figs. 9 and 10. Through those figures of mode shapes, the vibration behavior of the laminated shell with cut-out can be more instinctively reflected.

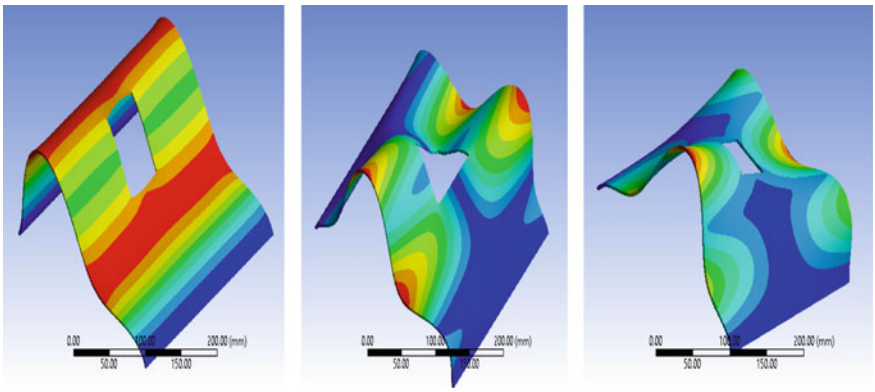

(a) First mode (b) Second Mode (c) Third Mode

Fig. 6 Theoretical mode shape for bidirectional cylindrical shell having straight edges simply supported and curved edges free with 0.2 cut-out ratio

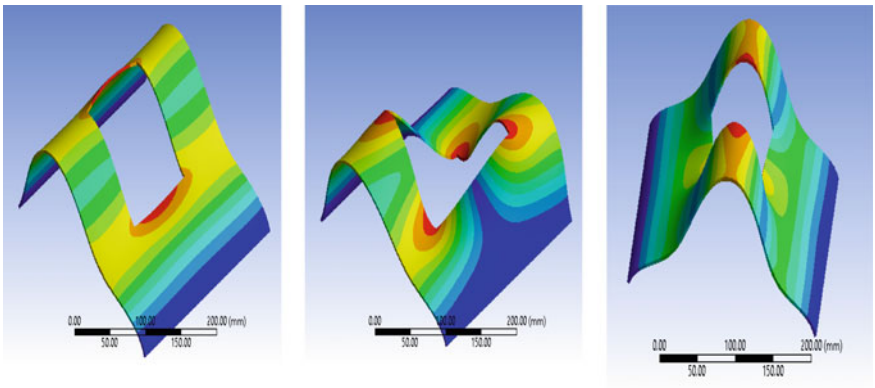

(a) First mode (b) Second Mode (c) Third Mode

Fig. 7 Theoretical mode shape for bidirectional cylindrical shell having straight edges simply supported and curved edges free with 0.4 cut-out ratio

5 Conclusions

The free vibration analysis of laminated composite shells with varying cut-outs is investigated in the present study. The bi-directional cross-ply symmetric glass fiber shells are taken for analysis. The numerical study has been performed using the finite element based software package ANSYS 16.0 using a triangular element with six DOFs per node. The comparison of numerical results with the literature shows very good agreement. A parametric study that includes the effects of the thickness ratio, curvature ratio, lamination schemes, and various support conditions on the non-dimensional natural frequency of cylindrical laminated shells with varying cut-out

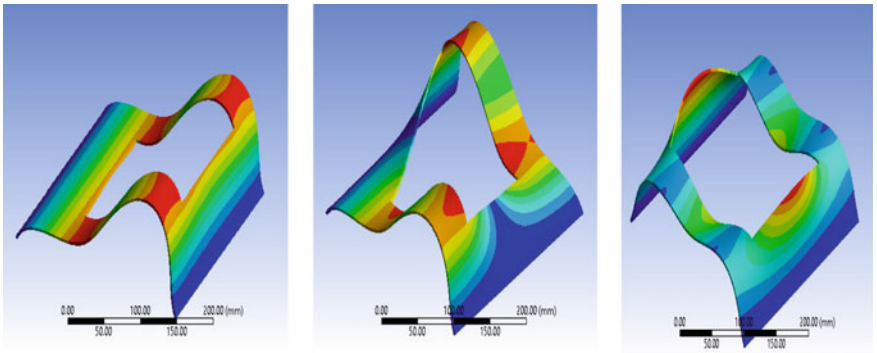

(a) First mode (b) Second Mode (c) Third Mode

Fig. 8 Theoretical mode shape for bidirectional cylindrical shell having straight edges simply supported and curved edges free with 0.6 cut-out ratio

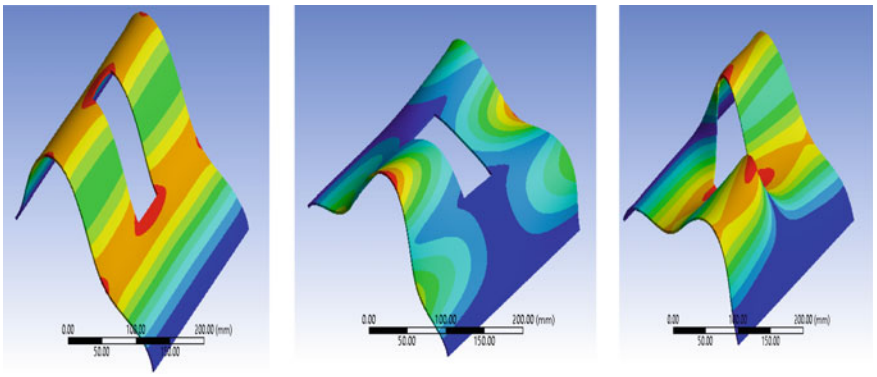

(a) First mode (b) Second Mode (c) Third Mode

Fig. 9 Theoretical mode shape for bidirectional cylindrical shell having straight edges simply supported and curved edges free with 0.2a × 0.4b cut-out ratio

percentages at the center is examined and can be treated as benchmark results for further research works.

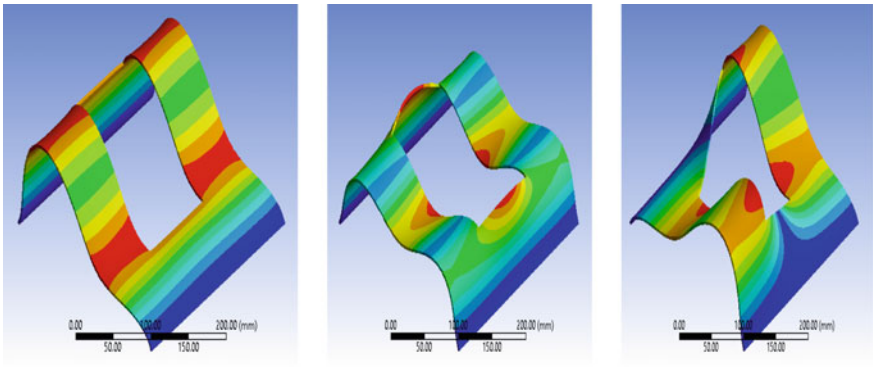

(a) First mode (b) Second Mode (c) Third Mode

Fig. 10 Theoretical mode shape for bidirectional cylindrical shell having straight edges simply supported and curved edges free with 0.4a × 0.6b cut-out ratio

References

1. Reddy JN, Liu CF (1985) A higher order shear deformation theory of laminated elastic shells. Int J Eng Sci 23(3):319–330
2. Chakravorty D, Sinha PK, Bandyopadhyay JN (1998) Applications of FEM on free and forced vibration of laminated shells. J Eng Mech 124:1–8
3. Hota SS, Chakravorty D (2007) Free vibration of stiffened conoidal shell roofs with cutouts. J Vib Control 13(3):221–240
4. Nanda N, Bandyopadhyay JN (2007) Nonlinear free vibration analysis of laminated composite cylindrical shells with cutouts. J Reinf Plast Compos 26:1413–1427
5. Poore AL, Barut A, Madenci E (2008) Free vibration of laminated cylindrical shells with a circular cutout. J Sound Vib 312(1–2):55–73
6. Malekzadeh P, Bahranifard F, Ziaee S (2013) Three-dimensional free vibration analysis of functionally graded cylindrical panels with cut-out using Chebyshev–Ritz method. Compos Struct 105:1–13
7. Hu HT, Peng HW (2013) Maximization of fundamental frequency of axially compressed laminated curved panels with cutouts. Compos Part B Eng 47:8–25
8. Biswas D, Ray C (2015) Comparative perspective of various shear deformation theories with experimental verification of hybrid laminates. J Vib Control 23:1321–1333
9. Mandal A, Ray C, Haldar S (2017) Free vibration analysis of laminated composite skew plates with cutout. Arch Appl Mech 87(9):1511–1523
10. Chaubey AK, Kumar A (2018) Vibration of laminated composite shells with cutouts and concentrated mass. AIAA J 56(4):1662–1678
11. Mandal A, Ray C, Haldar S (2019) Experimental and numerical modal analysis of composite laminated shells with cut-out. Intl J Maritime Eng 161:A1–A12

Numerical Study on Concrete-Filled Steel Tubes with Diagonal Binding Ribs and Longitudinal Stiffeners

Aiswarya M. Heman and K. G. Roshni

1 Introduction

Concrete-filled steel tubular (CFST) columns have high strength, superior seismic performance, and reasonable construction cost [4]. These are widely used as one of the main structural elements for resisting both vertical and lateral loads in high-rise buildings and bridges [5]. It consists of an outer thin steel tube and inner infilled concrete. If thin steel tubes are adopted, welding and construction will be easy. Also, steel plates tend to be slenderer when adopting high-strength steel. But the materials cannot be fully used. And the ductility is poor when high-strength concrete is used due to local buckling and also the increase in the deformation of the steel tube by the concreting is not negligible. Stiffened CFST have continuous strong confinement from the ribs or stiffeners to both concrete and steel tubes. This can relax the width-to-thickness ratio limit [6] and thus can facilitate the use of thin-walled and high-strength steel and concrete. Openings can act as shear connectors and can avoid the disengagement at interfaces between the concrete and the steel tube. It helps while pouring concrete. The ribs with square openings had larger strength but worse ductility than those with circular openings. Square and rectangular CFST columns [7] have easy beam-to-column connections hence lead to less construction cost. It helps to make flexible building layouts hence facilitate decoration, the layout of architectural space, and fireproof plates. Only a few numerical studies are available related to diagonal rib stiffened CFST columns. So, this paper presents the numerical

A. M. Heman (✉)
Thejus Engineering College, Manaladi House, Vadakkethara, Pazhayannur (P O), Thrissur, Kerala 680587, India

K. G. Roshni
Thejus Engineering College, Koottungal House, Kunnamkulam (P O), Vyssery, Thrissur, Kerala 680503, India
e-mail: roshnikg@thejusengg.com

D. K. Maiti et al. (eds.), *Recent Advances in Computational and Experimental Mechanics, Vol II*, Lecture Notes in Mechanical Engineering,
https://doi.org/10.1007/978-981-16-6490-8_2

study on the effect of ribs and stiffeners on axial load carrying capacity of nineteen various CFST column models and the seismic performance of three unstiffened square CFST columns and two octagonal CFST columns by nonlinear static analysis using ANSYS Workbench 16.2.

2 Numerical Study of Stiffened and Unstiffened CFST Columns Under Axial Load

2.1 General

The model of diagonal binding rib stiffened CFST column was validated with reference to the paper, "Improved composite effect of square concrete-filled steel tubes with diagonal binding ribs," [3].

A square column with 300 mm side and 900 mm height having 2 mm thick outer steel tube and ribs that are placed diagonally across the cross section. There are 60 mm diameter holes in the ribs at 225 mm center to center spacing. A 40 mm size meshing was provided. A multilinear isotropic hardening model was used. The bottom surface of the column was restrained against all degrees of freedom. The top of the column was free and axial load was applied with displacement control along the Y-axis. Due to the symmetry of geometry and loading, only one fourth of the model was established for efficiency. The axial load taken by the column is plotted against the strain and the failure mode (see Fig. 1).

By comparing experimental results and finite element analysis results by means of ultimate load-carrying capacity of the composite column and by means of strain, percentage variation of 1.92 and 3.03% was found. Thus, the model was validated.

The CFST column models used for further analysis are: unstiffened square columns, stiffened square columns with diagonal binding ribs, stiffened square columns with longitudinal stiffeners [8], and unstiffened octagonal columns. Here, a total of nineteen models are used. Here, on the naming of the models, U stands for unstiffened, R stands for rib stiffened, L stands for longitudinally stiffened, S stands for square-shaped cross section, O stands for octagonal-shaped cross section, the first digit indicates the thickness of steel tube, the second digit indicates the thickness of rib or stiffener, H, H1, and H2 indicates hollow opening with particular diameter and spacing between holes, W and W1 indicate square opening with particular spacing between the openings.

The width of stiffener or rib equals 141.42 mm and its height equals 900 mm. 2, 3, and 6 mm thick steel tubes and stiffeners or diagonal ribs were used. Square or circular openings with different spacing were provided on ribs.

A non-linear static analysis on the stiffened and unstiffened CFST columns was done by using the same method used for validation. The concrete, steel tube, and stiffeners or ribs were modeled by SOLID 186. The contact between steel tube and concrete, steel tube and ribs, ribs and concrete were modeled by CONTA 174. The

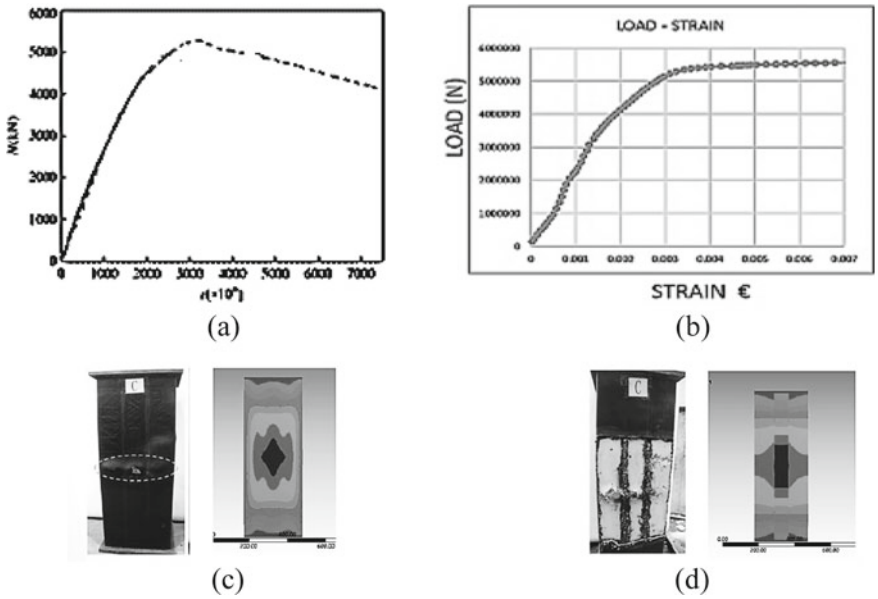

Fig. 1 **a** Load-strain graph from the experimental study [3], **b** load-strain graph from numerical analysis **c** failure mode on steel tube and **d** failure mode on concrete

connection between steel tube and ribs, between steel tube and concrete, between ribs and concrete was provided by using bonded, frictional and frictional, respectively with a frictional coefficient value of 0.2. A nonlinear isotropic hardening model was used. The material properties were as shown in Table 1. The ultimate axial load taken by the columns is plotted against the strain (see Fig. 2) and ultimate load values of different models are as shown in Table 2.

Table 1 Material properties

Type	Yield strength (MPa)	Ultimate strength (MPa)	Modulus of elasticity (GPa)	Poisson's ratio
2 mm steel	170	300	200	0.3
3 mm steel	350	490	195	0.3
6 mm steel	320	480	190	0.3
Concrete	60	–	39	0.15

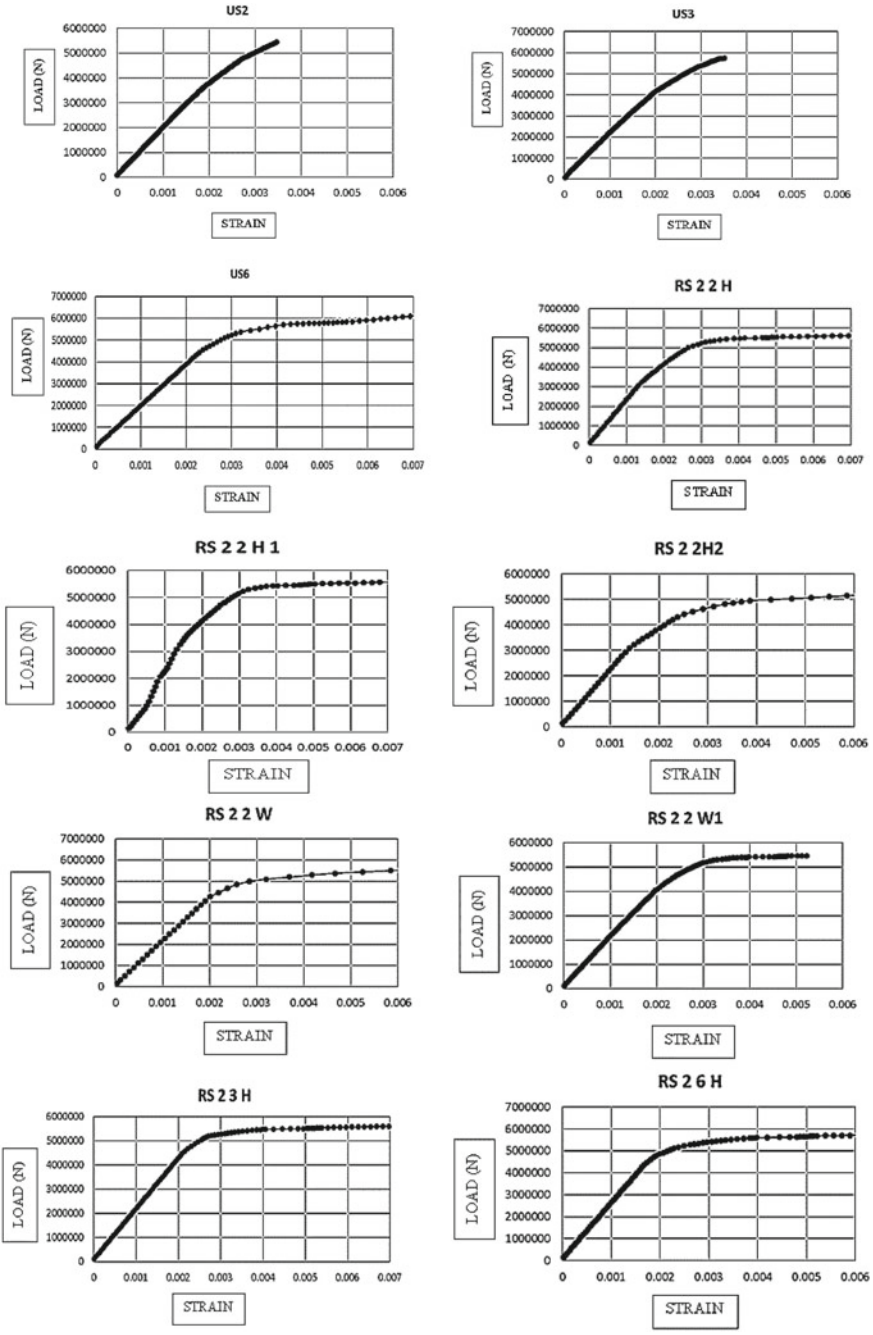

Fig. 2 Load-strain graph of CFST columns under axial load

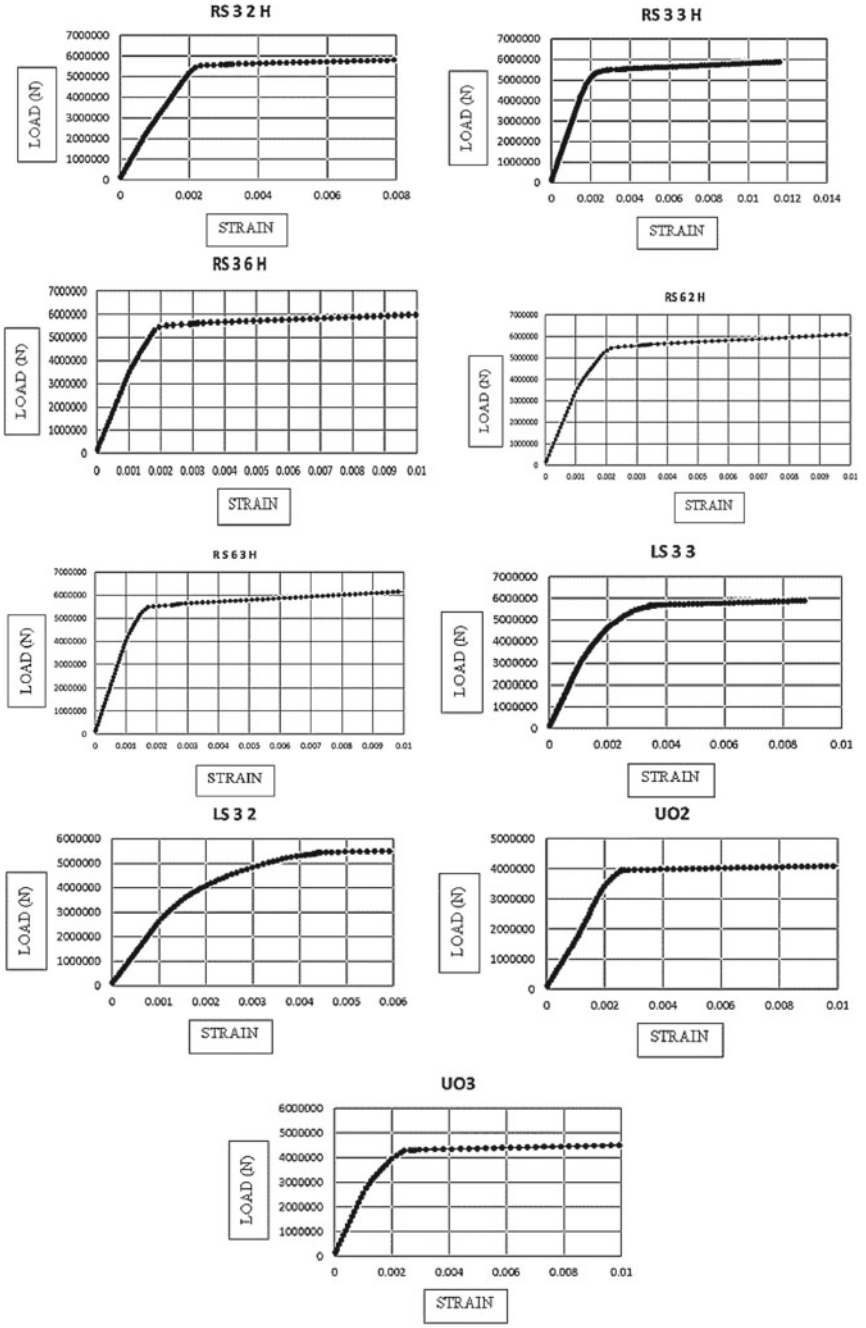

Fig. 2 (continued)

Table 2 Ultimate load values of CFST columns under axial load

Model	Steel tube thickness (t) (mm)	Stiffener thickness (ts) (mm)	Size of hole (d) (mm)	Spacing of hole (s) (mm)	Ultimate load (Nu) (kN)
US2	2				5342
US3	3				5646.4
US6	6				6456
RS22H	2	2	ϕ60	150	5518
RS22H1	2	2	ϕ60	225	5275.2
RS22H2	2	2	ϕ90	150	5182.4
RS22W	2	2	w55	225	5547.6
RS22W1	2	2	w80	150	5462.8
RS23H	2	3	ϕ60	150	5603.6
RS26H	2	6	ϕ60	150	5819.6
RS32H	3	2	ϕ60	150	6150.8
RS33H	3	3	ϕ60	150	6697
RS36H	3	6	ϕ60	150	6798.4
RS62H	6	2	ϕ60	150	7265
RS63H	6	3	ϕ60	150	7562.4
LS32	3	2			5653.6
LS33	3	3			6196.4
UO2	2				4095.7
UO3	3				4513.9

2.2 Results and Discussions

Unstiffened square CFST column with 6 mm-thick steel tube has 20.85% more axial load carrying capacity than that with 2 mm-thick steel tube. Because the increase in thickness of the steel tube helps more strongly to confine the concrete, hence reduce the local buckling and increase the load-carrying capacity. The ultimate strength of diagonal rib stiffened CFST with 6 mm-thick steel tube is 12.53% more than that of an unstiffened square CFST with 6 mm-thick steel tube. Because diagonal ribs effectively hold the concrete in corners of square CFST columns to be confined within the steel tube than the concrete on the middle of the sides of the steel tube. The ultimate strength of longitudinally stiffened square CFST columns with 3 mm-thick steel tube and a stiffener is 9.6% more than longitudinally stiffened square CFST columns with 3 mm-thick steel tube and 2 mm-thick stiffener due to the greater thickness value of the stiffener and a greater number of stiffeners per side. Because greater number and thickness value of the stiffener improves the confinement of the concrete effectively. The ultimate strength of the unstiffened octagonal CFST column with 3 mm-thick steel tube is 10.18% more than that with 2 mm-thick steel

tube due to greater steel thickness. Because if thicker the steel tube more strongly it confines the concrete, hence reduce the local buckling and increase the load-carrying capacity. The ultimate strength of unstiffened square CFST was 30.43% more than that of unstiffened octagonal CFST. Because the area of cross section of square CFST column model used is more than that of octagonal CFST column model used in this study. Diagonal binding rib stiffened CFST column with 6 mm-thick steel tube has 31.66% more axial load carrying capacity than that with 2 mm-thick steel tube. Because if thicker the steel tube it confines the concrete more strongly, hence reduce the local buckling and increase the load-carrying capacity. Diagonal binding rib stiffened CFST column with 6 mm-thick rib has 5.46% more axial load carrying capacity than that with 2 mm-thick rib. Because the increase in the thickness of ribs leads to improvement in the confinement of the concrete due to the high strength offered by the steel. The diagonal rib stiffened CFST with square openings had 5.16% more axial load carrying capacity than that with holes. Because the net cross-sectional steel area of the model with square openings was larger than that of those with circular openings, leading to greater strength. The ultimate strength decreased by 6.47% when increasing opening diameters from 0.4 to 0.6 times the diagonal rib width. Because, the net area of the rib available to effectively confine the concrete will be reduced, hence ultimate load-carrying capacity of the column will decrease. The ultimate strength decreased by 4.4% when the opening spacing is increased from 2.5 to 3.8 times the opening diameter. Because when increasing the spacing of openings on ribs, the number of openings or shear connectors decreases.

3 Behavior Under Lateral Cyclic Load

3.1 General

Concrete-filled steel tubular columns have become the preferred form for many seismic-resistant structures. Here, a total of 5 unstiffened models of CFST columns with different shapes and steel tube thickness were taken and were subjected to lateral cyclic loading based on codes such as FEMA or ATC protocol. After that, a hysteresis loop is drawn in order to find out the energy dissipated by the structure.

Cyclic loading is conducted by applying repeated cycles of loading on the lateral direction such as it resembles an actual earthquake. Here, the base of the column is fixed, i.e., displacement in X, Y, and Z directions are constrained and the top end is set free (displacement in Y and Z direction are constrained). The cyclic loading is given as displacement controlled. The displacement is given in alternating negative and positive cycles according to the FEMA protocol. From the ANSYS analysis, the hysteresis loop is drawn by plotting load on the Y-axis and the corresponding deformation on the X-axis. All the columns are tested with the loading of 23 cycles and a 1.2% drift ratio.

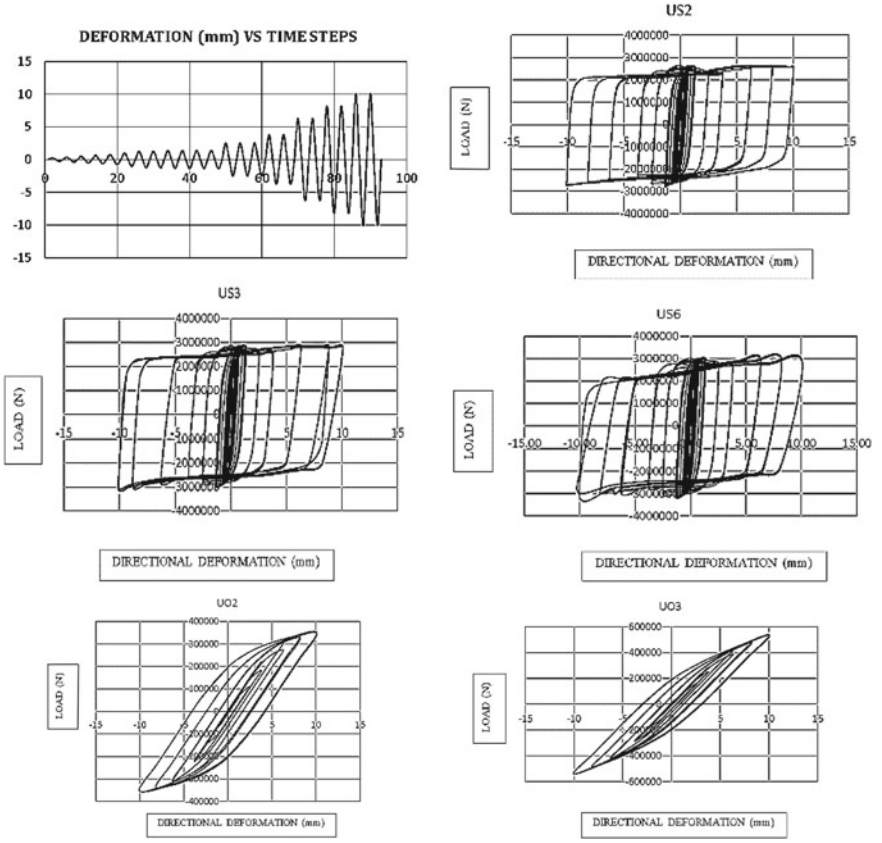

Fig. 3 Cyclic loading pattern and hysteresis loops of unstiffened square and octagonal CFST columns under lateral cyclic load

By using the load and deformation values obtained from ANSYS, the hysteresis loop [9] is drawn by plotting load on the Y-axis and the corresponding deformation on the X-axis. The loading pattern and hysteresis loops (see Fig. 3).

Total energy dissipated from the column is equal to the cumulative area enclosed by the loops in load-deformation hysteresis. It is calculated by using the software OriginPro 2020b version using the mathematical tool polygon area, which is shown in Table 3.

3.2 Results and Discussions

Unstiffened square CFST column with 6 mm-thick steel tube dissipates more seismic energy than unstiffened square CFST column with 3 mm- and 2 mm-thick steel tube

Table 3 Energy dissipation of unstiffened square and octagonal CFST columns under lateral cyclic load

Model	Thickness of steel tube (t) (mm)	Energy dissipation (kN m)
US6	6	580.32
US3	3	560.96
US2	2	557.05
UO3	3	497.74
U02	2	496.28

by 3.45% and 4.17%, respectively. Hence seismic performance improves with an increase in thickness of steel tube because confinement of the concrete by the steel tube will be more effective.

Unstiffened square CFST column with 3 mm- and 2 mm-thick steel tube dissipates more seismic energy than unstiffened octagonal CFST column with 3 mm and 2 mm-thick steel tube by 12.24% and 12.7%, respectively. Hence, unstiffened square CFST column has better seismic performance because more concrete and steel are available in the square column used in this study than in the octagonal column which makes it stronger to resist the seismic load.

Unstiffened square CFST column with 6 mm-thick steel tube, dissipated maximum amount of energy, indicates it is stronger to resist the seismic load. Because of its square shape and greater thickness of steel tube makes the concrete effectively confine within the steel tube.

4 Conclusions

From the study of various CFST column models under axial load, the diagonal rib stiffened column with thicker steel tube, thicker ribs with closely spaced square openings in it, is strong against axial load. Because, apart from thicker steel tube and ribs, triangular concrete prisms formed, due to four diagonal ribs with closely spaced openings which act as shear connectors, effectively confined at the corners by the steel tube and ribs.

From the study of various CFST column models under lateral cyclic load, unstiffened square CFST column with thicker steel tube, the dissipated maximum amount of energy, indicates it is stronger to resist the seismic load. Because of its square shape and greater thickness of steel tube makes the concrete effectively confine within the steel tube.

Acknowledgements I am especially grateful to our M. Tech coordinator Mrs. Geetha P. R., Assistant Professor, Department of Civil Engineering, Thejus Engineering College, for her great support, valuable suggestions, and guidance in completing this work. I am deeply indebted and gratefully

acknowledge the constant support and valuable patronage of my guide Mrs. Roshni. K. G., Assistant Professor, Department of Civil Engineering, Thejus Engineering College. I extend my heartfelt thanks to my family for their funding and sincere cooperation and to my friends for their encouragement.

References

1. Lee KC, Yoo CH (2012) Longitudinal stiffeners in concrete-filled tubes. J Struct Eng 138:753–758. https://doi.org/10.1061/(ASCE)ST.1943-541X.0000526
2. Dong H, Li Y, Cao W, Qiao Q, Li R (2018) Uniaxial compression performance of rectangular CFST columns with different internal construction characteristics. Eng Struct 176:763–775. https://doi.org/10.1016/j.engstruct.2018.09.051
3. Zhou Z, Gan D, Zhou X (2019) Improved composite effect of square concrete-filled steel tubes with diagonal binding ribs. J Struct Eng 145:1–12. https://doi.org/10.1061/(ASCE)ST.1943-541X.0002400
4. Kitada T (1998) Ultimate strength and ductility of state-of-the-art concrete-filled steel bridge piers in Japan. Eng Struct 20:347–354. https://doi.org/10.1016/S0141-0296(97)00026-6
5. Han L-H, Li W, Bjorhovde R (2014) Developments and advanced applications of concrete-filled steel tubular (CFST) structures: members. J Constr Steel Res 100:211–228. https://doi.org/10.1016/j.jcsr.2014.04.016
6. Evirgen B, Tuncan A, Taskin K (2014) Structural behavior of concrete filled steel tubular sections (CFT/CFSt) under axial compression. Thin Walled Struct 80:46–56. https://doi.org/10.1016/j.tws.2014.02.022
7. Ibanez C, Hernandez-Figueirido D, Piquer A (2018) Shape effect on axially loaded high strength CFST stub columns. J Constr Steel Res 147:247–256. https://doi.org/10.1016/j.jcsr.2018.04.005
8. Ge H, Usami T (1992) Strength of concrete-filled thin-walled steel box columns: experiment. J Struct Eng 118:3036–3054. https://doi.org/10.1061/(ASCE)0733-9445(1992)118:11(3036)
9. Wang Y-T, Cai J, Long Y-L (2017) Hysteretic behavior of square CFT columns with binding bars. J Constr Steel Res 131:162–175. https://doi.org/10.1016/j.jcsr.2017.01.001

Design of Graded Elastomeric Cellular Structures for Enhancing Energy Absorption

Gajendra K. Joshi and Anshul Faye

1 Introduction

Tremendous advances in manufacturing technologies (such as 3D printing) in the past few decades have opened limitless opportunities for designing artificial cellular materials. Cellular materials offer unique properties such as lightweight, high-energy absorption capabilities, and the ability to control the propagation of waves.

Cellular solids like polymeric, metallic foams, and honeycombs have been explored comprehensively and utilized for mechanical energy absorption during impact loading. The compaction of cells in these materials contributes to the desired capability. However, these materials are permanently deformed after compaction and cannot be reused. Adaptive design of an elastomeric cellular solid made of soft material opens an avenue to absorb mechanical energy and shielding the body or structures as they undergo large deformation at almost constant stress, once localization takes place. Cellular structures made of soft materials offer an additional advantage as they can retrieve their original shapes despite large deformations. Mullin et al. [1] observed that 2-D periodic elastomeric structures show a dramatic transformation of the original geometry because of the mechanical instability (buckling). For e.g. an elastomeric structure having circular holes arranged in a square array suddenly transforms into a periodic pattern of alternating, mutually orthogonal ellipses under uniaxial compression and they recover to their original shape after experiencing large deformations. They proposed that the mechanism will also be applicable for structures with a much smaller length scale. The same was demonstrated experimentally by Zhang et al. [2] for patterns with sub-100 nm features on an elastomeric

G. K. Joshi · A. Faye (✉)
Department of Mechanical Engineering, Indian Institute of Technology, Bhilai, India
e-mail: afaye@iitbhilai.ac.in

G. K. Joshi
e-mail: gajendraj@iitbhilai.ac.in

D. K. Maiti et al. (eds.), *Recent Advances in Computational and Experimental Mechanics, Vol II*, Lecture Notes in Mechanical Engineering,
https://doi.org/10.1007/978-981-16-6490-8_3

film. These results attracted considerable attention, and after Bertoldi et al. [3], soft porous materials have been studied rigorously for their applications to Auxetic materials by different groups of researchers [4–9]. The strong effect of topological changes in these materials on the wave directionality, directed another application of these materials in designing tunable phononic materials [10–13].

The instabilities in soft porous solid can be exploited to design reusable energy absorbing material [14]. Mostly, cellular materials made of metals, polymers, and ceramics have been investigated for efficient dissipation of mechanical energy, where plastic deformation, viscous effects, and fragmentation, respectively, are the mechanism of energy dissipation [15–27]. These systems have issues with either reusability or rate dependency. Architectured cellular material with a specific design pattern can undergo significant compaction because of microscopic buckling. Soft cellular structures have been primarily tested, and their energy-absorbing capability under quasi-static loading has been demonstrated successfully [1, 4, 28]. Cellular materials made of metals, polymers, and ceramics are very efficient under impact conditions [26, 27, 29, 30]. However, a similar characterization of soft polymeric materials is scarce in the literature. Utilization of these materials as energy-absorbing devices under impact loading and their characterization at high-strain rates obligate a better understanding of material behavior. Our objective is to investigate the mechanics of deformation and energy absorption in soft-porous materials under high strain-rate loading. We also explore the effects of the gradation of pore density on the compaction and the energy absorption behavior of the material.

2 Methodology

In the present study, numerical modeling was carried out with commercial finite element software ABAQUS/EXPLICIT. To investigate the deformation behavior, the effect of the gradation of pore density on the compaction behavior, and the energy absorption mechanism in soft porous materials under high strain rate, the following methodology was adopted: (a) dynamic simulation of elastomeric cellular structures with homogeneous porosity, (b) dynamic simulation of elastomeric cellular structures with non-homogeneous porosity, and (c) identification of buckling patterns for cellular structures with homogeneous and non-homogeneous porosity.

3 Description of Structure for Computational Analysis

The cellular structures are divided into two categories depending on their pore density and/or pore shape. These are: (a) cell of a circular hole with homogeneous porosity and (b) cell of a circular hole with non-homogeneous porosity. Non-homogeneous porosities are obtained by gradually varying the pore density and/or pore shape. Each structure comprises a microstructure of 11×11 square arrays of circular holes. To

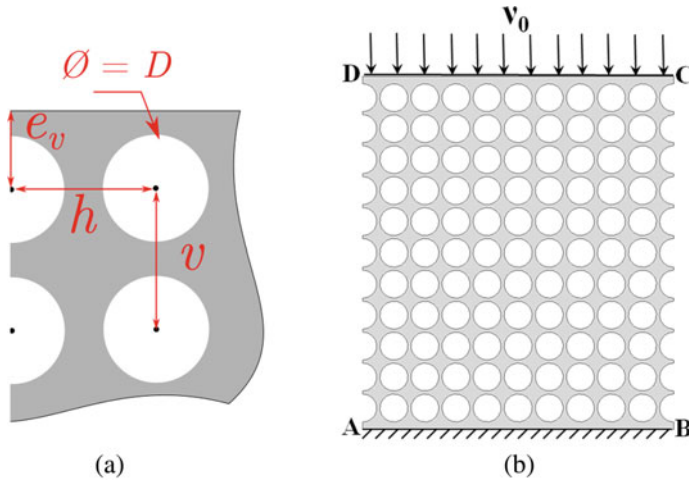

Fig. 1 **a** Parameters defining the configuration of cellular structure. **b** Loading of structure

Table 1 Parameters representing the structures consist of a cell of circular holes with homogeneous porosity

Configuration	D	h	v	e_v	Porosity (%)
1	7.8	8.6	8.6	6	≈62

avoid the effects of boundaries, the RVEs near the side walls were cut in half. The configuration of holes is shown in Fig. 1 with parameters defining the arrangements of holes. D denotes the diameter of the hole. h and v are horizontal, and vertical center to center distance between holes, and e_v indicate the distance between the edge of the specimen and the center of the lateral holes. The porosity is the ratio of the area (or volume) of holes to the overall area (or volume) of the structure. The details of the configurations are listed in Tables 1 and 2.

4 Finite Element Modeling

Numerical simulation was performed using the non-linear finite element software ABAQUS/Explicit. Six-nodded, plain strain, quadratic, triangular elements (CPE6M) were used. A sufficiently refined mesh is used.

Table 2 Parameters representing the structures consist of a cell of circular holes with non-homogeneous porosity

Configuration	Row	D	h	v	e_v	Porosity (%)	Overall porosity (%)
2	1–5	7.6	8.6	8.6	6	≈58	≈62
	6–11	8.0	8.6	8.6	6	≈66	
3	1–3	7.6	8.6	8.6	6	≈56	≈62
	4–7	7.8	8.6	8.6	6	≈64	
	8–11	8.0	8.6	8.6	6	≈66	
4	1–3	7.6	8.6	8.6	6	≈56	≈62
	4–6	7.8	8.6	8.6	6	≈64	
	7–9	8.0	8.6	8.6	6	≈66	
	10–11	8.2	8.6	8.6	6	≈68	

4.1 Material Behavior

The material is modeled as nearly incompressible Neo-Hookean hyperelastic material. The strain energy per unit of reference volume is $U = C_{10}(I_1 - 3) + 1/D_1(J - 1)$, with the initial shear modulus (μ) of 0.33 kPa and bulk modulus (K) of 555 kPa, where $C_{10} = \mu/2$ and $D_1 = 2/K$. Here, I_1 is the first invariant of right Cauchy–Green deformation tensor $\boldsymbol{C}$ and $J = \det\boldsymbol{F}$, where $\boldsymbol{F}$ is the deformation gradient [4]. The density of the material is used as 1250 kg/m^3.

Boundary Conditions. As shown in Fig. 1b, the bottom edge AB is fixed in both vertical and horizontal directions. At the top edge CD, a constant velocity is applied to compress the structure in the vertical direction. To simulate the impact conditions, the structures were compressed at different uniform velocities ranging from 1 to 50 mm/s.

5 Results and Discussion

5.1 Comparison of Structure with Homogeneous and Non-Homogeneous Porosity

Figure 2 shows the deformation behavior of the structures having homogenous and non-homogeneous porosities under large compressive strain. Nominal stress is obtained with the help of total force on edge AB. Nominal strain is the ratio of the applied displacement to the initial length of the specimen. At various stages, corresponding deformed shapes are also presented. The results have been plotted till the point where stable compression is prominent because this point can be interpreted as the maximum energy absorbed per unit volume of the cellular structure. We observe the typical behavior exhibited by cellular solid with three distinct regimes, a linear

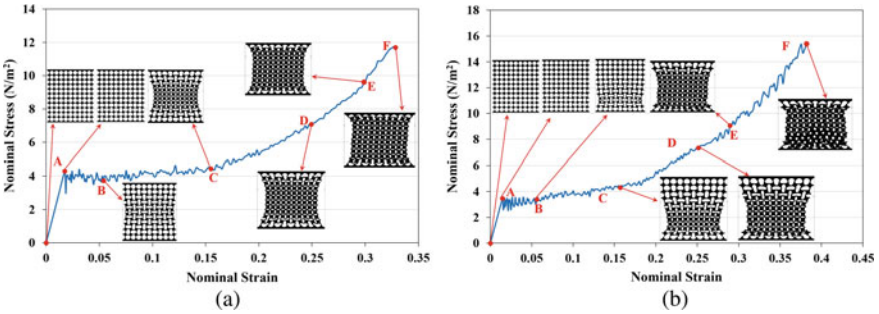

Fig. 2 Various stages of deformation of the cellular structure under compression for structures having **a** homogeneous porosity, and **b** non-homogeneous porosity. Porosity is ~62% for both the structures

elastic regime (up to point *A*), a stress plateau (from *A* to *C*), and densification by further compression (from *C* to *F*). Point *F* is referred to as a global buckling point, where the whole structure buckles. The energy absorption capacity of elastomeric cellular structures is primarily governed by these three regions. The area under the nominal stress–strain curve indicates the energy absorbed during compression. Note that by the time global buckling sets in the structure, it has gone under a significant strain of almost 32% for structure with homogeneous porosity (Fig. 2a) and ~38% for non-homogeneous structure (Fig. 2b), which dictates that the non-homogeneous structure offers greater advantages over homogeneous structure in terms of energy absorption capabilities and also provides better structural stability despite overall porosity being similar.

The nominal stress–strain response of configuration 3 up to a compressive strain of 0.1 at different impact velocities is shown in Fig. 3. With the increase in impact

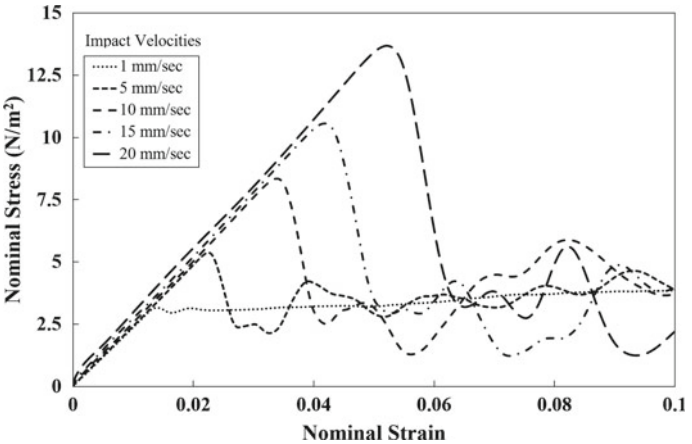

Fig. 3 Compressive stress–strain behavior of configuration 3 under different impact velocities

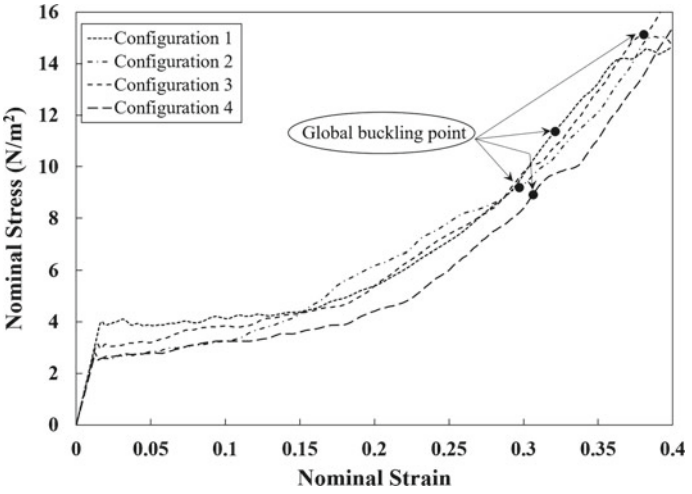

Fig. 4 Compression response of different configurations. Porosity is ~62% for all the configurations

velocity, the critical stress level after which the local elastic instabilities sets in the microstructure and sudden departure from linearity to plateau regime occurs also increases. With the rise in stress level, there is a slight increase in the area below the stress–strain curve which indicates the modest improvement in energy absorbed during compression. Therefore, these structures can be used for structural and load-bearing applications where elastic stiffness is significant.

Figure 4 includes the nominal stress versus nominal strain curve for the configurations listed in Tables 1 and 2. For each configuration, the global buckling point (the point up to which stable compression is obtained) is also highlighted with a filled dot. For all four configurations, the obtained global buckling point is different despite porosity being similar for all the structures. This suggests that with the variation in the local porosity, the compaction behavior can be altered. Also, it is seen that there is a variation in critical stress levels at the local instability point. This indicates that the specimen with the same overall porosity can also be designed to have different critical stress at local instability points by varying local porosity.

6 Conclusion

The elastomeric cellular structures made of soft porous material are designed and analyzed using finite element simulation to examine the deformation mechanism and energy absorption capabilities at a high strain rate. The elastomeric structure having variations of local porosity is explored. It is observed that the compression behavior of structures, having similar overall porosity can be altered by the gradation

of porosity within the structure. Observations from the finite element analysis are summarized below:

1. Precisely architecture elastomeric cellular structure with non-homogeneous porosity shows promising benefits over the structure with homogeneous porosity in terms of energy absorption. Also, it is seen that a non-homogeneous structure preserves better structural stability up to higher strain than the homogeneous structure.
2. The elastomeric cellular structures under different impact velocities are explored. It is seen that over the linear elastic regime the critical stress level at the local instability point increases with the increase in impact velocity which eventually enhances the energy absorption capability throughout the initial compression.
3. Elastomeric specimens having variations of local porosity are examined. It is regarded that the compression behavior of the structures having similar overall porosity can be altered by gradation of porosity within the structure to obtain different compaction strains as well as the critical stress level at local instability point as depicted in Fig. 4.

Acknowledgements The financial support through Grant number ECR/2018/001945 by Science and Engineering Research Board, India, is acknowledged.

References

1. Mullin T, Deschanel S, Bertoldi K, Boyce MC (2007) Pattern transformation triggered by deformation. Phys Rev Lett 99(8):084301
2. Zhang Y, Matsumoto EA, Peter A, Lin PC, Kamien RD, Yang S (2008) One-step nanoscale assembly of complex structures via harnessing of an elastic instability. Nano Lett 8(4):1192–1196
3. Bertoldi K, Reis PM, Willshaw S, Mullin T (2010) Negative Poisson's ratio behavior induced by an elastic instability. Adv Mater 22(3):361–366
4. Overvelde JT, Shan S, Bertoldi K (2012) Compaction through buckling in 2D periodic, soft and porous structures: effect of pore shape. Adv Mater 24(17):2337–2342
5. Babaee S, Shim J, Weaver JC, Chen ER, Patel N, Bertoldi K (2013) 3D soft metamaterials with negative Poisson's ratio. Adv Mater 25(36):5044–5049
6. Shim J, Shan S, Košmrlj A, Kang SH, Chen ER, Weaver JC, Bertoldi K (2013) Harnessing instabilities for design of soft reconfigurable auxetic/chiral materials. Soft Matter 9(34):8198–8202
7. Shen J, Zhou S, Huang X, Xie YM (2014) Simple cubic three-dimensional auxetic metamaterials. Phys Status Solidi B 251(8):1515–1522
8. Shan S, Kang SH, Zhao Z, Fang L, Bertoldi K (2015) Design of planar isotropic negative Poisson's ratio structures. Extrem Mech Lett 4:96–102
9. Javid F, Smith-Roberge E, Innes MC, Shanian A, Weaver JC, Bertoldi K (2015) Dimpled elastic sheets: a new class of non-porous negative Poisson's ratio materials. Sci Rep 5:18373
10. Bertoldi K, Boyce MC (2008) Mechanically triggered transformations of phononic band gaps in periodic elastomeric structures. Phys Rev B 77(5):052105

11. Wang P, Shim J, Bertoldi K (2013) Effects of geometric and material nonlinearities on tunable band gaps and low-frequency directionality of phononic crystals. Phys Rev B 88(1):014304
12. Wang P, Casadei F, Shan S, Weaver JC, Bertoldi K (2014) Harnessing buckling to design tunable locally resonant acoustic metamaterials. Phys Rev Lett 113(1):014301
13. Babaee S, Wang P, Bertoldi K (2015) Three-dimensional adaptive soft phononic crystals. J Appl Phys 117(24):244903
14. Bertoldi K (2017) Harnessing instabilities to design tunable architected cellular materials. Annu Rev Mater Res 47:51–61
15. Tattersall HG, Tappin G (1966) The work of fracture and its measurement in metals, ceramics and other materials. J Mater Sci 1(3):296–301
16. Gibson LJ, Ashby MF (1997) Cellular solids: structure and properties. Cambridge solid state science series. Cambridge University Press, Cambridge
17. Papka SD, Kyriakides S (1994) In-plane compressive response and crushing of honeycomb. J Mech Phys Solids 42(10):1499–1532
18. Ramachandra S, Kumar PS, Ramamurty U (2003) Impact energy absorption in an Al foam at low velocities. Scripta Mater 49(8):741–745
19. Gong L, Kyriakides S, Jang WY (2005) Compressive response of open-cell foams. Part I: morphology and elastic properties. Int J Solids Struct 42(5–6):1355–1379
20. Gong L, Kyriakides S (2005) Compressive response of open cell foams part II: initiation and evolution of crushing. Int J Solids Struct 42(5–6):1381–1399
21. Dawson MA, McKinley GH, Gibson LJ (2008) The dynamic compressive response of open-cell foam impregnated with a Newtonian fluid. J Appl Mech 75(4)
22. Raj RE, Daniel BSS (2009) Structural and compressive property correlation of closed-cell aluminum foam. J Alloy Compd 467(1–2):550–556
23. Raj RE, Parameswaran V, Daniel BSS (2009) Comparison of quasi-static and dynamic compression behavior of closed-cell aluminum foam. Mater Sci Eng A 526(1–2):11–15
24. Jang WY, Kyriakides S (2009) On the crushing of aluminum open-cell foams: part I. Experiments. Int J Solids Struct 46(3–4):617–634
25. Jang WY, Kyriakides S (2009) On the crushing of aluminum open-cell foams: part II analysis. Int J Solids Struct 46(3–4):635–650
26. Barnes AT, Ravi-Chandar K, Kyriakides S, Gaitanaros S (2014) Dynamic crushing of aluminum foams: part I-experiments. Int J Solids Struct 51(9):1631–1645
27. Gaitanaros S, Kyriakides S (2014) Dynamic crushing of aluminum foams: part II—analysis. Int J Solids Struct 51(9):1646–1661
28. Shan S, Kang SH, Raney JR, Wang P, Fang L, Candido F et al (2015) Multistable architected materials for trapping elastic strain energy. Adv Mater 27(29):4296–4301
29. Pinnoji PK, Mahajan P, Bourdet N, Deck C, Willinger R (2010) Impact dynamics of metal foam shells for motorcycle helmets: experiments & numerical modeling. Int J Impact Eng 37(3):274–284
30. Goel MD, Peroni M, Solomos G, Mondal DP, Matsagar VA, Gupta AK et al (2012) Dynamic compression behavior of cenosphere aluminum alloy syntactic foam. Mater Des 42:418–423

Dynamic Stiffness Method for Free Vibration Analysis of Stepped Plate Using the First-Order Shear Deformation Theory

Raj Kumar and Prasun Jana

1 Introduction

Stepped rectangular plates are generally used in the design of mechanical and aerospace structures. These structures are often exposed to mechanical vibrations [1]. Hence, for suitable designing of these structures, the dynamic behavior of different stepped plate configurations needs to be known [2]. Literature survey shows that the classical plate theory (CPT) has been used in most of the existing research pertaining to various non-uniform plates [3–6]. However, from the mechanics perspective, most of the plates used in different engineering applications can be considered thick and the effect of transverse shear cannot be neglected while studying the free vibration characteristics of plates. For these thicker plates, the first-order shear deformation theory (FSDT) can be used in which the transverse shear is also taken into account. However, the literature survey shows that research on exact free vibration analysis of stepped plates is very limited. Chopra [7] used the classical method based on CPT to obtain an exact solution for simply supported rectangular plates of varying thickness. Later, it was found that there was some unintended error in Chopra's work, where the same flexural stiffness is considered for the whole plate despite the varying thickness. Guo et al. [8] pointed out these errors and reported corrected results. But, the analysis method used in Guo et al. is based on classical plate theory and it is neither accurate nor as systematic as the dynamic stiffness method (DSM) that has been used in this study.

DSM is very similar to the finite element method (FEM). However, certain differences can be noted. In the finite element method, convergence of solution depends on the number of elements whereas DSM solution is independent of the number of

R. Kumar · P. Jana (✉)
Department of Aerospace Engineering, Indian Institute of Technology, Kharagpur, West Bengal 721302, India
e-mail: prasun@aero.iitkgp.ac.in

D. K. Maiti et al. (eds.), *Recent Advances in Computational and Experimental Mechanics, Vol II*, Lecture Notes in Mechanical Engineering,
https://doi.org/10.1007/978-981-16-6490-8_4

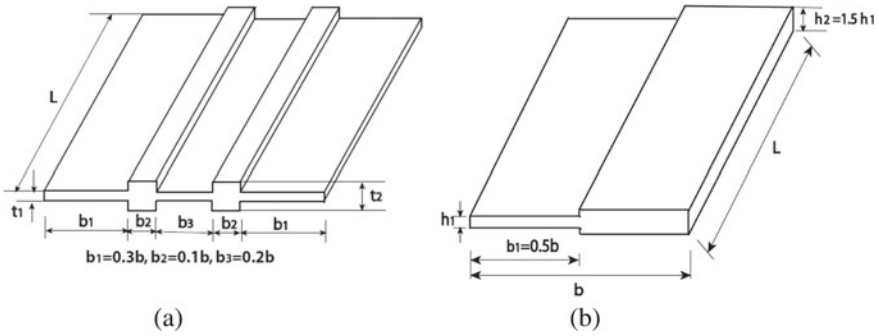

Fig. 1 Schematic of stepped plates considered in this study. **a** A double-stepped plate configuration was adopted from Boscolo and Banerjee [9]. **b** A single-stepped plate configuration adopted from Guo et al. [8]

elements as it uses the exact shape function obtained from the exact differential equations [9]. Therefore, DSM can be used to validate the result obtained by the finite element method (FEM). Initially, the work on DSM was published by Wittricks–Williams [10] in which the critical buckling stresses or natural frequencies of vibrations of thin prismatic structures, consisting of isotropic and anisotropic plate rigidly connected along longitudinal edges were computed. Later, Banerjee [11] showed that by using distinct analytical expressions rather than arithmetic procedures, computational effort for the complete process can be reduced. After that, several researchers [12, 13] have applied this DSM method for the structural analysis of various beam, bar, and plate problems.

In this work, the dynamic stiffness matrix is developed using FSDT for a very accurate free vibration analysis of thicker plates. And, for the first time, this DSM approach has been implemented to the free vibration analysis of a number of stepped plate configurations (See Fig. 1). Levy type boundary conditions (BCs) are used in developing the dynamic stiffness matrix where at least two opposite sides are simply supported. And, the other two sides can be a combination of either clamped (C), free (F), or simply supported (S) boundary conditions. For clamped and simply supported BCs, a particular degree of freedom of appropriate nodes will be constrained using the penalty method. In the penalty method, a significantly large stiffness is given to the relevant term of the principal diagonal of the dynamic stiffness matrix for constraining the boundary condition. The DS matrix developed for a single plate element is assembled to form the global DS matrix of the stepped plate. The global DSM is solved by the Wittricks–Williams (W–W) algorithm to compute the natural frequency very accurately. Another advantage of the W–W algorithm is that by adopting this approach no frequencies will be missed within a given frequency range of the plate. Here, the natural frequency results of the stepped plates are computed by varying different plate parameters. The results are compared with the corresponding results outlined in published literature wherever available. The comparison shows that results computed using DSM are more accurate and efficient than many of

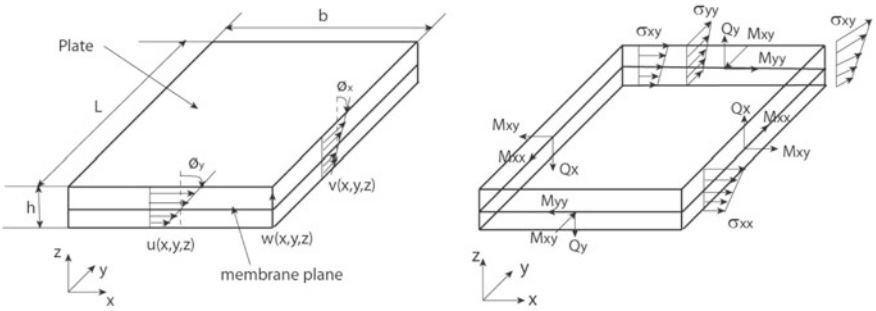

(a) Displacement field (b) Forces

Fig. 2 The Cartesian coordinate system and symbol for displacements and forces for a plate adopted from Boscolo and Banerjee [9]

the other approaches. And, these results can be used as benchmark values for the comparison of other methods.

2 Theory and Mathematical Modeling

2.1 Geometrical Properties

Let the length, width, and thickness of the rectangular plate used in the analysis are a, b, and h, respectively. A Cartesian coordinate system (x, y, z), as shown in Fig. 2a, b, is used for formulating the dynamic stiffness matrices. The sign convention as shown in Fig. 1a is used throughout the analysis.

2.2 Stress–Strain Relationship

The kinematic variables of a rectangular plate are defined by considering the first-order shear deformation theory [9] as follows:

$$\begin{aligned} u(x, y, z, t) &= u_0(x, y, t) + z\phi_y(x, y, t), \\ v(x, y, z, t) &= v_0(x, y, t) - z\phi_x(x, y, t), \\ w(x, y, z, t) &= w^{\mathrm{o}}(x, y, t). \end{aligned} \tag{1}$$

The quantities $\left(u_0, v_0, w^{\mathrm{o}}, \phi_x, \phi_y\right)$ are called generalized displacements. Here, (u_0, v_0) denotes the extensional deformation of the plate while w^{o} denotes the transverse deflection.

Assuming no motion in the membrane mode ($u_0, v_0 = 0$), the kinematic variables are written as

$$\begin{aligned} u(x, y, z, t) &= z\phi_y(x, y, t), \\ v(x, y, z, t) &= -z\phi_x(x, y, t), \\ w(x, y, z, t) &= w^{\mathrm{o}}(x, y, t) \end{aligned} \tag{2}$$

where ϕ_{x} and ϕ_{y} are the rotation of the transverse normal to midplane about the y- and x-axis, respectively.

The plane stress constitutive equations for the isotropic material can be expressed as

$$\begin{bmatrix} \sigma_{xx} \\ \sigma_{yy} \\ \sigma_{xy} \end{bmatrix} = \begin{bmatrix} Q_{11} & Q_{12} & 0 \\ Q_{11} & Q_{22} & 0 \\ 0 & 0 & Q_{11} \end{bmatrix} \begin{bmatrix} \varepsilon_{xx} \\ \varepsilon_{yy} \\ \gamma_{xy} \end{bmatrix} \tag{3}$$

where σ_{xx} and σ_{yy} denote the normal stresses in x- and y-directions and σ_{xy} denotes the shear stress in the plate's x–y plane. The reduced stiffness coefficients can be written as

$$Q_{11} = Q_{22} = \frac{E}{\left(1 - \nu^2\right)};\ Q_{12} = Q_{21} = \frac{\nu E}{\left(1 - \nu^2\right)};\ Q_{66} = \frac{E}{2(1 + \nu)}. \tag{4}$$

where E is Young's modulus and ν is the Poisson's ratio of the plate material.

2.3 Dynamic Stiffness Matrices Using FSDT

The governing differential equation of FSDT is derived from Hamilton's principle. In contrast to other methods, the Hamiltonian method provides the additional BCs as well as equations of motion for deriving the dynamic stiffness matrices. According to Hamilton's principle:

$$\delta \int (K - W)\mathrm{d}t = 0 \tag{5}$$

where K and W represent the kinetic and potential energy of the plate, respectively. The kinetic energy K can be written as

$$K = \frac{1}{2} \int_V \rho \left(\left(\frac{\partial u}{\partial t} \right)^2 + \left(\frac{\partial v}{\partial t} \right)^2 + \left(\frac{\partial w}{\partial t} \right)^2 \right) \mathrm{d}v \tag{6}$$

with ρ as the density of the plate.

The potential energy of the plate is given by

$$U = \frac{1}{2}\int_V \left(\sigma_{xx}\varepsilon_{xx} + \sigma_{yy}\varepsilon_{yy} + \tau_{xy}\gamma_{xy}\right)dv. \tag{7}$$

where ε_{xx} and ε_{yy} denote the normal strain in x- and y-directions, and γ_{xy} denotes the shear strain in the x–y plane.

By substituting Eq. (2) into non-linear von Karman strain and stress relation [9] and then applying Hamilton's principle (Eq. (5)), we get the following three coupled differential equations:

$$\begin{aligned}
&Ghk\left(\frac{\partial^2 w^{\mathrm{o}}}{\partial x^2} + \frac{\partial \phi_y}{\partial x} - \frac{\partial \phi_x}{\partial x} + \frac{\partial^2 w^{\mathrm{o}}}{\partial y^2}\right) - \rho h \frac{\partial^2 w^{\mathrm{o}}}{\partial t^2} = 0\\
&D\left(\frac{\partial^2 \phi_y}{\partial x^2} + \frac{1-\nu}{2}\frac{\partial^2 \phi_y}{\partial y^2} - \frac{\nu+1}{2}\frac{\partial^2 \phi_x}{\partial x \partial y}\right) - kGh\left(\frac{\partial w^{\mathrm{o}}}{\partial x} + \phi_y\right) - \frac{\rho h^3}{12}\frac{\partial^2 \phi_y}{\partial t^2} = 0\\
&D\left(\frac{\partial^2 \phi_x}{\partial y^2} + \frac{1-\nu}{2}\frac{\partial^2 \phi_x}{\partial x^2} - \frac{\nu+1}{2}\frac{\partial^2 \phi_y}{\partial x \partial y}\right) + kGh\left(\frac{\partial w^{\mathrm{o}}}{\partial y} - \phi_x\right) - \frac{\rho h^3}{12}\frac{\partial^2 \phi_x}{\partial t^2} = 0
\end{aligned} \tag{8}$$

where $D = \frac{Eh^3}{12(1-v^2)}$ is the plate bending or flexural stiffness, $G = \frac{E}{2(1+v)}$ is the shear modulus or modulus of rigidity and $k = 5/6$ is the shear correction factor.

The added advantage of using Hamilton's principle, it provides additional information on the connectivity of the displacement variables to the corresponding forces and moments, i.e. w^{o} to Q_x, ϕ_y to M_{xx}, and ϕ_x to M_{xy} (Eq. (9)).

The BCs resulting from the Hamiltonian formulation are:

$$\begin{aligned}
Q_x &: kGh\left(\frac{\partial w^{\mathrm{o}}}{\partial x} + \phi_y\right)\delta w^{\mathrm{o}},\\
M_{xx} &: D\left(\frac{\partial \phi_y}{\partial x} - v\frac{\partial \phi_x}{\partial y}\right)\delta \phi_y,\\
M_{xy} &: -\frac{Gh^3}{12}\left(\frac{\partial \phi_y}{\partial y} - \frac{\partial \phi_x}{\partial x}\right)\delta \phi_x,
\end{aligned} \tag{9}$$

As mentioned earlier, the BCs are considered as Levy type, where no less than two opposite edges are simply supported. The standard Levy type solution which satisfies Eq. (8) is

$$
\begin{aligned}
w^{o}(x, y, t) &= \sum_{m=1}^{y} W_m(x)\mathrm{e}^{i\omega t}\sin(\alpha_m y) \\
\phi_y(x, y, t) &= \sum_{m=1}^{y} \phi_{ym}(x)\mathrm{e}^{i\omega t}\sin(\alpha_m y) \\
\phi_x(x, y, t) &= \sum_{m=1}^{y} \phi_{xm}(x)\mathrm{e}^{i\omega t}\cos(\alpha_m y)
\end{aligned}
\tag{10}
$$

where ω is unknown frequency, $\alpha_m = m\pi/L$ and $m = 1, 2, \ldots \infty$.

Substituting Eq. (10) into (8) gives three ordinary differential equations, written in matrix form as

$$
\begin{bmatrix}
h\omega^2\rho + Ghk\left(\Delta^2 - \alpha^2\right) & Ghk\Delta & \alpha Ghk \\
-Ghk\Delta & D\left(\Delta^2 + \alpha^2\frac{\nu-1}{2}\right) - Ghk + \frac{\omega^2\rho h^3}{12} & \alpha D\frac{1+\nu}{2}\Delta \\
\alpha Ghk & \alpha D\frac{1+\nu}{2}\Delta & D\left(\frac{1-\nu}{2}\Delta^2 - \alpha\right) - Ghk + \frac{\omega^2\rho h^3}{12}
\end{bmatrix}
\begin{bmatrix} W_m \\ \phi_{ym} \\ \phi_{xm} \end{bmatrix} = \begin{bmatrix} 0 \\ 0 \\ 0 \end{bmatrix}
\tag{11}
$$

where Δ is the differential operator d/dx.

By expanding the determinant of Eq. (10), the following governing differential equation will be obtained:

$$
\left(\Delta^6 + a_1\Delta^4 + a_2\Delta^2 + a_3\Delta\right)\Theta = 0, \tag{12}
$$

where $\Theta = W_m$ or ϕ_{ym} or ϕ_{xm}.

Following the procedure mentioned in Boscolo and Banerjee [9], it can be found that the equation's discriminant is always positive, which means that the three roots are real. Eventually, the following four solutions are possible, i.e., (1) all roots are positive, (2) one negative and two positive roots, (3) two negative and one positive root, (4) all roots are negative. For presentational purposes, the derivation of dynamic stiffness matrices for case (1) is shown here. The same procedure is used for the derivation of dynamic stiffness matrices for other cases.

Case 1. All roots are positive:

The solution is expressed as

$$
\begin{aligned}
W_m(x) = A_1\cosh(r_1x) + A_2\sinh(r_1x) + A_3\cosh(r_2x) + A_4\sinh(r_2x) \\
+ A_5\cosh(r_3x) + A_6\sinh(r_3x) \\
\phi_y(x) = B_1\cosh(r_1x) + B_2\sinh(r_1x) + B_3\cosh(r_2x) + B_4\sinh(r_2x) \\
+ B_5\cosh(r_3x) + B_6\sinh(r_3x)
\end{aligned}
$$

$$\phi_x(x) = C_1\cosh(r_1x) + C_2\sinh(r_1x) + C_3\cosh(r_2x) + C_4\sinh(r_2x) + C_5\cosh(r_3x) + C_6\sinh(r_3x) \quad (13)$$

where $A_1 \ldots A_6$, $B_1 \ldots B_2$, $C_1 \ldots C_6$ are three sets of six constants, and r_1, r_2, and r_3 are the three roots of Eq. (11).

The relation between $A_1 \ldots A_6$, $B_1 \ldots B_6$, and $C_1 \ldots C_6$ is found out by substituting Eq. (13) into the governing differential equation (Eq. (10)). A cautious approach should be taken while manifesting the two sets of six constants in terms of the third, to avoid numerical congestion.

The relation between $A_1 \ldots A_6$, $B_1 \ldots B_6$, and $C_1 \ldots C_6$ is given as

$$\begin{aligned} A_1 &= -\delta_1 B_2,\ C_1 = -\gamma_1 B_2 \\ A_2 &= -\delta_1 B_1,\ C_2 = -\gamma_1 B_1 \\ A_3 &= -\delta_2 B_4,\ C_3 = -\gamma_2 B_4 \\ A_4 &= -\delta_2 B_3,\ C_4 = -\gamma_2 B_3 \\ A_5 &= -\delta_3 B_6,\ C_5 = -\gamma_3 B_6 \\ A_6 &= -\delta_3 B_5,\ C_6 = -\gamma_3 B_5 \end{aligned} \quad (14)$$

where

$$\delta_i = \frac{Gk\left(12Ghk - h^3\rho\omega^2 - 6D(-1+\nu)\left(\alpha^2 - r_i^2\right)\right)}{6r_i\left(2G^2hk^2 - DGk\alpha^2(1+\nu) + D(1+\nu)\rho\omega^2 + DGk(1+\nu)r_i^2\right)},$$

$$\gamma_i = \frac{\begin{array}{c}12Dr_i^2 - 12Ghk + 6D\alpha^2(\nu-1) + h^3\left(\rho\omega^2\right)\left(Gk\left(\alpha^2 - r_i^2\right) - \rho\omega^2\right) \\ -12G^2hk^2r_i^2\end{array}}{6\alpha r_i\left(-2G^2hk^2 + D(1+\nu)\left(-\rho\omega^2 + Gk\left(\alpha^2 - r_i^2\right)\right)\right)} \quad (15)$$

with $i = 1, 2, 3$.

Thus, Eq. (13) can be expressed in terms of one set of constants as

$$\begin{aligned} W_m(x) &= -\left(\begin{array}{l}B_2\delta_1\cosh(r_1x) + B_1\delta_1\sinh(r_1x) + B_4\delta_2\cosh(r_2x) + B_3\delta_2\sinh(r_2x) \\ +B_6\delta_3\cosh(r_3x) + B_5\delta_3\sinh(r_3x)\end{array}\right) \\ \phi_y(x) &= B_1\cosh(r_1x) + B_2\sinh(r_1x) + B_3\cosh(r_2x) + B_4\sinh(r_2x) \\ &\quad + B_5\cosh(r_3x) + B_6\sinh(r_3x) \\ \phi_x(x) &= -\left(\begin{array}{l}B_2\gamma_1\cosh(r_1x) + B_1\gamma_1\cosh(r_1x) + B_4\gamma_2\cosh(r_2x) + B_3\gamma_2\sinh(r_2x) \\ +B_6\gamma_3\cosh(r_3x) + B_5\delta_3\sinh(r_3x)\end{array}\right) \end{aligned} \quad (16)$$

By substituting Eq. (16) into (9), forces and moments can be rewritten as

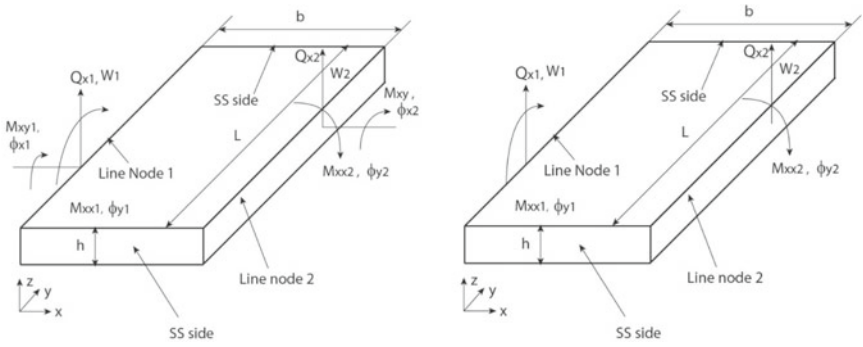

(a) Edge Conditions (b) Boundary Conditions

Fig. 3 Edge conditions and boundary conditions for a plate element adopted from Boscolo and Banerjee [9]

$$
\begin{aligned}
Q_x(x,y) = Q_x(x)\sin(\alpha y) = -Ghk \begin{pmatrix} B_1(1-\delta_1 r_1)\cosh(r_1 x) + B_2(1-\delta_1 r_1)\sinh(r_1 x) \\ +B_3(1-\delta_2 r_2)\cosh(r_2 x) + B_4(1-\delta_2 r_2)\sinh(r_2 x) \\ +B_5(1-\delta_3 r_3)\cosh(r_3 x) + B_6(1-\delta_3 r_3)\sinh(r_3 x) \end{pmatrix} \\
M_{xx}(x,y) = M_{xx}(x)\sin(\alpha y) = D \begin{pmatrix} B_2(r_1-\alpha\gamma_1\nu)\cosh(r_1 x) + B_1(r_1-\alpha\gamma_1\nu)\sinh(r_1 x) \\ +B_4(r_2-\alpha\gamma_2\nu)\cosh(r_2 x) + B_3(r_2-\alpha\gamma_2\nu)\sinh(r_2 x) \\ +B_6(r_3-\alpha\gamma_3\nu)\cosh(r_3 x) + B_5(r_3-\alpha\gamma_3\nu)\sinh(r_3 x) \end{pmatrix} \\
M_{xy}(x,y) = M_{xy}(x)\cos(\alpha y) = -\frac{Gh^3}{12} \begin{pmatrix} B_1(\alpha+\gamma_1 r_1)\cosh(r_1 x) + B_2(\alpha+\gamma_1 r_1)\sinh(r_1 x) \\ +B_3(\alpha+\gamma_2 r_2)\cosh(r_2 x) + B_4(\alpha+\gamma_2 r_2)\sinh(r_2 x) \\ +B_5(\alpha+\gamma_3 r_3)\cosh(r_3 x) + B_6(\alpha+\gamma_3 r_3)\sinh(r_3 x) \end{pmatrix}
\end{aligned} \tag{17}
$$

The BCs for the displacements and rotations as shown in Fig. 3b are

$$
\begin{aligned}
x = 0 &: W_m = W_1,\ \phi_y = \phi_{y1},\ \phi_x = \phi_{x1} \\
x = b &: W_m = W_2,\ \phi_y = \phi_{y2},\ \phi_x = \phi_{x2}
\end{aligned} \tag{18}
$$

The BCs for the forces and moments are

$$
\begin{aligned}
x = 0 &: Q_x = -Q_1,\ M_{xx} = -M_{xx1},\ M_{xy} = -M_{xy1} \\
x = b &: Q_x = -Q_2,\ M_{xx} = -M_{xx2},\ M_{xy} = -M_{xy2}
\end{aligned} \tag{19}
$$

Substituting Eq. (18) into (16), the subsequent relationship can be expressed in matrix form:

$$\begin{bmatrix} W_1 \\ \phi_{y1} \\ \phi_{x1} \\ W_2 \\ \phi_{y2} \\ \phi_{x2} \end{bmatrix} = \begin{bmatrix} 0 & -\delta_1 & 0 & -\delta_2 & 0 & -\delta_3 \\ 1 & 0 & 1 & 0 & 1 & 0 \\ 0 & -\gamma_1 & 0 & -\gamma_2 & 0 & -\gamma_3 \\ -\delta_1 S_{h1} & -\delta_1 C_{h1} & -\delta_2 S_{h2} & -\delta_2 C_{h2} & -\delta_3 S_{h3} & -\delta_3 C_{h3} \\ C_{h1} & S_{h1} & C_{h2} & S_{h2} & C_{h3} & S_{h3} \\ -\gamma_1 S_{h1} & -\gamma_1 C_{h1} & -\gamma_2 S_{h2} & -\gamma_2 C_{h2} & -\gamma_3 S_{h3} & -\gamma_3 C_{h3} \end{bmatrix} \begin{bmatrix} B_1 \\ B_2 \\ B_3 \\ B_4 \\ B_5 \\ B_6 \end{bmatrix} \tag{20}$$

$$\text{i.e. } \delta = \mathbf{AC}. \tag{21}$$

Substituting Eq. (19) into (17), the subsequent relationship can be expressed in matrix form:

$$\begin{bmatrix} Q_{x1} \\ M_{xx1} \\ M_{xy1} \\ Q_{x2} \\ M_{xx2} \\ M_{xy2} \end{bmatrix} = \begin{bmatrix} L_1 & 0 & L_2 & 0 & L_3 & 0 \\ 0 & R_1 & 0 & R_2 & 0 & R_3 \\ T_1 & 0 & T_2 & 0 & T_3 & 0 \\ -L_1 C_{h1} & -L_1 S_{h1} & -L_2 C_{h2} & -L_2 S_{h2} & -L_3 C_{h3} & -L_3 S_{h3} \\ -R_1 S_{h1} & -R_1 C_{h1} & -R_2 S_{h2} & -R_2 C_{h2} & -R_3 S_{h3} & -R_3 C_{h3} \\ -T_1 C_{h1} & -T_1 S_{h1} & -T_2 C_{h2} & -T_2 S_{h2} & -T_3 C_{h3} & -T_3 S_{h3} \end{bmatrix} \begin{bmatrix} B_1 \\ B_2 \\ B_3 \\ B_4 \\ B_5 \\ B_6 \end{bmatrix} \tag{22}$$

$$\text{i.e. } \mathbf{F} = \mathbf{RC}, \tag{23}$$

where

$$L_i = Ghk(\delta_i r_i - 1),\ R_i = D(\alpha\gamma_i \nu - r_i),\ T_i = \frac{Gh^3}{12}(\alpha + \gamma_i r_i) \quad \text{with } i = 1, 2, 3. \tag{24}$$

From Eqs. (21) and (23), the dynamic stiffness matrix $\mathbf{K}$ for an isotropic plate element is

$$\mathbf{F} = \mathbf{K}\delta, \text{ where } \mathbf{K} = \mathbf{RA}^{-1}. \tag{25}$$

2.4 Assembly Procedure

Assembly procedure in DSM follows the same steps as that of the FEM, and the only exception in DSM is, instead of single points or nodes, nodal lines are used to connect the plate elements (Fig. 4).

As mentioned earlier, penalty methods are used for the application of appropriate boundary constraints. The particular degree of freedom of nodes is constrained for different BCs as shown in Table 1.

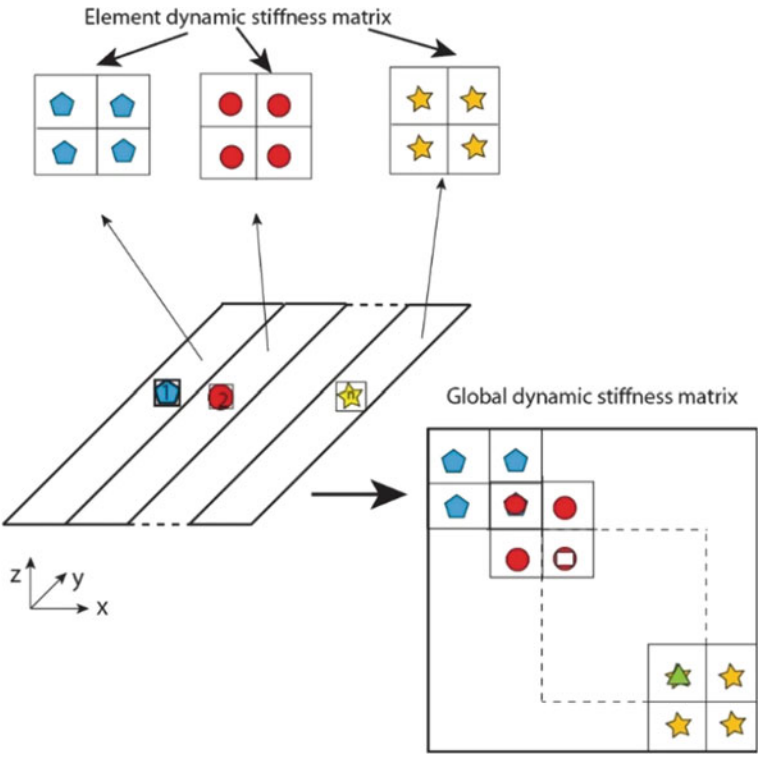

Fig. 4 Assembly of dynamic stiffness matrices

Table 1 The procedure for applying BCs are summarized as

Boundary conditions (BCs)	w_i [1]	ϕ_{yi}	ϕ_{xi}
Free (F)	No penalty	No penalty	No penalty
Simply supported (SS)	Penalized	No penalty	Penalized
Clamped (C)	Penalized	Penalized	Penalized

[1] Here, i is the node whose degree of freedom is restrained

Once the assembled global dynamic stiffness matrix is formed, the W-W algorithm is implemented for solving the eigenvalue problem which subsequently gives the natural frequencies [10]. The procedure of the W-W algorithm is not described here owing to space limitation, and it can be found in several other published literature.

3 Results and Conclusions

The complete process, beginning from the dynamic stiffness matrix and ending with the eigenvalue problem solution, is carried out in a computer program using MATLAB. Firstly, the natural frequencies for double-stepped plate (shown in Fig. 1a) and single-stepped plate (shown in Fig. 1b) are calculated using the DSM based on two plate theories: CPT and FSDT. The results are shown in Table 2 and compared with the published results [8, 9].

Natural frequencies for a single-stepped plate, shown in Fig. 1b, is calculated for varying thickness ratio are reported in Table 3. Results based on CPT and FSDT are

Table 2 Natural frequencies (rad/s) calculated for isotropic double-stepped plate shown in Fig. 1a and single-stepped plate shown in Fig. 1b based on different plate theories

Mode	Natural frequencies for double-stepped plate				Natural frequencies for single-stepped plate			
	S–S–S–S		S–C–S–C		S–S–S–S		S–C–S–C	
	Present (FSDT)	Ref [9] (FSDT)	Present (FSDT)	Ref [9] (FSDT)	Ref [8] (CPT)	Present (FSDT)	Ref [8] (CPT)	Present (FSDT)
1 1	3154.62	3154.61	4247.36	4247.36	3753.10	3558.93	5461.54	4862.73
1 2	7339.71	7339.71	8395.51	8395.51	9407.59	8359.57	10,471.40	8981.27
2 1	7704.14	7854.54	9416.91	9416.91	9544.23	8429.08	13,373.92	10,658.60
2 2	11,433.49	11,433.49	12,775.79	12,775.79	15,118.80	12,618.73	18,049.85	13,994.36
1 3	13,481.87	13,481.87	15,716.37	15,004.08	18,099.77	14,965.95	19,032.14	15,721.31
3 1	15,861.81	14,698.52	15,939.68	15,939.68	18,325.38	15,712.60	23,958.91	17,358.40
2 3	17,404.82	17,404.82	18,475.41	18,475.41	24,315.18	18,834.96	26,924.62	19,766.28
3 2	17,630.01	17,630.01	19,298.84	19,298.84	24,867.18	19,042.10	29,201.23	20,540.65

$E = 71.2$ GPa, $\vartheta = 0.3$, $\rho = 2700$ kg/m^3, $b/L = 1$, $k = 5/6$, $b_1 = 0.3b$, $b_2 = 0.1b$, $b_3 = 0.2b$

Table 3 Natural frequencies (rad/s) calculated for varying thickness ratio for isotropic single-stepped plate shown in Fig. 1b based on different plate theories: CPT and FSDT

Mode	$h_2/h_1 = 1.5$				$h_2/h_1 = 2$			
	S–S–S–S		S–C–S–C		S–S–S–S		S–C–S–C	
	CPT	FSDT	CPT	FSDT	CPT	FSDT	CPT	FSDT
1 1	3753.10	3558.93	5461.54	4862.73	4450.12	4093.98	6397.34	5462.19
1 2	9407.59	8359.58	10,471.45	8981.27	10,913.37	9329.50	12,402.73	10,077.86
2 1	9544.23	8429.09	13,373.94	10,658.61	11,016.68	9390.86	15,191.14	11,556.01
2 2	15,118.81	12,618.73	18,049.87	13,994.37	17,260.30	13,745.84	20,361.13	15,032.64
1 3	18,099.77	14,965.96	19,032.19	15,721.32	19,730.44	16,186.03	21,218.59	18,252.69
3 1	18,325.38	15,712.61	23,958.93	17,358.41	21,142.06	18,374.85	27,676.34	18,379.66
2 3	24,315.18	18,834.97	26,924.63	19,766.28	28,718.99	20,470.65	31,332.08	21,356.15

$E = 71.2$ GPa, $\vartheta = 0.3$, $\rho = 2700$ kg/m^3, $b/L = 1$, $k = 5/6$

Table 4 Natural frequencies (rad/s) for isotropic single-stepped plate shown in Fig. 1b computed by FEM (ANSYS) and compared with the exact value calculated by DSM

Mode	S–S–S–S			S–C–S–C		
	FSDT (DSM)	FSDT (FEM)	Percentage difference	FSDT (DSM)	FSDT (FEM)	%difference
$h_2/h_1 = 1.5$						
1 1	3558.93	3440.04	−3.4560	4862.73	4881.40	0.3839
1 2	8359.57	8450.88	1.0804	8981.278	9169.79	2.0767
2 1	8429.08	8580.31	1.7625	10,658.61	11,199.78	5.0773
2 2	12,618.73	12,730.36	0.8768	13,994.37	14,482.11	3.4853
1 3	18,834.96	19,518.09	3.4999	15,721.32	16,391.57	4.2633
3 1	19,042.10	19,958.54	4.5917	17,358.41	18,214.33	4.9308
2 3	23,472.87	23,808.87	1.4112	19,766.28	20,616.39	4.3007
$h_2/h_1 = 2$						
1 1	4093.98	4131.31	0.9035	5462.19	5432.31	-0.5501
1 2	9329.50	9415.98	0.9184	10,077.86	10,249.76	1.6771
2 1	9390.86	9544.18	1.6061	11,556.01	12,179.95	5.1227
2 2	13,745.84	13,913.49	1.2048	15,032.64	15,614.97	3.7293
1 3	16,186.03	16,720.18	3.1946	18,252.69	19,684.59	7.2742
3 1	18,374.85	18,737.72	1.9365	21,356.15	22,623.87	5.6034
2 3	20,470.65	20,703.72	1.1257	21,910.70	23,033.53	4.8747

$E = 71.2$ GPa, $\vartheta = 0.3$, $\rho = 2700$ kg/m^3, $b/L = 1$, $k = 5/6$

compared for different Levy-type BCs. It can be seen that the natural frequencies calculated using FSDT are less than the CPT, which is generally the case.

In Table 4, the first seven natural frequencies based on both CPT and FSDT, for different thickness ratios, are compared. It can be seen that the effect of shear deformation is not negligible and has a pronounced effect on the natural frequencies. To put the analysis in the broader context some comparative results using the FEM have also been reported in Table 4. ANSYS has been used for finite element analysis. Based on the FEM results, it is observed that the error between the DSM results and the FEM results in increases at high frequencies.

To summarize, in this work, natural frequency results for the stepped plate are calculated using the DSM approach and validated with the published results. The main contribution of the present work is the use of DSM to find out the natural frequencies of different stepped plate configurations using FSDT. In the future, this work will be extended to the stepped plate of orthotropic and functionally graded materials.

References

1. Mori T, Hiramatsu T, Shamoto E (2011) Simultaneous double-sided milling of flexible plates with high accuracy and high efficiency–suppression of forced chatter vibration with synchronized single-tooth cutters. Precis Eng 35(3):416–423
2. Stone B (2014) Chatter and machine tools. Springer International, New York
3. Lee J, Bergman L (1994) The vibration of stepped beams and rectangular plates by an elemental dynamic flexibility method J Sound Vib 171(5):617–40
4. Takabatake H, Imaizumi T, Okatomi K (1995) Simplified analysis of rectangular plates with stepped thickness. J Struct Eng 121(1):28–38
5. Jaworski J, Dowell E (2007) Free vibration of a cantilevered beam with multiple steps: comparison of several theoretical methods with experiment. J Sound Vib 312(4):713–725
6. Wang G, Unal A (2013) Free vibration of stepped thickness rectangular plates using spectral finite element method. J Sound Vib 332(18):4324–4338
7. Chopra I (1974) Vibration of stepped thickness plates. Int J Mech Sci 16:337–344
8. Guo S, Keane A, Moshrefi-Torbati M (1997) Vibration analysis of stepped thickness plates. J Sound Vib 204(4):645–657
9. Boscolo M, Banerjee JR (2011) Dynamic Stiffness elements and their application for plates using first order shear deformation theory. Comput Struct 89(3):395–410
10. Wittrick WH, Williams FW (1971) A general algorithm for computing natural frequencies of elastic structures. Quart J Mach Appl Math 24(3):263–284
11. Banerjee JR (1997) Dynamic stiffness formulation for structural elements: a general approach. Comput Struct 63(1):101–103
12. Kumar S, Ranjan V, Jana P (2018) Free vibration analysis of thin functionally graded rectangular plates using the dynamic stiffness method. Comput Struct 197:39–53
13. Kumar S, Jana P (2019) Application of dynamic stiffness method for accurate free vibration analysis of sigmoid and exponential functionally graded rectangular plates. Int J Mech Sci 163:105–121

Micromechanics-Based Technique of Material Homogenization and Determination of Fracture Plane in Advance Composites

Semayat Fanta, Y. S. C. Mouli, C. S. Upadhyay, and P. M. Mohite

1 Introduction

Unidirectional fiber-reinforced polymeric composite (UDFRPC) laminates are extensively used in many engineering fields due to their excellent mechanical properties and weight savings benefits. There are many modeling approaches to find the effective properties of UDFRPC lamina [1]. Standard mechanics is one of the homogenization techniques that uses Hill's concentration approach to find the material's effective properties [2]. Hill's concentration approach requires a sufficiently large RVE to accurately determine the effective mechanical properties. The size of RVE is essential when we use homogenization techniques. Literature on the size determination of RVE is presented in the work of Koley et al. [3]. In most cases, it requires randomly distributed fibers in cross section in a sufficiently large RVE to account for the fiber distribution stochastic nature in the lamina.

We determine the composite lamina effective properties using Hill's concentration factors approach on a few RVEs with randomly distributed fibers in the lamina's cross-section in the current work. The prime goal of micromechanics analysis is to predict a heterogeneous material's effective properties based on the constituent materials' properties (i.e., fiber and matrix), and their geometric arrangement, as shown in Fig. 1. The properties found from the current micromechanical analysis can be used for the composite laminate analysis.

Apart from finding the laminae's effective properties, an accurate prediction of the fracture plane angle in a lamina under transverse compression loading has been a challenging task due to the complexity of the failure mechanisms involved [4]. Even though various phenomenological and physically based models were proposed by

S. Fanta (✉) · Y. S. C. Mouli · C. S. Upadhyay · P. M. Mohite
Department of Aerospace Engineering, Indian Institute of Technology Kanpur, Kanpur Nagar, Uttar Pradesh 208016, India
e-mail: semayatf@iitk.ac.in

D. K. Maiti et al. (eds.), *Recent Advances in Computational and Experimental Mechanics, Vol II*, Lecture Notes in Mechanical Engineering,
https://doi.org/10.1007/978-981-16-6490-8_5

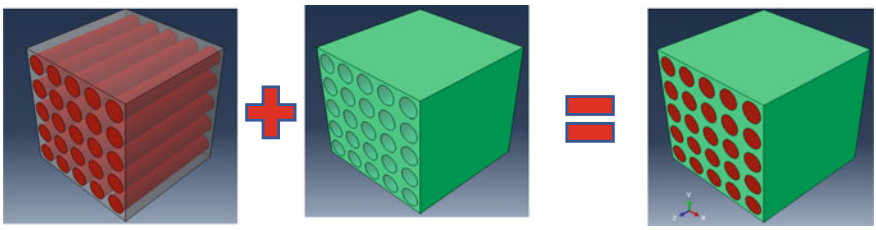

Fig. 1 Micromechanical modeling approach for unidirectional composite

Puck and Schürmann [5] and Pinho et al. [6], we need to go through rigorous experimentation, analytical approximations, and finite element method based numerical simulations to evolve the fracture condition in the materials as done by Daniel et al. [7], Soden et al. [8]. The present work addresses the problem with a simple elastic analysis on the RVE by loading it in transverse compression.

This study aims to provide micromechanics-based numerical simulation technique on RVEs of UDFRPC to predict homogenized material properties and determine the fracture plane angle when subjected to transverse compression loading.

2 Micromechanical Analysis

To obtain homogenized effective properties and determine the fracture plane angle in a composite lamina, RVE under consideration must be large enough to represent the whole material microstructure, Hollister et al. [1]. It has been shown that the RVE with at least 30 fibers is needed to sufficiently represent the material's macroscopic behavior as studied by González et al. [9], Totry et al. [10], and LLorca et al. [11].

In the current study, four RVEs with the random distribution of fibers are considered from the work of Koley et al. [3]. Four RVEs with 50 embedded fibers having a volume fraction nearly equal to 60% are employed to adequately capture the essential features of the material's microstructure while maintaining reasonable computational accuracy. The constituent materials considered are AS4 fiber and 3501-6 epoxy resin matrix for the micromechanical analysis, and their properties are taken from the experimental work by Soden et al. [8], as provided in Table 1.

Each RVE is modeled carefully, maintaining the periodicity using ABAQUS/CAE finite element software. Figure 2 illustrates the four RVEs considered in the analysis. Quadratic tetrahedral elements (C3D10) with fine meshing are considered for the analysis. The fiber and matrix are assumed to be perfectly bonded.

Table 1 Material properties of AS4 fiber and 3501-6 epoxy Soden et al. [8]

AS4 fiber				
E_1 (GPa)	E_2 (GPa)	G_{12} (GPa)	G_{23} (GPa)	ν_{12}
225	15	15	7	0.2
3501-6 Epoxy				
E_m (GPa)		ν_m		
4.2		0.35		

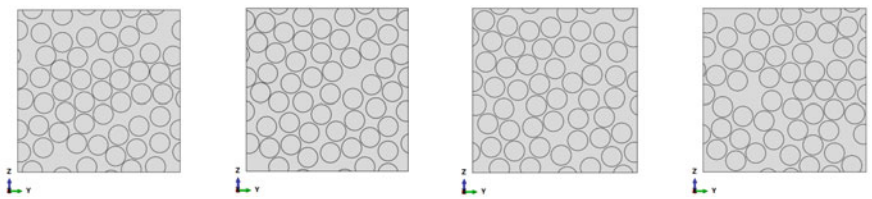

Fig. 2 RVE microstructures considered for analysis Koley et al. [3]. **a** RVE (1), **b** RVE (2), **c** RVE (3), **d** RVE (4)

2.1 Hill's Concentration Factor Approach

The effective properties of two or more constituent-based composite materials can be obtained using the volume averaging scheme of Hill's concentration factors approach [2]. In this approach, the composite's volume-averaged strains are equated to the phased volume averaged strains in individual phases to find the effective properties using the point-wise strain concentration factor. The average stress in the composite is given as in Eq. (1).

$$\overline{\sigma}_{ij} = \frac{V_f}{V_{RVE}}\overline{\sigma}_{ij}^{(f)} + \frac{V_m}{V_{RVE}}\overline{\sigma}_{ij}^{(m)} = v_f C_{ijkl}^{(f)}\overline{\varepsilon}_{kl}^{(f)} + v_m C_{ijkl}^{(m)}\overline{\varepsilon}_{kl}^{(m)} = \tilde{C}_{ijkl}\overline{\varepsilon}_{kl} \quad (1)$$

where $\overline{\varepsilon}_{ij}^{(f)}$, $\overline{\sigma}_{ij}^{(f)}$ and $\overline{\varepsilon}_{ij}^{(m)}$, $\overline{\sigma}_{ij}^{(m)}$ are averaged strains and stresses of fiber and matrix in the RVE; V_f, V_m and V_{RVE} are the volumes of fiber, matrix and the RVE; v_f and v_m are the volume fractions of fiber and matrix, respectively.

The phased volume averaged strain concentration factors for fiber and matrix are given as

$$\overline{A}_{ijkl}^{(f)} = \frac{1}{V_f}\iiint_V A_{ijkl}^{(f)}(x)dV_f \quad (2)$$

$$\overline{A}_{ijkl}^{(m)} = \frac{1}{V_m}\iiint_V A_{ijkl}^{(m)}(x)dV_m \quad (3)$$

Therefore, the phased averaged strains in the fiber and matrix are given as

$$\overline{\varepsilon}_{ij}^{(f)} = \overline{A}_{ijkl}^{(f)} \overline{\varepsilon}_{kl} \tag{4}$$

$$\overline{\varepsilon}_{ij}^{(m)} = \overline{A}_{ijkl}^{(m)} \overline{\varepsilon}_{kl} \tag{5}$$

where $A_{ijkl}^{(f)}(x)$ and $A_{ijkl}^{(m)}(x)$ are the local strain concentration tensors for fiber and matrix, respectively. The phased averaged strains in fiber and matrix as given in Eqs. (4) and (5) can be obtained in terms of phase averaged strain concentration factors $\overline{A}_{ijkl}^{(f)}$ and $\overline{A}_{ijkl}^{(m)}$ for fiber and matrix, respectively. The homogenized constitutive matrix ($\tilde{C}_{ijkl}$) in terms of phased averaged strain concentration factors of fiber and matrix is obtained by substituting Eqs. (4) and (5) in Eq. (1) as

$$\tilde{C}_{ijkl} = v_f C_{ijmn}^{(f)} \overline{A}_{mnkl}^{(f)} + v_m C_{ijmn}^{(m)} \overline{A}_{mnkl}^{(m)} \tag{6}$$

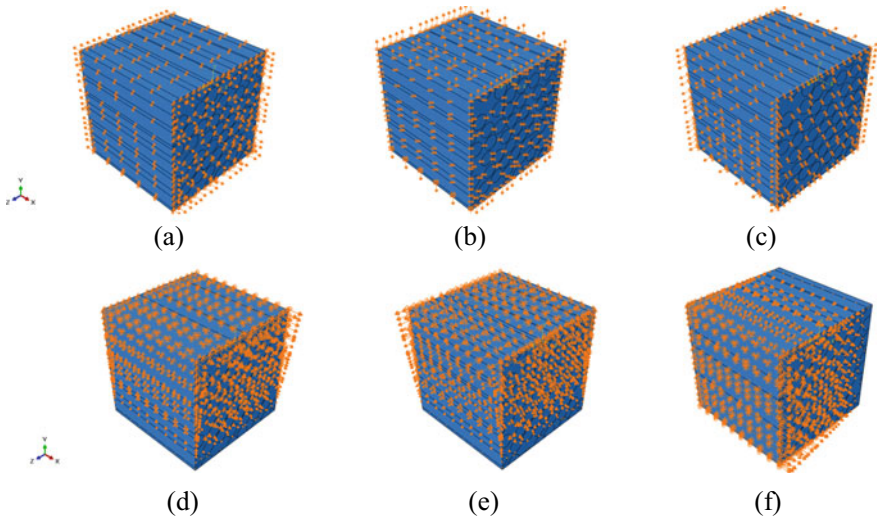

Fig. 3 Loading and boundary conditions applied for micromechanical analysis. **a** ϵ_{11} loading, **b** ϵ_{22} loading, **c** ϵ_{33} loading, **d** γ_{12} loading, **e** γ_{13} loading, **f** γ_{23} loading

2.2 Loading and Boundary Conditions

Each RVE is subjected to unit strain boundary conditions: three normal directions and three shear directions separately, as shown in Fig. 3. The elemental strains and elemental volumes are averaged over the fiber and matrix for each loading case.

2.3 Results and Discussion on Effective Material Properties

On performing the micromechanical analysis of four RVEs for determining the effective properties of the composite laminae using Hill's concentration factors approach, we have obtained the results as given in Table 2. In comparison to the computational results, the average values of E_1, G_{12}, and G_{13} are less than 10% of the deviation from the experimental values, whereas, ν_{12} and ν_{13} are around 10% and E_2, E_3, G_{23}, and ν_{23} are deviated by 17%, 17%, 15.6%, and 27.5%, respectively. However, the

Table 2 The comparison of effective material properties with data in the literature

Elastic property	Current micromechanics approach, note E_{ii} (GPa), G_{ij} (GPa)					Comparison
	RVE (1)	RVE (2)	RVE (3)	RVE (4)	Average	Error (%)
Effective properties of RVEs in the work of Soden et al. [8]						
E_1	137.23	137.56	137.54	137.54	**137.50**	0.36
E_2	9.21	9.10	9.10	9.17	**9.13**	17.00
E_3	9.14	9.0	9.15	9.169	**9.12**	17.00
G_{12}	6.09	5.98	5.89	5.96	**5.98**	9.40
G_{13}	6.00	5.95	5.97	6.03	**5.99**	9.40
G_{23}	3.61	3.66	3.61	3.61	**3.62**	15.60
ν_{12}	0.251	0.25	0.25	0.25	**0.25**	10.16
ν_{13}	0.254	0.25	0.25	0.25	**0.25**	9.93
ν_{23}	0.290	0.300	0.29	0.29	**0.29**	27.50
Effective properties of RVEs in the work of Koley et al. [3]						
E_1	136.19	136.01	136.04	136.73	**136.24**	0.92
E_2	9.20	9.10	9.20	9.27	**9.20**	0.76
E_3	9.28	9.14	9.24	9.26	**9.23**	1.10
G_{12}	4.93	5.01	4.24	5.45	**4.91**	17.90
G_{13}	5.20	5.16	5.05	5.41	**5.21**	13.00
G_{23}	3.53	3.61	3.57	3.60	**3.58**	1.10
ν_{12}	0.25	0.25	0.25	0.25	**0.25**	0.00
ν_{13}	0.25	0.25	0.25	0.25	**0.25**	0.00
ν_{23}	0.28	0.29	0.28	0.28	**0.28**	3.40

current analysis results are not much deviated from the experimental work of Soden et al. [8], and simulation results of Koley et al. [3], in which the mathematical theory of homogenization was used to determine the effective properties in the composite except the G_{12} and G_{13} properties. The unit strain boundary conditions used in the shear direction are overestimating the material elastic properties in the corresponding direction.

3 Determination of Fracture Plane Angle in RVE Subjected to Transverse Compression

Under transverse compression, the behavior of the fracture plane in composite lamina depends on the matrix behavior. We can observe the compressive stress–strain curves for composite laminates subjected to transverse compressive loading in Soden et al. [8]. The puck failure criterion is the most prominently used failure criterion to predict composite failure under transverse compression. However, this criterion is proposed on an analytical basis, and one can reiterate the possibility of various fracture planes in the UD composite laminates. Here in the current work, we have attempted to rebuild the fracture condition of composite RVE under transverse compression.

3.1 Determination of Micro-Stress from Macro-Strain

We can obtain the micro stress in the matrix from the macro unit macro strains applied in a transverse direction ε^0_{22} and ε^0_{33}. Since the matrix is weaker than the fiber, a resin reach region of the RVEs is emphasized to obtain the micro stresses, and the weak planes are determined. Using Hooke's law at the microscopic level for matrix material, the constitutive relation is given by

$$\sigma^{(m)}_{ij}(x) = C^{(m)}_{ijkl}\varepsilon^{(m)}_{kl}(x) \tag{7}$$

With

$$\varepsilon^{(m)}_{kl}(x) = A^{(m)}_{klmn}(x)\overline{\varepsilon}_{mn} \tag{8}$$

And writing macro strain in terms of unit macro strains in any directions as

$$\overline{\varepsilon}_{mn} = \varepsilon^0_{mn} \tag{9}$$

Therefore, the micro-stress from the macro-strain applied on RVE is calculated as

$$\sigma_{ij}^{(m)}(x) = C_{ijkl}^{(m)} A_{klmn}^{(m)}(x) \varepsilon_{mn}^{0} \tag{10}$$

where $\sigma_{ij}^{(m)}(x)$ are local stresses, $\varepsilon_{kl}^{(m)}(x)$ are local strains, $C_{ijkl}^{(m)}$ is local stiffness tensor of matrix, $A_{klmn}^{(m)}(x)$ is local strain concentration factor tensor, and ε_{mn}^{0} is the unit macro strain in any direction of the representative volume element.

3.2 Concept of Damage Stress Concentration Factor (DSCF)

To determine failure points in the RVE, we introduce a damage stress concentration factor (DSCF) and, is given by the ratio of the stress in a matrix material to the yield strength of matrix or the ratio of the stress in a fiber material to the ultimate strength of the fiber martial. Thus, the damage stress concentration factor for fiber and matrix, respectively, are defined as

$$(DSCF)_f = \left[\frac{\sigma_{kl}^{(f)}}{\sigma_{kl}^{ult}} \right]_{ij} \tag{11}$$

$$(DSCF)_m = \left[\frac{\sigma_{kl}^{(m)}}{\sigma_{kl}^{yield}} \right]_{ij} \tag{12}$$

where $\sigma_{kl}^{(f)}$ the stress in fiber, σ_{kl}^{ult} the ultimate strength of fiber material, $\sigma_{kl}^{(m)}$ the stress in the matrix, and σ_{kl}^{yield} the yield strength of matrix material, respectively.

3.3 Data Interpolation

Writing the Python script to extract the centroid (X, Y, Z) coordinates, the von-Misses stress σ_{vm} and the stress ratio $\frac{\sigma_{vm}}{\sigma_y}$ are calculated. The data in RVE for each load case at the centroid of each element are interpolated using the inverse distance interpolation technique of TECPLOT data extraction software. The assigned values to unknown points are calculated with a weighted average of the known point values. The interpolation is carried out on the destination mesh of $20 \times 100 \times 100$. The interpolation slice at $X = -2.5$, $X = 0.0$, and $X = +2.5$ are extracted, and the weak zones are identified at $X = 0$ (i.e., at mid-section of the specimen) shown in Figs. 4 and 5.

The four RVEs are interpolated through $X = -2.5$, $X = 0.0$ and $X = +2.5$ locations as shown in Fig. 4 and the emphasize is given to data obtained from the location $X = 0.0$. The fracture plane analysis on all RVEs was carried out by applying a unit macro strain in 22 and 33 directions. The data of damage stress concentration factors are

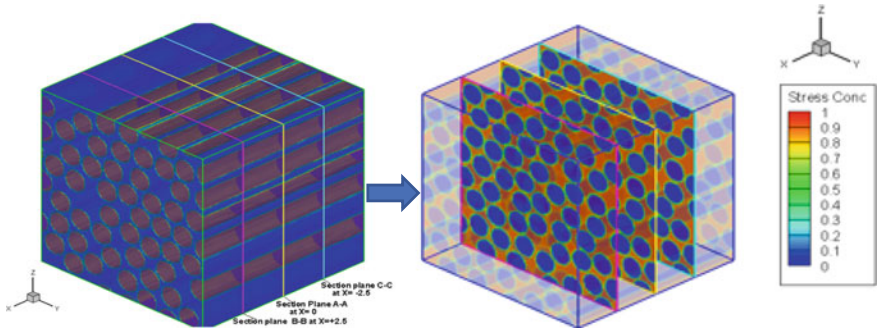

Fig. 4 Data interpolation slices at the various section for data extraction

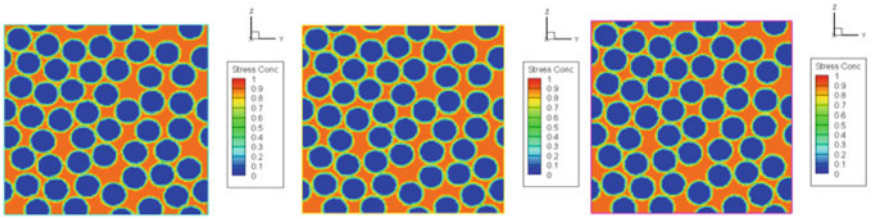

Fig. 5 Data slices at X (−2.5, 0.0, 2.5) using TECPLOT software. **a** X = −2.5, **b** X = 0.0, **c** X = +2.5

extracted at X = 0.0 location for both cases for RVE (1) and RVE (2) are illustrated in Figs. 6, 7 and 8.

The weak planes in ε_{22}^{c} and ε_{33}^{c} loading cases for all four RVEs at the locations X = 0.0 are extracted manually by visual identification, and their angles are identified with the help of ImageJ software. We performed for all four RVEs but reported only

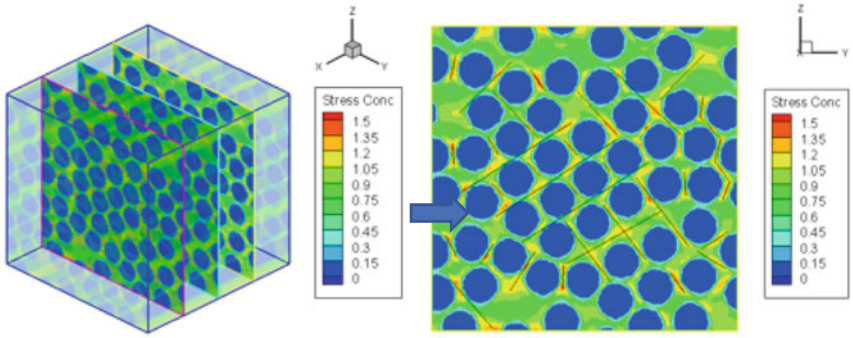

Fig. 6 Transverse compression ε_{22}^{c} loading on RVE (1)

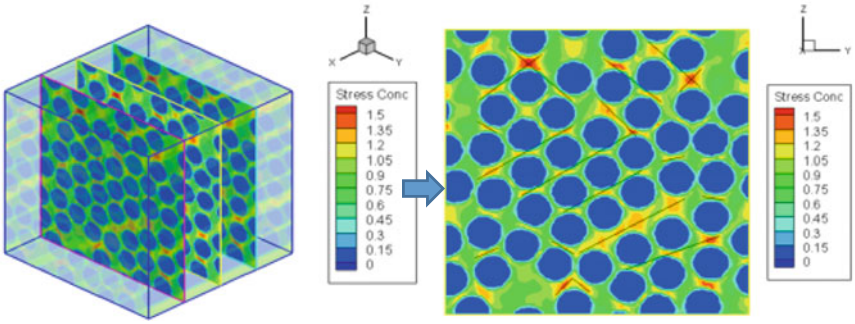

Fig. 7 Compression through-the-thickness ε_{33}^{c} loading on RVE (1)

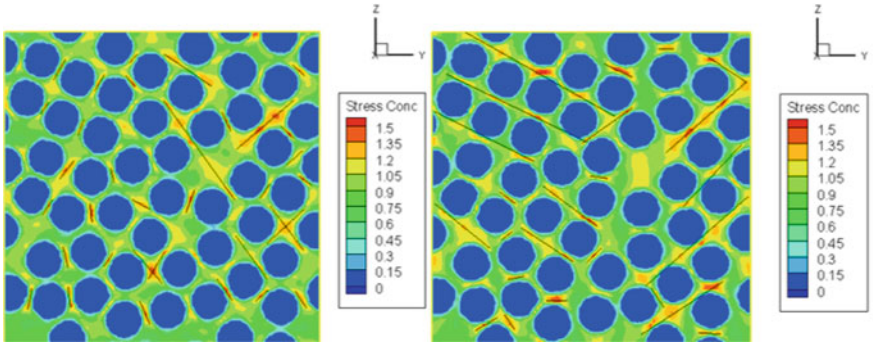

(a) (b)

Fig. 8 Transverse compression on RVE (2). **a** Compression along ε_{22}^{c}. **b** Compression along ε_{33}^{c} loading

the result of RVE (1) and (2) in this paper because of a large amount of data for which the scope of this paper cannot accommodate.

3.4 Weak Plane Analysis Using Weibull and Histogram Distribution

The weak plane angles for one RVE have been shown with normal distribution plotted in Fig. 9 to illustrate the scattering in the composite lamina's weak plane angle at macro compressive strains ε_{22}^{c} and ε_{33}^{c}.

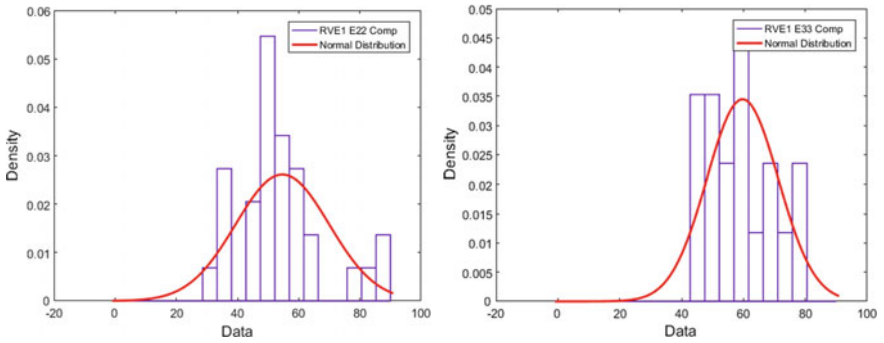

(a) (b)

Fig. 9 Normal distribution for fracture plane angle for RVE (1). **a** ε_{22}^{c} loading, **b** ε_{33}^{c} loading

3.5 Validation of the Result

According to González et al. [9], failure occurs along the plane perpendicular to the loading direction, as given in Fig. 10b. It is evident from Fig. 10b that microscopic cracks are due to shear band formation along an inclined plane.

Puck and Schürmann [5] and Pinho et al. [6] have found the value of weak plane as $53 \pm 2°$ for transverse compression of polymer matrix composite using the analytical technique. In the current work, the fracture angle is calculated with micromechanical analysis carried on the randomly distributed fibers in the RVEs, which reflects much more realistic in terms of fiber arrangement in the lamina cross-section. The fracture plane angles are found between 29.264 and 88.091° under transverse compression in ε_{22}^{c} case with a mean angle of fracture plane as 52.478°. Similarly, we can consider

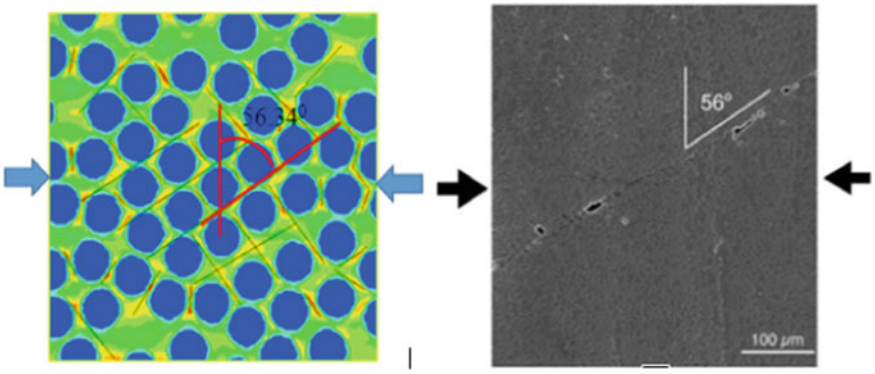

(a) (b)

Fig. 10 Comparison of fracture plane angle carbon/epoxy loaded under transverse compression. **a** Current analysis, **b** scanning electron microscope (SEM) [5]

Table 3 Fracture plane angle of the four RVEs and their average value when the RVE subjected to transverse compression (ε_{22}^{c}, ε_{33}^{c}) loading in current micromechanical analysis

RVE	RVE (1) (°)	RVE (2) (°)	RVE (3) (°)	RVE (4) (°)
ε_{22}^{c}**loading**				
Mean	52.478	56.036	58.942	56.748
Standard deviation	15.203	13.735	13.942	13.283
Minimum angle	29.264	28.610	35.455	38.290
Maximum angle	88.091	82.875	84.596	84.289
ε_{33}^{c}**loading**				
Mean	57.432	56.737	55.054	57.284
Standard deviation	11.538	16.424	13.900	11.785
minimum angle	41.987	32.881	32.470	37.875
Maximum angle	79.875	89.998	82.875	87.510
The average of the average mean value of ε_{22} and ε_{33} is equal to 56.34°				

ε_{33}^{c} case as a particular case of transverse loading, and we found a fracture plane angle between 41.987 and 79.875° with a mean angle of 57.432°. Table 3 shows the fracture plane angle values for each RVEs and their average of average mean values (as given in Fig. 8), which are taken to be a fracture plane angle of a particular UDFRPC. The average of averaged mean values of the fracture plane angle is observed to be 56.34°.

4 Conclusion

In this micromechanics-based approach, we obtained the homogenized material properties for four RVEs of carbon fiber reinforced polymer epoxy material. In the comparison of the computational results, the average values of E_1, G_{12}, and G_{13} are less than 10% of the deviation from the experimental values, whereas ν_{12} and ν_{13} are around 10% and E_2, E_3, G_{23}, and ν_{23} are deviated by 17%, 17%, 15.6%, and 27.5%, respectively. However, the current analysis results are not much deviated from the experimental work of Soden et al. [8], simulated results of Koley et al. [3], in which the mathematical theory of homogenization was used to determine the effective properties in the composite except the G_{12} and G_{13} properties. The unit strain boundary conditions used in the shear direction are overestimating the material elastic properties in the corresponding direction. The average fracture plane (or weak plane) angle for the transverse compression loading along ε_{22} and ε_{33} is found to as 56.34°. This value is comparable with both the analytical and experimental works of many authors.

To conclude, the current analysis provides the following advantage over the existing analytical models through the micromechanics of material homogenization.

1. This approach enables us to find both the effective properties and the fracture plane angle of UDFRPCs from a simple RVE analysis.
2. The statistical average fracture plane angle for the transverse compression loading along ε_{22} and ε_{33} is found to as 56.34°.

References

1. Hollister SJ, Kikuchi N (1992) A comparison of homogenization and standard mechanics analyses for periodic porous composites. Comput Mech 10(2):73–95
2. Hill R (1963) Elastic properties of reinforced solids: some theoretical principles. J Mech Phys Solids 11(5):357–372
3. Koley S, Mohite PM, Upadhyay CS (2019) A micromechanical study and uncertainty quantification for effective properties of unidirectional fibre reinforced composites. Compos Struct 225:111141
4. Semayat F, Mouli YSC, Upadhyay CS, Mohite PM (2020) Micromechanics based technique of material homogenization and determination of fracture plane in advanced composites, In: Maiti DK, Maiti D, Patra PK, Jana P, Mistry CS, Choshal R, Afzal MS (eds) Proceedings of the 1st online conference on international conference on recent advances in computational and experimental mechanics (ICRACEM), September 4–6, 2020, IIT Kharagpur, Papaer id: AM-20-051
5. Puck A, Schürmann H (2004) Failure analysis of FRP laminates by means of physically based phenomenological models. In: Failure criteria in fibre-reinforced-polymer composites. Elsevier, Amsterdam, pp 832–876
6. Pinho ST, Iannucci L, Robinson P (2006) Physically-based failure models and criteria for laminated fibre-reinforced composites with emphasis on fibre kinking: Part I: Development. Compos A Appl Sci Manuf 37(1):63–73
7. Daniel IM, Luo JJ, Schubel PM, Werner BT (2009) Interfiber/interlaminar failure of composites under multi-axial states of stress. Compos Sci Technol 69(6):764–771
8. Soden PD, Hinton MJ, Kaddour AS (2004) Lamina properties, lay-up configurations and loading conditions for a range of fibre reinforced composite laminates. In: Failure criteria in fibre-reinforced-polymer composites. Elsevier, Amsterdam, pp 30–51
9. González C, LLorca J (2007) Mechanical behavior of unidirectional fiber-reinforced polymers under transverse compression: microscopic mechanisms and modeling. Compos Sci Technol 67(13):2795–2806
10. Totry E, González C, LLorca J (2008) Failure locus of fiber-reinforced composites under transverse compression and out-of-plane shear. Compos Sci Technol 68(3–4):829–839
11. LLorca J, González C, Molina-Aldareguía JM, Segurado J, Seltzer R, Sket F, Rodríguez M, Sádaba S, Muñoz R, Canal LP (2011) Multiscale modeling of composite materials: a roadmap towards virtual testing. Adv Mater 23(44):5130–5147

A Review of Prediction of Stress State in a Concrete Member Using Ultrasonic Wave Velocity

Aayush Joshi and Kranti Jain

1 Introduction

Concrete structures are in a process of gradual deterioration and require routine maintenance [1]. On-time detection of distress is required so that proper preventive maintenance can be done. If the deterioration remains undetected at the early stages it can be hazardous and require costly repairs. Non-destructive testing is a very important tool to assess the condition of an existing concrete structure and they impart none or very insignificant damage to the concrete structure. On-time assessment of structural distress is also important so that proper retrofitting measures can be taken to prevent preterm failure of structure [2]. Ultrasonic pulse velocity testing is one of the NDT methods used to inspect the quality and homogeneity of concrete [3]. An ultrasonic wave (frequency more than 20 Hz) is made to pass through a concrete and the time of flight is recorded. This time of flight can be used to calculate the velocity of the wave. The wave velocity is directly related to the strength of the concrete. UPV is also used to find the elastic modulus of a material. The wave propagation in a material depends upon many factors such as surface condition, moisture content, path length, temperature, reinforcement bars, and stress [4]. Ultrasonic pulse velocity can be potentially used to evaluate the stress state of a member. This method for the evaluation of stress is based on the theory of acoustoelasticity. This method based on acoustoelasticity is harmless and advantageous as it can be used on real structures without any pre-treatment.

A. Joshi (✉)
Women Institute of Technology, Suddhowala, Dehradun, Uttarakhand 248001, India
e-mail: aayushjoshi.phd19@nituk.ac.in

A. Joshi · K. Jain
National Institute of Technology, Pauri Garhwal, Srinagar, Uttarakhand, India
e-mail: jainkranti08@nituk.ac.in

D. K. Maiti et al. (eds.), *Recent Advances in Computational and Experimental Mechanics, Vol II*, Lecture Notes in Mechanical Engineering,
https://doi.org/10.1007/978-981-16-6490-8_6

2 Theory

2.1 Acoustoelasticity

Acoustoelasticity is the stress dependency of a mechanical wave. Acoustoelastic refers to the change in propagation velocities of ultrasonic waves when a non-linear elastic solid is subjected to stress or strain [2]. The theory of acoustoelasticity is based on Murnaghan's [5] theory of finite deformation and non-linear elasticity. Based on this theory, equations representing the acoustoelastic effect were developed by Hughes and Kelly [6]. The velocities of waves derived are as follows.

$$\rho_o V_{11}^2 = \lambda + 2G + \frac{\sigma_{11}}{3K}\left[2l + \lambda + \frac{\lambda + 2G}{G}(4m + 4\lambda + 10G)\right] \tag{1}$$

$$\rho_o V_{12}^2 = \rho_o V_{13}^2 = G + \frac{\sigma_{11}}{3K}\left[m + \frac{\lambda n}{G} + 4\lambda + 4G\right] \tag{2}$$

$$\rho_o V_{22}^2 = \rho_o V_{33}^2 = \lambda + 2G + \frac{\sigma_{11}}{3K}\left[2l - \frac{2\lambda}{G}(m + \lambda + 2G)\right] \tag{3}$$

$$\rho_o V_{21}^2 = \rho_o V_{31}^2 = G + \frac{\sigma_{11}}{3K}\left[m + \frac{\lambda n}{4G} + \lambda + 2G\right] \tag{4}$$

$$\rho_o V_{23}^2 = \rho_o V_{32}^2 = G + \frac{\sigma_{11}}{3K}\left[m + \frac{\lambda + G}{4G}n - 2\lambda\right] \tag{5}$$

$$K = \lambda + \frac{2}{3}G \tag{6}$$

The Eqs. (1), (2), (3), (4) and (5) when linearized at first-order results in the Eq. (7) [7].

$$V_{ij}^{\sigma} = V_{ij}^{0}\left(A_{ij}\sigma_{11} + 1\right) \tag{7}$$

In the above equations, V_{ij} is the wave velocity where the first index represents the axis of propagation and the second index represents the axis of polarization (i, $j = 1, 2$ or 3). σ_{11} is stress applied, ρ_o is the initial density of a material, K is the bulk modulus, λ is lame's first parameter, G is dynamic shear modulus, l, m, n are Murnaghan's constant.

A_{ij} is the acoustoelastic constant and depends on Murnaghan's constants (l, m, n) and Lame's coefficient (λ, G), with the help of velocity of the ultrasonic wave the acoustoelastic constants can be calculated.

Initial researches were carried out on polystyrene, iron, and Pyrex glass by Huges and Kelly [6]. Propagation of Rayleigh wave under homogeneous stress in polymethylmethacrylate was studied by Wei et al. [8] and it was observed that wave

velocity and stress were linearly dependent. Chaki and Bourse [9] studied the tensile stress level in a pre-stressed steel tendon using acoustoelastic theory. Egle and Bray [10] predicted residual stress in rail-road steel and their results were following the theory of acoustoelasticity by Huges and Kelly. Payan et al. [11] calculated the third-order elastic constants in a uniaxial loaded concrete specimen using ultrasonic pulse velocity. This method was originally based on geophysics and used coda waves to evaluate stress in concrete. Sauris and Fernando [12] studied the effect of stress in the amplitude of the ultrasonic waves. Nougueira and William [13] also confirmed their observation. Lilamand et al. [7] studied the acoustoelastic effect in concrete prism at various load levels and confirmed the stress dependency of ultrasonic waves.

2.2 Microcracking

Apart from the acoustoelastic effect, the speed of the ultrasonic wave depends upon many other factors, the speed of ultrasonic waves in a solid is governed by microcracking. Microcracking plays a significant role in the propagation of a wave when the material is subjected to higher loads. Generally, with the increasing load, the microcracks are generated in concrete, initially, the microcracks are formed at the surface level and as the load increases the microcracks propagates towards the interior and then further gets converted into macro cracks which ultimately leads to failure of the member [14]. Hudson [15] devolved a crack model which was used to find the distribution and orientation of microcracking. The velocity of waves depends upon the intensity and orientation of microcracks [9]. Nougueira and William [13] estimated microcrack growth in concrete using changes in the amplitude of ultrasonic waves. Kroggel and Wilhelm [16] studied changes in amplitude for cyclic loading and found out that concrete preserves the stress memory following the Kaiser effect. At high stresses, the sensitivity of amplitude toward the stress state is higher than the velocity [2]

3 Experimental Setup

In the past researches, experiments were conducted on concrete prism and cylinders of various sizes [1, 2, 7, 14]. For the measurement of the ultrasonic wave velocity, an ultrasonic pulse velocity tester was used. The experiment setup used by most of the researchers was common and simple. The ultrasonic wave velocity was measured using two similar piezoelectric transducers (one used as an emitter and another as a receiver). Many researchers [1, 2, 7] measured the velocity of the longitudinal wave while some [1, 7] measured the velocity of both longitudinal and transverse waves. The direction of polarization and direction of propagation was also considered while experimenting. Some of the researchers [2] have measured ultrasonic velocity in both loading and unloading phases and interesting results were obtained. A common

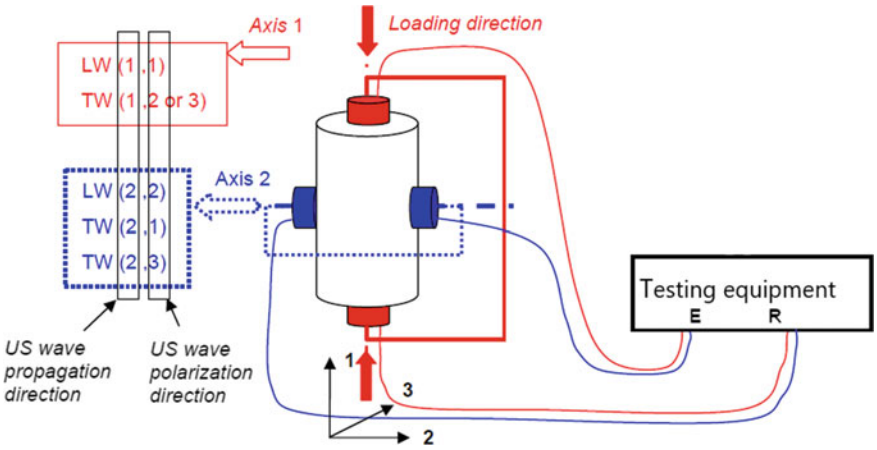

Fig. 1 Experimental setup and index meaning [7]

nomenclature system is followed for all the measurements, for example, LW*ij* stands for a longitudinal wave propagating along *i* direction and polarized along *j* direction and TW*ij* stands for a transverse wave propagating along *i* direction and polarized along *j* direction [7] (Fig. 1).

Microcracking patterns were recorded at different load levels using an acoustic emission testing machine. The sensors were placed on the surface of the material and were held in place using a wood casing. As the load increases, microcracks are generated, at every load level, the acoustic emission was measured for around 30 s after the last acoustic activity observed in the material [2]. The acoustic emission testing was done in parallel with wave velocity measurement and cyclic loading was applied to study the stress memory of concrete.

4 Result, Observation, and Discussion

The velocity of ultrasonic wave propagation in the material was observed to be stress-dependent, however, the dependency varies as the intensity of loading was changed. The velocity was also dependent on the direction of propagation of the wave, direction of polarization of wave, and direction of loading.

The following points were observed in this study.

1. At low-stress levels from 15 to 45% of ultimate load, the wave velocity increases almost linearly due to the closure of microcracks and the material particles come closer to each other. The acoustic emission observed was less and microcracking did not play any significant role at this load level. The relation between stress and wave velocity was simple here and the easiest to predict. Also, the stress level in

concrete in this load level can be predicted using the theory of acoustoelasticity only.

2. At stress levels from 45 to 80%, the velocity remains almost constant and there is a very slight increase as the microcracks expand and new microcracks were generated. The acoustic emission observed at this load level were significant and microcracking affected the ultrasonic wave velocity to a significant extent. The relation between stress and wave velocity is complex as microcracking comes into play, still, a correlation can be observed and stress level can be predicted.
3. At a stress level above 80%, the wave velocity drops drastically as microcracks develop into macro cracks. The acoustic emission observed here was the highest of all and microcracking dominated over the acoustoelastic effect. The relationship between stress and wave velocity is much more complex at this load level as microcracking dominates and macro cracks are generated. It is very difficult to predict stress levels using ultrasonic waves under this load level.
4. The wave velocity measured and acoustic emission data observed were found to be in good accordance with the Kaiser effect (stress memory effect).
5. The velocity was most sensitive when the direction of propagation and direction of polarization was along the direction of loading. The maximum velocity variation was observed for LW1. It was observed that the LW1 wave was 5 times more sensitive than the LW2 wave and the TW2 wave was 3 times more sensitive than TW1 or TW23 waves.
6. At higher stresses generally above 40% of the strength amplitude was more sensitive toward the stress as compared to velocity [12], generally at the same loading microcracks started to propagate inwards and new microcracks were generated extensively [2].
7. The acoustoelastic effect in concrete is 10 times more than that was observed in steel [7].

5 Conclusion

The review enhances the knowledge of stress dependency of ultrasonic waves. The ultrasonic wave velocity observed was observed highly stress dependent. The longitudinal and transverse wave polarizes along the direction of loading (LW1 and TW2) showed the largest variation. The stress evaluation using ultrasonic wave variation in concrete was possible by determining the acoustoelastic constants; however, in concrete measuring the ultrasonic velocity is difficult due to multiple scattering, a guided wave can be used which may overcome the problem to some extent. Also, it was observed in the study that the stress distribution while loading was not perfectly uniform, a further improved experimental setup can be used to develop the uniform stress in the specimen. Moreover, all the studies were performed under laboratory conditions and fresh concrete specimens were used; however, in situ conditions may

vary, and the results thus obtained may vary. This obstacle can be resolved in further study. An investigation can be done to assess the effect of creep and fatigue loading on the velocity of ultrasonic waves. This, in general, can improve the practicality of the non-destructive testing of concrete.

References

1. Bompan KF, Haach VG (2018) Ultrasonic tests in the evaluation of the stress level in concrete prisms based on the acoustoelasticity. Constr Build Mater 162:740–750. https://doi.org/10.1016/j.conbuildmat.2017.11.153
2. Shokouhi P, Zoëga A, Wiggenhauser H, Fischer G (2012) Surface wave velocity-stress relationship in uniaxially loaded concrete. ACI Mater J 109(2):141–148
3. Jhang K (2020) Applied sciences stress estimation using the acoustoelastic effect of surface waves in weak anisotropic materials
4. IS 13311(Part 1) (1992) Methods of non-destructive testing of concrete: part 1 ultrasonic pulse velocity. Bureau of Indian Standards, New Delhi
5. Murnaghan FD (1951) Finite deformation of an elastic solid (Applied mathematics series). Wiley, New York
6. Hughes DS, Kelly JL (1953) Second-order elastic deformation of solids. Phys Rev 92(5):1145–1149. https://doi.org/10.1103/PhysRev.92.1145
7. Lillamand I, Chaix JF, Ploix MA, Garnier V (2010) Acoustoelastic effect in concrete material under uni-axial compressive loading. NDT and E Int 43(8):655–660. https://doi.org/10.1016/j.ndteint.2010.07.001
8. Wei Z, Zhou X, Cheng Y (2000) Acoustoelastic determination of local surface stresses in polymethylmethacrylate. Appl Acoust 61(4):477–485
9. Chaki S, Bourse G (2009) Guided ultrasonic waves for non-destructive monitoring of the stress levels in prestressed steel strands. Ultrasonics 49(2):162–171
10. Egle DM, Bray DE (1976) Measurement of acoustoelastic and third-order elastic constants for rail steel. J Acoust Soc Am 60(3):741–744
11. Payan C, Garnier V, Moysen J (2009) Determination of third order elastic constants in a complex solid applying coda wave interferometry. Appl Phys Lett 94(1):3
12. Suaris W, Fernando V (1987) Detection of crack growth in concrete from ultrasonic intensity measurements. Mater Struct 20:214–220
13. Nogueira CL, Willam KJ (2001) Ultrasonic testing of damage in concrete under uniaxial compression. ACI Mater J 98(3):265–275
14. Jin J, Moreno MG, Riviere J, Shokouhi P (2017) Impact-based nonlinear acoustic testing for characterizing distributed damage in concrete. J Nondestr Eval 36(3):1–16
15. Hudson JA (1981) Wave speeds and attenuation of elastic waves in materials containing cracks. Geophys J Roy Astron Soc 64:133–150
16. Kroggel O, Wilhelm T (2006) Stress-memory of concrete—ultrasonic investigations. In: 2nd international RILEM symposium on advances in concrete through science and engineering. RILEM Publications SARL, pp 207–224

Simulation of Cyclic Mean Stress Relaxation and Ratcheting for Aluminium 7050 Alloy

Atri Nath, Ritwik Ghoshal, Sudhirkumar V. Barai, and Kalyan Kumar Ray

1 Introduction

Understanding of material behaviour through modelling and simulation under different loading conditions, especially in the elastic–plastic regime, is of extreme importance for the analysis and design of different engineering components made of conventional as well as advanced structural materials. The modelling of engineering components under cyclic loading requires attention to added complexities due to the consideration of the associated cyclic-plastic phenomena like Bauschinger effect, cyclic hardening/softening, and Masing/non-Masing behaviour. However, the fatigue loading in asymmetrical conditions under strain- and stress-controlled cyclic loading is characterized primarily by the two phenomena: (a) cyclic mean stress relaxation and (b) ratcheting respectively.

Cyclic mean stress-relaxation refers to the progressive shift of the hysteresis loops under asymmetric strain-controlled cycling such that the mean stress in a cycle stabilizes to zero mean stress level caused due to the plastic range [1–4]. A schematic representation of the stress–strain response for a metallic material under asymmetric strain-controlled cyclic loading is illustrated in Fig. 1a; the stabilization of the mean stress as the number of cycles are increased is demonstrated in Fig. 1b. The rate of mean stress relaxation for a material depends on the loading conditions and the

A. Nath (✉) · S. V. Barai
Department of Civil Engineering, IIT Kharagpur, Kharagpur, India

R. Ghoshal
Department of Ocean Engineering and Naval Architecture, IIT Kharagpur, Kharagpur, India

S. V. Barai
Department of Civil Engineering, BITS Pilani, Pilani, India

K. K. Ray
Department of Metallurgical and Materials Engineering, IIT Kharagpur, Kharagpur, India

D. K. Maiti et al. (eds.), *Recent Advances in Computational and Experimental Mechanics, Vol II*, Lecture Notes in Mechanical Engineering,
https://doi.org/10.1007/978-981-16-6490-8_7

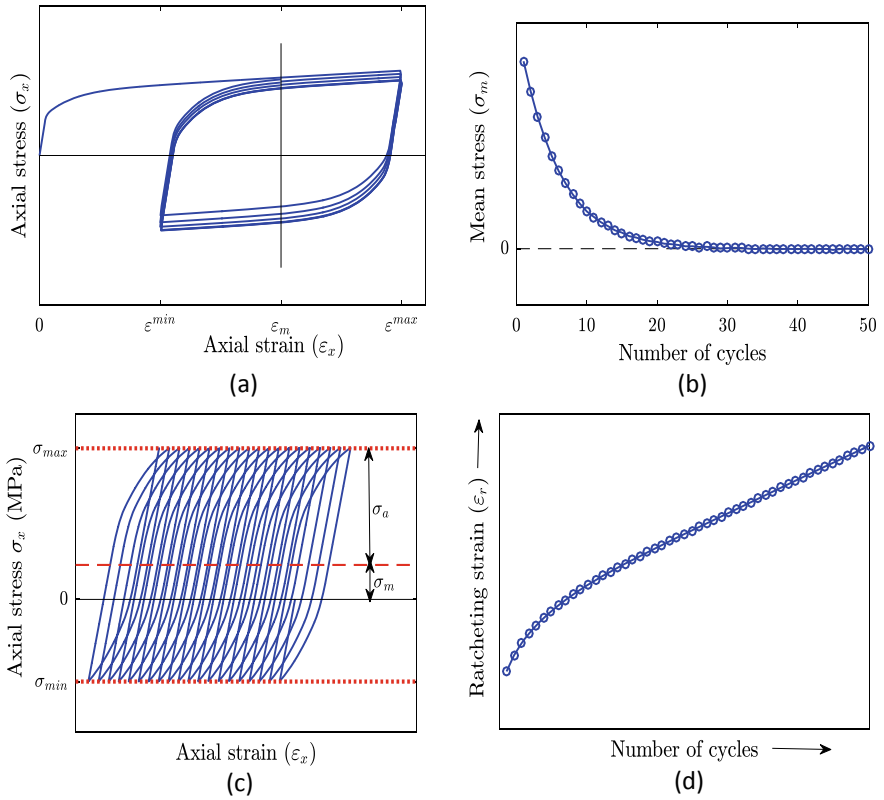

Fig. 1 Schematic representation of the mean-stress relaxation under asymmetric strain-controlled cycling and ratcheting response under asymmetric stress-controlled cycling. (**a**) Stress–strain response and (**b**) stabilization of mean stress (σ_m) with increasing number of cycles indicating mean stress relaxation. (**c**)Shift of hysteresis loops under asymmetric stress-controlled cycles, and (**d**) growth of ratcheting strain (ε_r) with increasing number of cycles

component geometry [3]. Typically, the mean stress in a cycle for asymmetric strain-controlled cycling stabilizes at an exponential rate, and the rate of relaxation decreases with the increasing number of cycles [4]. The rate of cyclic stress-relaxation increases with the increase in the magnitude of strain amplitude, but typically it is independent of the sign of the mean strain value for the asymmetric strain-controlled cycling [5].

A material subjected to asymmetric stress-controlled fatigue loading exhibits an accumulation of deformation (or plastic strain) in the direction of mean stress, if the loading is sufficiently high to induce plasticity; this phenomenon is termed as ratcheting [1, 2]. The ratcheting phenomenon is schematically demonstrated in Fig. 1c, where progressive movement of the hysteresis loops is observed in the direction of the mean stress with an increasing number of cycles, i.e., the mean strain in a cycle increases with the increasing number of cycles (Fig. 1d). Ratcheting is important from the design perspective as excessive strain accumulation may result in large

deformation leading to failure [2]. Experimental investigations on various metals and their alloys indicate that the ratcheting behaviour is dependent upon stress amplitude, mean stress, prehistory, as well as on the rate of loading [1–3].

The progressive shift of the hysteresis loops with the number of cycles typically encountered in asymmetric fatigue loading is usually replicated using only kinematic hardening [4–7]. The isotropic hardening component which is usually associated with cyclic hardening or softening behaviour is thus neglected while simulating the cyclic-plastic phenomena arising due to asymmetric loading conditions like mean stress relaxation and ratcheting for materials [4, 8]. The neglect of the contribution of the isotropic hardening component in the constitutive modelling questions the generalized nature of the existing approaches to model the cyclic-plastic response for a material under asymmetric loading cycles.

Nath et al. [1] have recently proposed a methodology considering combined isotropic-kinematic hardening model to obtain close predictions for the cyclic-plastic behaviour and have demonstrated its applicability to examine reported results on various ferrous and non-ferrous alloys [2, 9] under different strain-controlled and stress-controlled loading conditions. The major objective of this study is to demonstrate the applicability of this methodology for simulating the cyclic mean stress relaxation and ratcheting phenomena for AA7050 aluminium alloy reported by Hu et al. [10]; this is intended at the broader aim to assess the generalized nature of the proposed approach by Nath et al. [1]. The simulated cyclic-plastic response for the AA7050 alloy indicating mean stress relaxation under cyclic loading and the ratcheting behaviour obtained by the present approach is compared against the experimental (by Hu et al. [10]) and the reported predictions by Kourousis and Dafalias [8].

2 Methodology

The methodology proposed by Nath et al. [6] to simulate the cyclic-plastic response of metallic materials is used in the current study. The adopted approach considers the combined hardening model proposed by Chaboche [11]; the parameters of the Chaboche model are initially estimated from stabilized hysteresis loops. The preliminary set of parameters are subsequently optimized using genetic algorithm optimization technique to obtain closer cyclic-plastic simulations for a material. The methodology used in the present study is discussed in details in the following subsections.

2.1 Adopted Cyclic-Plastic Model

The approach considers the combined hardening model proposed by Chaboche et al. [11] incorporating nonlinear isotropic hardening component along with a kinematic

hardening part. Table 1 summarizes the mathematical formulation of the Chaboche's isotropic-kinematic hardening (CIKH) model used in the current study. The yield surface for the CIKH model considers the von-Mises yield criterion (Eq. (1), Table 1). The evolution of the isotropic hardening component (R) is governed by the parameters Q and b following Eq. (2). The kinematic hardening is constituted of four backstress components (Eq. (3), and the evolution of each of the backstress components ($\alpha_{i=1 \text{ to } 4}$) is nonlinear in nature. The parameter C_i physically represents the initial slope of the i^{th} backstress and the parameter γ_i which controls the rate of individual backstress evolution (Eq. (5), Table 1); consideration of $\gamma_i = 0$ results in a linear i^{th} backstress component [6, 7, 9–13].

2.2 *Preliminary Estimation of Isotropic Hardening Parameters*

The capability of a model to replicate the experimentally observed response under different loading modes depends not only on the model itself but also on the procedure to determine the parameters of the model. The adopted methodology considers the determination of the preliminary estimate of the parameters of the CIKH model from the stabilized hysteresis loops (SHL). The approach proposed by Nath et al. [6] utilizes the reported SHL under symmetric strain-controlled fatigue loading for different materials; however, SHL obtained under asymmetric loading conditions can also be considered for estimation of the preliminary set of parameters of the hardening model. The maximum variation of the yield surface is physically represented by the parameter Q. Consideration of a positive magnitude of this parameter results in the increase of stress amplitude with increasing cycles under symmetric strain-controlled fatigue loading as observed in cyclic hardening materials, while a negative Q is used to simulate cyclic softening behaviour [6]. The difference between the initial yield stress (σ_{y0}) and the stabilized yield stress is used as an estimate for the parameter Q, i.e.,

Table 1 Mathematical formulation of the CIKH model used in the present study [2]

$f = \sqrt{3/2(S-\alpha) : (S-\alpha)} - \left(\sigma_{y0} + R\right) = 0$
$\dot{R} = b(Q - R)\dot{p}$ (2)
$\dot{p} = \sqrt{\left(2/3\dot{\varepsilon}_p : \dot{\varepsilon}_p\right)}$ (3)
$\alpha = \sum_{i=1}^{4} \alpha_i$ (4)
$\dot{\alpha}_i = 2/3 C_i \dot{\varepsilon}_p - \gamma_i \alpha_i \dot{p} \quad i = 1, 2, 3, 4$ (5)

E = Young's modulus; S = deviatoric stress; R = isotropic hardening component governed by parameters b and Q; σ_{y0} = Initial yield stress; α = kinematic hardening component; α_i = backstress components governed by parameters C_i and γ_i; $\dot{p}$=accumulated plastic strain rate; $\dot{\varepsilon}_p$=plastic strain rate

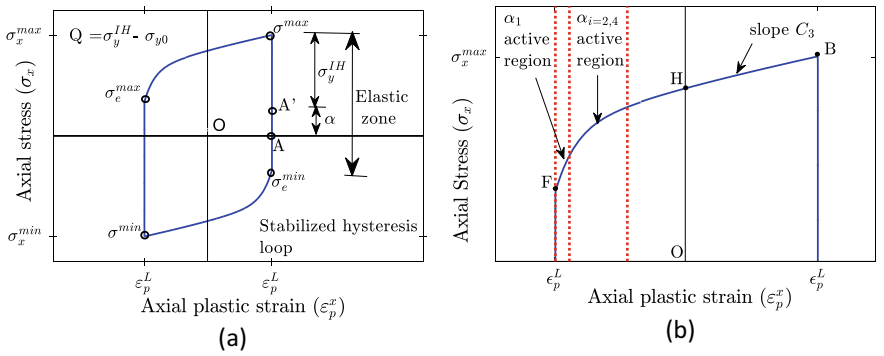

Fig. 2 Estimation of the CIKH model parameters from the stabilized hysteresis loops, (**a**) parameter Q from the size of the elastic zone and (**b**) kinematic hardening parameters following Rahman et al. [12]

$$Q = \sigma_y^{IH} - \sigma_{y0}, \tag{6}$$

where σ_y^{IH} is the yield stress of the stabilized hysteresis loops (SHL) determined as half of the length of the elastic zone for the SHL as indicated in Fig. 2a. The initial value of yield stress (σ_{y0}) is considered here as the maximum stress at which the stress–strain response under monotonic tensile test or in the tensile quarter of the first cycle in a tension to compression loading cycle deviates from the linear elastic portion, i.e., the slope of the stress–strain curve changes.

The parameter b governs the rate of saturation of the isotropic hardening component; a smaller magnitude (<20) of parameter b is used to simulate cyclic hardening or softening materials, whereas a larger magnitude of the same stabilizes the isotropic hardening rapidly indicating cyclic stable behaviour [1]. The influence of parameter b on the cyclic-plastic response under strain-controlled as well as stress-controlled fatigue loading, as well as the method to obtain its initial estimate for a material has been discussed in details by Nath et al. [6, 7]. The parameter b is estimated by fitting the variation of the size of the elastic zone with increasing number of cycles. Estimation of the isotropic hardening parameters Q and b considering the variation of the elastic zone size instead of that achieved from the fitting the variation of stress amplitude (or maximum stress) with increasing number of cycles provide closer predictions for the cyclic-plastic behaviour of materials [6, 7].

2.3 *Preliminary Estimation of Kinematic Hardening Parameters*

The preliminary estimate for the kinematic hardening parameters is obtained from the transition portion of the stabilized hysteresis loop, as depicted in Fig. 2b, following

the approach proposed by Rahman et al. [14]. Each of the backstresses dominates a part of the stress–strain response after the onset of yielding, the parameters related to each backstress can be estimated from their respective physical meanings. The first backstress component (α_1) is operative immediately after initiation of plastic deformation, thus has a high initial plastic modulus, but with rapid stabilization (Fig. 2b). This is simulated using a large values for the parameters C_1 and γ_1 [4]; the slope of the stress (σ_x) vs axial plastic strain (ε_x^p) curve after the yield point for the SHL (point F) is considered as the preliminary estimate for C_1. The third backstress component (γ_3) is almost linear, the small amount of non-linearity to its evolution by considering a non-zero value of the parameter γ_3 is considered for better ratcheting simulations [1, 4]; the slope of the linear portion (segment HB, Fig. 2b) of the σ_x vs ε_x^p curve obtained at high strain range provides the magnitude of the parameter C_3. The preliminary estimate of the remaining parameters of the CIKH model (i.e., C_2, C_4, γ_2, γ_3, γ_4) is obtained using the following expression [12]:

$$C_1/\gamma_1 + C_2/\gamma_2 + C_4/\gamma_4 + \sigma_{y0} + Q = \sigma_{sat}^{max} - C_3 * \varepsilon_p^L, \tag{7}$$

where σ_{sat}^{max} is the maximum axial stress for the stabilized hysteresis loops and ε_p^L is the limiting axial plastic strain. The obtained parameters are further optimized using genetic algorithm technique to obtain closer simulations for the varied loading conditions exhibiting the investigated cyclic-plastic phenomena.

2.4 Optimization Approach for Obtaining the Final Set of Parameters

The CIKH model (summarized in Table 1) considered in the present study contains 10 parameters other than the elastic parameters viz; modulus of elasticity, E, and the monotonic yield stress, also considered here as the initial yield stress (σ_{y0}). The closeness of fit of the cyclic-plastic predictions obtained by the current approach for a material to the experimental one is assessed by considering a root mean square error (RMSE) given by:

$$RMSE = \begin{cases} \sqrt{\frac{1}{n}\sum_{i=1}^{n}\left[\left(\sigma_i^{\exp} - \sigma_i^{\text{model}}\right)/\sigma_i^{\exp}\right]^2}, & for\ strain-controlled \\ \sqrt{\frac{1}{n}\sum_{i=1}^{n}\left[\left(\varepsilon_{r,i}^{\exp} - \varepsilon_{r,i}^{\text{model}}\right)/\sigma_{r,i}^{\exp}\right]^2}, & for\ stress-controlled \end{cases} \tag{8}$$

where n denotes the number of data points, σ_i^{exp} is the stress values, and $\varepsilon_{r,i}^{exp}$ is the ratcheting strain obtained from experiments. σ_i^{model} is the predicted stress, and

$\varepsilon_{r,i}^{model}$ is ratcheting strain obtained using CIKH model. The minimization of the RMSE serves as the objective function for the subsequent optimization technique.

The expression in Eq. (8) provides us with two objective functions for two different loading conditions. The optimization problem needs to be simultaneously capable of reducing the RMSE for both the cases; the determination of parameter for this type of problems is a multi-objective one. The magnitude of RMSE obtained for the strain-controlled loading cases and that for the stress-controlled conditions are combined in the present study considering equal weightage for the material to transform the multi-objective problem into a single objective one[1, 2].

Genetic algorithm (GA) optimization procedure is considered for tuning the initially estimated parameters of the hardening model to obtain cyclic-plastic simulations for a material that is suitably close to the experimental results, following Rahman et al. [12], and subsequently used by Nath et al. [1, 2, 9]. The GA technique performs a heuristic search of the feasible space defined by the upper and the lower bounds to find the global minima of a multi-variate function. The considered GA procedure iteratively reduces the magnitude of the RMSE; the number of generations of 20, a mutation rate of 20%, and a population size of 300 are considered in the present study.

3 Results and Discussions

The methodology detailed in Sect. 2 is next applied to simulate the deformation behaviour under asymmetric cyclic loading for aluminium alloy 7050–T7451, as reported by Hu et al. [10]. The mean and amplitude values for the examined loading conditions are estimated from the hysteresis loops reported by Hu et al. [10] for the considered material and are summarized in Table 2. The magnitude of yield stress and Young's moduli are estimated from the reported stress–strain curves in the tensile part of the first strain-controlled cycles (Fig. 4, Hu et al. [10]).

The methodology by Nath et al. [1] considers the estimation of the parameters for the Chaboche isotropic-kinematic hardening (CIKH) model based on the stabilized hysteresis loop obtained for symmetric strain-controlled cycling. However, Hu et al. [10] have not reported the cyclic-plastic response of the examined material under symmetric fatigue loading. For aluminium alloy 7050–T7451, Hu et al. [10] have

Table 2 Details of the considered loading parameters of the asymmetric cyclic loading for aluminium alloy 7050 reported by Hu et al. [10]

	Strain-controlled cyclic loading	Stress-controlled cyclic loading
Amplitude	0.9%	394 MPa
Mean	1.1%	70 MPa
Number of cycles	60	11

observed that the mean stress stabilizes to a zero value at approximately 60 cycles under asymmetric strain-controlled cyclic loading and have considered the stress–strain behaviour for the 60th cycle as the stabilized hysteresis loop; the reported hysteresis loop [10] for the 60th cycle has been used in the present study to estimate the parameters of the CIKH model.

The final set of CIKH model parameters for the aluminium alloy 7050–T7451 obtained by using the discussed approach is presented in Table 3; this set of parameters are used for the analysis of the cyclic-plastic response of the materials under asymmetrical loading conditions. Hu et al. [10] and Kourousis and Dafalias [8] have considered the peak strain (ε_{max}) in a cycle as a measure of the ratcheting strain (ε_r) for 7050 aluminium alloy; the ε_{max} in a cycle is used in the present study to analyze the ratcheting behaviour of the examined material for the sake of comparison.

The parameters summarized in Table 3 obtained using the present approach provide a suitable simulation of the cyclic mean stress relaxation phenomena as indicated in Fig. 3a. However, better ratcheting simulations are obtained using the present methodology than that reported by Kourousis and Dafalias [8] for the same material for the experimental behaviour [10], as is observed in Fig. 3b. The closeness of fit of the simulated response with the experimental behaviour for 7050 aluminium alloy under asymmetric loading conditions is quantified using the root mean square error (RMSE) and is compared against that computed for the reported predictions by Kourousis and Dafalias [8] as well as against predictions obtained with the parameters reported by Hu et al. [10] in Fig. 4.

Hu et al. [10] have used combined hardening model proposed by Chaboche [5]; the kinematic hardening component considered by Hu et al. [10] is composed of three

Table 3 Parameters of the cyclic-plastic model obtained using the present approach for aluminium alloy 7050 and that reported by Hu et al. [10] and Kourousis and Dafalias [8]

Parameters	CIKH model		MAFM model
	Present approach	Hu et al. [10]	Kourousis and Dafalias [8]
Elastic	$E = 69$ GPa $\sigma_{y0} = 289$ MPa	$E = 69$ GPa $\sigma_{y0} = 307$ MPa	$E = 69$ GPa $\sigma_{y0} = 200$ MPa
Isotropic hardening	$b = 11.9$ $Q = 12.1$ MPa	$b = 12$ $Q = 31$ MPa	Not considered
Kinematic hardening	$C_1 = 44{,}871.3$ MPa $C_2 = 29{,}087.5$ MPa $C_3 = 4847.5$ MPa $C_4 = 3059.3$ MPa $\gamma_1 = 638.5$ $\gamma_2 = 229.1$ $\gamma_3 = 4.3$ $\gamma_4 = 20.2$	$C_1 = 63{,}930$ MPa $C_2 = 9980$ MPa $C_3 = 6620$ MPa $\gamma_1 = 734$ $\gamma_2 = 728$ $\gamma_3 = 73$	$a_1^s = 1100$ MPa $a_2^s = 120$ MPa $a_3^s = 340$ MPa $a_4^s = 65$ MPa $a_4^{*s} = 0.16$ $c_1 = 4$ $c_2 = 1000$ $c_3 = 15$ $c_4 = 1800$ $c_4^* = 5000$

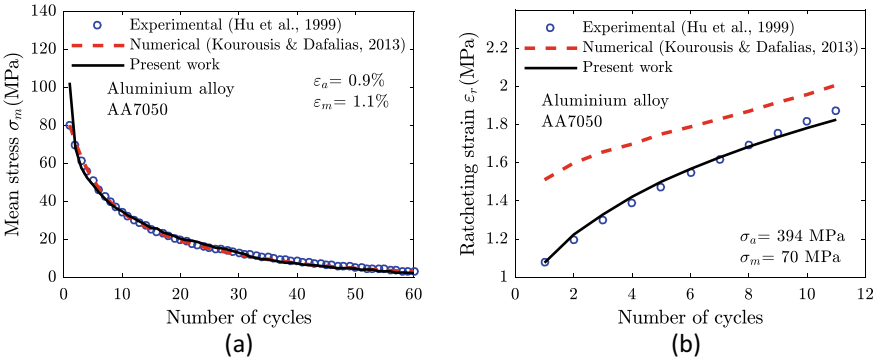

Fig. 3 Comparison of the simulated a) cyclic mean stress relaxation and b) ratcheting behaviour for AA7050 aluminium alloy obtained using the present methodology with the experimental [10] and reported simulations by Kourousis and Dafalias [8]

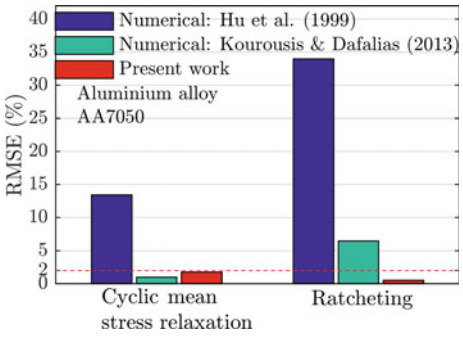

Fig. 4 Comparison of the root mean square error (RMSE) following Eq. (3) for the simulated cyclic-plastic response under asymmetric strain- and stress-controlled cyclic loading for aluminium alloy 7050 obtained using the present methodology against that reported by Hu et al. [10] and Kourousis and Dafalias [8]

backstresses, as presented in Table 3. However, the investigators have determined the parameters of the hardening model through a trial and error based approach. The magnitude of the RMSE for the simulations with the parameters reported by Hu et al. [10] are approximately 13 and 34% for strain-controlled and stress-controlled cycling, respectively. The RMSE values obtained by using the present approach is below 2% for both the cases (Fig. 4). The better simulations obtained using the present methodology than that for the parameters reported by Hu et al. [10] maybe ascribed to the adoption of genetic algorithm optimization technique for determining the parameters of the CIKH model.

Kourousis and Dafalias [8] have considered a multicomponent Armstrong-Frederick model with multiplier (MAFM) for simulating the response of aluminium alloy 7050; the investigators neglected the isotropic hardening constituent in their

constitutive model for the examined material, as summarized in Table 3. Excellent simulation for the cyclic mean stress relaxation response has been obtained by Kourousis and Dafalias [8] for 7050 aluminium alloy indicated by the low magnitude of the computed RMSE (approximately 1%), but the reported ratcheting predictions are compromised for the material (RMSE > 6%). The consistently low magnitude of RMSE for both the loading conditions (<2%) for the simulations obtained using the present methodology reveals its efficacy. The superior predictive capability of the present approach can thus be attributed to the incorporation of the isotropic hardening component coupled with a systematic approach to estimate the parameters of the combined hardening model using genetic algorithm optimization technique.

4 Conclusions

This work examines the applicability of a generalized approach based on Chaboche isotropic-kinematic hardening (CIKH) model for simulating the deformation behaviour of aluminium alloy 7050 reported by Hu et al. [10] under asymmetric fatigue loading. The adopted methodology generates a single set of parameters of the cyclic-plastic model through genetic algorithm optimization technique; the obtained parameters are used for simulating the response of the examined AA7050 alloy under asymmetric strain-controlled as well as stress-controlled fatigue. The used approach is found to generate superior cyclic-plastic simulations for the material for the considered loading conditions simulateaously, than those available in the literature. The root mean square error for the simulations obtained using the adopted methodology is below 2% for all the examined cyclic loading conditions for the material. The incorporation of the isotropic hardening component in the cyclic-plastic constitutive modelling is demonstrated to satisfactorily predict cyclic mean stress relaxation as well as ratcheting for the examined material with significant improvement in the later.

References

1. Hu W, Wang CH, Barter S (1999) Analysis of cyclic mean stress relaxation and strain ratchetting behaviour of aluminium 7050. DSTO-RR-0153. Aeronautical and Maritime Research Lab Melbourne (Australia)
2. Kourousis KI, Dafalias YF (2013) Constitutive modeling of aluminum alloy 7050 cyclic mean stress relaxation and ratcheting. Mech Res Commun 53:53–56. https://doi.org/10.1016/j.mechrescom.2013.08.001
3. Arcari A, Dowling NE (2012) Modeling mean stress relaxation in variable amplitude loading for 7075–T6511 and 7249–T76511 high strength aluminum alloys. Int J Fatigue 42:238–247. https://doi.org/10.1016/j.ijfatigue.2011.10.016
4. Meggiolaro MA, De Castro JTP, Wu H, Sanchez ECM (2016) A general class of non-linear kinematic models to predict mean stress relaxation and multiaxial ratcheting in fatigue problems

- Part II: generalized surface translation rule. Int J Fatigue 82:167–178. https://doi.org/10.1016/j.ijfatigue.2015.08.031
5. Hao H, Ye D, Chen Y, Feng M, Liu J (2015) A study on the mean stress relaxation behavior of 2124–T851 aluminum alloy during low-cycle fatigue at different strain ratios. Mater Des 67:272–279. https://doi.org/10.1016/j.matdes.2014.11.018
6. Nath A, Ray KK, Barai SV (2019) Evaluation of ratcheting behaviour in cyclically stable steels through use of a combined kinematic-isotropic hardening rule and a genetic algorithm optimization technique. Int J Mech Sci 152:138–150. https://doi.org/10.1016/j.ijmecsci.2018.12.047
7. Nath A, Barai SV, Ray KK (2019) Prediction of asymmetric cyclic-plastic behaviour for cyclically stable non-ferrous materials. Fatigue Fract Eng Mater Struct 42:2808–2822. https://doi.org/10.1111/ffe.13124
8. Paul SK, Sivaprasad S, Dhar S, Tarafder S (2011) Key issues in cyclic plastic deformation: experimentation. Mech Mater 43:705–720. https://doi.org/10.1016/j.mechmat.2011.07.011
9. Bari S, Hassan T (2000) Anatomy of coupled constitutive models for ratcheting simulation. Int J Plast 16:381–409. https://doi.org/10.1016/S0749-6419(99)00059-5
10. Chaboche JL (1986) Time-independent constitutive theories for cyclic plasticity. Int J Plast 2:149–188. https://doi.org/10.1016/0749-6419(86)90010-0
11. Chaboche JL (1991) On some modifications of kinematic hardening to improve the description of ratchetting effects. Int J Plast 7:661–678. https://doi.org/10.1016/0749-6419(91)90050-9
12. Arcari A, De Vita R, Dowling NE (2009) Mean stress relaxation during cyclic straining of high strength aluminum alloys. Int J Fatigue 31:1742–1750. https://doi.org/10.1016/j.ijfatigue.2009.01.021
13. Nath A, Barai SV, Ray KK (2019) A generalized model towards predicting monotonic and cyclic deformation behavior of cyclically stable materials. Procedia Struct Integr 23:263–268. https://doi.org/10.1016/j.prostr.2020.01.097
14. Rahman SM, Hassan T, Ranjithan SR (2005) Automated parameter determination of advanced constitutive models. In: Computer technology. ASME, vol 2, pp 261–272. https://doi.org/10.1115/PVP2005-71634

Modal Study on FGM Elliptical Plate Under Thermal Environment

Pankaj Sharma, Ashish Khinchi, and Rahul Singh

1 Introduction

Modal study is a tool required to evaluate the vibrational properties of the system such as eigenfrequencies and mode shapes. Importance of mode shapes and natural frequencies are needed to build structural components such as plate, shells, beams etc. [1]. Such modal analysis criteria can be used in many field (aeronautical field, ship construction industries, marine engineering etc.).

Elliptical plates are commonly employed in the aircraft structures (forward fuselage and aft fuselage), marine engineering (the bottom surface at the front part of a ship hull etc.), locomotive structures ("nose' of a bullet train is an ellipsoidal section etc.), mechanical and civil engineering [2, 3]. Thus modal study of elliptical shaped plate is essential. Often plate structures are required in engineering applications to support mounting and accessories. So different kind of plate structures are generally employed to modal study. As per the author's best knowledge, the modal analysis of elliptical shape plate is not explored.

Guo et al. [4] applied a modified Rayleigh–Ritz Method on modal characteristics of different shape plates such as triangular, elliptical, trapezoidal and rectangular plates. In this analysis simply supported and clamped end conditions are adopted by the author. Zhong et al. [5] examined the harmonic characteristics of multi directional FGM elliptical shaped plate, circular and sector plates. An isogeometric analysis (IGA) and high-order shear deformation theory (HSDT)-based numerical techniques

P. Sharma · R. Singh (✉)
Department of Mechanical Engineering, University Departments, Rajasthan Technical University, Kota, Rajasthan, India
e-mail: rahulsingh18@rtu.ac.in

A. Khinchi
Department of Mechanical Engineering, Vedant College of Engineering and Technology, Kota, Rajasthan, India

D. K. Maiti et al. (eds.), *Recent Advances in Computational and Experimental Mechanics, Vol II*, Lecture Notes in Mechanical Engineering,
https://doi.org/10.1007/978-981-16-6490-8_8

are implemented in this analysis. The effect of end conditions, parameters of material variation, and index of thickness variation are presented in this analysis. The modal analysis of composite thin super elliptical plate is studied by Altun-saray and Erkin [6] under clamped and simply supported end conditions. Rayleigh–Ritz approach for parametric analysis is adopted by the author. Modal study of thin elliptical shape shells carried out by Bryan [7].The eigenfrequencies and respective mode shapes are obtained with the help of angular and radial mathieu equations.

Talebitooti et al. [8] presented the modal characteristics of the FGM cylindrical shell under various end conditions under thermal effect. The author implemented the theory of Hamilton's principle, First-order shear deformation method (FSDT), Galerkin method and rule of mixture (P-FGM). Ansari et al. [9] developed the harmonic behaviour of elliptical plate. The material constants of elliptical plate are constantly varying in direction of thickness as per extended rule of mixture. In this analysis, the authors adopted the Hamilton's principle and HSDT. The harmonic behaviour of elliptical thin plate is carried out by Pradhan et al. [10] under different end conditions. The material constants of the FGM elliptical plate varied throughout direction of thickness using P-FGM. The 3D mode shapes of circular plate and elliptical plate are introduced under different boundary conditions.

Modal study of sandwich rectangular plate was carried out by Soleymani [11]. In this analysis natural frequencies are obtained by Navier analytical method. Hasheminejad [12] deals with modal study of eccentric clamped elliptical plate. Mathieu's functions are considered in this analysis. Altekin [13] presented the harmonic behaviour of super elliptical plate with uniform thickness under point supported and free end condition by using the Ritz method. Yuce and wang [14] dealt with free vibration analysis of the elliptical plate with core under simply supported and clamped support condition with the help of perturbation methods. Vibration characteristics of elliptical plate with the help of Ritz method were investigated by Hassan [15]. Elliptical plate thickness has been considered to vary linearly. Clamped or completely free boundary condition was used by author. The 3D deformed shapes and the related contours lines are plotted.

Free vibration study of plate and beam structure such as circular plate, annular plate, rectangular plate, trapezoidal plate and triangular plate were well examined. Literature review on various type of structures is available in references [16–27]. Several researchers have found theoretical approaches for the modal study of plate and beam structures under simply supported, clamped and free boundary conditions. Modal analysis of elliptical shape plate is found much less examined than that of other structures.

So far the researchers are interested to analyse free vibration behaviour of an elliptical plate with different methodology in the literature survey. But the authors contributed their efforts in this research article to determine whether the eigenfrequencies of an elliptical plate changes due to thermal effect or without thermal effect. The effect of temperature, material gradient index, boundary condition and aspect ratio throughout the elliptical plate's thickness direction are presented in this research using the FEM application software COMSOL.

Analytical techniques such as the Rayleigh–Ritz method, GDQ method and Galerkin techniques produce more efficient results which are time consuming. FEM application Software such as COMSOL, ABAQUS, ANSYS, and NASTRAN can be used to obtain efficient results in much less time as compared to the analytical method. The present analysis employs COMSOL 5.4.

2 Functionally Graded Elliptical Plate

FGM elliptical plate is composed of metal (Ti-6Al-4 V) and ceramic (ZrO_2). Modal study of FGM elliptical plate under rule of mixture (P-FGM) will be reported in this research. A FG elliptical plate of semi long axis a, semi short axis b and thickness of plate h is taken as shown in Fig. 1. The material parameters are assumed to vary in the thickness direction in accordance with the rule of mixture (P-FGM) from metal (Ti-6Al-4 V) at the lower surface to ceramic (ZrO_2) at the upper surface. Material constants are temperature dependent and are varying in direction of elliptical plate thickness. In this analysis, material constants are taken from Sharma et al. [17].

Material properties (Temperature dependent), according to power law gradation, are expressed as follows:

$$E_{z,T} = (E_c - E_m)V_f^n + E_m, \tag{1}$$

$$v_{z,T} = (v_c - v_m)V_f^n + v_m, \tag{2}$$

$$\rho_{z,T} = (\rho_c - \rho_m)V_f^n + \rho_m, \tag{3}$$

$$K_{z,T} = (K_c - K_m)V_f^n + K_m, \tag{4}$$

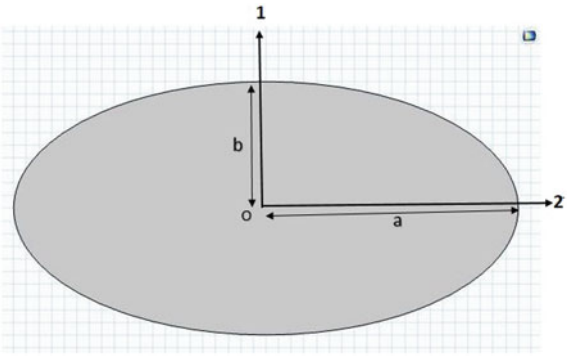

Fig. 1 Elliptical plate

$$\alpha_{z,T} = (\alpha_c - \alpha_m)V_f^n + \alpha_m, \tag{5}$$

$$V_f = \left(\frac{z}{h} + \frac{1}{2}\right), \tag{6}$$

$$H(T) = H_0\left(H_{-1}T^{-1} + H_1T^1 + H_2T^2 + H_3T^3\right), \tag{7}$$

where elasticity modulus, Poisson's ratio, density, thermal conductivity and volume fraction of the ceramic phase are E, v, ρ, K, α and V_f respectively. p represents material property gradient index. H_0,$H\text{-}_1$, H_1, H_2 and H_3 are coefficients. These are function of temperature for ceramic and metal materials. Subscripts c and m are denoted for ceramic and metal respectively.

3 Convergence Study

The free vibration analysis of isotropic elliptical plate (a = 2 m, b = 1 m and h = 0.02 m) is considered for convergence study. The natural frequencies are given in Hz. Table 1 displayed the convergence behaviour of natural frequencies under different modes using different meshing. Sufficient convergence is achieved using fine meshing. So fine meshing is used for further computation. The results are obtained using finite element software COMSOL (version 5.4) for five different modes displayed in Table 1 with different meshing (Fig. 2).

Table 1 Comparison of the natural frequencies of isotropic spherical cap with different physics controlled meshing using three dimensional finite element software COMSOL for different modes with [4]

Mesh size	No. of element	Natural frequencies (Hz)				
		Mode 1	Mode 2	Mode 3	Mode 4	Mode 5
Coarser	2094	34.882	50.491	71.981	90.273	99.454
Coarse	4410	34.506	49.825	70.678	88.449	97.327
Normal	10,552	34.301	49.474	70.094	87.597	96.406
Fine	33,163	34.188	49.299	69.832	87.189	87.107
Finer	62,652	34.161	49.261	69.778	87.107	95.933
Ref. [4]		34.153	49.292	69.893	87.359	90.228

Fig. 2 Fine meshing model

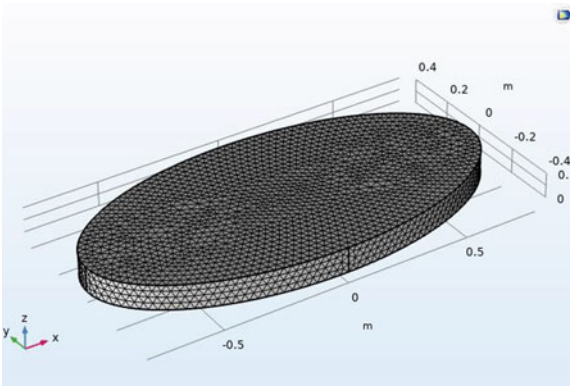

4 Basic Equations of Elliptical Plate

Displacement field of elliptical plate in 1, 2 and 3 direction can be represent as follows:

$$U(1,2,3,t) = u(1,2,t) - z.w_x(1,2,t), \tag{8}$$

$$V(1,2,3,t) = u(1,2,t) - z.w_y(1,2,t), \tag{9}$$

$$W(1,2,3,t) = w(1,2,t). \tag{10}$$

Here U, V and W are displacement in longitudinal direction, u and w are displacement in transverse direction 1, 2 and 3, and x and y in subscript represent first order differentiation with respect to corresponding coordinate.

According to Hooke's law, the stress (σ)-strain (e) relation can be expressed as follows [9]:

$$\sigma = Ce, \tag{11}$$

$$\mathrm{C} = \begin{bmatrix} \mathrm{Q11} & \mathrm{Q12} & 0 & 0 & 0 \\ \mathrm{Q21} & \mathrm{Q22} & 0 & 0 & 0 \\ 0 & 0 & \mathrm{Q66} & 0 & 0 \\ 0 & 0 & 0 & \mathrm{Q44} & 0 \\ 0 & 0 & 0 & 0 & \mathrm{Q55} \end{bmatrix} \tag{12}$$

The terms used in stiffness matrix (C) are as follows:

$$\begin{aligned} Q_{11} &= E_{11}/(1-v_{12.}v_{21}), \\ Q_{22} &= E_{22}/(1-v_{12.}v_{21}), \\ Q_{11} &= v_{21}E_{11}/(1-v_{12.}v_{21}), \\ Q_{44} &= kG_{23},\ Q_{55} = kG_{13},\ Q_{66} = kG_{12,} \end{aligned} \tag{13}$$

where E_{11}, E_{22} are the effective Young's modulus. $v_{12,}$ v_{21} are effective Poisson's ratio, and G_{13}, G_{23}, G_{12} are effective shear modulus. k is the Shear correction factor.

Kinetic energy (K) and potential energy (P) of elliptical plate are expressed as follows [2]:

$$\mathrm{K} = \frac{1}{2}\int\int_{A} \rho h w^2 \mathrm{dxdy}. \tag{14}$$

Here ρ, h are density and thickness of plate respectively.

$$P = \int\int_{A} 0.5D\begin{bmatrix} (w_{xx})^2+\left(w_{yy}\right)^2+2vw_{xx}w_{yy} \\ +2(1-v)W_{xy}^2 \end{bmatrix} dxdy. \tag{15}$$

Here D (flexural rigidity) = Eh^3 / 12(1- v^2).xx, yy and xy in subscript represent the second order differentiation with respect to corresponding coordinates.

4.1 Thermal Effect

A three-dimensional FGM plate model is used for present work. The eigenfrequencies of elliptical plate are calculated under thermal effect using FEA software COMSOL multiphysics using MUMPS eigensolver.

The present values of uniform temperature T can be obtained from following equation [20]. Here T_0 = 300 k is reference temperature and ΔT is change in temperature.

$$\mathrm{T} = \Delta\mathrm{T} + \mathrm{T}_0, \tag{16a}$$

$$H(T) = H_0\left(H_{-1}T^{-1} + H_1T^1 + H_2T^2 + H_3T^3\right). \tag{16b}$$

In this research work, the range of temperature difference is considered as ΔT = 100 K to ΔT = 600 K. For example if ΔT = 100 K, T_0 = 300 K then T would be equal to 400 K. At 400 K material properties are computed using Eq. 16b and then the computed values are incorporated in COMSOL software .

5 Results

5.1 Validation Study

An isotropic elliptical plate made of mild steel is considered for comparison purpose (Fig. 3, 4, 5, 6, 7, 8, 9, 10). For this clamped (CC) and simply supported (SS) end conditions for elliptical plate are used in this study. Material constants are taken from the reference [4]. An elliptical plate of semi long axis a, semi short axis b and thickness of plate h is considered (Table 2, 3, 4, 5, 6, 7). It may be observed that COMSOL-5.4 which is used for present study gives approximately same results and also shows good agreement with the results obtained by finite element method (FEM) [4]. The percentage error is computed with the help of following equation:

$$\text{Percentageerror} = \frac{(Reference - COMSOL)}{Reference} * 100\% \tag{17}$$

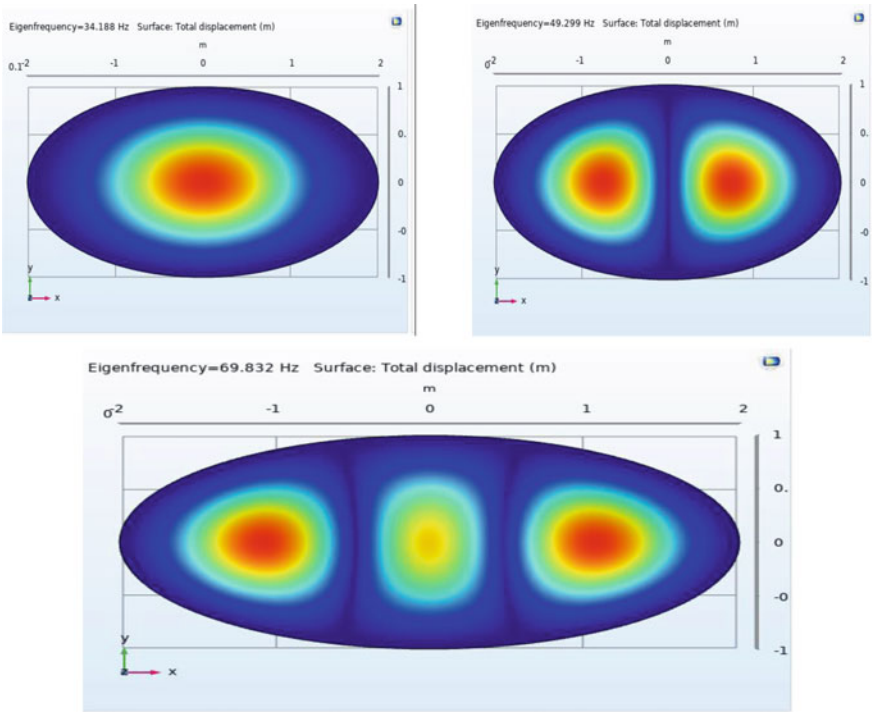

Fig. 3 First three mode shapes for isotropic elliptical shape plate under clamped–clamped (C−C) end conditions (a = 2 m, b = 1 m and h = 0.02 m)

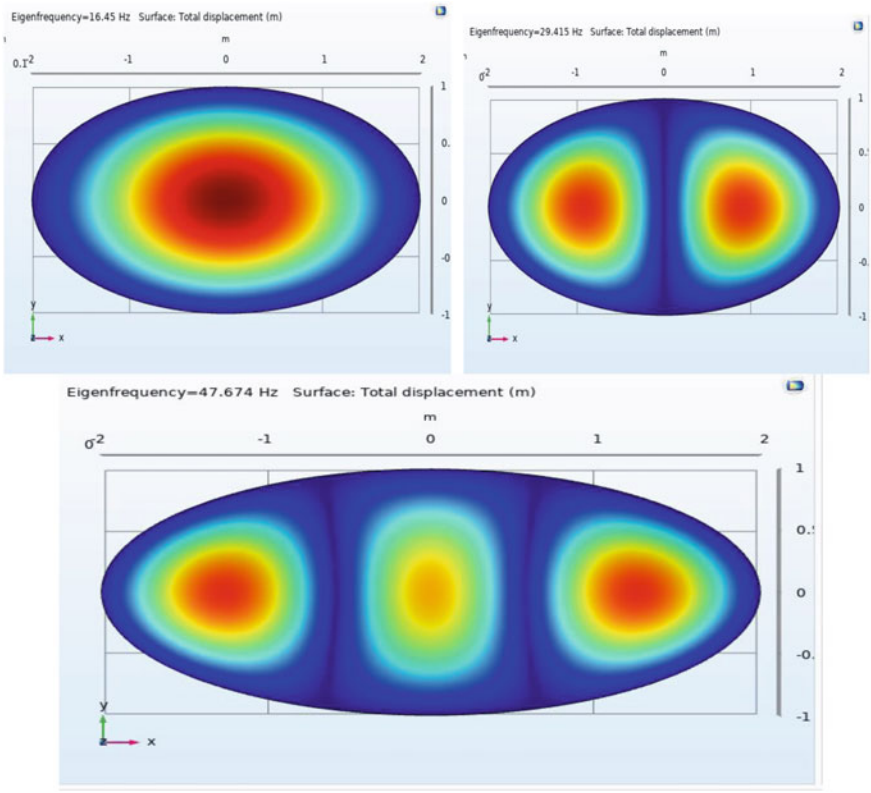

Fig. 4 First three mode shapes for isotropic elliptical shape plate under simply supported (S- end conditions (a = 2 m, b = 1 m and h = 0.02 m)

5.2 Parametric Study

In this analysis, 3D elliptical plate with semi long axis (a = 2 m), semi short axis (b = 1 m) and thickness of plate (h = 0.1 m) are used to obtain the modal characteristics with or without thermal effect. For this work, temperature difference (ΔT) is varied in the range $\Delta T = 100$ K to $\Delta T = 600$ K. The effects of temperature rise, material gradient index, and aspect ratio and end conditions on the eigenfrequencies of FGM elliptical plate are reported.

6 Conclusions

The modal study of FGM elliptical plate under thermal effect is studied. The eigenfrequencies and respective mode shapes is obtained for different boundary conditions

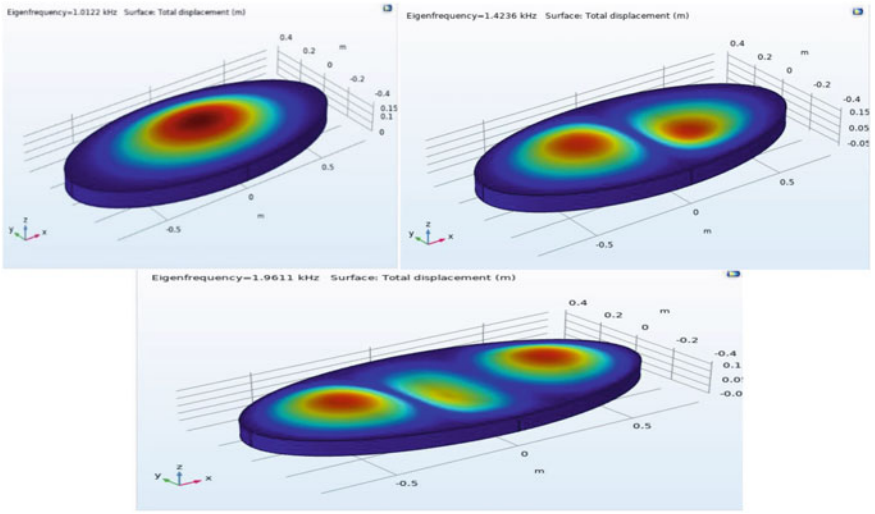

Fig. 5 Mode shapes with related eigenfrequencies for clamped FGM elliptical shape plate without thermal effect under power law (p = 1)

Fig. 6 Effect of temperature rise on the eigenfrequencies (Hz) of clamped FGM elliptical plate under power law (a/b = 2, h = 0.1 m, p = 1 and ΔT = 100 K to ΔT = 600 K)

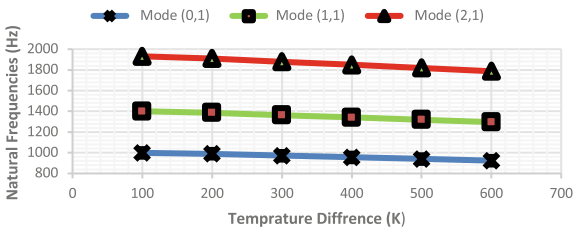

Fig. 7 Effect of material gradient index on the eigrnfrequencies (Hz) of clamped FGM elliptical plate with thermal effect under power law (a/b = 2, h = 0.1 m, ΔT = 800 K and p = 1 to 6)

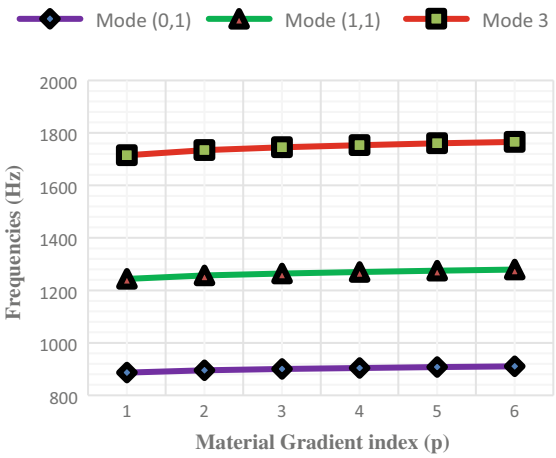

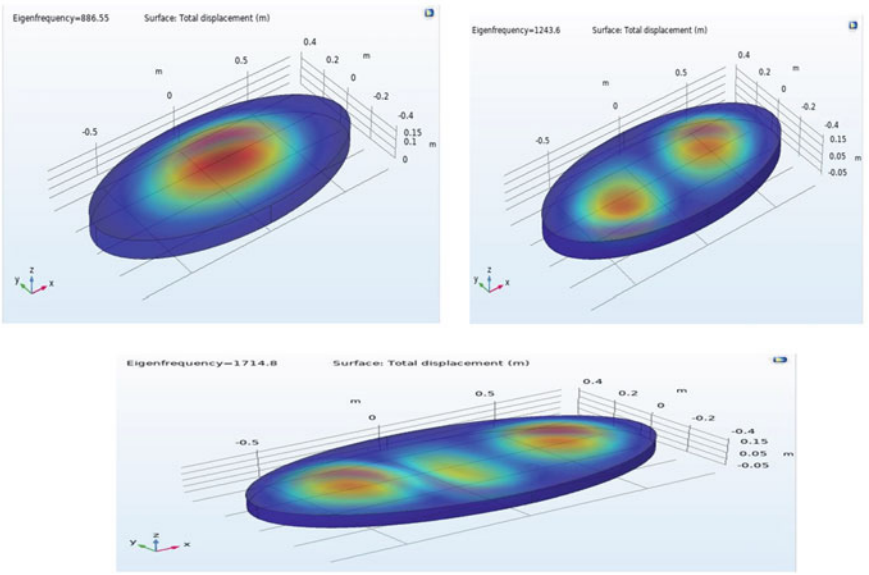

Fig. 8 First three mode shapes of FGM elliptical shape plate for clamped (C−C) end conditions with thermal effect under power law (a/b = 2, h = 0.1 m, p = 1 and ΔT = 800 K)

Fig. 9 Effect of various aspect ratio (δ) on the eigenfrequencies (Hz) of clamped FGM elliptical plate with thermal effect under power law (a/b = 2, h = 0.1 m, p = 1, δ = 0.25 to 2 and ΔT = 800 K)

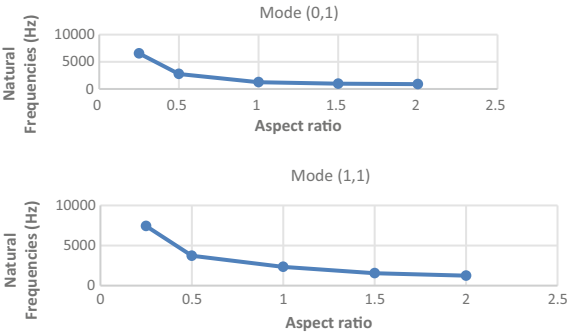

Fig. 10 Effect of different end condition on the eigenfrequencies (Hz) of FGM elliptical plate with thermal effect under power law (a/b = 2, h = 0.1 m, p = 1 and ΔT = 800 K)

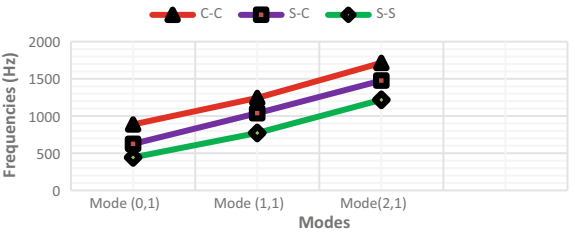

Table 2 Comparative study of first ten eigenfrequencies (Hz) of isotropic elliptical shape plate under clamped (C–C) and simply supported end condition (a = 2 m, b = 1 m and h = 0.02 m)

Boundary Conditions						
Modes	Clamped (C–C)			Simply Supported (S–S)		
	Ref[4]	COMSOL	Error%	Ref[4]	COMSOL	Error%
1	34.153	34.188	0.1	16.45	16.45	0
2	49.292	42.299	0.016	29.45	29.415	0.11
3	69.893	69.832	0.087	47.69	47.674	0.03
4	87.359	87.189	0.19	57.29	57.436	0.25
5	96.228	96.02	0.22	71.6	71.49	0.15
6	110.09	109.85	0.21	78.19	78.061	0.16
7	128.47	127.94	0.41	101.01	100.95	0.05
8	137.5	137.09	0.29	103.05	103.2	0.14
9	166.37	165.06	0.78	121.99	122.89	0.73
10	166.64	165.03	0.96	133.4	133.08	0.29

Table 3 First three eigenfrequencies (KHz) of a clamped FGM elliptical plate without thermal effect (a/b = 2, h = 0.1 m, p = 1)

S.No	Mode	COMSOL
1	(0,1)	1.01
2	(1,1)	1.42
3	(2,1)	1.96

Table 4 First three eigenfrequencies (Hz) of a clamped FGM elliptical plate with thermal effect (a/b = 2, h = 0.1 m, p = 1 and ΔT = 100 K to ΔT = 600 K)

Temp diff (ΔT)	Mode (0,1)	Mode (1,1)	Mode (2,1)
100	998.94	1401	1931.10
200	988.99	1387	1911
300	971.6	1362.6	1878.3
400	956.7	1341.8	1849.5
500	940.84	1319.50	1819
600	923.97	1295.90	1786.9

Table 5 The eigenfrequencies (Hz) of FGM clamped elliptical plate with different material gradient index under thermal effect (a/b = 2, h = 0.1 m, ΔT = 800 K and p = 1 to 6)

Mode/p	p = 1	p = 2	p = 3	p = 4	p = 5	p = 6
Mode 1	886.55	895.23	900.13	904.09	907.49	910.43
Mode 2	1243.6	1256.9	1264.2	1270	1274.9	1279.2
Mode 3	1714.8	1734.5	1745.2	1753.4	1760.1	1765.8

Table 6 First three eigenfrequencies (Hz) of a clamped FGM elliptical plate for various aspect ratio (δ) under thermal effect (a/b = 2, h = 0.1 m, p = 1, δ = 0.25 to 2 and ΔT = 800 K)

Aspect ratio/Mode	Mode (0,1)	Mode (1,1)	Mode (2,1)
0.25	6546	7428.6	8504.9
0.5	2761.5	3725	4927.5
1	1246.5	2338.1	–
1.5	971.77	1548	2301.4
2	886.55	1243.60	1714.8

Table 7 First three eigenfrequencies (Hz) of a FGM elliptical plate for different end conditions under thermal effect (a/b = 2, h = 0.1 m, p = 1 and ΔT = 800 K)

Boundary conditions / Mode	C−C	S−C	S−S
Mode (0,1)	886.55	625.43	443.74
Mode (1,1)	1243.6	1038.6	771.9
Mode (2,1)	1714.8	1476.4	1218.6

under thermal effect. The thermal effect on the FGM elliptical is accomplished by employing specific temperatures on the top surface and keeping a constant temperature (T = 300 K) at a bottom surface region. Material parameters of the elliptical shape plate vary continuously across the thickness direction as per rule of mixture (P-FGM).

The following conclusions are made using FGM elliptical plate under thermal effect.

- With temperature rise, the eigenfrequencies decrease for ΔT = 100 K to ΔT = 600 K for all modes under clamped boundary condition.
- It is also noted that with increase material gradient index from p = 1 to p = 6, the natural frequencies for all three modes increases.
- Under clamped FGM elliptical plate, with the increase in aspect ratio, the eigenfrequency decreases for all modes under thermal effect at p = 1.
- Increasing order of eigenfrequencies for various end condition are as SS, SC and CC end conditions.

References

1. Sharma P (2019) Vibration analysis of functionally graded piezoelectric actuators. Springer, New York, NY
2. Merneedi A, Nalluri MR, Vissakodeti V (2017) Free vibration analysis of an elliptical plate with cut-out. J Vibroengineering 19(4):2341–2353
3. Lim TC (2016) Simply-supported elliptical auxetic plates. J Mech 32(4):413–419
4. Guo W, Feng Q (2019) Free vibration analysis of arbitrary-shaped plates based on the improved Rayleigh–Ritz Method. Adv Civ Eng 2019

5. Zhong S, Jin G, Ye T, Zhang J, Xue Y, Chen M (2020) Isogeometric vibration analysis of multi-directional functionally gradient circular, elliptical and sector plates with variable thickness. May. Compos Struct 30:112470
6. Altunsaray E (2018) Free vibration of symmetrically laminated quasi-isotropic super-elliptical thin plates. Steel Compos Struct 29(4):493–508
7. Bryan A (2018) Free vibration of thin shallow elliptical shells. J Vib Acoust 140(1)
8. Talebitooti M, Ghasemi M, Hosseini SM (2017) Vibration analysis of functionally graded cylindrical shells with different boundary conditions subjected to thermal loads. J Comput & Appl Res Mech Eng (JCARME) 6(2):103–114
9. Ansari R, Torabi J, Shakouri AH (2017) Vibration analysis of functionally graded carbon nanotube-reinforced composite elliptical plates using a numerical strategy. Aerosp Sci Technol 60:152–161
10. Pradhan KK, Chakraverty S (2015) Free vibration of functionally graded thin elliptic plates with various edge supports. Struct Eng Mech 53(2):337–354
11. Soleymani MM, Hajabasi MA, ElahiMahani S (2015) Free vibrations analysis of a sandwich rectangular plate with electrorheological fluid core. J Comput & Appl Res Mech Eng (JCARME) 5(1):71–81
12. Hasheminejad SM, Ghaheri A (2014) Exact solution for free vibration analysis of an eccentric elliptical plate. Arch Appl Mech 84(4):543–552
13. Altekin M (2011) Free in-plane vibration of super-elliptical plates. Shock Vib 18(3):471–484
14. Yüce H, Wang CY (2010) Perturbation methods for moderately elliptical plates with a core. Actamechanica 215(1–4):105–117
15. Hassan SM (2004) Free transverse vibration of elliptical plates of variable thickness with half of the boundary clamped and the rest free. Int J Mech Sci 46(12):1861–1882
16. Sharma P, Parashar SK (2016) Free vibration analysis of shear-induced flexural vibration of FGPM annular plate using generalized differential quadrature method. Compos Struct 155:213–222
17. Sharma P, Singh R (2019) Investigation on modal behaviour of FGM annular plate under hygrothermal effect. In IOP Conference series: materials science and engineering, October, vol 624, no 1. IOP Publishing, p 012001
18. Parashar SK, Sharma P (2016) Modal analysis of shear-induced flexural vibration of FGPM beam using Generalized Differential Quadrature method. Compos Struct 139:222–232
19. Khinchi A, Sharma P (2020) Free vibration analysis of isotropic spherical cap and FG-spherical cap with cut-out using COMSOL. In AIP Conference Proceedings, May, vol 2220, no 1. AIP Publishing LLC, p 130074
20. Sharma P, Singh R, Hussain M (2020) On modal analysis of axially functionally graded material beam under hygrothermal effect. Proc Inst Mech Eng C J Mech Eng Sci 234(5):1085–1101
21. Tran TT, Nguyen PC, Pham QH (2021) Vibration analysis of FGM plate in thermal environment resting on elastic foundation using ES-MITC3 element and prediction of ANN. Case Stud Therm Eng 100852
22. Singh R, Sharma P (2019) A review on modal characteristics of FGM structures. In AIP conference proceedings, September, vol 2148, no 1. AIP Publishing LLC, p 030037
23. Sharma P, Singh R (2021) A numerical study on free vibration analysis of axial FGM beam. Mater Today: Proc 1(44):1664–1668
24. Singh R, Sharma P (2021) Free vibration analysis of axially functionally graded tapered beam using harmonic differential quadrature method. Mater Today: Proc 1(44):2223–2227
25. Sharma P, Singh R (2021) Effect of selection of mesh distribution on efficacy of natural frequency of Timoshenko beam in HDQ analysis. Mater Today: Proc
26. Singh R, Sharma P (2021) Vibration analysis of an axially functionally graded material non-prismatic beam under axial thermal variation in humid environment. J Vib Control. https://doi.org/10.1177/10775463211037150
27. Sharma P, Singh R (2020) On frequency analysis of functionally graded nano beam under hygrothermal effect. In AIP Conference Proceedings, October, vol 2276, no 1. AIP Publishing LLC, p 020008

Fluid Structure Interaction Analysis Under Earthquake Loading and Its Application to Concrete Gravity Dam

Angshuman Mandal and Damodar Maity

1 Introduction

The interaction of dam-reservoir coupled system is essentially a fluid–structure interaction problem. Mutual interaction of an elastic dam and its adjacent compressible fluid has been extensively studied in recent years. Under dynamic loading, the elastic dam moves into and away from the reservoir water. Under the influence of this disturbances, reservoir water exerts hydrodynamic pressure on the dam surface. Initially "Added mass approach" proposed by Westergaard [1] was implemented to study the effect of hydrodynamic pressure on the dam body. Consideration of rigid structure and incompressible fluid were the limitations of "Added Mass Approach". The analytical solution of the wave equation considering compressible fluid for vertical and inclined upstream faces of the dam had been conducted by Chopra [2] and Chwang [3], respectively. The study later extended to the elastic nature of the dam, which is practical in nature. In order to study the interaction between the compressible fluid and elastic dam, two coupling approaches have been proposed by the researchers, namely, direct or monolithic approach [4, 6] and indirect or iterative approach [5, 6]. It is observed from the literatures that, being iterative in nature, indirect coupling is sensitive to the pre-specified tolerance value for converged solution and with increase in flexibility of the dam body, and the time taken to solve the coupled problem is drastically increased. On the other hand, direct coupling method does not suffer from such limitations.

A. Mandal (✉)
Civil Engineering Department, Birla Institute of Technology Mesra, Patna Campus, Patna, India
e-mail: angshuman.mandal8@bitmesra.ac.in

D. Maity
Civil Engineering Department, Indian Institute of Technology Kharagpur, Kharagpur, India
e-mail: dmaity@civil.iitkgp.ac.in

D. K. Maiti et al. (eds.), *Recent Advances in Computational and Experimental Mechanics, Vol II*, Lecture Notes in Mechanical Engineering,
https://doi.org/10.1007/978-981-16-6490-8_9

The present study focuses on the earthquake analysis of fluid structure interaction and its application on the concrete gravity dam. The derivation finite element formulation of the reservoir domain from the classical Navier–Stokes equation has been addressed in systematic manner. The boundary conditions of all the four sides of the reservoir domain and their implementation technique in finite element framework is mentioned. The finite element discritization, constitutive relationship, and construction of the elemental property matrices of the concrete gravity dam is addressed in details. Direct coupling approach is followed in the fluid structure interaction study. The natural frequencies of the Pine Flat dam, adjacent reservoir, and the dam reservoir coupled system are compared with the existing literatures for validation of the MATLAB based finite element coding. The seismic responses of the dam-reservoir coupled system are obtained for Koyna dam under Koyna earthquake (1967) acceleration using Newmark beta average acceleration algorithm [7].

2 Finite Element Formulation of the Reservoir Water

The theoretical developments and the finite element formulation of the reservoir domain are discussed in the following sections.

2.1 Mathematical Formulation for the Reservoir Domain

2.1.1 Governing Equation of Motion for Reservoir Water

The equation of motion of a viscous, Newtonian fluid in two-dimensions may be expressed by the well-known Navier–Stokes equation as follows [8]:

$$\dot{V}_i + V_j V_{i,j} + \frac{1}{\rho_f} p_{,i} - \nu V_{i,ji} = f_i, \tag{1}$$

where V_i and V_j are the two mutually orthogonal velocity components along 'i' and 'j' directions, respectively, 'p' is the hydrodynamic pressure, 'ρ_f' is the mass density of the fluid, and 'ν' is the kinematic viscosity. The subscripts attached to the velocity and pressure variables represent the derivatives along the preferred directions. The term 'f_i' represents the body forces present in the fluid domain acting along the 'i' direction. The overhead dot represents the derivative with respect to time. Considering the fluid as in-viscid and neglecting non-linear convective terms for small amplitude of vibration, the simplified form of Eq. (1) is expressed as follows:

$$\rho_f \dot{V}_i + p_{,i} = 0. \tag{2}$$

The continuity equation of the fluid may be expressed as follows:

$$\rho_f c^2 V_{k,k} + \dot{p} = 0, \tag{3}$$

where 'c' is the acoustic wave speed in the fluid. In order to obtain a single variable formulation for the fluid in terms of pressure, Eqs. (2) and (3) are combined together. The resulting equation is widely known as the 'Helmholtz wave equation' and is expressed as follows:

$$\nabla^2 p\,(x, y, t) = \frac{1}{c^2}\ddot{p}\,(x, y, t), \tag{4}$$

where $p(x, y, t)$ is the hydrodynamic pressure with spatial and temporal position as (x, y) and *'t'*, respectively.

2.1.2 Boundary Conditions of the Reservoir Domain

In a dam-reservoir coupled system, reservoir domain is generally consisted of four boundaries as follows: (a) free surface (Γ_f), (b) dam-reservoir interface (Γ_s), (c) reservoir-reservoir bed interface (Γ_r), and (d) truncation surface (Γ_t). All these boundaries are shown in Fig. 1. The boundary conditions of the reservoir domain and their mathematical expressions are shown in Table 1.

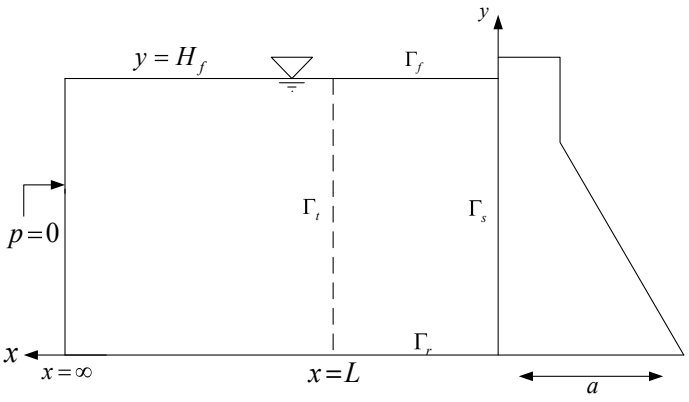

Fig.1 Boundaries of the infinite reservoir domain adjacent to a concrete gravity dam

Table 1 Boundary conditions of the reservoir domain

Boundary	Boundary Type	Boundary Condition	Remarks
Γ_f	Free Surface	$p(x, H_f, t) = 0$	Surface wave neglected
		$\frac{\partial p}{\partial y} = -\frac{1}{g}\ddot{p}$	Surface wave considered [4]
Γ_s	Dam-reservoir interface	$\frac{\partial p}{\partial n}(0, y, t) = -\rho_f a e^{iwt}$	Horizontal ground acceleration component=ae^{iwt}
Γ_r	Reservoir- reservoir bed interface	$\frac{\partial p}{\partial n}(x, 0, t) = 0$	Reservoir bottom absorption neglected
		$\frac{\partial p}{\partial n}(x, 0, t) = -q\dot{p}(x, 0, t)$ $q = \frac{1}{c}\left(\frac{1-\alpha}{1+\alpha}\right)$	Reservoir bottom absorption effect [9]
Γ_t	Truncation surface	$\frac{\partial p}{\partial n}(L, y, t) = 0$	Sommerfeld's boundary condition [10]
		$\frac{\partial p}{\partial n}(L, y, t) = -\frac{\zeta}{2H_f}p - \frac{1}{c}\dot{p}$	Sharan boundary condition [11]
		$\frac{\partial p}{\partial n}(L, y, t) = \left(\zeta_m - \frac{1}{c}\right)\dot{p}$	Gogoi and Maity Boundary condition [12]

2.2 Property Matrices of the Reservoir Domain

The wave equation (Eq. 4) may be written in two-dimensional form using Galerkin approach as follows:

$$\int_{\Omega} N_{rj}\left[\nabla^2 \sum N_{ri}\, p_i - \frac{1}{c^2}\sum N_{ri}\, p_i\right] d\Omega = 0, \tag{5}$$

where N_r is the shape function for the finite elements used in the reservoir domain and Ω is the region under consideration. Implementing Green's theorem, the following expressions are obtained:

$$-\int_{\Omega}\left[\frac{\partial N_{rj}}{\partial x}\sum\frac{\partial N_{ri}}{\partial x}p_i + \frac{\partial N_{rj}}{\partial y}\sum\frac{\partial N_{ri}}{\partial y}p_i\right]d\Omega - \frac{1}{c^2}\left[\int_{\Omega} N_{rj}\sum N_{ri}\, d\Omega\right]\ddot{p}i$$
$$+\left[\int_{\Gamma} N_{rj}\sum\frac{\partial N_{ri}}{\partial n}d\Gamma\right]p_i = 0, \tag{6}$$

where Γ indicates the boundary surfaces. The standard dynamic equation of motion in matrix form may be obtained from Eq. (6) as follows:

$$\left[\overline{E}\right]\{\ddot{p}\} + [G]\{p\} = \{B\}. \tag{7}$$

The matrices in Eq. (7) may be expressed as follows:

$$\left[\overline{E}\right] = \frac{1}{c^2}\sum \int_{\Omega} N_r^T N_r d\Omega, \tag{8}$$

$$[G] = \sum \int_{\Omega} \left(\frac{\partial}{\partial x}[N_r]^T \frac{\partial}{\partial x}[N_r] + \frac{\partial}{\partial y}[N_r]^T \frac{\partial}{\partial y}[N_r] \right) d\Omega, \tag{9}$$

$$\{B\} = \left\{B_f\right\} + \{B_s\} + \{B_r\} + \{B_t\} = \sum \int_{\Gamma} N_r^T \frac{\partial p}{\partial n} d\Gamma. \tag{10}$$

The finite element description of each boundary side has been expressed and shown in Table 2. Substituting these boundary conditions in Eq. (7), the following general dynamic equation in matrix form are obtained:

$$[E]\{\ddot{p}\} + [A]\{\dot{p}\} + [G_c]\{p\} = -\rho_f [R_s]\{a\}, \tag{11}$$

$$\text{where} \qquad [E] = \left[\overline{E}\right] + \frac{1}{g}\left[R_f\right], \tag{12}$$

$$[A] = [R_{tc}] + \frac{1}{c}[R_t], \tag{13}$$

$$[G_c] = [G] - iwq[R_r]. \tag{14}$$

3 Finite Element Formulation of the Gravity Dam

The important aspects of the standard finite element scheme [13] for the analysis of the dam are outlined in the following sub-sections. It is to be mentioned that eight noded isoparametric quadratic elements have been considered for discretizing the dam body.

Table 2 Boundary conditions of the reservoir in finite element form

Boundary Description	Boundary Type	Boundary Condition	Remarks
Γ_f	Free Surface	$\{B_f\} = 0$	Surface wave neglected
		$\{B_f\} = -\frac{1}{g}[R_f]\{\ddot{p}\}$ $[R_f] =$ $\sum \int_{\Gamma_f} [N_r]^T [N_r]\, d\Gamma$	Surface wave considered
Γ_s	Dam-reservoir interface	$\{B_s\} = -\rho_f [R_s]\{a\}$ $[R_s] =$ $\sum \int_{\Gamma_s} [N_r]^T [T]\, [N_s]\, d\Gamma_s$	[T] is transformation matrix and $[N]$ is the shape function matrix
Γ_r	Reservoir- reservoir bed interface	$\{B_r\} = 0$	Reservoir bottom absorption neglected
		$\{B_r\} = -q[R_r]\{\dot{p}\}$ $[R_r] =$ $\sum \int_{\Gamma_r} [N_r]^T [N_r] d\Gamma_r$	Reservoir bottom absorption modeled [9]
Γ_t	Truncation surface	$\{B_t\} = 0$	Sommerfeld's boundary condition [10]
		$\{B_t\} =$ $-\left([R_{tc}]\{p\} + \frac{1}{c}[R_t]\{\dot{p}\}\right)$ $[R_{tc}] =$ $\sum \int_{\Gamma_t} [N_r]^T \zeta\, [N_r]\, d\Gamma_t$	Sharan boundary condition [11]
		$\{B_t\} =$ $-\left([R_{tc}] + \frac{1}{c}[R_t]\right)\{\dot{p}\}$ $[R_{tc}] =$ $\sum \int_{\Gamma_t} [N_r]^T \zeta_m\, [N_r]\, d\Gamma_t$ $[R_t] =$ $\sum \int_{\Gamma_t} [N_r]^T [N_r]\, d\Gamma_t$	Gogoi and Maity Boundary condition [12]

3.1 Constitutive Matrix

Plane strain formulation is suitable (Hall and Chopra [9]) for the analysis of concrete gravity dam. In plane strain formulations, it is assumed that the strains along the longitudinal axis are negligible. Therefore, the constitutive relation for isotropic elastic material may be expressed as follows:

$$\begin{Bmatrix} \sigma_x \\ \sigma_y \\ \tau_{xy} \end{Bmatrix} = [D] \begin{Bmatrix} \varepsilon_x \\ \varepsilon_y \\ \gamma_{xy} \end{Bmatrix} = \frac{E_d}{(1+\nu)(1-2\nu)} \begin{bmatrix} (1-\nu) & \nu & 0 \\ \nu & (1-\nu) & 0 \\ 0 & 0 & \frac{(1-\nu)}{2} \end{bmatrix} \begin{Bmatrix} \varepsilon_x \\ \varepsilon_y \\ \gamma_{xy} \end{Bmatrix}. \tag{15}$$

In Eq. (15), the stress and strain vectors are referred as $\{\sigma\}^T = \{\sigma_x, \sigma_y, \tau_{xy}\}$ and $\{\varepsilon\}^T = \{\varepsilon_x, \varepsilon_y, \gamma_{xy}\}$, respectively. The matrix [D] relates the stress and the strain terms hence defined as the constitutive matrix. Here, in the constitutive matrix,E_d and ν are the elastic modulus and Poisson's ratio of the dam, respectively.

3.2 Property Matrices of the Dam

In the FEM framework, for a single element, the work balance relation can be written as follows:

$$\begin{aligned} &\int_{\Omega_e} \{\delta d\}_i^T \{F\} d\Omega + \int_{\Gamma_e} \{\delta d\}_i^T \{S\} d\Gamma + \sum_{i=1}^{n_i} \{\delta d\}_i^T \{F_c\}_i \\ &= \int_{\Omega_e} \left(\{\delta \varepsilon\}_i^T \{\sigma\} + \{\delta d\}^T \rho_d \{\ddot{d}\} + \{\delta d\}^T c_d \{\dot{d}\} \right) d\Omega, \end{aligned} \tag{16}$$

where $\{\delta d\}$ and $\{\delta \varepsilon\}$ are the small arbitrary displacements and their corresponding strains, respectively, $\{F\}$ are the body forces, $\{S\}$ are the prescribed surface tractions, $\{F_c\}_i$ are the concentrated loads that act at a total of n_c points on the element, $\{\delta d\}_i^T$ is the displacement of the point at which load $\{F_c\}_i$ is applied, ρ_d is the mass density of the dam material, c_d is the material damping parameter analogous to viscosity, and volume integration is carried out over the elemental volume Ω_e. The displacement field $\{d\}$ and its first two derivatives may be expressed as follows:

$$\{d\} = [N_d] \{\overline{d}\}; \quad \{\dot{d}\} = [N_d] \left\{\dot{\overline{d}}\right\}; \quad \{\ddot{d}\} = [N_d] \left\{\ddot{\overline{d}}\right\}. \tag{17}$$

In the above equation, shape functions $[N_d]$ are functions of space and the nodal degree of freedom $\{\overline{d}\}$ are functions of time only. Combining Eqs. (16) and (17), the

following expressions may be derived:

$$\begin{aligned}\left\{\delta\bar{d}\right\}^T\Bigg[&\int_{\Omega_e}[B]^T[D][B]d\Omega\left\{\bar{d}\right\}+\int_{\Omega_e}[N_d]^T\rho_d[N_d]d\Omega\left\{\ddot{\bar{d}}\right\}\\&+\int_{\Omega_e}[N_d]^Tk_d[N_d]d\Omega\left\{\dot{\bar{d}}\right\}-\int_{\Omega_e}[N_d]^T\{F\}d\Omega\\&-\int_{\Gamma_e}[N_d]^T\{S\}d\Gamma-\sum_{i=1}^{n_c}\{F_c\}_i\Bigg]=0.\end{aligned}\tag{18}$$

It is assumed in the finite element analysis that the locations of concentrated load $\{F_c\}_i$ are coincident with node point locations otherwise the load has to be properly distributed on all the nodes. Since $\left\{\delta\bar{d}\right\}$ is arbitrary, Eq. (18) can be rewritten as follows:

$$\left[M_d^e\right]\left\{\ddot{\bar{d}}\right\}+\left[C_d^e\right]\left\{\dot{\bar{d}}\right\}+\left[K_d^e\right]\left\{\bar{d}\right\}=\left\{F_d^e\right\},\tag{19}$$

where M_d^e,C_d^e and K_d^e are the elemental mass, damping, and stiffness matrices, respectively, and are defined as follows:

$$\begin{aligned}\left[M_d^e\right]&=\int_{\Omega_e}[N_d]^T\rho_d\,[N_d]\,d\Omega\ ,\left[C_d^e\right]=\int_{\Omega_e}[N_d]^Tk_d\,[N_d]\,d\Omega\ ,\\\left[K_d^e\right]&=\int_{\Omega_e}[B]^T[D]\,[B]\,d\Omega\ .\end{aligned}\tag{20}$$

The external load vector is defined as follows:

$$\left\{F_d^e\right\}=\int_{\Omega_e}[N_d]^T\{F\}\,d\Omega\ +\int_{\Gamma_e}[N_d]^T\{S\}\,d\Gamma\ +\sum_{i=1}^{n_c}\{F_c\}_i.\tag{21}$$

For plane strain formulation, considering t as the dimension along the longitudinal direction of the structural element, the stiffness and mass matrix may be written as follows:

$$\left[M_d^e\right]=t\int_A\int[N_d]^T\rho_d[N_d]\,dxdy\ ,\quad\left[K_d^e\right]=t\int_A\int[B]^T[D]\,[B]\,dxdy\ ,\tag{22}$$

The area integral in Eq. (22) is computed using the standard Gauss quadrature integration technique. The global property matrices are then obtained by assembling technique utilizing all the elements,

$$[M_d] = \sum_{e=1}^{Ne} \left[M_d^e\right], \quad [K_d] = \sum_{e=1}^{Ne} \left[K_d^e\right], \tag{23}$$

where $N_e$is the total number of elements present in the finite element mesh. Rayleigh or proportional damping scheme has been considered in the present analysis.

The dynamic equilibrium equation of a system is defined as follows:

$$[M_d]\left\{\ddot{\overline{d}}\right\} + [C_d]\left\{\dot{\overline{d}}\right\} + [K_d]\{\overline{d}\} = \{F_d\}, \tag{24}$$

where the matrices defined as M_d, C_d, and K_d are representing the global mass, damping, and stiffness, respectively. The vector F_d represents the global force vector.

4 Fluid Structure Interaction

4.1 Theoratical Formulation of the Direct Coupling Approach

The equation of motion of the dam domain is expressed as follows:

$$M_d\ddot{u}_d + C_d\dot{u}_d + K_d u_d - Rp - M_d\ddot{U}_g = 0. \tag{25}$$

The coupling matrix R in Eq. (25) comes into picture to satisfy the compatibility condition at the dam-reservoir interface and may be expressed as follows:

$$\int_{\Gamma_s} N_d^T npd\Gamma = \left(\int_{\Gamma_s} N_d^T n N_r d\Gamma\right) p = Rp, \tag{26}$$

where n is the unit normal vector to the dam-reservoir interface N_d and N_r are the shape functions of the dam and reservoir, respectively. The equation of motion of the fluid domain may be expressed as follows:

$$E\ddot{p} + A\dot{p} + Gp + R^T\ddot{u}_d - F_l = 0. \tag{27}$$

Both the Eqs. (25) and (27) are coupled together and mathematically define the equation of motion of the coupled system. In matrix form, these two equations may be expressed as follows:

Table 3 Comparison of the first two natural frequencies (Hz) of the dam, reservoir, and the coupled system

Mode No	Dam		Reservoir		Dam-Reservoir	
	Sami and Lotfi [14]	Present Study	Sami and Lotfi [14]	Present Study	Sami and Lotfi [14]	Present Study
1	3.15	3.18	3.11	3.11	2.53	2.55
2	6.48	6.43	4.75	4.76	3.27	3.30

$$\begin{bmatrix} E & R^T \\ 0 & M_d \end{bmatrix} \begin{Bmatrix} \ddot{p} \\ \ddot{u}_d \end{Bmatrix} + \begin{bmatrix} A & 0 \\ 0 & C_d \end{bmatrix} \begin{Bmatrix} \dot{p} \\ \dot{u}_d \end{Bmatrix} + \begin{bmatrix} G & 0 \\ -R & K_d \end{bmatrix} \begin{Bmatrix} p \\ u_d \end{Bmatrix} = \begin{Bmatrix} F_l \\ M_d \ddot{U}_g \end{Bmatrix}. \tag{28}$$

4.2 Modal Analysis Using the Direct Coupling Approach

For the free vibration analysis, the coupled system may be solved using the following:

$$\begin{bmatrix} E & R^T \\ 0 & M_d \end{bmatrix} \begin{Bmatrix} \ddot{p} \\ \ddot{x}_d \end{Bmatrix} + \begin{bmatrix} G & 0 \\ -R & K_d \end{bmatrix} \begin{Bmatrix} p \\ x_d \end{Bmatrix} = \begin{Bmatrix} 0 \\ 0 \end{Bmatrix}. \tag{29}$$

5 Results and Discussions

5.1 Validation Study Based on Pine Falt Dam

The first two natural frequencies of the dam, reservoir, and dam-reservoir coupled system have been listed and compared with the values obtained by Sami and Lotfi [14] in Table 3. The slight discrepancy arises in the responses which may be due to the slight variation in the geometry of the dam domain.

5.2 Earthquake Response of Koyna Dam and Its Adjacent Reservoir

The geometry and the material properties for the Koyna dam are considered from the research conducted by Burman et al. [15] as follows: modulus of elasticity is E_d = 31,500 MPa, Poisson's ratio $\nu = 0.235$, mass density $\rho_d = 2415.816$ kg/m^3, and material damping is $\xi_d = 5\%$. The geometry of the Koyna dam is shown in Fig. 2.

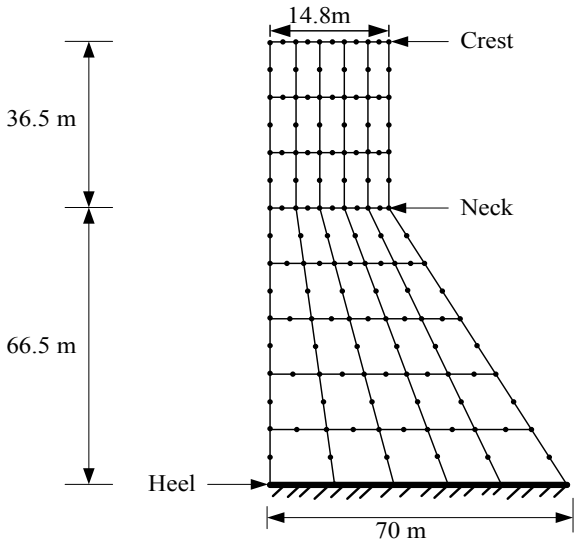

Fig. 2 Geometry and finite element discretization of Koyna dam

Koyna earthquake (1967) acceleration has been considered for the present study. The base of the dam is assumed as rigid. The reservoir water is considered to be compressible with unit weight $\gamma_w = 9.81$ kN/m^3 and pressure wave velocity $c = 1440$ m/s. The depth of the reservoir (H_f) and the truncation length are considered as 103 m and 51.5 m ($0.5H_f$), respectively [16]. Sommerfeld boundary condition has been implemented at the truncated surface. The time history response of the hydrodynamic pressure coefficient at the heel of the dam is shown in Fig. 3. Distribution of the hydrodynamic pressure at the upstream face of the dam when it is maximum at the heel is shown in Fig. 4.

Now the time history responses of the horizontal crest displacement, major, and minor principal stress histories at the neck of the dam are obtained with and without

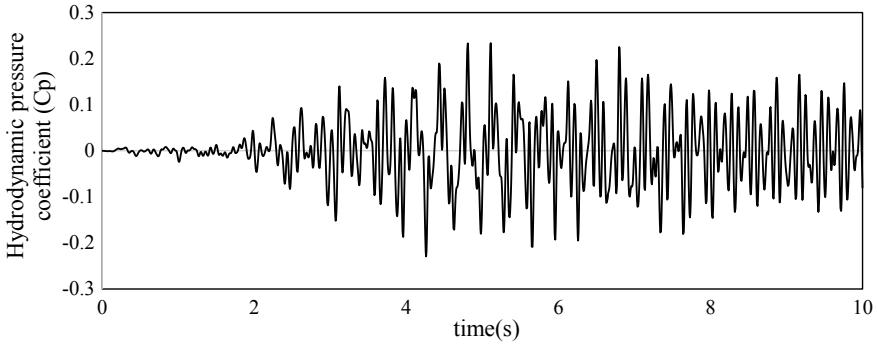

Fig. 3 Time history response of the Hydrodynamic Pressure coefficient at the heel of the dam

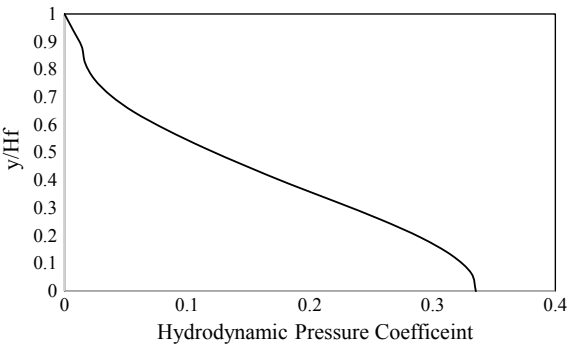

Fig. 4 Distribution of the Hydrodynamic Pressure coefficient at upstream face of the dam

the presence of the reservoir water and are shown in Figs. 5–7. The stress contours are obtained for major and minor principal stresses with empty and full reservoir condition and shown in Figs. 8–9.

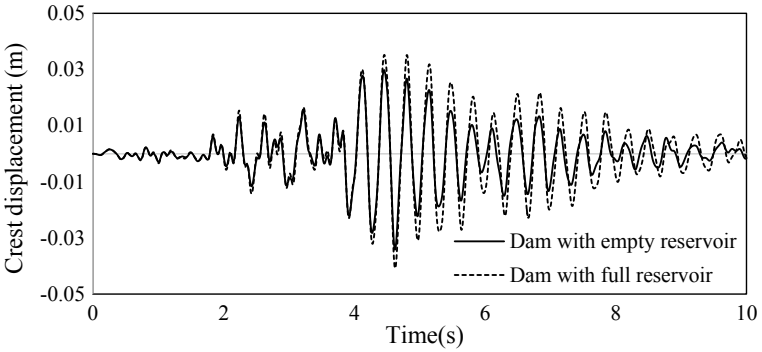

Fig. 5 Variation of the crest displacement of the Koyna dam for the upstream reservoir

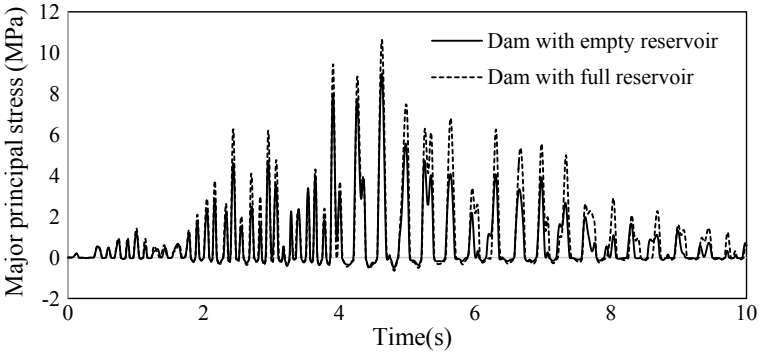

Fig. 6 Time history responses showing the variation of minor principal stress at neck of the dam

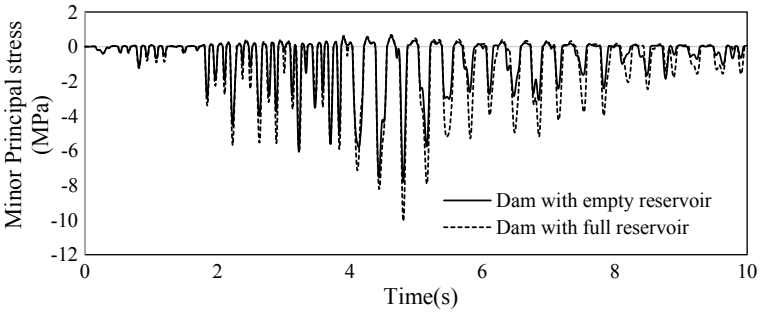

Fig. 7 Time history responses showing the variation of minor principal stress at neck of the dam

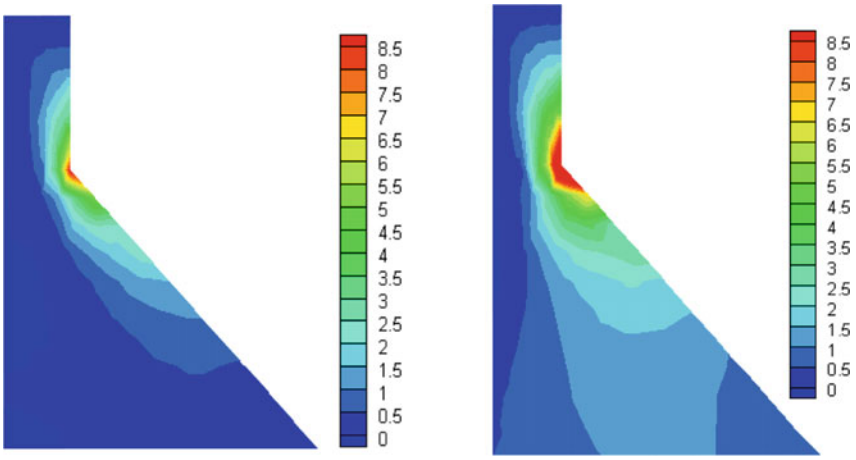

(a) Only Dam (b) Dam Reservoir Interaction

Fig. 8 Major Principal stress contours for the dam and dam reservoir interaction system

It is observed that the displacement at the crest of the dam and stress responses at the neck of the dam body is significantly altered in the presence of the reservoir water. Hence, consideration of the proper coupling approach between the dam and the reservoir domain is necessary and significant from the earthquake analysis point of view of a concrete gravity dam. Otherwise under severe earthquakes, cracks may get initiated at the neck of the dam due to the effect of the reservoir water.

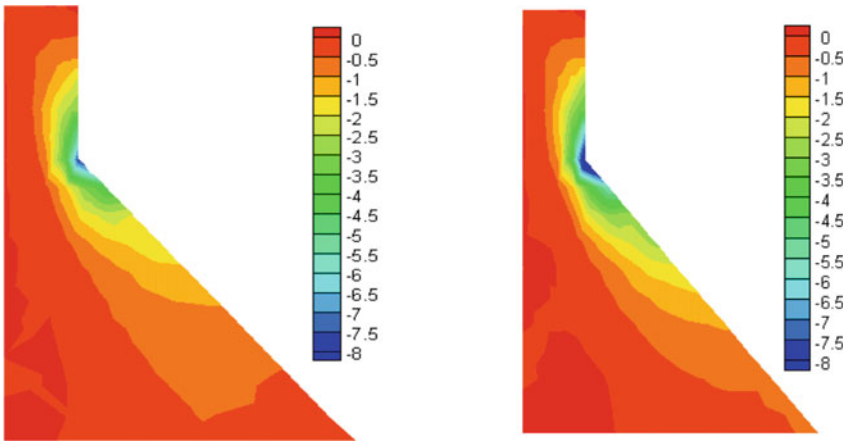

(a) Only Dam (b) Dam Reservoir Interaction

Fig. 9 Minor Principal stress contours for the dam and dam reservoir interaction system

References

1. Westergaard HM (1933) Water pressure on dams during earthquakes. Trans ASCE 98:418–472
2. Chopra AK (1967) Hydrodynamic pressures on dams during earthquakes. J Eng Mech, ASCE 93:205–223
3. Chwang AT (1978) Hydrodynamic pressure on sloping dams during earthquakes, part-2 exact theory. J Fluid Mech 87:343–348
4. Zeinkiewicz OC, Bettess P (1978) Fluid-structure dynamic interaction and Wave forces. An introduction to numerical treatment. Int J Numer Meth Eng 13:1–16
5. Maity D, Bhattacharya SK (2003) A parametric study on fluid-structure interaction problems. J Sound Vib 263:917–935
6. Mandal KK, Maity D (2015) Comparison between direct and indirect coupling for seismic analysis of fluid structure coupled system. Asian J Sci Technol 6(12):2030–2042
7. Chopra AK (2007) Dynamics of structure: theory and applications to earthquake engineering, 2nd edn. Prentice Hall of India, New Delhi
8. Modi PN, Seth SM (1989) Hydraulic and fluid mechanic, 9th edn. Standard Book House, New Delhi, India
9. Hall JF, Chopra AK (1982) Two dimensional dynamic analysis of concrete gravity and embankment dams including hydrodynamic effects. Earthq Eng Struct Dynam 10:305–332
10. Sommerfeld A (1949) Partial differential equations in physics, 1st edn. Academic Press, New York
11. Sharan SK (1992) Efficient finite element analysis of hydrodynamic pressure on dams. Comput Struct 42(5):713–723
12. Gogoi I, Maity D (2006) A non-reflecting boundary condition for the finite element modeling of infinite reservoir with layered sediment. Adv Water Resour 29:1515–1527
13. Bathe KJ (2009) Finite element procedures. Prentice Hall of India, New Delhi
14. Sami A, Lotfi V (2007) Comparison of coupled and decoupled modal approaches in seismic analysis of concrete gravity dams in time domain. Finite Elem Anal Des 43:1003–1012
15. Burman A, Nayak P, Agarwal P, Maity D (2012) Coupled gravity dam-foundation analysis using a simplified direct method of soil structure interaction. Soil Dyn Earthq Eng 34:62–68
16. Gogoi I, Maity D (2010) A novel procedure for determination of hydrodynamic pressure along upstream face of dams due to earthquakes. Comput Struct 88:539–548

Dr. Damodar Maity is Professor in the Department of Civil Engineering, Indian Institute of Technology, Kharagpur. He has more than 150 research publications in journals and conference proceedings of national and international repute. His research area of interest includes computation mechanics, structural health monitoring, fluid-structure interaction. He has received two best paper awards from The Institution of Engineers (India). Prof. Maity is author of a book titled, "Computer Analysis of Framed Structures" published by I.K. International Pvt. Ltd. He has served as scientific/advisory board member of several international conferences. He served as secretary for The Indian Society of Theoretical and Applied Mechanics for three consecutive years. Prof. Maity has developed a video course on "Design of Steel Structures" and a web course on "Finite Element Analysis" under NPTEL, MHRD.

Effect of Limb Position on U Plan Shaped Tall Building Under Wind Load

Shanku Mandal, Sujit Kumar Dalui, and Soumya Bhattacharjya

1 Introduction

Increasing the vertical orientation of a building to cope up with the rapid urban development and exponential growth of population facilitates the unavailability of the necessary space for horizontal development. The construction of buildings is often unconventional, resulting in a lack of land and architectonic esthetic. Depending on the building configuration, the wind forces behave differently. Within those unorthodox structures, wind structure interaction is quite different from regular plan shaped structures which creating additional complexity in structural design problem. The information about the wind effect on various alphabetical plan shape structures is beyond the scope of various codal provisions. The experimental and numerical approach is the available option to study the effect of wind on this type of structures. In the recent past, several researchers have explored the wind behaviour on alphabetic shapes. Gomes et al. [1] observed that the pressure variations in internal faces of the L and U shape buildings on various tested wind angels are mainly due to the influence of the extra wing on U shape building. The interference effect of the closely spaced T and L shaped pattern group buildings has been studied by Zhao and Lam [2]. Amin and Ahuja [3] presented the distribution of pressure on T and L shaped building models at an extended wind angle range. The wind effect has been evaluated by Raj and Ahuja [4] on the varying cross plan shaped structure having an equal plan area. The Shear Stress Transport (SST) and k-ε turbulence model have been used in Computational Fluid Dynamics (CFD) code by Mukherjee et al. [5] to find out the pressure on Y shape building on wind load. The wind effect on interfered and isolated case of T shape building has been studied by Ahlawat and Ahuja [6]. Cheng et al. [7] examined the variation in dynamic responses of H and square shape building

S. Mandal (✉) · S. K. Dalui · S. Bhattacharjya
Department of Civil Engineering, Indian Institute of Engineering Science and Technology, Shibpur, Howrah, India

D. K. Maiti et al. (eds.), *Recent Advances in Computational and Experimental Mechanics, Vol II*, Lecture Notes in Mechanical Engineering,
https://doi.org/10.1007/978-981-16-6490-8_10

by the wind tunnel and proper orthogonal decomposition technique. Mashalkar et al. [8] evaluated the design loads on C, I, L and T type building. Li and Li [9] provided a reliable and simple procedure to evaluate the effect of dynamic load on L shaped buildings across wind direction. Ranka and Shingade [10] compared the drag and pressure coefficients of T, rectangular, L and square shape buildings on 0°, 45° and 90° wind angle. Paul and Dalui [11] investigated the wind exerted pressure and force coefficients on Z shaped buildings. Ullas and P [12] inspect the wind responses on +, V and Y shape buildings. Bhattacharyya and Dalui [13] calculated the wind pressure on the E plan shaped tall buildings. Mallick et al. [14] experimentally investigate the surface pressure of C shape models for 0°–180° wind angle taking 30° intervals. The comparison of wind effect on chamfered, rounded and shape corner U shape building has been presented by Shanku et al. [15]. The study of Bhattacharyya and Dalui [16] using CFD and wind tunnel showed the pressure distribution on E shaped building.

The alphabetic E, T, I, C, U, Y and T shapes are widespread structural form in modern construction practices. The past research covers various fundamental wind effects on such structures. Among those shapes, U shaped building is a popular choice to build residential complex, shopping malls, academic buildings etc. The construction of a primary shape U building can often not be feasible due to the space availability and its forces to build a peculiar U shape building. In our present study, the change in aerodynamic behaviour has been investigated around the U shape buildings due to the shifting of limbs for 0° and 90° wind induced angle. The various sifting length cases have been considered in our present for numerical simulation using CFD. The comparison of force and pressure coefficients has been presented to understand the variation in wind responses.

2 Scope of the Work

The wind behaviour of the original U shape has been measured at the mentioned induced angle. This study further extended with the shifting of two limbs by 0.05L, 0.1L, 0.15L, 0.2L and 0.3L from each side (L is the length of the building taken as 250 mm) keeping the plan area same. The different cases of shifted models have been presented in Fig. 1.

The building models are marked as U1, U2, U3, U4, U5 and U6. The presence of two limbs at the extreme corners is the original shape (U1). The U2 model has sifted limbs by 12.5 mm from both ends. In the case of U3, U4, U5 and U6 model, the sifting length of 25, 37.5, 50 and 75 mm has been adopted. The height and width of the building are taken 500 and 150 mm. The limb width is 50 mm, and the 150 mm initial gap is considered in between two limbs.

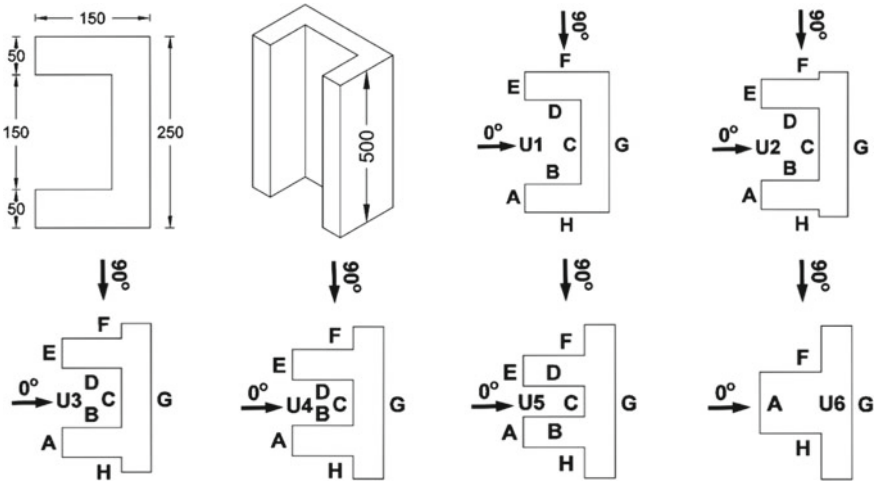

Fig. 1 The building models for this study (all dimensions are in mm)

3 Solution Methodology

The wind flow around the buildings has been simulated using computational fluid dynamics (CFD). The CFD technique in the recent past has become advance, and it is capable enough to predict the fluid–structure interaction (Löhner et al. [17]). However, CFD approaches need validation to gain credibility in the calculated results.

3.1 Computational Domain Setup

All the building (see Fig. 2) has been modelled at 1:300 scale and analyzed by considering the k-ε turbulence model using the Computational Fluid Dynamics (CFD) module of Ansys CFX. Where k represents the turbulence kinetic energy and the turbulence eddy dissipation is termed as ε. To avoid blockage correction,

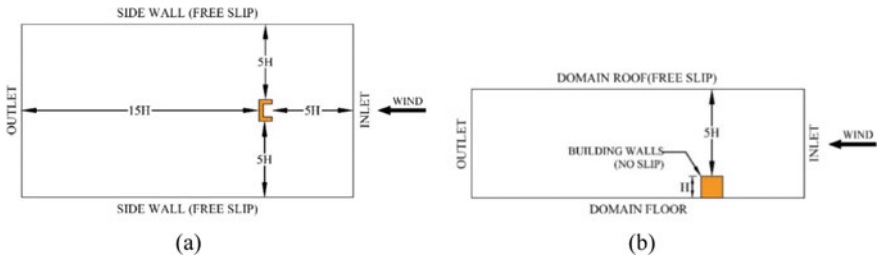

Fig. 2 The domain used for numerical simulation. **a** Plan View **b** Elevation View

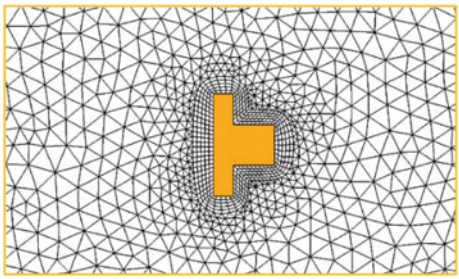

Fig. 3 The mesh details of the U6 building case

5H distance from the building has been maintained from the sidewalls, inlet and roof. The domain outlet has been considered at a distance of 15H (H = height of the building = 500 mm). Free slip condition has been taken on sidewalls and roof on the domain. This large size domain (Revuz et al. [18]) is suitable for unrestricted wind flow. No slip condition has been adopted on the faces of the building and floor of the domain. 10 m/s wind velocity has been provided at the inlet. The boundary layer velocity profile has been generated in the domain by the power-law equation (see Eq. 1). The length of the Atmospheric Boundary Layer (ABL) is taken 1 m.

$$\mathbf{U}_x/\mathbf{U}_\infty = |\mathbf{x}/\mathbf{x}_0|^\alpha. \tag{1}$$

Here, any point height from the ground and the atmospheric boundary layer height are denoted as 'x' and 'x_0'. The wind velocity at any point at x-height and the velocity of free steam are noted as 'U_x' and 'U_∞' respectively. The power low exponent α has been taken as 0.133, which is dependent on the surroundings.

3.2 Generation of Mesh

The tetrahedral type meshing elements (Bhattacharyya and Dalui [16]) are infiltrated in the entire domain expect the building model. The delicate layers of meshing have been adopted around the building. This technique is helpful to simulate good wind flow around the building and effective in the calculation of better wind induced responses. In Fig. 3, the meshing patterns of a typical U6 model has been demonstrated in which it is visible that some delicate layers of mesh have been generated near the buildings.

3.3 Grid Sensitivity Study

The grid sensitivity study has been carried out to find out the suitable mesh size for the numerical study. The results' accuracy depends on the adopted meshing. This

Table 1 The variation in the drag coefficient of primary shape (U1) model for different mesh types

Mesh type	Total elements	Drag coefficient	% of Error
M1	2,884,984	0.8754	−20.264
M2	5,165,448	0.9476	−13.688
M3	12,546,748	1.0142	−7.625
M4	19,853,472	1.0453	−4.791
M5	26,709,214	1.0716	−2.396
M6	33,935,947	1.0959	−0.182
M7	41,093,375	1.0977	–

study initially started on the original U shape with coarser meshing (M1), which involves low computational time and step by step the fine meshing (M2–M7) has been implemented in each step until the calculated response of the current case matches with the previous one. The drag coefficient of the primary U shape model at a wind angle of 0° has been calculated for each case and corresponding errors in results have been estimated, as shown in Table 1.

The M6 meshing pattern has been adopted for the numerical study though the error is almost negligible and also it saves some computation time.

3.4 Validation

The validity of the software package has been checked with the horizontal pressure coefficient values along the horizontal centerline of Face C and D data of the previous research article. For the validation, the model and numerical details are adapted from the article published by Gomes et al. [1]. The wind pressure along the horizontal centreline of mentioned faces for 180° wind angle has been calculated. The comparison of the extracted values has been presented in Fig. 4. The obtained results of the current numerical simulation follow almost the same trend as given in the published article.

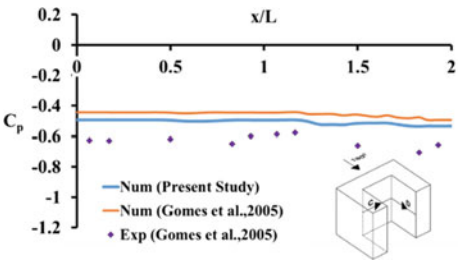

Fig. 4 The pressure variation along the horizontal line for Face C and D

4 Results and Discussion

The change in limb position has a significant impact on the nature of wind behaviour around the building shapes. The various important wind induced responses of different building cases has been extracted from the numerical analysis at 0° and 90° wind angle.

4.1 Wind Flow Streamline

The flow streamlines around the building shape for examined wind angles has been demonstrated in Fig. 5. The position of the limbs greatly affected the wind flow around the building model. However, the axisymmetry in each building case creates an asymmetric flow pattern on both sides. The symmetry in the wind flow has been disturbed by the change in wind angle because of the two limbs. The limbs of the U shape not only irregularize the plan shape but also creates unpredictable wind behaviours around the building. The vortex has been generated in the leeward side of the building and at the wake zone. Those pattern of the vortex reforms because of the shifts. With the change in angle, the vortices are also formed in between the two limbs and the variation in vortex formation is also visible when those limbs are gradually shifted to the centre.

The variation in flow pattern causes a variation in wind induced responses on those limbs shifted U shape buildings. The velocity has been increased at the flow separated corners.

4.2 Comparison of Force Coefficients

The force coefficient values have been extracted for two limbs shifted buildings at 0° and 90° wind angle and presented in Fig. 6 to understand across and along wind response of those buildings.

It is visible that the along wind response decreases with the shifting up to a specific limit and the axisymmetric position of limb manages the effect of across wind response at 0° angle. The drag coefficient of the building has minimized gradually due to the shifting of both limb from 0.05 to 0.2 L for 0° wind angle but some increment is observed with the further shifting. However, the change in wind angle causes some concern. The drag coefficient and lift coefficient has increased gradually up to the extreme sifting length of 0.3L for 90° wind angle. This indicates that the sifting of the limb is effective in drag coefficient reduction when the wind angle is 0°, but when the angle of wind changes, these benefits are no longer exists instead it creates huge variation in wind responses.

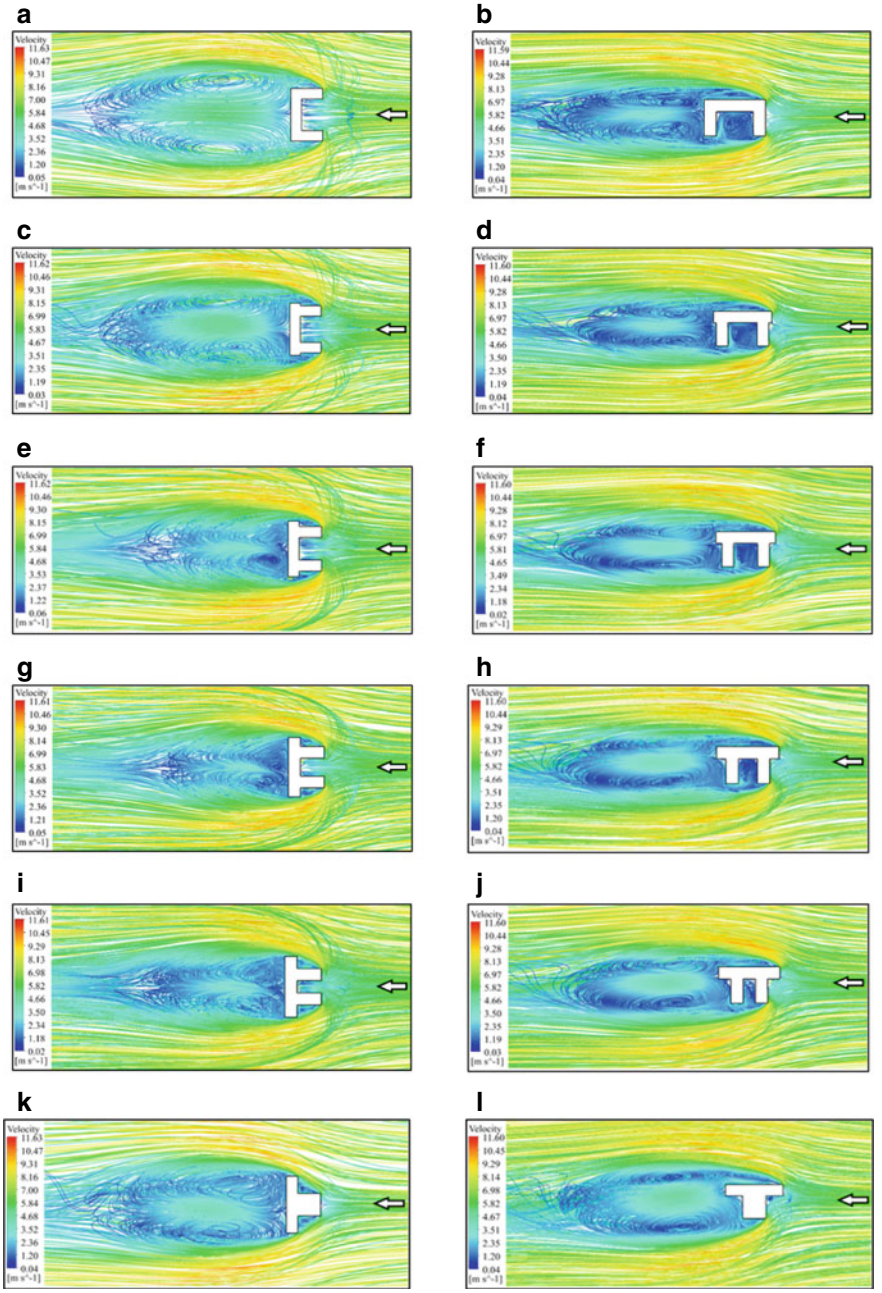

Fig. 5 The wind velocity streamlines around the various building for 0° and 90° wind angle **a** U1 Building at 0° wind angle, **b** U1 Building at 90° wind angle, **c** U2 Building at 0° wind angle, **d** U2 Building at 90° wind angle, **e** U3 Building at 0° wind angle, **f** U3 Building at 90° wind angle, **g** U4 Building at 0° wind angle, **h** U4 Building at 90° wind angle, **i** U5 Building at 0° wind angle, **j** U5 Building at 90° wind angle, **k** U6 Building at 0° wind angle, **l** U6 Building at 90° wind angle

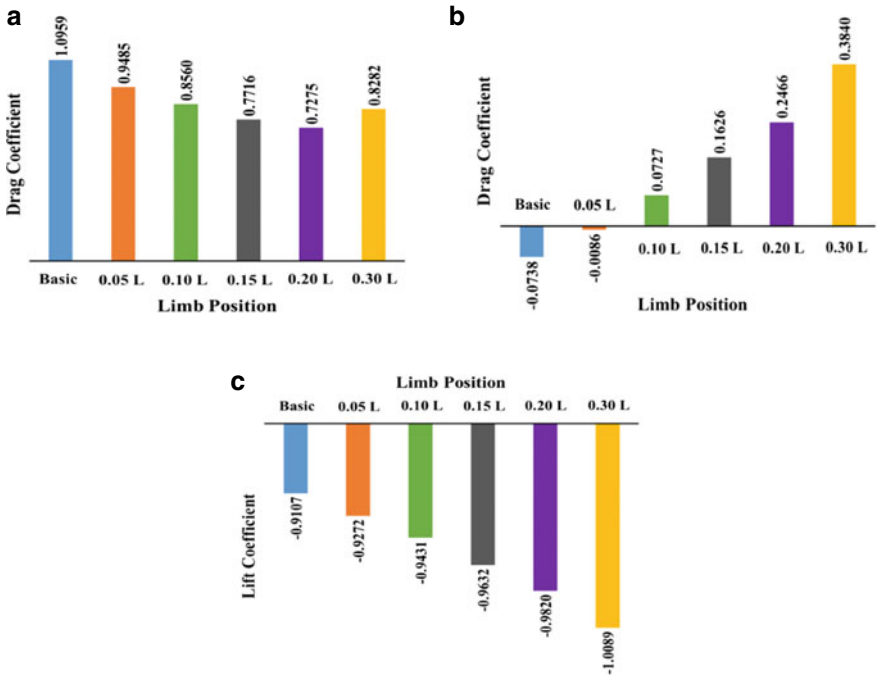

Fig. 6 The variation in force coefficients for limb shifting, **a** Drag Coefficient for 0° angle, **b** Drag Coefficient for 90° angle, **c** Lift Coefficient for 90° angle

4.3 Comparison of Pressure Coefficients

The mean pressure coefficient on the faces of different cases is presented in Tables 2, 3, 4 and 5. The flow pattern around the shape directly influences the pressure distribution on the building face.

For 0° wind angle, the mean positive pressure on face A increases with the shifting. However, on the interior faces (B, C and D) the mean pressure decreases because of

Table 2 The mean pressure coefficient on primary faces of the various shape for 0° angle

Limb Position (L)	Face A	Face B	Face C	Face D	Face E	Face F	Face G	Face H
0.00	0.4100	0.8275	0.8702	0.8275	0.4100	−0.5610	−0.3805	−0.5610
0.05	0.4385	0.8239	0.8636	0.8239	0.4357	−0.5714	−0.3554	−0.5714
0.10	0.4435	0.8224	0.8617	0.8224	0.4435	−0.6621	−0.4086	−0.6621
0.15	0.4726	0.8098	0.8470	0.8098	0.4726	−0.6159	−0.4152	−0.6159
0.20	0.5525	0.7912	0.8257	0.7912	0.5525	−0.4002	−0.3962	−0.4002
0.30	0.6995	–	–	–	–	0.0793	−0.3771	0.0793

Table 3 The mean pressure coefficient on the corner faces of the various shape for 0° angle

Limb Position (L)	Face F1	Face F2	Face H1	Face H2
0.00	–	–	–	–
0.05	−0.4576	−0.4521	−0.4576	−0.4521
0.10	−0.4277	−0.4890	−0.4277	−0.4890
0.15	−0.4013	−0.4941	−0.4013	−0.4941
0.20	−0.2332	−0.5454	−0.2332	−0.5454
0.30	0.2065	−0.5502	0.2065	−0.5502

Table 4 The mean pressure coefficient on primary faces of the various shape for 90° angle

Limb Position (L)	Face A	Face B	Face C	Face D	Face E	Face F	Face G	Face H
0.00	−0.4369	−0.5730	−0.5450	−0.5493	−0.6747	0.5671	−0.4764	−0.2803
0.05	−0.4711	−0.5990	−0.5739	−0.5796	−0.7344	0.6351	−0.4959	−0.2908
0.10	−0.4810	−0.5787	−0.5570	−0.5626	−0.7156	0.6288	−0.4881	−0.3066
0.15	−0.4928	−0.5637	−0.5460	−0.5496	−0.6912	0.6256	−0.4948	−0.3233
0.20	−0.4954	−0.5499	−0.5362	−0.5390	−0.6747	0.6198	−0.5040	−0.3401
0.30	−0.5124	–	–	–	–	0.6056	−0.4892	−0.3624

Table 5 The mean pressure coefficient on the corner faces of the various shape for 90° angle

Limb Position (L)	Face F1	Face F2	Face H1	Face H2
0.00	–	–	–	–
0.05	0.8585	0.5228	−0.2684	−0.2902
0.10	0.8480	0.5324	−0.2921	−0.2958
0.15	0.8224	0.5444	−0.3166	−0.3091
0.20	0.7874	0.5477	−0.3427	−0.3270
0.30	0.7046	0.5574	−0.3834	−0.3558

the increase in suction pressure due to the interference between shifted two limbs when the limbs are shifted. The suction on leeward faces increases with the sifting up to 0.15L after that the suction is decreased due to the presence of positive pressure on shifted position. The suction on face F1 and H1 decreases with the increase in sifting length but an increase in suction is observed in face F2 and H2. The axisymmetric faces exerted the same pressure variation at 0° wind angle (Fig. 7).

At 90° wind angle, all the faces exerted suction except face F, F1 and F2. The suction in face A, H, H1 and H2 increases with limb shifting. The increase in suction is noticed on face B, C, D and E up to the sifting of 0.05L, but after that, it decreases with further shifting. The increase in positive pressure is observed in face F2, but a

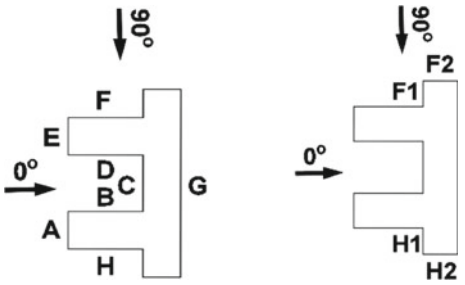

Fig. 7 The building faces of a typical shifted case

decrease in positive pressure occurs in face F1 with the sifting. At face F, the positive pressure increases up to 0.05L then decrement observed till 0.3L limb shifting.

Figure 8 is showing the various faces of the original U shape, a typical limb shifted case and 0.30L shifted case. These figures are also showing the direction of measured horizontal pressure. The pressure has been calculated at mid-height (250 mm) for each case. The pressure coefficient along the horizontal centerline for all the shapes has been presented in Fig. 9 to visualize the pressure variation along the perimeter of those shapes due to the shifting.

From Fig. 9 it is clear that the variation in pressure is visible mainly at the corner faces (A, E, F, F1, F2, H, H1 and H2) of shifted limbs. The shifting of 75 mm from each side has a significant variation compared to all other shifts for each wind angle. The inner faces (B, C and D) are experiencing almost similar wind pressure in all limb locations.

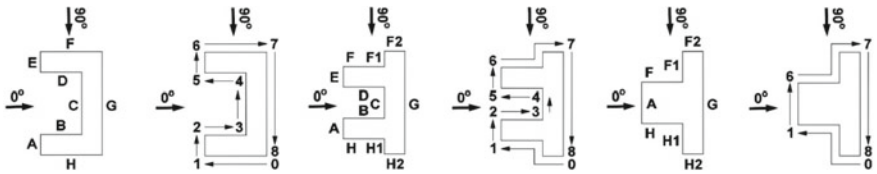

Fig. 8 The building faces of typical cases and the measured pressure coefficient direction

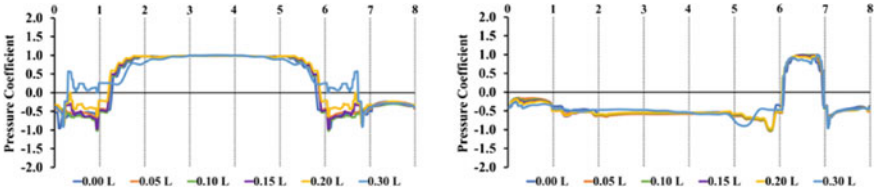

(a) 0° (b) 90°

Fig. 9 The pressure coefficient along the horizontal centerline for various cases **a** 0°, **b** 90°

5 Conclusions

In the present study, the variation in wind effect has been investigated because of both limbs shifting from extreme end to centre points at 0° and 90° wind angle. The shifting of both limbs has the advantage to have an axisymmetry shape in each shifting case. The wind induced pressure, lift and drag coefficient has been measured and compared. The comparison of those value indicates the impact of wind on those altered shape. The observations from this study can be summed up as follows.

- The drag coefficient of the building minimizes with the increase in shifting length from both sides of the end up to a distance of 50 mm for 0° wind angle, but further increase in sifting length attracts more drag force than the previous shifting length case. The axisymmetric shape does not draw significant lift force on that mentioned angle.
- The change in wind angle attracts more drag and lift force in shifted shape than the basic shape. The drag and lift coefficient both gradually increase with the increase in shifting length.
- The suction and pressure both are increased at the outer surfaces of those shifted shapes for 0 and 90° wind angle respectively. However, the inner surface of those shape exerted less suction and pressure in these cases. The significant pressure variations are observed on the outer faces of the entirely shifted (0.30L) shape. Those points should be considered for the cladding design of those buildings.

From the above discussion, it is quite clear that limb shifting has the benefit over basic shape when the wind flows at a normal angle, but the benefits no longer exist when the wind angle changes because of the increase in both lift and drag force. So, these factors have to be taken with special care. Therefore, this research indicates the benefits as well as the drawback of the limb shifting under wind loads which fulfils the objective of the study. The explored information from this study is significant and unique since no past literature has information about the effect of limb position on U plan shaped tall building. This study also indicates the requirements of a detailed study in different wind direction if the designer wants to construct a U shape building having shifted limbs from both sides. This study will guide the designer about the factors which should be considered for a safe design.

References

1. Gomes MG, Rodrigues AM, Mendes P (2005) Experimental and numerical study of wind pressures on irregular-plan shapes. J Wind Eng Ind Aerodyn 93(10):741–756
2. Zhao JG, Lam KM (2008) Interference effects in a group of tall buildings closely arranged in an L- or T-shaped pattern. Wind Struct An Int J 11(1):1–18
3. Amin J, Ahuja A (2011) Experimental study of wind-induced pressures on buildings of various geometries. Int J Eng Sci Technol 3(5):1–19
4. Raj R, Ahuja AK (2013) Wind loads on cross shape tall buildings. J Acad Ind Res 2(2):111–113

5. Mukherjee S, Chakraborty S, Dalui SK, Ahuja AK (2014) Wind induced pressure on 'Y' plan shape tall building. Wind Struct An Int J 19(5):523–540
6. Ahlawat R, Ahuja AK (2015) Wind loads on 'T' plan shape tall buildings. J Acad Ind Res 4(1):27–30
7. Cheng L, Lam KM, Wong SY (2015) POD analysis of crosswind forces on a tall building with square and H-shaped cross sections. Wind Struct An Int J 21(1):63–84
8. Mashalkar BS, Patil GR, Jadhav AS (2015) Effect of plan shapes on the response of buildings subjected to wind vibrations. IOSR J Mech Civ Eng 1:80–89
9. Li Y, Li QS (2016) Across-wind dynamic loads on L-shaped tall buildings. Wind Struct An Int J 23(5):385–403
10. Ranka S, Shingade PVS (2016) Analytical and numerical analysis of wind load on tall buildings. Int J Eng Sci Technol 5(11):3188–3197
11. Paul R, Dalui SK (2016) Wind effects on 'Z' plan-shaped tall building: a case study. Int J Adv Struct Eng 8(3):319–335
12. Ullas A, Nimisha P (2017) Response of buildings of different plan shapes subjected to wind vibrations. Int Res J Eng Technol **4(**5):1625–1628
13. Bhattacharyya B, Dalui SK (2018) Investigation of mean wind pressures on ' E ' plan shaped tall building. Wind Struct An Int J 26(2):99–114
14. Mallick M, Kumar A, Patra KC (2019) Experimental investigation on the wind-induced pressures on C-Shaped buildings. KSCE J Civ Eng 23(8):3535–3546
15. Mandal S, Dalui SK, Bhattacharjya S (2020) Effect of aerodynamic modifications on a tall building with horizontal irregularity. Adv In Struc Sys Mat 99–107
16. Bhattacharyya B, Dalui SK (2020) Experimental and numerical study of wind-pressure distribution on irregular-plan-shaped building. J Struct Eng (United States) 146(7):1–14
17. Löhner R et al (2015) Journal of wind engineering recent advances in computational wind engineering and fluid-structure interaction. J Wind Eng Ind Aerodyn 144:14–23
18. Revuz J, Hargreaves DM, Owen JS (2012) On the domain size for the steady-state CFD modelling of a tall building. Wind Struct An Int J 15(4):313–329

Cross-stream Deployment of Delta Vortex Generators in Finned Tube Arrays for Flow Modification and Capacity Augmentation

Amit Arora and P. M. V. Subbarao

1 Introduction

Development of high effectiveness heat exchange modules is an important research area as it promises lower material cost. Liquid-to-gas heat exchangers are widely used for building domestic as well as industrial air-conditioning systems. There is a large range of designs available depending up on the tube and fin shapes. Apart from their physical design, the heat exchange capacity of such heat exchangers is largely controlled by the gas-side thermal resistance [1, 2]. Generally there are plain or corrugated fins on the gas-side; accordingly they are referred as finned tube array (or bank). A schematic view of finned tube array is shown in Fig. 1a. The air flow over the tubes is essentially a case of cross flow [3], and the flow separation is a common phenomenon in these heat exchangers. Such an occurrence makes a large fin area ineffective for the heat exchange which mainly lies in the tube wakes. Apparently thermal management of the tube wake region is essential to improve the effectiveness of finned tube arrays.

Incorporating longitudinal vortex generators (LVGs) is an effective way of passively curtailing the occurrence of wake region [1, 5]. Generation of longitudinal vortices (LVs) in the baseline flows results in large scale mixing of the core and near wall fluid, thereby producing large augmentation in the heat transfer coefficients [6, 7]. Among various types of LVGs, the toe-out type winglets are a preferred design for the wake management as it directs the approaching flow behind the tubes [8–10]. They should be deployed, in pair, behind each tube. Fins with a pair of toe-out type triangular vortex generator erected behind each hole, meant for inserting tubes, are

A. Arora (✉)
Department of Mechanical Engineering, MNIT Jaipur, Jaipur 302017, India
e-mail: amit.mech@mnit.ac.in

P. M. V. Subbarao
Department of Mechanical Engineering, IIT Delhi, New Delhi 110016, India

D. K. Maiti et al. (eds.), *Recent Advances in Computational and Experimental Mechanics, Vol II*, Lecture Notes in Mechanical Engineering,
https://doi.org/10.1007/978-981-16-6490-8_11

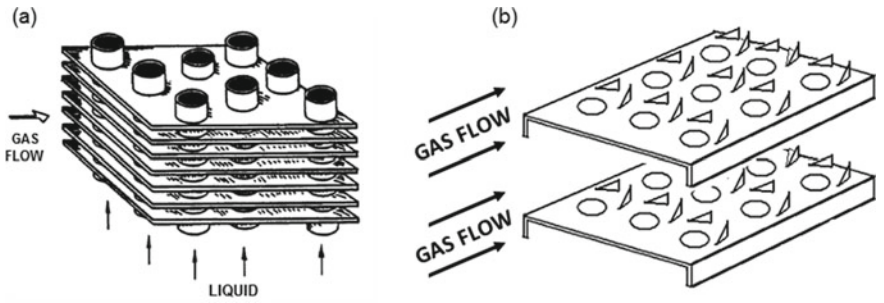

Fig. 1. **a** Finned tube array [4], **b** Fins with toe-out type LVGs

shown in Fig. 1b. It is apparent that their ability to modify the wake region depends on their position around the tube, accordingly they require thoughtful deployment in order to use them effectively for the stipulated task. Here, it may be noted that the triangular winglets are commonly referred as delta winglets.

In an experimental study of finned tube array with delta winglets, the percentage augmentation in the gas-side heat transfer coefficient is found to be dependent on the number of winglet rows in the flow direction [11]. When the winglets were deployed behind the first tube row, the heat transfer coefficient increased by 16.5–44% over the Reynolds number range 220 to 960. But when the winglets were deployed behind each alternate tube row, a large jump in the heat transfer augmentation was noticed which lies in the range 30–68.8%. Another study also reported the effect of number of winglet rows, in the flow direction, by deploying toe-out type rectangular winglets in an inline finned tube heat exchanger [12]. This numerical investigation indicated that the average heat transfer coefficient as well as the pressure drop increases with the number of winglet rows. Some other numerical studies considered toe-out type delta winglets, erected adjacent to the tubes, and found that they too are effective in achieving large capacity augmentation of such heat exchangers [8, 9]. The effect of longitudinal displacement of the winglets, in an inline finned tube array, is studied numerically in the Reynolds number range 500–3000 [13]. It is observed that the winglets result in increased vorticity which manifests as the rise in temperature gradients, hence the heat transfer rate. Further it is reported that the thermal augmentation is achieved at the cost of higher pressure drop. In another numerical study [8], the effect of varying attack angle of toe-out type delta winglets placed in an inline finned tube heat exchanger was investigated at a fixed Reynolds number (Re = 800). The attack angle was varied in a narrow range from 10–20°, and it is realized that the Nusselt number as well as the pressure drop increases with the attack angle. Also, the numerical simulations showed that the deployment of toe-out winglets at the tube upstream produces higher thermal augmentation compared to the downstream locations, but at the cost of higher pressure drop [14]. Despite higher augmentation, such a deployment is not preferred as it is unsuitable for causing the desired flow modifications by way of directing approaching flow in the tube wake region.

Although both rectangular and triangular (or delta) winglets are equally popular in the literature, triangular winglets deliver higher thermal augmentation compared to rectangular winglets under same area constraint [15]. Therefore, the present study uses toe-out type delta winglets for improving the heat exchange rates particularly in the poorly utilized fin area that exists in the tube wake of plain finned tube arrays. Since spatial positioning of the winglets in the tube downstream has a critical role in determining the degree of augmentation, their cross-stream position is changed in discrete steps to analyze the effect on the wake modification, and the heat exchange capacity.

2 Numerical Formulations

Three dimensional numerical simulations are performed to analyze the effect of winglet position on the flow modifications. As RNG k-ε model is adopted for modelling turbulence [13, 16, 17], the governing equations catering to steady incompressible turbulent flow through the finned tube array include mass, momentum (RANS), energy, turbulent kinetic energy (k), and turbulent energy dissipation rate (ε) equations. The governing equations are discretized by using finite volume method [18], and SIMPLE (semi-implicit method for pressure linked equations) algorithm is used for the pressure–velocity coupling [19]. A commercial CFD code, ANSYS Fluent 14.0, is used to solve the governing equations which are expressed below with indexed notations.

Continuity equation:

$$\frac{\partial\left(\rho u_i\right)}{\partial x_i} = 0. \tag{1}$$

Momentum (RANS) equation:

$$\frac{\partial\left(\rho u_i u_j\right)}{\partial x_i} = -\frac{\partial p}{\partial x_j} + \frac{\partial}{\partial x_i}\left[\mu\left(\frac{\partial u_i}{\partial x_j} + \frac{\partial u_j}{\partial x_i} - \frac{2}{3}\delta_{ij}\frac{\partial u_k}{\partial x_k}\right)\right] + \frac{\partial}{\partial x_i}\left(-\rho\overline{u_i' u_j'}\right). \tag{2}$$

Reynolds stress term is calculated by using Boussinesq hypothesis as expressed below,

$$-\rho\overline{u_i' u_j'} = \mu_t\left(\frac{\partial u_i}{\partial x_j} + \frac{\partial u_j}{\partial x_i}\right) - \frac{2}{3}\left(\rho k + \mu_t\frac{\partial u_k}{\partial x_k}\right)\delta_{ij}. \tag{3}$$

Energy equation:

$$\frac{\partial[u_i(\rho E + p)]}{\partial x_i} = \frac{\partial}{\partial x_i}\left(k_{eff}\frac{\partial T}{\partial x_i}\right), \tag{4}$$

where 'E' is the total energy and k_{eff} is the effective thermal conductivity.

The transport equations for the turbulent kinetic energy 'k' and dissipation rate 'ε' are expressed as follows:

$$\frac{\partial}{\partial x_i}(\rho k u_i) = \frac{\partial}{\partial x_i}\left(\alpha_k \mu_{eff} \frac{\partial k}{\partial x_i}\right) + \mu_t S^2 - \rho\varepsilon, \tag{5}$$

$$\frac{\partial}{\partial x_i}(\rho \varepsilon u_i) = \frac{\partial}{\partial x_i}\left(\alpha_\varepsilon \mu_{eff} \frac{\partial \varepsilon}{\partial x_i}\right) + C_{1\varepsilon}\frac{\varepsilon}{k}\mu_t S^2 - C_{2\varepsilon}\rho\frac{\varepsilon^2}{k} - R_\varepsilon, \tag{6}$$

where (α_k and α_ε) are inverse effective Prandtl numbers for (k and ε) respectively, (S) is the modulus of the mean rate of strain tensor, (μ_t) is the turbulent (or eddy) viscosity, (μ_{eff}) the is effective viscosity, ($C_{1\varepsilon}$, $C_{2\varepsilon}$) are the model constants and (R_ε) is the rate of strain term. Their mathematical definition/value is available in literature [13, 20].

In order to check the mesh quality, multi-block hybrid approach is used; and second-order upwind scheme is used to model the convective terms. The effects of buoyancy forces and the viscous dissipation are disregarded [17], and the thermo-physical properties of air are treated constant which are computed at the bulk mean temperature. The solid is assumed isotropic, and the tube wall is considered isothermal [6, 13]. The heat exchange through the fins is modeled as conjugate heat transfer problem. The convergence was concluded when the normalized residuals of the energy equation and rest of the equations were $\leq 10^{-8}$ and $\leq 10^{-5}$ respectively.

2.1 Computational Domain and Boundary Conditions

Finned tube array adopted for the study has three tube rows in the flow direction. Its geometric specifications are presented in Table 1. A pair of delta winglet type LVG is deployed in the downstream of each tube, as depicted in Fig. 1b.

Although degree of heat transfer enhancement increases with the attack angle, the pressure loss increases at a faster rate due to the flow separation occurring at the leading edge of the vortex generators [22]. Therefore the delta winglets are erected

Table 1 Heat exchanger design [21]

Geometric feature	Symbol	Dimension (m)
Tube diameter	D	0.038
Longitudinal tube pitch	P_L	0.1
Transverse tube pitch	P_T	0.1
Fin space	H	0.012
Fin pitch	P_f	0.013
Tube length	L_t	0.3
Fin thickness	t	0.001

with a conservative yet conducive attack angle of 30°. The aspect ratio 'AR' of the winglets is kept equal to unity [23]. The computational expense is restricted by modelling a periodic section in the tube axial direction, and a symmetric section in the transverse direction, as shown in Fig. 2. Various boundary conditions applied for solving the flow are given in Table 2.

Extended flow lengths equal to 10H and 30H are provided at the inlet and exit to capture the entry and exit effects respectively. The conditions prescribed at the far-field inlet and exit boundaries are "uniform velocity" and "outflow" respectively [21]. Additionally, turbulent intensity is prescribed at the inlet boundary which is determined by an empirical correlation [16, 20].

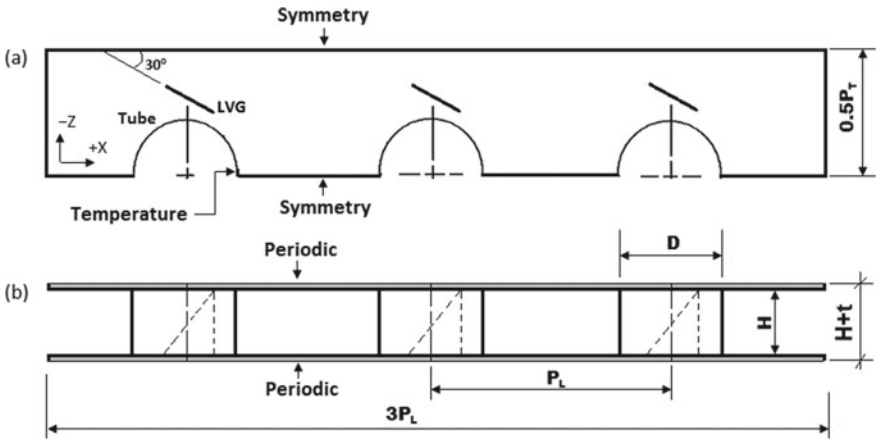

Fig. 2 Computational domain. **a** Plan, **b** elevation

Table 2 Boundary conditions in the computational domain

Physical boundary	Velocity B.C	Thermal B.C
Flow inlet	Uniform velocity	Uniform temperature
Flow exit	Outflow	Outflow
LVG surface	No slip	Adiabatic
Tube surface	No slip	Isothermal
Upper and lower bounds (y-direction)	Periodic	Periodic
Front and rear bounds (z-direction)	Symmetry	Symmetry

2.2 Grid Selection and Model Validation

The viscosity affected regions were resolved by placing the wall adjacent nodes at y^+ value less than unity. In order to contain the total mesh volumes, graded mesh is adopted to a large extent as shown in Fig. 3. An iterative test was carried out at highest Reynolds number to obtain the mesh. The models for the heat exchangers with and without LVGs have approximately 4.3 and 4.2 million cells respectively. Thereafter, the computational model was validated in reference to the published experimental data [21], as depicted in Fig. 4. The Reynolds number varies in the range 1415–7075. The characteristic dimension for defining the Reynolds number equals twice the fin-space, and the characteristic velocity is far-field inlet velocity [10, 24]. The pressure drop across the fin array may be expressed in a dimensionless form which is referred as apparent friction factor 'f_{app}' as given by Eq. (8). Here, A_{min} is the minimum flow

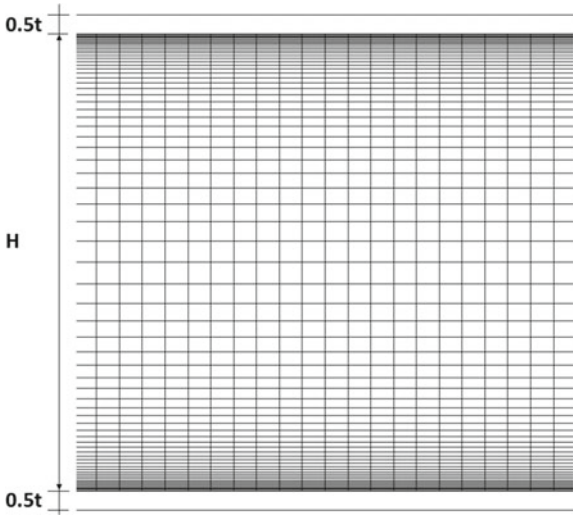

Fig. 3 Graded meshing

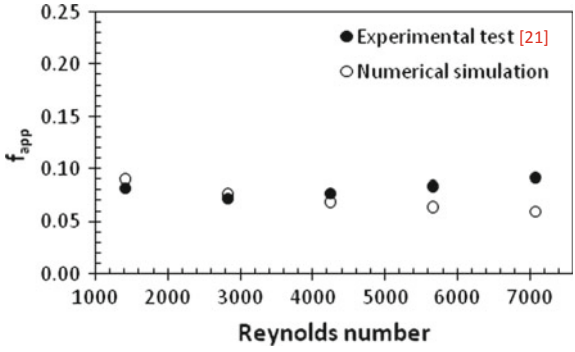

Fig. 4 Model validation based on friction factor

area (m^2), A_o is the total heat transfer area (m^2), Δp is the pressure drop (Pa).

$$\text{Reynolds number, Re} = \frac{\rho L_c U_\infty}{\mu}. \tag{7}$$

$$\text{Friction factor, } f_{app} = \frac{2.\Delta p}{\rho U_\infty^2}.\frac{A_{min}}{A_o}. \tag{8}$$

3 Results and Discussions

Once the computational model was duly validated, it was used for studying the effect of LVG deployment on the tube-wake modification followed by the study of change in LVG position on the flow structures and consequent effects on the heat transfer. The finned tube array comprises of three tube rows in the flow direction, and the LVGs make 30° angle with the main flow direction. In order to analyze the effect of winglet position on the performance change, the vortex generators were displaced in small steps in the cross-stream direction (i.e. z-axis) while keeping their streamwise position fixed. For a detailed study, two different stream-wise locations were selected in the tube downstream (i.e. X/D = 0.5 and X/D = 0.9). The LVGs were displaced in the cross-stream direction in small steps with step-size equal to Z/D = 0.2, as apparent in Fig. 5. Here, X/D is the dimensionless distance of the LVGs in the streamwise direction and Z/D is the distance in the cross-stream direction. Furthermore, 'P_L' is the longitudinal tube pitch, 'P_T' is the transverse tube pitch, and 'D' is the tube diameter. Their geometric values are given in Table 1.

As evident, nearest LVG position in the z-direction is Z/D = 0.5 in case of first stream-wise position (i.e. X/D = 0.5) and it is Z/D = 0.3 in case of X/D = 0.9.

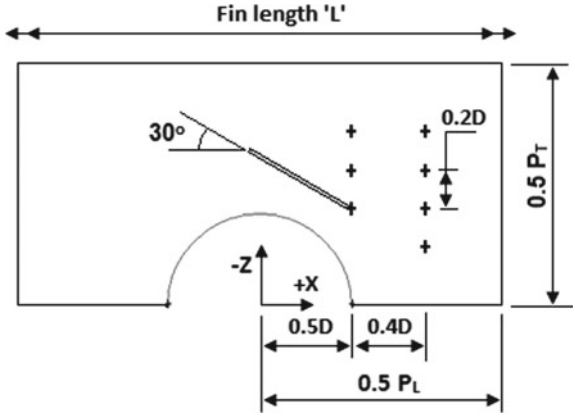

Fig. 5 Locations for deploying longitudinal vortex generators (LVGs)

There are three different cross-stream positions for erecting LVGs at the first stream-wise position. In contrast, there are four different cross-stream positions for erecting LVGs corresponding to the second stream-wise position. The results and discussions in the remaining part of the manuscript correspond to a fixed Reynolds number (Re = 4245).

3.1 Change in Wake Structures Due to LVG Deployment

As convective heat transfer is mainly attributed to the bulk motion resulting due to the prevailing flow structures, it is important to first appreciate and acknowledge the principal structures in the baseline flow and the effect of LVG deployment on the flow modifications. For that purpose, pathlines are first generated in the baseline flow, as shown in Fig. 6a. Thereafter, pathlines are generated at the same Reynolds number for two different cross-stream positions, one nearest and other farthest, of the LVGs held at the same stream-wise position (i.e. X/D = 0.9), as shown in Fig. 6b, c.

In Fig. 6a, it is evident that all the tubes have large recirculation regions in their downstream. Such an occurrence is likely to make the affected fin surface virtually ineffective for heat exchange with the adjacent fluid. It is encouraging to observe that the deployment of LVGs has resulted in dramatic reduction in the spread of baseline wakes, as apparent in Fig. 6b, c. Such a visible change is expected to produce large augmentation in the heat transfer coefficients.

Further comparison of Fig. 6b, c tells that despite of same stream-wise location, the two cases of LVGs have different impact on the baseline wakes. The LVGs positioned at Z/D = 0.3 are largely immersed in the tube wake whereas the LVGs corresponding to Z/D = 0.9 are totally away from it. It is observed that the LVGs placed at the former cross-stream position are able to effectively pump the approaching flow in the tube wakes but they are ineffective in generating large scale longitudinal vortical motion. In contrast, the LVGs in the second case are less effective in curtailing the wake spread but they are able to generate three dimensional longitudinal vortex over a large fin area. Such a noticeable change in the flow characteristics is expected to produce significant rise in the heat transfer coefficients on the affected parts of the fin surface.

The effect of change in LVG position on the wake modification is analyzed by comparing the velocity profiles corresponding to all four cross-stream positions of the LVGs, as shown in Fig. 7. The velocity profiles are drawn in a plane that passes through the center of fin space. The vortex generators are positioned at a fixed stream-wise location (i.e. X/D = 0.9), and they are displaced in the transverse direction with a small step wise of Z/D = 0.2. Evidently, LVGs at all positions, except Z/D = 0.3, have caused visible shrinkage in the spread of recirculation regions. Further it may be noticed that the span of the recirculation zone initially decreases with the outward cross-wise movement of the LVGs followed by the eventual growth as the vortex generators move away too far.

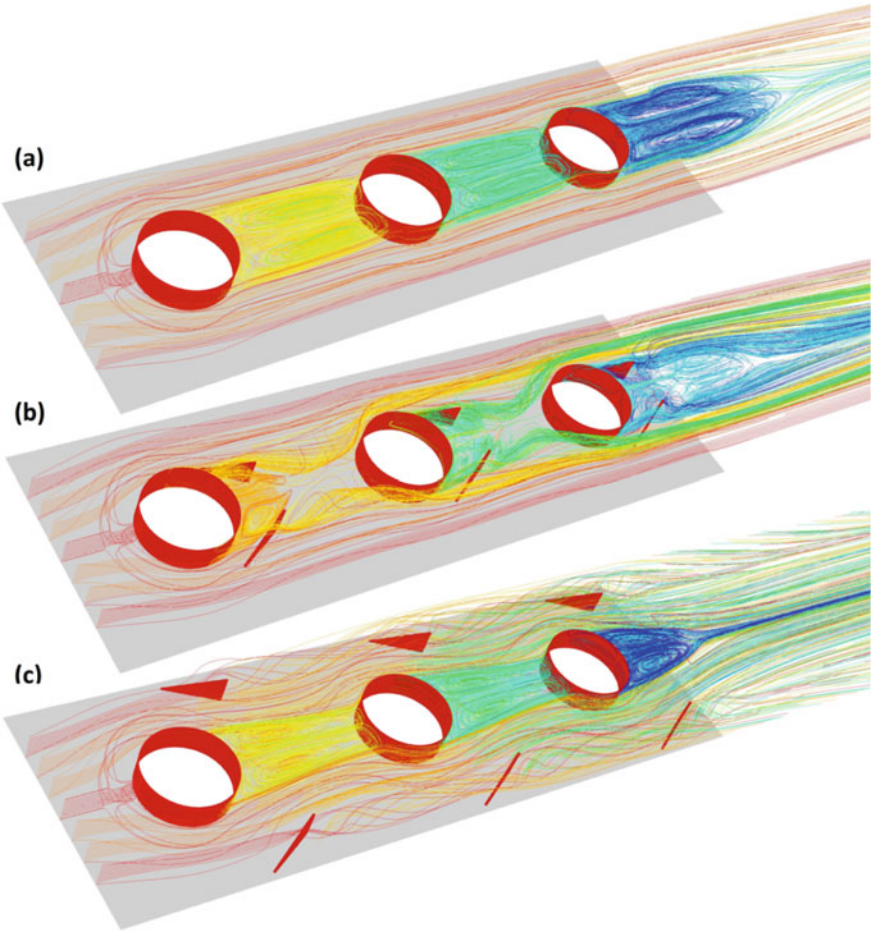

Fig. 6 Pathlines. **a** No LVG, **b** LVG at Z/D = ±0.3, **c** LVG at Z/D = ±0.9

3.2 Thermal Management of Tube Wake

Changes in the flow structure are expected to have a direct bearing on the heat fluxes. The combined effect of redirecting the approaching flow and the generation of longitudinal vortices caused by the LVGs should produce large thermal augmentations particularly on the downstream tubes and the fin surface hiding behind the tubes. In order to analyze the effect of flow modifications on the thermal characteristics, average heat transfer coefficients of all tubes as well as the fin area affected by the tube wakes are separately computed and compared with the baseline case.

In Fig. 8, the average heat transfer coefficients, of the three tube rows, corresponding to the two stream-wise LVG positions are compared in reference to the baseline heat exchanger. Evidently, all cases of the finned tube array with LVGs are

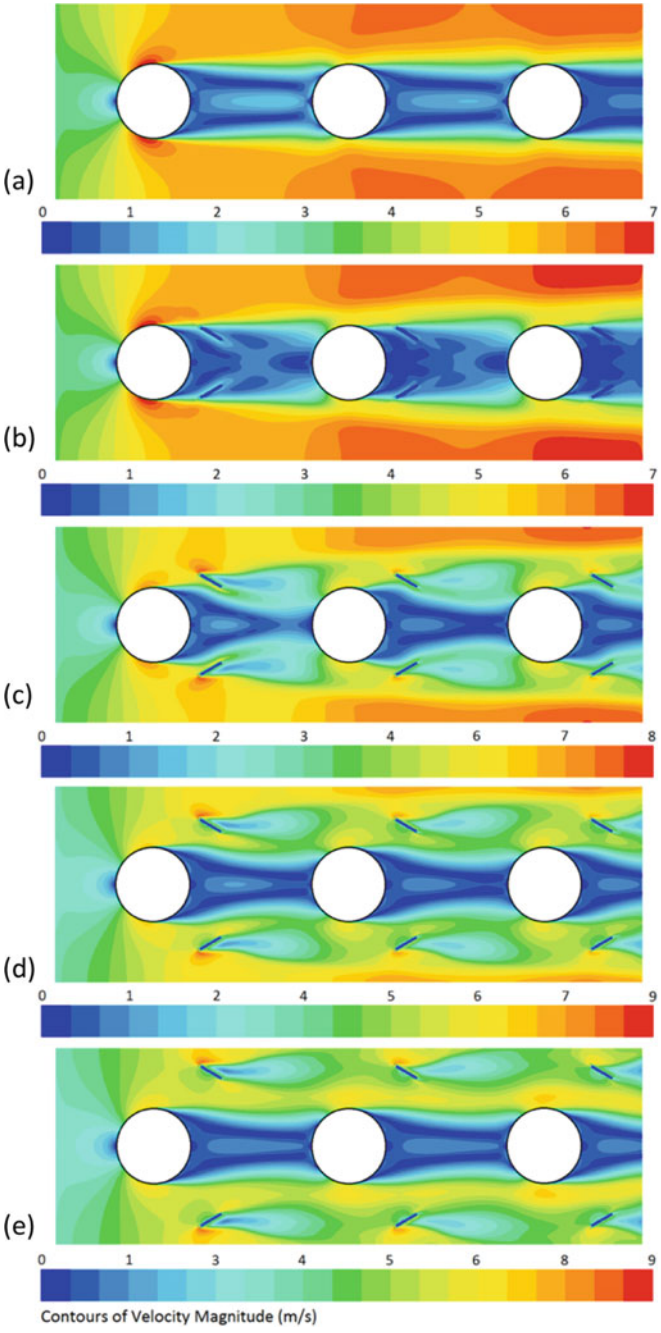

Fig. 7 Velocity profiles. **a** No LVG, **b** LVG at Z/D = ±0.3, **c** LVG at Z/D = ±0.5, **d** LVG at Z/D = ±0.7, **e** LVG at Z/D = ±0.9

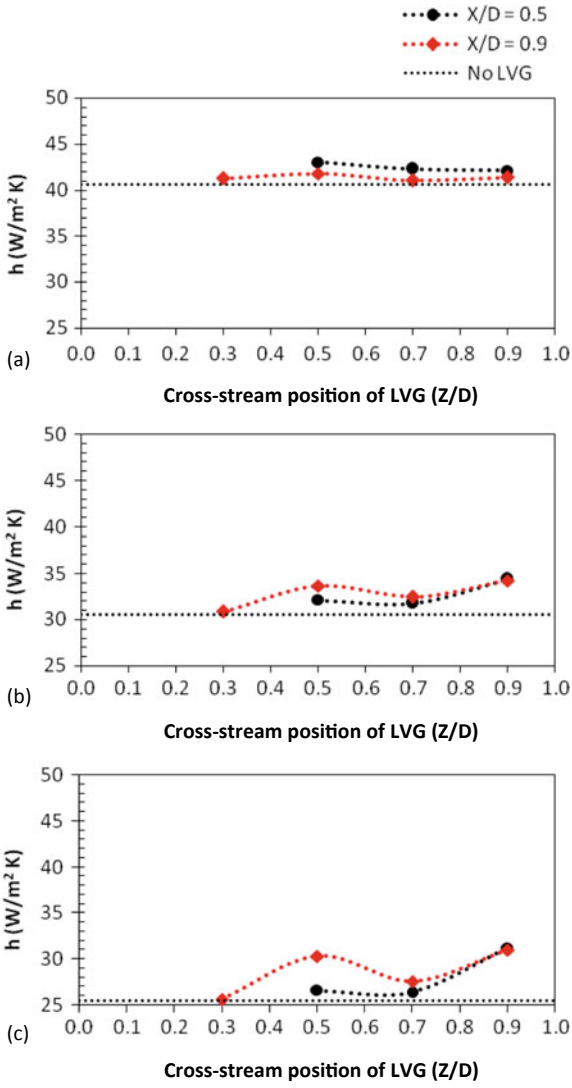

Fig. 8 Average heat transfer coefficient of each tube row. **a** First row, **b** second row, **c** third row

performing better than the baseline case. Further it may be noticed that the leading tube experiences least augmentation which is virtually insensitive to the cross-wise LVG translation. Such a behaviour may be attributed to no wake present at the upstream of the leading tube. Unlike leading tube, the heat transfer enhancement on the downstream tubes have same pattern irrespective of different stream-wise locations but there is no one-to-one correspondence with the cross-wise change in the LVG position. Apart from the downstream tubes, there is a large fin surface which is seriously affected by the tube wakes. The flow structures in the plain finned tube array, shown in Figs. 6a and 7a, make it pretty evident that the fin area hiding behind

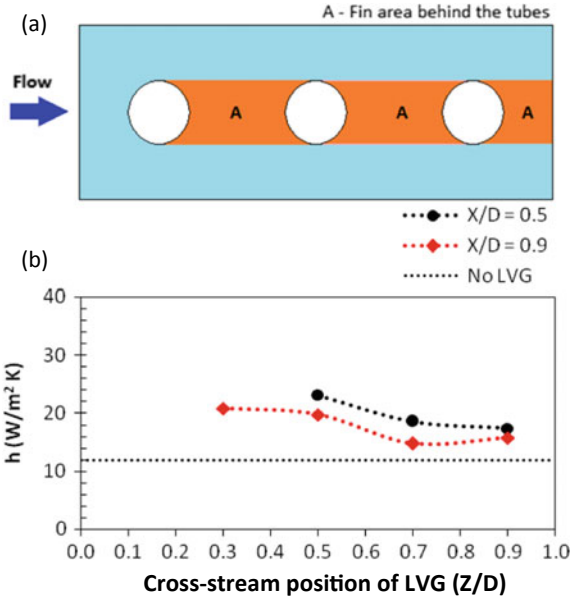

Fig. 9. **a** Fin area hiding behind the tubes, **b** heat transfer coefficient of the fin area behind the tubes

the tubes, shown in Fig. 9a, is a close representative of the fin surface affected by tube wakes.

The average heat transfer coefficients corresponding to the fin area hiding behind the tubes are compared in reference to the baseline heat exchanger in Fig. 9b. Evidently, the degree of augmentation is highest when the LVGs are held close to the tubes in the transverse direction. The augmentation gradually decays to eventually become asymptotic, but it remains better than the plain finned tube array.

3.3 Overall Capacity Augmentation

The combined effect of augmentations in the heat transfer coefficients on the tubes, the fin surface behind the tubes, and the fin area beyond wake regions results in overall increase in the heat transfer capacity of the heat exchanger at the same Reynolds number.

It is apparent from Fig. 10 that the deployment of LVGs at the two streamwise locations resulted in confirmed augmentation. When the LVGs are largely hidden behind the tubes (i.e. Z/D = 0.3), the degree of augmentation is least which grows monotonically with the outward displacement in the cross-stream direction. The highest augmentation corresponding to the nearer streamwise position (i.e. X/D = 0.5) is 124.9%, and it is 121.7% for the LVGs positioned at X/D = 0.9.

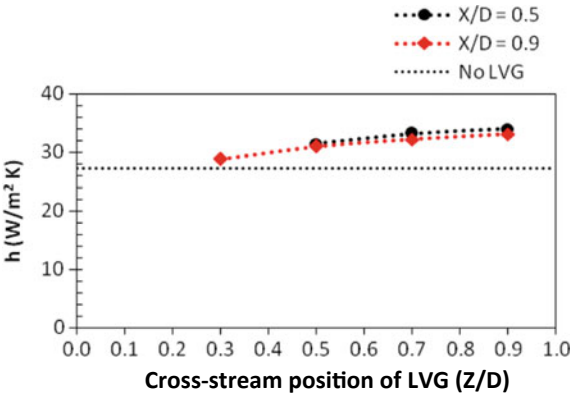

Fig. 10 Average heat transfer coefficient of the finned tube array

4 Conclusions

All the tubes in the plain finned tube array are found to have large recirculation regions in their downstream. The deployment of toe-out type delta winglets, erected with 30° attack angle, has resulted in significant reduction in the spread of baseline wakes. The span of the recirculation zone is found to initially decrease with the outward cross-wise movement of the vortex generators followed by re-enlargement. The combined effect of redirecting the approaching flow in the tube wakes and the generation of longitudinal vortices, by the LVGs, produced appreciable thermal augmentations at the same Reynolds number particularly on the downstream tubes and the fin surface hiding behind the tubes. When the winglets largely hide behind the tubes, degree of overall thermal augmentation is least, which is found to increase with the outward displacement of winglets in the cross-stream direction. The highest augmentation at Re = 4245 is 124.9% which is resulted by the winglets positioned at X/D = 0.5 and Z/D = 0.9.

Acknowledgements This work was financially supported by the Indian Institute of Technology Delhi, New Delhi, India. The authours are grateful to the Institute and its administration for providing a conducive environment. Furthermore, we sincerely acknowledge the incessant encouragement and support provided by the laboratory staff.

References

1. Webb RL, Kim NH (2005) Principles of enhanced heat transfer. Taylor & Francis, New York
2. Arora A, Subbarao PMV, Agarwal RS (2015) Numerical optimization of location of 'common flow up' delta winglets for inline aligned finned tube heat exchanger. Appl Therm Eng 82:329–340. https://doi.org/10.1016/j.applthermaleng.2015.02.071
3. Bergman TL, Lavine AS, Incropera FP, Dewitt DW (2011) Introduction to heat transfer. John Wiley & Sons Inc., NJ

4. Fiebig M, Kallweit P, Mitra N, Tiggelbeck S (1991) Heat transfer enhancement and drag by longitudinal vortex generators in channel flow. Exp Thermal Fluid Sci 4:103–114. https://doi.org/10.1016/0894-1777(91)90024-l
5. Jacobi AM, Shah RK (1995) Heat transfer surface enhancement through the use of longitudinal vortices: a review of recent progress. Exp Thermal Fluid Sci 11:295–309. https://doi.org/10.1016/0894-1777(95)00066-u
6. Joardar A, Jacobi AM (2007) A numerical study of flow and heat transfer enhancement using an array of delta-winglet vortex generators in a fin-and-tube heat exchanger. J Heat Transf 129:1156–1167. https://doi.org/10.1115/1.2740308
7. Jain A, Biswas G, Maurya D (2003) Winglet-type vortex generators with common-flow-up configuration for fin-tube heat exchangers. Numer Heat Transf Part A: Appl 43(2):201–219. https://doi.org/10.1080/10407780307325
8. Pal A, Bandyopadhyay D, Biswas G, Eswaran V (2012) Enhancement of heat transfer using delta-winglet type vortex generators with a common-flow-up arrangement. Numer Heat Transf Part A 61:912–928. https://doi.org/10.1080/10407782.2012.677322
9. Lei YG, He YL, Tian LT, Chu P, Tao WQ (2010) Hydrodynamics and heat transfer characteristics of a novel heat exchanger with delta-winglet vortex generators. Chem Eng Sci 65:1551–1562. https://doi.org/10.1016/j.ces.2009.10.017
10. Kwak KM, Torii K, Nishino K (2005) Simultaneous heat transfer enhancement and pressure loss reduction for finned-tube bundles with the first or two transverse rows of built-in winglets. Exp Thermal Fluid Sci 29:625–632. https://doi.org/10.1016/j.expthermflusci.2004.08.005
11. Joardar A, Jacobi AM (2008) Heat transfer enhancement by winglet-type vortex generator arrays in compact plain-fin-and-tube heat exchangers. Int J Refrig 31:87–97. https://doi.org/10.1016/j.ijrefrig.2007.04.011
12. He YL, Chu P, Tao WQ, Zhang YW, Xie T (2013) Analysis of heat transfer and pressure drop for fin-and-tube heat exchangers with rectangular winglet-type vortex generators. Appl Therm Eng 61:770–783. https://doi.org/10.1016/j.applthermaleng.2012.02.040
13. Gorji M, Mirgolbabaei H, Barari A, Domairry G, Nadim N (2011) Numerical analysis on longitudinal location optimization of vortex generator in compact heat exchangers. Int J Numer Meth Fluids 66:705–713. https://doi.org/10.1002/fld.2278
14. He YL, Han H, Tao W, Zhang Y (2012) Numerical study of heat-transfer enhancement by punched winglet-type vortex generator arrays in fin-and-tube heat exchangers. Int J Heat Mass Transf 55:5449–5458. https://doi.org/10.1016/j.ijheatmasstransfer.2012.04.059
15. Wu JM, Tao WQ (2008) Numerical study on laminar convection heat transfer in a channel with longitudinal vortex generator, Part B: Parametric study of major influence factors. Int J Heat Mass Transf 51:3683–3692. https://doi.org/10.1016/j.ijheatmasstransfer.2007.03.031
16. Tian L, He Y, Tao Y, Tao W (2009) A comparative study on the air-side performance of wavy fin-and-tube heat exchanger with punched delta winglets in staggered and in-line arrangements. Int J Therm Sci 48:1765–1776. https://doi.org/10.1016/j.ijthermalsci.2009.02.007
17. Lu G, Zhou G (2016) Numerical simulation on performances of plane and curved winglet type vortex generator pairs with punched holes. Int J Heat Mass Transf 102:679–690. https://doi.org/10.1016/j.ijheatmasstransfer.2016.06.063
18. Dezan DJ, Salviano LO, Yanagihara JI (2015) Interaction effects between parameters in a flat-tube louvered fin compact heat exchanger with delta-winglets vortex generators. Appl Therm Eng 91:1092–1105. https://doi.org/10.1016/j.applthermaleng.2015.08.072
19. Gong J, Min C, Qi C, Wang E, Tian L (2013) Numerical simulation of flow and heat transfer characteristics in wavy fin-and-tube heat exchanger with combined longitudinal vortex generators. Int Commun Heat Mass Transf 43:53–56. https://doi.org/10.1016/j.icheatmasstransfer.2013.01.004
20. FLUENT 6.2 User guide (2004) Fluent incorporated Lebanon. NH, USA
21. Arora A, Subbarao PMV, Agarwal RS (2016) Development of parametric space for the vortex generator location for improving thermal compactness of an existing inline fin and tube heat exchanger. Appl Therm Eng 98:727–742. https://doi.org/10.1016/j.applthermaleng.2015.12.117

22. Biswas G, Torii K, Fujii D, Nishino K (1996) Numerical and experimental determination of flow structure and heat transfer effects of longitudinal vortices in a channel flow. Int J Heat Mass Transf 39:3441–3451. https://doi.org/10.1016/0017-9310(95)00398-3
23. Fiebig M, Valencia A, Mitra NK (1993) Wing-type vortex generators for fin-and-tube heat exchangers. Exp Thermal Fluid Sci 7:287–295. https://doi.org/10.1016/0894-1777(93)90052-k
24. Sinha A, Chattopadhyay H, Iyengar AK, Biswas G (2016) Enhancement of heat transfer in a fin-tube heat exchanger using rectangular winglet type vortex generators. Int J Heat Mass Transf 101:667–681. https://doi.org/10.1016/j.ijheatmasstransfer.2016.05.032

Flood Inundation Mapping Using HEC-RAS 2D in Sangli City of Krishna River Basin, Maharashtra (India)

Lalit Kumar, Mohammad Saud Afzal, and Shivshankar Chalwad

1 Introduction

India has a large population and a high gross domestic product (GDP) that is mainly affected by river floods annually [1]. According to the World Resources Institute, India is the world's second-most populous country, where flooding has a huge impact on its economy. India's population is one-fourth of the total population of the world, where an estimated 4.84 million people's lives are in danger due to the occurrence of floods in rivers annually. India's population is rapidly increasing, and it is anticipated to surpass China's by 2022 [2]. This increase in population leads to increased urbanization and agricultural expansion, which degrades the environment and causes floodplains to be occupied. The floodplain can be better understood and managed, which can help minimize the effects of riverine floods. Most of the rivers in India are not gauged, which results in the unavailability of a hydrologic/hydraulic dataset. Due to the unavailability of dataset, hydraulic model development becomes a significant challenge to the researchers. Moreover, the data observed is not always available and is of the required quality for the development of a hydrologic model.

The Hydrologic Engineering Centre-River Analysis System (HEC-RAS) is a widely utilized hydraulic modeling program that is dependable and is publicly accessible [3]. The HEC-RAS 5.0 includes a two-dimensional capability that enhances the model accuracy. The surface roughness, digital elevation model (DEM), and observed stage and discharge data are required to develop a hydraulic model. The surface roughness can be easily approximated from satellite images in absence of land use/land cover (LULC) information [4].

The DEM defines the model's conveyance region and has a substantial impact on hydraulic model output. Patro et al. (2009) analyzed the hydrodynamic model on a

L. Kumar (✉) · M. S. Afzal · S. Chalwad
Department of Civil Engineering, Indian Institute of Technology, Kharagpur, India
e-mail: lkumar@iitkgp.ac.in

D. K. Maiti et al. (eds.), *Recent Advances in Computational and Experimental Mechanics, Vol II*, Lecture Notes in Mechanical Engineering,
https://doi.org/10.1007/978-981-16-6490-8_12

large river system of India using Shuttle Radar Topography Mission (SRTM) DEM datasets [5]. They determined that the use of SRTM dataset as a source of topographic data is a viable alternative. Paiva (2011) developed a hydrologic model for the Purus river basin in Brazil using the SRTM dataset and reported that the SRTM dataset can be used for large basin systems [6]. Further, Sanders (2007) reported that the SRTM dataset provides a worldwide source of topography data that may be used to predict floods when other sources are unavailable [7].

Generally, the hydraulic characteristics of the water channel and flood plain area are analyzed by HEC-2 simulation model. HEC-2 was developed to measure river surface level for floodplain management by the United States Army Corps of Engineers [8]. Similarly, this program also examines the impact of artificial embankment and water channel. Over the years HEC has extended its product services to include development of applications in water resources and water supply systems [9]. Flood plains are the adjacent geographic areas of rivers and streams which carry a huge volume of water during floods. When flow enters a floodplain, it poses a threat to the lives and structures [10, 11].

Pramanik et al. (2009) performed 1D hydrodynamic modeling over the Brahmani river basin using SRTM DEM data [12]. They examined the hydraulic characteristics of the cross-section and observed that in absence of measured cross-section, the modified cross-sections are suitable for the development for hydraulic model. Further, Wahid et al. (2017) made a study for Inundation modeling in the Koshi for assessing flood risk [13]. They calibrated their model for the monsoon of 2006 with a correlation coefficient (R^2) of 0.57 at Basuwa and 0.70 at Baltara. The Flood inundation simulation due to embankment breach was done for the frequency analysis of return period (25, 50, and 100 years) at Chatara station. The HEC-RAS was simulated from 2006 to 2007 and was calibrated and validated against observed outflow from Koshi barrage, observed water level at Basuwa, and Bal-tara. Similarly, the model was validated for the monsoon of 2007 with R2 value of 0.51 at Basuwa and 0.69 at Baltara. Further, the extreme rainfall events were analyzed based on past critical events [14, 15].

The present study develops a HEC-RAS 2D model in extreme flood events at Sangli city of Krishna river basin, Maharastra (India). The results of HEC-RAS 2D are validated with recent floods during august 2019 in the Sangli city of Krishna river basin, Maharastra (India).

2 Study Area

The Sangli city of Krishna river basin is situated in Maharashtra, India (shown in Fig. 1). The Sangli city of Krishna river basin has minimal data availability that might benefit from hydraulic modeling. The Maharashtra, Telangana, Karnataka, and Andhra Pradesh are the four states that drain into the Krishna river basin in southern India [16]. The mountains of Balaghat in the north, the Western Ghats in the west, and the Eastern Ghats in the south and east define the boundary of the Krishna river

Fig. 1 Location of the central Krishna river basin in India (Source: https://earth.google.com/)

basin (India). The Maharashtra, a state of India consists of 308,000 Km^2 geographical area. Maharashtra experiences monsoon rains from both the south-west and north-east. The precipitation occurs mainly between June and September, with rainy days varying from 40 to 100 mm. The State is experiencing flash floods particularly in the Western Ghats, including the basins of Krishna and Upper Bhima. Similarly, the districts of Sangli, Satara and Kolhapur in the Krishna Basin, and the districts of Pune and Solapur in the Bhima Basin have experienced extreme flooding many times over the last decade.

The Maharashtra state of India consists of 308,000 Km^2 geographical area. Maharashtra experiences monsoon rains from both the south-west and north-east. The precipitation occurs mainly between June and September, with rainy days varying from 40 to 100 mm. The State is experiencing flash floods particularly in the Western Ghats, including the basins of Krishna and Upper Bhima. Similarly, the districts of Sangli, Satara, and Kolhapur in the Krishna Basin, and the districts of Pune and Solapur in the Bhima Basin have experienced extreme flooding many times over the last decade.

3 Materials

3.1 Hydrological and Satellite Data

The hydrological discharge data is obtained from Mahahp website of Maharastra, India (www.mahahp.org). The hydrological datasets of Sangli city of Maharastra, India are used to model HEC-RAS 2D model. Due to the channel discharge, the flow data for free surface flow is often unreliable. That occurs due to the temporal characteristics of the storm event causing floods. The precipitation data is obtained from the Indian metrological department (IMD) that is used as a input parameter to

HEC-RAS 2D model. The Sentinel-2 satellite data are used in the present study for flood inundation mapping. The DEMs of 30 m spatial resolution are observed from satellite, i.e., SRTM [17].

3.2 HEC-RAS Model

Hydrologic Engineering Center developed the HEC-RAS program in the early 1990s. The capabilities of HEC-RAS have grown significantly as it is capable enough to perform large calculation to determine water surface elevation. The HEC-RAS 2D is used in the present study which performs two-dimensional unsteady flow calculation. The 2D diffusive wave equation and 2D Saint–Venant equations were used in the HEC-RAS flood model to perform flood simulation [18]. Generally, the diffusive wave equation is used to perform flood routing simulation. The implicit finite volume approach is used in HEC-RAS 2D that allows maximum computational time step. The normal depth, flood hydrograph, and rating curve are used HEC-RAS 2D models boundary conditions. The HEC-RAS 2D model simulation results are obtained in the RAS Mapper that shows velocity, depth, water surface elevation, duration, and period of arrival and recession.

3.3 Methods

The DEM (SRTM) data collected from USGS website is imported to the ArcGIS to perform fill up/ burning of DEM. Further, the delineation of the watershed basin using flow direction, flow accumulation was performed in ArcGIS, as shown in Fig. 2.

Fig. 2 Delineated basin using flow accumulation

The land use and land cover maps are imported to extract Manning's coefficient that is used to calibrate the HEC-RAS 2D model. Further, the geometry (River, banks, flow paths, bridges, barrages) of the basin is developed using ArcGIS, as shown in Fig. 3.

This developed geometry is imported to HEC-RAS using HEC-GeoRAS extension. Further, the cross-section and terrain profile data were generated using ArcGIS, as shown in Fig. 4.

The cross-section and terrain profile data are introduced into the HEC-RAS 2D model. The channel terrain layer is generated by interpolating an elevation for each grid cells between two cross-sections using the channel bathymetry data from the cross-sections [3].

The terrain layers were made up of 12 raster images, each measuring 5,000 feet by 5,000 feet. Each raster image comprises of 4,000,000 pixels, with each pixel or GIS cell measuring 2.5 ft × 2.5 ft. Therefore, the present terrain model consists

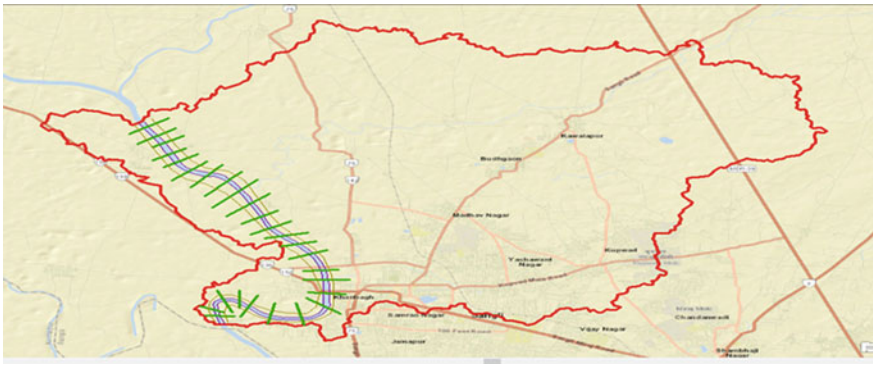

Fig. 3 Delineated basin with required river geometry in ArcGIS

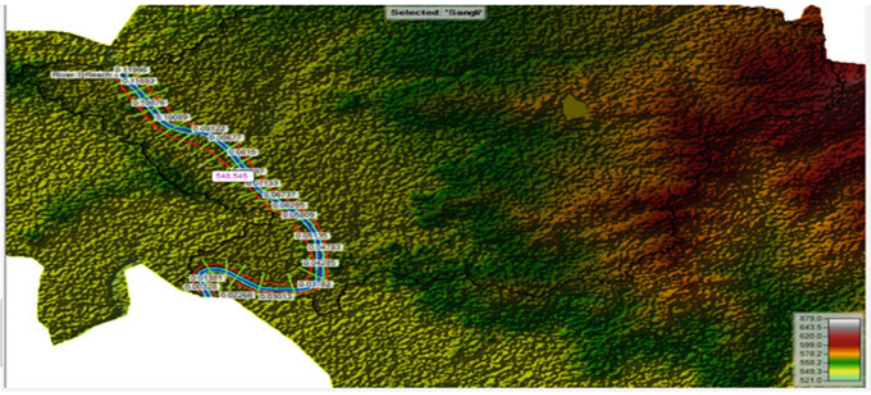

Fig. 4 Extracted cross-section data, terrain profile data in HEC-RAS 2D

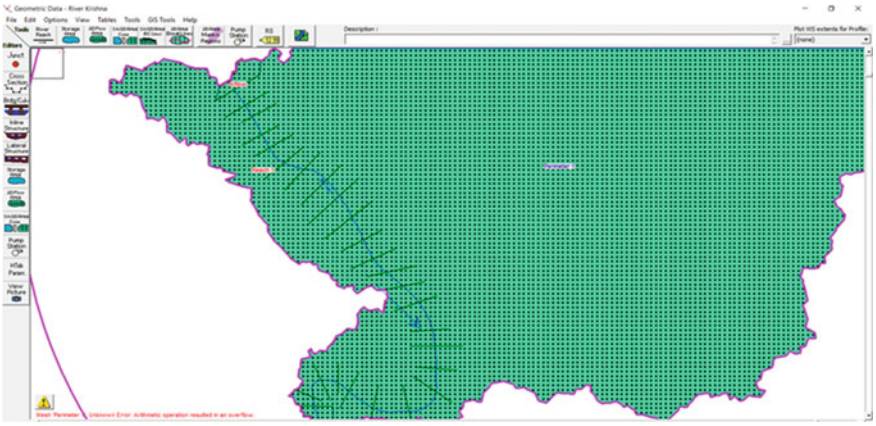

Fig. 5 Computational mesh generated in Geometric editor

of 48,000,000 distinct GIS cells, each with its own elevation. Further, the mesh is generated in HEC-RAS 2D using the boundary condition of unsteady flow, as shown in Fig. 5.

The present study contains 13 km of the Krishna river stretch in Sangli city with 24 cross-sections. As boundary condition includes a random flow hydrograph at the upstream end and the downstream end is set to normal depth. The computational points are created for the 2D flow area, where precipitation is considered as input to the model. Further, the flow direction is developed from each cell using Multiple Flow Direction method.

The HEC-RAS model computes water surface elevations at the center of each computational grid cell for each computational time step using a combination of a finite-volume and finite-difference approach. The user can construct the computational mesh using HEC-RAS 2D modeling features. The modeler can specify the boundaries of the computational mesh that surrounds the channel and any neighboring floodplain regions in the Geometric Data Editor. Further, the unsteady state simulations are performed using 1D geometry and 2D mesh dataset. A flow hydrograph is the most often used boundary condition in HEC-RAS 2D model. A flow hydrograph at Irwin bridge gauge Sangli, Maharastra is shown in Fig. 6.

The HEC-RAS allows to designate a flow hydrograph to the upstream or downstream end of a 2D flow. However, for most applications, the hydrograph and normal depth are used as upstream and downstream boundary conditions respectively. In most cases, the channel slope is utilized instead of the friction slope. Further, HEC-RAS 2D computes the stage-based discharge received from the unsteady flow analysis at the downstream boundary using Manning's equation.

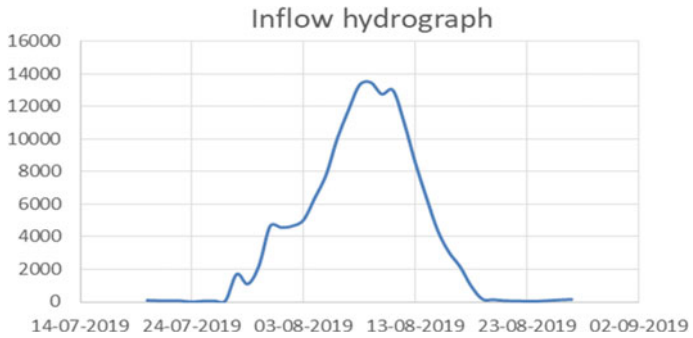

Fig. 6 Inflow hydrograph at Irwin bridge gauge Sangli

4 Results

The present study represents the simulation inundation results in Sangli city of Krishna river basin floodplain. A SRTM data collects the information about the storage area and the lateral structure or weir in the HEC-RAS 2D model. The weir is a small, low dam constructed across the river to increase the water depth upstream. Generally, the weir is also known as gauging weir or measuring weir.

The HEC-RAS 2D model is an upgraded version of the HEC-RAS 1D unsteady model which divides the floodplain into many large storage areas rather than discretizing it. The HEC-RAS 2D model relies on explicit mass conservation and momentum conservation. The land inundation maps are prepared using HEC-RAS 2D from 20th July to 12th August 2019. The result of HEC-RAS 2D model is validated with the flood inundation map reported by National Remote Sensing Centre (NRSC). The flood inundation map (HEC-RAS 2D) on 9th August 2009 shows good similar patterns with the NRSC flood inundation map qualitatively. The flood inundation maps from 22nd July 2019 to 11th August 2019 are shown during the period as shown in Fig. 7.

5 Conclusions

The HEC-RAS 1D model with storage area requires large time consumption and effort. However, it is observed in the present study that the HEC-RAS 2D model provides accurate inundation mapping of flood with less time and effort. The HEC-RAS 2D model includes a terrain map/model that is used to develop computational mesh and explore the land cover with a spatial bed roughness. The HEC-RAS 2D portrays weirs and captures all filling and emptying processes locations similar as in case of 1D model. Due to pre-configuration of HEC-RAS 2D model, the storage area is constructed very easily as compared to the 1D model. The locations where data

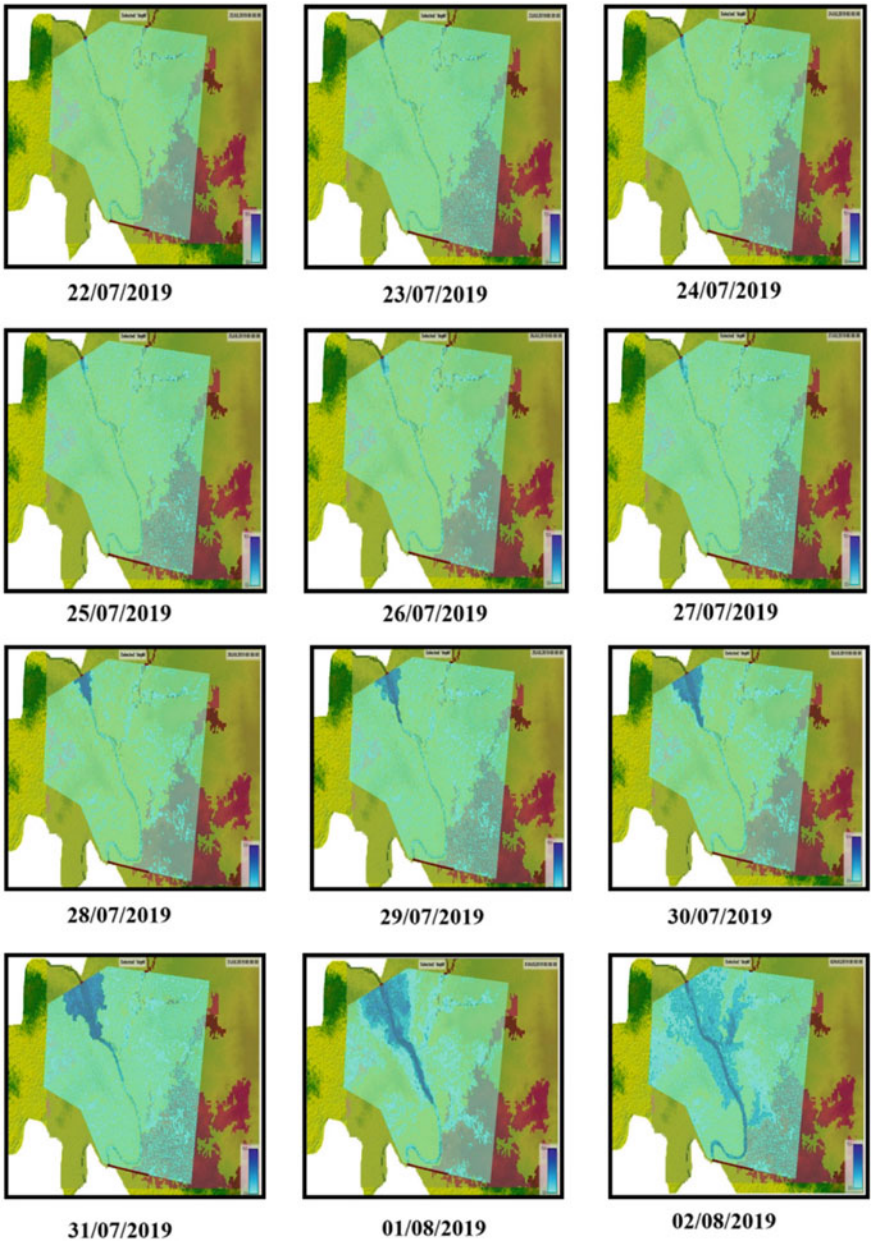

Fig. 7 Flood inundation maps extracted from HEC-RAS 2D

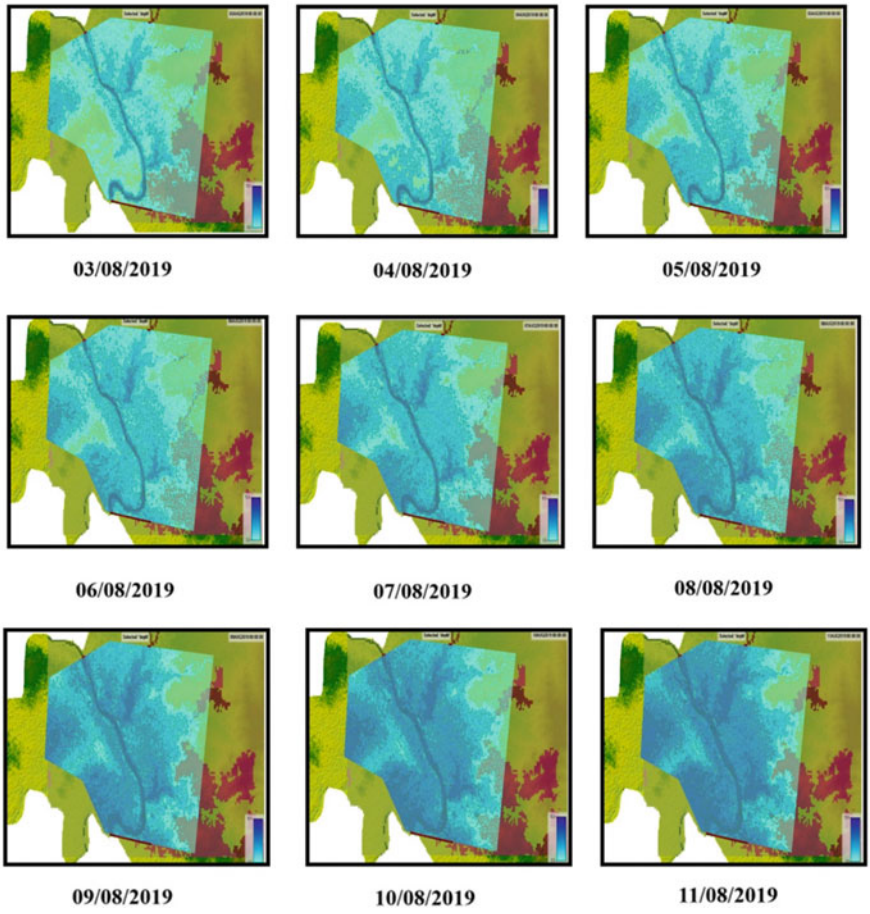

Fig. 7 (continued)

for hydraulic modeling is missing, an uncalibrated HEC-RAS 2D model can be used. Therefore, HEC-RAS 2D model is recommended for flood inundation mapping.

The present study shows the path of modeling unsteady flow with the storage area as a 2D model by using HEC-RAS. Future mitigation strategies might be developed using the two-dimensional HEC-RAS model. Further, the hydrologic model like HEC-HMS can be used to calculate streamflow in a catchment of ungauged streams or having limited datasets [19].

Acknowledgements We would like to thank Google earth pro for the image of the Krishna river basin used in the present study. This work was carried out as a part of the project titled "Predictive Tool for Arctic Coastal Hydrodynamics and Sediment Transport" funded by the National Centre for Polar and Ocean Research (NCPOR). Authors also acknowledge support by SRIC, IIT Kharagpur, under the ISIRD project titled "3D CFD Modeling of the Hydrodynamics and Local Scour Around

Offshore Structures Under Combined Action of Current and Waves." We would also like to thank google earth pro.

References

1. Searchinger T, Hanson C, Ranganathan J et al (2014) Creating a sustainable food future. A menu of solutions to sustainably feed more than 9 billion people by 2050. World resources report 2013–14: interim findings
2. Rath P. India's Population Growth-Issues, Challenges and Future Trajectory
3. Brunner GW (1995) HEC-RAS River Analysis System. Hydraulic Reference Manual. Version 1.0
4. Anderson MC, Allen RG, Morse A, Kustas WP (2012) Use of Landsat thermal imagery in monitoring evapotranspiration and managing water resources. Remote Sens Environ 122:50–65
5. Patro S, Chatterjee C, Singh R, Raghuwanshi NS (2009) Hydrodynamic modelling of a large flood-prone river system in India with limited data. Hydrol Process an Int J 23(19):2774–2791
6. Paiva RCD, Collischonn W, Tucci CEM (2011) Large scale hydrologic and hydrodynamic modeling using limited data and a GIS based approach. J Hydrol 406(3–4):170–181
7. Sanders BF (2007) Evaluation of on-line DEMs for flood inundation modeling. Adv Water Resour 30(8):1831–1843
8. Moore RJ, Bell VA, Jones DA (2005) Forecasting for flood warning. Comptes Rendus Geosci 337(1–2):203–217
9. Kim J, Lee J-K, Ahn J-S (2010) Optimization for roughness coefficient of river in Korea-review of application and Han river project water elevation. J Korean Soc Civ Eng 30(6B):571–578
10. Tayefi V, Lane SN, Hardy RJ, Yu D (2007) A comparison of one-and two-dimensional approaches to modelling flood inundation over complex upland floodplains. Hydrol Process an Int J 21(23):3190–3202
11. Shrestha A, Bhattacharjee L, Baral S et al (2020) Understanding Suitability of MIKE 21 and HEC-RAS for 2D Floodplain Modeling. World Environmental and Water Resources Congress 2020: Hydraulics, Waterways, and Water Distribution Systems Analysis, pp 237–253
12. Pramanik N, Panda RK, Sen D (2010) One dimensional hydrodynamic modeling of river flow using DEM extracted river cross-sections. Water Resour Manag 24(5):835–852
13. Wahid SM, Kilroy G, Shrestha AB, Bajracharya SR, Hunzai K (2017) Opportunities and challenges in the trans-boundary Koshi River Basin. River system analysis and management. Springer, pp 341–352
14. Rangari VA, Umamahesh NV, Bhatt CM (2019) Assessment of inundation risk in urban floods using HEC RAS 2D. Model Earth Syst Environ 5(4):1839–1851
15. Pedrozo-Acuña A, Rodr'iguez-Rincón JP, Arganis-Juárez M, Dom'inguez-Mora R, González Villareal FJ (2015) Estimation of probabilistic flood inundation maps for an extreme event: Pánuco River, México. J Flood Risk Manag 8(2):177–192
16. Thornton III JC (2016) 2D HEC-RAS model development in data poor areas of India case study: Central Krishna River Basin
17. Werner M (2001) Shuttle radar topography mission (SRTM) mission overview. Frequenz 55(3–4):75–79
18. Farooq M, Shafique M, Khattak MS (2019) Flood hazard assessment and mapping of River Swat using HEC-RAS 2D model and high-resolution 12-m TanDEM-X DEM (WorldDEM). Nat Hazards 97(2):477–492
19. Chu X, Steinman A (2009) Event and continuous hydrologic modeling with HEC-HMS. J Irrig Drain Eng 135(1):119–124

Stream-wise Deployment of Vortex Generators in Finned Tube Arrays for Capacity Enhancement Through Flow Modification

Amit Arora and P. M. V. Subbarao

1 Introduction

Low heat transfer coefficients associated with the gas flows necessitate the use of extended surfaces in gas-to-liquid heat exchangers [1]. These heat exchangers are commonly referred as finned tube arrays or fin-and-tube heat exchangers due to the presence of thin fins, made of high thermal conductivity material, fitted on a tube bank. The air flows on the fin-side and the liquid flows through the tubes. The effectiveness of such heat exchangers does not increase much until its gas-side thermal conductance undergoes large augmentation [2]. There is a relentless effort to improve their thermal compactness. Several review articles [3, 4] provide consolidated summaries of valuable studies which attempted to improve the effectiveness of commercial heat exchangers. Flow separation over the tubes is a common occurrence on the gas side, and a large fin area is affected by the tube wake region. Low flow velocities prevail in the wake region, thereby making the heat fluxes dismally low in magnitude. Apparently, flow modifications in the tube wake region are vital to improve the thermal effectiveness of finned tube arrays.

Literature talks about several ways which can be effectively used to contain the spread of flow separation and its consequent effects. Using longitudinal vortex generators (LVGs) for producing large thermal augmentation on the gas side is a preferred passive enhancement technique. The existence of longitudinal vortices is found to prevail over lengths which are many times the height of the generators [5, 6]. It is worth noting that the winglet type LVGs is a preferred choice because it produces

A. Arora (✉)
Department of Mechanical Engineering, MNIT Jaipur, JLN Marg, Jaipur, Rajasthan 302017, India
e-mail: amit.mech@mnit.ac.in

P. M. V. Subbarao
Department of Mechanical Engineering, IIT Delhi, Hauz Khas New Delhi 110016, India
e-mail: pmvs@mech.iitd.ac.in

D. K. Maiti et al. (eds.), *Recent Advances in Computational and Experimental Mechanics, Vol II*, Lecture Notes in Mechanical Engineering,
https://doi.org/10.1007/978-981-16-6490-8_13

performance augmentation by invoking all three mechanisms of passive heat transfer enhancement i.e. developing boundary layers, swirl, and flow destabilization [7]. Their deployment in pair adjacent to the tubes, as shown in Fig. 1, results in redirecting the approaching flow behind the tubes. As the ability of a pair of winglets, to redirect the approaching flow, depends on its position around the tube; therefore their position selection needs careful consideration. Accordingly, a study of the effect of change in winglet position on the wake management, of finned tube arrays, is essential to use them effectively for the augmentation in the heat transfer rates.

In a three-dimensional numerical study [9], rectangular winglets were deployed in a fin-and-tube heat exchanger for its capacity augmentation. It was observed that the winglets effectively produced significant thermal augmentation. Another numerical investigation of winglets in a channel flow suggests that the degree of thermal augmentation as well as pressure loss increases with the LVG area [10]. Further, it was found that under same area constraint, a pair of triangular (or delta) winglet delivers greater thermal augmentation compared to rectangular winglets. In fact, a numerical investigation has demonstrated the potential of delta winglets in a novel finned tube array built with the tubes having varying diameter [11]. Here, it is reaffirmed that the delta winglet type LVG is abbreviated as DVG. The effect of winglet geometry and its location was studied by conducting numerical simulations of delta winglets deployed in a compound fin-and-tube heat exchanger [12]. It was reported that the aspect ratio of the winglets should be neither too large nor too small. Further, it was suggested that the winglet location should be mindfully selected as it has a strong bearing on the improved performance. If the winglets are completely located in the tube wakes, they do not produce any appreciable augmentation in the heat exchange.

In the present study, toe-out type delta winglet LVGs are considered for the thermal management of the baseline wakes due to their ability to redirect high momentum fluid in the wake of all tubes. As their ability to favourably modify the flow characteristics depends on their position around the tube, their streamwise position is changed in discrete steps to analyze the effect on the wake modification, and the heat exchange capacity.

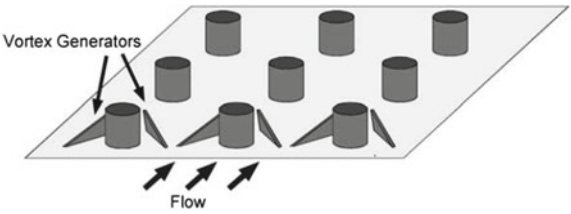

Fig. 1 Toe-out type delta winglets in the tube downstream [8]

2 Numerical Simulations

2.1 Numerical Methods

Three-dimensional numerical simulations are performed to analyze the effect of change in winglet positions on the flow modifications. As RNG k-ε model is adopted for modelling turbulence [13–15], the governing equations catering to steady incompressible turbulent flow through the finned tube array include mass, momentum (RANS), energy, turbulent kinetic energy (k), and turbulent energy dissipation rate (ε) equations. The governing equations are discretized by using finite volume method [16], and SIMPLE (semi-implicit method for pressure linked equations) algorithm is used for the pressure–velocity coupling [17].

A commercial CFD code, ANSYS Fluent 14.0, is used to solve the governing equations which are expressed below with indexed notations.

Continuity equation:

$$\frac{\partial(\rho u_i)}{\partial x_i} = 0 \tag{1}$$

Momentum (RANS) equation:

$$\frac{\partial\left(\rho u_i u_j\right)}{\partial x_i} = -\frac{\partial p}{\partial x_j} + \frac{\partial}{\partial x_i}\left[\mu\left(\frac{\partial u_i}{\partial x_j} + \frac{\partial u_j}{\partial x_i} - \frac{2}{3}\delta_{ij}\frac{\partial u_k}{\partial x_k}\right)\right] + \frac{\partial}{\partial x_i}\left(-\rho\overline{u_i' u_j'}\right) \tag{2}$$

Reynolds stress term is calculated by using Boussinesq hypothesis as expressed below,

$$-\rho\overline{u_i' u_j'} = \mu_t\left(\frac{\partial u_i}{\partial x_j} + \frac{\partial u_j}{\partial x_i}\right) - \frac{2}{3}\left(\rho k + \mu_t\frac{\partial u_k}{\partial x_k}\right)\delta_{ij} \tag{3}$$

Energy equation:

$$\frac{\partial[u_i(\rho E + p)]}{\partial x_i} = \frac{\partial}{\partial x_i}\left(k_{eff}\frac{\partial T}{\partial x_i}\right) \tag{4}$$

where ‘E’ is the total energy and k_{eff} is the effective thermal conductivity.

The transport equations for the turbulent kinetic energy ‘k’ and dissipation rate ‘ε’ are expressed as,

$$\frac{\partial}{\partial x_i}(\rho k u_i) = \frac{\partial}{\partial x_i}\left(\alpha_k\mu_{eff}\frac{\partial k}{\partial x_i}\right) + \mu_t S^2 - \rho\varepsilon \tag{5}$$

$$\frac{\partial}{\partial x_i}(\rho\varepsilon u_i) = \frac{\partial}{\partial x_i}\left(\alpha_\varepsilon\mu_{eff}\frac{\partial \varepsilon}{\partial x_i}\right) + C_{1\varepsilon}\frac{\varepsilon}{k}\mu_t S^2 - C_{2\varepsilon}\rho\frac{\varepsilon^2}{k} - R_\varepsilon \tag{6}$$

where ($\alpha_k and \alpha_\varepsilon$) are inverse effective Prandtl numbers for (k and ε) respectively, (S) is the modulus of the mean rate of strain tensor, (μ_t) is turbulent (or eddy) viscosity, (μ_{eff}) is effective viscosity, ($C_{1\varepsilon}$, $C_{2\varepsilon}$) are model constants and (R_ε) is the rate of strain term. Their mathematical definition/ value is available in literature [14].

In order to check the mesh quality, multi-block hybrid approach is used; and second-order upwind scheme is used to model the convective terms. The effects of buoyancy forces and the viscous dissipation are disregarded [15], and the thermophysical properties of air are treated constant which are computed at the bulk mean temperature. The solid is assumed isotropic and the tube wall is considered isothermal [14, 18]. The heat exchange through fins is modeled as conjugate heat transfer problem. The convergence was concluded when the normalized residuals of the energy equation and rest of the equations were $\leq 10^{-8}$ and $\leq 10^{-5}$ respectively.

2.2 Computational Domain and Model Validation

Finned tube array adopted for the study has three tube rows in the flow direction. Its geometric specifications are presented in Table 1. A pair of delta winglet type LVG is deployed in the downstream of each tube, as depicted in Fig. 2, and the winglets are aligned with 30° attack angle. The height-to-base ratio borne by the winglets equals 0.5 [19].

The computational expense is restricted by modelling a periodic section in the tube axial direction and a symmetric section in the transverse direction, as shown in Fig. 2. Various boundary conditions applied for solving the flow are given in Table 2. Extended flow lengths equal to 10H and 30H are provided at the inlet and exit respectively. The conditions prescribed at the far-field inlet and exit boundaries are "uniform velocity" and "outflow" respectively [20]. Additionally, turbulent intensity is prescribed at the inlet boundary which is determined by an empirical correlation [13]. The viscosity affected regions were resolved by placing the wall adjacent nodes at y^+ value less than unity. In order to contain the total mesh volumes, graded mesh is adopted to a large extent as shown in Fig. 3. An iterative test was carried out at highest Reynolds number to obtain the mesh. The models for the heat exchangers with and

Table 1 Heat exchanger design [20]

Geometric feature	Symbol	Dimension
Tube diameter	D	0.038 m
Longitudinal tube pitch	P_L	0.1 m
Transverse tube pitch	P_T	0.1 m
Fin space	H	0.012 m
Fin pitch	P_f	0.013 m
Tube length	L_t	0.3 m
Fin thickness	t	0.001 m

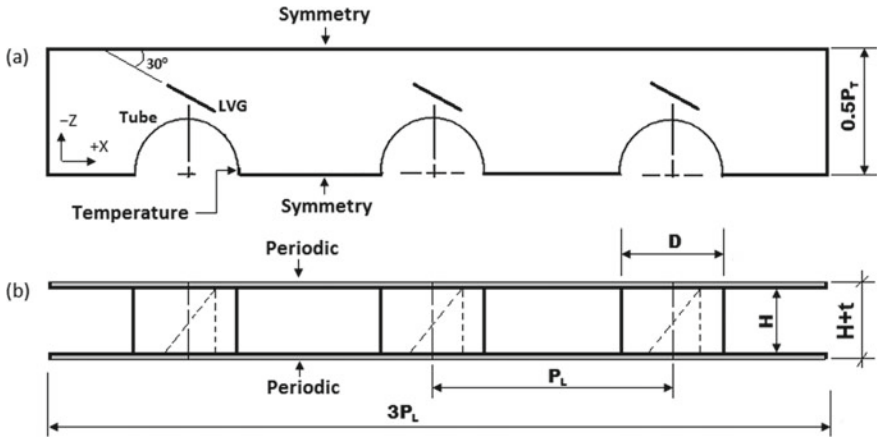

Fig. 2 Computational domain **a** Plan **b** Elevation

Table 2 Boundary conditions in the computational domain

Physical boundary	Velocity B.C	Thermal B.C
Flow inlet	Uniform velocity	Uniform temperature
Flow exit	Outflow	Outflow
LVG surface	No slip	Adiabatic
Tube surface	No slip	Isothermal
Upper and lower bounds (y-direction)	Periodic	Periodic
Front and rear bounds (z-direction)	Symmetry	Symmetry

without LVGs have approximately 4.3 and 4.2 million cells respectively. Thereafter, the computational model was validated in reference to the published experimental data [20], as depicted in Fig. 4. The Reynolds number varies in the range 1415–7075.

The characteristic dimension for defining the Reynolds number equals twice the fin-space and the characteristic velocity is far-field inlet velocity [21, 22]. The pressure drop across the fin array may be expressed in a dimensionless form which is referred as apparent friction factor 'f_{app}' as given by Eq. 8. Here, A_{min} is the minimum flow area (m^2), A_o is the total heat transfer area (m^2), Δp is the pressure drop (Pa).

$$\text{Reynolds number, Re} = \frac{\rho L_c U_\infty}{\mu} \tag{7}$$

$$\text{Friction factor, } f_{app} = \frac{2.\Delta p}{\rho U_\infty^2}.\frac{A_{min}}{A_o} \tag{8}$$

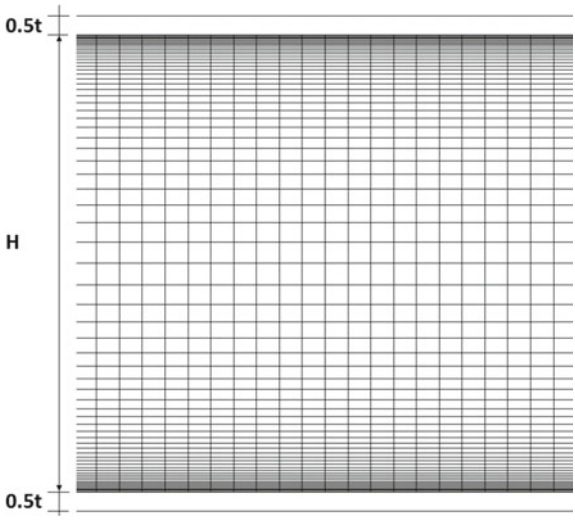

Fig. 3 Graded meshing

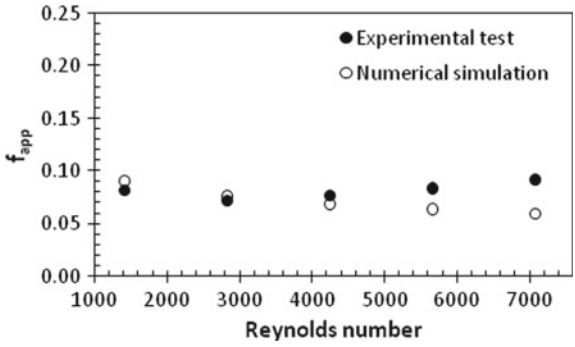

Fig. 4 Model validation

3 Results and Discussions

Main thrust of this investigation is to analyze the effect of streamwise change in the LVG position on the tube-wake modifications. The finned tube array comprises of three tube rows in the flow direction, and the LVGs make 30° angle with the main flow direction. The vortex generators were displaced in the streamwise direction (i.e. x-axis) while keeping their cross-stream position fixed. For a detailed study, two different cross-stream positions are selected (i.e. Z/D = 0.5 and Z/D = 0.9) where LVGs are made to undergo stream-wise translation with a fixed but small step-size equal to X/D = 0.2, as apparent in Fig. 5. Here, X/D is the dimensionless distance of the LVGs in the streamwise direction and Z/D is the distance in the cross-stream direction. Furthermore, 'P_L' is the longitudinal tube pitch, 'P_T' is the transverse tube pitch, and 'D' is the tube diameter. Their geometric values are given in Table 1.

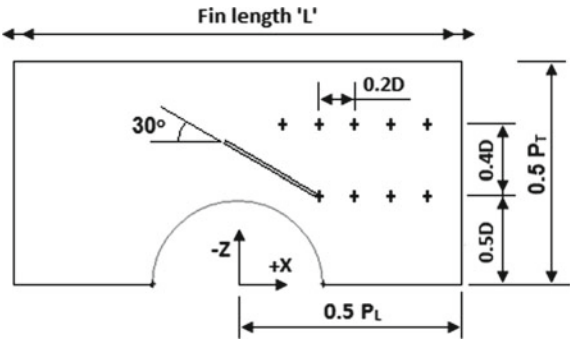

Fig. 5 Locations for deploying longitudinal vortex generators (LVGs)

As evident in Fig. 5, the foremost and the rearmost LVG positions in the flow direction are X/D = 0.5 and 1.1 in case of first cross-stream position (i.e. Z/D = 0.5). The two LVG positions in case of second cross-stream position (i.e. Z/D = 0.9) are X/D = 0.3 and 1.1, respectively. There are four different streamwise positions for erecting LVGs at the first cross-stream position. In contrast, there are five streamwise positions for erecting LVGs corresponding to the second cross-stream position. The results and discussions in the remaining part of the manuscript correspond to a fixed Reynolds number (Re = 4245).

3.1 Change in Wake structures due to LVG Deployment

Deployment of LVGs is going to certainly change the flow characteristics particularly in the wake region but those changes can be appreciated fairly only when we are familiar with the flow field existing in the plain finned tube arrays. For that purpose, pathlines are generated in the plain finned tube arrays, as shown in Fig. 6a. Evidently, the flow field in the absence of LVGs is characterized by significantly large recirculation regions behind all tubes. Such an occurrence is known to have low values of flow velocities thereby making the affected fin surface virtually ineffective for the convection.

After gaining familiarity with the flow field in the plain finned tube arrays, pathlines are generated at the same Reynolds number for a selected LVG location, say X/D = Z/D = 0.5, as shown in Fig. 6b. Apparently, the deployment of LVGs has brought in visible changes in the flow characteristics particularly in the wake region. It is encouraging to see that the recirculation regions associated with all the tubes are no more present which existed prominently otherwise. Further, it may be noticed that the deployment of toe-out delta LVGs has brought in two major changes in the flow field, first it is effective in redirecting the approaching flow in the tube wake and the second is the generation of longitudinal vortices.

Next, velocity profiles are compared in order to gain further understanding about the change in flow characteristics resulting due to the deployment of LVGs and

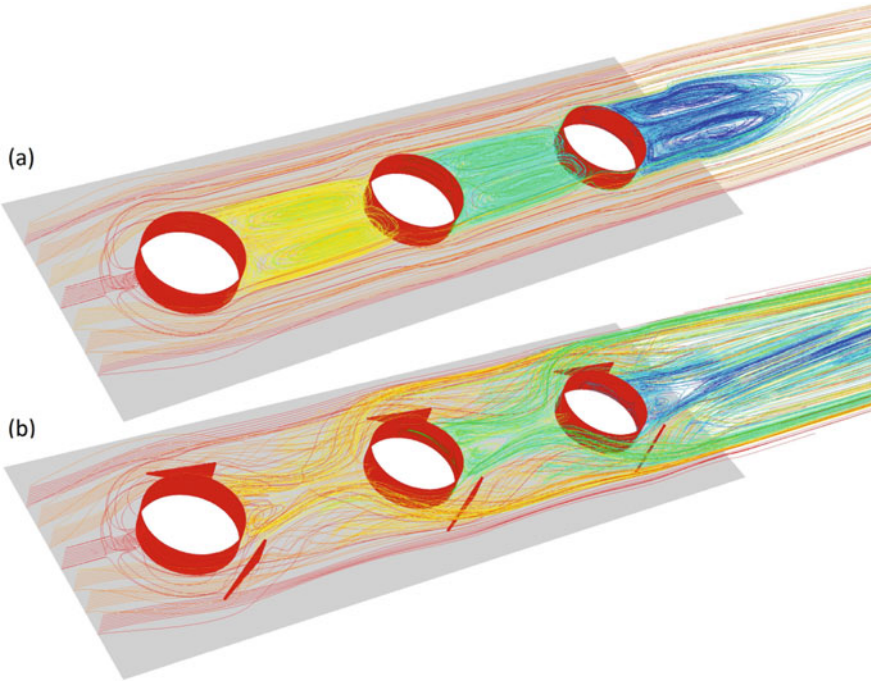

Fig. 6 Pathlines **a** No LVG **b** LVG at X/D = Y/D = 0.5

change in its position in the streamwise direction, as depicted in Fig. 7. These velocity profiles are drawn in a plane that passes through the center of the fin space. The LVGs bear a fixed cross-stream coordinate (i.e. Z/D = 0.5), and they are displaced in the streamwise direction with a small stepwise of Z/D = 0.2. Evidently, there is a large region of small flow velocities behind each tube in the absence of LVGs which is expected to have serious adverse effect on the heat transfer in the affected region. But the deployment of LVGs has caused visible shrinkage in the aforementioned region of small flow velocities, as evident in Fig. 7b–e. Such a visible change is expected to produce large augmentation in the heat transfer coefficients over the affected fin area. Further, it is observed that the fin area affected by the small flow velocities is least when the LVGs are positioned at the foremost location in the streamwise direction, and it is gradually increasing with the streamwise displacement of the LVGs.

3.2 Effect of Flow Modifications on Wake Affected Heat Transfer

Flow modifications in the wake region due to the deployment of toe-out type LVGs, and change in its streamwise position is going to have direct impact on the heat

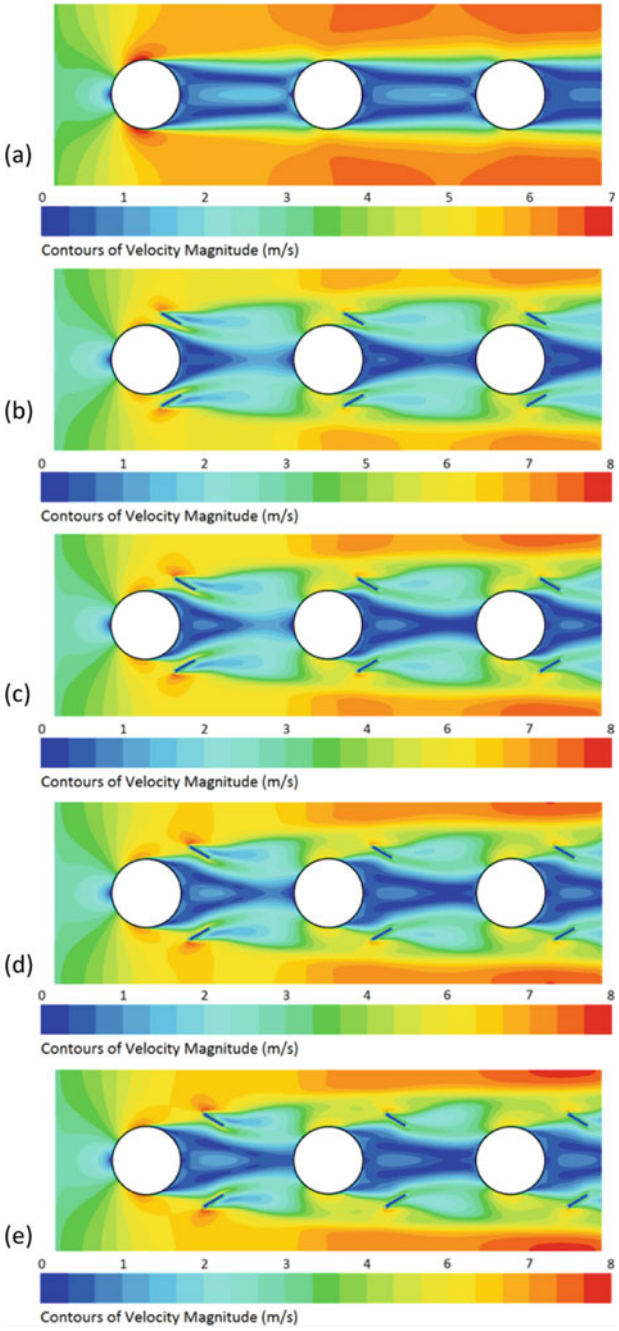

Fig. 7 Velocity profiles **a** No LVG **b** LVG at X/D = 0.5 **c** LVG at X/D = 0.7 **d** LVG at X/D = 0.9 **e** LVG at X/D = 1.1

exchange scenario. The combined effect of redirecting the approaching flow and the generation of longitudinal vortices caused by the LVGs should produce large thermal augmentations particularly on the downstream tubes and the fin surface hiding behind the tubes. The average heat transfer coefficients, of various tubes, in the presence of LVGs are compared in reference to the plain finned tube array, as shown in Fig. 8. Evidently, the deployment of LVGs has a favourable effect on all tubes. The leading tube row experiences least augmentation which does not change much with the streamwise change in the LVG position. At the nearer cross-stream

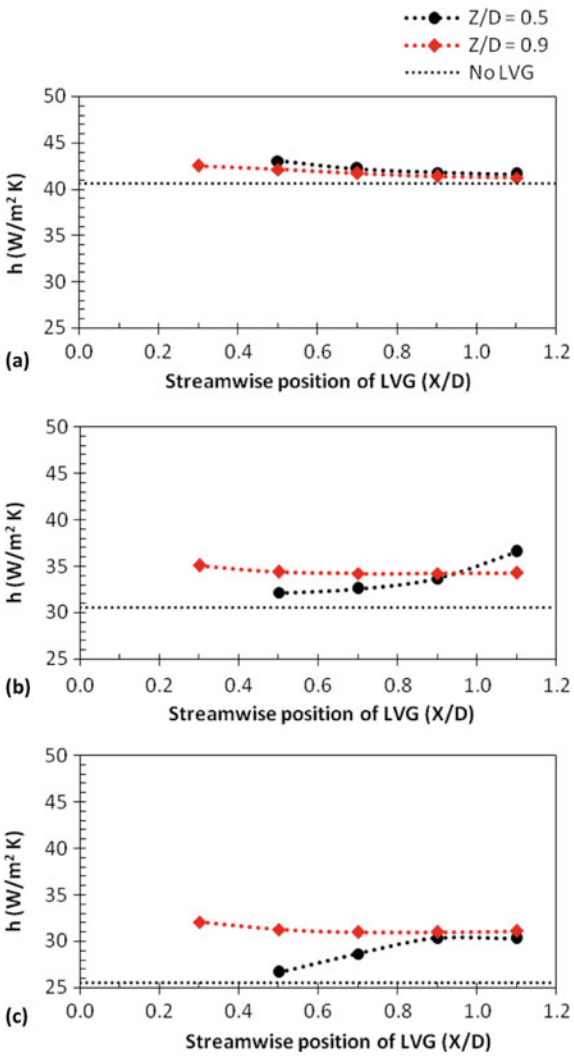

Fig. 8 Average heat transfer coefficient of each tube row **a** First row **b** Second row **c** Third row

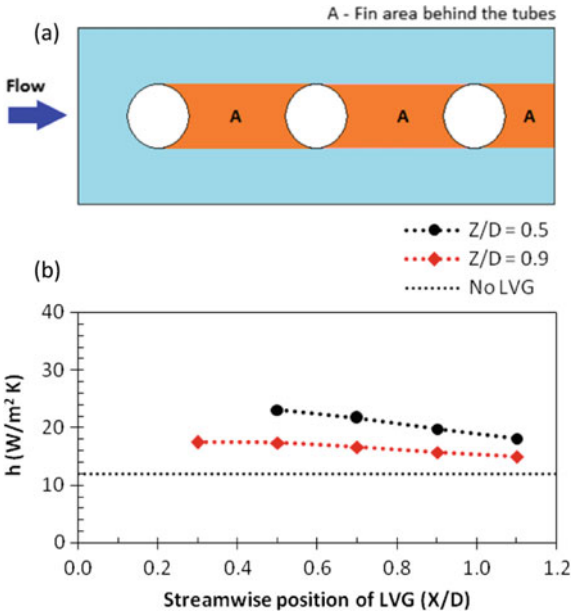

Fig. 9 **a** Fin area hiding behind the tubes **b** Heat transfer coefficient of the fin area hiding behind tubes

coordinate (i.e. Z/D = 0.5), the heat transfer coefficient of the downstream tubes increases with the streamwise shift in the LVG position whereas a weak opposite trend is noticed when the LVGs are placed at the farther cross-stream coordinate.

Just like tubes, fins are also expected to experience thermal augmentation particularly in the wake regions. Figure 6a makes it evident that the fin area hiding behind the tubes, shown in Fig. 9a, is a close representative of the fin surface affected by tube wakes. The effect of LVG position on the average heat transfer coefficient corresponding to the aforesaid fin area is shown in Fig. 9b. Evidently, the degree of augmentation is higher when the LVGs are placed at the nearer cross-stream position. At both cross-stream positions, the degree of augmentation is observed to be decreasing with the streamwise shift in the LVG position. Such a declining change is attributed to the increasing fin area, subjected to small flow velocities, resulting due to streamwise displacement of the LVGs, as discussed in Sect. 3.1.

3.3 Change in Heat Exchanger Effectiveness

Local augmentations on various affected surfaces in the plain finned tube arrays are going to contribute in the overall increase in the heat transfer capacity at the same Reynolds number. It is apparent from Fig. 10 that the deployment of LVGs at the two cross-stream locations resulted in confirmed augmentation. But the streamwise

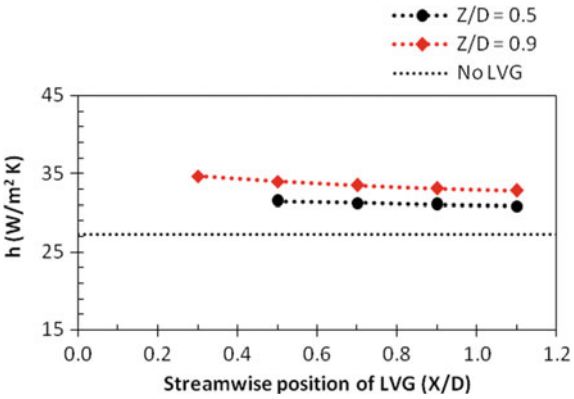

Fig. 10 Average heat transfer coefficient of the finned tube array

change in the LVG position has a weak effect on the overall degree of augmentation despite of change in the cross-stream coordinate. The highest augmentation corresponding to the nearer cross-stream position (i.e. Z/D = 0.5) is 115.6% and it is 127.2% for the LVGs positioned at Z/D = 0.9.

4 Conclusions

There is a large recirculation region of low heat transfer coefficients existing behind all tubes in a plain finned tube array. The deployment of toe-out type delta winglets, erected with 30° attack angle, produces favorable changes in the flow characteristics particularly in the tube wake regions. The flow modifications performed by the vortex generators bring about appreciable thermal augmentations over a large fin area at the same Reynolds number particularly on the fin surface hiding behind the tubes. Despite change in the cross-stream coordinate, the streamwise shift in the generator's position has a decreasing effect on the degree of overall augmentation but the effect is weak. The highest augmentation at Re = 4245 is 127.2% which is resulted by the delta winglets positioned at X/D = 0.3 and Z/D = 0.9.

Acknowledgements This work was financially supported by the Indian Institute of Technology Delhi, New Delhi, India. The authors are grateful to the Institute and its administration for providing a conducive environment. Furthermore, we sincerely acknowledge the incessant encouragement & support provided by the laboratory staff.

References

1. Bergman TL, Lavine AS, Incropera FP, Dewitt DP (2011) Introduction to Heat Transfer. John Wiley & Sons Inc., NJ, USA
2. Arora A, Subarea PMV, Agarwal RS (2015) Numerical optimization of location of 'common flow up' delta winglets for inline aligned finned tube heat exchanger. Appl Therm Eng 82:329–340
3. Jacobi AM, Shah RK (1995) Heat transfer surface enhancement through the use of longitudinal vortices: A review of recent progress. Exp Thermal Fluid Sci 11:295–309
4. Wang Q, Zeng M, Ma T, Du X, Yang J (2014) Recent development and application of several high efficiency surface heat exchangers for energy conversion and utilization. Appl Energy 135:748–777
5. Webb RL, Kim NH (2005) Principles of enhanced heat transfer. Taylor & Francis, New York
6. Hiravennavar SR, Tulapurkara EG, Biswas G (2007) A note on the flow and heat transfer enhancement in a channel with built-in winglet pair. Int J Heat Fluid Flow 28:299–305
7. Chu P, He YL, Lei YG, Tian LT, Li R (2009) Three-dimensional numerical study on fin-and-oval-tube heat exchanger with longitudinal vortex generators. Appl Therm Eng 29:859–876
8. Torii K, Kwak KM, Nishino K (2002) Heat transfer enhancement accompanying pressure-loss reduction with winglet-type vortex generators for fin-tube heat exchangers. Int J Heat Mass Transf 45:3795–3801
9. Gholami AA, Wahid MA, Mohammed HA (2014) Heat transfer enhancement and pressure drop for fin-and-tube compact heat exchangers with wavy rectangular winglet-type vortex generators. Int Commun Heat Mass Transfer 54:132–140
10. Wu JM, Tao WQ (2008) Numerical study on laminar convection heat transfer in a channel with longitudinal vortex generator, Part B: Parametric study of major influence factors. Int J Heat Mass Transf 51:3683–3692
11. Wu JM, Tao WQ (2011) Impact of delta winglet vortex generators on the performance of a novel fin-tube surfaces with two rows of tubes in different diameters. Energy Convers Manage 52:2895–2901
12. Huisseune H, T'Joen C, Jaeger PD, Ameel B, Schampheleire SD, Paepe MD (2013) Influence of the louver and delta winglet geometry on the thermal hydraulic performance of a compound heat exchanger. Int J Heat Mass Transf 57:58–72
13. Tian L, He Y, Tao Y, Tao W (2009) A comparative study on the air-side performance of wavy fin-and-tube heat exchanger with punched delta winglets in staggered and in-line arrangements. Int J Therm Sci 48:1765–1776
14. Gorji M, Mirgolbabaei H, Barari A, Domairry G, Nadim N (2011) Numerical analysis on longitudinal location optimization of vortex generator in compact heat exchangers. Int J Numer Meth Fluids 66:705–713
15. Lu G, Zhou G (2016) Numerical simulation on performances of plane and curved winglet type vortex generator pairs with punched holes. Int J Heat Mass Transf 102:679–690
16. Dezan DJ, Salviano LO, Yanagihara JI (2015) Interaction effects between parameters in a flat-tube louvered fin compact heat exchanger with delta-winglets vortex generators. Appl Therm Eng 91:1092–1105
17. Gong J, Min C, Qi C, Wang E, Tian L (2013) Numerical simulation of flow and heat transfer characteristics in wavy fin-and-tube heat exchanger with combined longitudinal vortex generators. Int Commun Heat Mass Transfer 43:53–56
18. Joardar A, Jacobi AM (2007) A numerical study of flow and heat transfer enhancement using an array of delta-winglet vortex generators in a fin-and-tube heat exchanger. J Heat Transfer 129:1156–1167
19. Fiebig M, Valencia A, Mitra NK (1993) Wing-type vortex generators for fin-and-tube heat exchangers. Exp Thermal Fluid Sci 7:287–295
20. Arora A, Subbarao PMV, Agarwal RS (2016) Development of parametric space for the vortex generator location for improving thermal compactness of an existing inline fin and tube heat exchanger. Appl Therm Eng 98:727–742

21. Kwak KM, Torii K, Nishino K (2005) Simultaneous heat transfer enhancement and pressure loss reduction for finned-tube bundles with the first or two transverse rows of built-in winglets. Exp Thermal Fluid Sci 29:625–632
22. Sinha A, Chattopadhyay H, Iyengar AK, Biswas G (2016) Enhancement of heat transfer in a fin-tube heat exchanger using rectangular winglet type vortex generators. Int J Heat Mass Transf 101:667–681

Hydrodynamic Study of the Flows Caused by Dam Break Around a Rectangular Obstacle

Debasish Dutta, Lalit Kumar, Mohammad Saud Afzal, and Prashant Rathore

1 Introduction

A dam is a boundary that stops or controls the movement of water or the underground stream. These dams control floods and provide water for irrigation, human use, navigation, aquaculture, etc. Since dams stores a huge volume of water. Therefore, it causes some of the most dangerous disasters. Dam break study is essential to forecast, characterize, and reduce threats due to dam failure, and therefore, it attracts the interest of hydraulic engineers and researchers. Dam failure is often caused by poor initial design, structural deficiencies, poor construction, or lack of maintenance [1]. The dam failure occurs because of various causes like landslides, earthquakes, heavy rainfall, or other triggering factors [2]. Floods from dam failure are typically much more dangerous than the hydrologic flood from heavy precipitations, and thus need early precautionary measures [3]. In the worst condition, complete dam structure is removed suddenly, and stored water is released rapidly to the downstream of the river valley, huge damage to wealth and life occurs from such a failure mode. Therefore, Dam break analysis is essential for managing floods. The estimation of submergence areas and the effect of flood waves is necessary for mitigation of hazards [4, 5]. Ritter (1892) was the first to study dam break analytically and derived a solution for instantons dam break [6]. He took horizontal and frictionless channels and infinite lengths of both channels and reservoirs. Later it was further studied by many researchers by changing the downstream slope and lengths [7]. Some researchers also analyzed dam break on the sloping bed [8–11]. To better understand the flows due to dam break in a laboratory experiment is a vital tool; only a few researchers have analyzed dam break experimentally due to the complexity in its setup. Yeh and Petroff (2004) performed an experimental study about the effect of dam break on a

D. Dutta (✉) · L. Kumar · M. Saud Afzal · P. Rathore
Indian Institute of Technology Kharagpur, Kharagpur, India
e-mail: debasish.dutta@iitkgp.ac.in

D. K. Maiti et al. (eds.), *Recent Advances in Computational and Experimental Mechanics, Vol II*, Lecture Notes in Mechanical Engineering,
https://doi.org/10.1007/978-981-16-6490-8_14

structure that has widely been used in literature and used as validation [12]. Ismail et al. (2013) obtained the velocity profile from dam break experiments and validated the results from simulation done in Ansys fluent, for measuring velocities they used Ultrasonic Doppler Velocity profilers and observe that turbulence modelling does not affect upstream velocity profile but has a significant effect at downstream of the obstacle [13]. Aureli et al. (2008) conducted an experiment, but the acquisition of data was performed through imaging techniques [14]. The test was also simulated in a 2D MUSCL-Hancock finite volume numerical model. Soares and Zech (2007) studied the dam break experimentally and obtained the changes in velocity and water level using ADV and resistive gauges [15]. Several numerical models of dam break have been developed by solving the continuity and momentum equation. Lariyah et al. (2013) analyzed dam break study for water supply projects based on the Kahang dam and later classified dam break consequences as minor, moderate, major [16]. They investigated and generated an inundation map at the downstream area and also predicted breach ow hydrograph. Feizi (2018) studied the effect of downstream obstacles (bridges and piers) caused by dam breaks on various flood patterns [17]. He used fluent 3D software for hydraulic analysis and model for free surface flow. The VOF technique was used to model the free surface. Demaio et al. (2004) also used fluent 3D software and studied the wave formed after the dam break. They modeled the wave formed at the starting of the dam break and compared the results with the actual experimental result [18]. Bai et. al. (2007) find the effect of the curvature on the dam break flows, and they found that small curvature has a minimum effect on flows due to dam break, while a greater curvature has a broad effect, causes the decrease of downstream water depth and fluctuations [19]. Yi Xiong (2011) understands dam break mechanics, peak out-flow prediction, and other essentials of dam break using the HEC-RAS model [20]. The study also predicted the submergence area and the number of villages affected due to dam failure with rehabilitation costs. The objective of the present study is to obtain the velocities magnitude upstream and downstream of the obstacle when flood waves strike the obstacle in dam break simulation in REEF3D. The simulated results are compared with experimental results for the validation of the CFD framework.

2 Experimental Set-up

The experiments have been conducted in Hydraulics and water resources engineering Laboratory, Department of Civil Engineering, Indian Institute of Technology Kharagpur. The experiments have been done in a rectangular flume of length 6 m, width 0.3 m, and height 0.6 m. The walls of the flume were made of 5 mm thick Plexiglas with metal bottom, as shown in Fig. 1.

The dam has been demonstrated by a metallic plate, hinged from top corners, and a silicone sealant is used to stop the seepage through the edges of the dam and minimize the error. The dam is located at 4 m downstream from the water's entrance and separates upstream and downstream parts of the channel. The upper

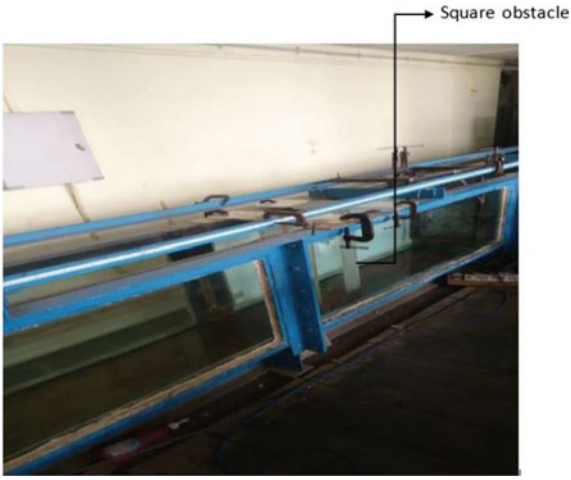

Fig. 1 Flume used for the experiment on dam break analysis

part represents the reservoir, in which water is filled up to certain different heights, and the inflow was then stopped. The water supply system comprises a constant head reservoir (dam reservoir) at an elevation of about 2 m above the ground level. Pumps are used to lift water from the underground reservoir to the dam reservoir. The constant discharge was maintained to minimize the waves formed in the storage behind the dam.

2.1 Setup of Obstacle

A square bottom obstacle has been made up of 5 mm thick Plexiglas with sides of 0.8 m, and a height of 0.6 m was placed at 0.9 m downstream of the dam. V1 and V2 are two points 8 cm upstream of the obstacle and 8 cm downstream of the obstacle where ADV is placed, and velocities at different reservoir levels are calculated. The water surface profile has been captured using a video recorder placed along the flume at different reservoir levels (i.e., h = 20, 25, 30, 35, and 40). The Schematic diagram of the experimental setup with a single obstacle is shown in Fig. 2.

The Acoustic Doppler velocimeter (ADV) is an instrument used to record immediate velocity components at a point with a generally high frequency in the present study. Measurements are performed by estimating the speed of particles in a remote sampling volume dependent on the Doppler shift effect. A pulse is sent from the center transducer, and the Doppler shift presented by the reflections from particles suspended in the water is collected by the 4 (four) recipients. ADV is situated at 0.82 m and one at 1.06 m downstream of the dam (i.e., point v1 and v2). ADV tests ought to be put at least 0.05 m range from the base to take precise readings. The examining recurrence was taken to be 100 Hz.

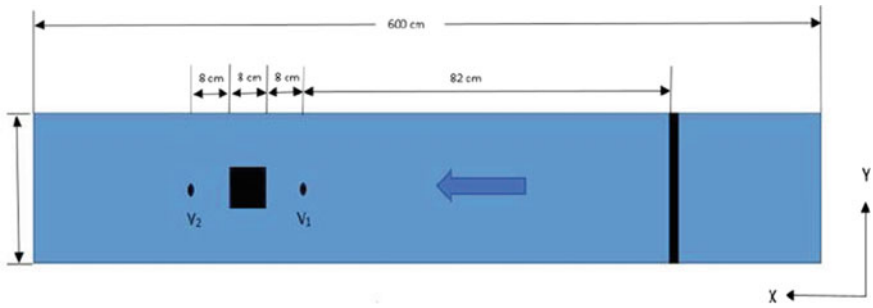

Fig. 2 Schematic diagram of the experimental setup with obstacle of top view

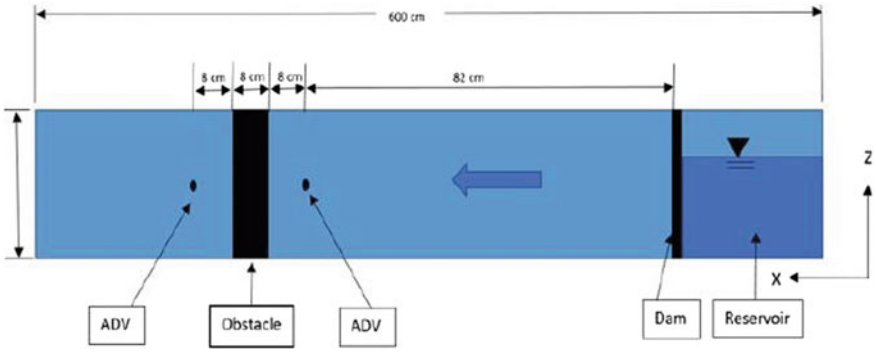

Fig. 3 Schematic diagram of the experimental setup with obstacle of side view

Figures 2 and 3 show the dam located at 4 m downstream of the inlet, water is filled up to the desired height, and inflow is stopped, waves in the reservoir are allowed to settle for some time. The channel bed is kept horizontal, then the breaking procedure was done by suddenly lifting the radial gate (t less than 98 2 s). Gate was lifted manually, and the water is allowed to pass through the flume and strike the obstacle downstream. The ADV used to measure velocity at a point is placed at point v1 and v2, as shown in Fig. 2. The readings were observed by ADV and processed in a computer connected to ADV. A DSLR camera was also placed along the flume to capture the video for calculating water height, and water sur-face profile. Dam break Experiment was conducted for five different heights (i.e., 0.20, 0.25, 0.30, 0.35, and 0.40 m).

3 Numerical Model

The dam break analysis has drawn the interest of CFD researchers due to its (Dam) increasing size in recent years, which increases the threat to the people residing

downstream of the dam. A number of CFD techniques have been developed in the past few years. Among that, REEF3D is more user-friendly than others and also shows the flow of water in a very realistic manner [21].

3.1 Governing Equations

The fluid hydrodynamics inside the Numerical wave Tank (NWT) is solved by incompressible RANS equation along with the continuity equation as shown below.

$$\frac{\partial u_i}{\partial x_i} = 0. \tag{1}$$

$$\frac{\partial u_i}{\partial t} + u_j \frac{\partial u_i}{\partial x_j} = -\frac{1}{\rho}\frac{\partial p}{\partial x_j} + \frac{\partial}{\partial x_j}\left[(\upsilon + \upsilon_t)\left(\frac{\partial u_i}{\partial x_j} + \frac{\partial u_j}{\partial x_i}\right)\right] + g_i \tag{2}$$

where u_i is the velocity of the flow, P is the pressure, water density is denoted by ρ, υ is termed as the fluid kinematic viscosity, υ_t is the eddy-viscosity, and g is the gravitational acceleration.

The dimension of the model is 10.0 m long, 0.30 m wide, and 0.60 m deep, as shown in Fig. 3. The dimension of the model's geometry is saved in a file named a control file, which can be seen in the ParaView. When the simulation is completed, the simulation results can be obtained by using ParaView software. A wake zone can be noticed at the downstream side of the obstacle.

4 Results and Discussion

During the experiment the ow changes rapidly, the velocity distribution of the hydraulic jump is very much complicated and changes with time. Through the ADV probe, the velocity in the x-direction is obtained at 7 cm above the bed level. Due to fast transient flow, no conclusion can be made about the velocity profile.

4.1 Dam Break with One Obstacle

ADV placed in upstream of the obstacle: With a single obstacle and ADV placed in front of the obstacle, velocity measurements have been observed for different reservoir depths. Velocity measurement is obtained by the ADV probe is shown in Fig. 5. The hydraulic jump was developed by striking water with an obstacle. The hydraulic jump can be recognized as the limit between high velocity upstream of the

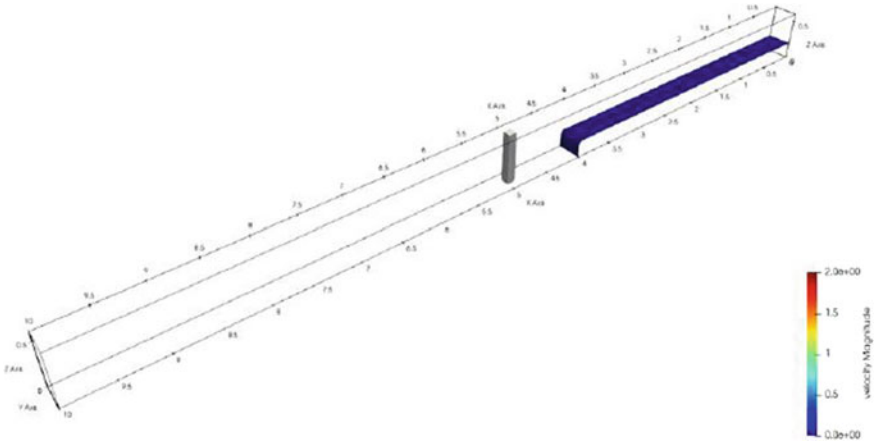

Fig. 4 Geometry of single obstacle model in ParaView

obstacle and a part of water almost at rest. The water separates around the obstacle, and a wake is formed behind this. After some time, the hydraulic jump slowly moves in an upward direction the upstream reservoir empties, the wake zone is as yet present, but the velocities reduce its amplitude.

ADV placed downstream of the obstacle: Figure 6 represents the velocity magnitude in x-direction downstream of the obstacle at different reservoir heights obtained by the ADV.

4.2 Comparison of Velocity Magnitude

ADV placed in upstream of the obstacle: The velocity magnitude results of numerical simulation and velocity magnitude of the experiment is shown in Figs. 7 and 8. Although there is a scatter of data in ADV readings, but a general trend can be obtained.

The velocity magnitude measurement shows the change in velocity from supercritical to subcritical through a hydraulic jump. During the supercritical period, the magnitude of the flow velocity is very high (approximately 2 m/s). Then after the hydraulic jump, the amplitude of the flow velocity decreases rapidly around a value $u = 0.5$ m/s. Finally, the interesting results are obtained at V2, located downstream of the obstacle where the wake zone occurs. The oscillation (periodic change in signs of velocity) proves the wake eddy's presence, which was clearly observed during the experiment.

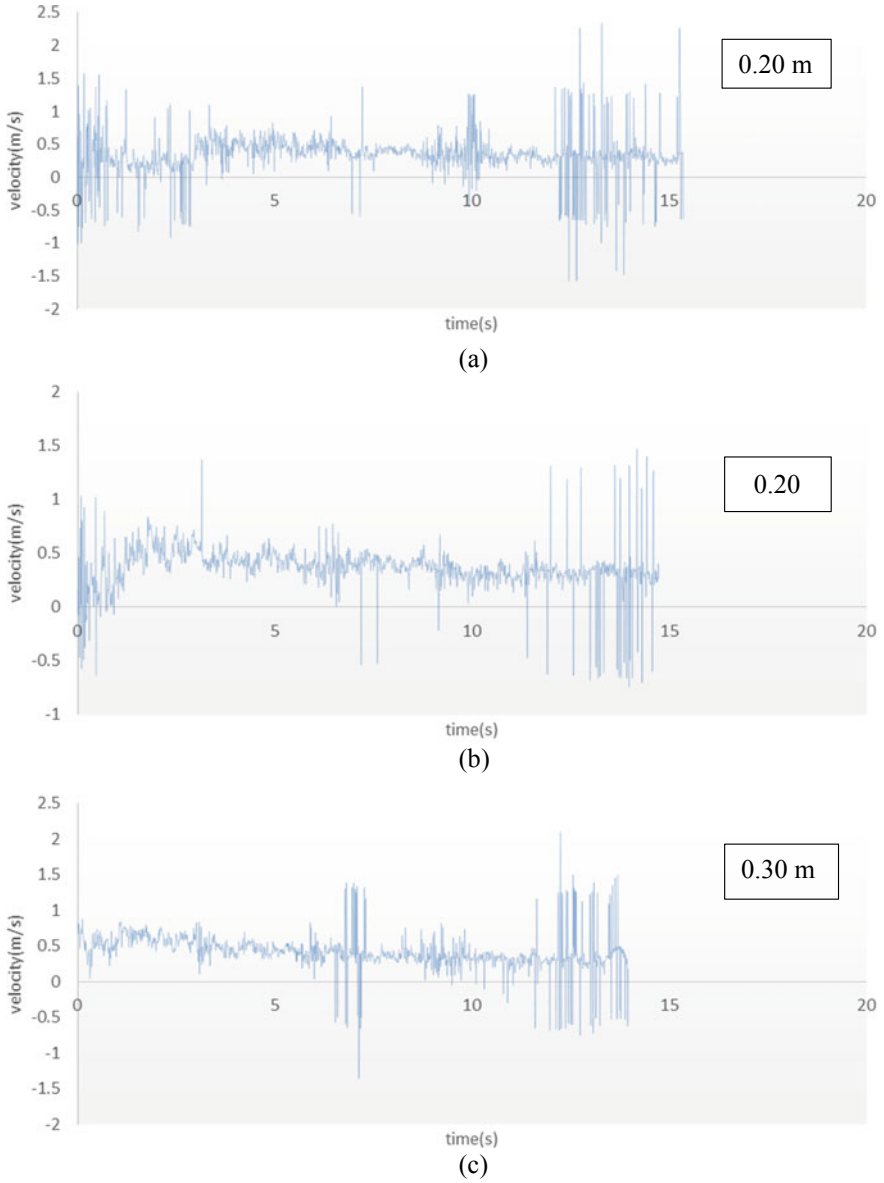

Fig. 5 Velocity magnitude in x-direction upstream of obstacle at different height

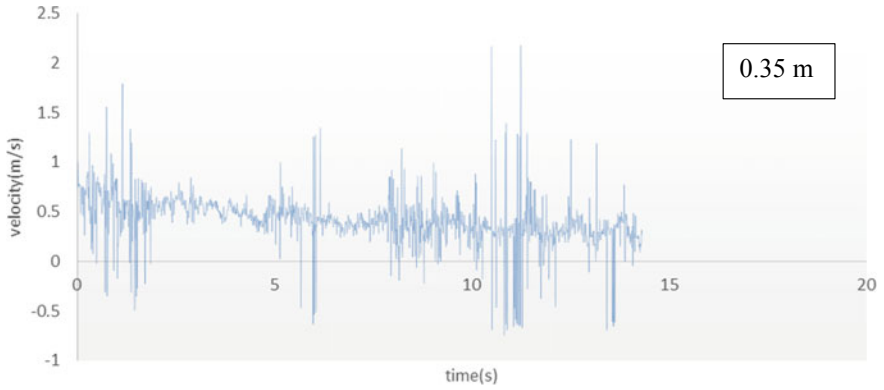

(d)

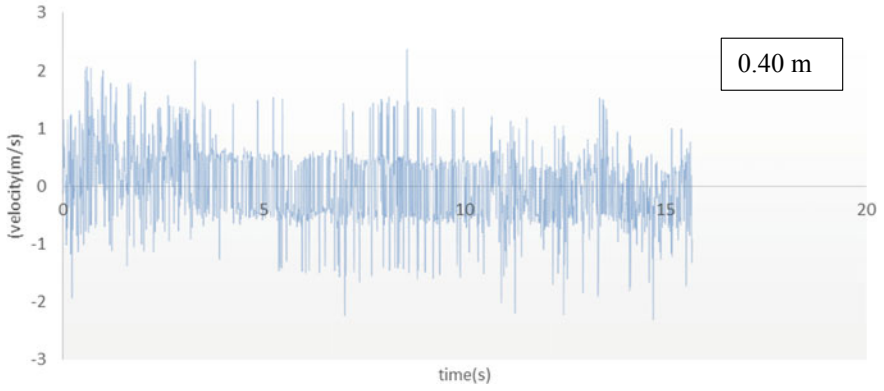

(e)

Fig. 5 (continued)

5 Conclusion

In this study, a dam break ow in a flume with a rectangular obstacle is presented. Experimentally and numerically, it is possible to characterize the flow almost completely. In numerical analysis, the level set method is used in REEF3D to visualize the free surface of the fluid, which shows the fluid surface in a very realistic manner. Data measurement from the experimental data set is used to validate the numerical model, aiming to solve complex fast-transient ow problems, which is one of the problem's objectives. The experiments have been performed for different depths upstream. The asymmetrical velocity fluctuation is obtained on the lower depth, and when the depth of the water level is increased, there is the symmetrical velocity fluctuation. After comparing both results, it can be seen that there is an almost similar plot in REEF3D and in experimental work. Therefore, it can be concluded that the

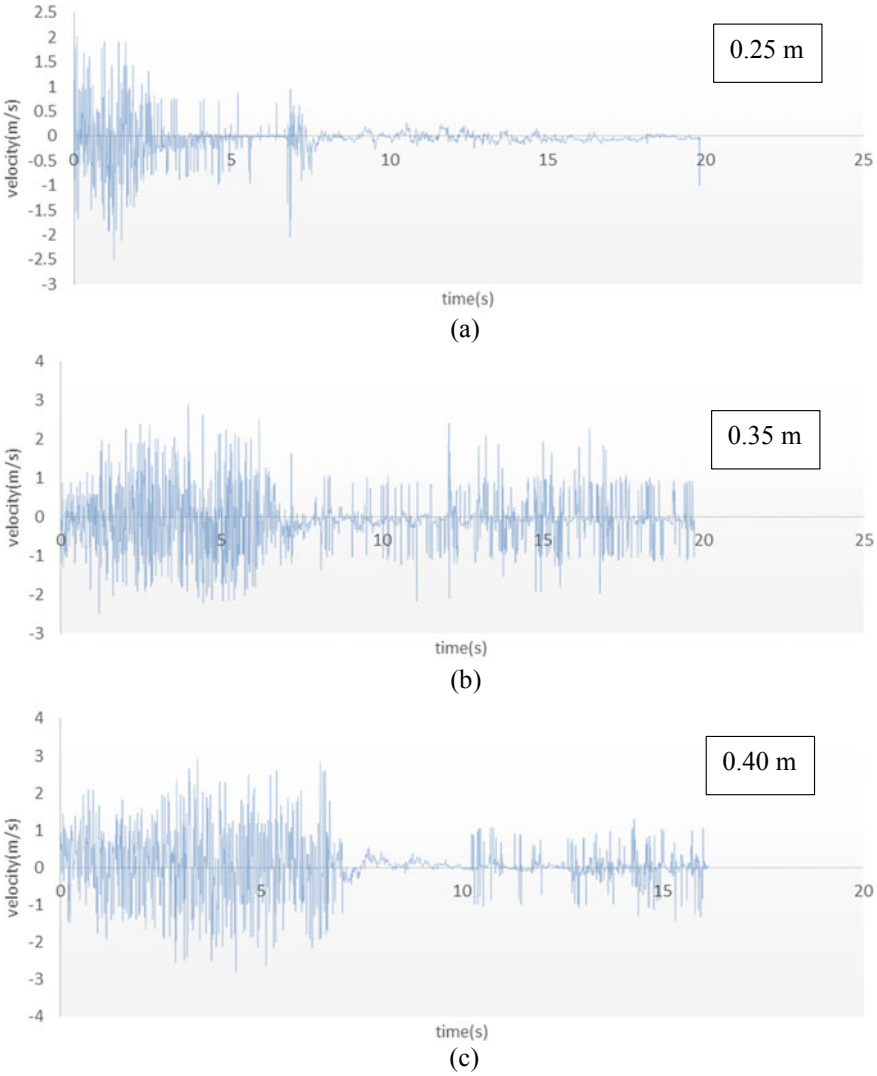

Fig. 6 Velocity magnitude in x-direction downstream of the obstacle at different reservoir height

REEF3D framework can perform the dam break analysis. The present study can be performed with waves and current in future research work. The obstacle shape, size, and position can be changed to determine the velocity fluctuations and ow characteristics. The angles between the two obstacles can be varied to observe the ow hydrodynamics.

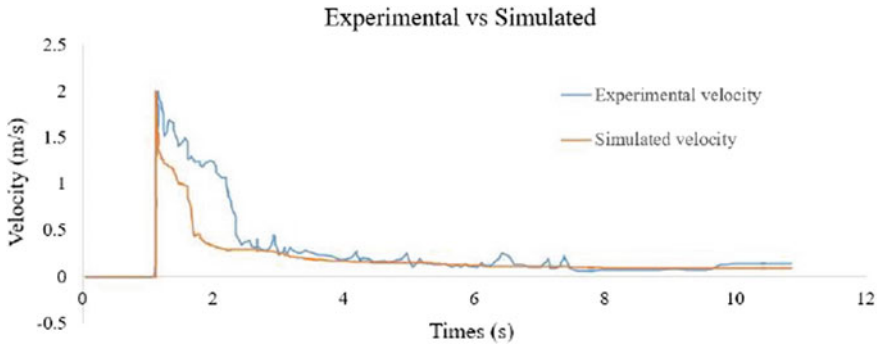

Fig. 7 The comparison of velocity magnitude results obtained in front of obstacle

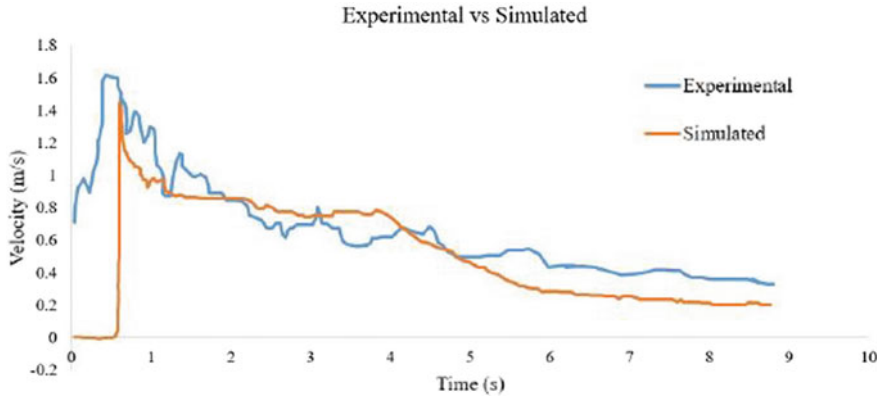

Fig. 8 The comparison of velocity magnitude results obtained after the obstacle

Acknowledgements Authors acknowledge support by SRIC, IIT Kharagpur, under the ISIRD project titled 3D CFD Modelling of the Hydrodynamics and Local Scour Around Off-shore Structures Under Combined Action of Current and Waves.

References

1. Bell SW, Elliot RC, Chaudhry MH (1992) Experimental results of two-dimensional dam-break flows. J Hydraul Res 30(2):225–252
2. Leal JG, Ferreira RM, Cardoso AH (2006) Dam-break wave-front celerity. J Hydraul Eng 132(1):69–76
3. Dutta D, Mandal A, Afzal MS (2020) Discharge performance of plan view of multi cycle W-form and circular arc labyrinth weir using machine learning. Flow Meas Instrum 73:101740
4. Gazi AH, Afzal MS, Dey S (2019) Scour around piers under waves: Current status of research and its future prospect. Water 11(11):1–14

5. Kumar L, Afzal MS, Afzal MM (2020) Mapping shoreline change using machine learning: a case study from the eastern Indian coast. Acta Geophys 1–17
6. Ritterm A (1892) Die fortpanzung der wasserwellen. Zeitschrift des Vereines Dtsch Ingenieure 36(33):947–954
7. Hunt JD (1984) Steady state columnar and equiaxed growth of dendrites and eutectic. Mater Sci Eng 65(1):75–83
8. Nsom B, Debiane K, Piau J-M (2000) Bed slope effect on the dam break problem. J Hydraul Res 38(6):459–464
9. Chanson H (2004) Hydraulics of open channel flow, 2nd edn. Elsevier
10. Ancey C, Iverson RM, Rentschler M, Denlinger RP (2008) An exact solution for ideal dam-break floods on steep slopes. Water Resour Res 44(1)
11. Liu W, Wang B, Guo Y, Zhang J, Chen Y (2016) Experimental investigation on the effects of bed slope and tailwater on dam-break flows. J Hydrol (590):125256
12. Froehlich DC (1989) Proceedings of the 1989 national conference on hydraulic engineering. ASCE,New Orleans, Louisiana, United States
13. Ismail H, Ann Larocque L, Bastianon E, Hanif Chaudhry M, Imran J (2020) Propagation of tributary dam-break flows through a channel junction. J Hydraul Res 1–10
14. Aureli F, Maranzoni A, Mignosa P, Ziveri C (2008) Dam-break flows: acquisition of experimental data through an imaging technique and 2D numerical modeling. J Hydraul Eng 134(8):1089–1101
15. Soares-Frazo S, Zech Y (2007) Experimental study of dam-break flow against an isolated obstacle. J Hydraul Res 45(sup1):27–36
16. Lariyah MS, Vikneswaran M, Hidayah B, Muda ZC, Thiruchelvam S, Abd Isham AK, Rohani H (2013) IOP conference series: earth and environmental science, IOP Conference Series 2013, vol. 16, pp. 012044.https://doi.org/10.1088/1755-1315/16/1/012044
17. Feizi A (2018) Hydrodynamic study of the flows caused by dam break around downstream obstacles. Open Civil Eng J 12(1)
18. DeMaio A, Savi F, Sclafani L (2004) 3D mathematical simulation of dam-break flow. In: Proceeding of the IASTED international conference environmental modeling and simulation 2004, pp 22–24
19. Bai Y, Dong XU, Lu D (2007) Numerical simulation of two-dimensional dam-break flows in curved channels. J Hydrodyn Ser B 19(6):726–735
20. Yi X (2021)A dam break analysis using HEC-RAS. J Water Resour Prot
21. Afzal MS, Bihs H, Kumar L (2020) Computational fluid dynamics modeling of abutment scour under steady current using the level set method. Int J Sedim Res 35(4):355–364
22. Bihs H, Afzal MS, Kamath A, Arntsen A REEF3D: an advanced wave energy design tool for the simulation of wave hydrodynamics and sediment transport.
23. Ahmad N, Bihs H, Myrhaug D, Kamath A, Arntsen A (2018) Three-dimensional numerical modelling of waveinduced scour around piles in a side-by-side arrangement. Coast Eng 138:132–151

Effect of Changing Aspect Ratios on U Plan Shaped Tall Building Under Wind Excitation

Shanku Mandal, Sujit Kumar Dalui, and Soumya Bhattacharjya

1 Introduction

The new global scenario shows the problem of growing population growth. The existing buildings are not enough to accommodate all. The only solution to overcome this problem is to construct new buildings that also face land scarcity. So, the increasing length in the vertical direction is the suitable option for the designers. The elevated structures are very much responsive to wind force. The design of such structures has significant involvement in the calculation of wind-induced responses. The different international wind codes cover the procedure to calculate the wind effects on some regular shapes. The alphabetic plan shapes are the popular choice from both factors; one is utility purpose and the other one is the architectural beauty. But the information is limited for those shapes. Some researchers concentrate on analysing the wind effect on unusual structures, but to a certain extent, they are also limited. The differences in pressure distribution on the L- and U-shaped buildings have been demonstrated by Gomes et al. [1] at various wind angel range. The rms, max, mean and min pressure on the face of T- and L-shaped buildings has been calculated by Amin and Ahuja [2]. A study has been performed on the dynamic effect of H plan shape tall building by Lam et al. [3] to find out the effect of the size of recessed cavities. Menon et al. [4] measured the variation in temperature of air with the change in wind speed and aspect ratio of the building. Afiq et al. [5] presented a review on the pollutant dispersion and flow pattern in symmetric street canyons due to the change in an aspect ratio of building, direction of wind and wind speed. Tong and Leung [6] explored the influence of aspect ratio, wind speed and diurnal heating on the

S. Mandal (✉) · S. K. Dalui · S. Bhattacharjya
Department of Civil Engineering, Indian Institute of Engineering Science and Technology, Howrah, Shibpur, India

S. Bhattacharjya
e-mail: soumya@civil.iiests.ac.in

D. K. Maiti et al. (eds.), *Recent Advances in Computational and Experimental Mechanics, Vol II*, Lecture Notes in Mechanical Engineering,
https://doi.org/10.1007/978-981-16-6490-8_15

dispersion of the pollutant in street canyons of the urban area. Amin and Ahuja [7] demonstrated the effect of the side ratio on the difference in pressure variation on the faces of the rectangular building. Haritha and Srivalli [8] studied the wind effect on the rectangular shape tall building of different aspect ratio. The computational Fluid Dynamics (CFD) and wind tunnel experiment is executed by Mukherjee et al. [9] to calculate the wind-induced pressure on Y-shaped building. Bhattacharyya et al. [10] find out the pressure variation on the faces of E-shaped building with the application of CFD and wind tunnel. The variation in wind responses due to interfered and isolated Y-shaped building has been investigated by Ahlawat and Ahuja [11]. Vikram and Chandradhara [12] calculated the differences in the axial force and the bending moment of the leeward and windward column for the change in height and aspect ratio of a building. Li and Li [13] investigated the across wind responses of L shape model of various geometry on dynamic-wind force. Kumar and Dalui [14] showed the pressure differences between the angular and regular cross shaped building at various range of wind-induced angle. The impact of wind on the change in the height of a square building has been investigated by Gedam and Bhaskar [15]. Shelke and Joshi [16] explored the seismic and wind forces dependency on the changing aspect ratio of buildings. Mallick et al. [17] investigated the pressure distribution on the C shape structure with and without curved for different wind angle cases. Shanku et al. [18] illustrated the wind-induced effect on aerodynamically modified U-shaped building. Sanyal and Dalui [19] compared the force and moment coefficients of different cross-sectional Y-shaped building. The effect of terrain, turbulence, building dimensions and wind direction on pressure characteristics at L shape models has been investigated by Li et al. [20]. Thordal et al. [21] demonstrated the structural responses of corner transformed buildings. Guzmán-Solís et al. [22] proposed an equation to calculate the torsional response of rectangular tall building. Zhang et. al. [23] generated strong and low wind velocity around a super-tall building in the CFD domain and measured the dependency of wind comfort on the buildings having major and minor modifications. The impact of openings in tall buildings on wind pressure, speed and flow has been measured by Chen et al. [24]. Jiang and Cheng [25] illustrated the flow variation around a square shape with the change in Reynolds numbers. Li et al. [26] investigated the impact of different turbulence intensity and turbulence scale ratio on pressure variation at building faces. Du et al. [27] demonstrated the power spectrum densities curves, fluctuating and mean component of force and pressure coefficients, Strouhal numbers, spanwise correlations of two square-shaped in close proximity. Jafari and Alipour 28 discussed various approaches to reduce the tall building's vibration because of the wind flow. Bairagi and Dalui [29] measured the pressure on setback buildings using CFD and stated that these roof pressure variation could be adopted for roof design. Kim [30] used CFD simulation on a double-skin façade to assessed the thermal responses of office buildings located in Saudi Arabia. Noormohamadian and Salajegheh [31] applied the CFD and polynomial regression technique to evaluate the influence of exterior geometry on wind aerodynamic responses of a triangular section.

The wind impact on various alphabetical-shaped buildings has been studied considering different structural reformation and other prospects of wind but the information related to the effect of change in height on alphabetic plan shaped irregular tall buildings is not available in previous articles. Though the variation in height is a crucial parameter in designing a wind-resistant structure, it is necessary to conduct a study incorporating this effect. Some of the articles cover this important wind aspect on the square and rectangular shape and this information is not enough to predict the behaviour of alphabetic figures. The U alphabetic irregular plan shaped tall building is considered in the presented study because this shape is suggested most of the time to construct academic buildings, public buildings and shopping malls, etc. The differences in pressure, force and moment coefficients due to change in aspect ratio has been calculated by numerical analysis. The variation in surface pressure of those buildings has been illustrated by plotting pressure contours of the surface.

2 Details of the Building Models

In the current study, the wind loads on the buildings with different aspect ratios have been analyzed at a 0° angle of flow. The aspect ratio has been varied by changing the height of the structure without changing the side ratio. The aspect ratio 0.5, 1, 1.5, 2, 2.5, 3, 3.5, 4, 4.5 and 5 were considered for present study. The ratio has been calculated by dividing the height to length of the building (H/L). The buildings are modelled as a 1:300 geometric scale. The length (L), limb width (b') and width (b) of the building are adopted as 250 mm, 50 mm and 150 mm, respectively. So the varying height of the building for 0.5–5 ratio is taken as 125 mm, 250 mm, 375 mm, 500 mm, 625 mm, 750 mm, 875 mm, 1000 mm, 1125 mm and 1250 mm, respectively as shown in Fig. 1.

3 Solution Methodology

The wind force on structures depends on the shape and height of the structure. The extreme size attracts wind force and the considered building models in our current study are irregulars in shape. Those two factors are well enough to become vulnerable to the wind flow. To understand the exact wind effect around the building, the computational fluid dynamics (CFD) code of Ansys CFX has been utilized, which simulates wind flow around the building models. In recent years, advances in CFD are capable of predicting the interaction of the fluid structure. (Löhner et al. [32]).

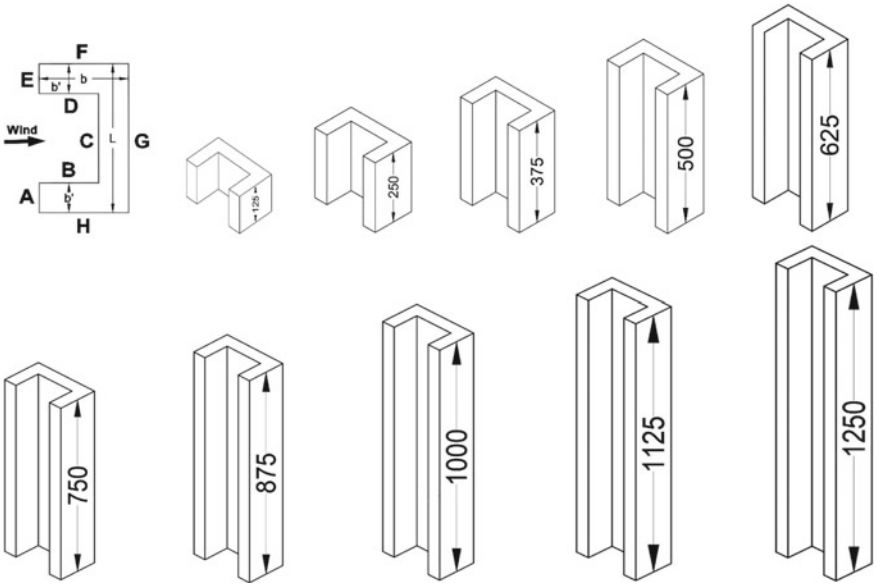

Fig. 1 Analytical building models for numerical simulation (all the dimensions are in mm)

3.1 Computational Domain Setup

The various buildings, as shown in Fig. 1, have been numerically simulated by k-ε turbulence model in an atmospheric boundary layer (ABL) flow generate domain (Revuz et al. [33]) having a close boundary of 5H from the building model in case of the inlet, roof and sidewalls. However, the close boundary at a 15H distance is taken for the outlet. The selection of a large domain is free from the restriction of wind flow and the calculation of blockage correction. The power-law equation (see Eq. 1) creates the boundary layer. The exponent (α) has been taken as 0.133.

$$U/U_H = |Z/Z_H|^{\alpha} \tag{1}$$

Where, The wind speed in any point in Z elevation is denoted by $\boldsymbol{U}$. $\boldsymbol{U}_H$ signifies the wind speed at any reference height $\boldsymbol{Z}_H$. The height of $\boldsymbol{Z}_H$ is considered as 1.0 m in the current study and 10 m/s velocity is generated from in the inlet of the domain.

Figure 2 is showing a specific domain of 125 mm height (H) building of aspect ratio 0.5 for numerical simulation. The corresponding length of the bounding box has been calculated, as mentioned earlier. For different building cases, the domain size has been changed according to the height of the building. The operating pressure in between the domain is 1 atm and the pressure at the outlet has been taken 0 Pa.

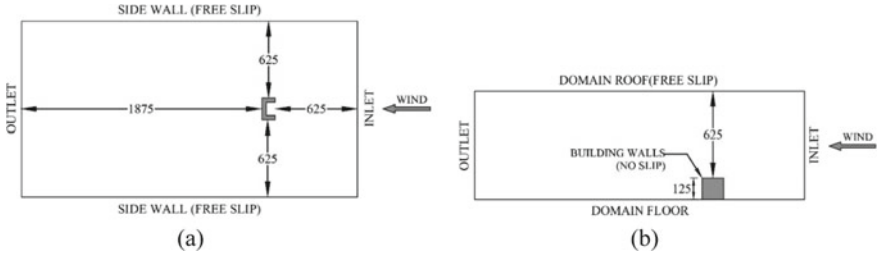

Fig. 2 The details of the numerical analysis domain **a** Plan view **b** Elevation view

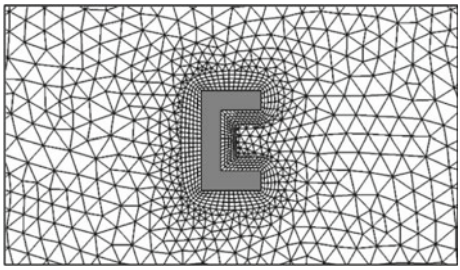

Fig. 3 The mesh pattern for a typical model case

3.2 Generation of Mesh

The entire domain has meshed with the tetrahedral type elements (Bhattacharyya et al. [10]) but to tackle higher differential flow efficiently relatively very fine layers of hexagonal elements are filtered around the model. Figure 3 demonstrates the mesh pattern of a typical model in which the entire domain has meshed with tetrahedral elements which are relatively larger as compare to the meshing provided around the building.

3.3 Mesh Refinement Study

The mesh refinement study is basically done to select the suitable mesh size for the numerical simulation. This study is one of the vital parameters for CFD analysis. The simulated results accuracy depends on the chosen mesh size for analytical research. This study is based on the trial and error technique. Various mesh refinement trails (MT1–MT7) have been performed and the results are noted in each step. A mesh refinement study is executed on a 500 mm height (aspect ratio 2) building for a 0° wind angle. The elements in each stage and the corresponding drag coefficient values are noted. The trails continue with various mesh size till a significant variation is not found. The errors are also calculated to show the importance of the mesh refinement study. The MT6 trail mesh size is adopted in the entire study because

Table 1 The mesh refinement study on 500 mm height building (aspect ratio 2.5) at 0° angle

Mesh Trial	Total Elements	Drag Coefficient	% of Error
MT1	2.885×10^6	0.875	−20.264
MT2	5.165×10^6	0.948	−13.669
MT3	12.547×10^6	1.014	−7.645
MT4	19.853×10^6	1.045	−4.812
MT5	26.709×10^6	1.072	−2.396
MT6	33.936×10^6	1.096	−0.182
MT7	41.093×10^6	1.098	–

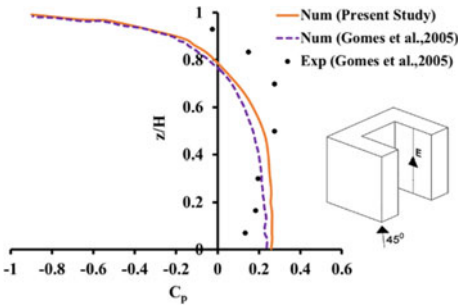

Fig. 4 The pressure coefficients comparison of face E for 45° wind incidence angle

the error is almost negligible and this will save some computational time for each analysis (Table 1).

3.4 Validation of Numerical Simulation

The pressure coefficient along the vertical axis of face E at 45° wind angle has been taken from a published article by Gomes et al. [1]. To validate the current numerical analysis result, a study has been performed with the model as per the article and other analysis methodology. The corresponding pressure values have been extracted from the numerical simulation and compared with the taken values of the article, as shown in Fig. 4. The data extracted from Ansys CFX is well-matched with the published results. However, there is some discrepancy but those are within acceptable limits.

4 Results and Discussion

The impact of wind has been studied by calculating various wind-induced responses on the U-shaped building with changing aspect ratio for 0° wind angle. This section presents the variation in wind flow patterns, force coefficient, moment coefficient

and pressure coefficient due to change in height. The contour plot of pressure on the surface of those buildings also represents the variation in pressure distribution with the height. Because of the axisymmetry shape of U-shaped building and the usual wind induce angle, the mean pressure coefficient values are the same for symmetric faces. The pressure contour plot also represents the same variation for the symmetric faces.

4.1 Wind Velocity Streamline

The pattern of wind flow and the velocity of the flow in different locations are illustrated by plotting streamlines, as shown in Fig. 5. The height of the building is a vital factor for variation in flow streamline. The symmetric flow pattern is visible on both sides of the building for the axisymmetry shape of U building. However, the generated vortex patterns in the wake zone, influenced by the height. With the increase in height, the lengthy vortex is formed. At the side faces and the backside of the building, the velocity of the flow decreased significantly due to side wash and vortex generation respectively. The sudden increase in speed has been observed in the corner points where the flow separation occurs.

4.2 Comparison of Force and Moment Coefficients

The force and moment coefficient has been calculated for each building at 0° wind angle and illustrated in Fig. 6. The comparison of those coefficients displays that the increase in the height of a building with keeping other parameters fixed leads to great attraction to wind. The drag coefficient and the moment coefficients along Y-axis (M_y) are demonstrated in Fig. 6 because the lift coefficient and the moment along X-axis (M_x) are close to zero. The force and moment coefficient both are increasing as aspect ratio changes to 0.5–5. The drag force coefficient of the buildings has been raised with the increase in aspect ratio gradually from 0.5 to 3.5 and the moment coefficient along Y-axis also increasing with the change in ratio up to 4. The drag coefficient and moment coefficient along Y-axis (M_y) is almost the same for the changing height from 875 to 1000 mm and 1000 mm to 1125 mm, respectively. This signifies that the change in building height in between the range will not attract extra force and moment but further increase in height leads to increase in force and moment. This point should keep in mind while designing such a structure. This will give a benefit to the designer that they can be fixed the high limit value for the building because it will not involve any extra precaution to build the structural members.

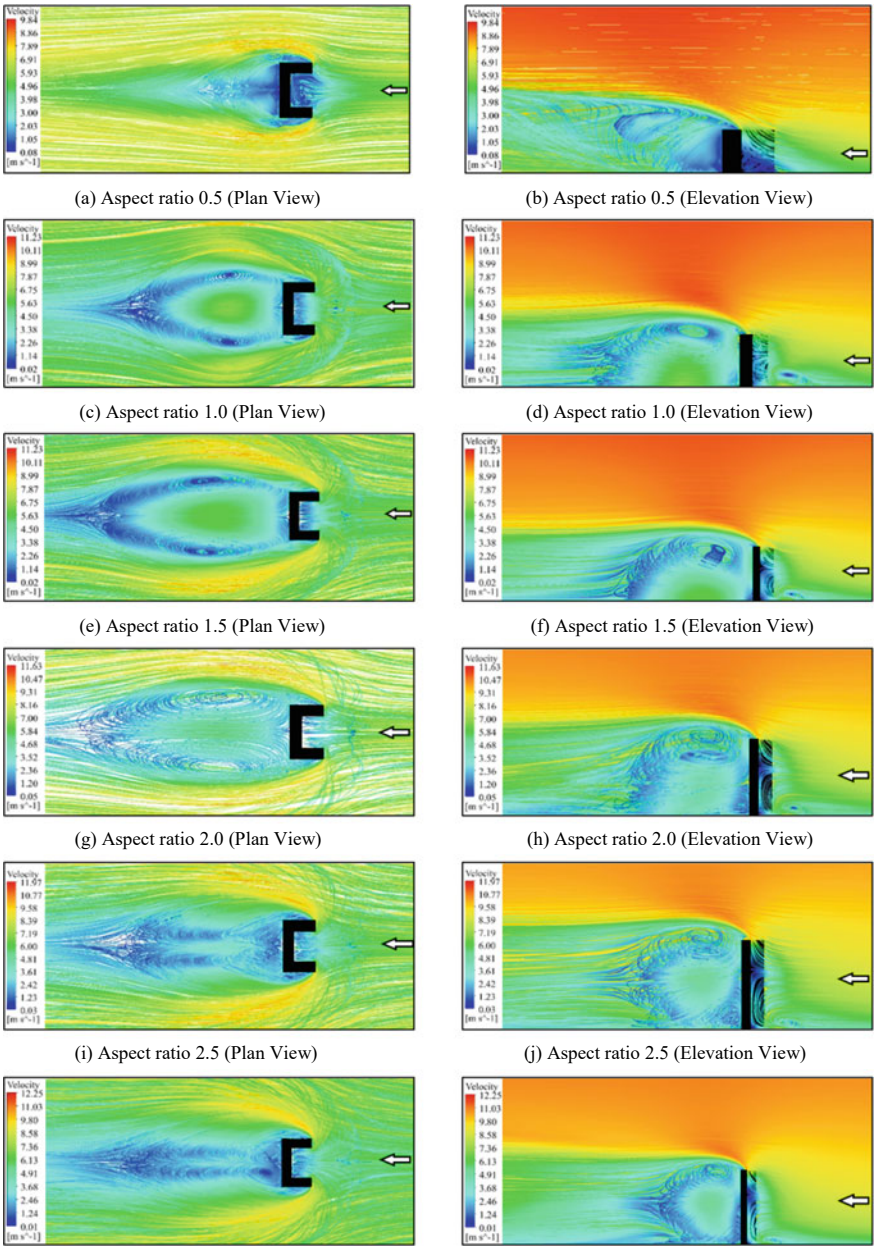

(a) Aspect ratio 0.5 (Plan View)

(b) Aspect ratio 0.5 (Elevation View)

(c) Aspect ratio 1.0 (Plan View)

(d) Aspect ratio 1.0 (Elevation View)

(e) Aspect ratio 1.5 (Plan View)

(f) Aspect ratio 1.5 (Elevation View)

(g) Aspect ratio 2.0 (Plan View)

(h) Aspect ratio 2.0 (Elevation View)

(i) Aspect ratio 2.5 (Plan View)

(j) Aspect ratio 2.5 (Elevation View)

(k) Aspect ratio 3.0 (Plan View)

(l) Aspect ratio 3.0 (Elevation View)

Fig. 5 The plan and elevation view of wind flow pattern around the various building for 0° wind angle

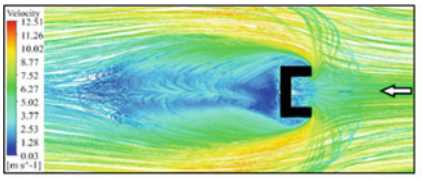

(m) Aspect ratio 3.5 (Plan View)

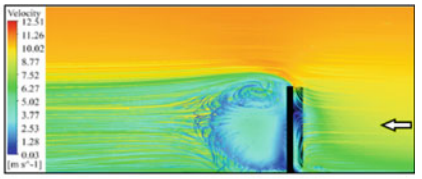

(n) Aspect ratio 3.5 (Elevation View)

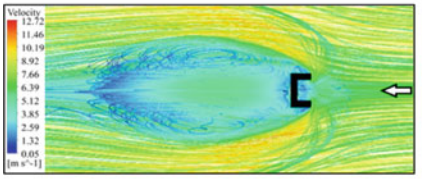

(o) Aspect ratio 4.0 (Plan View)

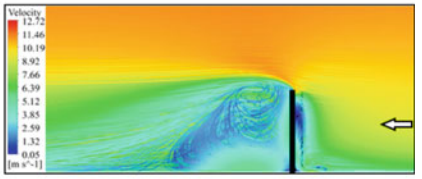

(p) Aspect ratio 4.0 (Elevation View)

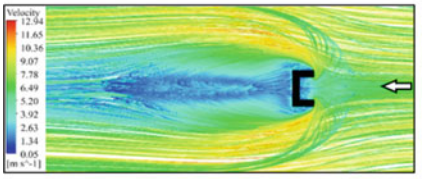

(q) Aspect ratio 4.5 (Plan View)

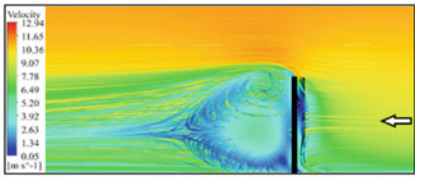

(r) Aspect ratio 4.5 (Elevation View)

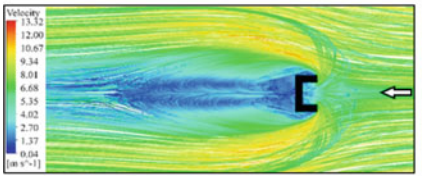

(s) Aspect ratio 5.0 (Plan View)

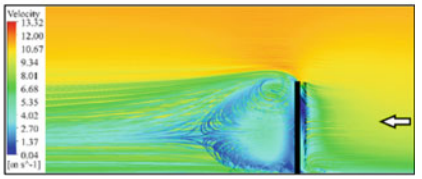

(t) Aspect ratio 5.0 (Elevation View)

Fig. 5 (continued)

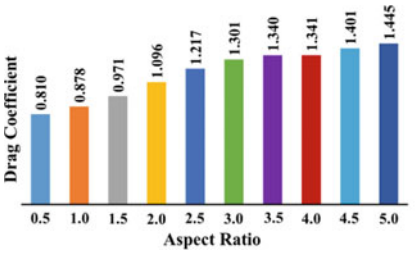

(a) Drag coefficient for 0° angle

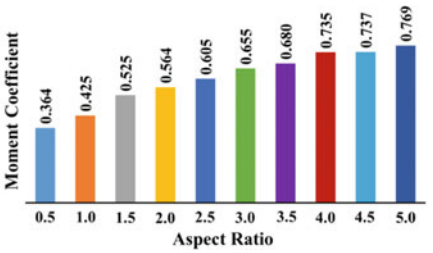

(b) Moment coefficient for 0° angle

Fig. 6 The variation in drag and moment coefficient with the change in an aspect ratio

Table 2 The comparison of mean pressure coefficient of various cases for 0° wind angle

Aspect Ratio	Face A	Face B	Face C	Face D	Face E	Face F	Face G	Face H
0.5	0.336	0.377	0.404	0.377	0.336	−0.252	−0.189	−0.252
1.0	0.352	0.584	0.697	0.584	0.352	−0.293	−0.191	−0.293
1.5	0.365	0.750	0.802	0.750	0.365	−0.386	−0.288	−0.386
2.0	0.389	0.826	0.870	0.826	0.389	−0.549	−0.381	−0.549
2.5	0.391	0.891	0.928	0.891	0.391	−0.655	−0.468	−0.655
3.0	0.396	0.939	0.971	0.939	0.396	−0.698	−0.526	−0.698
3.5	0.413	0.987	1.019	0.987	0.413	−0.722	−0.531	−0.722
4.0	0.451	1.034	1.063	1.034	0.451	−0.727	−0.537	−0.727
4.5	0.454	1.063	1.090	1.063	0.454	−0.732	−0.550	−0.732
5.0	0.456	1.096	1.122	1.096	0.456	−0.747	−0.562	−0.747

4.3 Comparison of Mean Pressure Coefficients

The change in mean pressure coefficients for the height increment has been demonstrated in Table 2. The pressure has been calculated on the surface of the building for each case. The mean pressure also increases with height. The same pressure variation is observed at the symmetric faces of the building. That means the mean pressure on face A, B and F are the same with face E, D and H, respectively. The positive pressure is exerted on face A, B, C, D and E but the negative pressure is observed on the face F, G and H because of the side wash and formation of the vortex on that face. Face C has the maximum positive pressure in each case and the maximum negative pressure is on face F and H. The side wash from these faces causes immense negative pressure.

The contour of pressure has been plotted to visualize the pressure variations on the different locations of the building face. The contour helps to understand max and min pressure locations and it is utilized in the time of design of the elements on this location. In Fig. 7, the pressure contour of face A, B, C, D, E, F, G and H

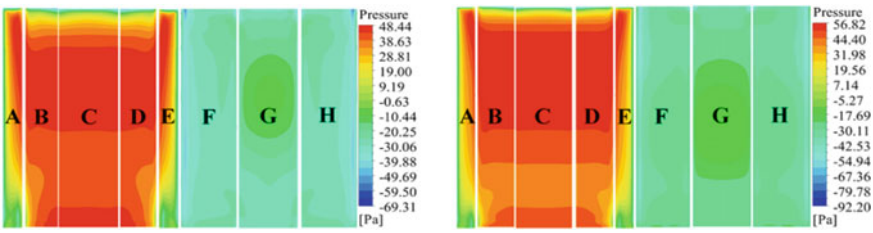

(a) Aspect Ratio 2.5 (b) Aspect ratio 4.5

Fig. 7 Pressure contour plot of all the faces of typical buildings

are shown for 2.5 and 4.5 aspect ratio models. The symmetric faces are showing the same pressure variations on the surface.

The distribution of pressure on the surface of the buildings is almost identical for each case but in the higher aspect ratio building, the magnitude of pressure is relatively high. Tremendous positive pressure has been exerted on most surfaces of B, C and D. The suction is occurring at the corners of surface A and C due to flow separation. The negative pressure is noticeable all over the face F, G and H. The maximum suction is evident at some portion of the corners in face F. The pressure contour plot is a useful illustration of pressure variation, which helps the designer to recognize the critical region.

5 Conclusions

The current study demonstrated the impact of wind on U-shaped building having a different height ratio. The irregular flow pattern around the alphabetic shape influences the wind-induced responses and also the extreme height is susceptible to wind force. The initial aim of this study is to highlight the change in wind behaviour and the effect of changing aspect ratio on the alphabetic shape. This numerical analysis measures the effect of different aspect ratio and illustrated the variation in moment, pressure and force coefficients. This article described the information regarding the impact of aspect ratio on an alphabetical shape. So, these calculated responses are significant and unique because the past articles only cover the effect of changing aspect ratio on regular building shapes. The wind flow around the buildings depends on both the shape and height of the structure. The building irregular shape promotes abrupt flow all around the building and the increased height produces a wider vortex shedding field at the wake region. With the increase in aspect ratio, the higher values of the drag and moment coefficient are monitored. The significant findings are that the negligible rise in force and moment is observed at the height ratio of 3.5 to 4 and 4 to 4.5 height ratio. That means the building height in between the range does not attract extra wind forces. This indicates that the construction of a building in between the range does not require any extra design consideration and it will be economical as well because the increase in building height in between the range does not involve a higher section of the structural members. The mean pressure coefficients at different faces have a higher value with the building height. This signifies that the cladding elements design should be done with extra care and the material will be strong enough to withstand the enormous pressure. As the construction of the tall building has high demand in the current era, the critical findings from this study will help the design engineers to select an appropriate height for the U plan shape high rise building construction and also guide to take precautionary actions for the structural safety.

References

1. Gomes MG, Moret Rodrigues A, Mendes P (2005) Experimental and numerical study of wind pressures on irregular-plan shapes. J Wind Eng Ind Aerodyn 93(10):741–756
2. Amin JA, Ahuja AK (2008) Experimental study of wind pressures on irregular-plan shape buildings. In: BBAA VI Int Colloq Bluff Bodies Aerodyn Appl Milano, Italy, pp 1–9
3. Lam KM, Wong SY, To AP (2009) Dynamic wind loading of H-shaped tall buildings. In: 7th Asia-Pacific conference wind engineering APCWE-VII, Taiwan
4. Memon RA, Leung DYC, Liu CH (2010) Effects of building aspect ratio and wind speed on air temperatures in urban-like street canyons. Build Environ 45(1):176–188
5. Afiq MW, Azwadi CSN, Saqr KM (2012) Effects of buildings aspect ratio, wind speed and wind direction on flow structure and pollutant dispersion in symmetric street canyons: a review. Int J Mech Mater Eng 7(2):158–165
6. Tong NYO, Leung DYC (2012) Effects of building aspect ratio, diurnal heating scenario, and wind speed on reactive pollutant dispersion in urban street canyons. J Envir Sci 24(12):2091–2103
7. Amin JA, Ahuja AK (2013) Effects of side ratio on wind-induced pressure distribution on rectangular buildings. J Struct 2013:1–12
8. Haritha KV, Srivalli IY (2013) Effect of wind on tall building frames-influence of aspect ratio. Int J Res Civil Eng Arch Des 1(1):1–6
9. Mukherjee S, Chakraborty S, Dalui SK, Ahuja AK (2014) Wind induced pressure on 'Y' plan shape tall building. Wind Struct 19(5):523–540
10. Bhattacharyya B, Dalui SK, Ahuja AK (2014) Wind induced pressure on 'E' plan shaped tall buildings. Jordan J Civ Eng 8(2):120–134
11. Ahlawat R, Ahuja AK (2015) Wind loads on Y plan shape tall building. Int J Eng Appl Sci 2(4):80–83
12. Vikram MB, Chandradhara GP (2016) Behavior of windward and leeward columns with aspect ratio and height of the building. Ind J Adv Chem Sci:169–172
13. Li Y, Li QS (2016) Across-wind dynamic loads on L-shaped tall buildings. Wind Struct 23(5):385–403
14. Kumar D, Dalui SK (2017) Effect of internal angles between limbs of cross plan shaped tall building under wind load. Wind Struct 24(2):95–118
15. Gedam HV, Bhaskar GB (2018) Effect of wind load on high rise buildings considering aspect ratio. Int J Res Appl Sci Eng Technol 6(6):903–907
16. Shelke MB, Kuwar VA (2018) Effect of wind and earthquake forces on different aspect ratio of building. Int J Adv Res Ideas Innov Technol 4(3):873–875
17. Mallick M, Kumar A, Patra KC (2019) Analysis of curvature effect on C-shaped buildings. ACM Int. Conf. Proceeding Ser., pp 260–266
18. Mandal S, Dalui SK, Bhattacharjya S (2020) Effect of aerodynamic modifications on a tall building with horizontal irregularity. In: Vinyas M et al (eds), Adv. In struc. Sys. Mat. (pp 99–107)
19. Sanyal P, Dalui SK (2020) Effect of corner modifications on Y' plan shaped tall building under wind load. Wind Struct 30(3):245–260
20. Li Y, Duan RB, Li QS, Li YG, Li C (2020) Research on the characteristics of wind pressures on L-shaped tall buildings. Adv Struct Eng 23(10):2070–2085
21. Thordal MS, Bennetsen JC, Capra S, Kragh AK, Koss HHH (2020) Towards a standard CFD setup for wind load assessment of high-rise buildings: Part 2–Blind test of chamfered and rounded corner high-rise buildings. J Wind Eng Ind Aerodyn205:104282
22. Guzmán-Solís V, Pozos-Estrada A, Gómez R (2020) Experimental study of wind-induced shear, bending, and torsional loads on rectangular tall buildings. Adv Struct Eng 23(14):2982–2995
23. Zhang X, Weerasuriya AU, Zhang X, Tse KT, Lu B, Li CY, Liu C (2020) Pedestrian wind comfort near a super-tall building with various configurations in an urban-like setting. Build Simul 13(6):1385–1408

24. Chen FB, Wang X, Zhao Y, Li Y, Li Q, Xiang P, Li Y (2020) Study of wind loads and wind speed amplifications on high-rise building with opening by numerical simulation and wind tunnel test. Adv Civ Eng 2020:8850688
25. Jiang H, Cheng L (2020) Flow separation around a square cylinder at low to moderate Reynolds numbers. Phys Fluids32(4):044103
26. Li Y, Yan J, Chen X, Li Q, Li Y (2020) Investigation of surface pressures on CAARC tall building concerning effects of turbulence. Wind Struct 31(4):287–298
27. Du X, Chen R, Dong H, Ma W, Xu H, Zhao Y (2021) Aerodynamic characteristics of two closely spaced square cylinders in different arrangements. J Wind Eng Ind Aerodyn 208:104462
28. Jafari M, Alipour A (2021) Methodologies to mitigate wind-induced vibration of tall buildings: a state-of-the-art review. J Build Eng33:101582
29. Bairagi AK, Dalui SK (2021) Estimation of wind load on stepped tall building using CFD simulation. Iran J Sci Technol Trans Civ Eng. 45:707–727
30. Kim DD (2021) Computational fluid dynamics assessment for the thermal performance of double-skin façades in office buildings under hot climatic condition. Build Serv Eng Res Technol 42(1):45–61
31. Noormohamadian M, Salajegheh E (2021) Evaluation and minimization of moment coefficient of tall buildings with trilateral cross-section via a surrogate model. SN Appl Sci 3:234
32. Löhner R, Haug E, Michalski A, Muhammad B, Drego A, Nanjundaiah R, Zarfam R (2015) Recent advances in computational wind engineering and fluid-structure interaction. Jnl Wind Eng Ind Aerodyn 144:14–23
33. Revuz J, Hargreaves DM, Owen JS (2012) On the domain size for the steady-state CFD modelling of a tall building. Wind Struct 15(4):313–329

Development of Flow and Acoustic Calculation Method for Design of Tunable Acoustics Combustion Test Rig

Rohit Mohan Jiwane and Krishnakant Agrawal

1 Introduction

Increasing overall thermal efficiency of gas turbines requires higher combustor firing temperatures, which increase the thermal NO_x emissions [1]. To overcome this issue, a Lean Premixed (LP) combustion strategy is used [2] which can provide lower flame temperatures and hence lower NOx. However, lower temperatures lead to fall in reaction rates due to which the flame becomes weak and has stability issues, and it becomes susceptible to thermoacoustic oscillations [3]. These oscillations can cause undesirable fluctuations in pressure and heat release fluxes in the combustor, which can induce fatigue failure and also increase in wear and tear of engine components [4]. In extreme cases, it can even cause structural damage and conditions unsafe for operation.

Combustion instability is a consequence of the interaction between flame, flow and acoustics [3, 5]. Acoustic field affects the fluid mechanics which affects the combustion. The unsteady heat release is an efficient acoustic source which generates pressure wave propagating in the system. This establishes a combustion instability cycle through feedback between acoustics and combustion. To suppress combustion-driven oscillation we have two methods, active control and passive control, both targeting elimination of the coupling between heat release and acoustics field [6]. While there are many studies focusing on the effect of flow perturbation and burner design on the dynamic flame response, combustion dynamics is also affected by its coupling with

R. M. Jiwane · K. Agrawal (✉)
Department of Mechanical Engineering, Indian Institute of Technology Delhi, New Delhi, Hauz Khas, India
e-mail: kkant@mech.iitd.ac.in

R. M. Jiwane
e-mail: rohitjiwane07@gmail.com

D. K. Maiti et al. (eds.), *Recent Advances in Computational and Experimental Mechanics, Vol II*, Lecture Notes in Mechanical Engineering,
https://doi.org/10.1007/978-981-16-6490-8_16

the chamber acoustics [7]. Hence, while studying combustion dynamics in a laboratory scale setup, care should be taken on design of its acoustic aspects, as they might not always be equivalent to that observed in real scale combustor due to difference in geometric dimensions and operating conditions. In a general case, it is desirable to have a lab scale test setup where the acoustic behaviour can be continuously varied or "tuned" to be able to match the actual combustor acoustic behaviour. It is well known that by changing the combustor length, natural resonant frequency of the combustor chamber volume can be varied. Further, there are other methods such as varying the end boundary conditions or inducing global modes such as Helmholtz resonance to have variable chamber acoustics [8]. Some of such designs from literature are shown in Fig. 1. Knadler et al. [9] validated the physics-based low-order thermoacoustic model of a liquid fueled gas turbine combustor shown in Fig. 1a, by fixing of acoustics boundary conditions. Air siren is used at the rig inlet and choked exit is used at the end of the combustion chamber transition tube. Terhaar et al. [10] present a tunable acoustics feature in the test rig as shown in Fig. 1b, which consists of a generic combustor with a premixed swirl-stabilized natural gas flame. Here variation of the length of upstream plenum section can be done in a continuous manner to generate continuous variation in the acoustic resonant frequencies. At the upstream of tube, speakers are mounted to excite resonance over the desired frequency range.

In a study by Kim et al. [11], adjustable length was used along with plug nozzle in the exit section of the combustion chamber shown in Fig. 1c. The plug nozzle leads to flow acceleration leading to choking conditions and acts as a closed boundary condition for acoustics. By varying location of the plug nozzle, the length of acoustically

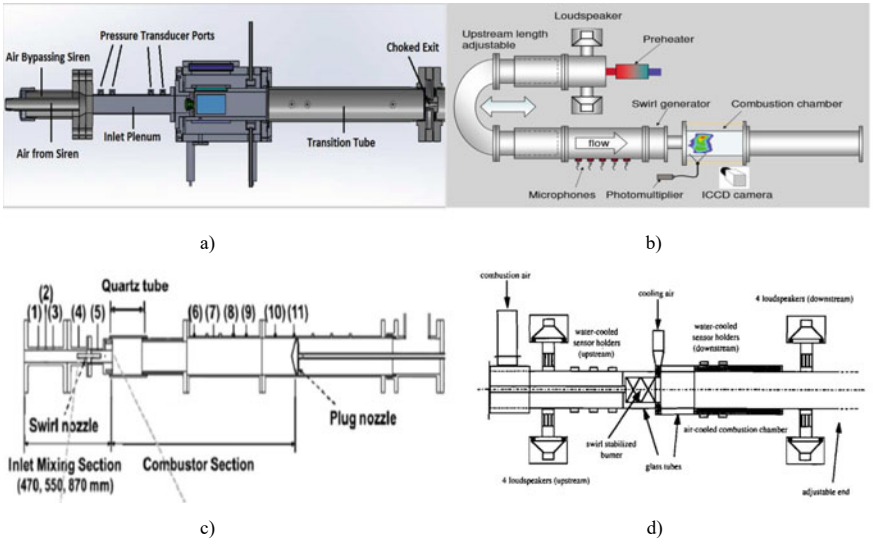

Fig. 1 Few designs of tunable acoustic test rig for combustion dynamics studies from literature [9–12]

resonating column can be varied to vary its resonant frequencies. Paschereit [12] has used four loudspeakers (two at upstream and two at downstream end) shown in Fig. 1d, to change the acoustic boundary conditions by varying the phase difference between the acoustic waves from the two speakers at each end. A microphone picks acoustic resonance in combustion chamber and feeds the signal to the speakers, which can vary their phase from 0 to 360 deg. to create the required impedance conditions, thus tuning the acoustics.

In the above examples, the tunable acoustics is achieved either with geometry or boundary condition modification. One more example of controlled acoustics is through having flow choking plates in two inlet plenums of the combustor chamber [13], which will be shown in the next section, as it also forms the basis for validation of our numerical setup. However, it is observed that details on a systematic design of these arrangements to obtain the controlled acoustics are missing in available literature, on which an initial attempt is made in present work utilizing studies on the chamber acoustics.

2 Numerical Setup and Validation

In present project, three-dimensional finite-element-based COMSOL software is used for analyzing the chamber acoustics of the test rig, after validation with chamber acoustic results from a similar rig from literature [13]. Incorporation of the mean flow effects on the standing acoustic wave pattern was achieved by coupling the compressible flow solver (for mean flow) module with the linearized oscillating potential flow (for acoustics) module in COMSOL [14]. This is required to have an impact of mean background flow on the chamber acoustics, as a similar situation exists in industrial combustion chamber applications. To achieve this coupling, the acoustic pressure is solved with velocity as the principal variable. This helps in having all governing equations (acoustic or mean flow) in terms of velocity itself, through which the mean flow and the acoustic field can be coupled [14].

Assuming the flow to be irrotational, the velocity potential field, Φ, can be defined such that $\boldsymbol{V} = \nabla\Phi$, where $\boldsymbol{V}$ is the mean velocity field. This can be used for solving the mean flow velocity field in the domain with conditions like mass or velocity inlet and flow outlet. This is referred to as the Compressible Potential Flow (CPF) module in COMSOL. Compressibility effects are inherent by use of an equation of state for an ideal gas (assuming the flow is isentropic) is then included to close the system of equations [15].

With the mean flow field calculated, the oscillating acoustic velocity field is solved using the Linearized Potential Flow (LPF) module equations in COMSOL. Here again, the acoustic potential, ϕ, is related to the acoustic particle velocity (v) by $\boldsymbol{V} = \nabla\phi$. For deriving the LPF equation, equations for conservation of mass, momentum and state for an ideal gas (assuming the fluctuations to be isentropic) are combined. The equation is then decomposed into time-independent and acoustic components, and linearized about the mean flow (neglecting nonlinear terms). The second order

wave equation, thus achieved, can be written as

$$\frac{\rho}{c^2} i\omega(i\omega\phi + V.V\phi) + \nabla.\left[\rho\nabla\phi - \frac{\rho}{c^2}(i\omega\phi + V.V\phi)V\right] = 0$$

which is commonly referred to as the Helmholtz equation (expressed here in frequency domain in terms of the acoustic velocity potential ϕ). The term capital V, is the background mean flow velocity field which is obtained by solving the CPF module. The LPF equation can be solved, subject to appropriate boundary conditions, to obtain the acoustic potential. Once the acoustic potential is known, the acoustic pressure can be found as

$$P = -\rho(i\omega\varnothing + V.\nabla\varnothing)$$

With proper selection of the acoustic boundary conditions, and domain conditions such as variation of temperature in combustion chamber (affecting speed of sound and fluid density), frequencies and the acoustic mode shapes can be predicted by solving the CPF and LPF equations in tandem.

For validation, we are taking case study of the burner in [13] with combustion chamber and the air and fuel supplies as shown in Fig. 2a. It consists of two plenums to supply air to two flow swirlers, through which the fuel-air mixture is issued to stabilize the counter-rotating swirl flame. The two plenum inlets have orifice plates which help in maintaining sonic flow or choking conditions. Since flow velocity cannot fluctuate at the choking boundary, it is acoustically treated as a sound hard wall and the same is applied in the COMSOL simulations in present study. At the downstream exit of the combustion chamber, a perfectly matched layer is applied. For

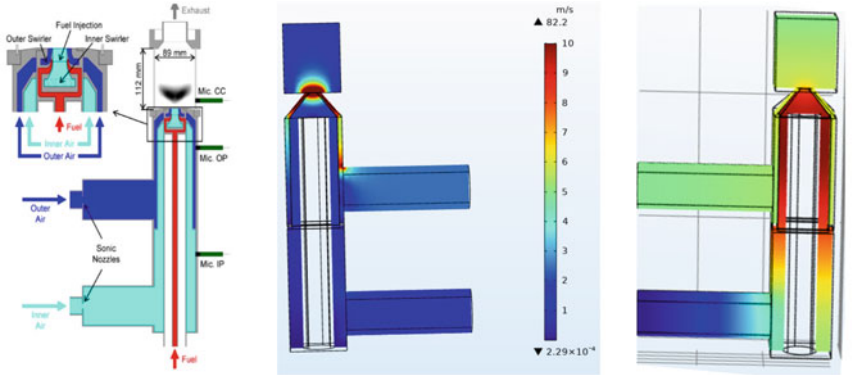

a) b) c)

Fig. 2 Contours from present simulations for the validation case, **a** Test rig for combustion chamber acoustics validation [13], **b** CPF solution in terms of mean flow velocity, **c** LPF solution in terms of the acoustic pressure mode shape at resonant frequency near 392 Hz

Table 1 Comparison of eigenfrequency (Hz) obtained from COMSOL simulations of the validation case, with varying modelling assumptions

COMSOL simulation without domain temperature variation	COMSOL simulation with domain temperature variation	COMSOL simulation with domain temperature and mean background flow
92	91	110
119	118	140
383	389	392
521	519	530
566	565	910
886	895	1050

the mean flow CPF module, mass flow inlet is applied at the plenum inlet boundary and flow outlet is used at the downstream combustion exit.

The CPF module is solved first to provide input of mean flow velocity to the LPF (or acoustics) module, which is solved with a frequency sweep with constant acoustic forcing. A sinusoidally oscillating velocity forcing of 1 m/s was applied at the sonic nozzle from where the outer air is supplied. Sensitivity studies to various modelling assumptions were carried out as: (1) simple chamber acoustics without any effect of domain temperature variation or mean flow, (2) chamber acoustics with domain temperature variation (having effect on the speed of sound and fluid density) but no mean flow and (3) chamber acoustics with domain temperature variation as well as the mean background flow effect. Resonant frequencies are captured using acoustic pressure probes at multiple points in the domain and their values for these cases are listed in Table 1. The experimentally observed frequency peak in power spectrum of acoustic signal is near 392 Hz [13]. It is observed that with the addition of temperature profile, the frequency range goes closer to the experimental value (from ~383 Hz to ~389 Hz). Also, with the addition of background flow, the simulated frequency is almost completely matching with the experimental value (~392 Hz). Hence, it could be concluded that by including more details of physics in the modelling, the acoustic frequency predictions are getting better. Contours of mean flow velocity and acoustic pressure from the simulation are shown in Fig. 2b and c respectively.

It could also be observed that even the sensitivity to the modelling refinements is also not that strong, probably due to low flow velocity (~82 m/s) compared to sound speed. In such case, one might even consider simulating the phenomenon with simple pressure acoustics without any background flow coupling. This might help while dealing with complex geometries leading to large computational mesh. However, in present work, the effect of background flow is incorporated for better accuracy as well as considering scenario where small passage dimensions could arise while trying various dimensions in the conceptual rig design. Such locations could lead to flow acceleration leading to flow choking conditions due to compressible flow effects. In such a case, the background flow would have substantial impact on the chamber acoustics and hence should be included.

3 Design of Tunable Acoustic Test Rig

In this section, a preliminary design of overall rig dimensions is described. This design will eventually be analyzed to understand its natural-resonant frequencies using the method developed in previous section and targeted to achieve tunable acoustics. Also, the overall pressure drop in flow through the rig, with various modifications of the geometry of the test rig is evaluated. Schematic of the proposed combustion test rig is shown in Fig. 3. The rig consists of inlet plenum, diffuser, honeycomb and screen, mixing section, combustor and the exhaust section. Basic dimensions of different components of test rig as were selected based on literature, available tank capacity to provide continuous flow for at least 1-min duration from an available pressurized air tank of 1000 L capacity at 22 bars. Calculations target to achieve flow velocities of ~30 m/s in primary combustion zone, which are typical in stationary gas turbine combustors [16]. Then the pressure drop in the rig was calculated based on pressure loss coefficients of different components from the literature [17].

Preliminary dimensions of the diffuser, honeycomb, plenum and screen parameters and other dimensions thus calculated are as below:

Cone angle of diffuser—10 degree [18], L/D ratio for honeycomb—6 to 8 [18], Wire diameter of screen mesh—0.254mm [19]. The diameter of inlet plenum used is 2-inch, L/D ratio for mixing section and combustor—4 and 10, respectively. Primary combustion zone cross-section = 10×10 cm^2. Exhaust cross-section = 7×7 cm^2, mixing section is circular with 4 cm diameter and settling chamber cross-section = 10×10 cm^2.

The pressure drop across different sections is calculated using the above dimensions and the pressure loss coefficients from literature. In the first calculation iteration, the density is assumed constant at all stations and in further iterations it is varied based on updated pressure from the previous iteration. This helps to incorporate the effect of fluid compressibility in the pressure drop calculation. This procedure was repeated until the static pressure values were converged at different stations. The final values of static pressure at different stations (components) of the rig are shown

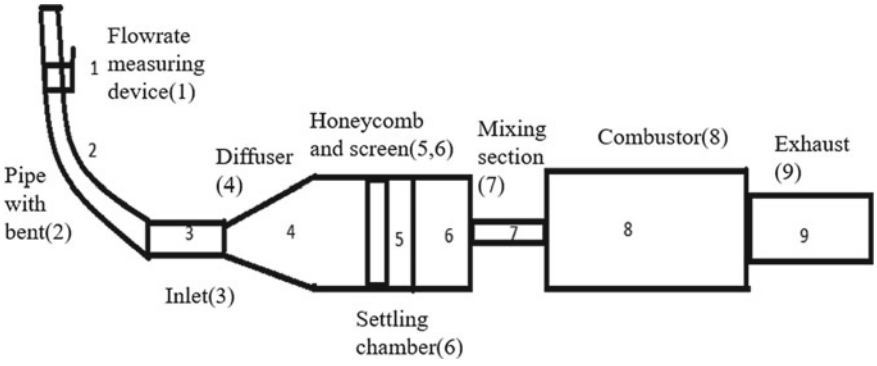

Fig. 3 Outline of the proposed combustion test rig

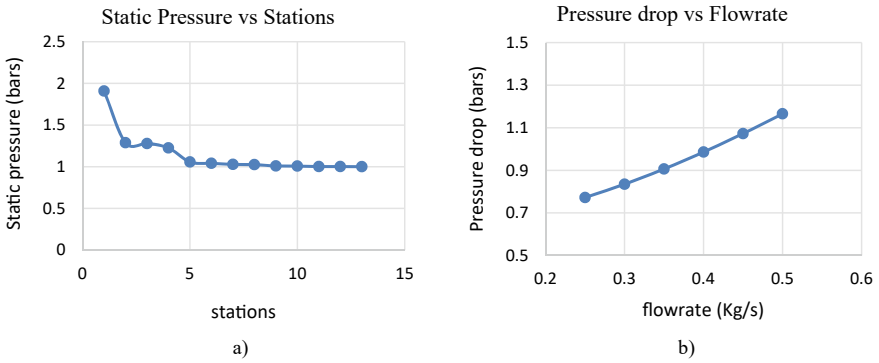

Fig. 4 Graph of **a** static pressure versus different stations(components) in the rig, **b** pressure drop versus flow rate

in Fig. 4a. It is observed that overall pressure drop with current arrangements remain below 1 bar and could be easily supplied by a compressed air tank having pressure of 22 bars. For higher flow rates, the increase in pressure drop is shown in Fig. 4b and is still within acceptable limits.

4 Acoustic Analysis of the Proposed Test Rig

It is targeted that the rig has to replicate the acoustic behaviour of the real scale combustor used in land-based gas turbines, where the typical combustion dynamics frequencies are observed in range of 30–400 Hz for the longitudinal modes. The test rig should be capable of having tunable acoustics, or continuously varying the natural chamber frequency in this range. Modelling details of the preliminary test rig in COMSOL are shown in Fig. 5 in terms of the geometry, boundary conditions, and domain conditions, and the computational mesh is shown in Fig. 6. A step-wise increasing temperature profile was assumed at different sections of the geometry to simulate the effect on material properties due to combustion-related temperature increase. The effect of mean flow was modelled to have better accuracy. As described, mean flow velocity assessment is also important to know and avoid potentially flow-choking conditions at different rig sections. Sample results from the CPF module for

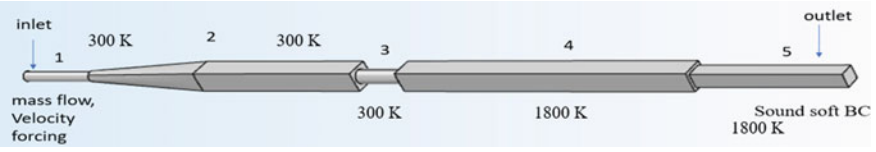

Fig. 5 Experimental test rig with boundary and domain conditions

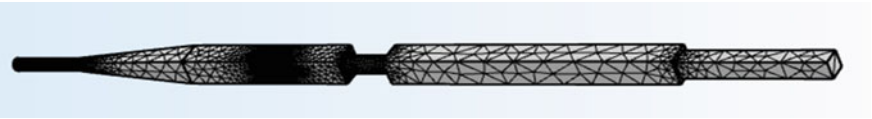

Fig. 6 Meshing in COMSOL

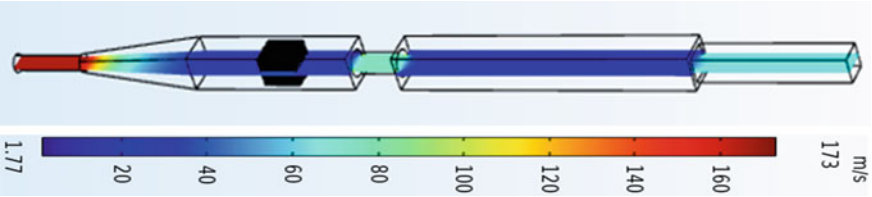

Fig. 7 Velocity variation in the rig

the mean flow velocity are shown in Fig. 7 and the acoustic mode shapes from the LPF module (with background flow from the CPF module) are shown in Fig. 8.

5 Variation In Test Rig Geometry To Achieve Tunable Acoustics

To achieve the target of tunable acoustics and get the different frequency range of chamber acoustics, changes in geometry were made and modelling of chamber acoustics was done to assess the frequency variations. Some of these are variation in combustion chamber length, reduction in the exhaust area and change in mixing section diameter.

5.1 Variation of the Geometry Length

The baseline rig geometry derived from calculations in previous sections with exhaust section length of 0.5 m. In first geometry variations, the length of exhaust section is increased by 1.5 m and then the length of the settling chamber is increased by 2 m just after the honeycomb section. Increase in length was targeted at capturing low acoustic frequencies. The results of the acoustic analysis in terms of resonant frequency for the baseline as well as geometry modification cases are shown in Table 2.

It is observed that as the length is increased for the exhaust section, the first mode frequency changes from 54 to 38 Hz. Also, when we increase the settling chamber length, we get the first mode frequency at 22 Hz. Hence, we can achieve all the

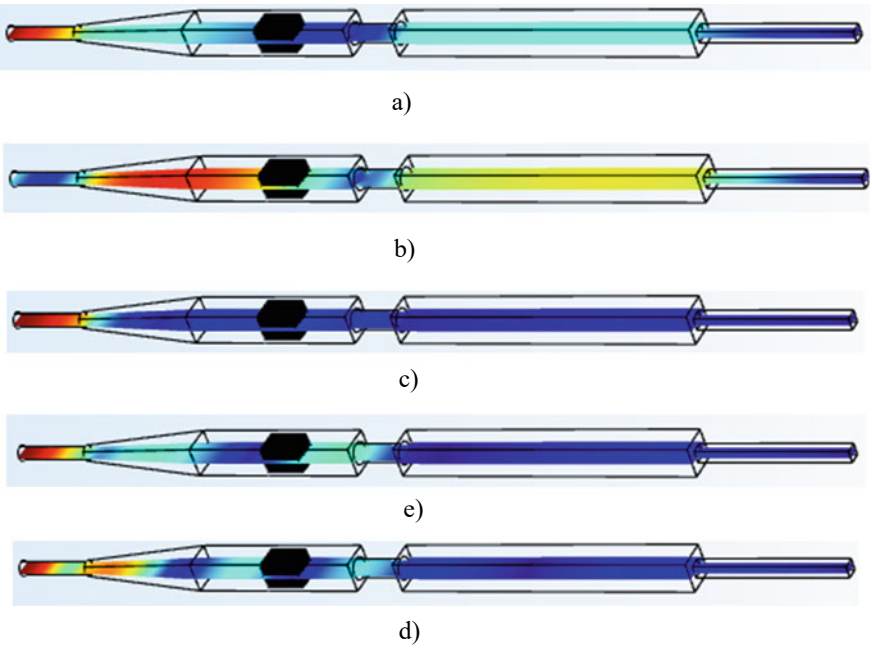

Fig. 8 Acoustic mode shapes (magnitude irrelevant due to no modelling of damping) with background flow for preliminary test rig configuration **a** 1st mode shape corresponding to the frequency of 86 Hz, **b** 2nd mode shape—102 Hz, **c** 3rd mode shape—170 Hz, **d** 4th mode shape—258 Hz, **e** 5th mode shape—378 Hz

Table 2 Comparison between resonant frequency (Hz) for the exhaust section of length 0.5m, 2m and of settling length increase of 2m

Exhaust length 0.5m	54	122	170	258	378	434	518
Exhaust length 2m	38	86	166	256	366	386	478
Settling chamber length 2m	22	70	110	138	170	206	258

intermediate frequencies by having an intermediate length of the exhaust section or settling. Furthermore, the higher modes frequencies also vary with the length variation to achieve the desired frequency range.

However, to cover more frequency range we need to alter the length by larger magnitude, which is limited due to space constraints. Hence, other methods are explored on geometry variation to achieve the complete target frequency range of 30 to 500 Hz.

Table 3 Comparison of frequencies with different geometry variations

Case 1 (Hz)	Case 2 (Hz)	Case 3 (Hz)	Case 4 (Hz)	Case 5 (Hz)
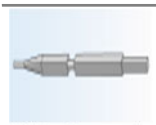 Original rig (exhaust section 0.5m x 0.5m)	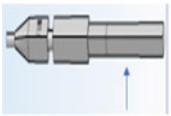 Exhaust length =2m	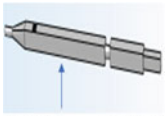 Settling chamber length increased by 2m	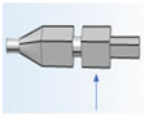 Combustion section length reduced to 0.5m	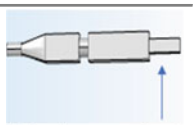 Exhaust area reduced to half of combustor area
54	38	22	46	42
122	86	70	134	102
170	166	110	178	170
258	258	138	266	258
378	386	170	382	378
434	478	206	514	434

5.2 *Variation of the Exhaust Cross-Section*

In the next geometry variation, the exhaust cross-section is reduced to 4 cm x 4 cm which is lower than half of the combustor area. This is done basically to explore presence of the Helmholtz resonance mode. The Helmholtz mode is different from the standing longitudinal wave as it a global resonance and not along any specific direction. This makes it useful to capture entirely different range of frequencies. Along with exhaust cross-section area variation, there were other geometric variations done, which are compiled in Table 3 along with the frequencies obtained from the analysis.

It was observed that the exhaust area variation is also having impact on the acoustic resonance frequencies. This provides one more way of obtaining the desired frequency range by geometry variation. However, with the present range of exhaust area reduction, the Helmholtz mode was not captured.

5.3 *Variation in the Mixing Section Diameter*

When the diameter of the mixing section is changed or reduced, we could see the longitudinal wave in upstream section and in the downstream section separately. This is because with the area reduction, mean flow velocity will increase and can approach the flow choking conditions, which would mean a sound hard acoustic boundary condition at the location. Due to this, we can have the upstream and downstream resonances separated and can make the changes in individual section, as needed. Mostly we will prefer changing the geometry in the upstream side rather than in the downstream side because the high temperature gases in the downstream side will

make hardware variations somewhat difficult. For modelling acoustics, both the CPF and LPF flow modules are solved together in COMSOL and other model settings also remain same as described earlier. The mode shapes of the rig with different diameter such as 5, 6, 7 and 8 cm of mixing sections are compared in Figs. 9 and 10.

The resonant frequencies of different diameter such as 5, 6, 7 and 8 cm of mixing sections are compared. Although the mode shapes and resonant frequency are varying with different diameter of the mixing chamber there is no sharp change which could indicate a mode separation between the upstream and downstream side. The variations are more or less gradual, which is due to variation of acoustic impedance in the mixing chamber section as well as due to impact of higher velocity background flow at lower mixing chamber diameters.

It must be highlighted here that on reducing the mixing chamber diameter below 4 cm, there was no converged solution achieved from the software. This might be

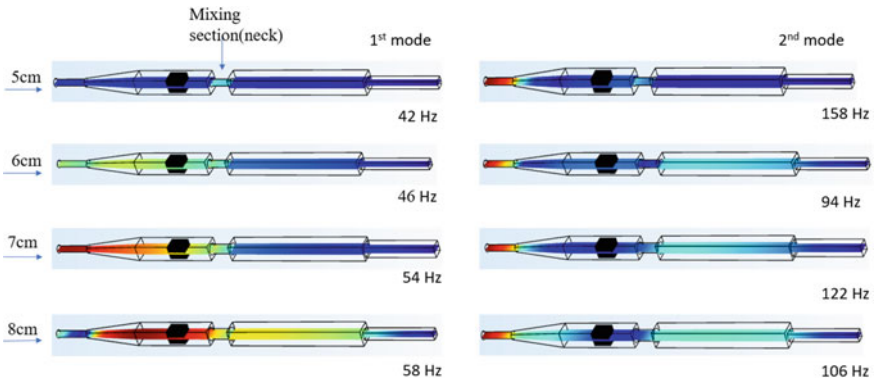

Fig. 9 Mode shape comparison for the diameter of mixing sections of 5, 6, 7 and 8 cm between 1st and 2nd mode

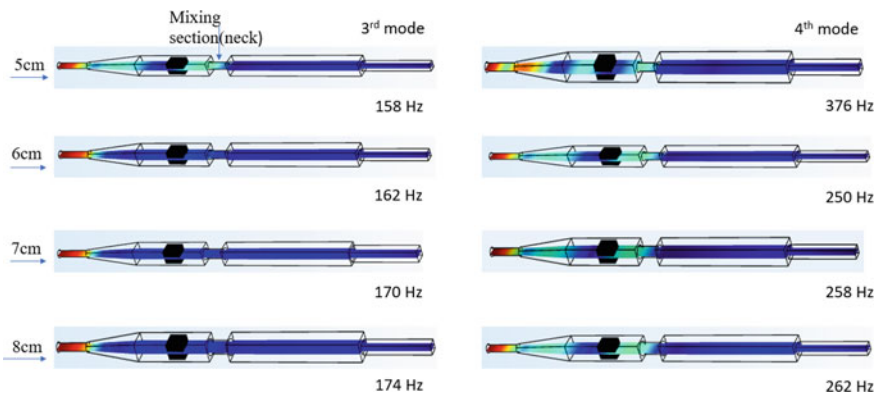

Fig.10 Mode shape comparison for the diameter of mixing sections of 5, 6, 7 and 8 cm between 3rd and 4th mode

indicative of a singularity where the flow conditions reach to the choking condition and there is an indeed a mode separation happening. However, from a practical perspective such high mean flow velocities in the mixing section are unrealistic and hence this geometry change was not further explored. Nevertheless, varying the mixing chamber cross-section still remains a potential option to vary chamber acoustics in some frequency range.

6 Conclusion

Present studies highlight key aspects of modelling method needed to capture the chamber acoustic physics with presence of mean background flow and temperature variation. Dimensions and pressure drop of different components of the test rig such as diffuser, plenum, flow conditioner and straightener, mixing and burner section, combustion chamber, transition and exhaust tube, etc., were calculated based on study requirements and literature. Then to achieve the purpose of having tunable acoustics, dimensions of various rig components were varied targeting the frequency range for a real scale combustor (~30–500 Hz). Results show that varying length of both upstream and downstream side as well as varying cross-section of the mixing and the exhaust section is effective in achieving the variation of the resonant acoustic frequencies. However, a Helmholtz mode behaviour and mode separation due to flow acceleration were not captured in simulations of the explored configurations. Further detailed studies would be needed to make the rig compact and get simple arrangements to achieve the tunable acoustics over the entire frequency range of interest.

References

1. Kim G, Lee YD, Sohn CH, Choi KW, Kim HS (2015) Experimental investigation on combustion and emission characteristics of a premixed flame in a gas-turbine combustor with a vortex generator. Appl Therm Eng 77:57–64
2. Lieuwen T, Chang M, Amato A (2013) Stationary gas turbine combustion: Technology needs and policy considerations. Combust Flame 160(8):1311–1314
3. Lieuwen TC, Yang V (2006) Combustion instabilities in gas turbine engines. Combust Instab Gas Turbine Engines
4. Zhao D, Li XY (2015) A review of acoustic dampers applied to combustion chambers in aerospace industry. Prog Aerosp Sci 74:114–130
5. Lieuwen T (2014) Unsteady combustor processes
6. Bothien MR (2008) Impedance tuning : a method for active control of the acoustic boundary conditions of combustion test rigs
7. Tran N (2009) Influence of inlet acoustic boundary condition on large amplitude combustion instabilities : design of a robust impedance control system. Thesis
8. Richards GA, Gemmen RS, Yip MJ (1996) A test device for premixed gas turbine combustion oscillations technical note 1027(304):1–24

9. Knadler M, Caley T, Lee JG, Jung S, Kim S, Park H (2018) Validation of a physics-based low-order thermo-acoustic model of combustion driven oscillations in a liquid fueled gas turbine combustor. Proc ASME Turbo Expo 4A
10. Terhaar S, Moeck JP, Paschereit CO, Bernhard C (2015) Response of a swirl-stabilized flame to simultaneous perturbations in equivalence ratio and velocity at high oscillation amplitudes 162:.1046–1062
11. Kim MK, Yoon J, Oh J, Lee J, Yoon Y (2013) An experimental study of fueleair mixing section on unstable combustion in a dump combustor. Appl Therm Eng 61(2):662–670
12. Paschereit CO, Gutmark E, Weisenstein W (1998) Structure and control of thermoacoustic instabilities in a gas-turbine combustor. Combust Sci Technol 138(1–6):213–232
13. Arndt CM, Severin M, Dem C, Stöhr M, Steinberg AM, Meier W (2015) Experimental analysis of thermo-acoustic instabilities in a generic gas turbine combustor by phase-correlated PIV, chemiluminescence, and laser Raman scattering measurements. Exp Fluids 56(4):1–23
14. Introduction I (2018) Developed with COMSOL multiphysics
15. Rienstra SW, Hirschberg A (1952) An introduction to acoustics. Phys Today 5(11):24
16. COMSOL (2014) Introduction to the acoustics module. Manual
17. Kharagpur (2013) System measurement:1–15
18. Kudela H (2010) Hydraulic losses in pipes 3:1–9
19. Cattafesta L, Bahr C, Mathew J (2010) Fundamentals of wind-tunnel design. Encycl Aerosp Eng
20. Farell C, Youssef S (1996) Experiments on turbulence management using screens and honeycombs. J Fluids Eng Trans ASME 118(1):26–62

Development of a Numerical Tool for Studying Turbulent Fuel–air Mixing in Swirl-Based Gas Turbine Combustion Chambers

Rahul Pandey and Krishnakant Agrawal

1 Introduction

Use of fossil fuel combustion-based devices is likely to continue in a foreseeable future due to the ever-growing energy needs of the human society. Even with growing share of renewables among power sources [1], the ever-increasing power demand particularly from developing countries with improving living standards, overall nullifies this benefit. For a foreseeable future, steady demand in combustion-based devices for power generation such as Gas Turbines is envisaged [2]. Combined Cycle Gas Turbines are one of the most-efficient, clean, compact, reliable, and readily available technology for large scale power generation. However, they are subjected to stringent pollution regulations due to their large capacity and target markets. Hence, research efforts are still ongoing to have ultra-low emissions of NO_X, CO, particulate matter, unburned hydrocarbons, and greenhouse gases [2–6]. Lean premixed combustion is one of the most promising and cost-effective strategy to achieve these targets. However, a major challenge is to achieve complete premixing of fuel and air in the limited space and time in the combustor, due to high mass flow throughput in industrial devices. Effective design of flow field and use of turbulence creating devices is taken to meet this target [4, 5]. The swirling flow strategy is one of the promising technologies to meet requirements of good mixing and flame stabilization in lean-premixed combustion [5]. Swirling flow induces radial pressure gradients, which help in creation of the recirculation zones in the expansion region in primary combustion zone, which helps to stabilize the combustion process. It helps in improved mixing due to the longer flow travel path and enhanced shear and turbulence.

R. Pandey (✉) · K. Agrawal
Department of Mechanical Engineering, Indian Institute of Technology Delhi, New Delhi, India

K. Agrawal
e-mail: kkant@iitd.ac.in

D. K. Maiti et al. (eds.), *Recent Advances in Computational and Experimental Mechanics, Vol II*, Lecture Notes in Mechanical Engineering,
https://doi.org/10.1007/978-981-16-6490-8_17

While there are some studies on modelling of bulk-flow features in turbulent swirling flows using Computational Fluid Dynamics (CFD), studies dedicated to studying mixing of different streams (fuel and air in present case) in such flows are scarce. Eiamsa-ard et al. [7] simulated swirling flow induced by means of a loose-fit twisted tape in a circular tube and associated heat transfer with five Reynolds Average Navier Stokes (RANS) turbulence models. These were Standard k-ε, Re-normalized (RNG) k-ε, Realizable k-ε, Standard k-ω and SST k-ω, where that last one was found to be in better agreement with experimental results in terms of bulk-flow velocity profile. Engdar et al. [8] did a numerical study on a swirl stabilized burner and found that for swirl number 0.58, the k-ω model captures inner recirculation zone (IRZ) better than the standard k-ε model. In a similar case [9], mixed results were obtained using standard k-ε model for simple turbulent flows and swirling reacting flows as well. In general, standard k-ε model predicts high level of turbulence diffusivity in a swirling flow. This overestimation is due to use of isotropic eddy viscosity assumption with all such two-equation turbulence models, as swirling flows are generally anisotropic [10]. A lot of investigations [7–12] have clearly demonstrated superiority of anisotropic turbulence modelling methods such as Reynolds Stress Models (RSM) for swirling flows. Yılmaz [11] studied the effect of swirl number on combustion characteristics such as IRZ etc. in a natural gas diffusion flame with best predictions with RSM turbulence model compared to two-equation models. Escue [12] found RNG k-ε model better for low swirl cases and RSM model better for higher swirl cases. Shih [13] presented a study on rotating pipe flow and swirling flow with recirculation and found nonlinear cubic RSM to be a better than the standard k-ε model. Jakirlic [14] for various Reynolds Number and rotation rates or swirl numbers, also found RSM to better predict the experimental results compared to the standard k-ε model. Najafi [15] found RSM predictions realistic when modelling turbulent swirl decay rate. Although RSM proves its superiority in highly anisotropic flows such as with swirl, it is computationally expensive due to involvement of equations for six stress components. It is more desirable to achieve a two-equation turbulence model for having computationally affordable simulations for industrial design studies. In present work, various two-equation and RSM models are evaluated for prediction of fuel–air mixing in swirling flow for a gas turbine model burner.

2 Validation Case and Experimental Data

Galley et al. [16] presented experimental studies on a 300 kW swirl stabilized lean-premixed laboratory scale burner (Fig. 1) to study effect of the fuel–air un-mixedness on flame-stabilization and flashback potential. The swirler is a radial type of swirl generator which is having 18 rectangular-shaped radial air inlets inclined at an average swirl angle 35.3º to the normal radial direction, which eventually produced a flow swirl number of 1.1. The fuel used was propane (C_3H_8) which was injected axially into the mixing tube from a concentric smaller tube of 6 mm diameter. Such central fuel injection leads to gradual mixing evolution with distance. Short distance

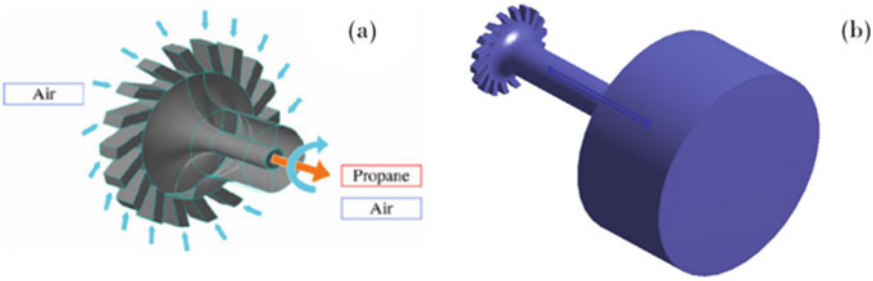

Fig. 1. **a** Swirling flow burner design [17] with air and propane inlets shown and **b** Numerical computational domain of the present study

is not enough for complete mixing when fuel is injected axially because radial pressure gradient traps the fuel in the core of the vortex as air has the natural tendency to flow towards low-pressure zones [17]. This was done intentionally to control un-mixedness or partial premixing and investigate its effects on flame stabilization. There was a relatively long cylindrical mixing tube of length 100 mm and diameter 25 mm with optical access, followed by a combustion chamber of 300 mm length and 150 mm diameter after fuel injection plane as shown in Fig. 2. The mixing field was visualized by measuring concentration of acetone gas seeded in the fuel, through Planar Laser-Induced Fluorescence (PLIF) technique. It provides detailed spatial and temporal data of the mixing field before combustion, which is very useful for validating the numerical models used in the present study. One sample image showing instantaneous acetone contours in midplane of mixing tube [16] is shown in Fig. 3. Such detailed spatio-temporal data on the mixing field is one of the main reasons why this case was chosen for validation purposes. In most of other studies, combustion is immediate after swirler and usually there is no detailed measurement of the fuel–air mixing profile.

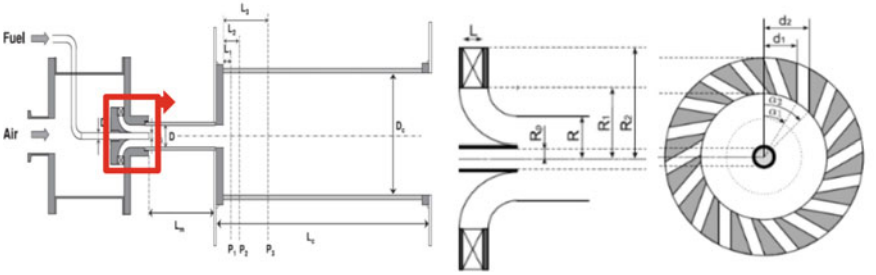

(a) Side view of the entire geometry; (b) Air inlet enlarged (c) Section A-A

Fig. 2. The burner dimensions are as follows: **a** L = 6 mm, Lm = 100 mm, Di = 6 mm, D = 25 mm, De = 8 mm, LC = 300 mm, DC = 150 mm, De = 8 mm. **b** R1 = 22.5 mm, R2 = 32.5 mm, Rp = 3 mm, R = 12.5 mm. **c** d1 = 11 mm, d2 = 15 mm, α1 = 29.27°, and α 2 = 41.81°

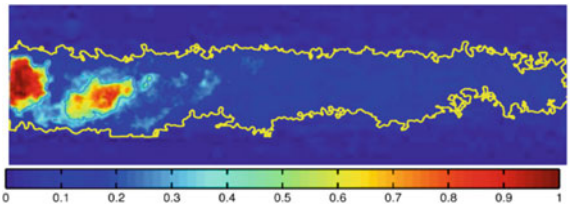

Fig. 3. Sample instantaneous acetone contour of fuel mass fraction in midplane of mixing tube obtained by PLIF technique [14]

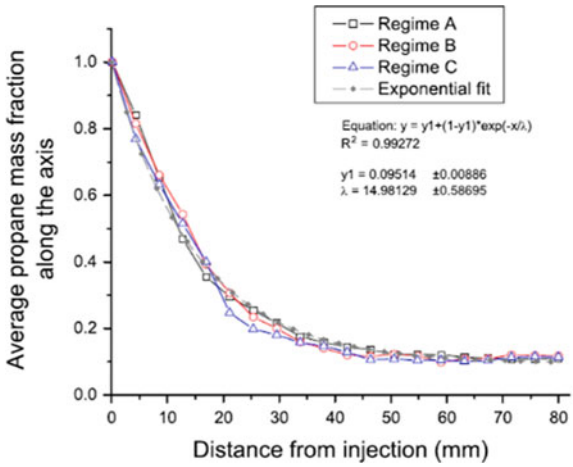

Fig. 4 Measured fuel concentration along the centerline of the mixing tube [17]

Three different regimes were discussed experimentally to study flame flashback and flame stability. Mixing profile for regime 1 is presented in Fig. 4 for which air mass flow rate was 40 g/s and fuel mass flow rate was 1.93 g/s were fixed. These are time-averaged values of fuel concentration, which decays exponentially along the axis which is shown in Fig. 4. These plots are used for validating the simulation results in the present study.

3 Numerical Setup and Simulation

A numerical model is created in ANSYS Workbench 19.2 [18]. As the purpose of this study is to characterize the flow field and not to study the flame behavior, the length of the combustion chamber is reduced in the model to reduce the mesh count hence saving computational time and resources.

3.1 Governing Equations and Boundary Conditions

The Reynolds Averaged Navier Stokes (RANS) have been used in the present study for turbulent flow modelling, which for the SST k-ω turbulence model are as follows:

Continuity Equation [18]:

$$\frac{\partial}{\partial_i}(\rho u_i) = 0 \tag{1}$$

Momentum Equation [18]:

$$\frac{\partial}{\partial x_j}\left(\rho u_i u_j\right) = -\frac{\partial p}{\partial x_i} + \frac{\partial}{\partial x_j}\left[\mu\left(\frac{\partial u_i}{\partial x_j} + \frac{\partial u_j}{\partial x_i} - \frac{2}{3}\delta_{lj}\frac{\partial u_l}{\partial x_l}\right)\right] + \frac{\partial}{\partial x_j}\left(-\rho\overline{u_i' u u_j'}\right) \tag{2}$$

The turbulent kinetic energy equation: and specific dissipation for k-ω model can be obtained from the following governing transport equations [18]:

$$\frac{\partial}{\partial t}(\rho k) + \frac{\partial}{\partial X_i}(\rho k u_i) = \frac{\partial}{\partial x_j}\left(\Gamma_k \frac{\partial k}{\partial x_j}\right) + G_k - Y_k + S_k \tag{3}$$

$$\frac{\partial}{\partial t}(\rho \omega) + \frac{\partial}{\partial X_i}(\rho \omega u_i) = \frac{\partial}{\partial x_j}\left(\Gamma_\omega \frac{\partial \omega}{\partial x_j}\right) + G_\omega - Y_\omega + S_\omega \tag{4}$$

Computational Fluid Dynamics (CFD) is a numerical technique that can determine the fluid flow and heat transfer in a fluid domain by discretizing the domain and solving a few partial differential equations that govern the fluid flow and energy transfer. For a simple non-turbulent flow without heat transfer, a mass conservation equation (Eq. 1 ρ—density, u_i—velocity component) and three momentum conservation Eq. (2) known as the Navier Stokes equations are required to be solved. The commercially available software package FLUENT from ANSYS is used for all the simulations in the present project. Since flow is turbulent, a turbulence model is required. A Reynolds Average Navier Stokes approach has been used and standard two-equation k-ω turbulence model equations for modelling turbulence are presented (Eqs. 3 and 4). It solves Reynolds transport equations for the turbulent kinetic energy—k and its specific dissipation—ω with source and sink terms as explained further. In above equations, Gk represents the turbulence kinetic energy generation because of mean velocity gradients. Γ_k and Γ_ω represent the effective diffusivity of k and ω respectively and Gω represents the generation of ω and Yk and Y ω represent the dissipation of k and ω due to turbulence.

As the key parameter of investigation is the fuel–air mixing profile, hence species transport equation for fuel and air species are needed. A general species transport equation for ith specie is presented in Eq. 5. Modelling species diffusion accurately is important for capturing the fuel–air mixing profile, for which the diffusion flux of species (Ji) is detailed in Eq. 6. Since the case is isothermal, there is negligible effect expected due to the thermal gradient-driven diffusion term in Eq. 6.

The conservation equation for ith specie takes the following general form, Yi being the local mass fraction of each species [18]:

$$\frac{\partial}{\partial t}(\rho Y_i) + \frac{\partial}{\partial X_i}(\rho v Y_i) = -\frac{\partial}{\partial x_i}(J_i) + R_i + S_i \tag{5}$$

Where Ri and Si are the net rate of production and destruction of the species which are zero in present non-reacting flow and Ji is the mass diffusion term in turbulent flow given by the following relation [18]

$$J_i = -\left(\rho D_{i,m} + \frac{\mu_t}{Sc_t}\right)\frac{\partial}{\partial x_i}Y_i - \frac{D_{t,i}}{T}\nabla T \tag{6}$$

Since the case is isothermal, there is negligible effect expected due to the thermal gradient-driven diffusion term in Eq. 6.

Boundary Conditions and Fluid Properties:

The air mass flow rate was set as 40/18 g/s in the sector model (as it is 40 g/s in the full 360º model) and propane mass flow rate was set as 1.93/18 g/s (1.93 g/s in the full 360º model). The direction of the flow at all inlets was set as perpendicular to the inlet boundary. Turbulence was specified using turbulent intensity of 5% being the borderline of simple flows (like pipe flow) and complex flows (like turbine and swirl flows) for all inlets and 'hydraulic diameter' calculated according to the dimensions of the inlet, which was 4.8 mm for air inlet, 6 mm for fuel inlet and 150 mm for the outlet. The outlet condition was set as 'pressure outlet' with absolute static pressure set as 1 bar and zero guage pressure. The walls were set as stationary with no slip condition and standard wall roughness. It is assumed that there is no combustion in the mixing tube or before mixing tube hence all walls were considered as adiabatic. The calculation of density was done using the incompressible ideal gas law and the specific heat was calculated using the mixing law.

3.2 Solution Method and Convergence

Steady state pressure-based solver was used to solve the governing equations using the 'Semi Implicit Method for Pressure Linked Equations' (or SIMPLE) algorithm for pressure–velocity coupling. Combination of first and second order schemes for discretization were used to achieve satisfactory convergence of the solution, while underrelaxation parameters were found to be of not much use. There are various surface and point monitors created in the domain on which the values of fuel mass fraction and velocity magnitude (Fig. 5) were monitored with solution iteration progress to assess the solution convergence. Along with this, the solution residuals were also monitored and found to be much below order of 10^{-3} for all solution variables for a converged solution.

3.3 Domain Reduction Strategy

Initially, a full geometry model having 18 swirlers was created for validation, where the total number of cells were 36 lacs. This resulted in significant computational time

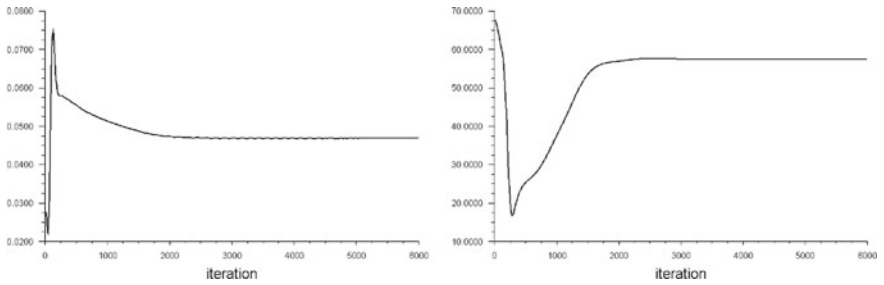

Fig. 5 Vertex average of fuel mass fraction (left) and vertex average of velocity magnitude (right)

requirement and average duration of one week for a single simulation with available resources.

To overcome this problem, the number of cells was required to be reduced without compromising the mesh refinement at critical locations such as the fuel-air mixing region (presented later).

A series of iterations were performed to obtain correct method of extracting the sector model to reduce the domain and hence the computation time and resources. The model was cut by a V-Shaped sketch, a combination of V-Shaped and curve sketch, a combination of V-shaped and straight-line sketch and a completely curved geometry. First method provided distorted results because of two body creation. Second and third methods provided close results to experiments and fourth method provided overlapping results.

A 20º periodic sector model representing 1/18th part of the geometry with a single air inlet slot was used, which provided with 1.7 lacs cell count keeping with similar mesh refinement. Simulations were carried out both for the full domain and the sector model and the results showed that with appropriate choice of the segmentation method, the sector model is able to provide same prediction as the full model. It was observed that the cut method is always not trivial, and some of the seemingly simple cut methods can provide inaccurate predictions. Verification with the full model hence becomes important.

As shown in Fig. 6, when the geometry was cut in a straight V-shape sector, two material bodies were created due to inclination of the inlet air slot which is required to create the swirl. Simulation with this showed some unreasonable results in terms of reverse flow near the fuel injection tube as shown in second image in Fig. 6. This could be due to inaccurate prediction of the flow swirl when the periodicity is not captured accurately with such segmentation method. Then to avoid creation of two bodies, few methods of cutting were tried like cutting with curved lines (method #2) and using combination of sector and parallel inclined lines (method #3) and sector and diverging inclined lines (method #4) as shown in Fig. 6. Fuel-air mixing profiles (axial) with these methods (except method #1 which provided unrealistic flow) are shown in the same figure and compared with the full 360º model. It is observed that the sector method #4 provided closest agreement with the full model and hence it is chosen for all further studies.

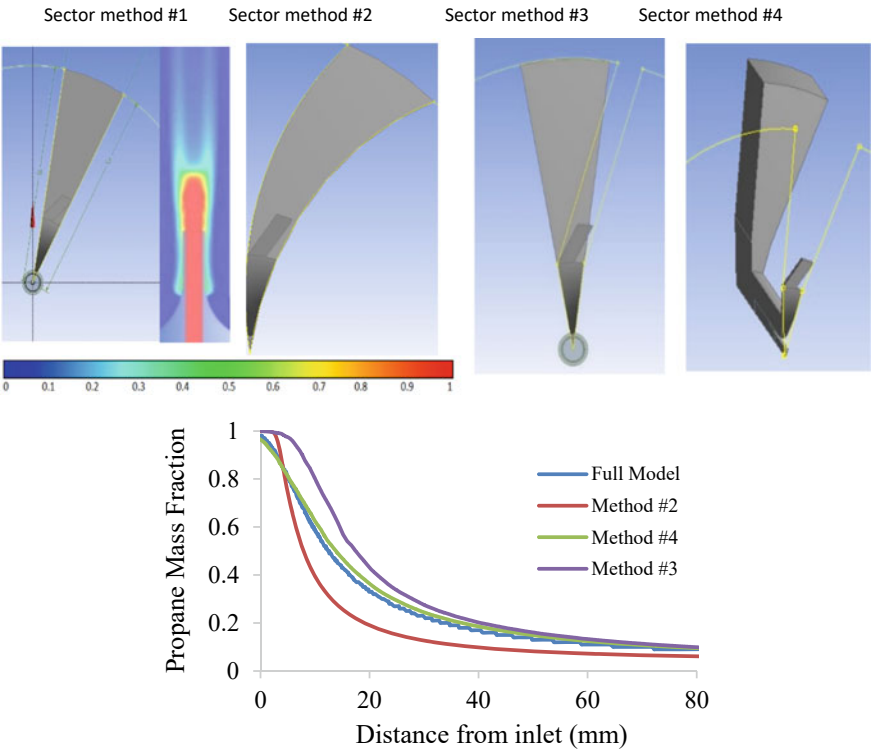

Fig. 6. Sector model creating strategies (top) and corresponding fuel mixing results (below); Axial fuel decay profile for three strategies of sector creation (middle); Comparison of axial fuel decay profile for sector model and full model at optimum refinement

3.4 Meshing

Meshing is shown from different views and at different locations in Fig. 7. Different sizes of elements were used at different locations according to need which is visible in the first image.

The most sensitive locations are the region where fuel and air interact with each other. These regions were meshed with fine elements while relatively coarser mesh was employed elsewhere to make the simulation computationally affordable. The second image shows the meshing at the rim area. This region was meshed carefully as the mixing starts from this location; hence it will have significant impact on mixing profile at all downstream locations. This was also observed in few initial cases with coarse mesh, the results for which are not included in this paper. In the final mesh, for the rim wall thickness of 1 mm, 8 to 9 mesh elements were used to ensure capturing the mixing behavior accurately. The air swirler zone is more like a diverging turning tube through air flows and enters the mixing tube. Although this section induces swirl effect to the incoming airflow, it is mostly a straight flow in a channel and does not

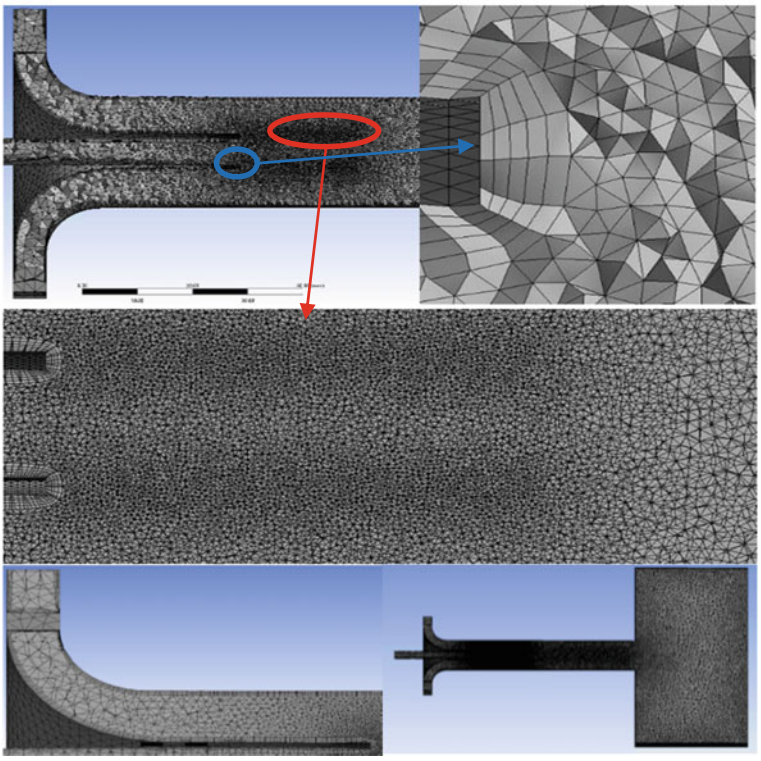

Fig. 7. Final mesh shown on the full scale 360º model showing the refinement at different sections created using body of influence method

involve mixing phenomena, hence does not need fine meshing. Width of this tube varies from 5 to 12 mm having 7 to 11 unstructured cells. The tetrahedral mesh is accompanied by inflation or prismatic cell mesh layers of 0.8 mm width having 5 layers on all walls of the domain to accurately capture the flow boundary layer.

3.5 Grid Independence Study

The grid independence study is performed to assess optimum level of grid refinement, going from course mesh with 37,200 cells and the most refined mesh with 783,000 cells. Intermediate refinement levels were 190,000 cells and 453,000 cells. As shown in Fig. 8, 190 k (k representing × 1000), 453 k and 783 k cell-count meshes produced almost same results, while the coarsest mesh having 37.2 k cells produced some deviation. As more than 190 k mesh cells produced similar profiles, it would be a waste of resources working on highly refined mesh cells hence, mesh refined with 190 k cells was accepted as the grid-independent refinement.

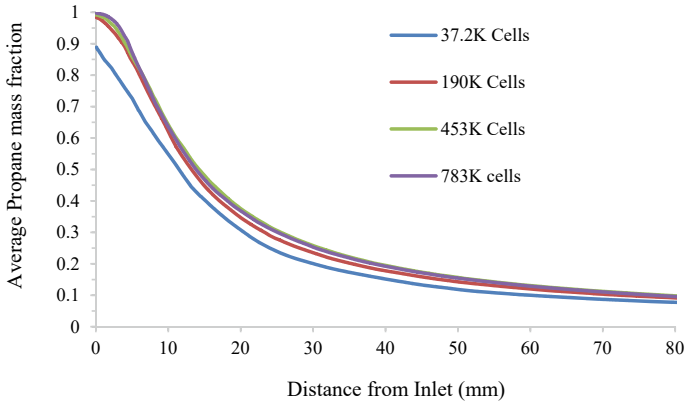

Fig. 8. Axial fuel fraction decay at various refinements

4 Model Validation Results and Discussion on Choice of the Turbulence Model

With appropriate strategies for domain reduction and meshing presented in previous section, simulations are carried out with various RANS-based turbulence models in the present section to find the most appropriate model for capturing the fuel-air mixing in swirling flows, as discussed in the introduction. Both the two-equation models such as k-ε, k-ω and their variants, as well as the Reynolds Stress Model (RSM) variants with detailed turbulent stress components modelling were assessed for the purpose.

The various turbulence models tried were namely the standard k-ε, Realizable k-ε, RNG k-ε, Standard k-ω, BSL k-ω, SST k-ω, RSM Linear Pressure Strain (LPS), RSM Stress-Omega and RSM Stress-BSL. Results with these models in the developed numerical setup, are shown in Fig. 9 in terms of centerline fuel mass fraction vs axial distance. This axial decay of fuel mass fraction is also available from the experimental results and is also plotted in the same graph for comparison. All turbulence models show exponential decay of fuel mass fraction along the length of the mixing tube, though some of them overestimate and some underestimate the centerline fuel concentration decay which is related to mixing process moving downstream. It can be observed that SST k-ω model as well as the RSM Stress Baseline (BSL) model have been able to reproduce the results well. This is also in some agreement with the literature discussed earlier, where the SST k-ω and RSM were observed to have good prediction capability for swirling flows. However, in present work they are now observed to work well for capturing the mixing behavior of different flow streams in swirling flow as well. A variation of k-ω model, which is the baseline (BSL) k-ω model also seem to be in close agreement with the experimental result, except for some deviation near the mixing tube inlet. However, the standard k-ε turbulence model and the standard k-ω turbulence model have grossly underpredicted the mixing

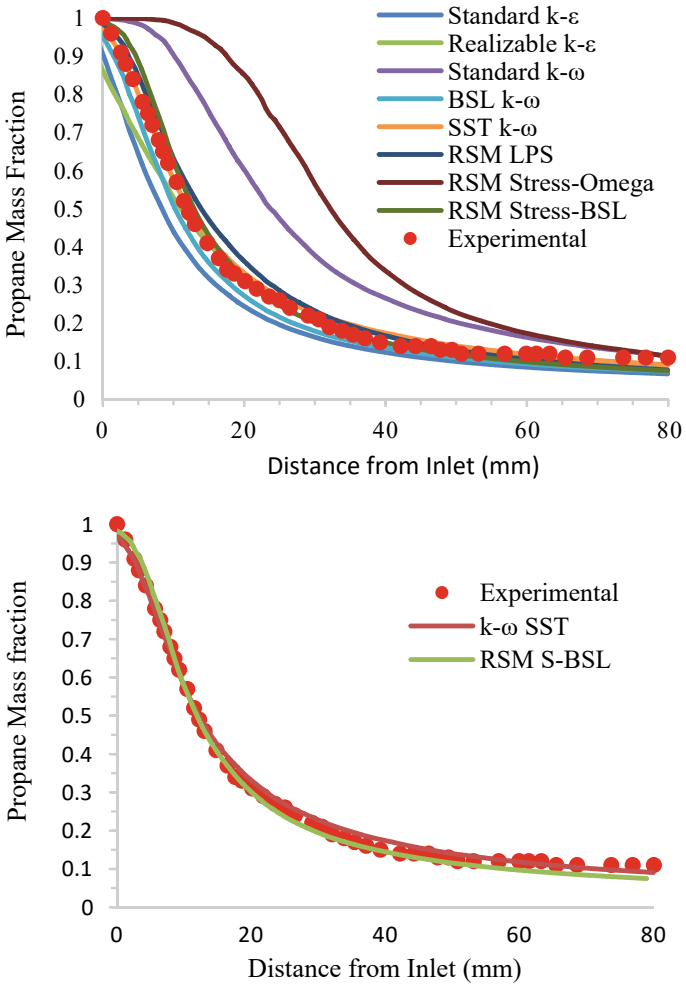

Fig. 9. Axial decay of fuel fraction for all RANS turbulence models

leading to very slow decay of the centerline fuel mass fraction. The two models, SST k-ω and RSM stress-BSL models which reproduced the experimental axial fuel mass fraction decay very accurately are also shown separately at bottom in same figure of Fig. 9 provide a closer view to assess level of accuracy obtained with the present numerical setup. Out of these two, the SST k-ω was chosen for further studies as it is a two-equation model, which means lower demand on computations resources, while giving similar level of accuracy to the more detailed RSM which models six components of the turbulent strain and hence requires more calculations.

5 Conclusion

In present work, strategies for simulating the fuel–air mixing phenomena in swirling flows in a computationally affordable as well as accurate manner are evaluated and presented. The experimental validation case chosen provides detailed data on the fuel–air mixing field in space and time for this purpose. The domain reduction strategy in terms of sector creation was found non-trivial for the flow with swirl, and a particular sector-cut strategy produced best agreement with the full 360º model. Optimum refinement of the computational mesh was also assessed through the grid-independence study, while highlighting the important mesh refinement regions for capturing the mixing accurately. Finally, many of the available RANS-based turbulence model in ANSYS, including two-equation turbulence models and Reynolds stress model variants were validated. Among these, the k-ω SST and RSM stress-BSL were the two models which reproduced the flow field in the mixing tube very close to the experimental data. Out of these the k-ω SST is recommended for further studies as it is a two-equation model and hence computationally more efficient than the RSM based models.

References

1. OCED Green growth studies: Energy preliminary version. 10.1.1.500.1397
2. AL-Halbouni A, Giese A, Tali E, Leicher J, Albus R, Gorner K (2017) Combustor concept for industrial gas turbines with single digit NOx and CO emission values
3. A Clean Techn Environ Policy (2015) Kemal AltinişikAli Keskin
4. Surjosatyo A, Ani FN (2011) Study of enhancing the swirl burner performance on a small-scale biomass gasification
5. Patel V, Shah R (2019) Effect of swirl and number of swirler vanes on combustion characteristics of methane inverse diffusion flame. J Mech Sci Technol 33:1947–1958. https://doi.org/10.1007/s12206-019-0345-7
6. Agbonzikilo FE, Owen I, Stewart J, Sadasivuni SK (2014) Experimental and numerical investigation of fuel–air mixing in a radial swirler slot of a dry low emission gas turbine combustor. https://doi.org/10.1115/1.4031735
7. Eiamsa-ard S, Wongcharee K, Sripattanapipat S (2009) 3-D Numerical simulation of swirling flow and convective heat transfer in a circular tube induced by means of loose-fit twisted tapes. Int Commun Heat Mass Transfer 36(9):947–955. ISSN 0735-1933, https://doi.org/10.1016/j.icheatmasstransfer.2009.06.014
8. Ulf E, Jens K (2002) Investigation of two-equation turbulence models applied to a confined axis-symmetric swirling flow. In: Proceedings of the ASME 2002 pressure vessels and piping conference. Computational technologies for fluid/thermal/structural/chemical systems with industrial applications, vol 2, Vancouver, BC, Canada, 5–9 Aug 2002, pp 199–206. ASME. https://doi.org/10.1115/PVP2002-1590
9. Datta A, Som SK (1999) Combustion and emission characteristics in a gas turbine combustor at different pressure and swirl conditions. Appl Therm Eng 19:949–967. https://doi.org/10.1016/S1359-4311(98)00102-1
10. Sharif MAR, Wong YKE (1995) Evaluation of the performance of three turbulence closure models in the prediction of confined swirling flows. Comput Fluids 24(1):81–100. ISSN 0045-7930, https://doi.org/10.1016/0045-7930(94)E0004-H

11. Yılmaz I (2013) Effect of swirl number on combustion characteristics in a natural gas diffusion flame. J Energy Resour Technol 135(4):042204. https://doi.org/10.1115/1.4024222
12. Escue A, Cui J (2010) Comparison of turbulence models in simulating swirling pipe flows. Appl Math Model 34(10):2840–2849. https://doi.org/10.1016/j.apm.2009.12.018
13. Shih T, Zhu J, Liou W, Chen K, Liu N, Lumley J (1997) Modeling of turbulent swirling flows, NASA Technical Memorandum, No. 113112, Aug 1997, 54p
14. Jakirlic S, Hanjalic K, Tropea C (2002) Modeling rotating and swirling turbulent flows: a perpetual challenge. AIAA J 40(10):1984–1996. https://doi.org/10.2514/2.1560
15. Najafi A, Sadeghipour M, Saidi M, Souhar M (2003) Boundary layer solution for the turbulent swirling decay flow through a fixed pipe: SBR at the Inlet, vol. 259. American Society of Mechanical Engineers, Fluids Engineering Division (Publication) FED, pp 449–456
16. Galley D, Ducruix S, Lacas F, Veynante D (2011) Mixing and stabilization study of a partially premixed swirling flame using laser induced fluorescence. Combus Flame 158(1):155–171, ISSN 0010-2180, https://doi.org/10.1016/j.combustflame.2010.08.004.
17. https://www.castsafety.org/pdf/3_engine_fundamentals.pdf
18. ANSYS FLUENT® Theory Guide

Wind Impact on U Plan Shaped Tall Building Having Various Sifted Single Limb Positions

Shanku Mandal, Sujit Kumar Dalui, and Soumya Bhattacharjya

1 Introduction

The construction of modern age building confronted with challenges that involve horizontal expansion. This promotes not only the vertical development of building but also innovative shape. Those shapes are looking attractive and also fulfilling the demands of the architect. The reactions on those shape due to wind flow is rather peculiar from traditional building shapes. The design of alphabetic shapes is quite problematic and need close observations on various important wind behaviours. The existing codes are not contained such information. The manuscripts provided by several authors have shown the crucial effect of wind on distinctive shapes. Stathopoulos and Zhou [1] explored the wind instigate pressure on peculiar shape buildings formed by connecting two rectangular shapes in different positions. Gomes et al. [2] demonstrated the distribution of surface pressure of 1:100 scaled U- and L-shaped models. Zhao and Lam [3] oriented five square models in the T and L pattern to explore the effect of wind due to the interference. Lam et al. [4] analyzed the dynamic wind effect of depth and width variant recessed cavities H-shaped building. Amin and Ahuja [5] investigate the difference in surface pressure of T and L shaped models at a various range of wind incidence angle. Kushal et al. [6] considered an isolated rectangle and square shape and transformed those into T shape to understand the pressure difference and the spacing effect of T shape. Chakraborty et al. [7] studied the flow variation, pressure differences due to varying wind flow on + shape building. Mukherjee et al. [8] utilized the experimental and numerical approaches to determine the surface pressure of the Y-shaped building. The measurement of the

S. Mandal (✉) · S. K. Dalui · S. Bhattacharjya
Department of Civil Engineering, Indian Institute of Engineering Science and Technology, Shibpur, Howrah, India

S. Bhattacharjya
e-mail: soumya@civil.iiests.ac.in

D. K. Maiti et al. (eds.), *Recent Advances in Computational and Experimental Mechanics, Vol II*, Lecture Notes in Mechanical Engineering,
https://doi.org/10.1007/978-981-16-6490-8_18

torsional moment, overturning moment and base shear of interference and isolate T-shaped buildings has been presented by Ahlawat and Ahuja [9]. Mashalkar et al. [10] measured the lateral displacement, wind force and storey drifts of C, I, T, C and L type building. Cheng et al. [11] compared the wind responses of H- and square-shaped model and concluded that the shape factor has a remarkable impact on change in wind force and dynamic response. Paul and Dalui [12] showed pressure contours, vertical and horizontal pressure on various faces of Z-shaped buildings using Ansys CFX for 0° to 180° wind angle. Ranka and Shingade [13] demonstrated the force at a different height, pressure contour and drag coefficient of square, T, L and rectangular-shaped buildings at different wind angle. Pashine et al. [14] calculated the wind force of L- and T-shaped models with different height and wind angle. Hemanthkumar and Kiran [15] presented the various wind responses of L, C, H and T-shaped buildings. Hocine et al. [16] explored the numerical variation among the different turbulence models and also incorporated the proper orthogonal decomposition technique in large eddy simulation results to calculate the mean dynamics flow value of a D section. Kareem and Wan [17] stated the comprehensive applications of CFD simulation to estimate the aerodynamic performance of the structure. Mallick et al. [18] presented the wind pressure variations on without curved and curved surface of the building having C shape. The artificial neural network approach has been applied by Nikose and Sonparote [19] to predicted the along and across wind response of tall buildings. Shanku et al. [20] examined the variation in pressure and force coefficient of corner altered U-shaped building. Yang et al. [21] assessed the square model's wind aerodynamics variation with the different arrangements' splitter plates. Bhattacharyya and Dalui [22] investigate the pressure variation on asymmetric E-shaped building with the help of CFD and wind tunnel experiment. Khodaie [23] suggested both taper modification and a tuned mass damper system to control the excessive vibration in a tall structure. The CFD and wind tunnel experiments have been utilized by Tse et al. [24] to study the influence of topography in wind structure interaction. The wind turbulence around the square building has been studied by Zhang et al. [25] to assess the wind comfort at the pedestrian level. Guzmán-Solís et al. [26] investigated the wind response of rectangular building at different terrain categories by wind tunnel experiment. Choi and Kwon [27] proposed a new technique to evaluate the Strouhal number of rectangular shapes. Li et al. [28] measured the impact of wind turbulence on pressure fluctuations in the surface of a rectangular shape. Du et al. [29] investigated the critical aerodynamic behaviour on closely spaced structures in the diagonal and horizontal arrangement at a wide range of wind directions. The moment, force and pressure coefficients have been calculated by Sanyal and Dalui [30] on Y-shaped building with different limb angle using CFD. Moorjani et al. [31] explored the effectiveness of vent treatments in the building floor and suggested the suitable locations of vent arrangement.

In the modern-day, the construction of alphabetic shapes such as I, L, E, C, T, Y and U shapes are prevalent for residential and commercial purpose. The wind responses of this structure differ greatly from square and rectangular structures. Some researchers had explored the responses considering various aspects as illustrated in the previous paragraph. The previous articles contain minimal data about widespread U-shaped

buildings, so further study should be carried out with top priority. The lack of necessary space is a critical issue that can often lead to constructing a U shape in which the limbs are not located at the extreme ends. Therefore, this study investigates the influence of limb position of U-shaped buildings. This study illustrates the differences in wind pressure and forces of such building at 0° and 90° wind angel using the Computational Fluid Dynamics (CFD) technique.

2 Scope of the Work

The impact of wind has been measured for basic U shape at the said angle. The change in wind behaviour has been identified by shifting one limb of basic U shape at a location of 12.5 (0.05L), 25 (0.10L), 37.5 (0.15L), 50 (0.20L), 62.5 (0.25L), 75 (0.30L), 87.5 (0.35L), 100 (0.40L) and 150 (0.60L) mm from one corner keeping other limb at same location (L is 250 mm, the building length). Figure 1 demonstrates the various shifted building cases.

The two limbs are located at the extreme corners in the basic model (U1). In U2, U3, U4, U5, U6, U7, U8, U9 and U10 model the one limb has been sifted at a distance of 12.5, 25, 37.5, 50, 62.5, 75, 87.5, 100 and 150 mm without moving the opposite limb. A similar plan area is maintained for each case. The 50 mm limb width, 500 mm height, 150 mm width and 150 mm initial gap is adopted in the study.

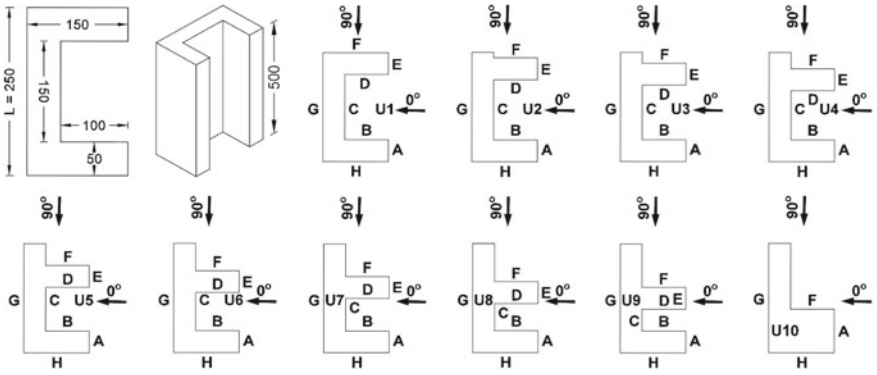

Fig. 1 Various analytical building models considered for numerical simulation (all dimensions are in mm)

3 Solution Methodology

The Ansys CFX module has been adopted for numerical simulation based on computational fluid dynamics (CFD). The advances in CFD technique promotes its application in complicated wind-related problem (Tamura and Phuc [32]).

3.1 Computational Domain Setup

The analysis has been carried out in the blockage free computational domain (Revuz et al. [33]) in which inlet and outlet are placed at 5H and 15H distance from the 1:300 scaled building model. The two side and top clearance from the building are taken 5H. The wind effect can be measured in domain floor and all faces of the buildings where no slip wall condition provided, whereas no responses have been generated in domain roof and sides where free slip wall condition is taken. The atmospheric boundary layer (ABL) flow is simulated using the power-law equation. The operating pressure at the domain and relative pressure at the outlet is considered 1 atm and 0 Pa, respectively.

$$U = U_0|\mathbf{z}/\mathbf{z}_0|^{\alpha} \tag{1}$$

Here, 'z_0' is the height of the boundary layer which has been fixed to 1 m. 'z' is the height of any point taken from the ground. $\boldsymbol{U}_0$ is the flow velocity at inlet taken as 10 m/s and $\boldsymbol{U}$ is any point velocity of the wind. The equation's exponent (α) is based on terrain category and 0.133 is adopted value for the simulation (Fig. 2).

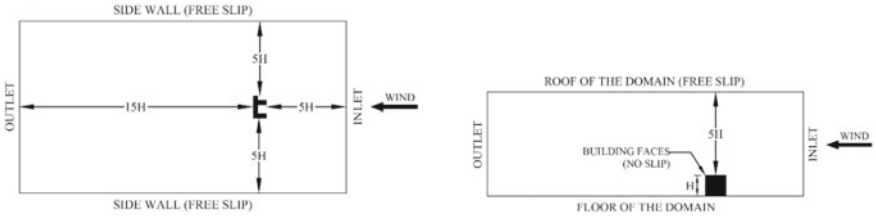

Fig. 2 The **a** Plan View **b** Elevation View of numerical analysis domain

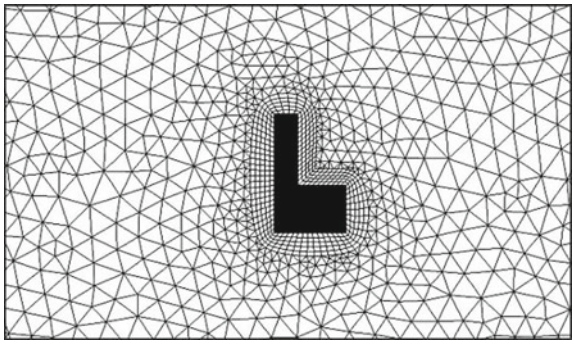

Fig. 3 The mesh pattern around the U10 building and the entire domain

3.2 Generation of Mesh

Figure 3 illustrates the meshing arrangements for the U10 building model where fine meshing has been employed around the building and for the remaining domain, tetrahedral elements are used. This meshing technique has been adopted from the article of Bhattacharyya and Dalui [22]. This method of meshing is useful for recording high-intensity flow in major regions (near building faces) without utilizing massive computational resources.

3.3 Mesh Refinement Study

Findings a suitable mesh size is an essential parameter for CFD simulation since its influence the analytical results. The mesh has been refined until convenient results have been calculated from the simulation. Table 1 demonstrated the difference in drag coefficient values of the basic model (U1) at 0° wind angle for each trail and % of error in this trail as compared to the final one. The mistake in calculated results for MT6 and MT7 is almost negligible, so the MT6 mesh trail is considered for further simulation to save the overall time for one computation.

Table 1 The mesh refinement study of primary shape (U1) model at 0° wind angle

Mesh Trial	No of Elements	Drag Coefficient	% of Error
MT1	28.850×10^5	0.8754	−20.264
MT2	51.655×10^5	0.9476	−13.688
MT3	12.547×10^6	1.0142	−7.625
MT4	19.853×10^6	1.0453	−4.791
MT5	26.709×10^6	1.0716	−2.396
MT6	33.935×10^6	1.0959	−0.182
MT7	41.093×10^6	1.0977	–

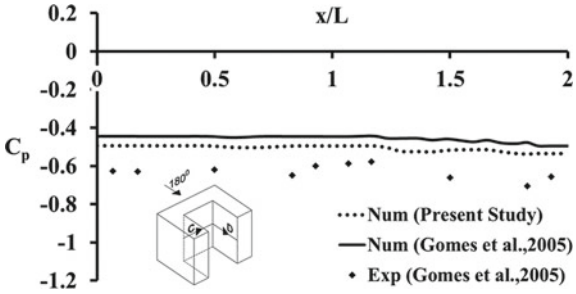

Fig. 4 The comparison of horizontal pressure coefficients of Face C and D for 180° wind incidence angle

3.4 Validation of Numerical Study

The pressure coefficient at 180° wind angle for Face C and D through horizontal centreline has been adopted from Gomes et al. [2] to check the variation in current numerical results. The model dimension for this validation study is considered as presented in the article. The numerical results have been validated since the negligible variation is noted and it also follows almost similar trends (see Fig. 4).

4 Results and Discussion

The location of the limb plays a crucial role in altering the wind behaviour around the U-shaped building model. The numerical study at 0° and 90° wind angle have recorded critical change in wind responses because of single-limb relocation.

4.1 Wind Velocity Streamline

The position of a limb on a U-shaped building influence the wind-induced responses by changing the nature of wind flow around the building. The velocity streamline represents the velocity fluctuations and the pattern of wind flow. Figure 5 delineates the flow characteristics near the basic U building and some critical cases of limb-shifted U building. The axisymmetric composition of U shape no longer exists when one of the limbs is transfer systematically from one end to the other end. This rearrangement causes the unsymmetrical flow at both ends and originated irregular vortices at the backside of the buildings at 0° angle. The vortices are also generated between the two limbs due to the backflow of wind. The vortices have been formed on the side faces of the shifted locations. The zone of separation also has been moved with the shifting. The low wind velocity has been noted at each side faces of the primary building due to flow circulation but when one limb is shifting, due to the

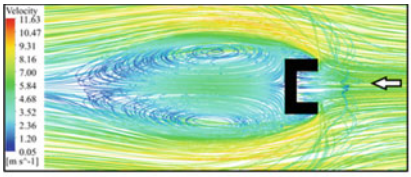

(a) Primary Building (U1) at 0° angle

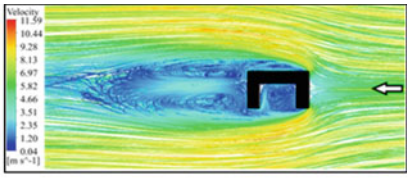

(b) Primary Building (U1) at 90° angle

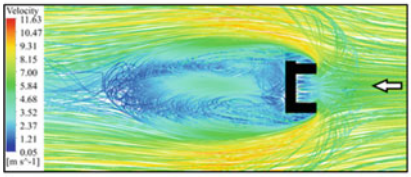

(c) Limb Shifted Building (U2) at 0° angle

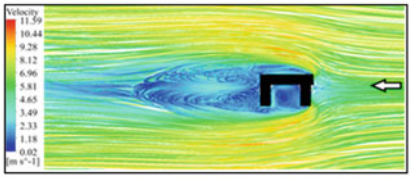

(d) Limb Shifted Building (U2) at 90° angle

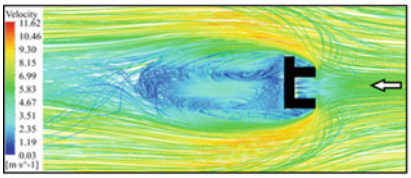

(e) Limb Shifted Building (U5) at 0° angle

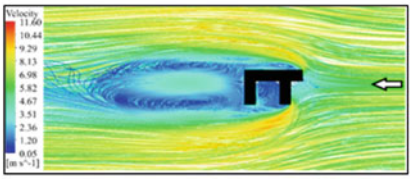

(f) Limb Shifted Building (U5) at 90° angle

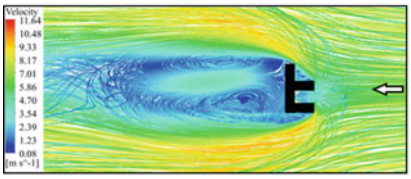

(g) Limb Shifted Building (U8) at 0° angle

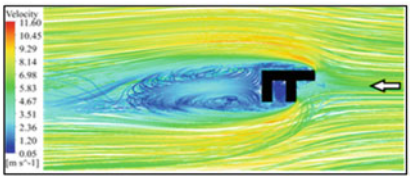

(h) Limb Shifted Building (U8) at 90° angle

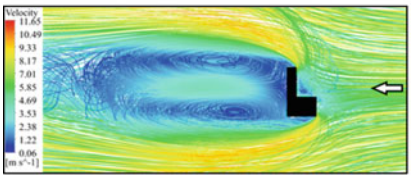

(i) Limb Shifted Building (U10) at 0° angle

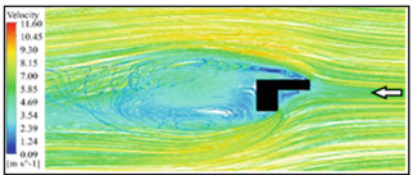

(j) Limb Shifted Building (U10) at 90° angle

Fig. 5 The wind velocity streamlines around the various building for 0° and 90° wind angle

change in the flow separation zone, the velocity at this end changes dramatically and this causes remarkable fluctuations in wind responses.

The variation in pattern is also visible for the change in the angle of flow. The tremendous increase in velocity is noted at flow separation regions. The extreme low wind velocity is produced between the two limbs of the basic building and U2–U9 building cases at a 90° angle due to the vortex formation. The same phenomenon is observed in the wake region. But for the U10 building, where both limbs are located

at the same corner, the velocity is slightly high in these regions compared to other cases.

The zone of the vortex at the wake region up to specific shifted cases is comparatively small at both wind direction as compared to the primary case. But the increase in shifts length again formed the large vortex zone.

Small vortices are also formed at the shifted locations. Those variations in flow pattern influence the wind responses of those buildings.

4.2 Comparison of Force Coefficients

The notable variation in force coefficient has been detected for the shifting and the pictorial comparison of the calculated value is presented in Fig. 6. The drag coefficient of the building has been decreased gradually due to the sifting of one limb from 12.5 mm (0.05L) to 75 mm (0.30L). However, further shifting of the limb causes an increase in the drag coefficient. The drag coefficient is comparatively low in each shifted building as compared to the basic building at 0° angle. This indicates that the pattern of flow regulates the wind responses. The shifting of one limb by 0.30L is the most suitable position to minimize the effect of wind in along wind direction since the value (0.8509) of drag coefficient is lowest among all the cases. Nevertheless, a remarkable increase in the lift coefficient is observed with the increase in shifting length. A tremendous increase in lift coefficient is noted while shifting of limbs from 0.30L to 0.35L (−0.0963 to −0.5422). The relocation of the limb from

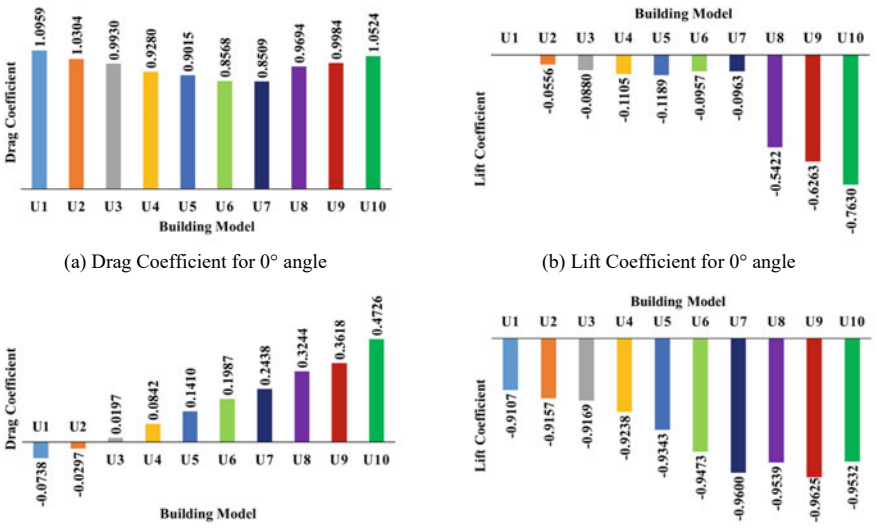

(a) Drag Coefficient for 0° angle

(b) Lift Coefficient for 0° angle

(c) Drag Coefficient for 90° angle

(d) Lift Coefficient for 90° angle

Fig. 6 The comparison of drag and lift coefficient between limb shifted buildings

0.35 L position to 0.60 L position indicates severe across wind responses because the responses gradually increase from −0.5422 to −0.7630. If the wind angle shifts to 90°, the drag coefficient no longer diminishes with the limb relocation. The shifting of limb induces a considerable increase in both lift and drag coefficient as the flow around the building varies significantly when shifts in wind direction are considered.

4.3 Comparison of Pressure Coefficients

Figure 7 demonstrate the various faces of a basic building and typical limb shifted buildings. The variation in pressure values indicates the fact that the transfer of the limbs to the other corner influence the wind flow significantly (see Tables 2, 3, 4 and 5). At face A and B for 0° angle, the increase in mean pressure has been noted up to 0.25L shifting but further shifts up to 0.40L decrease the pressure because the flow separation point changes and wind velocity decreases near those faces due

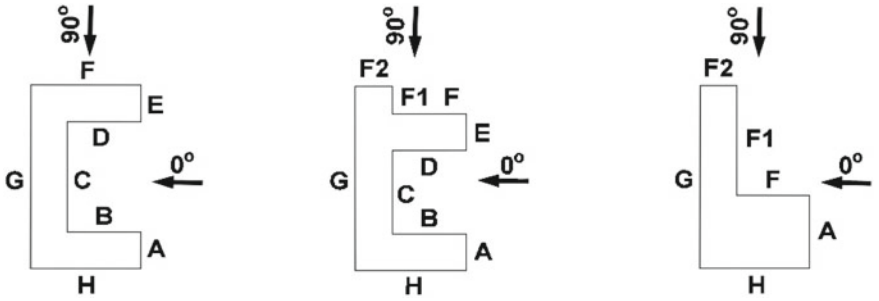

Fig. 7 The various faces of a basic building and typical limb shifted buildings

Table 2 The mean pressure coefficient on the primary faces for 0° angle

Limb Position	Face A	Face B	Face C	Face D	Face E	Face F	Face G	Face H
0.00 L	0.410	0.828	0.870	0.828	0.410	−0.561	−0.381	−0.561
0.05 L	0.434	0.823	0.866	0.821	0.408	−0.597	−0.378	−0.526
0.10 L	0.437	0.823	0.864	0.821	0.393	−0.686	−0.415	−0.558
0.15 L	0.437	0.824	0.864	0.820	0.433	−0.629	−0.399	−0.588
0.20 L	0.439	0.828	0.856	0.814	0.498	−0.431	−0.388	−0.572
0.25 L	0.518	0.834	0.870	0.834	0.587	−0.182	−0.308	−0.369
0.30 L	0.515	0.833	0.868	0.831	0.589	−0.181	−0.308	−0.371
0.35 L	0.461	0.817	0.854	0.807	0.728	0.223	−0.374	−0.564
0.40 L	0.458	0.794	0.836	0.781	0.774	0.340	−0.380	−0.572
0.60 L	0.633	–	–	–	–	0.615	−0.375	−0.532

Table 3 The mean pressure coefficient on the shifted faces for 0° angle

Limb Position	Face F1	Face F2
0.00 L	–	–
0.05 L	−0.488	−0.492
0.10 L	−0.537	−0.515
0.15 L	−0.429	−0.456
0.20 L	−0.253	−0.478
0.25 L	−0.058	−0.421
0.30 L	−0.050	−0.433
0.35 L	0.305	−0.510
0.40 L	0.408	−0.516
0.60 L	0.628	−0.526

Table 4 The mean pressure coefficient on the primary faces for 90° angle

Limb Position	Face A	Face B	Face C	Face D	Face E	Face F	Face G	Face H
0.00 L	−0.437	−0.573	−0.545	−0.549	−0.675	0.567	−0.476	−0.280
0.05 L	−0.466	−0.610	−0.582	−0.587	−0.747	0.631	−0.491	−0.287
0.10 L	−0.467	−0.601	−0.573	−0.580	−0.741	0.622	−0.477	−0.283
0.15 L	−0.478	−0.594	−0.568	−0.575	−0.737	0.615	−0.468	−0.288
0.20 L	−0.485	−0.581	−0.558	−0.564	−0.722	0.608	−0.459	−0.295
0.25 L	−0.494	−0.576	−0.556	−0.560	−0.701	0.601	−0.453	−0.309
0.30 L	−0.516	−0.590	−0.572	−0.576	−0.728	0.583	−0.460	−0.330
0.35 L	−0.441	−0.495	−0.485	−0.488	−0.607	0.603	−0.515	−0.316
0.40 L	−0.507	−0.569	−0.556	−0.560	−0.707	0.560	−0.478	−0.344
0.60 L	−0.499	–	–	–	–	0.488	−0.429	−0.371

Table 5 The mean pressure coefficient on the shifted faces for 90° angle

Limb Position	Face F1	Face F2
0.00 L	–	–
0.05 L	0.857	0.523
0.10 L	0.845	0.541
0.15 L	0.817	0.550
0.20 L	0.780	0.561
0.25 L	0.736	0.570
0.30 L	0.684	0.576
0.35 L	0.662	0.551
0.40 L	0.591	0.571
0.60 L	0.428	0.590

to vortex generation. This causes suction on those faces. The sudden increase in pressure is calculated at 0.60L shift on face A since two limbs are connected in this case, so no vortex has been formed in between those limbs. The mean positive pressure gradually decreases at face C and D up to 0.20L sifting length. At 0.25L shifting case, the increase in positive pressure is observed on those faces but further relocation to the other end reduces the mean pressure. In face E, the shifting till 0.10L minimizes the mean pressure but beyond 0.10L shifting the pressure again increasing as the flow separation point shifts. The mean negative pressure at face F and F1 gradually increases up to the transfer of 0.10L but further transfer lowered the negative pressure and ultimately the mean positive pressure is noted on this face from 0.35L shifting but the mean negative pressure is measured on the surface of the face F2, G and H since in this locations wind velocity is very low and the vortex has been formed. The magnitude of pressure fluctuates with the relocation of the limb has been observed due to the variation in the wind flow pattern.

At 90° wind angle, the mean negative pressure is measured on all the faces except the face F, F1 and F2. The increment in mean negative pressure is visible at face A up to 0.30L shifting. The sudden decrease in pressure is noted at 0.35L but further increase in pressure is measured at 0.40L shifts. At face B, C, D, E, G and H remarkable fluctuation of mean pressure is calculated in each step of the shifting case. At Face F1, the mean positive pressure decreases with the increment in shifting length but the exact opposite situation arises at face F2 up to the 0.30L shifting. It is evident that the location of the limb has dramatically affected the wind movement. Therefore, variations in mean pressure are observed in each step of systemic relocation of the single limb.

The pressure coefficients variation of basic and shifted buildings are illustrated in Fig. 9, through the perimeter of the buildings at a distance of 250 mm from the ground. Figure 8 demonstrated the direction of the calculated pressure coefficients.

The comparison of the pressure coefficient clearly shows that the limb position has a remarkable impact on the variation of pressure distribution on the faces of the building. The significant variation is visible in the region of Face E, F and F1 at 0° wind angle. The negative pressure on that region converted gradually to positive pressure with the increase in shifting length. At a 0.60L sifting case, tremendous variation is observed at the said angle. For a 90° wind angle, the pressure variation

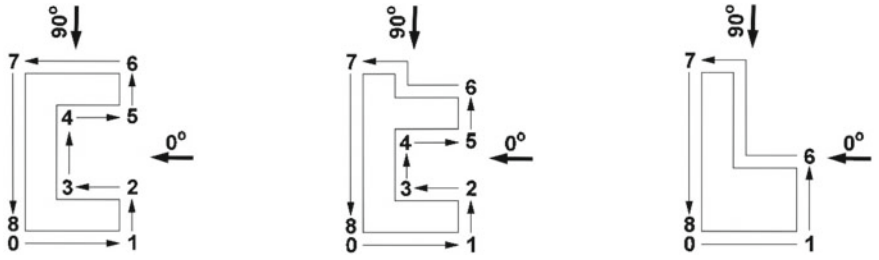

Fig. 8 The various faces of typical buildings and the direction of the measured pressure coefficient

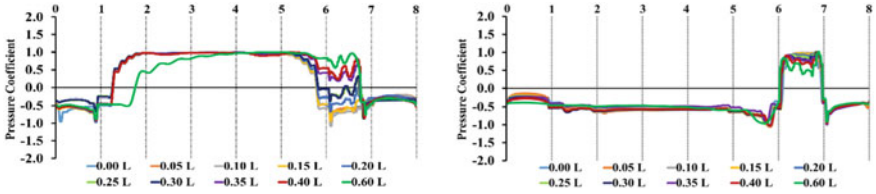

(a) 0° (b) 90°

Fig. 9 The comparison of pressure coefficient along with the horizontal centerline **a** 0° **b** 90°

due to sifting is almost negligible. However, for this angle, a slight difference is present in the sifting length of 150 mm (0.60L).

5 Conclusions

The influence of the limb transfer of a U-shaped building from one extreme corner to other corner is investigated in the current study considering the wind angle of 0° and 90°. Different position of the limb has been considered to measure the variation in pressure and force coefficients. Because of the limb shifting the irregularity in plan shape not only prevail but also the advantages of axisymmetry shape in the primary building got vanished. The impact of the shifting is explored by understanding the variation in wind responses, which can be summarized as follows.

- The drag force coefficient in shifted buildings cases is far less than the basic building at 0° angle of the wind. The 0.30L limb position is showing better response compare to other shifting position. However, the basic building attracts less drag force with the change in wind angle.
- The across wind response of reformed building left a critical concern at both 0° and 90° angle of the wind. A dramatic increment in lift coefficient is noticed at higher sifted length cases. The axisymmetric shape of basic building induces almost negligible lift force at the wind angle of 0°. The basic shape has some benefit over other shifting forms since there is no such concern of across wind response.
- The wind flow patterns and the flow velocity near the building faces generate unpredictable pressure distribution on the building surface. Comparing the mean pressure coefficient and the pressure coefficient through horizontal centerline indicates that detailed observations and careful cladding design are required if shifting is considered.

The information obtained from this study is quite unique since no such previous data is available from which the effect of limb position on U-shaped building can be explored. The initial purpose of this study is to explore the wind impact on those shape and present a set of information which will guide to construct the limb shifted

U buildings. This study will help to figure out the critical aspects of this type of shape and the data from this study can be applied to wind-resistant design. This article reveals that the sifting of the limb is beneficial to minimize the along wind response at normal wind direction. However, this shifting can stimulate severe across wind response. This study therefore suggests that the sifting of limbs of a U-shaped building should be avoided as far as the situation not permits. If the situation arises, this study will assist the designer to understand the implications of limb shifting so that the necessary precautions can be incorporated in the design stage of the building.

References

1. Stathopoulos T, Zhou YS (1993) Numerical simulation of wind-induced pressures on buildings of various geometries. J Wind Eng Ind Aerodyn 46–47:419–430
2. Gomes MG, Moret Rodrigues A, Mendes P (2005) Experimental and numerical study of wind pressures on irregular-plan shapes. J Wind Eng Ind Aerodyn 93(10):741–756
3. Zhao JG, Lam KM (2008) Interference effects in a group of tall buildings closely arranged in an L- or T-shaped pattern. Wind Struct 11(1):1–18
4. Lam KM, Wong SY, To AP (2009) Dynamic wind loading of H-shaped tall buildings. In: 7th Asia-pacific conf wind eng APCWE-VII. Taiwan
5. Amin J, Ahuja A (2011) Experimental study of wind-induced pressures on buildings of various geometries. Int J Eng Sci Technol 3(5):1–19
6. Kushal T, Ahuja AK, Chakrabarti A (2013) An experimental investigation of wind pressure developed in tall buildings for different plan shape. Int J Innov Res Stud2(6):605–614
7. Chakraborty S, Dalui SK, Ahuja AK (2014) Wind load on irregular plan shaped tall building–a case study. Wind Struct 19(1):59–73
8. Mukherjee S, Chakraborty S, Dalui SK, Ahuja AK (2014) Wind induced pressure on 'Y' plan shape tall building. Wind Struct 19(5):523–540
9. Ahlawat R, Ahuja AK (2015) Wind loads on 't' plan shape tall buildings. J Acad Ind Res 4(1):27–30
10. Mashalkar BS, Patil GR, Jadhav AS (2015) effect of plan shapes on the response of buildings subjected to wind vibrations. IOSR J Mech Civ Eng 1:80–89
11. Cheng L, Lam KM, Wong SY (2015) POD analysis of crosswind forces on a tall building with square and H-shaped cross sections. Wind Struct 21(1):63–84
12. Paul R, Dalui SK (2016) Wind effects on 'Z' plan-shaped tall building: a case study. Int J Adv Struct Eng 8(3):319–335
13. Ranka S, Shingade PVS (2016) analytical and numerical analysis of wind load on tall buildings. Int J Eng Sci Technol 5(11):3188–3197
14. Pashine B, Vaidya VD, Singh DP (2016) Wind analysis of multistoried structure with T shape and L Shape geometry. Int J Eng Dev Res 4(3):70–77
15. Hemanthkumar MS, Kiran T (2017) Analysis of wind response on different shapes of high rise mivan wall buildings by using gust factor method. Int Res J Eng Technol 4(9):211–222
16. Hocine AEBL, Lacey RWJ, Poncet S (2019) Turbulent flow over a D-section bluff body: a numerical benchmark. Environ Fluid Mech 19(2):435–456
17. Kareem A, Wan J (2019) Aerodynamic tailoring of structures using computational fluid dynamics. Struct Eng Int 29:26–39
18. Mallick M, Kumar A, Patra KC (2019) Analysis of curvature effect on C-shaped buildings. In: ACM Int. Conf. Proceeding Ser., pp 260–266
19. Nikose TJ, Sonparote RS (2019) Dynamic wind response of tall buildings using artificial neural network. Struct Design Tall Spec Build 28:1–18

20. Mandal S, Dalui SK, Bhattacharjya S (2020) Effect of aerodynamic modifications on a tall building with horizontal irregularity. Adv struc Sys Mat:99–107
21. Yang Q, Liu Z, Hui Y, Li Z (2020) Modification of aerodynamic force characteristics on high-rise buildings with arrangement of vertical plates. J Wind Eng Ind Aerodyn 200:104155
22. Bhattacharyya B, Dalui SK (2020) Experimental and numerical study of wind-pressure distribution on irregular-plan-shaped building. J Struct Eng 146(7):1–14
23. Khodaie N (2020) Vibration control of super-tall buildings using combination of tapering method and TMD system. J Wind Eng Ind Aerodyn 196:104031
24. Tse KT, Weerasuriya AU, Hu G (2020) Integrating topography-modified wind flows into structural and environmental wind engineering applications. J Wind Eng Ind Aerodyn204:104270
25. Zhang B, Ooka R, Kikumoto H (2020) Analysis of turbulent structures around a rectangular prism building model using spectral proper orthogonal decomposition. J Wind Eng Ind Aerodyn206:104213
26. Guzmán-Solís V, Pozos-Estrada A, Gómez R (2020) Experimental study of wind-induced shear, bending, and torsional loads on rectangular tall buildings. Adv Struc Eng 23(14):2982-2995
27. Choi CK, Kwon DK (2000) Determination of the Strouhal number based on the aerodynamic behavior of rectangular cylinders. Wind Struct Int J 3(3):209–220
28. Li Y, Yan J, Chen X, Li Q, Li Y (2020) Investigation of surface pressures on CAARC tall building concerning effects of turbulence. Wind Struct 31(4):287–298
29. Du X, Chen R, Dong H, Ma W, Xu H, Zhao Y (2021) Aerodynamic characteristics of two closely spaced square cylinders in different arrangements. J Wind Eng Ind Aerodyn 208:104462
30. Sanyal P, Dalui SK (2021) Effects of internal angle between limbs of 'Y' plan shaped tall building under wind load. J Build Eng33:101843
31. Moorjani RR, Lombardo FT, Devin AF, Young BS, Baker WF, Ray SD (2021) Influence of vented floors on the across-wind response of tall buildings. J Wind Eng Ind Aerodyn 209:104480
32. Tamura Y, Phuc PV (2015) Development of CFD and applications: Monologue by a non-CFD-expert. J Wind Eng Ind Aerodyn 144:3–13
33. Revuz J, Hargreaves DM, Owen JS (2012) On the domain size for the steady-state CFD modelling of a tall building. Wind Struct 15(4):313–329

Integrated Numerical Model and Coupled Analysis of V-Shaped Semisubmersible Under Metocean Condition

Swarnadip Dey and Atul K. Banik

1 Introduction

Wind energy has been identified as a suitable alternative to conventional energy sources. The advantage of offshore wind is manifold. Offshore wind blows over long stretches without obstruction. More power can be generated from fewer turbines owing to larger wind speeds. Densely populated coastal cities can be served and valuable land can be saved. Also, the noise pollution can be avoided. Harnessing offshore wind energy at a viable cost, per unit of production, requires a close interdisciplinary collaboration among researchers. From a structural point of view, the rotation of turbine blades influences the dynamic responses of a floating platform while the movement of the platform affects the position and orientation of the turbine and consequently its aerodynamic performance. Musial et al. [13] and Butterfield et al. [2] highlighted the engineering challenges that need to be overcome for the successful and economical deployment of FOWTs. Nielson et al. [14] developed simulation models for dynamic analysis of FOWTs and compared their results with those of a scaled model test. They emphasized the need for an integrated aero-hydro-servo approach in design. Thus, the need for an integrated approach to the analysis and design of FOWTs is well established. The most common approach for design of the floating wind turbines nowadays is wind-wave basin test where the wind is generated by the wind tunnel fans and wave fields are generated by the wave generator separately [4, 5]. But in reality the waves are mainly induced by winds, hence such studies may not provide reliable results. It is therefore crucial to have realistic metocean conditions available that accurately characterize the physical behaviour of the

S. Dey (✉) · A. K. Banik
Civil Engineering Department, NIT Durgapur, Mahatma Gandhi Road, A Zone, Durgapur 713209, India

A. K. Banik
e-mail: atul.banik@ce.nitdgp.ac.in

D. K. Maiti et al. (eds.), *Recent Advances in Computational and Experimental Mechanics, Vol II*, Lecture Notes in Mechanical Engineering,
https://doi.org/10.1007/978-981-16-6490-8_19

offshore environment [15]. In wide range of offshore wind turbines research, design and analysis activities, Dey et al. [3] have highlighted the necessity of inclusion of operational and survival design condition in the analysis of FOWTs. To reduce the computational effort, often the researchers have adopted a frequency domain approach [6, 16] where the paramount limitation is in its capability of capturing the nonlinear dynamic characteristics or modelling dynamic loading events. The best representation of responses should be in time domain.

Amongst the various offshore floating platforms available nowadays, semi-submersible platforms has found great acceptance in the offshore industry mainly because of its better hydrodynamic stability, higher roll and pitch stability and lesser cost of installation than other types of floating platforms [12]. However, the conventional semi-submersible platforms consist of cylindrical columns which are connected by braces. Over a period of time, the braces are subjected to fatigue damage as a result of cyclic loading which occurs due to the repeated application of waves having a specific phase. The fatigue damage in the braces may have serious implications on the performance of the platform. Therefore, to overcome this shortcoming, the concept of a braceless or a V-shaped semi-submersible platform was developed by Karimirad and Michailides [10]. Although, the V-shaped semi-submersible platform is an asymmetric structure but has found that its performance is not affected in an undesirable way under misaligned wind and wave conditions.

This paper deals with three different V-shaped semisubmersible, the details of which in the following section, designs as mentioned in the work of Karimirad and Michailides [9] and their applicability in three different geographical locations, i.e., East coast, West coast of USA and the Gulf of Mexico coast [15]. Realistic metocean data set released by National Data Buoy Centre were used for the assessment. An integrated numerical modelling of the V-shaped semisubmersible and its coupled dynamic responses are studied in time domain under the combined action of turbulent wind and irregular waves. Variable wind speed data has been generated by the simulator TurbSim [7], using Kaimal spectrum [8] with a turbulence intensity of 0.1 and irregular wave train was represented by JONSWAP spectrum. MATLAB code was also used to generate the time history of the dynamic thrust force from the turbulent wind speed data. The responses of the wind turbine and tensions in mooring line have been statistically compared for each of the design cases under the operational and survival environmental conditions [11] by using hydrodynamic software AQWA [1].

2 V-shaped Semisubmersible—An Alternative Concept

The V-shaped semi-submersible platform in the present paper consists of three cylindrical columns of equal diameter connected by two rectangular pontoons and over the top of the central column, the turbine tower is placed. The turbine considered here is the NREL 5 MW baseline and details are given in Table 2. A catenary mooring cable is suspended from each of the column base and is anchored to the seabed. The angle

between the pontoons is kept constant at 60°. Vcd60 is chosen as the base configuration while the size of the pontoons and the distance between the pontoons is varied for the other two designs, Vcd50 and Vcd70. The characteristics of the three alternative designs of the V-shaped semi-submersible platform are mentioned in Table 1 from the work of Karimirad and Michailides [9]. For describing the response behavior of the FOWT, a body-fixed reference axis is considered with its origin at center of gravity and initially it is parallel to the global reference axis, where the still water surface signifies the x–y plane while the z-axis points vertically upwards (Fig. 1).

Table 1 Properties details of the three chosen V-shaped semisubmersible platforms

Properties	Design parameters of V-shaped semisubmersibles		
	$V_{cd}50$	$V_{cd}70$	$V_{cd}60$
Distance between columns (m)	50	70	60
Pontoons width (m)	9	7	9
Pontoons depth (m)	5	4	5
Column dia (m)	9	7	9
Total mass (kg)	9,340,000	6,954,000	10,263,000
Submerged volume (m^3)	9113	6785	10,013
CoG (x, y, z) (m)	(−25.8, 0.0, −14.9)	(−35.2, 0.0, −14.2)	(−30.6, 0.0, −16)
CoB (x, y, z) (m)	(−28.5, 0.0, −19.1)	(−36.8, 0.0, −20.5)	(−32.8, 0.0, −19.6)
K_{xx} (m)	35.44	35.45	35.45
K_{yy} (m)	46.09	46.09	46.09
K_{zz} (m)	41.76	41.75	41.76

Table 2 Characteristics of NREL Base 5 MW wind turbine

Properties	Values
Hub height (m)	87.6
Wind turbine CoG (x, y, z) (m)	(−0.2, 0.0, 70)
K_{xx} (m)	79.267
K_{yy} (m)	78.102
K_{zz} (m)	13.663

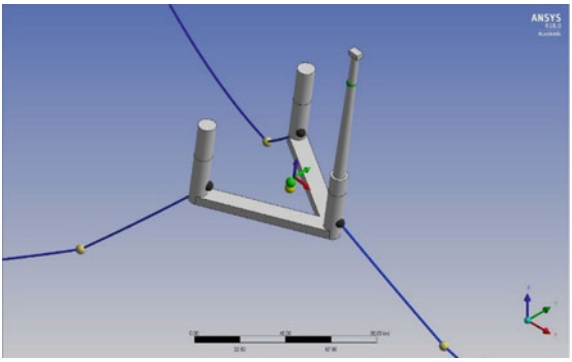

Fig. 1 V-shaped semisubmersible model in AQWA [1]

2.1 Free Decay Analysis

Free decay analysis of the structure has been carried out to obtain the natural periods. The natural periods thus obtained were compared with those reported by Karimirad and Michailides [9] and a good match was observed as shown in Table 3. It is also observed that at free-floating condition Vcd50 and Vcd70 platforms act similarly in heave and pitch modes while the Vcd60 is exceptionally showing low natural frequencies in all the modes.

The Response Amplitude Operators (RAOs) are determined or calculated as par the attribution of the system versus the wave frequencies. Normally, if a periodical excitation of a certain frequency under a regular wave is acting, the response would also be regular. In this work, the calculation was made with a series of regular waves which were propagating −1800 towards the platform. Figure 2a–c shows the comparison of RAOs in the surge, heave, and pitch for the three different semisubmersibles in the present study. The RAOs follow a similar pattern for the three cases thereby validating the present model. This signifies a good agreement has been made between the models presented in this paper.

Table 3 Comparison of natural periods

V-shaped semisubmersible	Unit	Heave	Roll	Pitch
$V_{cd}50$	Periods (s)	18	25	15
$V_{cd}70$		18	30	13
$V_{cd}60$ (present)		24	41	17
$V_{cd}60$ [9]		25	31	20

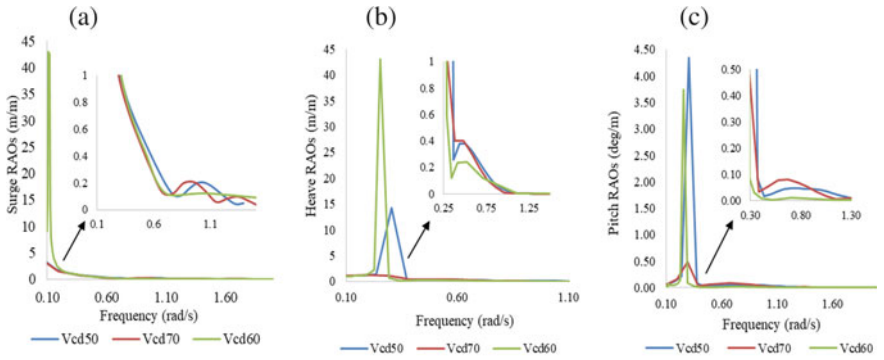

Fig. 2 RAO comparison of Vcd50, Vcd70 and Vcd60. **a** Surge, **b** heave and **c** pitch

3 Metocean Conditions

Stewart et al. [15] have provided a comprehensive metocean data set for use in offshore wind energy applications. The data were obtained from the National Data Buoy Centre which is run by National Oceanic and Atmospheric Administration. Twenty-three ocean sites around USA which yielded the parameters needed for offshore wind energy use namely wind speed, significant wave height, wave peak-spectral period, wind direction and wave direction were chosen. The sites with at least 5 years of data were selected. The sites were then grouped according to their geographic locations and were combined to create three representative sites—a West coast site, an East coast site and a Gulf of Mexico site. The West coast site was characterized as the site having highest waves.

The wind-driven wave parameters were selected based on data measurement in the offshore region according to the sites mentioned by Stewart et al. [15]. JONSWAP spectrum was used to define the wave load in the undeveloped sea, on the structure. Here, wind load was turbulent in nature with turbulence intensity 0.1 and followed Kaimal spectrum [8]. To account for the operationality of the turbine, two different environmental conditions (operational and survival) have been considered (Table 4).

4 Coupled Dynamic Analysis of Rigid Body in Time Domain

For describing the motion behavior of the FOWT, a body-fixed reference axis was considered with its origin at the center of gravity and initially, it was parallel to the global reference axis, where the still water surface signifies the x–y plane while the z-axis points vertically upwards. In a time-domain dynamic analysis of structure, a convolution integral form of the equation was used to account for the frequency-dependent added mass matrix and damping matrix. The equation of motion as given

Table 4 External loading conditions in the analysis of different analyses

Regions	Environment conditions	Wind speeds (m/s)	Significant wave heights (m)	Wave peak spectral periods (s)	Directionality (°)
West coast	Operational	11.4	2.410	11.194	−10.674
	Survival	35	9.110	8.888	47.742
East coast	Operational	11.4	1.750	7.503	−14.423
	Survival	35	7.10	12.10	26.511
Gulf of Mexico	Operational	11.4	1.623	6.373	−0.479
	Survival	35	6.29	11.528	20.149

in AQWA [1] in wave frequency with slow drift may be represented as,

$$\{\mathbf{M}+\mathbf{A}(\infty)\}\ddot{\mathbf{X}}(t)+\mathbf{c}\dot{\mathbf{X}}(t)+\mathbf{K}\mathbf{X}(t)+\int_0^t \mathbf{h}(t-\tau)\ddot{\mathbf{X}}(\tau)\partial\tau=\mathbf{F}_{\text{hydro}}+\mathbf{F}_{\text{aero}}+\mathbf{F}_{\text{moor}} \tag{1}$$

Here, **M** is the system mass matrix consisting of the mass component of the system and $\mathbf{A}(\infty)$ is the added mass matrix component in infinite frequency; **c** is the linear frequency independent damping matrix, **K** is the system stiffness matrix consisting of the contributions from the hydrostatic stiffness, **X** is the displacement vector, $\dot{\mathbf{X}}$ is the velocity vector while $\ddot{\mathbf{X}}$ is the acceleration vector $\mathbf{F}_{\text{hydro}}$ includes the first order and second order wave excitation forces. $\mathbf{F}_{\text{aero}}$ is the aerodynamic forces. $\mathbf{F}_{\text{moor}}$ is the mooring dynamic force.

Here, $\mathbf{h}(\tau)$ is the acceleration impulse function computed by the transform of the frequency-dependent added-mass matrix $\mathbf{A}(\omega)$ or hydrodynamic damping matrix $\mathbf{C}(\omega)$ in wave frequency ω is represented as given in AQWA (ANSYS 16):

$$\mathbf{h}(\tau)=\frac{2}{\pi}\int_0^\infty\left[\mathbf{C}(\omega)\frac{\sin(\omega t)}{\omega}\right]d\omega=\frac{2}{\pi}\int_0^\infty\{\mathbf{A}(\omega)-\mathbf{A}(\infty)\}cos(\omega t)d\omega \tag{2}$$

4.1 Cable Dynamics Model

As mooring lines are slender structures the mooring loads were not computed by diffraction theory. Thus, often a semi-empirical Morison equation was used which describes the load per unit length of cable as a sum of a drag term and an inertia term given as

$$dF_m = \frac{1}{2}\rho_w C_d D|u_r|u_r + \rho_w C_m \frac{\pi D^2}{4}\dot{u}_w - \rho_w \frac{\pi D^2}{4}(C_m - 1)\dot{u}_m \tag{3}$$

$$u_r = u_w - u_m \tag{4}$$

Here ρ_w is the density of water, C_d is the drag coefficient, C_m is the inertia coefficient, D is the diameter of mooring line, $\dot{u}_r$ and u_r are the transverse directional relative acceleration and the relative velocity between water particle velocity (u_w) and mooring body velocity (u_m) respectively. The design parameters of the mooring cables were taken from the work of Karimirad and Michailides [9] as the self-weight of the cable is 117 kg per metre length, equivalent diameter is 0.138 m and axial stiffness is 3.0E+6 kN. Three set of single mooring lines are used with a clump mass for each and the weight is 37,000 kg, displaced water volume 4.4 m^3 and the drag coefficient is 1.2.

5 Results and Discussions

The coupled analysis is conducted for the floating platform Vcd60 was carried out under turbulent wind and irregular waves. Total simulation time was 4000 s and to avoid transitional part the initial 1500 s have been avoided. To account for the wind and its effect in the analysis time step of the analysis has been chosen as 0.05 s. Over the periodical range of one wave cycle, the platform motion responses create aerodynamic oscillations which can all be called as aerodynamic damping. Furthermore, the propagation of waves also affects the airflow indicated by decrease of wind speed above crests, this emphasizes the coupling between wind and wave in FOWT simulations. Among the East, West and Gulf of Mexico coasts West coast is deemed to be the most appropriate for the chosen Vcd60 as the mooring line tension and responses of the platform especially for the survival condition has been found to be the critical one. A marked difference was observed in the responses of the platform during the operational and survival condition. The presence of aerodynamic damping decreased the platform surge and pitch responses during operational condition. In all the design cases it is shown (Figs. 3, 4, 5, 6, 7, 8, 9, 10, 11, 12, 13 and 14) that the presence of aerodynamic damping decreased the platform surge and pitch responses during operational condition. The deviation in the surge response in the survival condition was found to be 4-times than that in the operational condition, while the deviation in the pitch responses in the survival was found to be 5.33 times the deviation in the operating condition. Significant pitch response was seen in the Gulf of Mexico coast and deviation in the pitch response in survival condition was found to be almost 6 times than that in the operating condition. In the East coast, the maximum value of the pitch response is found to be lesser than that in the Gulf and West coast. The mooring line tension and the responses along surge and heave directions were also found to be much lesser. Thus it can be said that the East coast is the most appropriate for the Vcd60 semisubmersible platform to perform.

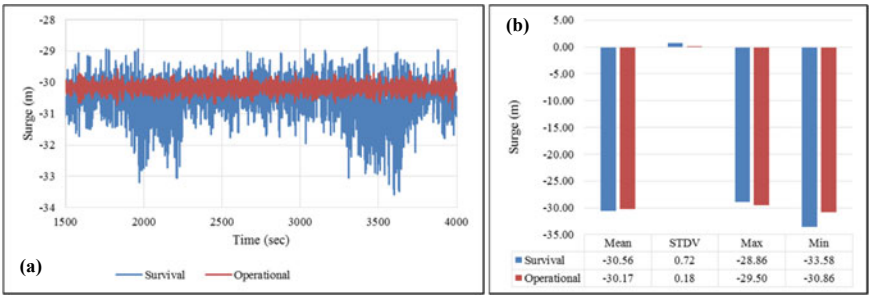

Fig. 3 Comparison of coupled dynamic surge responses of the Vcd60 in West coast under survival and operational conditions **a** in time domain and **b** statistically

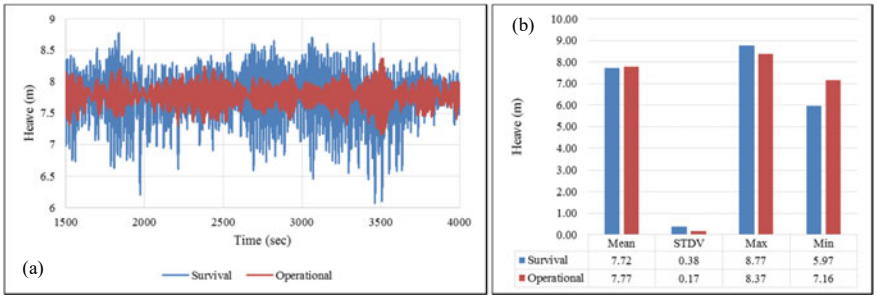

Fig. 4 Comparison of coupled dynamic heave responses of the Vcd60 in West coast under survival and operational conditions **a** in time domain and **b** statistically

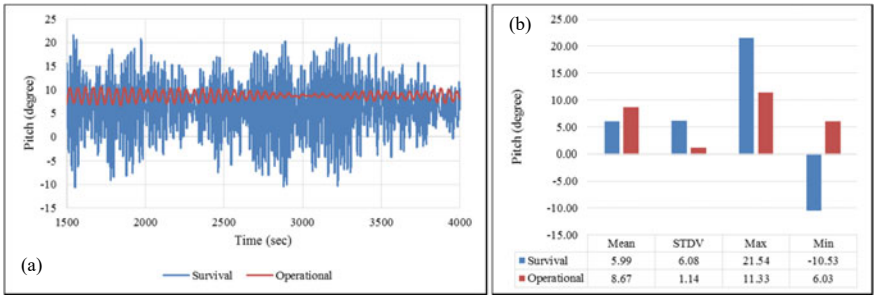

Fig. 5 Comparison of coupled dynamic pitch responses of the Vcd60 in West coast under survival and operational conditions **a** in time domain and **b** statistically

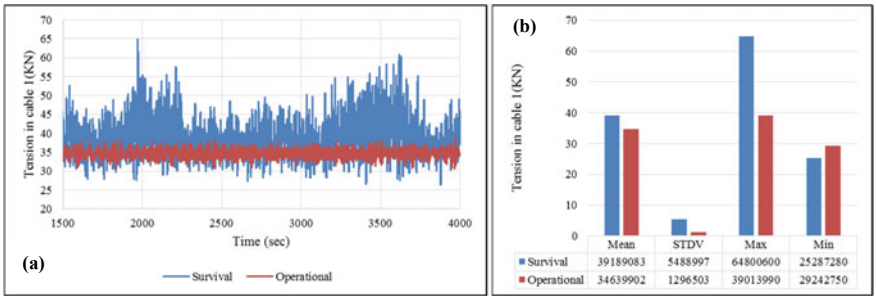

Fig. 6 Comparison of tension at cable 1 responses of the Vcd60 in West coast under survival and operational conditions **a** in time domain and **b** statistically

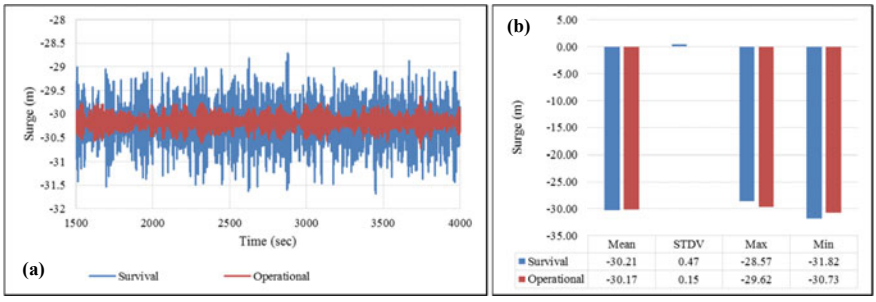

Fig. 7 Comparison of coupled dynamic surge responses of the Vcd60 in East coast under survival and operational conditions **a** in time domain and **b** statistically

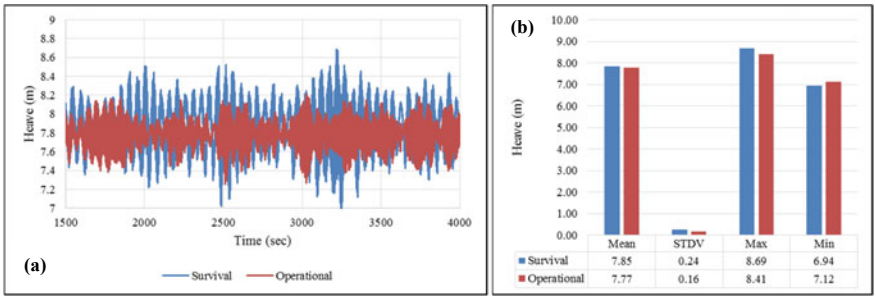

Fig. 8 Comparison of coupled dynamic heave responses of the Vcd60 in East coast under survival and operational conditions **a** in time domain and **b** statistically

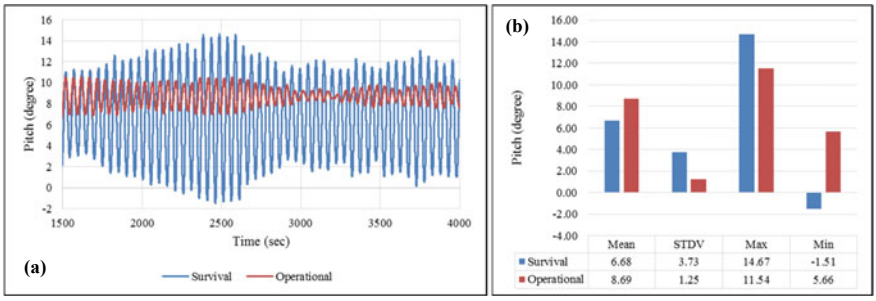

Fig. 9 Comparison of coupled dynamic pitch responses of the Vcd60 in East coast under survival and operational conditions **a** in time domain and **b** statistically

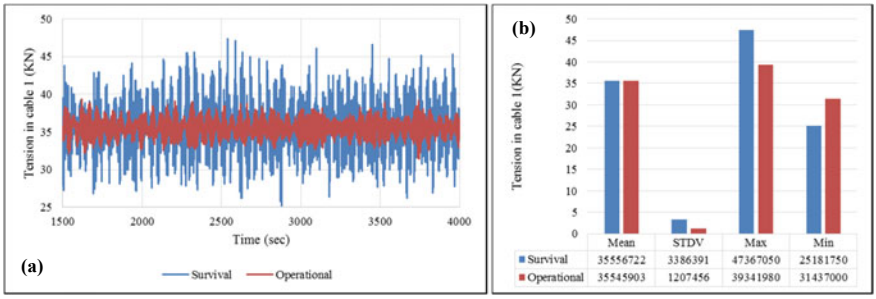

Fig. 10 Comparison of tension in cable 1 of the Vcd60 in East coast under survival and operational conditions **a** in time domain and **b** statistically

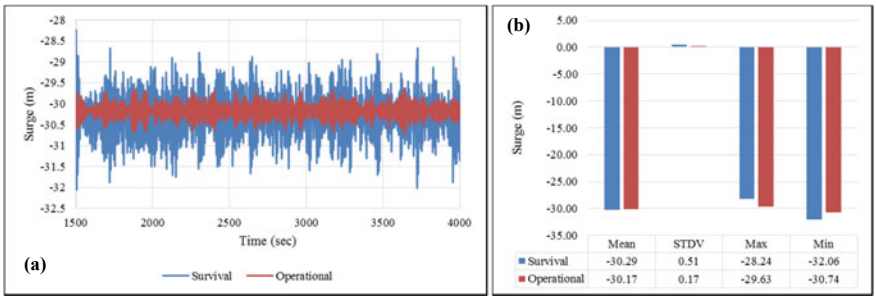

Fig. 11 Comparison of coupled dynamic surge responses of the Vcd60 in Gulf of Mexico coast under survival and operational conditions **a** in time domain and **b** statistically

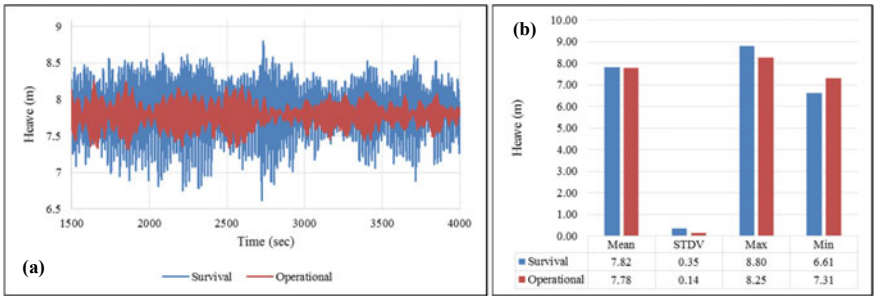

Fig. 12 Comparison of coupled dynamic heave responses of the Vcd60 in Gulf of Mexico coast under survival and operational conditions **a** in time domain and **b** statistically

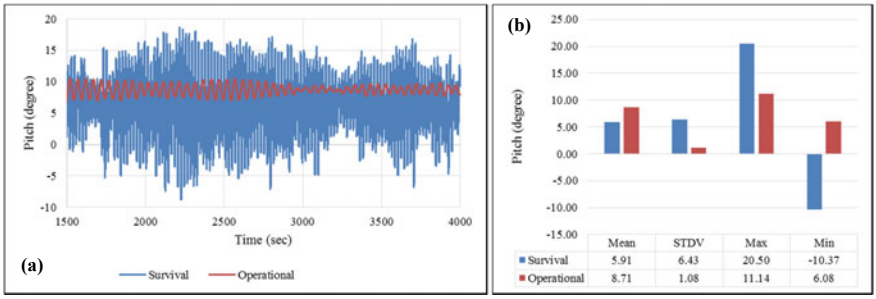

Fig. 13 Comparison of coupled dynamic pitch responses of the Vcd60 in Gulf of Mexico coast under survival and operational conditions **a** in time domain and **b** statistically

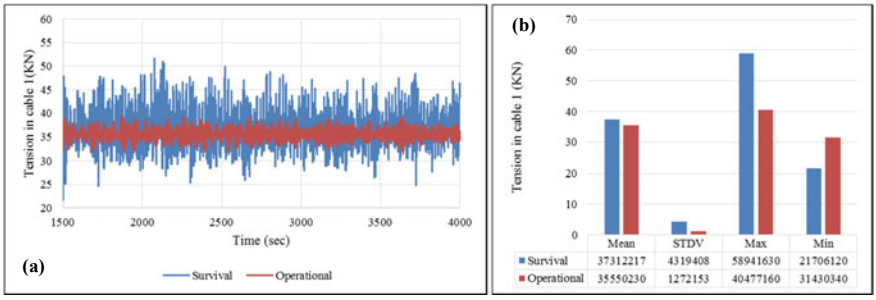

Fig. 14 Comparison of tension in cable 1 of the Vcd60 in Gulf of Mexico coast under survival and operational conditions **a** in time domain and **b** statistically

Through this present study, the application of the fluid–structure interaction enables detailed investigation into the complex fluid flow around the FOWT system. However, there is limitation in the matrix solver of AQWA [1], in the current model the part of the viscous damping effects cannot be included which means the cross-terms of the damping matrix are zero.

6 Conclusions

The applicability of V-shaped semi-submersible platforms in three different geographical locations (East, West and Gulf of Mexico coast) of USA has been assessed. Real metocean data of these regions obtained from National Data Buoy Centre were made use of during analysis. These data include wind speed, significant wave height, wave peak spectral period, wind direction and wave direction. Dynamic coupled analysis was carried out for a V-shaped platform under both the operational and survival conditions. The responses of the platform along three DOF namely surge, heave and pitch and the mooring line tension were analysed. The results showed that,

- West coast is the most inappropriate for the V-shaped platform as the responses of the platform were exceedingly large which is mainly due to the high waves in this region.
- A significant difference was observed in the responses of the platform under operational and survival conditions. The deviation in the surge response in the survival condition was found to be 4 times than that in the operational condition while the deviation in the pitch response in the survival condition was found to be 5.33 times the deviation in the operating condition.
- In the Gulf of Mexico coast significant pitch response was observed. The deviation in the pitch response in the survival condition was found to be almost 6 times as compared to that in the operational condition. The large pitch response may have a significant impact on the turbine performance.
- East coast has been found to be the most appropriate for deployment of a V-shaped semisubmersible platform as the responses along surge and heave directions and maximum pitch response are found to be much lesser.

Overall it can be said that the V-shaped or braceless semisubmersible platform is a promising new concept and can be used extensively in the offshore wind industry. Careful choice of diameter at the water line and pontoon radius can lead to an improvement of the V-shaped platform performance in different environmental conditions and water depths. Energy-absorbing devices can also be used for suppression of horizontal motion and vertical rotations of the V-shaped platforms. And lastly, for design and analysis of floating offshore platforms at a particular region, it is essential that realistic metocean data of that region are used so that accurate results are obtained.

Acknowledgements This work is funded by National Institute of Technology Durgapur.

References

1. ANSYS AQWA (2016) AQWA user's manual release 17.0. ANSYS Inc., Canonsburg (PA), USA
2. Butterfield S, Musial W, Jonkman J, Sclavounos P, Wayman L (2005) Engineering challenges for floating offshore wind turbines. In: Proceedings of the Copenhagen offshore wind conference, Copenhagen, Denmark, pp 377–382, 25–27 Oct 2005
3. Dey S, Saha K, Acharya P, Roy S, Banik AK (2017) Coupled dynamic responses of a semisubmersible-type Floating Offshore Wind Turbine (FOWT) under the combined action of irregular wave and turbulent wind. In: Proceedings of the international conference on ships and offshore structures, Shenzhen, China, 11–13 Sept 2017
4. Duan F, Hu Z, Liu G, Wang J (2016) Experimental comparisons of dynamic properties of floating wind turbine systems based on two different rotor concepts. Appl Ocean Res 58(2016):266–280
5. Duan F, Hu Z, Niedzwecki JM (2016) Model test investigation of a spar floating wind turbine. Mar Struct 49(2016):76–96
6. Huijs F, Bruijn RD, Savenije F (2014) Concept design verification of a semi-submersible floating wind turbine using coupled simulations. Energy Procedia 53(2014):2–12
7. Jonkman, BJ, Kilcher L (2012) TurbSim user's guide: version 1.06.00. Technical report, DEAC36-08-GO28308, National Renewable Energy Laboratory, Golden, Colorado
8. Kaimal JC, Wyngaard JC, Izumi Y, Cote OR (1972) Spectral characteristics of surface-layer turbulence. Q J R Meteorol Soc 98:563–589
9. Karimirad M, Michailides C (2015) V-shaped semisubmersible offshore wind turbine: an alternative concept for offshore wind technology. Renew Energy 83(2015):126–143
10. Karimirad M, Michailides C (2016) V-shaped semisubmersible offshore wind turbine subjected to misaligned wave and wind. J Renew Sustain Energy 8:023305
11. Koo BJ, Goupee AJ, Kimball RW, Lambrakos KF (2014) Model tests for a floating wind turbine on three different floaters. J Offshore Mech Arct Eng 136(2):020907
12. Liu Y, Li S, Yi Q, Chen D (2016) Developments in semi-submersible floating foundations supporting wind turbines: a comprehensive review. J Renew Sustain Energy Rev 60:433–449
13. Musial W, Butterfield S, Boone A (2004) Feasibility of floating platform systems for wind turbines. In: 42nd AIAA aerospace sciences meeting and exhibit, p 1007
14. Nielson FG, Hanson TD, Skaare B (2006) Integrated dynamic analysis of floating offshore wind turbines. In: Proceedings of the 25th international conference on offshore mechanics and arctic engineering. American Society of Mechanical Engineers, Hamburg, Germany, pp 671–679, 4–9 June 2006
15. Stewart GM, Robertson A, Jonkman J, Lackner MA (2015) The creation of a comprehensive metocean data set for offshore wind turbine simulations. Wind Energy 2016 19:1151–1159
16. Wang K, Ji C, Xue H, Tang W (2017) Frequency domain approach for the coupled analysis of floating wind turbine system. J Ships Offshore Struct 12(6):767–774

The Flow Hydrodynamics Around Tandem Cylinders

Ainal Hoque Gazi and Mohammad Saud Afzal

1 Introduction

From life science to engineering applications, turbulent flows are found everywhere in daily life. The practical application of flow past a bluff body in the domain of thermal and structure system is huge, some of the related such applications can be observed in [1–4]. A flow field is considered either laminar or turbulent based on Reynolds number, which is the ratio of the inertia force to the viscous force. With the change of Reynolds number, the random motion of fluid develops a variation in velocity and pressure [5]. Consequently, the momentum, the mass, and the energy of the flowing fluids are exchanged. The largest turbulent eddies interact with the mean flow and extract energy from it through a process known as vortex stretching. The angular momentum of the larger eddies is conserved during the process of vortex stretching, which maintains turbulence in the flow. Over time these large eddies become unstable and break into further smaller eddies. In this process, there is a cascading of energy from small to the smallest eddies. The energy cascading stops when the Reynolds number of the smallest eddies becomes unity. At this point, the viscosity dominates, and the energy dissipation occurs [6] and the intensity of the turbulence becomes more acute.

The turbulence created around the bridge pier loosens the sediment particles around the pier and the sediments are carried away from the vicinity of the pier, resulting in scour formation. The scour is considered as one of the major reasons behind the failure of bridges. The recent studies dealing with the scour are but not limited to [7–9]. To analysis this, fluid engineers require a potent tool for simulating the turbulence around the pier. Generally, Reynolds Averaged Navier Stokes (RANS), Large Eddy Simulation (LES), Direct Numerical Simulation (DNS) are used to model the turbulence phenomenon. In RANS model, the mean flow and the

A. H. Gazi (✉) · M. S. Afzal
Department of Civil Engineering, Indian Institute of Technology Kharagpur, Kharagpur, India

D. K. Maiti et al. (eds.), *Recent Advances in Computational and Experimental Mechanics, Vol II*, Lecture Notes in Mechanical Engineering,
https://doi.org/10.1007/978-981-16-6490-8_20

impact of the turbulence on the mean flow are the main features, which need a closure rule. The Boussinesq hypothesis are the classical closure method, which were formulated in 1872. Also in the RANS model, no care is taken when smoothing out the model equation, meaning the whole spectrum of the fluctuations are averaged out, and no special preference is given to any mode or scale. A different procedure for modeling more strong eddies is the LES. In LES, a filter is added to the vector fields which remove the specific fluctuating modes. Thus LES captures larger eddies by considering space filtering of the Navier Stokes equations in spite of time averaging.

In this paper, a comparative study of the flow hydrodynamics around tandem cylinders have been carried out using OpenFOAM toolbox for circular cylinders. The RANS and LES models are applied to observe flow hydrodynamics around tandem cylinders. The authors found that the study of flow around the tandem cylinder for both RANS and LES in the same study in an open channel flow is limited. Here, the authors have presented a detailed study of the flow physics around two tandem cylinder mainly highlighting the behavior of force coefficients and the vorticity with the variation of Reynolds number and gap ratios. This study can be further enhanced by performing laboratory experiment for further confirmation.

2 Numerical Model

The simulations presented in this paper are carried out in OpenFOAM5.0, which is a freely available source of C++ codes [10]. PisoFoam, an editable solver in OpenFOAM, was chosen for the purpose of simulation, which solves three-dimensional Navier–Stokes equations (NSE) for a transient, incompressible and turbulent flow. The solver is based on a finite-volume method and PISO (pressure-implicit with the splitting of operators) algorithm for pressure–velocity coupling. For the convective terms in the Navier Stokes equation, the central difference scheme is used; for pressure gradient and inviscid conditions, fourth-order accuracy is applied; for time integration, second-order implicit Euler method is applied. The volume of fluid (VOF) is used to capture the air–water interface. Further, a fraction function, α, is defined as the volume fraction of water in each cell. α is 0 means the cell is filled with air, and α is 1 means the cell is occupied by water; otherwise, $0 < \alpha < 1$ means cells are bisected by the free water surface.

The continuity and the Navier Stokes equation, in their simplified form, adopted in OpenFOAM are given by Eqs. (1) and (2).

$$\frac{\partial u_i}{\partial x_i} = 0 \tag{1}$$

$$\frac{\partial u_i}{\partial t} + u_j \frac{\partial u_i}{\partial x_j} = -\frac{1}{\rho}\frac{\partial p}{\partial x_i} + \frac{\partial}{\partial x_j}\left[(\nu + \nu_t)\left(\frac{\partial u_i}{\partial x_j} + \frac{\partial u_j}{\partial x_i}\right)\right] + g_i \tag{2}$$

where u is time-averaged velocity, p is pressure component, v is eddy viscosity, v_t is kinematic eddy viscosity and g_i is the body force.

2.1 Rans

RANS reduces the computational cost by averaging the flow quantity. In RANS equations the main focus is given to model the Reynolds stress $-\rho u_i u_j$. The turbulence closure is provided by k–ε [11] model as given by Eqs. (3) and (4).

$$\frac{\partial k}{\partial t} + u\frac{\partial k}{\partial x} + v\frac{\partial k}{\partial y} + w\frac{\partial k}{\partial z} = \frac{\partial}{\partial z}\left(\frac{v_t}{\sigma_k}\frac{\partial k}{\partial z}\right) + v_t\left(\left(\frac{\partial u}{\partial z}\right)^2 + \left(\frac{\partial v}{\partial z}\right)^2\right) - \varepsilon \quad (3)$$

$$\frac{\partial \varepsilon}{\partial t} + u\frac{\partial \varepsilon}{\partial x} + v\frac{\partial \varepsilon}{\partial y} + w\frac{\partial \varepsilon}{\partial z} = \frac{\partial}{\partial z}\left(\frac{v_t}{\sigma_\varepsilon}\frac{\partial \varepsilon}{\partial z}\right) + C_{\varepsilon 1}\frac{\varepsilon}{k}v_t\left(\left(\frac{\partial u}{\partial z}\right)^2 + \left(\frac{\partial v}{\partial z}\right)^2\right) - C_{\varepsilon 2}\frac{\varepsilon^2}{k} \quad (4)$$

where k is the turbulent kinetic energy and ε is the turbulent dissipation rate. The eddy viscosity is expressed by Eq. (5).

$$v_t = C_1\frac{k^2}{\varepsilon} \quad (5)$$

For the non-linear k-ε model, the following Boussinesq hypothesis is assumed to model the Reynolds stress ($\tau_{i,j}$)

$$\tau_{i,j} = 2v_t S_{i,j} - \frac{2}{3}k\partial_{i,j} \quad (6)$$

where $S_{i,j}$ is the average strain rate tensor. Constants for Eqs. (3), (4) and (5) have been used from [12], i.e., C_1,$C_{\varepsilon 1}$, $C_{\varepsilon 2}$, σ_k, $\sigma_\varepsilon = 0.09$, 1.44, 1.92, 1.0 and 1.3, respectively. First, the model geometry is defined, and meshes are constructed in blockMesh, with all the necessary boundary conditions in the respective directions. After setting all other parameters, simulation is started by the command PisoFOAM (the name of the solver in openFOAM is treated as a simulating command). The final results are viewed in third-party software paraview. The density of water is taken as 1000 kg/m^3 and the dynamic viscosity of the water is considered as 1.002×10^{-3} kg m^{-1} s^{-1} and kept constant for all of the cases.

2.2 Les

The LES has the capability to solve the 3D turbulence flow condition. The small eddies created in the flow field are modelled by sub-grid scale model, whereas the large scale eddies are calculated directly in the LES. To make this demarcation between small scale and large scale eddies, a filter function is used in NSE. The main equations in LES are obtained by filtering the NSE, as given below-

$$\frac{\partial \overline{u_i}}{\partial x_i} = 0 \tag{7}$$

$$\frac{\partial \overline{u_i}}{\partial t} + \overline{u_j}\frac{\partial \overline{u_i}}{\partial x_j} = -\frac{1}{\rho}\frac{\partial \overline{p}}{\partial x_i} + \frac{\partial}{\partial x_j}\left[\nu\left(\frac{\partial \overline{u_i}}{\partial x_j} + \frac{\partial \overline{u_j}}{\partial x_i}\right)\right] - \frac{\partial \tau_{i,j}}{\partial x_j} \tag{8}$$

where $\bar{u}_{i,j}$ = velocity component along the flow direction of the resolved scale and p = corresponding pressure. Here, the Reynolds stress is considered as SGS tensor, which is expressed as following-

$$\tau_{i,j} = \overline{u_{i,j}u_{i,j}} - \overline{u_{i,j}u_{i,j}} \tag{9}$$

For the Smagoinsky-Lilly model, the SGS eddy viscosity is modelled as

$$\mu_t = \rho L_s^2 \sqrt{2\overline{S}_{i,j}\overline{S}_{i,j}} \tag{10}$$

where L_s = min (kd, $C_s(\Delta x \Delta y \Delta z)^{1/3}$) = mixing length for subgride scale; d = distance between the nearest walls; κ = von-Karman constant, and C_s = Smagorinsky coefficients.

3 Mesh Convergence Study

Mesh convergence studies are performed to lower the cost of the simulation without affecting the accuracy of the results. In this study meshes are divided into three categories based on the number of elements, viz., coarse (A, D), medium (B, E), and fine (C, F) (Tables 1 and 2). Coefficient of drag (C_d) and coefficient of lift (C_l) are

Table 1 Mesh convergence study for RANS

Mesh	Element number	C_d	C_l
Coarse (A)	57,430	1.07	0.0693
Medium (B)	141,820	1.180	0.0694
Fine (C)	262,700	1.198	0.0711

Table 2 Mesh convergence study for LES

Mesh	Element number	C_d	C_l
Coarse (D)	281,423	1.089	0.701
Medium (E)	564,440	1.210	0.704
Fine (F)	712,310	1.230	0.721

considered for the convergence test, which are calculated as $C_d = 2F_x/\rho u^2 D$ and $C_l = 2F_y/\rho v^2 D$, where u and F_x denote stream wise velocity and force; v and F_y denote spanwise velocity and force.

From Tables 1 and 2 it can be observed that the difference between the coefficient of lift for coarse and medium meshes, for both RANS and LES, are insignificant (0.14% between A and B; 0.42% between D and E). However, the observed difference between the coefficient of drag for coarse and medium are quite high (10.28% between A and B; 11.11% between D and E). Further investigating, the difference between the coefficient of lift as well as the difference between the coefficient of drag for medium and fine meshes, for both RANS and LES, are negligible (the difference of C_l between B and C is 2.44%, the difference of C_l between E and F is 2.7%, the difference of C_d between B and C is 1.52%, and the difference of C_d between E and F is 1.65%, respectively). Hence, mesh B for RANS and E for LES are considered in this study.

4 Validation

To validate the model, the coefficients of drag and lift obtained in this paper are compared with the coefficients of drag and lift presented by previous researchers. For the validation, coefficients of drag and lift in tandem cylinders are calculated based on Reynolds number, $R_e = 25{,}348$.

At gap ratio $(S/D) = 4$ and Reynolds number $R_e = 25{,}348$, the values of $C_{d1} = 1.1$ and $C_{d2} = 0.45$ for circular cylinder in tandeare obtained in this study, respectively. Similarly, At the gap ratio $(S/D) = 4$ and Reynolds number $R_e = 25{,}348$, the values of $C_{l1} = 0.2$ and $C_{l2} = 0.7$ for circular cylinder in tandem are obtained in this study, respectively (Table 3). This result agree well with the results of [13, 14]

5 Results and Discussions

In this section, all of the configurations for different Reynolds numbers and gap ratios are analyzed. For all of the cases, smallest grid size is chosen as 1.2, 1.5 and 0.30 mm along x, y and z directions, respectively. Time-steps $\Delta t = 0.0001$, 0.0002 and 0.00001 s are used in the simulations and the Courant number is maintained lesser than unity. Melville and Chiew [15] concluded that for getting equilibrium

Table 3 Comparative results for tandem cylinders. C_{d1} and C_{d2} are the drag coefficients at the upstream and the downstream of the cylinder, C_{l1} and C_{l2} are the lift coefficients at the upstream and the downstream of the cylinder, respectively

Researches	R_e	S/D	C_{d1}	C_{d2}	C_{l1}	C_{l2}
Alam et al. [13]	20,000	2	1.05	−0.24	0.03	0.55
	20,000	5	1.22	0.29	0.44	0.71
Kitagawa and Ohta [14]	22,000	2	0.88	0.02	0.13	0.58
	22,000	5	1.17	0.50	0.20	1.00
Present study						
Circular cylinder	25,348	2	1.01	0.32	0.17	0.55
	25,348	3	1.08	0.33	0.19	0.58
	25,348	4	1.10	0.45	0.20	0.70

scour depth in a small-scale laboratory experiment, the experiment should be done for several days. However, the main objective of this study is to compare the flow hydrodynamics around twin piers in between RANS and LES; hence, the test duration is not considered very important.

The flow hydrodynamics around single cylinder are different compared to the flow hydrodynamics around two cylinders. The reason is that the flow at the downstream becomes unsteady and produces different vortex shedding zones in the middle of two cylinders and a discontinuity in the flow pattern is observed. This discontinuity depends on Reynolds number and center to center distance between two cylinders [16]. Zdravkovich [17] described the wake interference in tandem cylinder, where the upstream cylinder behaves as a single body and the wake created around the downstream cylinder is strongly influenced by the upstream cylinder.

Here, simulations have been carried out around two circular cylinders placed in tandem for Reynolds number, $R_e = 25{,}348$ and 126,746 with gap ratio, $S/D = 2$, 3 and 4. The velocity at the inlet is considered as 0.5 m/s and 2.5 m/s. A comparison of flow hydrodynamics simulated by Reynolds Average Navier Stoke simulations (RANS) and Large Eddy Simulations (LES) have been made. In RANS k-ε turbulence model and in LES Smagorinsky-Lilly turbulence model is used. Results of velocity distributions simulated in RANS and LES are displayed in Fig. 1 for Reynolds numbers, $R_e = 126{,}746$.

As can be seen from Fig. 1 that at gap ratio, $S/D = 2$ and Reynold number, $R_e = 126{,}746$, vortices do not shed in the gap in RANS but it starts to form at gap ratio $S/D = 2$ in LES. This process of developing vorticity keeps on moving alternately with the increase of gap ratios, $S/D = 3$ to 4. However, the downstream cylinder interference interacts with this increasing vortex and hence modifying the forces experienced by the two cylinders. For smaller spacing ($S/D = 2$), vortices are not observed in the gap between the cylinders, although, the interaction with the surrounding (bottom or top side) of the downstream cylinder is observed. Whereas, at a higher gap ratio ($S/D = 3$, 4), vortices are affected more by the surrounding (bottom, top and front sides) of the cylinders, which leads to form a chaotic flow in the flow field.

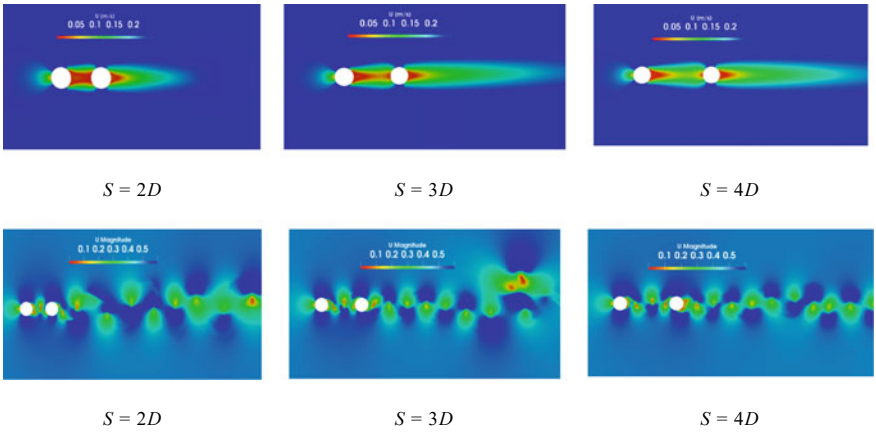

Fig. 1 Velocity variation around tandem cylinders simulated in RANS and LES for circular piers. Upper row is for RANS and lower row is for LES. S = center to center distance of piers, D = diameter of piers. $R_e = 126{,}746$

On the other hand, when fluid particles past by the cylinders, then slow-moving fluid layers create boundary layers. Due to the presence of strong viscosity resistance, flow momentum becomes less in boundary layers. Further increasing the pressure in the flow direction, fluid particles have to overcome this increasing pressure with the addition of high viscosity resistance. Hence, fluid particles either stop or reverse. In this way, fluid layers detached from the solid surface. These separated layers create a high amount of turbulence at the rear side of the cylinder, which is called a wake vortex. It is observed that narrow and wide wakes are generated in the gap region and moved from one cylinder to another cylinder. Streamline plot for Reynolds numbers, $R_e = 25{,}348$ and 126,746 in RANS and LES are shown in Fig. 2, which showed that the flow intensity in the gap region is more complicated than the surroundings of the cylinders. At Reynolds numbers, $R_e = 253$ (laminar flow), a symmetric pattern of streamlines is noticed (not shown here). At Reynolds number, $R_e = 25{,}348$, a series of unsteady pattern is observed in LES. At Reynolds number, $R_e = 126{,}746$, present more comparative results between RANS and LES (Fig. 2). The formation of recirculation zones is noticed earlier in LES than RANS. The random pattern is explained as the irregular breakup of vortices..

The Reynolds number plays a vital role on the wake of two cylinders. Igarashi [18] reported six types of flow pattern in tandem cylinders for $R_e = (0.87\text{–}5.2) \times 10^4$. Similar kind of flow patterns were noticed by [17] at $R_e = 6.0 \times 10^4$.

The only difference in between their observation is that the former found two asymmetric and symmetric vortices in the gap in the cylinders. To study the effect of R_e on the force coefficients in tandem cylinders, simulated in the LES and RANS, a plot of R_e versus C_d and R_e versus C_l is shown in Fig. 3. At low R_e, the variation in the values of C_d and C_l are more in LES than in RANS is observed, whereas at higher R_e the variation in the values of C_d and C_l become negligible. Also, for same

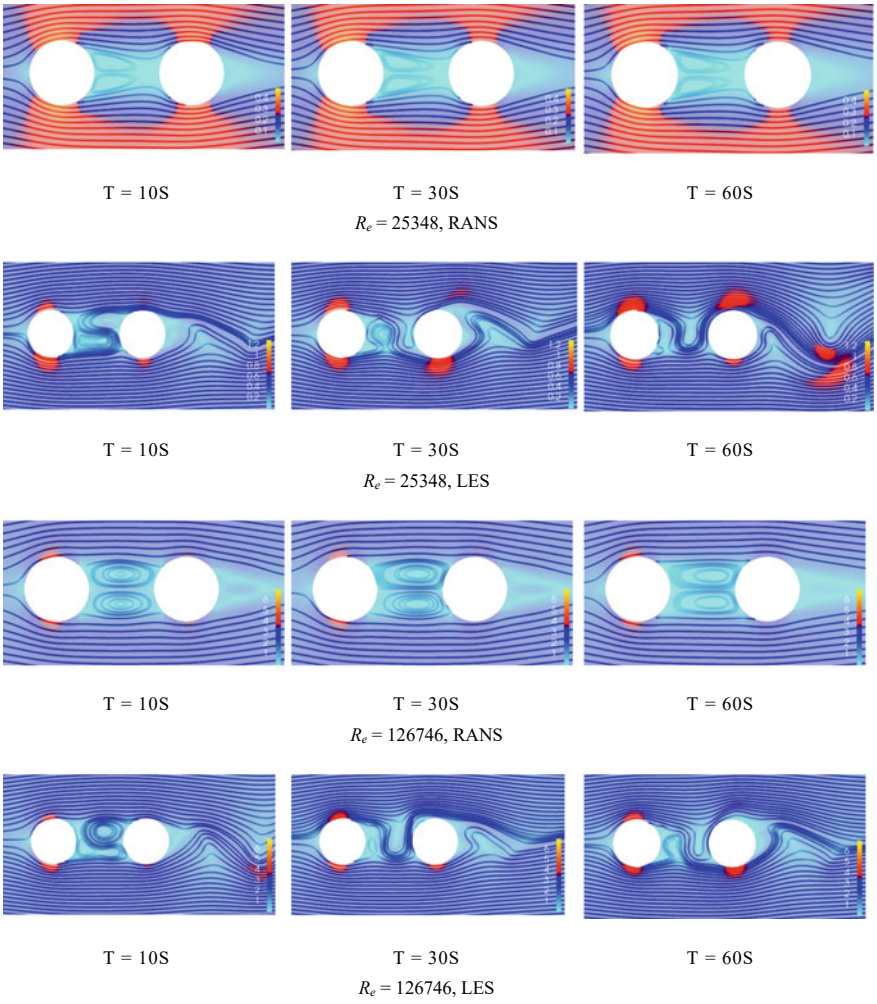

Fig. 2 Evolution of velocity contour for $R_e = 25{,}348$ and $126{,}746$ at the gap $S = 3D$

R_e the values of the coefficients C_d and C_l increase as the gap between the cylinders increases until a critical point ($S = 4D$) is reached, whereafter a fixed value of C_d and C_l are obtained. The force coefficients are calculated in this study as $C_d = 2F_x/\rho u^2 D$ and $C_l = 2F_y/\rho u^2 D$, where F_x is stream-wise force and F_y is spanwise force. The average drag coefficients on the upstream cylinder are about 0.86 in RANS and 0.88 in LES and in the downstream cylinder it is 0.28 in RANS and 0.31 in the LES for $S/D = 2$ and $R_e = 126{,}746$, respectively.

The reason is that the downstream cylinder is affected by the wake of the upstream cylinder, resulting in lower mean drag concerning the upstream cylinder at smaller spacing. Further increasing of spacing, the average drag coefficients on the upstream

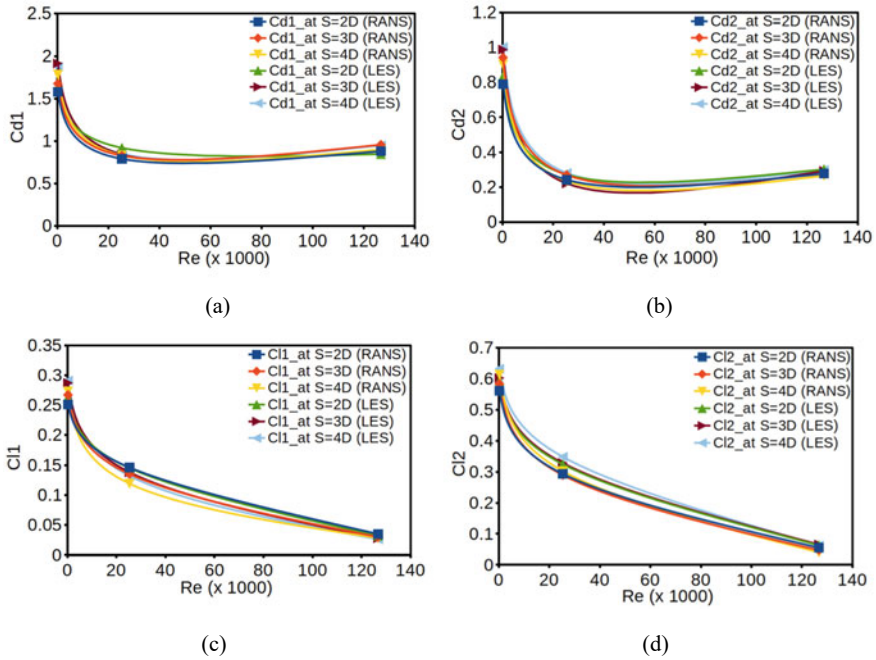

Fig. 3 C_d versus R_e for tandem circular cylinders simulated in RANS and LES

cylinder becomes about 0.89 in RANS and 1.05 in LES and in the downstream cylinder it is 0.29 in RANS and 0.32 in the LES for $S/D = 4$ and $R_e = 126{,}746$, respectively. These results are compatible with the existing experimental data [14].

It is noticed that for smaller spacing ($S/D = 2$), the drag on the first cylinder is almost unaltered in RANS simulation, but in LES alteration in the value is observed. However, the drag on the downstream cylinder is found periodic for both RANS and LES. The present result agreed well with previously existing data. When the spacing in between the cylinder is large ($S/D \geq 4$), vortex shedding from each of the cylinder dominates. This is confirmed by [19]. At smaller spacing, stronger interaction is noticed. The mean value of lift coefficients for a large number of cycles is found to be almost zero at higher spacing. The fluctuation of lift coefficients in RANS is more symmetric than in the LES is also observed. At lower spacing, there is higher pressure in the middle of the cylinders compared to the higher spacing. This makes lower drag on the downstream cylinder at smaller spacing.

Acknowledgements The support from the project of the Institute Scheme for Innovative Research and Development (ISIRD) titled "3D CFD modeling of the hydrodynamics and local scour around offshore structures under combined action of waves and current" from IIT Kharagpur is recognized.

References

1. Derakhshandeh JF, Alam MM (2020) Reynolds number effect on the flow past two tandem cylinders. Wind Struct 30(5):475–483
2. Arif MR, Hasan N (2020) Large-scale heating effects on global parameters for flow past a square cylinder at different cylinder inclinations. Int J Heat Mass Transf 161:120237
3. Arif MR, Hasan N (2019) Vortex shedding suppression in mixed convective flow past a square cylinder subjected to large-scale heating using a non-Boussinesq model. Phys Fluids 31(2):023602
4. Arif MR, Hasan N (2020) Effect of thermal buoyancy on vortex-shedding and aerodynamic characteristics for fluid flow past an inclined square cylinder 38(2):463–471. http://iieta.org/journals/ijht
5. Xu S, Zhou Y, So R (2003) Reynolds number effects on the flow structure behind two side-by-side cylinders. Phys Fluids 15:1214–1219
6. Dey S (2014) Fluvial hydrodynamics. Springer, Berlin
7. Gazi AH, Afzal MS, Dey S (2019) Scour around Piers under Waves: Current Status of Research and Its Future Prospect. Water 11:2212
8. Gazi AH, Afzal MS (2019) A new mathematical model to calculate the equilibrium scour depth around a pier. Acta Geophys 1–7
9. Gazi AH, Purkayastha S, Afzal MS (2020) The equilibrium scour depth around a pier under the action of collinear waves and current. J Marine Sci Eng 8:36
10. Weller HG, Tabor G, Jasak H, Fureby C (1998) A tensorial approach to computational continuum mechanics using object-oriented techniques. Comput phys 12:620–631
11. Jones W, Launder BE (1972) The prediction of laminarization with a two-equation model of turbulence. Int J Heat Mass Trans 15:301–314
12. Rodi W, Mansour N (1993) Low Reynolds number k-ε modelling with the aid of direct simulation data. J Fluid Mech 250:509–529
13. Alam MM, Moriya M, Takai K, Sakamoto H (2003) Fluctuating fluid forces acting on two circular cylinders in a tandem arrangement at a subcritical Reynolds number. J Wind Eng Ind Aero 91:139–154
14. Kitagawa T, Ohta H (2008) Numerical investigation on flow around circular cylinders in tandem arrangement at a subcritical Reynolds number. J Fluids Struc 24:680–699
15. Melville BW, Chiew YM (1999) Time scale for local scour at bridge piers. J Hydraul Eng 125:59–65
16. Mizushima J; Suehiro N (2005) Instability and transition of flow past two tandem circular cylinders. Phys Fluids 17:104107
17. Zdravkovich M (1988) Review of interference-induced oscillations in flow past two parallel circular cylinders in various arrangements. J Wind Eng Ind Aero 28:183–199
18. Igarashi T (1981) *Characteristics of the flow around two circular cylinders arranged in tandem*: 1st report. Bulletin of JSME 24:323–331
19. Prsic MA, Ong MC, Pettersen B, Myrhaug D (2014) Large Eddy Simulations of flow around a smooth circular cylinder in a uniform current in the subcritical flow regime. Ocean Eng 77:61–73

Machine Learning-Based Molecular Dynamics Simulations of Monolayered Graphene

Kritesh Kumar Gupta, Lintu Roy, and Sudip Dey

1 Introduction

Molecular dynamics (MD) simulations are widely adopted by the research community for nano-scale characterization of materials and simulation of nano-scale applications. Following the first experimental realization of monolayer graphene in 2004, an extensive amount of experimental and theoretical research has been carried out to explore the potential of this 2D wonder material. For instance, Lee et al. [1] experimentally investigated the mechanical strength and stiffness of monolayer graphene and reported that graphene is strongest and lightest material known.

Being a nano-scale 2D material, the graphene has limited experimental results published, moreover the experimental characterization of monolayer graphene has few limitations in terms of time, cost and precision. In this regard, the molecular dynamics simulation arises as an alternative approach to characterize nano-scale materials such as graphene. To this end, an extensive molecular simulation has been carried out by a lot of researchers to explore the mechanical characteristics of monolayer graphene [2–6]. The findings of these literature revealed that there are few external parameters which influences the fracture characteristics of graphene. These factors are reported as temperature, strain rate, topological defects and atomic inclusions [7–11]. However, the molecular simulations are intensive and computationally expensive in nature. The complex material systems with large number of atoms even require a supercomputing facility to conduct the molecular simulations. So it becomes next to impossible to conduct the simulations iteratively to carry out the robust and comprehensive analysis such as sensitivity analysis and optimization [12]. This calls for an alternative approach, which starts with fewer molecular simulations and predicts the characteristics for large number of unknown samples. A few

K. K. Gupta (✉) · L. Roy · S. Dey
Department of Mechanical Engineering, National Institute of Technology Silchar, Silchar, India
e-mail: kritesh_rs@mech.nits.ac.in

D. K. Maiti et al. (eds.), *Recent Advances in Computational and Experimental Mechanics, Vol II*, Lecture Notes in Mechanical Engineering,
https://doi.org/10.1007/978-981-16-6490-8_21

groups have come up with the solution for this by implementing machine learning approaches with MD simulations to predict the characteristics of nano-scale materials [13–16]. These studies revealed that the huge numbers of molecular simulations were carried out to create the training and test data samples for constructing machine learning models. Few other groups combined soft computing methods and MD simulation to form a prediction-based models by running comparatively lesser molecular simulations [17–20].

With the concise literature review presented in the preceded section, it can be observed that there are statistical ways available which can be clubbed with MD simulations in order to make the molecular simulations more robust and lesser computationally expensive. In the present study, our objective is to club the design of experiment, MD simulations and machine learning approach (support vector machines) to construct the prediction-based model which predicts the fracture strength of graphene subjected to variation in temperature and applied strain rate. In this order, Sect. 2 briefly describes the overview of support vector machines, molecular dynamics simulation and methodology of machine learning-based molecular dynamics simulation (MLBMD). The validation and interpretation of results are provided in Sect. 3. Section 4 provides the conclusion of the present study.

2 Methodology

2.1 Support Vector Regression (SVR)

The Support Vector Machine (SVM) is one of the most versatile approaches of supervised machine learning. It is popularly used for the classification problems and utilizes the kernel tricks to model non-linear decision boundaries. It was further used for the regression problems due to its robust nature, sparse solution and good generalization. In the present study, we employed Statistics and Machine Learning Toolbox of MATLAB [21] which applies the nonlinear epsilon-insensitive SVM (ε-SVM) regression. The training dataset comprises the input features and corresponding observed responses where each instance is synchronized to high dimensional space. The objective of SVR is to reach at a function *f(x)* that deviates from the observed response variables 'y_n' by a value 'ε' and is as flat as possible. For linear function, f may be defined as-

$$f(x) = wx + b \qquad w \in X,\ b \in \Re \tag{1}$$

For the minimization of Euclidean norm-

$$\begin{aligned} &\min \frac{1}{2}\|w\|^2 \\ Subject\ to- \\ &y_i - wx_i - b \leq \varepsilon \\ &wx_i + b - y_i \leq \varepsilon \end{aligned} \tag{2}$$

The above problem is applied when function exists and approximates all the elements of sample space with precise ε. SVR can further extend the problem for nonlinear functions, due to the presence of dual formulation. With the implementation of Lagrange multipliers, the standard dualization method is expressed as-

$$L(\alpha) = \frac{1}{2}\sum_{i=1}^{N}\sum_{j=1}^{N}(\lambda_i - \lambda_i^*)(\lambda_j - \lambda_j^*)K(x_i, x_j) + \varepsilon\sum_{i=1}^{N}(\lambda_i - \lambda_i^*) - \sum_{i=1}^{N} y_i(\lambda_i - \lambda_i^*)$$

Subject to -

$$\sum_{i=1}^{N}(\lambda_n - \lambda_n^*) = 0, \quad \text{where } \lambda_i,\ \lambda_i^* \in (0, C) \tag{3}$$

where C refers to the trade-off between the flatness of the *f(x)* and the threshold deviation larger than ε are tolerated. The new values are predicted using the function-

$$f(x) = \sum_{n=1}^{N}(\lambda_n - \lambda_n^*)K(x_n, x) + b \tag{4}$$

The further details of the SVR approach may be referred from the article by Trafalis and Ince [22]. To evaluate the accuracy and performance of SVR-based prediction model the correlation coefficient (R^2 value) is observed. The R-square (correlation coefficient) is calculated by-

$$R^2 = 1 - \frac{\sum_{i=1}^{n}(y_i - f_i)^2}{\sum_{i=1}^{n}(y_i - \overline{y})^2} \tag{5}$$

where, y is the observed value, f is the predicted value, $\overline{y}$ is the mean of observed value, and i denotes the sample index. The value of R^2 provides the statistical signification of closeness of the predicted points to the regression line. It determines goodness of fit for any model, and its value is always in between 0 to 1 [23].

2.2 Molecular Dynamics (MD) Simulation

The uniaxial tensile deformation is performed by employing the open-source molecular dynamics package LAMMPS [24], while the Tersoff [25] potential is used as the interatomic potential between an individual carbon atoms. Another open source tool, VMD [26] is utilized to construct the pristine graphene sheet of 5 nm (nanometers) edge dimensions and for the generation of data files required for running MD simulations. The periodic boundary conditions were implemented in each direction of modeled 2D material. The application of periodic boundary removes the boundary effects induced by the finite size. Before the molecular simulation of uniaxial tensile deformation, the energy minimization for the pristine structure is carried out by adopting conjugate gradient method; while to make sure that the pressure in the perpendicular directions of tensile deformation is zero, NPT ensemble is utilized. The timestep (interval of each iteration) of 1 fs (femtoseconds) is used in the whole process of uniaxial deformation of graphene. The simulation is conducted with the temperature in the range of 200 K to 1000 K, and applied strain rate in the range of 0.0005/ps to 0.005/ps. The range of temperature is selected on the basis of conditions the graphene sample may experience while synthesis and the range of strain rate is selected on the basis of the strain rate used in earlier theoretical studies [13]. The precision of the findings drawn from the molecular simulations relies on using an appropriate force field. Tersoff potential is one of the majorly used force field to mimic the carbon nanostructures. It has been reported by the researchers in the past that in general the original Tersoff potential overestimates the characteristics of graphene while conducting MD simulations. The change in the few parameters of Tersoff potential has been suggested by these groups to produce accurate mechanical properties of graphene [27–29]. The changes proposed by these groups are found useful when it comes to produce exact mechanical characteristics of pristine graphene. In the present study we used the modified interatomic potential parameters of Tersoff (refer to the Table 1) suggested by Rajsekaran et al. [29].

The atomic forces of the material system in consideration are determined with the help of potential field, by which further atomistic pressure and stress can be determined. The present study calculates the virial stress, which denotes the stress times volume (stress X volume). So the stress values determined by the LAMMPS are further divided by the volume of the material system.

2.3 Simulation Methodology

In the present study, we used temperature (T in the range of 200 K-1000 K) and strain rate (SR in the range of 0.0005/ps to 0.005/ps) as the input features and the design of experiment (DOE) algorithm is used to create a sample space for full factorial design with six levels of variation in each parameter. Further, the D-optimal approach is used to optimally select the N (32) samples as the training data from the sample

Table 1 Modified Tersoff potential parameters (modification depicted by bold blue letters)

Parameters	γ	***A(eV)***	***B(eV)***	$\lambda_1(\text{Å}^{-1})$	$\lambda_2(\text{Å}^{-1})$	***N***	***C***	$\beta\ (\times 10^{-7})$	***d***	***h***	***R(Å)***	***D(Å)***
Original Tersoff	1.0	1393.6	346.74	3.4879	2.2119	0.72751	38,049	1.5724	4.3484	-0.57058	1.8	0.15
Modified Tersoff [29]	1.0	1393.6	**430**	3.4879	2.2119	0.72751	38,049	1.5724	4.3484	**-0.930**	**2.1**	**0.00**

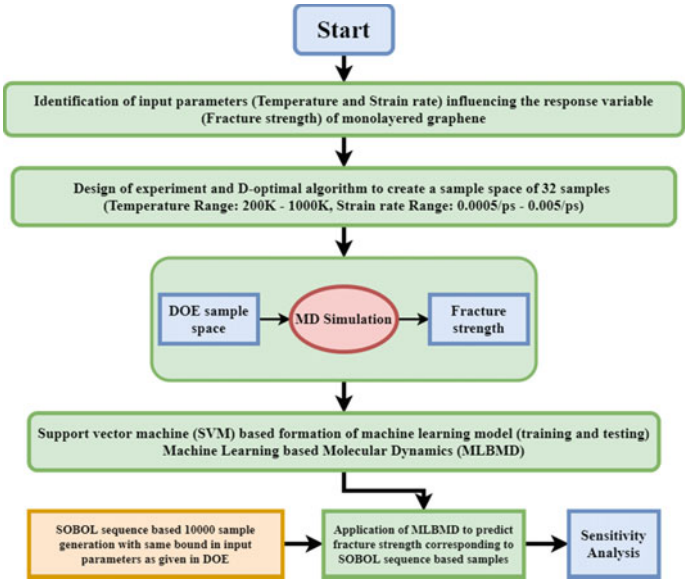

Fig. 1 The flowchart of MLBMD

space created by DOE. The MD simulations are carried out for these 32 samples to determine the fracture strength of graphene. The N input features (temperature and strain rate) and their corresponding response variable (fracture strength) are used to train the SVM-based machine learning model. The testing sample space (16 in no.s) is created with the help of SOBOL sequence sampling with the same bound (T: 200-1000 K & SR: 0.0005–0.005/ps) of input features. The prediction for the fracture strengths of the test sample is carried out with the help of SVM based machine learning model. The predicted values are compared with the corresponding MD simulation results with the help of scatter plots to assess the accuracy (error plot) of the model. Figure 1 illustrates the flowchart of the simulation methodology. Once the accuracy of the SVM-based machine learning model is established, the large number (10,000) of samples are generated by employing SOBOL sequence sampling, and these samples are generated within the same bound of input parameters as the training and testing sample space. The SVM-based model is used to predict the fracture strength for these large number of samples.

3 Results and Discussion

At first, the fracture strength of monolayered graphene determined by MD simulation is validated with the values reported in the earlier published literatures. The uniaxial deformation of monolayered graphene is carried out at room temperature (300 K)

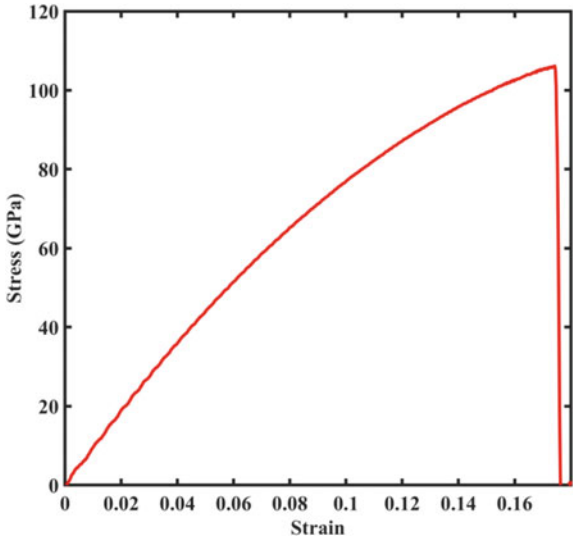

Fig. 2 Stress–strain plot of graphene

and with the applied strain rate of 0.001 /ps. The graphene is found to be failing at 106.1 GPa which is in the vicinity of the experimental observation of 130 ± 10 GPa [1], and few MD-based studies which reported failure strength in the range of 90–132 GPa [3, 28–30]. The stress–strain plot for the graphene at the conditions of validation is illustrated in Fig. 2. Once the adequate confidence is acquired with the validation of the fracture strength determined by MD simulation, further studies are carried out.

3.1 Parametric Study

The uniaxial tensile deformation of monolayer graphene is carried out in the present study at various temperatures in the range of 200 K–1000 K. Similarly the effect of.

variation in applied strain rate on the fracture strength of graphene is studied. It is observed that the variation in temperature has the drastic adverse effect on the fracture strength of graphene, while the variation in strain rate shows very small influence on it. From the variation plots illustrated in Fig. 3, it is revealed that the fracture strength reduces by 27% when the temperature is varied from 200 to 1000 K, whereas around 1% increase is observed in the fracture strength when strain rate is varied from 0.0005 /ps to 0.005 /ps. While varying the temperature, the strain rate is kept at 0.0005 /ps and while varying strain rate a temperature of 200 K is maintained.

The dominance of temperature over strain rate is confirmed by the Pareto analysis depicted in Fig. 4. Figure 4 illustrates the significance of individual input parameters and their interaction on the fracture strength of graphene. The bars crossing the

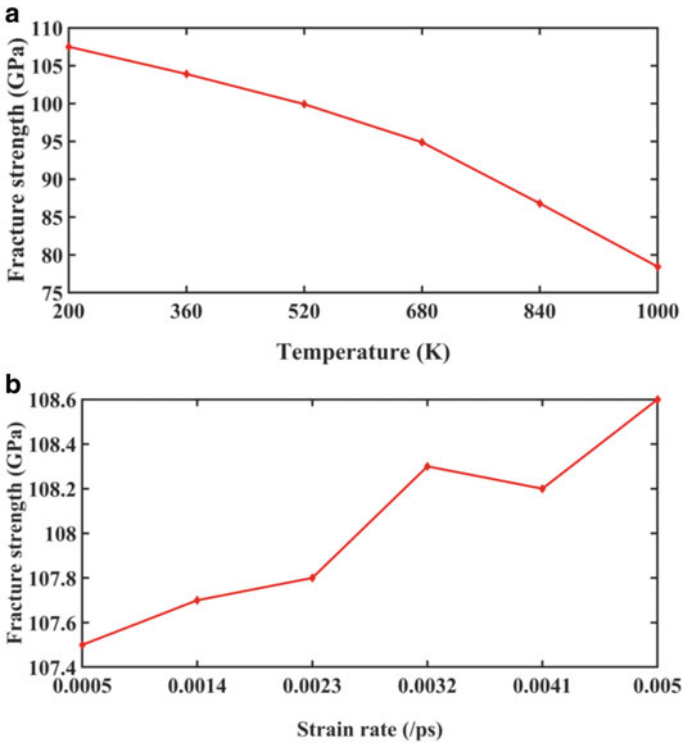

Fig. 3 Variation in fracture strength of monolayer graphene **a** with respect to variation in temperature **b** with respect to variation in strain rate

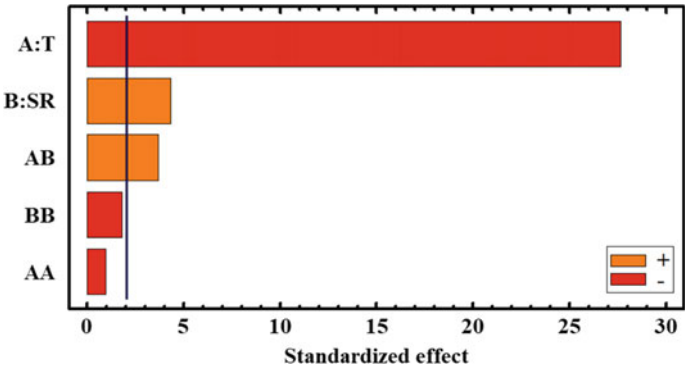

Fig. 4 Pareto analysis for the significance of individual parameters on the fracture strength of graphene

vertical blue line (A, B, and their interaction AB) are most significant in the determination of fracture strength of graphene. "A" refers to the temperature, and "B" refers to the strain rate.

3.2 Machine Learning-Based Molecular Dynamics (MLBMD)

The analysis carried out in the preceded section is based on the MD simulations conducted for the 32 samples derived through DOE. The fracture strength of graphene is determined for each instance of 32 samples with the help of MD simulations. In the next step, the dataset created with the MD simulation is used to train the SVM-based machine learning model. The accuracy of the trained model is assessed by observing R^2 value, which was found 0.95 for the training scatter plot (refer to Fig. 5a). After the model was successfully trained, the test dataset of 16 samples was created with the SOBOL sequence sampling using the same bound of the input parameters (T: 200 K–1000 K, SR: 0.0005/ps-0.005/ps) as used for training the model.

The different sampling techniques are utilized for constructing the training (DOE) and testing (SOBOL sequence) datasets to enforce the sound generalization ability of SVM-based machine learning model toward the unknown sample points. The MD simulation is conducted for the instances in test dataset and the corresponding results of MD simulations are compared with the predicted results derived from the SVM trained model (refer to Fig. 5b). The error analysis is carried out for the test dataset which is illustrated by the probability density function (pdf) plot depicted in Fig. 5c. The error plot reveals that the percentage error in the predicted fracture strength was within $\pm$ 5%. With the adequate confidence corroborated with the accuracy of SVM-based machine learning model to predict fracture strength of graphene. The 30,000 unknown samples were generated with the help of SOBOL sequence sampling with the same upper and lower bound in the input parameters as kept while training and testing the model. These 30,000 samples comprised with 10,000 samples containing variation in only temperature and constant strain rate maintained at 0.0005 /ps, another 10,000 samples containing variations in strain rate and constant temperature maintained at 200 K, and 10,000 samples of data which contains the variation in both (compound) the input parameters. The fracture strength of graphene predicted for these 30,000 samples is illustrated as pdf plots shown in Fig. 6a. The prediction results for these unknown large number of samples revealed that the occurrence bound of predicted fracture strength is similar to the fracture strength determined using MD simulations (on comparing Figs. 5a and 6a). The relative coefficient of variation (sensitivity index) is determined to back up the dominance of variation in temperature over the variation in strain rate for the corresponding variation in fracture strength of graphene (refer to Fig. 6b).

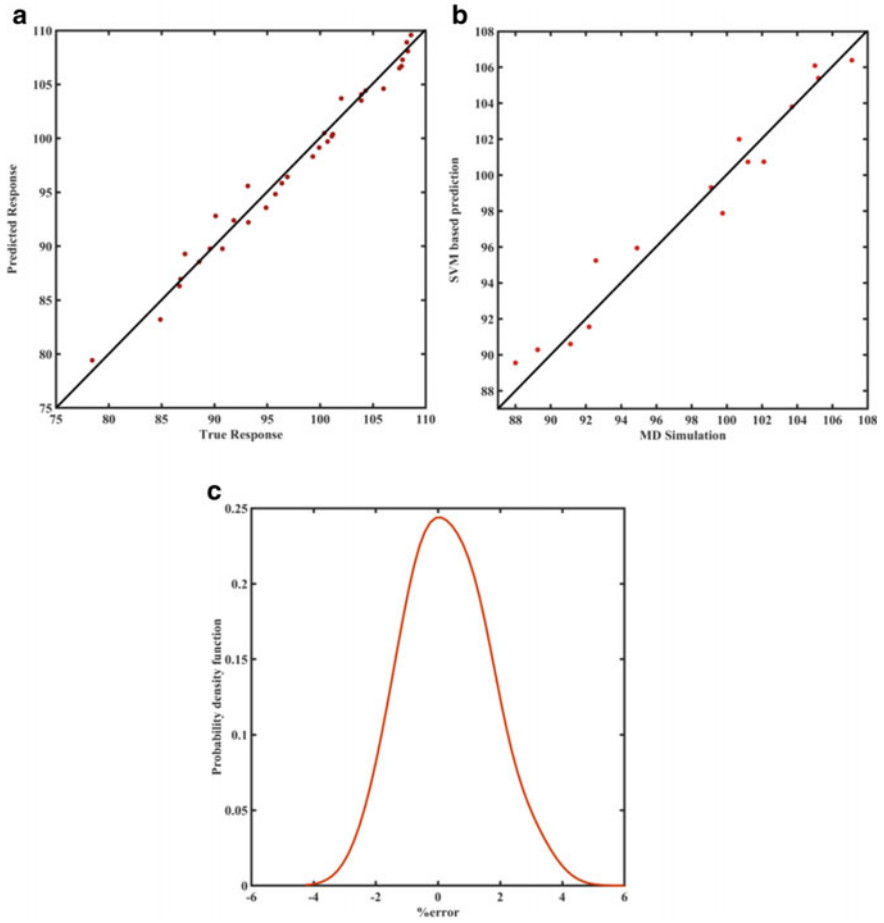

Fig. 5 Validation of SVM-based machine learning model. **a** Training the SVM-based machine learning model with 32 samples derived through DOE and MD simulations **b** Testing the model with the 16 samples derived from SOBOL sequence sampling and MD simulation **c** The error plot (pdf) depicting the percentage error of predicted results with respect to the MD simulation

4 Conclusion

In the present study, we presented a support vector machine-based prediction of fracture strength of graphene. The model is formed with the help of dataset derived by running few set of MD simulations. The model is trained with the MD simulation results of 32 samples derived from DOE and tested with the different set of 16 samples generated by using SOBOL sequence sampling. However, the upper and lower bound of the input features i.e. temperature and strain rate is kept same (T: 200 K-1000 K, SR: 0.0005/ps-0.005/ps). It is observed that the SVR-based machine learning demonstrates the impressive generalization ability, where the prediction

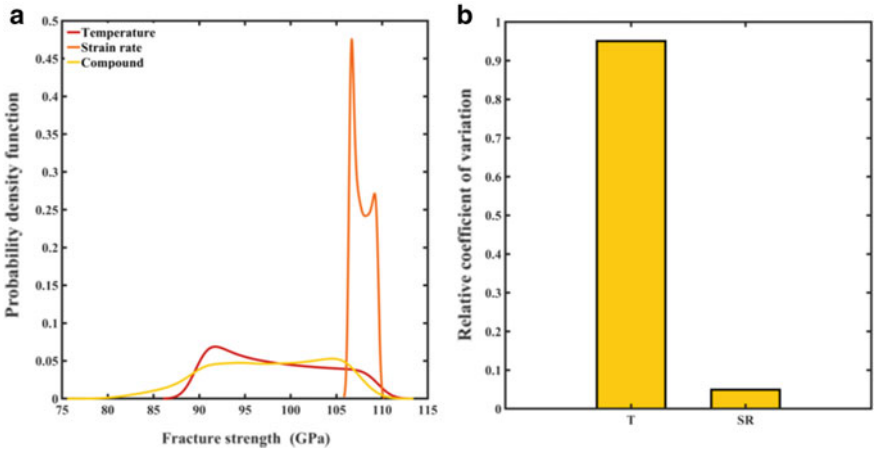

Fig. 6 SVM-based prediction of fracture strength of graphene. **a** The pdf plots of predicted fracture strength subjected to variation in temperature, strain rate, and compound variation in both. **b** The relative coefficient of variation of fracture strength with respect to temperature and strain rate

made for unknown test samples was found within the error bound of ± 5%. The SVR model is further used to predict the results for unknown 30,000 samples which are obtained using SOBOL sequence sampling.

These 30,000 samples comprised with 10,000 samples containing variation in only temperature and constant strain rate maintained at 0.0005 /ps, another 10,000 samples containing variations in strain rate and constant temperature maintained at 200 K, and 10,000 samples of data which contains the variation in both (compound) the input parameters. The prediction results for these unknown large number of samples revealed that the occurrence bound of predicted fracture strength is similar to the fracture strength determined using MD simulations (on comparing Figs. 5a and 6a). Further, the data-driven sensitivity analysis carried out with the predicted fracture strength back up the dominance of variation in temperature over the variation in strain rate for the corresponding variation in fracture strength of graphene (refer to Fig. 6b), similar to the deterministic results (refer to Fig. 4). In this manner by running merely 48 (32 training samples and 16 test samples) number of MD simulations the prediction of 30,000 samples are obtained.

Acknowledgements KKG is glad to acknowledge the financial support provided by Ministry of Education (MoE), Govt. of India during conducting the present study.

References

1. Lee C, Wei X, Kysar JW, Hone J (2008) "Measurement of the elastic properties and intrinsic strength of monolayer graphene", science, vol 321(5887), pp 385–388
2. Thomas S, Ajith KM (2014) Molecular dynamics simulation of the thermo-mechanical properties of monolayer graphene sheet. Procedia Materials Science. 5:489–498
3. Ansari R, Ajori S, Motevalli B (2012) Mechanical properties of defective single-layered graphene sheets via molecular dynamics simulation. Superlattices Microstruct 51(2):274–289
4. Agius Anastasi A, Ritos K, Cassar G, Borg MK (2016) "Mechanical properties of pristine and nanoporous graphene", Molecular Simulation, vol 42(18), pp 1502–1511
5. Gupta KK, Roy A, Dey S (2020) "Comparative Study of Various Defects in Monolayer Graphene Using Molecular Dynamics Simulation", in Advances in Applied Mechanical Engineering, Springer, Singapore, pp 539–546
6. Tsai JL, Tu JF (2010) Characterizing mechanical properties of graphite using molecular dynamics simulation. Mater Des 31(1):194–199
7. Gupta KK, Dey S (2019) "Effect of Temperature on the Fracture Strength of Perfect and Defective MonoLayered Graphene", in Advances in Computational Methods in Manufacturing, Springer, Singapore, pp 793–804
8. Dewapriya MAN, Rajapakse RKND (2014) "Molecular dynamics simulations and continuum modeling of temperature and strain rate dependent fracture strength of graphene with vacancy defects", J Appl Mech, vol 81(8)
9. Zhang YY, Gu Y (2013) Mechanical properties of graphene: Effects of layer number, temperature and isotope. Comput Mater Sci 71:197–200
10. Gupta KK, Mukhopadhyay T, Roy A, Dey S (2020) "Probing the compound effect of spatially varying intrinsic defects and doping on mechanical properties of hybrid graphene monolayers", J Mater Sci Technol
11. Rajasekaran G, Parashar A (2018) Effect of topological defects on mechanical properties of graphene sheets: a molecular dynamics study. Materials Today: Proceedings. 5(2):6780–6788
12. Mukhopadhyay T, Mahata A, Dey S, Adhikari S (2016) Probabilistic analysis and design of HCP nanowires: an efficient surrogate based molecular dynamics simulation approach. J Mater Sci Technol 32(12):1345–1351
13. Dewapriya MAN, Rajapakse RKND, Dias WPS (2020) "Characterizing fracture stress of defective graphene samples using shallow and deep artificial neural networks", Carbon
14. Zhang Z, Hong Y, Hou B, Zhang Z, Negahban M, Zhang J (2019) Accelerated discoveries of mechanical properties of graphene using machine learning and high-throughput computation. Carbon 148:115–123
15. Wang X, Han D, Hong Y, Sun H, Zhang J, Zhang J (2019) Machine learning enabled prediction of mechanical properties of tungsten disulfide monolayer. ACS Omega 4(6):10121–10128
16. Yang H, Zhang Z, Zhang J, Zeng XC (2018) Machine learning and artificial neural network prediction of interfacial thermal resistance between graphene and hexagonal boron nitride. Nanoscale 10(40):19092–19099
17. Garg A, Vijayaraghavan V, Wong CH, Tai K, Gao L (2014) An embedded simulation approach for modeling the thermal conductivity of 2D nanoscale material. Simul Model Pract Theory 44:1–13
18. Vijayaraghavan V, Garg A, Wong CH, Tai K, Singru PM (2015) An integrated computational approach for determining the elastic properties of boron nitride nanotubes. Int J Mech Mater Des 11(1):1–14
19. Garg A, Tai K (2014) Stepwise approach for the evolution of generalized genetic programming model in prediction of surface finish of the turning process. Adv Eng Softw 78:16–27
20. Garg A, Vijayaraghavan V, Lam JSL, Singru PM, Gao L (2015) A molecular simulation based computational intelligence study of a nano-machining process with implications on its environmental performance. Swarm Evol Comput 21:54–63
21. MATLAB 2018a, The MathWorks, Inc., Natick, Massachusetts, United States.

22. Trafalis TB, Ince H (2000) “Support vector machine for regression and applications to financial forecasting”. In Proceedings of the IEEE-INNS-ENNS International Joint Conference on Neural Networks. IJCNN 2000. Neural Computing: New Challenges and Perspectives for the New Millennium, IEEE, vol. 6, pp 348–353
23. Saunders LJ, Russell RA, Crabb DP (2012) The coefficient of determination: what determines a useful R2 statistic? Invest Ophthalmol Vis Sci 53(11):6830–6832
24. Plimpton S (1993) “Fast parallel algorithms for short-range molecular dynamics”, Sandia National Labs., Albuquerque, NM (United States), No. SAND-91–1144
25. Tersoff J (1988) New empirical approach for the structure and energy of covalent systems. Phys Rev B 37(12):6991
26. Humphrey W, Dalke A, Schulten K (1996) VMD: visual molecular dynamics. J Mol Graph 14(1):33–38
27. Lindsay L, Broido DA (2010) “Optimized Tersoff and Brenner empirical potential parameters for lattice dynamics and phonon thermal transport in carbon nanotubes and graphene”, Physical Review B,vol 81(20), pp 205441
28. Mortazavi B, Fan Z, Pereira LFC, Harju A, Rabczuk T (2016) Amorphized graphene: a stiff material with low thermal conductivity. Carbon 103:318–326
29. Rajasekaran G, Kumar R, Parashar A (2016) “Tersoff potential with improved accuracy for simulating graphene in molecular dynamics environment”, Materials Research Express, vol 3(3), pp 035011
30. Wang MC, Yan C, Ma L, Hu N, Chen MW (2012) Effect of defects on fracture strength of graphene sheets. Comput Mater Sci 54:236–239

Comparison of Mean and Peak Pressure Coefficient for Cross-Plan-Shaped Tall Buildings Under Wind

Debasish Kumar and Sujit Kumar Dalui

1 Introduction

With the advent of construction technology and scarcity of land, the high-rise building construction is increasing rapidly in important cities. It becomes a challenging role for designers to design tall buildings in the wind environment. Different international codes like IS: 875 (Part-3):2015 [1], AS-NZS: 1180:2002 [2], ASCE-7-10 [3], etc. are available for the design of regular and conventional tall buildings. Nowadays, building shapes are smell out from these conventional shapes instead becoming more irregular and unconventional in plan and elevation. Wind tunnel testing is a very suitable method for such kinds of buildings. With the development of modern computational techniques, CFD becomes a reliable method to deal with those building models.

Gomes et al. [4] investigated L- and U-shaped model wind-induced responses with a 1:100 length scale using an experimental and numerical approach. Bhattacharyya and Dalui [5] investigated an 'E' plan-shaped building to evaluate the mean pressure coefficient, pressure distribution and pressure contours for various wind flow directions and the results showed good agreement between numerical and experimental techniques. A detailed comparison of pressure coefficients and force coefficients for different cross-plan-shaped buildings was conducted by Kumar and Dalui [6] by CFD simulation using ANSYS CFX. A study of '+' plan-shaped tall building models for 0° and 45° wind flow was demonstrated by Chakraborty et al. [7]. Mukherjee et al. [8] conducted a study to evaluate wind pressure variation on 'Y' plan-shaped tall buildings under various wind flow directions through wind tunnel testing. The wind-induced responses of different irregular plan-shaped building like Z-type [9], Y-type [8, 10], C-type [11] and L-type [12] were studied. Li et al. [13] experimentally investigated aerodynamic treatment to reduce wind forces on four

D. Kumar (✉) · S. K. Dalui
Indian Institute of Engineering Science and Technology, Shibpur, Howrah 711201, India

D. K. Maiti et al. (eds.), *Recent Advances in Computational and Experimental Mechanics, Vol II*, Lecture Notes in Mechanical Engineering,
https://doi.org/10.1007/978-981-16-6490-8_22

different models. Lui et al. [14] studied the mean, fluctuating and peak wall pressure coefficient for the rectangular tall high-rise building for various plan ratios. Amin and Ahuja [15] pointed out that wind pressure on windward faces is independent of the side ratio for rectangular plan-shaped tall buildings, while the side ratio of such buildings significantly influences wind pressure of side and leeward faces.

Moreover, CFD offers more flexibility for the designer to choose any ground-surface conditions, any approaching wind flow situations, building configurations and various surrounding building arrangements. Different research work was performed to understand the flaws and strength of various influential parameters like appropriate grid size, turbulence profiles, velocity profiles, etc. [16]. Thordal et al. [17] focussed on the essential aspects of atmospheric boundary layer wind flow simulation for numerical approach.

2 Objectives

This paper investigates the comprehensive study of mean and peak pressure coefficient over different surfaces for two cross-plan-shaped tall buildings at various wind flow directions ranging from 0° to 180° at an interval of 30°. Here, one regular cross-plan-shaped tall building is considered a basic model, and angular cross-plan-shaped tall buildings are formed by shifting the limb position by 15°. The overall plan area of these two buildings remains the same. However, the total angle between each limb, i.e. $\alpha_1 + \alpha_2 = 180°$, should be satisfied. To keep the plan area remains the same, and the length of the limbs for the angular cross-plan-shaped model is required to be increased marginally. The detailed dimension of the two building models is shown in Fig. 1a, b.

The regular cross-plan-shaped model prototype dimensions are 30 m in length, 15 m in width and 150 m in height, respectively. The building models are scaled down to a scale of 1:300. The overall plan area of the model is 22500 mm^2. The mean pressure coefficient at each face is derived for both models. Furthermore, peak pressure and power spectral density plot of pressure are also evaluated for both models and compared to comprehend the cross-sectional variation.

3 Numerical Analysis

Computational fluid dynamics (CFD) are proficiently developed boundary layer wind profiles around the building, and the wind-induced responses on and around the building can be evaluated. Here, the ANSYS CFX package is used for numerical simulation. There are various turbulence models available for numerical simulation, such as k-ε model, k-ω model and SST model. Generally, the k-ε model predicts better results for medium turbulence conditions and Chakraborty et al. [7] and Mukherjee et al. [8] used k-ε turbulence model in their numerical study. Thus, the k-ε model is

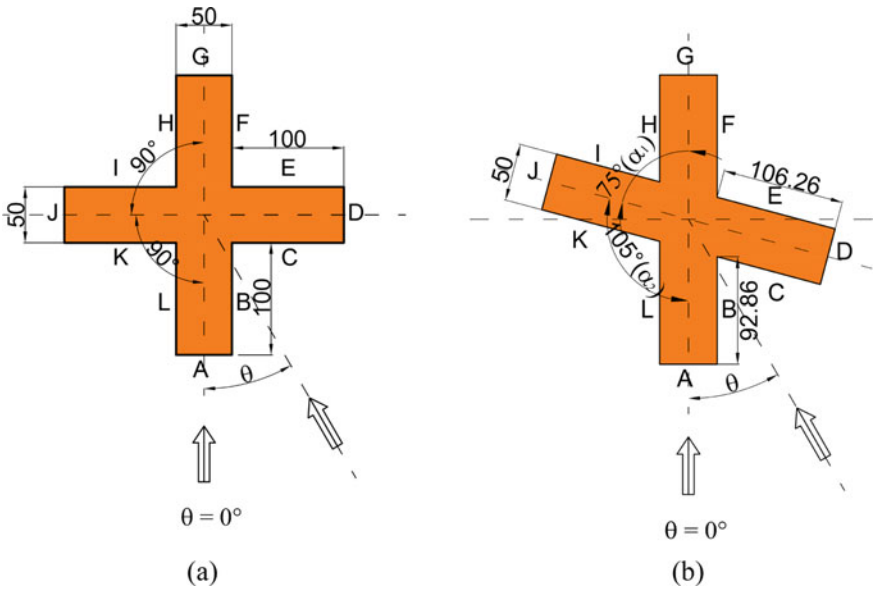

Fig. 1 Typical layout of the regular and angular cross-plan-shaped tall building models with dimensions and face notations

opted here for the present simulation. Furthermore, a comparison is made between the numerical analysis (using the ANSYS CFX package) and Chakraborty et al. [7] results. The dimensional parameter and wind flow parameters related to wind flow are kept similar.

3.1 Velocity Profiles and Meshing Information

To fully incorporate the vortex generations and velocity fluctuations in the wake region of the building [18], upstream, downstream, side clearances and top clearance are 5H, 15H, 5H and 5H, respectively. H is the overall height of the building (shown in Fig. 2a, b). No-slip condition is considered at the building surfaces to obtain the pressure contour. Thus, there is no relative movement between building surfaces and the wind flow layer. The free slip condition is maintained at the domain side and top surfaces. At the interface between wind flow and sidewalls, the velocity field's normal component is zero, but the tangential component is unrestricted. The tangential force is zero. The velocity scale is 1:5 and the velocity at the inlet is 10 m/s. Here, the power law is used with a power index of 0.133 to generate boundary layer wind flow at the domain inlet. A comparison of the velocity profile between numerical simulation and experimental data used by Chakraborty et al. [7] is shown in Fig. 3 and found to be within the acceptable range. The equation of power law is noted

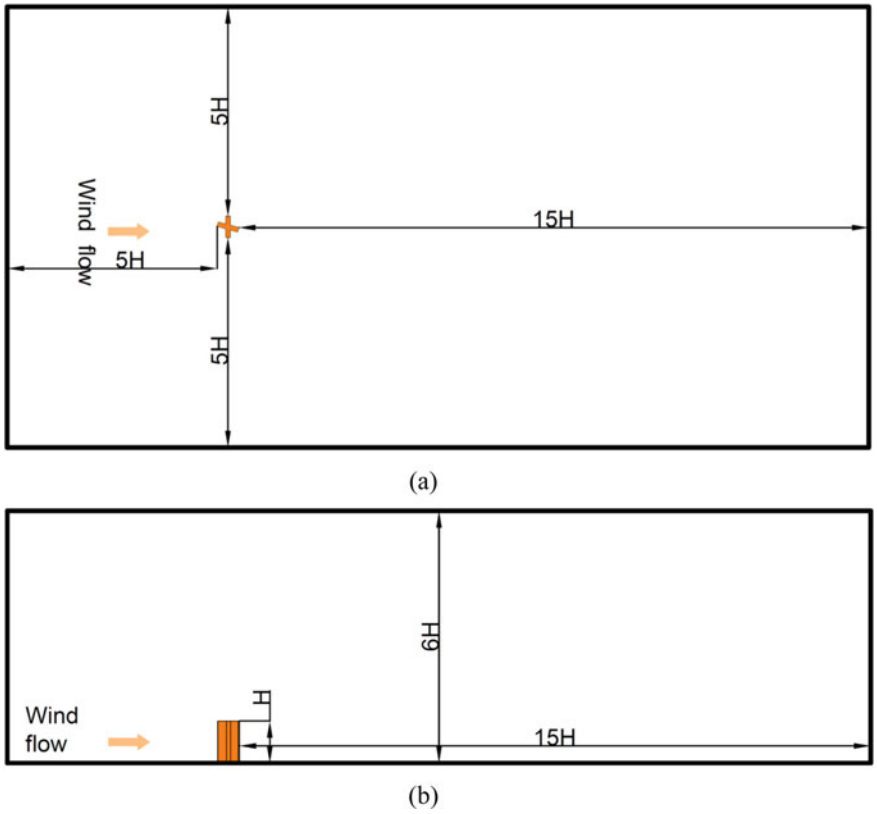

Fig. 2 The domain around the building. **a** Plan. **b** Side elevation

below as:

$$\frac{U}{U_o} = \left(\frac{z}{z_o}\right)^{\alpha} \tag{1}$$

where U_o is the basic wind speed taken as 10 m/s,

Z_o is boundary layer height scaled down to 1 m and

α is power index taken as 0.133.

Velocity in other directions is zero. Moreover, a combination of hexagonal and tetrahedral meshing is chosen for meshing the building surface and the rest of the domain. To accurately access the actual pressure fluctuations on the building surfaces, finer meshing is generated. In contrast, the coarse mesh is judicially chosen for the rest of the domain to reduce the time of calculation without losing the accuracy of the obtained results.

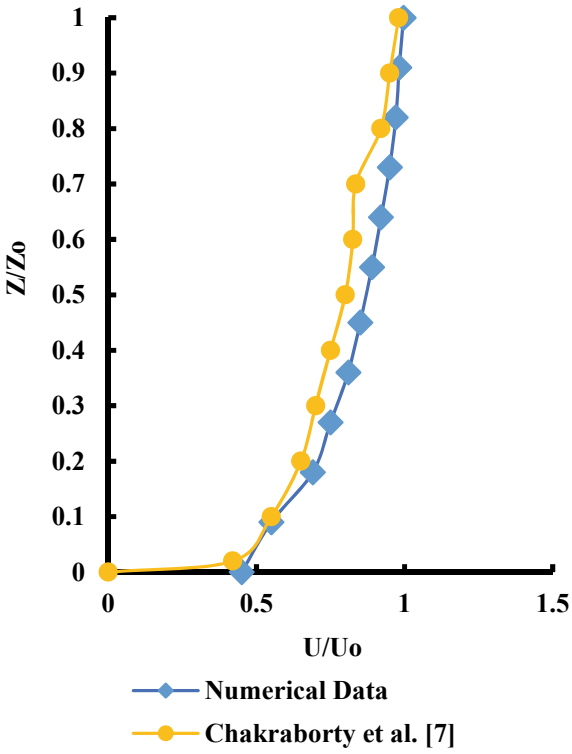

Fig. 3 Velocity profile along with height

4 Comparison of Numerical Analysis with Experimental Data

The results obtained from numerical analysis using the ANSYS CFX package should be validated with experimental data. The wind tunnel test setup used by Chakraborty et al. [7] and model details of the '+' plan-shaped building were summarized here.

A blower fan of 125HP is used to generate a continuous flow of wind through the wind tunnel, having a cross-section of 2 m (width) × 2 m (height) and a length of 38 m. A 6 m (width) and 6 m (depth) square-holed honeycomb wire mesh is located at the wind tunnel entrance to generate a streamline of flow with a very mild velocity with less turbulence. An elliptical effuse profile of 6 m in length with a contraction ratio of 9:5:1 is used to increase wind flow velocity. The wind must pass through the vortex generator and barrier wall to simulate a small desired and controlled degree of turbulence in the wind velocity. The experiments are conducted considering terrain category-II, which corresponds to open terrain with well-scattered obstructions having heights generally between 1.5 and 10 m, as per IS 875 (Part-III):2015. Square cubes of different sizes are positioned on the wind tunnel upstream side. A dyno drive is attached with a diffuser or fan at the outlet to control wind flow velocity. A pitot tube is attached to the wind tunnel at a distance of 7.8 m from

the elliptical effuse to measure wind velocity in the wind tunnel and reference point. The wind tunnel is also mechanized with a hot-wire anemometer and a manometer. A pressure transducer is connected with the pressure tapping point and the reference pressure point to measure the pressure through Barron instruments. The Perspex sheet is generally used for a pressure measurement model having a thickness of 4 mm. Pressure points are installed on surfaces of the models with suitable spacing, both along with height and width, to predict pressure fluctuation on the surface and the edges more precisely. The pressure tapings are made of stainless steel tubes with 1 mm internal diameter and 15–20 mm-long, placed flush with the mode surfaces by drilling holes at each grid point.

The mean pressure coefficients for different faces evaluated from the numerical analysis are compared with the experimental results by Chakraborty et al. [7] at 0° wind flow direction which is represented in Fig. 6. The dimensional parameter and wind flow parameters are maintained analogous for these two cases. Marginal deviations are noted on the few selected faces like Face A and Face K, but discrepancies are within the acceptable limits. These differences are due to the insufficiency of pressure tapping points on the surfaces and edges to acquire pressure fluctuations in experimental analysis. It has been observed that the numerical result is slightly higher than the experimental results but within the acceptable range.

5 Results and Discussions

5.1 Mean Pressure Coefficients (C_p)

The mean pressure coefficients on different surfaces for both building models at 0°, 30°, 60° and 90° wind incidence angles are depicted in Table 1. For the regular cross-plan-shaped model, the maximum positive mean C_p at Face A is observed for 0° wind incidence angle and maximum suction depicted for 60° angle of attack. The mean C_p is reduced at Face A for the angular building model at 0° wind flow. The most unfavourable mean negative C_p is observed at Face D for regular cross-plan-shaped building at 30° angle of attack due to a larger separation of flow. A maximum positive mean C_p is depicted at Face B for angular cross-plan-shaped buildings at 30° wind flow due to the combined effect of mutual interference and the larger frontal surface facing the approaching wind directly. Moderate suction is prevailing in the side and leeward faces of both building models.

5.2 Peak Pressure Coefficients ($\widehat{C_p}$)

The peak pressure coefficients at each face for both cross-plan-shaped building models at 0° wind incidence angle are represented in Fig. 4. The peak pressure

Table 1 Pressure coefficient on different surfaces of regular and angular cross-plan-shaped tall buildings at 0°, 30°, 60° and 90° wind incidence angles

Faces	Mean pressure coefficients							
	0° wind flow		30° wind flow		60° wind flow		90° wind flow	
	Regular	Angular	Regular	Angular	Regular	Angular	Regular	Angular
Face A	0.871	0.855	0.222	0.324	−0.819	−0.627	−0.505	−0.543
Face B	0.511	0.630	0.914	0.919	0.784	0.796	0.540	0.206
Face C	0.553	0.654	0.783	0.872	0.917	0.896	0.503	0.113
Face D	−0.476	−0.478	−0.858	−0.311	0.226	0.625	0.869	0.754
Face E	−0.360	−0.349	−0.557	−0.574	−0.665	−0.276	0.506	0.821
Face F	−0.395	−0.406	−0.550	−0.542	−0.468	−0.125	0.540	0.702
Face G	−0.396	−0.372	−0.451	−0.406	−0.455	−0.413	−0.515	−0.455
Face H	−0.417	−0.371	−0.395	−0.347	−0.367	−0.327	−0.369	−0.395
Face I	−0.374	−0.346	−0.378	−0.333	−0.384	−0.351	−0.405	−0.427
Face J	−0.503	−0.447	−0.466	−0.412	−0.448	−0.368	−0.398	−0.396
Face K	0.539	0.424	−0.466	−0.547	−0.546	−0.433	−0.415	−0.506
Face L	0.500	0.234	−0.663	−0.713	−0.547	−0.391	−0.371	−0.448

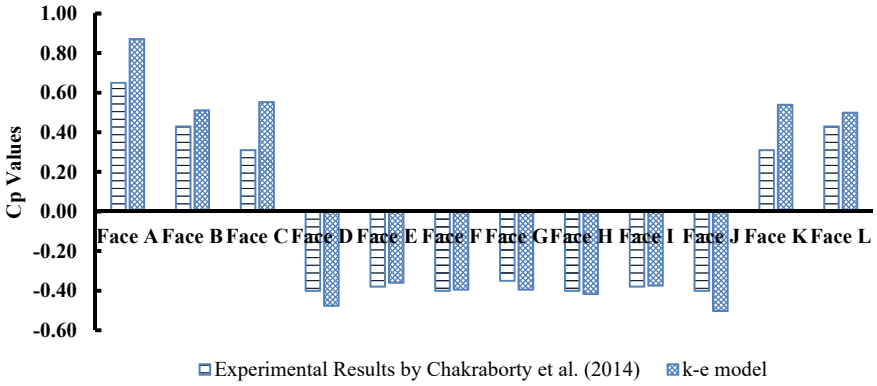

Fig. 4 Comparison of mean pressure coefficients on different surface of building for regular cross-plan-shaped building model at 0° wind incidence angle for numerical and experimental results by Chakraborty et al. [7]

coefficients are higher than the mean pressure coefficients, and these differences are noticed mainly at the top, bottom and edges of the building surfaces. The difference between the $\widehat{C_p}$ and C_p is mainly attributed to the existence of body-generated turbulence and normalization of 3-s gust speed to obtain peak pressure value. The peak pressure coefficients are obtained by measured instantaneous pressure normalized over 3-s gust speed.

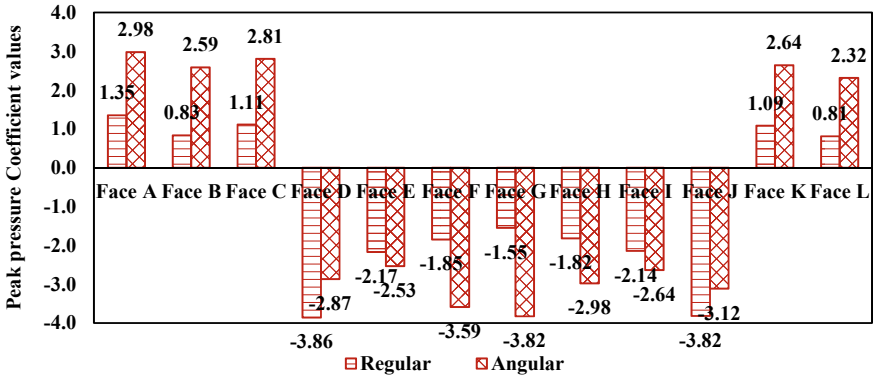

Fig. 5 Peak pressure coefficient at different surfaces (Face A to Face L) for regular and angular cross-building models at 0° wind flow

The maximum positive $\widehat{C_p}$ value is observed at Face A with a magnitude of (+)1.35 for regular cross-plan-shaped building. The critical negative $\widehat{C_p}$ value of (−)3.86 is noted at Face D for the regular building model. A much higher positive peak pressure coefficient (+)2.98 is noticed at Face A for angular building model at 0° wind flow. Face D and Face J are subjected to critical negative peak pressure coefficients due to the larger separation of flow for both building models. The negative $\widehat{C_p}$ at Face D is reduced to (−)2.87 for the angular cross-building model due to asymmetry in the building plan and lesser separation of flow. Larger difference between peak $\widehat{C_p}$ and mean C_p is noticed in the side and leeward faces for angular building model compared to regular building model (Fig. 5).

5.3 *Power Spectral Density (PSD)*

The power spectral density (PSD) of pressure is evaluated for all the surfaces at the height of 470 mm from the base of the building. The gauge time is considered as 3 s. Here, PSD is modified to reduced power spectral densities ($nS(n)/\sigma^2$), and frequency (n) is modified to reduced frequency (nD/U_h),

where n = frequency,
$S(n)$ = power spectral density of pressure,
σ = standard deviation of pressure variation with respect to time at that point,
D = the dimension of the cross-section in the across wind direction and
U_h = static velocity of wind at height H.

Figure 6a–l represents the PSDs plot at each surface (Face A to Face L) for both cross-plan-shaped building models for 0° wind flow direction at 470 mm height from base. The higher peak value for regular cross-plan-shaped buildings is noticed at Face A and Face B compared to the angular model. Turbulence in the flow is increased for

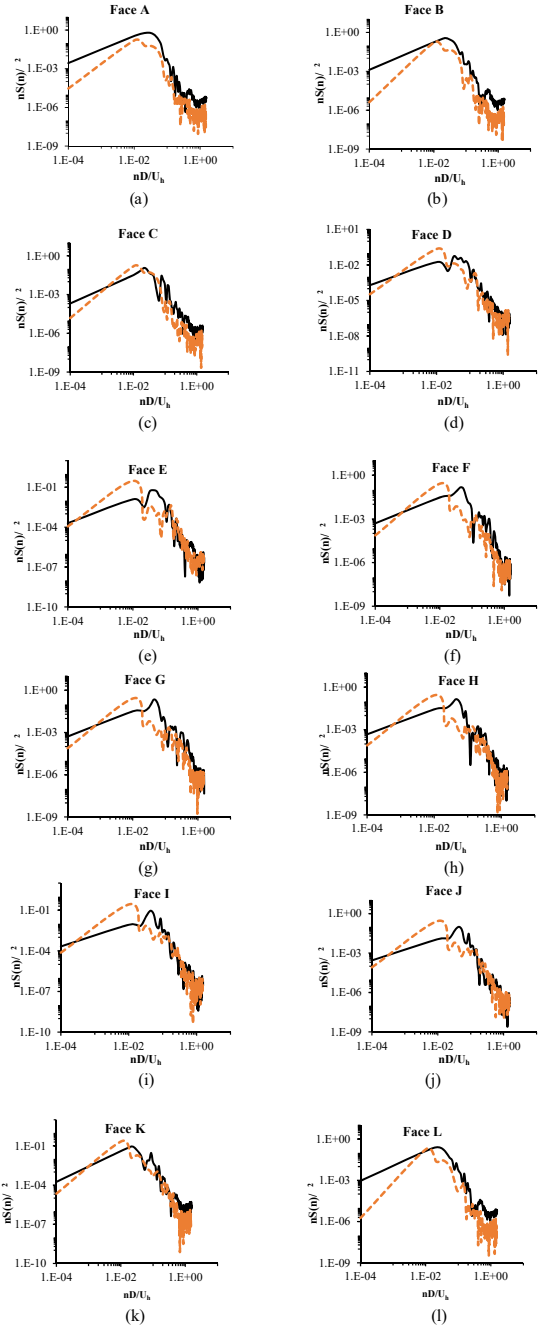

Fig. 6 The plot of reduced power spectral density with reduced frequency for regular and angular cross-plan-shaped building models at different faces for 0° wind incidence angle. **a** Face A, **b** Face B, **c** Face C, **d** Face D, **e** Face E, **f** Face F, **g** Face G, **h** Face H, **i** Face I, **j** Face J, **k** Face K, **l** Face L

the angular building model owing to the lowering of the first peak and slightly shift of peak to lower reduced frequencies. The spectral peak becomes much flat, and the spectral shape becomes much wider at Face C for angular building models, indicating vortex shedding is more random and irregular. The second peak in the PSDs pointed out the effect of strong reattachment and subsequent re-separation of the shear layer flow or flapping. Thus, the impact of mutual interference between the side faces of frontal limbs and frontal faces of the side limbs is enlightened. Being positioned on the leeward side, similar PSDs are observed for Face E to Face I for both building models. Moreover, higher turbulences on these faces are more prominent for angular cross-plan building due to gently lowering the peak and shift of peak to a slightly lower reduced frequency. Flatter spectral peak with similar spectral values is noticed for both building models at Face L.

6 Conclusions

This paper compares wind-induced responses of regular and angular cross-plan-shaped buildings through a comprehensive investigation of mean and peak pressure coefficient and power spectral densities. The numerical modelling (k-ε model) using ANSYS CFX package is used to predict the wind-induced responses for both building models at various WIA ranging from 0° to 180° at an interval of 30°. The noteworthy outcomes of the present study are summarized as follows:

- The frontal face of the frontal limb for the regular cross-plan-shaped building model is subjected to maximum mean positive pressure, which is similar to the frontal faces of regular rectangular or square plan-shaped buildings at 0° wind incidence angle. There is a reduction in the mean C_p values for angular cross-plan-shaped building at Face A for 0° wind flow conditions. The combined effect of mutual interference between the adjacent faces and being positioned on the confined region with respect to the approaching wind for 30° skew angle of flow, Face B has suffered the most critical positive mean C_p value for regular building model.
- The highest separation of wind flow leads to developing the most unfavourable mean negative Cp at the side faces of side limb (Face D and Face J) for regular cross-plan-shaped tall buildings at a critical skew angle of wind flow.
- The peak pressure coefficient for the windward face (Face A) is close to the mean pressure coefficient, while a more significant difference between peak pressure and mean pressure coefficient is noticed for the wake region (leeward and side faces) due to the high separation of flow.
- A good agreement between numerical data and experimental results indicates that numerical analysis using ANSYS CFX with k-ε turbulence model can be effectively used to evaluate wind-induced responses.
- The vortex shedding mainly influences the single peak of PSDs of Face A and Face B for regular cross-plan-shaped buildings. In contrast, the sharp second peak

is noticed for all the faces of angular cross-plan-shaped buildings, indicating both vortex shedding and the reattachment of the separated flow on the side walls.

The results obtained from numerical analysis are essential for designing a similar nature of the building. The numerical method can be an excellent weapon to handle typical irregular plan-shaped buildings.

References

1. IS:875 (Part-III) (2015) Indian standard code of practice for design loads (other than earthquake) for buildings and structures. Part 3 (wind loads). Bureau of Indian Standards, New Delhi, India
2. AS/NZS: 1170.2:2002 (2002) Structure design actions, part-2: wind actions. Australian/New Zealand Standard; Sydney and Wellington
3. ASCE: 7-10 (2010) Minimum design loads for buildings and other structures. Structural Engineering Institute of the American Society of Civil Engineering, Reston
4. Gomes MG, Rodrigues AM, Mendes P (2005) Experimental and numerical study of wind pressures on irregular-plan shapes. J Wind Eng Ind Aerodyn 93:741–756. https://doi.org/10.1016/j.jweia.2005.08.008
5. Bhattacharyya B, Dalui SK (2020) Experimental and numerical study of wind-pressure distribution on irregular-plan-shaped building. J Struct Eng 146(7):04020137. https://doi.org/10.1061/(ASCE)ST.1943-541X.0002686
6. Kumar D, Dalui SK (2017) Effect of internal angles between limbs of cross plan shaped tall building under wind load. Wind Struct 24(2):95–118. https://doi.org/10.12989/was.2017.24.2.095
7. Chakraborty S, Dalui SK, Ahuja AK (2014) Wind Load on irregular plan shaped tall building—a case study. Wind Struct 19(1):59–73. https://doi.org/10.12989/was.2014.19.1.059
8. Mukherjee S, Chakraborty S, Dalui SK, Ahuja AK (2014) Wind Induced pressure on 'Y' plan shape tall building. Wind Struct 19(5):523–540. https://doi.org/10.12989/was.2014.19.5.523
9. Pal R, Dalui SK (2016) Wind effects on 'Z' plan shaped tall building: a case study. Int J Adv Struct Eng 8:319–335. https://doi.org/10.1007/s40091-016-0134-9
10. Sanyal P, Dalui SK (2020) Effect of corner modifications on Y plan shaped tall building under wind load. Wind Struct 30(3):245–260. https://doi.org/10.12989/was.2020.30.3.245
11. Mallick M, Mohanta A, Kumar A, Patra K (2020) Gene-expression programming for the assessment of surface mean pressure coefficient on building surfaces. Build Simul 13:401–418. https://doi.org/10.1007/s12273-019-0583-8
12. Li B, Liu J, Li M (2013) Wind tunnel study on the morphological parameterization of building non-uniformity. J Wind Eng Ind Aerodyn 121:60–69
13. Li Y, Tian X, Tee KF, Li QS, Li YG (2018) Aerodynamic treatments for the reduction of wind loads on high-rise buildings. J Wind Eng Ind Aerodyn 172:107–115. https://doi.org/10.1016/j.jweia.2017.11.006
14. Liu Y, Kopp GA, Chen S (2019) Effects of plan dimensions on gust wind loads for high-rise buildings. J Wind Eng Ind Aerodyn 194:103980. https://doi.org/10.1016/j.jweia.2019.103980
15. Amin JA, Ahuja AK (2014) Characteristics of wind forces and responses of rectangular tall buildings. Int J Adv Struct Eng 6(3):1–14. https://doi.org/10.1007/s40091-014-0066-1
16. Meng F, He B, Zhu J, Zhao Amos D, Darko A, Zhao Z (2018) Sensitivity analysis of wind pressure coefficients on CAARC standard tall buildings in CFD simulations. J Build Eng 16:146–158. https://doi.org/10.1016/j.jobe.2018.01.004

17. Thordal MS, Bennetsen JC, Koss HHH (2019) Review of the practical application of CFD for the determination of wind load on high-rise buildings. J Wind Eng Ind Aerodyn 186:155–168. https://doi.org/10.1016/j.jweia.2018.12.019
18. Revuz J, Hargreaves DM, Owen JS (2012) On the domain size of steady-state CFD modeling of a tall building. Wind Struct 15(4):313–329. https://doi.org/10.12989/was.2012.15.4.313

A Computational Approach to Investigate the Properties of Geopolymer Concrete

B. Ramya Madhuri and K. Srinivasa Rao

1 Introduction

In this concrete era, research has been carried out to find out alternatives to conventional concrete. In this hunt for new materials, geopolymer concrete has emerged as one of the best alternatives for conventional concrete. Geopolymer concrete is a sustainable material as its production is pollution-free, unlike conventional concrete. This can be developed using precursor materials such as fly ash, Ground Granulated Blast Furnace Slag (GGBS), red mud, rice-husk ash, etc., which are silica-rich materials and industrial by-products. Moreover, it prevents the depletion of limestone as well as the emission of carbon dioxide.

Geopolymer concrete can be developed by combining the precursors and the hardeners. The hardeners such as sodium or potassium hydroxide in combination with sodium or potassium silicate can be used. The chemistry involved in the production of geopolymer concrete is quite different from that of conventional concrete. The synthesis of geopolymer involves the dissolution of alumina and silica oxides from the precursor materials under highly alkaline environment, transportation of the dissolved oxide minerals followed by coagulation and then finally polycondensation to form 3-D network of silico-aluminate structures [1]. This process involves the expulsion of water quite contrary to the hydration of cement in conventional concrete. The water present in the chemicals and the water which is expelled out is merely used to provide workability for the mix [2].

B. Ramya Madhuri (✉) · K. Srinivasa Rao
Andhra University College of Engineering (A), Visakhapatnam, AP, India

D. K. Maiti et al. (eds.), *Recent Advances in Computational and Experimental Mechanics, Vol II*, Lecture Notes in Mechanical Engineering,
https://doi.org/10.1007/978-981-16-6490-8_23

Table 1 Properties of Alccofine 1203 (data as furnished by the manufacturer)

Property	Unit	Value
Average particle size	Microns	4–6
Fineness as specific surface	cm^2/gm	12,000
Specific gravity	–	2.86 ± 0.02
Bulk density	kg/m^3	600 to 700

Table 2 Chemical composition of Alccofine 1203 [3]

Constituents	Composition (%)
SiO_2	35.30
MgO	6.20
Al_2O_3	21.40
Fe_2O_3	1.20
SO_3	0.13
CaO	32.30

2 Experimental Programme

2.1 Materials

In this study, geopolymer concrete is prepared by using class F fly ash and Alccofine 1203 as the precursors. Class F fly ash is collected from NTPC Simhadri. Alccofine 1203 is a low-calcium silicate-based micro-fine mineral additive. The physical properties and chemical composition of Alccofine 1203 are listed in Tables 1 and 2, respectively. The hardeners used are sodium hydroxide and sodium silicate. Sodium hydroxide is available as solid flakes and sodium silicate is available in solution form. The modulus of sodium silicate (Na_2O—15%, SiO_2—34.5%) is approximately 2.3. It is the ratio of percentage composition of SiO_2 to Na_2O by weight.

2.2 Mix Design

The mix design is done as per IS 10262:2019, but in case of geopolymer concrete, the alkaline liquid–binder ratio is considered instead of the water–cement ratio [4]. Alkaline liquid or hardener refers to the mixture of sodium hydroxide and sodium silicate solutions. In addition to the alkaline liquid, extra water is also added to the geopolymer concrete mix to increase the workability of the mixture. Extra water is added based on water to geopolymer solid ratio, such that the total mass of water present in the mix is equal to the water contained in the sodium hydroxide and sodium silicate solutions and the extra water. Geopolymer solids refer to the binder (fly ash

Table 3 Geopolymer concrete mixture proportions

Materials	Mass (kg/m^3)
Fly ash (ASTM class F)	361
Alccofine 1203	19
Fine aggregate	726
Coarse aggregate	1224
Sodium silicate solution ($SiO_2/Na_2O = 2.3$)	91.2
Sodium hydroxide solution	60.8
Extra water	38.11

and Alccofine) as well as the solids present in sodium hydroxide and sodium silicate solutions [5].

The binder content of 380 kg is taken to develop an M30-grade geopolymer concrete. The alkaline liquid to binder ratio is 0.4 and water to geopolymer solid ratio of 0.3 is adopted after conducting several trials. The amount of total alkaline liquid required is computed and the quantities of NaOH and Na_2SiO_3 are determined based on their proportions. The mixture proportions for trial No. 4 are shown in Table 3.

2.3 Mixing, Casting and Curing

The sodium hydroxide solution with the required concentration should be prepared 24 h prior to the mixing so that the heat gets dissipated. And the sodium silicate solution is added to the sodium hydroxide solution 1 h before the mixing of concrete. This allows dissociation of silica in the solution which assists the process of geopolymerization. The geopolymer concrete is mixed using a pan mixer. Initially, the dry contents (binder and aggregates) are mixed well and then the hardener followed by the extra water is added gradually to the mix. The mixing time maintained is 6–8 min. The casting of specimens should be carried out within 2–3 min after mixing as the concrete mix gets stiffer with time and the workability decreases. The specimens are demoulded after 24 h and cured in ambient condition. Geopolymer concrete developed using only fly ash needs to be cured in an oven for 24 h maintaining the temperature at 60 °C, and this concrete exhibits low strength when cured in ambient condition. The addition of Alccofine accelerates the geopolymerization resulting in the development of strength even under ambient conditions. The trials were conducted by replacing fly ash with 30% Alccofine but it was found that the mix is too stiff to be handled and even its setting time is too low and cannot be mixed. It's getting hardened while mixing itself. This is due to the high percentage of Alccofine. Moreover, using higher percentages of Alccofine will result in increasing the cost of the concrete.

The compressive strength is determined by conducting the experiment on 150 × 150 × 150 mm cubes after 28 days of ambient curing as per IS 516–1959.

2.4 Taguchi Method of Optimization

Taguchi method of orthogonal arrays is an experimental methodology based on statistics, developed by Genichi Taguchi. Taguchi method is used to study the influence of various factors affecting the output of a process. In other words, it gives the mathematical relationship between input parameters and the response in any process. This method gives the S/N (signal/noise) ratio to evaluate the performance of the response. It is nothing but the ratio of the mean (signal) to the standard deviation (noise) [7]. The S/N ratio is also denoted by η. It is given by a loss function shown in Eq. (1):

$$\text{Larger the better S/N (dB)} = -10 \times \log_{10}\left(\frac{1}{n}\sum_{i=1}^{n}\frac{1}{y_i^2}\right) \tag{1}$$

where n = the number of times an experiment is performed and y_i = the response or the output.

Taguchi method is used for its robustness. It is originated from fractional factorial method and in the more simplified form which can be easily applied to optimization problems. The number of experiments to be conducted is reduced considerably, when compared to methods such as full factorial method and response surface method. All the three variables can be varied at the same time unlike in one factor at a time method, reducing the number of experiments to almost one-third of the required. This saves time, resources, effort and money.

In this study, different mixes are prepared by varying the proportion of Alccofine in the binder, concentration of sodium hydroxide solution and the ratio of Na_2SiO_3 to NaOH. The percentage of Alccofine is varied from 0 to 25 with an increment of 5% in each trial. The concentration of NaOH taken is 8, 10 and 12 M. The ratio of Na_2SiO_3 to NaOH considered is 1.5, 2 and 2.5. By considering all these variations, the total number of experiments required to be conducted are 54 (6 × 3 × 3). The results of all the 54 trials can be predicted by conducting one-third (18) of the total number of experiments. Taguchi method of optimization is chosen to perform the parametric study on the geopolymer concrete. The different levels considered for the input parameters are shown in Table 4. The standard L18 orthogonal array design is developed in software 'Minitab 18' as shown in Table 5.

Table 4 Levels of the three factors

Factor	Symbol	Levels						Output parameters
		1	2	3	4	5	6	
Proportion of Alccofine	A	0	5	10	15	20	25	Compressive strength
Molarity of NaOH	M	8	10	12	–	–	–	
Ratio of Na_2SiO_3 to NaOH	R	1.5	2.0	2.5	–	–	–	

Table 5 Trials conducted as per Taguchi standard L18 array

Trial no	Alccofine proportion (%) (A)	Molarity of NaOH (M)	Ratio of Na_2SiO_3 to NaOH (R)	Compressive strength (Comp) (MPa)
1	0	8	1.5	8.74
2	0	10	2.0	12.22
3	0	12	2.5	10.67
4	5	8	1.5	28.00
5	5	10	2.0	19.34
6	5	12	2.5	24.74
7	10	8	2.0	31.23
8	10	10	2.5	32.67
9	10	12	1.5	42.96
10	15	8	2.5	37.04
11	15	10	1.5	40.89
12	15	12	2.0	50.67
13	20	8	2.0	58.00
14	20	10	2.5	46.07
15	20	12	1.5	60.00
16	25	8	2.5	65.33
17	25	10	1.5	75.56
18	25	12	2.0	58.67

3 Results and Discussions

The influence of all the three parameters, namely, proportion of Alccofine (A), molarity of NaOH (M) and the ratio of Na_2SiO_3 to NaOH (R) are graphically represented in Fig. 1. The three-dimensional surface plots are obtained as shown in Fig. 2.

From Figs. 1 and 2, it is clear that the compressive strength of the geopolymer concrete increases with an increase in the proportion of Alccofine in the binder. Alccofine is a micro-fine material so it helps in accelerating the rate of geopolymerization. Moreover, the addition of Alccofine to the binder allows the reaction to take place in ambient condition. It is clear that the proportion of Alccofine is the most influential factor among the three.

The average S/N values of all the factors at different levels are given in Table 6. The rank in the ninth column of Table 6 denotes the order of importance of the three factors. The factor with rank 1, i.e. the proportion of Alccofine is the most influential parameter among the three. And the ratio of Na_2SiO_3 to NaOH is the second most influential parameter among the three.

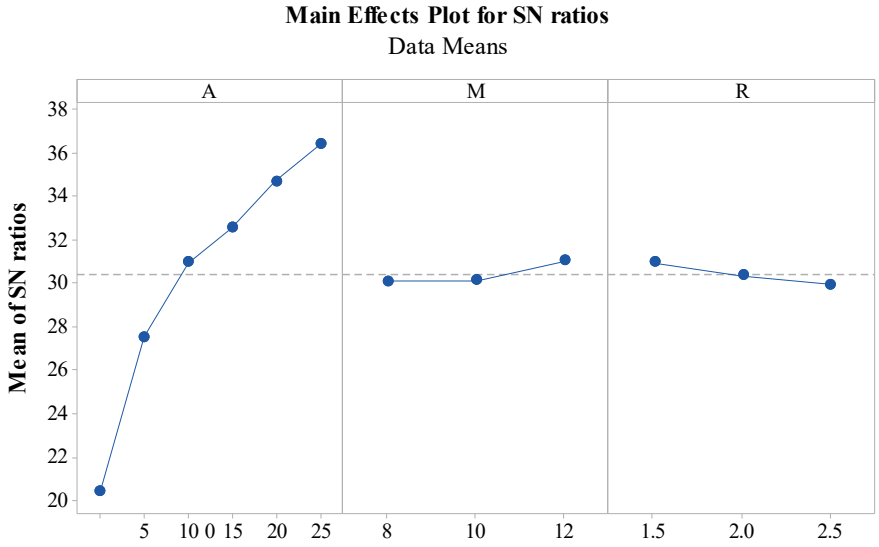

Fig. 1 Main effects plot for S/N ratios

The numerical value of the maximum point in each graph in Fig. 1 shows the optimum value or the best value of that particular parameter. The maximum S/N values are obtained at level 6 for 'A', at level 3 for 'M' at level 1 for 'R'. Therefore, the compressive strength of geopolymer concrete is maximum when the proportion of Alccofine is 25%, the concentration of NaOH is 12 M and the ratio of Na_2SiO_3 to NaOH is 1.5.

The objective of this study is to develop geopolymer concrete of M30 grade economically. The target strength of M30-grade concrete is 38.25, so the target strength is set at 38.25 MPa and the corresponding factors are determined. It is found that the target strength is achieved when the proportion of Alccofine is 12.5%, the concentration of NaOH is 9.02 M and the ratio of Na_2SiO_3 to NaOH is 2.0. The same is shown graphically in Fig. 3. The value of compressive strength can be obtained for all the values of factors within their constraints and for any specific value of compressive strength the values of three factors can be obtained. This is the advantage of optimization as this can be done without following the hectic experimental procedures. The required quantities are obtained by computation instead of experiments. The computation is performed by feeding the minimum required data to the program.

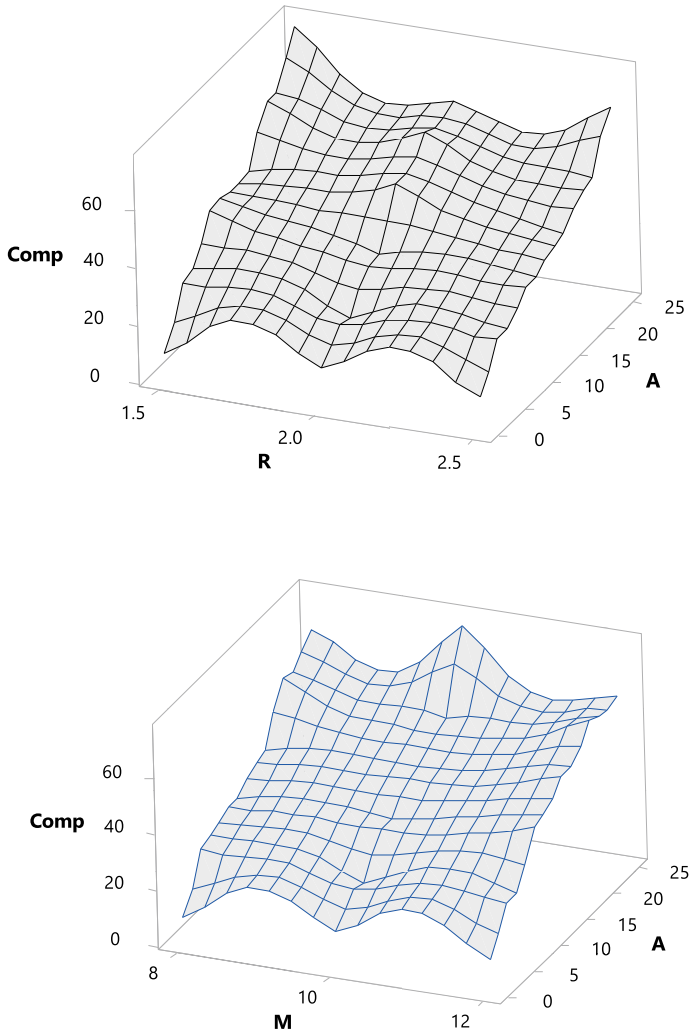

Fig. 2 3-D surface plots of compressive strength versus the input parameters

Table 6 Average S/N values of factors at different levels

	Average η (S/N) by factor level (dB)							
Parameter	1	2	3	4	5	6	Delta	Rank
Proportion of Alccofine	20.38	27.51	30.95	32.57	34.70	36.41	16.03	1
Molarity of NaOH	30.10	30.14	31.02				0.92	3
Ratio of Na_2SiO_3 to NaOH	30.97	30.35	29.94				1.02	2

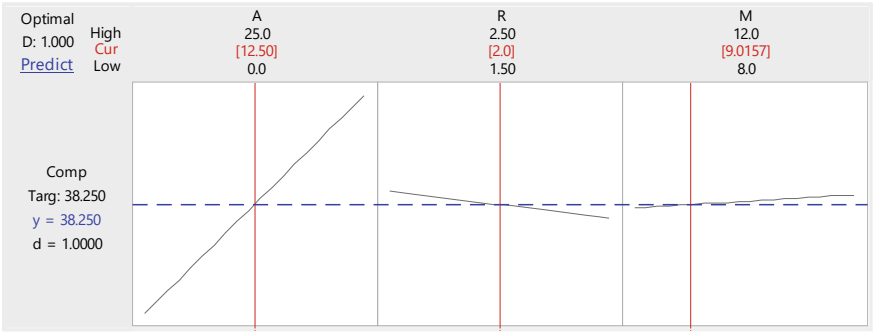

Fig. 3 Graph showing the factors at which target strength is obtained

3.1 Mathematical Modelling

The influence of all the input parameters on the response (compressive strength) can be predicted from Table 6 and also from the three-dimensional surface plots. However, a mathematical formulation of any phenomenon will serve better. The impact of the three input parameters on the response is mathematically formulated as shown in Eq. (2). The equation is developed by using regression analysis [8]. The linear regression curve is developed as it is the best fit for the available data.

$$\text{Comp}=17.10+2.17\text{A}+0.81\text{M}-6.61\text{R} \tag{2}$$

The compressive strength can be computed for any values of A, M and R, within their constraints using Eq. (2).

4 Conclusion

The target strength for the M30-grade geopolymer concrete is obtained when the proportion of Alccofine is 12.5%, the concentration of NaOH is 9.02 M and the ratio of Na_2SiO_3 to NaOH is 2.0.

The results of present study are encouraging to achieve a sustainable concrete which can address the global issues such as disposal of huge quantities of fly ash and prevention of depletion of natural resources such as limestone. The usage of water can also be reduced as it is ambient cured.

References

1. Part WK, Ramli M, Cheah CB (2015) An overview on the influence of various factors on the properties of geopolymer concrete derived from industrial by-products. Constr Build Mater 77:370–395. https://doi.org/10.1016/j.conbuildmat.2014.12.065
2. Singh B, Ishwarya G, Gupta M, Bhattacharyya SK (2015) Geopolymer concrete: a review of some recent developments. Constr Build Mater 85:78–90. https://doi.org/10.1016/j.conbuildmat.2015.03.036
3. Singhal DP, Junaid MT, Jindal BB, Mehta A (2018) Mechanical and microstructural properties of fly ash based geopolymer concrete incorporating alccofine at ambient curing. Constr Build Mater 180:298–307. https://doi.org/10.1016/j.conbuildmat.2018.05.286
4. IS 10262 : (2019) Concrete mix proportioning guidelines. Second Revision, Bureau of Indian Standards
5. Rangan BV (2008) Fly Ash-based Geopolymer Concrete, Research Report GC 4. Curtin University of Technology, Perth, Australia, Engineering Faculty
6. IS 516 : (1959) Methods of tests for strength of concrete. Bureau of Indian Standards
7. Karna SK, Sahai R (2012) An overview on Taguchi method. Int J Eng Math Sci 1:11–18, Jan–June
8. Raymond HM, Douglas CM, Christine MAC: Response surface methodology–process and product optimization using designed experiments. Wiley Publications. ISBN: 978-1-118-91601-8

Prediction of Resistance of Layered Toughened Glass Under Low-Velocity Impact

K. Senthil, G. S. Chauhan, S. Rupali, and K. Pravesh

1 Introduction

The toughened glass as a basic material has low strength and is fragile against projectile impact as compared to the metal, composite and ceramic material [1, 2]. The major benefit of layered toughened glass is to prevent glass shards from flying away and causing injuries, with the interlayer holding the glass shards and stopping shattered glass from flying into the occupants [2–4]. The transparent laminated glass plate consists of two or more layers of float glass sheets combined by an adhesive interlayer of tough PVB under heat treatment. Due to the composite action of layers of glass plies and interlayer-glass adhesion PVB, it is very difficult to understand the behaviour of laminated toughened glasses. Owing to a poor understanding of the interaction between intermediate layer and glass, the use of laminated toughened glass could be extended to larger areas in need of investigation. Sakai et al. 2013 [5] performed experiments and numerical studies to determine the fracture behaviour of LG under impact. It was observed that when the adhesion between the interlayer and glass was low and the tensile strength was high it resulted in laminated glass that was difficult to break. Del Linz et al., 2017 [6] conducted a finite element analysis and experimental test to study the delamination occurring at the interface of glass plates and interlayer. Numerous experiments were performed at varying velocities and varied thicknesses of PVB. The results showed that the intermediate layer with thickness less than 1.52 mm fails quickly in comparison to thicker ones, because as delamination starts a high value of strain develops. Xu et al., 2010 [7] performed numerical simulation for velocity impact on windshield plate. It was observed that from crack pattern characteristics critical information like the velocity of impact

K. Senthil (✉) · G. S. Chauhan · S. Rupali · K. Pravesh
Department of Civil Engineering, National Institute of Technology Jalandhar, Jalandhar 144011, India
e-mail: kasilingams@nitj.ac.in

D. K. Maiti et al. (eds.), *Recent Advances in Computational and Experimental Mechanics, Vol II*, Lecture Notes in Mechanical Engineering,
https://doi.org/10.1007/978-981-16-6490-8_24

and failure stress can be calculated. It also concludes that for the study of the low-velocity impact on windshield plate, XFEM is a valuable tool for reproducing cracks that develops due to impact. Zhang et al., 2020 [8] performed an experimental study to analyse the behaviour of laminated glass under low-velocity impact by varying intermediate layers. The different types of interlayers SGP, PVB and TPU were used. The results have shown that the performance of LG is greatly affected by the impact energy and the type of intermediate layer used. It was observed that when impact was made at energy levels of 3 J and 5 J the intermediate layers of TPU and PVB performed better. But when impacted at higher energy levels of 10 J and 15 J the intermediate layer with SGP exhibited greater load-resisting capacity. Yuan et al., 2017 [9] developed an analytical model to study the behaviour of LG under low-velocity impact. Numerous studies were conducted using both analytical and experimental tests using two different intermediate layers, PVB and SGP. The analytical results obtained were validated with experimental results which were found in good agreement with each other. Wei et al., 2005 [10] performed hypervelocity impact tests velocity in the range of 1.5–5 km/s at normal angles to the surface of the laminated glass. The numerical simulation was carried out using smooth particle hydrodynamics (SPH) on laminated glass, to investigate the impact effect and to evaluate the damage characteristics. The material model adopted for glass material was the Johnson-Holmquist strength and failure model. It was observed that glass plies bound with plastic PVB interlayer lead to effective enhancement of the protection efficiency than glass plies put together without any interlayer like PVB at almost the same areal density.

The major benefit of toughened glass is to prevent glass shards from flying away and causing injuries, with the interlayer holding the glass shards and stopping shattered glass from flying into the occupants [11–14]. The transparent laminated glass plate consists of two or more layers of float glass sheets combined by an adhesive interlayer of tough PVB under heat treatment. Due to the composite action of layers of glass plies and interlayer glass adhesion (PVB), it is very difficult to understand the behaviour of laminated toughened glasses. The mechanism of rupture of laminated glass under impact is different since the glass and plastics will be laminated together and the failure mechanism depends on the number of layers of glass, projectile type, properties of plastics (PVB) and mechanical properties of the glass. Bulletproof glass is more correctly called bullet-resistant glass because no glass is totally bulletproof. Also, it is observed that it is difficult to simulate the complete fracture behaviour from a crack growth of the glass to the failure of the interlayer for the laminated plate using finite element analysis available in commercial packages (ABAQUS/AUTO-DYN) [15–17]. For reliable predictions of performances of structural glasses under impact loadings, an accurate constitutive model, strong coupling algorithms and solver are therefore needed [18–23]. The performance of toughened glass will be determined by many factors, such as laminate mass, post breakage stiffness, interlayer glass adhesion, interlayer tearing energy etc. Therefore, it is concluded that further studies on transparent glass are required to accurately analyse the response of chemically toughened laminated glass against small arms projectile impact using finite element simulations [18–22] by ABAQUS/AUTO-DYN/LS-Dyna solver.

Based on the detailed literature, it has been observed that the response of layered toughened glass against low-velocity impact was found to be limited. Therefore, the present study is focused to estimate the impact response of laminated glass under low-velocity impact using ABAQUS finite element technique. In addition to that, the performance of laminated glass plates subjected to varying velocities was thoroughly examined. The damage behaviour of laminated glass was incorporated through the linear elastic material model and brittle fracture model. However, the behaviour of polyvinyl butyral (PVB) is incorporated through a linear elastic material model. The numerical results were further validated with the experimental results available in the literature. The prediction results include time histories of impactor glasses acceleration and velocity during impact under various parameters such as different shapes, masses and velocities.

2 Constitutive Behaviour and Numerical Modelling

The constitutive behaviour of materials was incorporated using the linear elastic and brittle fracture model of glass and nonlinear finite element model available in ABAQUS/Explicit, as well as modelling of target and impactor and mesh convergence study were presented in this section.

2.1 Constitutive Behaviour of Target

The elastoplastic response of laminated glass such as glass and PVB was predicted using the linear elastic material model as well as the brittle fracture model. The parameters required in the model are material density, Poisson's ratio (v) and Young's modulus (E) (see Table 1).

This material model is available in ABAQUS which is usually used to model the failure of materials like concrete. This model can be further extended to glass and ceramics which are brittle in nature. Using this material model the impact damage initiation, evolution and failure patterns can be obtained. The smeared crack model is often used for concrete crack modelling when using the brittle fracture model. This

Table 1 Material properties of glass and PVB interlayer (Yuan et al., 2017) [9]

Material	Density (kg/m^3)	Young's modulus (MPa)	Poisson's ratio
Glass	2500	70,000	0.22
Interlayer (PVB)	2000	253	0.435

Table 2 Fracture properties of glass

Energy (N/m)	09.40
Stress (MPa)	74.00
Displacement (m)	1.081×10^{-7}

Table 3 Non-zero parameters of mode 2 failure of glass

p	2
e_{max}	0.002

material model takes into account the degradation of material stiffness at suitable points, instead of tracking individual cracks.

The brittle fracture model was used to predict the damage behaviour of glass material. There are two modes of failure associated with this model, i.e. crack initiation and crack propagation stages. In order to predict the starting point of failure at the crack initiation stage, the cracking failure stress has to be incorporated in the designed model. The initiation of damage starts when the principal stresses developed, and the maximum of all exceeds the failure stress pre-defined in the model. The fracture energy is associated with the first mode of failure. The parameters associated with this mode are shown in Table 2. The fracture energy of glass was 9.40 N/m available in the literature [24]**.** The direct cracking failure stress of glass was 74 MPa [25]. The non-zero parameters p and e_{max} were obtained from Don [25] (see Table 3). The direct cracking failure displacement was 1.081×10^{-7} m and the non-zero parameters p and e_{max} [25], respectively. For the linear elastic material model properties of PVB refer to Ref. (9). After crack initiation, the prorogation of crack is also referred to as post-failure mode in which only power-law technique needs to be considered. At the crack propagation stage, the failure of glass in brittle cracking model ABAQUS considers only two non-zero material parameters. The material was assumed to be failed when the local cracking displacement becomes equals to or exceeds the failure displacement at any point.

2.2 Numerical Modelling

The simulations were carried out using linear elastic and brittle fracture model of glass and three-dimensional nonlinear finite element model available in ABAQUS/Explicit [26]. The projectile used was a spherical impactor of radius 82.5 mm and mass of 4.52 kg. The length and breadth of the glass panel and PVB were taken as 1.26 and 0.79 m, respectively. The glass plates and PVB interlayer were modelled as deformable and fixed boundary whereas the impactor was modelled as analytic rigid as the elastic stiffness of steel is three times larger than the glass. The laminated glass was used in the experiment [9] comprising 4.76 mm thickness and contains two glass plates of 2 mm thicknesses as the outer layer with PVB sheet of 0.76 mm thickness as an interlayer was considered in the present study. The penalty contact algorithm

was defined between the target and impactor as well as glass and PVB. The friction between the target and the impactor as well as glass and PVB was defined as 0.002. The numerical model geometry was used as symmetric and full section, incorporating 8-noded brick elements with a reduced integration method. The element deletion option is available in the ABAQUS and the same is incorporated in the simulation in order to remove the element when the stress exceeds the limit defined for materials.

2.3 Mesh Convergence Study

The mesh convergence was carried out in order to estimate the mesh density and computational cost. The target with varying mesh sizes such as 3, 2 and 1 mm along with a spherical impactor is shown in Fig. 1. The mesh size was varied as 3, 2 and 1 mm and corresponding to the total number of elements as 19,872, 36,648 and 100,416, respectively. The CPU hour for 3, 2 and 1 mm mesh size was 2.5, 4.1 and 21 h, respectively.

The acceleration predicted from the simulations on target with 3, 2 and 1 mm mesh size against the impactor was 43, 40 and 42 *g*, respectively. It was observed that the target acceleration and deformations were shown in Fig. 2a and b, and the differences were found to be insignificant (40–43 *g*) at the initial rise time. A significant deviation between the experiment and simulations was observed in the case of 3 and 2 mm at 10 ms; however, the acceleration was somehow close to the experimental result. The predicted acceleration in the target with a 1 mm mesh size was 40 *g*, whereas the measured acceleration was 32 *g*. Therefore, the size of mesh of 1 mm was considered in the impact zone for both validation of simulation with the experiment as well as other parametric studies. However, the authors have attempted on 2, 3 and 4 mm mesh sizes considering entire targets of the same size in order to verify the results and it was observed that the target is sensitive to the mesh size. Further, the investigations such as the influence of nose shapes, 3 mm mesh size

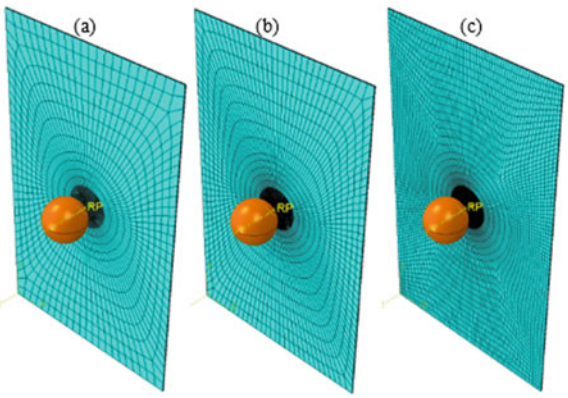

Fig. 1 Meshing density of **a** 3, **b** 2 and **c** 1 mm target with impactor

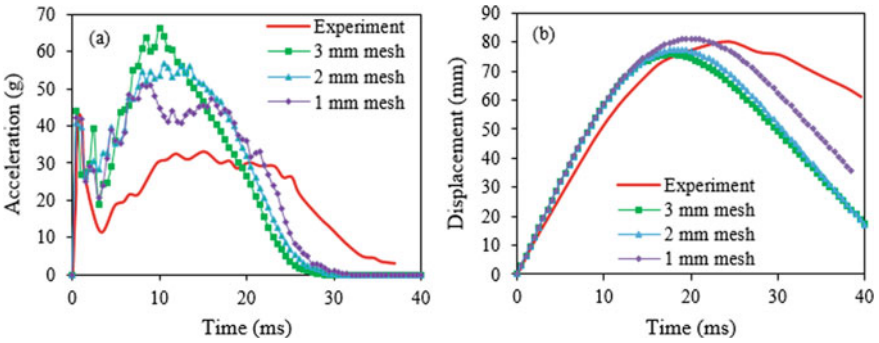

Fig. 2 Acceleration (g) (**a**) and **b** displacement (mm) of the target with varying mesh function of time

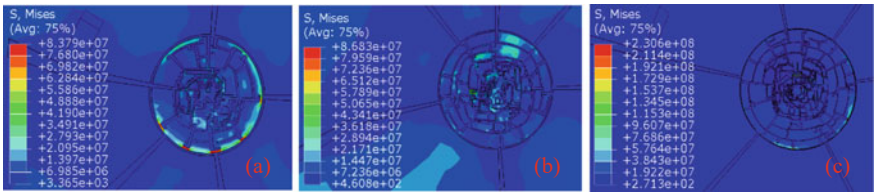

Fig. 3 Mises stresses (Pa) in **a** 3, **b** 2 and **c** 1 mm target at 40 ms

was considered the same mesh configuration in order to reduce the computational cost; however, the extended version of the paper is under preparation and thorough mesh-sensitive investigations will be presented. The Mises stresses of the target with varying mesh size at 40 ms (millisecond) are shown in Fig. 3.

In order to understand more about the propagation of cracks, the target with 3 mm size at the impact region and the target with 3 mm size in the entire region were compared (see Fig. 4). It was observed that there is a significant difference in crack propagation in the case of a target having finer mesh in the entire region. Also, it was observed that the Mises stresses on target with finer mesh in impact region and finer mesh in entire target region at 40 ms was found to be 83 and 67 MPa, respectively. Similarly, the displacement on target with finer mesh in impact region and finer mesh in the entire target region was found to be 14 and 31 mm, respectively. In order to verify the sensitivity of the mesh, further simulations were performed considering the same mesh size of 4, 3 and 2 mm in the entire target. The Mises stresses on glass with 4, 3 and 2 mm mesh sizes were found to be 45, 109 and 76 MPa, respectively, at 25 ms, whereas the same on PVB was 32, 29 and 32, respectively, see Fig. 5. Similarly, the displacement on target with 4, 3 and 2 mm mesh sizes was found to be 17, 53 and 24 mm, respectively. The CPU time for completing the simulation on 4, 3 and 2 mm mesh size targets was 16.5, 22 and 33 CPU hours, respectively. However, detailed investigations may be required in order to identify the mesh sensitivity in the target.

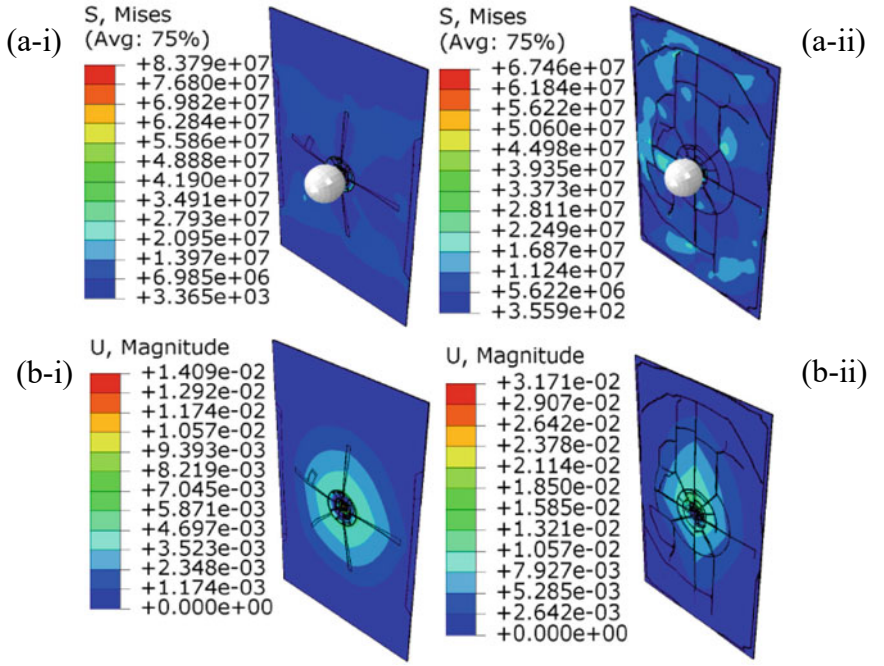

Fig. 4 **(a)** Mises stresses (Pa) and **(b)** displacement (m) on target with (i) finer mesh in impact region and (ii) finer mesh in entire target region at 40 ms **a** (a-i), **b** (a-ii), **c** (b-i), **d** (b-ii)

3 Comparison of Simulation with the Experiment

The simulations were performed on 4.76 mm thick-layered glass using ABAQUS finite element technique and the results thus predicted were compared with the experimental results. The response of laminated glass was studied against 4.52 kg mass of sphere which is the proximity of the experiment available in the literature [9]. Overall, the results thus obtained from the simulations were found in good agreement with the experiment [9] (see Fig. 6). The percentage of error between the experiment [9] and simulations is shown in Table 4 and it was found to be insignificant in the case of 6.39 m/s velocity.

4 Influence of Nose Shapes

The influence of nose shapes such as flat, hemisphere and ogival nose of 4.52 kg mass on layered toughened glass was studied and compared with the spherical nose shape. The influence of nose shapes was studied considering 3 mm mesh size in order to reduce the computational cost (see Figs. 7–9). The Mises stresses in the target against

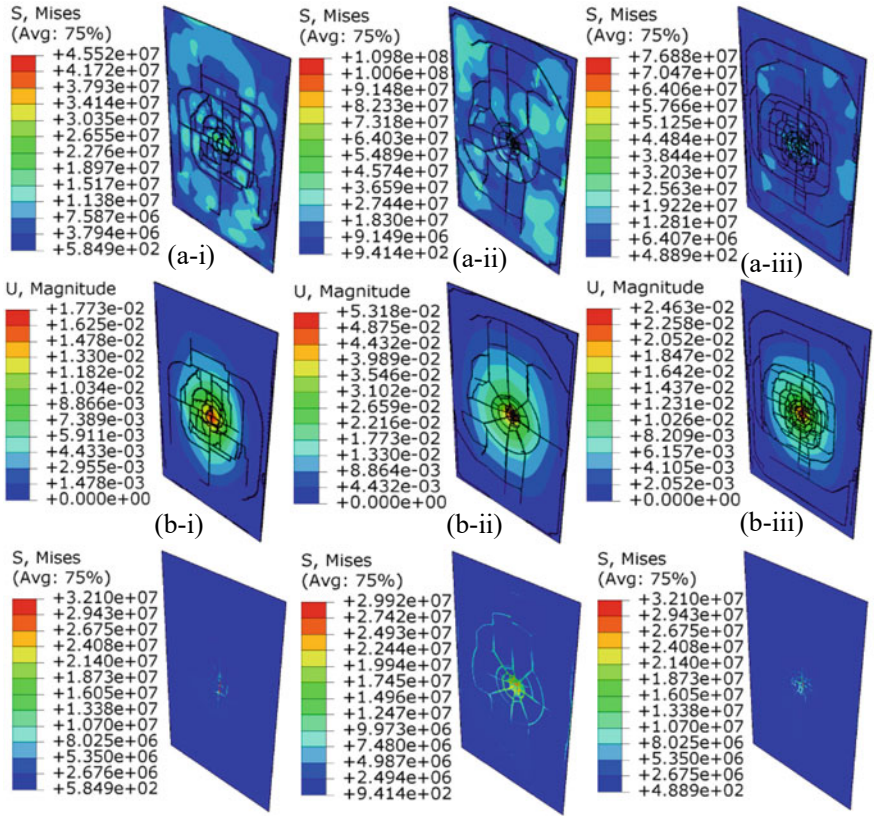

Fig. 5 **(a)** Mises stresses (Pa) on glass **(b)** displacement (m) and **(c)** Mises stresses (Pa) on PVB with (i) 4 mm, (ii) 3 mm and (iii) 2 mm at 25 ms

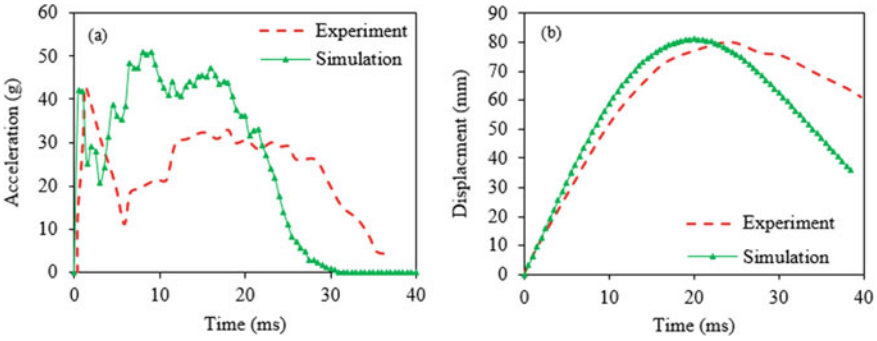

Fig. 6 Acceleration (*g*) **a** and **b** displacement (mm) of target against 6.39 m/s incidence velocity

Table 4 Comparison of experiment and simulations

Velocity (m/s)	Initial rise of acceleration (m/s^2)			Maximum displacement (mm)		
	Experiment	Simulation	% of error	Experiment	Simulation	% of error
6.39	435.8	431.3	1.05	80.6	74.8	7.18

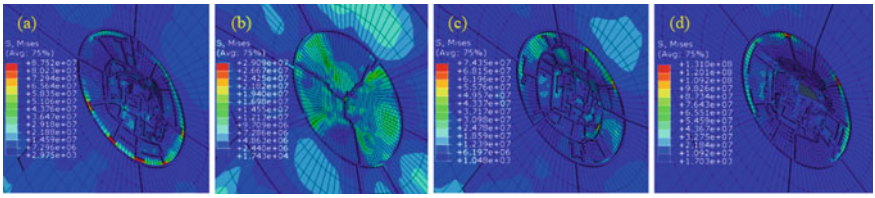

Fig. 7 Mises stresses (Pa) on target against **a** spherical, **b** flat, **c** hemisphere and **d** ogive nose impactor

spherical, flat, hemisphere and ogival nose impactor are shown in Fig. 7a–d. Overall, the impacted glass target exhibited two different failures such as cone and radial cracks. However, none of the impactors perforates the 4.76 mm thick-layered glass target against 6.39 m/s incidence velocity. It was observed that the failure pattern of glass against the sphere and hemisphere was found to be almost the same as radial cracks (see Fig. 7a and c). The glass failed into small pieces and the pieces of the target were found stuck with the target due to PVB. In the case of a flat nose impactor, the glass was deformed under cone failure and it was observed that few wider cracks originated from the centre of the target (see Fig. 7b). It was also observed that local failure such as small holes on the glass plate against ogival nose impactor at the same incidence velocity of 6.39 m/s. Based on the observation, the only ogival nose impactor pierces the target and it may be due to the fact that the sharp tip of the nose causes the hole in the target. Therefore, it is concluded that the ogival nose shape was found to be an efficient impactor among the chosen impactor shapes. The acceleration of the target against the spherical, flat, hemisphere and ogival nose impactor is shown in Fig. 8. The pattern and trend of acceleration in the target against spherical and hemispherical shapes were found to be almost the same. However, the highest acceleration was noticed in the case of flat nose impactor and the initial rise was found to be higher than second rise acceleration. However, the trend was found reverse in the case of the ogive, hemisphere and spherical nose shapes. In the case of the ogive nose impactor, the acceleration history resulted in a larger period due to the pointed tip; however, it follows the trend of hemispherical and spherical shape impactor.

The deformed profile and maximum displacement of the target against the spherical, flat, hemisphere and ogival nose impactor are shown in Fig. 9a–d. The maximum displacement in the target was found to be 58, 32, 52 and 70 mm against sphere, blunt, hemisphere and ogive nose impactor, respectively. It was observed that the maximum displacement was found in the target in the case of an ogive nose impactor and there is

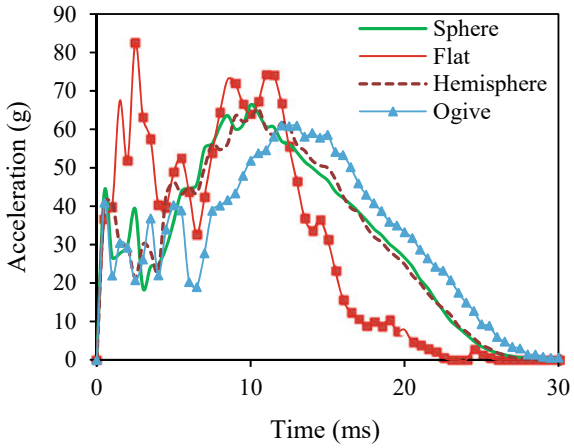

Fig. 8 Acceleration in target against varying nose shapes

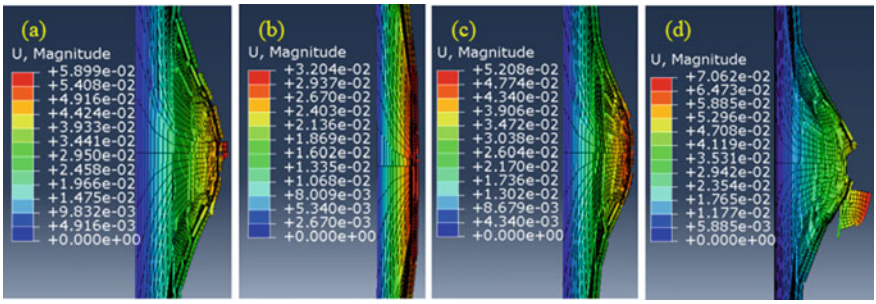

Fig. 9 Maximum displacement on target against **a** sphere, **b** blunt, **c** hemisphere and **d** ogive nose impactor

a scaping in the target (see Fig. 9d). It was also observed that the least displacement as well as least damage in the target against flat nose impactor. It was concluded that the flat nose impactor was found to be the least efficient penetrator whereas the ogival nose shape was found to be conservative and efficient among the chosen nose shapes.

5 Conclusions

The study is focused on estimating the impact resistance of 4.76 mm laminated toughened glass under 6.39 m/s velocity against 4.52 kg mass of impactor using ABAQUS, a commercial software. The damage behaviour of laminated glass was incorporated through the linear elastic material model and brittle fracture model.

The behaviour of PVB is incorporated through a linear elastic material model. The numerical results were further validated with the experimental results available in the literature. Further, the influence of nose shapes was studied and the following conclusions were drawn:

- The results obtained from numerical methods were found in good agreement with the experiments. The numerical methods provide reliable and extensive analysis which can be used in future large-scale modelling. The peak acceleration of the target varies significantly with varying incidence velocity, however, displacement was found to be almost the same.
- It was concluded that the flat nose impactor was found to be the least efficient penetrator whereas the ogival nose shape was found to be conservative and efficient among the chosen nose shapes. It was observed that the failure pattern of glass against the sphere and hemisphere was found to be almost the same as radial cracks.

References

1. Zhang X, Hao H, Ma G (2013) Parametric study of laminated glass window response to blast loads. Eng Struct 56:1707–1717
2. Hooper PA, Sukhram RAM, Blackman BRK, Dear JP (2012) On the blast resistance of laminated glass. Int J Solids Struct 49:899–918
3. Zhang X, Hao H, Ma G (2013) Laboratory test and numerical simulation of laminated glass window vulnerability to debris impact. Int J Impact Eng 55:49–62
4. Shetty MS, Wei J, Dharani LR, Stutts DS (2013) Analysis of damage in laminated architectural glazing subjected to wind loading and windborne debris impact. Buildings 3:422–441
5. Sakai S, Maenaka K, Kakuda H, Yamazaki K (2013) Optimum design of impact resistance of laminated glass plate. 10th World Congress on structural and multi-disciplinary optimization
6. Del Linz P, Hooper PA, Arora H, Wang Y, Smith D, Blackman BR, Dear JP (2017) Delamination properties of laminated glass windows subject to blast loading. Int J Impact Eng 105:39–53
7. Xu J, Li Y, Chen X, Yan Y, Ge D, Zhu M, Liu B (2010) Characteristics of windshield cracking upon low-speed impact: numerical simulation based on the extended finite element method. Comput Mater Sci 48(3):582–588
8. Zhang X, Liu H, Maharaj C, Zheng M, Mohagheghian I, Zhang G, Dear JP (2020) Impact response of laminated glass with varying interlayer materials. Int J Impact Eng 139:103505
9. Yuan Y, Xu C, Xu T, Sun Y, Liu B, Li Y (2017) An analytical model for deformation and damage of rectangular laminated glass under low-velocity impact. Comp Struct 176:833–843
10. Wei Z, Yue H, Gongshun G, Baojun P (2005) Experimental and numerical studies of laminated glass subject to hypervelocity impact. In: Proceedings of the fourth European Conference on Space Debris
11. Mecholsky JJ, Rice RW, Freiman SW (1974) Prediction of fracture energy and flaw size in glasses from measurements of mirror size. J Am Ceram Soc 57:440–443
12. Zhang X, Hao H (2016) The response of glass window systems to blast loadings: An overview. Int J Prot Struct 7(1):1–32
13. Linz PD, Hooper PA, Arora H, Wang Y, Smith D (2017) Delamination properties of laminated glass windows subject to blast loading. Int J Impact Eng 105:39–53
14. Adachi T, Osada M, Watanabe K (2016) Measuring behavior of impactor penetrating through polymer sheet based on electromagnetic induction. Key Eng Mat 715:122–127

15. Grujicic M, Bell WC, Pandurangan B, Cheeseman BA, Fountzoulas C, Patel P, Templeton DW, Bishnoi KD (2011) The effect of high-pressure densification on ballistic-penetration resistance of a soda-lime glass. Proc Inst Mech Eng Part L: J Mat Des Appl 298–315
16. Ralston AD, Weggel DC, Whelan MJ, Fang H (2015) Experimental and numerical investigations of glass curtain walls subjected to low- level blast loads. Int J Comput Meth Exp Measur 3(2):121–138
17. Chaudhri MM Dynamic fracture of inorganic glasses by hard spherical and conical projectiles. Philo Trans R Soc A **373**:20140135
18. Gautam PC, Gupta R, Sharma AC (2017) Manjit Singh, Determination of Hugoniot elastic limit and equation of state of ceramic materials in the pressure region 20 GPa to 100 GPa. Proc Eng 173:198–205
19. Rabczuk T, Belytschko T, Xiao SP (2004) Stable particle methods based on Lagrangian kernels. Comp Metho Appl Mech Eng 193:1035–1063
20. Rabczuk T, Areias PMA, Belytschko T (2007) A mesh-free thin shell for non-linear dynamic fracture. Int J Numer Meth Eng 72(5):524–548
21. Rabczuk T, Gracie R, Song JH, Belytschko T (2010) Immersed particle method for fluid–structure interaction. Int J Numer Meth Eng 81:48–71
22. Khawaja H, Messahel R, Souli M, Al-Bahkali E, Moatamedi M (2017) Fluid solid interaction simulation of CFRP shell structure. Mathe Eng Sci Aero 8(3):311–324
23. Badnava H, Msekh MA, Etemadi E, Rabczuk T (2017) An h-adaptive thermo-Mechanical phase field model for fracture. Finite Elem Ana Des 138:31–47
24. Bouzid S, Nyoungue A, Azari Z, Bouaouadja N, Pluvinage G (2001) Fracture criterion for glass under impact loading. Int J Impact Eng 25:831–845
25. Don PK (2013) Low-velocity impact analysis of monolithic and laminated glass using finite element method, Mater of Science. University of Birmingham
26. ABAQUS User Manual, Simulia, (2020)

Robotic Detection of Damage in Autonomously Assembled Structures Via Synthetically Trained Classification Models

Melanie R. Anderson, Conner Pulling, and Erik Komendera

1 Introduction

A global effort to establish a permanent human presence on the lunar and Martian surfaces is underway. Accordingly, the ability of robotic agents to autonomously assemble structures in uncertain environments is becoming increasingly imperative. Without these enabling technologies, the deployment of large structures such as instruments, habitats, communication infrastructures, solar array farms, etc. becomes prohibitively expensive and even hazardous if their construction requires astronaut assistance. Consequently, solutions to the many facets of the in-space assembly (ISA) problem are of considerable value to space-faring organizations across the world. Of the numerous unsolved ISA problems, the autonomous detection of damage states and assembly errors is among the most consequential. Without this capability, the mechanics of an assembled structure may be insufficiently known during assembly and over the lifetime of the structure. Furthermore, because computational capability and communications bandwidth to the Earth are strongly limited in space environments, assembly agents are required to perform detection locally and with limited resources. Therefore, to enable the incorporation of structures with predictable behaviors into current ISA initiatives, a computationally efficient autonomous detection capability must be first developed.

Structural health monitoring (SHM) research has been conducted and advanced for many decades; however, the state-of-the-art techniques have not been designed with the constraints of ISA missions in mind. They often require leave-in-place sensors, involve the monitoring of specific damage modes, and/or require human actors [1, 2]. In recent years, researchers have turned to the classification power of machine learning algorithms to overcome this lack of generality, but the training

M. R. Anderson (✉) · C. Pulling · E. Komendera
Virginia Tech, Blacksburg, VA 24061, USA
e-mail: mra2pz@vt.edu

D. K. Maiti et al. (eds.), *Recent Advances in Computational and Experimental Mechanics, Vol II*, Lecture Notes in Mechanical Engineering,
https://doi.org/10.1007/978-981-16-6490-8_25

of such algorithms for SHM purposes often requires the costly damaging of monitored structures or replicas thereof to determine the resulting damage metrics [3]. To circumvent this shortcoming, model-driven methods have also been developed in which the characteristics of the structure are compared to those of a finite element (FE) model to infer damage. Although this approach eliminates the need for manufacturing multiple copies of the same structure, it does require the generation of high-fidelity finite element models which must be correlated with the actual structure (usually via digital image correlation); otherwise, it is not guaranteeable that the model entirely captures the mechanics of the structure. The generation of such models is not trivial. It is also noteworthy that high-fidelity FE simulations (e.g. any simulation implementing 3D brick elements or other high degree-of-freedom elements, full quadrature schemes, highly refined meshes, etc.) can be computationally expensive. The research conducted by Schwarz et al. [4] and Cobb and Liebst [5] is only a couple of the many efforts that have demonstrated the applicability of model-driven methods for SHM. Considering their limitations though, the state-of-the-art approaches described above are unsatisfactory for the SHM of autonomously assembled structures in unstructured space environments (e.g. the lunar surface) as they are either economically infeasible, require human actors, or require computational powers outside the limits of the existing embedded system paradigm.

2 High-Level Description of Methodology

To overcome the obstacles preventing the deployment of autonomous SHM missions in uncertain environments, a synergistic approach has been developed in which model-driven methods and classification algorithms are employed such that robotic agents can be empowered to autonomously identify the health status of a structure and react accordingly. In this approach, thousands of simplified FE models for every suspected damage state are generated with joint positions that are varied via the addition of a noise vector sampled from a Gaussian multivariate distribution at each assembly step. Despite the increased computational time (which can be significantly mitigated by selecting parameters that simplify the FE models), it is important to generate multiple noise-varied models so as to capture the full breadth of behaviors that can be introduced to the actual structure as a result of assembly imprecision. Each of these models is then subjected to various loading conditions (representing a strategic prodding of the structure by a robotic agent) to induce a sustained static deflection. The resulting structural responses are used to train classification models, one for each loading condition. Once these models have been trained, they are able to predict which damage state (if any) is present in a structure given the loading condition and resulting behaviors. However, since structural responses are heavily dependent on loading configuration, an ensemble can also be employed such that the model predictions are weighted proportionally to their classification abilities for that damage scenario.

It is important to note that, in order for the above methodology to be effective, the FE models from which the training data is derived must be well-correlated with the actual deployed structure. This potentially poses stringent limitations on the methodology, as it is not trivial to correlate simulated models with structures that have not yet been assembled. Although this correlation is partially accounted for by the addition of assembly noise in the simulated assembly, a concept of operations has been designed for the purpose of improving the likelihood of model-structure correlation. A complete description of this ConOps is beyond the scope of this paper; however, it involves a mock ground assembly in which state estimations are used to inform the FE models, and material properties are adjusted to correlate damage indicators.

3 Structural Definitions and Finite Element Simulations

In this preliminary study, truss structures were exclusively examined. These structures have a high stiffness-to-weight ratio and possess redundant supports which provide stiffness in all three dimensions. These properties and the simplicity of assembly have granted ubiquity to these structures in aerospace and civilian applications; trusses are commonly used to erect communications towers, provide support structures to solar array panels, etc.

3.1 Structure Definitions

The following truss structures were examined in this study and are shown in Fig. 1:

1. *Communications Tower Analog* (CTA): three-bay (16-noded) square truss of base dimensions 0.3048 m

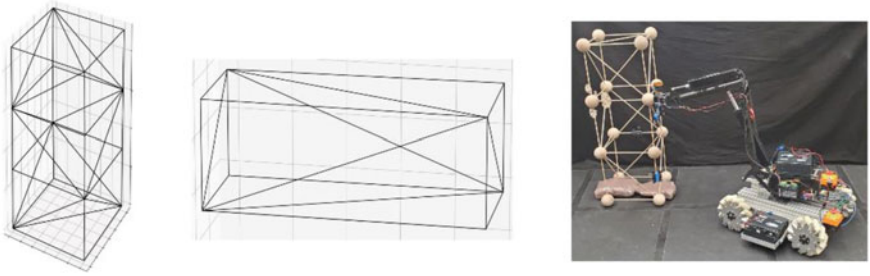

Fig. 1 Two examples of the simulated truss models developed in Python for FEA and a preliminary hardware model. On the left is shown the CTA. In the middle is shown the SASA. On the right is shown a hardware CTA model being probed by a Mobile Assembling Robotic Collaborator (MARC)

2. *Solar Array Support Analog* (SASA): one-bay (eight-noded) rectangular truss of base dimensions 2.5 m × 1 m × 1 m

To accommodate near-term hardware trials, these trusses were assigned Young's modulus, E, consistent with that of a softwood (E 8,000 MPa) and a cross-sectional area, A, of 31.67 mm^2 (properties of commercial off-the-shelf wooden struts).

During the simulated assemblies of these structures, the noise-varied nodal positions of the trusses were determined by adding a Gaussian multivariate noise vector to the nominal strut vector corresponding to the next assembly step. In this way, the accumulation of assembly error is preserved. This process was performed for uniform variances of $\sigma^2 = 0.45, 7.20, 14.40, 28.8$ mm^2 to later ascertain the effect of assembly imprecision on classification accuracies.

3.2 Damage Definitions and Indicators

For this early investigation, a damage metric was defined in which only the stiffness of struts was affected by the imposed damage. A strut damaged in this way is analogous to a structural member with a manufacturing defect, crack, or some other miscellaneous form of physical damage. The effects of such damage are illustrated in Fig. 2. Within the FE formulation, the damage was accomplished by multiplying the local elemental stiffness equation by a stiffness loss scalar, $\delta = 0.3$ as shown in Eqs. (1) and (2). This stiffness loss was applied one at a time to each of the struts in the set of possible damage classes for each structure. However, in the SASA studies, all 13 unfixed struts were considered, and only a subset of 14 struts was selected for the CTA study because the tower consists of 37 unfixed struts.

Once loads have been applied to the damaged structure, damage can only be identified if the structure exhibits some form of observable behavior that is indicative of the incurred stiffness loss. Two such damage indicators were explored: nodal displacements (the resulting global displacements of every truss joint) and elemental strains (the strain incurred in each strut).

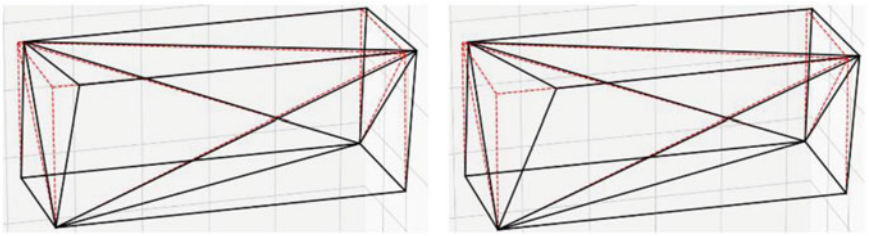

Fig. 2 Demonstration of effects of stiffness damage in a strut on the behavior of a loaded truss. On the left is shown a truss without damage and on the right is shown a truss in which the top-front horizontal member is damaged. Dotted lines represent the undisplaced trusses, and solid lines represent the displaced trusses

Although both were examined, not all damage indicators were included in each sub-study. During the CTA studies, in which only a subset of the potential damage classes was considered, displacements were exclusively included in an attempt to demonstrate that classification could be possible without any on-structure sensors. During the SASA studies, in which the full set of damage classes were considered, both were considered.

As mentioned above, these damage indicators must also be observable. Although a complete description of the data acquisition methods necessary for the observation of these features is outside the scope of this paper, it is envisioned that with external sensors in the workspace, onboard sensor suites, and removable sensors on the truss itself (e.g. strain gauges), the robotic agents will be capable of measuring these indicators within an acceptable noise envelope.

With these structure and damage definitions, an FE formulation could then be completely described.

3.3 Finite Element Formulations and Solutions

In order to minimize computational time, a partitioned direct stiffness formulation of 3D space truss elements was chosen and developed in Python in which the struts possess stiffness only in their axial directions. As is generally the case, the struts' stiffness matrices were developed in their local coordinate systems, as demonstrated in the internal force–displacement equations shown below in (1) and (2), and are then transformed such that they can contribute to the global stiffness matrix of the entire structure. The contributions of these stiffnesses were added to a partitioned global stiffness matrix to simplify the solving of the global system of equations.

$$\delta^{(i)}[K]^{(i)}\{u\}^{(i)} = \{f\}^{(i)} \tag{1}$$

$$\delta^{(i)}\frac{A^{(i)}E^{(i)}}{L^{(i)}}\begin{bmatrix} 1 & 0\,0 & -1 & 0\,0 \\ 0 & 0\,0 & 0 & 0\,0 \\ 0 & 0\,0 & 0 & 0\,0 \\ -1 & 0\,0 & -1 & 0\,0 \\ 0 & 0\,0 & 0 & 0\,0 \\ 0 & 0\,0 & 0 & 0\,0 \end{bmatrix}\begin{Bmatrix} u_{0,x}^{(i)} \\ u_{0,y}^{(i)} \\ u_{0,z}^{(i)} \\ u_{1,x}^{(i)} \\ u_{1,y}^{(i)} \\ u_{1,z}^{(i)} \end{Bmatrix} = \begin{Bmatrix} f_{0,x}^{(i)} \\ f_{0,y}^{(i)} \\ f_{0,z}^{(i)} \\ f_{l,x}^{(i)} \\ f_{l,y}^{(i)} \\ f_{l,z}^{(i)} \end{Bmatrix}, \delta^{(i)} = \begin{cases} \delta < 1 & (i)\text{damaged} \\ 1 & \text{else} \end{cases} \tag{2}$$

In (1), K represents the local stiffness matrix of an element, u represents the displacement vector of an element, and f represents the internal force vector of an element. In (2), the superscript i signifies the ith element, u represents the displacements of a specific node, f represents the elemental internal forces at a specific node, subscript 0 denotes the 0th node of that element, and the subscript l denotes the node

of that element attached at its length. This equation was developed assuming that, in each local coordinate frame, the strut's 0th node is attached to the local origin and the *x*-axis is aligned with the neutral axis of the element. It is also important to note that, in each assembly state, the three degrees of freedom (dofs) of each base node were fixed, as would presumably be the case for any deployed equipment-supporting truss.

In order to express the aforementioned stiffness loss, sustained static deflections were applied to the structure by simulated robotic agents. Because the effect of an applied load on the behavior of a damaged truss is a function of the direction and location of the applied load relative to the location of damage, various robotic loading configurations were applied to the system. These loads were strategically placed on nodes near possible damaged struts and in directions that were easily applied by robotic agents. Additionally, all applied forces were of a magnitude equal to 150 Newtons. These varying loads were simply incorporated into the FE simulation during the assembling of the partitioned global force vector.

Upon assembling the partitioned global stiffness matrix and injecting the known applied loads into the system, the unknown global displacements could be calculated using (3).

$$\{U_u\}=[K_{uu}]^{-1}\left(\{F_u\}-\left[K_{up}\right]\left\{U_p\right\}\right) \tag{3}$$

In this well-known solution, K_{uu} is the stiffness partition whose rows and columns correspond to the unknown dofs, K_{up} is the stiffness partition whose rows correspond to the unknown dofs and whose columns correspond to the known dofs, F_u is the force partition that corresponds to the prescribed dofs, U_p is the prescribed displacement vector, and U_u represents the unknown (i.e. those that are not fixed to the ground) displacements of the structure's joints as a result of the applied loading. This last vector is important because it is a robot-trackable feature of the structure that can be used to train classification algorithms.

Once these displacements were known, elemental strains, another trackable feature, could also be computed for the purpose of classification. Since they are 3D space truss elements, the elemental strains are constant throughout their cross-sections and along their lengths and were calculated using the strain–displacement definition, $\in= L^{-1}\Delta L$, where $\in$ is the elemental strain, L is the undisplaced length of a strut, and ΔL is the change in length of the strut as a result of the applied force.

4 Classification Algorithms

Many classification algorithms were evaluated during this preliminary study as described below; however, before these models could be trained and tested, the raw finite element data needed to be appropriately organized as input data.

4.1 Data Organization

Each of the implemented classification algorithms required the generation of design matrices, X, composed of feature row vectors containing either displacements or strains as discussed in Sect. 3.2. Each of these row vectors of damage features corresponds to a single generated instance of the truss being examined, and each column corresponds to either a displacement or strain at a particular tracked location on that truss. Also required by these algorithms are the related label vectors, y, that contain the damage class labels for each row of damage indicators. Each of these damage class labels corresponds to a truss containing damage in a particular strut. For instance, in the SASA studies, damage class 1 corresponded to a truss with damage in strut number 3. When combined with the design matrices, these label vectors defined a range of correspondence between the damage indicators and the present damage class.

Although numerous values were tested, it was determined that past n 2000 truss instances per damage class (15 classes for CTA and 14 classes for SASA), the tradeoff between improved training capabilities and increased computational time began to become less favorable. As such, for every model, 30,000 or 28,000 uniquely varied trusses were generated using the FE formulation, and the damage indicators of each truss as a result of its loading condition, damage class, and noise level were recorded in a design matrix. These design matrices were then constructed for each loading condition (ten for the CTA and eight for the SASA).

Additionally, another architecture was evaluated during the SASA studies for the purpose of classification with only partial datasets. Such a scheme is important because it is not trivial to obtain full-truss sets of damage features (especially those requiring visual sensing) in an uncertain environment with limited sensing capacity. In this strut-wise architecture, design matrices were constructed from data pertaining to one strut at a time. Although this required the generation of additional design matrices, the feature space was diminished which expedited training times. Furthermore, this allowed for the framing of a binary classification problem instead of a multiclass problem in which the struts were individually examined for damage. In this architecture, strains were primarily employed since nearby damage can significantly influence the global displacements of a strut's nodes.

All of these design matrices were then scaled, preprocessed, and split into training, validation, and testing sets before finally being fed as input data into the classification algorithms described below.

4.2 Classification Models and Ensembles

This study began with the employment of multiclass support vector classifiers (SVCs) evaluated with a grid search over a range of hyperparameters including the kernel

type, regularization parameter, etc. These models only considered one loading condition at a time; however, because some loads express certain damage classes more than others, an ensemble method was required for accuracy across all damage classes. This led to the development of an F1-score voting ensemble, a voting system in which each model's vote was weighted using the F1 scores (the harmonic mean of precision and recall) calculated from each model's validation set. In a multiclass model, there exist c F1 scores, one corresponding to each class. This allowed for the weighting of each model's vote by the F1 score corresponding to its prediction. This ensemble drastically increased the classification accuracy, but it was noted that this improvement did not scale with the number of loading conditions examined. This led to the development of an integer programming formulation that maximized the F1 score for each class by tuning the number of loads included.

Auto-Sklearn [6] was then employed to efficiently automate hyperparameter tuning and explore additional classification models. This meta-learning library revealed interesting model and hyperparameter selections when applied to individual loading condition datasets. Random forests classifiers were selected 60% of the time and an extra trees classifier yielded the highest performance. These models were then placed in an F1 ensemble to further improve the testing accuracy; however, the ensembles were inadequate at classifying the undamaged case. To overcome this, Bayesian model combination (BMC) [7] ensembles were implemented.

Unlike the F1 ensembles, BMCs consider misclassification tendencies, an important consideration when attempting to overcome grossly misclassified classes, when scaling a model's vote. To construct these ensembles, the hypothesis space for each model was approximated by the posterior probability matrix computed from the confusion matrix generated from validation set testing. These conditional probabilities represented the probability that a damage class was present given a model's predicted damage class and were used to weight each model's prediction. The BMCs were much more capable at correctly classifying the undamaged class, but led to only marginal overall accuracy gains.

Neural networks (NNs) were lastly considered during the final stages of this study. Another meta-learning library, Auto-Pytorch [8] was employed to perform efficient architecture selection and hyperparameter tuning. After several runs, it became clear that Auto-Pytorch favored a fully connected layer-based network with residual shortcut connections based on ResNet's residual building block [9]. Although only slight improvements were observed, an interesting discovery was made about this model. The NN was employed on the SASA datasets with nearly the same hyperparameters and architecture and performed almost identically, indicating that it may be a more generalized model.

5 Results and Conclusion

In Tables 1 and 2, an incomplete compilation of classification results for the various algorithms tested on CTA and SASA data is described. The average model/ensemble Top-1, Top-2, and Top-3 accuracies are shown, which indicate how often the actual damage class was included in the models' first choice, top two choices, and top three choices, respectively. For the sake of brevity, hyperparameters, training times, inference times, and detailed NN architectural details are not included; interested parties may contact the authors for this information. Results for NNs are averaged over three trials.

Table 1 Top-1, Top-2, and Top-3 accuracies of five evaluated classification algorithms for the CTA structure using nodal displacement damage indicators. These results correspond to trusses assembled with variances, $\sigma^2 = 28.8$ mm^2

Model	CTA (displacements)		
	Top-1 (%)	Top-2 (%)	Top-3 (%)
SVC w/optimized F1 ensemble	72.3	78.0	82.0
Auto-Sklearn	69.3	74.9	80.0
Auto-Sklearn w/optimized F1 ensemble	83.9	87.8	91.5
Auto-Sklearn w/ BMC	85.8	90.7	94.8
NN w/o shortcut	81.1	92.3	99.2
NN w/residual shortcut	85.9	92.1	99.3

Table 2 Top-1, Top-2, and Top-3 accuracies of five evaluated classification algorithms for the SASA structure using nodal displacement and elemental strain damage indicators. These results correspond to trusses assembled with variances, $\sigma^2 = 28.8$ mm^2

Model	SASA (displacements)			SASA (strains)		
	Top-1 (%)	Top-2 (%)	Top-3 (%)	Top-1 (%)	Top-2 (%)	Top-3 (%)
SVC w/optimized F1 ensemble	84.1	87.9	91.1	88.1	91.6	93.9
Auto-Sklearn	70.9	77.9	81.9	72.6	79.5	83.3
Auto-Sklearn w/optimized F1 ensemble	83.6	87.1	90.0	87.8	90.6	92.4
Auto-Sklearn w/BMC	86.2	90.4	93.4	90.3	94.8	96.0
NN w/o shortcut	85.7	92.8	100	85.7	92.8	100
NN w/ residual shortcut	85.4	92.6	100	85.7	92.8	100

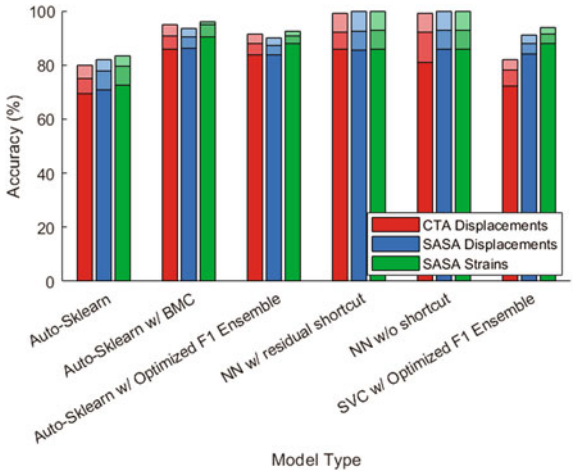

Fig. 3 Graphical representation of Top-1 (foreground), Top-2 (middleground), and Top-3 (background) classification accuracies for CTA displacements, SASA displacements, and SASA strains

As demonstrated in Fig. 3 and Table 1, most of the algorithms were capable of correctly identifying the damaged strut in more than 80% of the CTA trusses. The BMC ensemble and the residual fully connected NN were the top classifiers; however, it is of note that the NN was able to make inferences 35 times faster. In addition, the residual shortcut connection improves the Top-1 accuracy by an appreciable margin while not significantly reducing the Top-2 or Top-3 accuracies is shown. Lastly, the residual shortcut yielded faster convergence times as shown in Fig. 4 in the Appendix.

It is apparent from a comparison between the results for the two structures that the SASA classifiers had significant increases in performance over the CTA despite the inclusion of the SASA's full damage class set. It was initially expected that, although there is one less damage class in this full SASA class set than in the CTA class set, the classifiers would struggle with the SASA since the damage classes are not as geometrically distributed as they are in the CTA; however, it is clear that the decreased complexity of the structure simplified the classification problem. Furthermore, unlike for the CTA, the BMC significantly outperformed all other methods for the SASA strain datasets. This indicates that knowledge of the misclassification tendencies was of more value for this structure. That being said, the NNs were the only models capable of achieving 100% Top-3 accuracy. Also evident in Table 2 is the increased value of the strain indicators over the nodal displacement indicators to all but the NN models, since the models exposed to the strain experienced an average accuracy increase of approximately 4%. Each of these data trends is represented graphically in Fig. 3 for both structures.

Table 3 shows that NNs were able to determine whether each individual strut (except for struts 3 or 10) was damaged with 100% accuracy. For struts 3 and 10, these algorithms did not perform as well, but this is not unexpected considering strut 10 is a mirror image of strut 3 and the loads applied to the struts are also mirrored images. Since strains only preserve directionality in one dimension, these two struts should have nearly identical strains for mirrored loading conditions. This demonstrates the necessity of strategically applying probing loads, especially for

Table 3 Average classification accuracies using the strut-wise scheme on the SASA datasets. The results for two subsets of the struts are presented. These results correspond to trusses assembled with variance, $\sigma^2 = 28.8\ \text{mm}^2$

Strut-wise scheme; SASA (strain only)		
Model	Struts	Binary accuracy (%)
NN w/residual shortcut and upsampling	3, 10	80–81
NN w/residual shortcut and upsampling	All other struts	100

structures with similar elements. Despite this, these results are important because they show that, with only strain readings from one strut for eight separate probes, robotic agents were capable of determining its health with impressive levels of certainty.

As near-100% Top-1 accuracy is desired, the preliminary trials described above have perhaps demonstrated that these procedures by themselves are not yet sufficient for the purpose of monitoring actual structures. However, since some models were capable of achieving near-100% Top-3 accuracies, it has also been demonstrated that the proposed methodology can tremendously refine the space of potential damage cases. This is significant because it allows for the employment of a specialized investigation in which only three struts are considered instead of the entire structure. In fact, because the BMC's inadequacies are misaligned with those of the strut-wise scheme, it may be possible to achieve 100% accuracy by performing a limited scope strut-wise classification upon narrowing the damage set to three struts.

Although these are meaningful results, there are many subsequent avenues of research that need to be traversed before such a methodology can be implemented in an actual ISA mission. This includes but is not limited to validating the methodologies on hardware (initial tests with hardware are currently being performed as shown in Fig. 1), evaluating alternative damage modes (e.g. improperly attached or misaligned joints), examining alternative damage indicators, exploring new feature space combinations, and determining formally the algorithms' dependence on assembly variance and the number of generated trusses.

Acknowledgements This research was funded by the Assemblers: A Modular and Reconfigurable Manipulation System for Autonomous In-Space Assembly NASA Early Career Initiative grant.

Appendix

See Fig. 4.

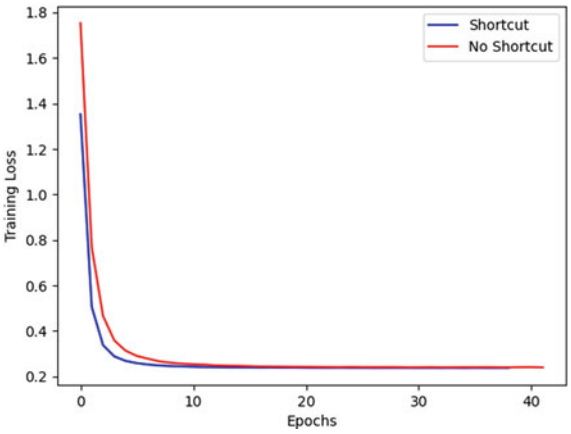

Fig. 4 Plot of training loss as a function of epoch illustrating faster convergence of neural network models with residual shortcut during SASA strain study

References

1. Zhao X, Gao H, Zhang G, Ayhan B, Yan F, Kwan C, Rose JL (2007) Active health monitoring of an aircraft wing with embedded piezoelectric sensor/actuator network: I. defect detection, localization and growth monitoring. Smart Mater Struct 16(4):1208–1217. https://doi.org/10.1088/0964-1726/16/4/032
2. Velsor JKV, Gao H, Rose JL (2007) Guided-wave tomographic imaging of defects in pipe using a probabilistic reconstruction algorithm.https://doi.org/10.1784/insi.2007.49.9.532
3. Worden K, Manson G (2007) The application of machine learning to structural health monitoring. Philos Trans R Soc A: Math Phys Eng Sci 365:515–537. https://doi.org/10.1098/rsta.2006.1938
4. Richardson SM, Formenti DL (2007) FEA model updating using SDM, p 7
5. Cobb RG, Liebst BS (1997) Structural damage identification using assigned partial eigenstructure. AIAA J 35:152–158. https://doi.org/10.2514/2.77
6. Feurer M, et al (2015) Efficient and automated machine learning. Adv Neural Inf Process Syst
7. Monteith K, Carroll JL, Seppi K, Martinez T (2011) Turning Bayesian model averaging into Bayesian model combination. In: The 2011 international joint conference on neural networks, San Jose, CA, 2011, pp 2657–2663. https://doi.org/10.1109/IJCNN.2011.6033566
8. Mendoza H, Klein A, Feurer M, Springenberg JT, Hutter F (2018) Towards automatically-tuned neural networks. https://doi.org/10.1007/978-3-030-05318-57
9. He K, Zhang X, Ren S, Sun J (2016) Deep residual learning for image recognition. In: 2016 IEEE conference on computer vision and pattern recognition (CVPR), Las Vegas, NV, 2016, pp 770–778. https://doi.org/10.1109/CVPR.2016.90

Construction Industry with 3D Printer: A New Era

Shivam Sharma, Soham Mitra, Adeyemi Adesina, and Sreekanta Das

1 Introduction

The concept of 3D printing started with the invention of stereolithography by Charles W. Hull of the USA in 1983. This technology, also known as rapid prototyping (RP), uses a photochemical process to polymerize synthetic resins, leading to a fast, precise, and repeatable production of elements with the help of computer support. Using this technology objects with very high precision and extremely complicated geometry can be built. Hence this technology found its use in various fields such as medicine and automotive industries [1]. The first commercially available 3D printing system, built using RP technology, known as SLA-1 was developed in 1987 [2].

The foundation for additive manufacturing using cement-based materials was laid through the work of Pegna [3]. This study used the techniques of depositing layers of reactive material over layers of the matrix material. Currently, the techniques used in large-scale concrete 3D printing are contour crafting, D-shape, and concrete printing [4]. The N2MBuild or the nano to meter build technique is used along with other concrete 3D printing techniques for building the utilities [5]. There has been a

S. Sharma · S. Mitra · A. Adesina · S. Das (✉)
University of Windsor, Windsor, ON, Canada
e-mail: sdas@uwindsor.ca

S. Sharma
e-mail: sharm189@uwindsor.ca

S. Mitra
e-mail: mitras@uwindsor.ca

A. Adesina
e-mail: adesina1@uwindsor.ca

S. Das
Department of Civil and Environmental Engineering, University of Windsor, 401 Sunset Avenue, Windsor, ON, Canada

D. K. Maiti et al. (eds.), *Recent Advances in Computational and Experimental Mechanics, Vol II*, Lecture Notes in Mechanical Engineering,
https://doi.org/10.1007/978-981-16-6490-8_26

huge growth in 3D concrete printing activities since its inception by Pegna in 1997. Figure 1 shows the growth in activities in 3D printing since 1997.

Contour crafting: Khoshnevis through his studies conducted during the period of 1998–2004 developed the contour crafting technique, in which a cement-based paste is continuously deposited in the form of layers and involves the use of a trowel to smoothen the printed material [7, 8]. The printing for this process is done using a gantry-based setup. This layer-by-layer method has the potential to render a paradigm shift, thus leading to a revolutionary change in the construction industry [9]. Moreover, contour crafting was chosen by NASA to explore its potential to build a swift and reliable lunar infrastructure [10]. Figure 2 shows the layer-by-layer contour crafting printing using a gantry-based system.

D-shape: The D-shape method, developed by Enrico Dini, was first exhibited in 2007 in London [12]. In this process, a 3D printer is used with sand as a building material.

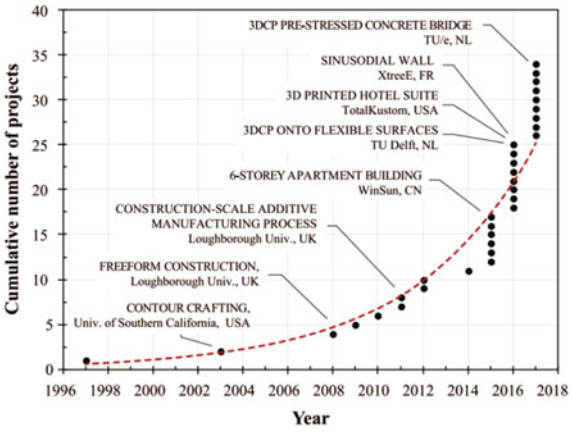

Fig. 1 Growth in projects involving 3D concrete printing [6]

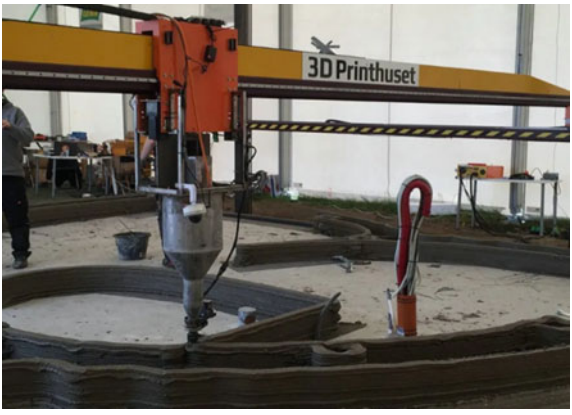

Fig. 2 Contour crafting printing using a gantry-based system [11]

Fig. 3 Structure printed using the D-shape method [4]

It uses a stereolithography 3D printing process in which sand, a binder, is sprayed on the surface of each sequential layer, hardening the surface selectively. The process is repeated several times for the full structure to develop as per the digital model. Any material that is not glued by the binder is used as a support to the subsequent layers and can be removed from the printed structure using a vacuum cleaner. Thus, this method is beneficial to print complex structures that have overhangs and voids. This process like contour crafting uses a gantry for the printing process but the structures are printed off-site with much human intervention. Figure 3 shows an egg-shaped structure printed using the D-shape method.

Concrete printing: Concrete printing is also an off-site manufacturing process using a gantry system. This process, like the other two processes, is also based on the extrusion of cement mortar. But this process has more control over internal and external geometries. It uses a single deposition nozzle through which only the required material volume is deposited in the structure. The print resolution for concrete printing can vary from 4 to 6 mm. However, this layer-by-layer printing method introduces anisotropy to the structure and can cause a staircase—sausage-like—effect on the printed surface. This layering error—staircase effect—can substantially affect the quality of external surfaces. Furthermore, the deposition rate for this process is slower than that of the other two processes. Figure 4 shows a full-scale build using the concrete printing process [4].

N2MBuild: The N2MBuild or the nano to meter build was developed to reduce the number of raw materials, pollution, and energy consumption that is caused by traditional building technologies. This process utilized carbon dioxide to print the structures by extracting carbon dioxide from the atmosphere. Nanorobots, controlled

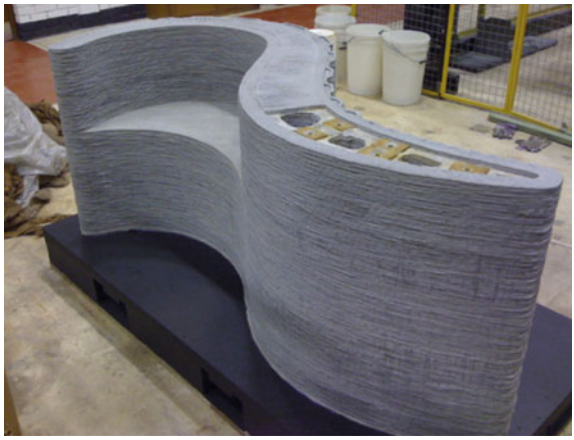

Fig. 4 A full-scale build using the concrete printing process [4]

and powered by light, are used for printing. Light of a particular wavelength is emitted by a projector, which uses a detailed 3D digital model as an input, from above the site. This is used mostly to print the utilities of a building such as pipelines, communication lines, etc. [5].

2 Critical Properties of Concrete Used in 3D Printing

It is not viable to use conventional concrete as a raw material for 3D printing due to its composition and fresh properties. Since 3D concrete printing is done without any supporting framework [4], the printed layers should be able to bear the weight of subsequent layers without a large deformation. Additionally, the material, in its fresh state, should be able to smoothly extrude through the pipes and the nozzles [13, 14]. Hence, concrete (cementitious material) used in 3D printing needs to be workable enough to pass through the printing nozzle and set as quickly as possible in order to have the capacity to support layers of the concrete. Buildability and flowability are also found to be crucial for 3D printing and have a certain mutual relationship [15]. Therefore, high-performance materials are required to obtain a high extent of control during the printing process [16]. The fresh and hardened properties of 3D concrete can be enhanced with the use of various mineral and chemical admixtures alongside additives such as fibres. The following sub-sections discuss various properties that are needed for 3D concrete printing.

2.1 Rheological Properties

The rheological properties of concrete are indicators that describe the fresh properties of concrete in terms of its flowability and deformation. To ensure proper 3D printing of concrete, the viscosity of the concrete must be low initially and increase significantly soon after it is extruded from the nozzle to be able to support the self-weight of the printed layers. Therefore, it is of utmost importance to have adequate control of rheological properties for smoother pumpability and the rapid setting of the concrete after it is extruded from the nozzle [17]. In the past, researchers have been able to influence the rheological properties of concrete by tailoring the mix designs using various methods. For instance, rheological parameters such as viscosity and yield stress can be significantly improved by increasing the coarse aggregate (CA) and fine aggregate content in the mix [18]. However, the size of coarse aggregates used must be small enough for easy printing of the concrete and preventing clogging of the printer. Chemical admixtures such as superplasticizer (SP) and viscosity modifying admixture (VMA) can also be used to improve the rheology properties. The SP can be used to increase the workability of the concrete mixture without any significant determinantal impact on the mechanical properties while the use of VMA will prevent possible segregation of bleeding of the concrete. Mineral admixtures such as fly ash and silica fume can also be incorporated as the binder component to improve the workability of the concrete. It is worth mentioning that majority of the mineral admixtures are wastes products from various industrial processes, hence, their use in concrete will improve the overall sustainability of the 3D printed concrete.

Another critical rheology property of concrete used in 3D printing is the setting time. The concrete used for 3D should be able to be set within a timeframe such that it is fluid enough to be printed and set fast before the next layer is printed. Hence, a shorter set times (i.e. initial and final) lower than that of the conventional concrete is required for the concrete to be used in 3D printing. The setting time can be controlled with the use of chemical admixtures such as accelerators which accelerates the hydration process.

2.2 Pumpability of Concrete

As the name implies, the pumpability of concrete for 3D printing is an indication of the ability to pump the concrete without any detrimental impact on the performance of the concrete and the 3D printer. Mobilizing the ability of concrete under pressure and keeping its initial properties unchanged is termed concrete pumpability [19]. The applied pressure, required to move the concrete through the pipes, causes some deformation in the concrete material in the direction of the applied force. Since fresh mortar gets deformed more easily than the coarse aggregate (CA), the deformation characteristic of the concrete significantly depends on the fresh mortar. Therefore,

carefully tailored mix designs are required to optimize the rheological properties of the fresh concrete [20].

2.3 Extrudability of Concrete

The capability to steadily print concrete by passing it through pipes and nozzles of the 3D printer is referred to as extrudability. It has been reported that the particle sizes of the constituent materials used for the production of concrete significantly affect the corresponding extrudability for 3D printing. Segregation can be caused due to the high content of sand, therefore, it should be avoided [13, 14]. Zareiyan and Khoshnevis demonstrated a concrete mixture that can be extruded without a framework. In that study, to analyze the extrudability of the concrete, four key factors were considered, and these factors included bonding agents (cementitious and supplementary cementitious materials), water-cement ratio, fibres for reinforcement, and superplasticizers [21]. Generally, to improve the extrudability of concrete used in 3D printing, the components of the concrete should be made up of particles possessing spherical morphology instead of angular.

2.4 Buildability of Concrete

The buildability of concrete which is an indication of the capability of printed concrete to maintain its form during the printing process is essential to the overall performance of the 3D concrete. Shear strength of fresh concrete can be varied by varying the dosage of superplasticizer and ultimately resulting in optimum buildability [13, 14]. Apart from modifying the constituent material properties, buildability can be improved by changing the type of nozzle. For instance, making use of a rectangular or square nozzle instead of a circular nozzle can increase the contact area between the subsequent layers [22]. Le et al. found that the buildability of a given mix can be improved by increasing the number of adjacent filament layers [13, 14].

2.5 Mechanical Properties

Regardless of how concrete is produced; the mechanical properties are critical to its overall performance as it is an indication of the ability of the produced concrete to withstand various loads. A review by Paul et al. suggests that limited research has been conducted on the mechanical properties of 3D printed concrete [22]. Wolfs et al. did a recent experimental study on the effect of 3D concrete printing parameters (interlayer print-time, nozzle height, and surface dehydration) on the mechanical

properties (compressive strength and tensile strength) [23]. Intriguingly, the study has exhibited the use of geotechnical (soil) tests to evaluate the properties of early age printed concrete, in the range of 0–90 min after deposition [24]. They posit Mohr–Coulomb theory as a satisfactory failure criterion for early age 3D printed concrete. Furthermore, it was found that cohesion varied linearly with time, and internal friction was independent of age. The study also concluded that Young's modulus, shear strength, and compressive strength were a linear function of time for a freshly printed concrete.

In a study conducted by Nerella et al., compressive and flexural strengths of printed concrete were found to be higher than the conventionally casted prism specimens produced from the same batch of mortar [25]. However, recent research at the Eindhoven University of Technology indicates that the compressive strength of printed specimens was about 31% lower than that of casted specimens [23]. It is interesting to note that the compressive strength of the printed material had no directional dependency. In contrast, Feng et al. have concluded that the loading direction and the size of the specimen influence mechanical properties like elastic modulus, strength, and Poisson's ratio [26]. Their research exhibited a higher compressive strength when the specimens were tested parallel to the layer depositions compared to when loaded perpendicular to the printed layers. Therefore, suggesting that 3D printed materials are orthotropic. The finite element analysis of a thin shell structure conducted by them also indicated the influence of the printing direction on the overall structural performance.

2.6 Inter-layer Bond Strength of 3D Printed Concrete

Weak inter-layer strength of printed concrete is regarded as one of the major challenges in the extrusion-based 3D printing method since there is a high possibility of flaws occurring in-between the extruded layers. Sanjayan et al. found that the moisture level at the surface of the printed layers significantly affects the inter-layer strength. The moisture level was further found to be a function of various parameters: the evaporation rate, the printing process, and the rate of the bleeding of the mixes [27].

The structural performance of 3D printed concrete is critically affected by the bond strength between the layers and it was found that the manufacturing process has a clear impact on this bond strength [23]. The bond between the substrate and overlay of the cast-in-mould concrete is influenced by several factors such as the moisture content and interface texture of the existing concrete surface [28]. However, in 3D concrete printing, the layers are in a fresh state and their inter-layer strength is majorly influenced by the adhesion between them. This adhesion further depends on the print-time between subsequent layers, which should be optimized in such a way that the delay time is long enough to let the extruded layers be strong enough to support the upper layers, but not that long to ensure proper bonding between the layers [13, 14, 27]. In the study carried out by Le et al., it was found that increasing

the print-time between two layers led to weak tensile bond strength. Further, the study established a relationship between characteristic bond strength and print-time [13, 14].

3 Reinforcement in 3D Printed Concrete

As concrete is weak in tension, concrete structures require reinforcement for better structural performance. Current techniques of additive manufacturing of concrete do not cater to the ductility and tensile capacity of the structure since most of the approaches focus on the placement of concrete. In addition, the current solutions for automation in reinforcement are still rudimentary. Therefore, there is a need to resolve this recurring issue [29–31].

The 3D printing of fibre-reinforced geopolymer was studied, leading to an improvement in flexural and tensile strength [32]. However, the fibre content of up to only 1% was investigated to avoid clogging during the extrusion process. Hack and Lauer developed the Mesh Mould approach, where the first step is to print a corrugated framework of thermoplastic polymers. Then, concrete is poured over this framework, and finally, to achieve a smoother finish, the surface is troweled manually [32]. As polymers have low stiffness and to increase the functionality of this method, the study further enhanced the method by allowing the automation of metal reinforcement [33].

A reinforcement entrainment device has been developed at the Eindhoven University of Technology that can insert the steel reinforcement into the concrete filament before it is released from the nozzle. The beams printed with this device had a significant post-crack moment capacity [29, 30]. They further refined the method by establishing pull-out characteristics such as the bond strength and anchorage length of both the printed and the traditionally cast concrete. It was found that the bond strength of printed concrete was significantly lower than that of the traditionally cast concrete [29, 30].

Mechtcherine et al. developed a novel technique of 3D printing steel bars with geometric precision and freedom, using gas-metal arc welding. The printed steel bars exhibited a lower yield stress by 28% and a lower tensile strength by 16% than the conventionally used reinforcement rebars. Nonetheless, a ductile mode of failure was observed in the printed steel bars [31].

4 Structures Built Using Concrete 3D Printing Technology

In the recent past, many commercial structures have been build using 3D printing technology. The DFAB House in Switzerland is the world's first inhabited house, with a floor area of about 200 sq. meters, that was both digitally planned and built. This project was completed in 2019 by the professors at ETH Zurich in collaboration

Fig. 5 DFAB house in Switzerland [36]

with various industry partners. The project combined six new digital fabrication technologies in the building. These technologies are in situ fabricator, which is a mobile onsite construction robot equipped with sensing and feedback systems to operate autonomously in the construction sites in any environment; Mesh Mould, which is a formwork free fabrication process for the cast-in-situ concrete structures; Smart Slab, which is a prefabricated concrete slab introducing large-scale 3D sand print technology as formwork; Smart Dynamic Casting, which is an automated concrete slip-forming process, a process in which a reusable moving formwork is used, eliminating the need for disposable formwork; Spatial Timber Assemblies, which are robotic prefabrication processes for timber frame system and Lightweight translucent façade, which was developed to integrate the facade systems of the project. This project exemplifies the first inhabited house which is both digitally planned and digitally built [35]. The picture of the completed DFAB house is shown in Fig. 5.

The BOD which stands for "Building on Demand", built-in Denmark is Europe's first 3D printed house completed in 2017. This building has a floor area of about 50 sq. m. This project was designed by the construction company, COBOD. This building illustrates the economic and architectural advantage of applying 3D printing in construction. The entire building is 3D printed, including its foundations and does not contain any straight elements or reinforcements. This would be a challenge both technically and with respect to cost if using traditional construction practices for construction and hence demonstrates the effectiveness of 3D printing. The 3D rendering of this building is shown in Fig. 6 [37].

A 40-foot-long Pedestrian Bridge in Madrid, Spain built in 2016 using concrete 3D printing technology is one of the first 3D printed bridges in the world. The bridge was built in eight parts using fused concrete powder with micro-reinforced thermoplastic polypropylene. This bridge was designed by the Advanced Architecture Institute of Catalonia (IAAC) and constructed by the infrastructure and renewable energy

Fig. 6 3D rendering of BOD building, Denmark [37]

Fig. 7 Forty-foot-long 3D printed Pedestrian Bridge in Madrid, Spain [39]

corporation, ACCIONA with assistance from Enrico Dini, who is the inventor of D-shape [38]. The bridge was opened to the public in December 2016 [39]. A picture of the 3D printed bridge is shown in Fig. 7.

The largest concrete 3D building built to date is constructed by the robotic construction company, Apis Cor and this building was completed in 2019. This building is a two-story-high office building located in Dubai with a floor area of 640 sq. m and a height of about 9.5 m. The building was built at the site on a conventionally built foundation work without using any extra assembly works using a mobile 3D printer. The material used for the construction was a gypsum-based mixture developed by Apis Cor. and procured locally. For constructing the columns, the formworks were first built using 3D printing and the reinforcements were then added manually, and finally, the formwork was filled with concrete. The entire construction of the building was conducted in the open area. This proved that the printing technology was resilient to harsh environments [40]. A picture of the office building during its construction process is shown in Fig. 8. These structures took much less construction time to complete than the time required for the traditional construction method. These infrastructures demonstrate the potential of concrete 3D buildings in the construction industry as well as call for conducting more research on this area.

Fig. 8 Construction of 3D printed office in Dubai [40]

The robotic construction company, Apis Cor has also taken up projects in the USA for building affordable houses. One such project is in Santa Barbara County, California. Once completed this project will be the first 3-D printed affordable home in the USA.

5 Potential of 3DCP and Research Need

The advent of concrete 3D printing technology has paved the way and increased the feasibility of conducting more innovative research into various types of building constructions with various art effects and also research needed for suitable concrete or other green materials that can be adopted in 3D printing. 3D printing makes it possible to use different building materials and build components of various shapes and sizes without the requirement of any formwork or mould, which is one of the main hurdles to cast components of various shapes and sizes. The development and testing of components of various shapes and sizes using various building materials will help to establish the feasibility of these building materials in the construction industry, as well as it will help to optimize the use of materials and labour for future constructions. Since 3D printing technology does not generate any waste or very little waste in materials, the use of 3D concrete printing will prove a greener method of constructing buildings and other infrastructures.

Geopolymer which is a green alternative to Portland cement, engineered cementitious composites (ECC) which is a high-performance concrete, and rubber infused concrete which uses recycled tire materials are being developed, and performances of these materials are being evaluated. However, applications of these materials in construction have been limited or none. The availability of 3DCP will allow researchers to use these materials for making various building components and elements for determining the structural performance and durability properties. It is hoped that the research outcomes from these studies will open the door for the applications of these materials in large-scale constructions. Additionally, 3DCP will

allow the construction of various curved shape buildings that could not be done using the traditional construction method. Since 3DCP allows a cheaper and faster way of constructing dwelling houses, it is believed that the housing problem in many developing countries like India, Brazil, Nigeria, Mexico, and Bangladesh can be resolved using 3DCP technology and these houses can be made even more affordable and sustainable if geopolymers or durable clay products instead of Portland cement is used in making concrete materials for 3D concrete printing. Availability of 3DCP and sustainable and cheaper concrete materials does have the potential to solve the housing problem of homeless problem currently faced by megacities of developed countries like Canada and the USA. Additionally, with further research on materials and structures using 3DCP, houses, hospitals for emergency, and disaster relief operations due to flood, earthquake, hurricane, and even due to incidents like COVID-19 can be built within a short period of time and at a very low cost.

6 Concluding Remarks

This study is important for the researchers who are interested in research and development in the emerging technology of 3DCP, as this paper provides the general trend of research development of 3DCP. The review of the development of 3DCP in the recent past and the various works completed to date using this technology show the potential of 3DCP in bringing a significant upgrade and overhaul in the traditional construction process as well as in developing alternate and efficient building materials and their applications. This technology, with its numerous advantages, can provide cost-effective housing solutions which can be beneficial to the developing nations as well as to the megacities of developed countries. Hence this technology has a huge potential and working towards realizing its full potential should be the way forward.

Acknowledgements This research was undertaken with the financial assistance of the Natural Sciences and Engineering Research Council of Canada (NSERC).

References

1. Moussion A (2014) Interview d'Alain Le Méhauté, l'un des pères de l'impression 3D. Primante 3D. http://www.primante3d.com/inventeur/. Accessed 2 Feb 2020
2. Uppalla S, Tadikamalla M. A review on 3D printing of concrete—the future of sustainable construction. I-Manager's J Civ Eng 7(3):49–62. https://doi.org/10.26634/jce.7.3.13610
3. Pegna J (1997) Exploratory investigation of solid freeform construction. Autom Constr 5(5):427–437
4. Lim S, Buswell RA, Le T, Austin SA, Gibb AGF, Thorpe T (2012) Developments in construction-scale additive manufacturing processes. Autom Constr 21:262–268. https://doi.org/10.1016/j.autcon.2011.06.010

5. Rebolj D, Fischer M, Endy D, Moore T, Šorgo A (2011) Can we grow buildings? Concepts and requirements for automated nano- to meter-scale building. Adv Eng Inform 25(2):390–398. https://doi.org/10.1016/j.aei.2010.08.006
6. Buswell RA, Leal De Silva WR, Jones SZ, Dirrenberger J (2018) Cement and concrete research 3D printing using concrete extrusion: a roadmap for research. Cem Concr Res 112:37–49. https://doi.org/10.1016/j.cemconres.2018.05.006
7. Khoshnevis B (1998) Innovative rapid prototyping process making large sized, smooth surface complex shapes in a wide variety of materials. Mater Technol 13(2):53–56. https://doi.org/10.1080/10667857.1998.11752766
8. Khoshnevis B (2004) Automated construction by contour crafting—related robotics and information technologies 13:5–19. https://doi.org/10.1016/j.autcon.2003.08.012
9. Hwang, Dooil, and Behrokh Khoshnevis. 2004. "Concrete Wall Fabrication by Contour Crafting." In International Symposium on Automation and Robotics in Construction, 2004 Proceedings of the 21st ISARC, Jeju, South Korea. https://doi.org/10.22260/ISARC2004/0057
10. Khoshnevis, B, Carlson A, Leach N, Thangavelu M (2012) Contour crafting simulation plan for lunar settlement infrastructure buildup. Thangavelu 2000:1458–67
11. Contour Crafting, Architecture computing design engineering industry technology https://www.hisour.com/contour-crafting-40687/. Accessed 12 Mar 2020
12. Dini E (2009) D-SHAPE—the 21st century revolution in building technology has a name. http://www.cadblog.pl/podcasty/luty_2012/d_shape_presentation.pdf. Accessed 25 June 2020
13. Le TT, Austin SA, Lim S, Buswell RA, Gibb AGF, Thorpe T (2012) Mix Design and fresh properties for high-performance printing concrete. Mater Struct J 45:1221–1232. https://doi.org/10.1617/s11527-012-9828-z
14. Le TT, Austin SA, Lim S, Buswell RA, Law R, Gibb AGF, Thorpe T (2012) Hardened properties of high-performance printing concrete. Cem Concr Res 42(3):558–566. https://doi.org/10.1016/j.cemconres.2011.12.003
15. Zhang Y, Zhang Y, Liu G, Yang Y, Wu M, Pang B (2018) Fresh properties of a novel 3D printing concrete ink. Constr Build Mater 174:263–71. https://doi.org/10.1016/j.conbuildmat.2018.04.115
16. Lim S, Buswell R, Le T, Wackrow R, Austin S, Gibb A, Thorpe T (2011) Development of a Viable Concrete Printing Process. In: Proceedings of the 28th international symposium on automation and robotics in construction, ISARC 2011. 29 Jun–2 Jul 2011, Seoul, South Korea, pp 665–670. https://doi.org/10.22260/ISARC2011/0124
17. Weng Y, Lu B, Jen Tan M, Qian S (2016) Rheology and printability of engineered cementitious composites-a literature review. In: Proc. of the 2nd intl. conf. on progress in additive manufacturing, 427–32. Singapore. 16–19 May 2016
18. Hu J, Wang K (2011) Effect of coarse aggregate characteristics on concrete rheology. Constr Build Mater 25(3):1196–1204. https://doi.org/10.1016/j.conbuildmat.2010.09.035
19. Jolin M, Burns D, Bissonnette B, Gagnon F, Bolduc L-S (2009) Understanding the pumpability of concrete. In: Shotcrete for underground support XI. Davos, Switzerland, June 7–10, 2009
20. Mechtcherine V, Nerella VN, Kasten K (2014) Testing pumpability of concrete using sliding pipe rheometer. Constr Build Mater 53:312–323. https://doi.org/10.1016/j.conbuildmat.2013.11.037
21. Zareiyan B, Khoshnevis B (2018) Effects of mixture ingredients on extrudability of concrete in contour crafting. Rapid Prototyping Journal 24(4):722–730. https://doi.org/10.1108/RPJ-01-2017-0006
22. Paul SC, Van Zijl GPAG, Tan MJ, Gibson I (2017) A review of 3D concrete printing systems and materials properties: current status and future research prospects, no. September 2016. https://doi.org/10.1108/RPJ-09-2016-0154
23. Wolfs RJM, Bos FP, Salet TAM (2019) Hardened properties of 3D printed concrete: the influence of process parameters on interlayer adhesion. Cem Concr Res 119(February):132–140. https://doi.org/10.1016/j.cemconres.2019.02.017
24. Wolfs RJM, Bos FP, Salet TAM (2018) Early age mechanical behaviour of 3d printed concrete: numerical modelling and experimental testing. Cem Concr Res 106(January):103–116. https://doi.org/10.1016/j.cemconres.2018.02.001

25. Nerella VN, Krause M, Nather M, Mechtcherine V (2016) Studying the printability of fresh concrete for formwork-free concrete onsite 3D printing technology (CONPrint3D). In: Proceeding for the 25th conference on rheology of building materials, pp 333–47. https://doi.org/10.1016/b978-0-12-815481-6.00016-6
26. Feng P, Meng X, Chen JF, Ye L (2015) Mechanical properties of structures 3D printed with cementitious powders. Constr Build Mater 93:486–497. https://doi.org/10.1016/j.conbuildmat.2015.05.132
27. Sanjayan JG, Nematollahi B, Xia M, Marchment T (2018) Effect of surface moisture on inter-layer strength of 3D printed concrete. Constr Build Mater 172:468–475. https://doi.org/10.1016/j.conbuildmat.2018.03.232
28. Beushausen H, Alexander MG (2008) Bond strength development between concretes of different ages. Mag Concr Res 60(1):65–74. https://doi.org/10.1680/macr.2007.00108
29. Bos, Freek P., Zeeshan Y. Ahmed, Evgeniy R. Jutinov, and Theo A.M. Salet. 2017. "Experimental Exploration of Metal Cable as Reinforcement in 3D Printed Concrete." Materials 10 (11). https://doi.org/10.3390/ma10111314.
30. Bos FP, Ahmed ZY, Wolfs RJM, Salet TAM (2017) 3D printing concrete with reinforcement. In: Proceedings of the 2017 fib symposium, Maastricht, The Netherlands, 12–14 June 2017. https://doi.org/10.1007/978-3-319-59471-2
31. Mechtcherine V, Grafe J, Nerella VN, Spaniol E, Hertel M, Füssel U (2018) 3D-printed steel reinforcement for digital concrete construction—manufacture, mechanical properties and bond behaviour. Constr Build Mater 179:125–137. https://doi.org/10.1016/j.conbuildmat.2018.05.202
32. Panda B, Paul SC, Tan MJ (2017) Anisotropic mechanical performance of 3D printed fiber reinforced sustainable construction material. Mater Lett 209:146–149. https://doi.org/10.1016/j.matlet.2017.07.123
33. Hack N, Lauer WV (2014) Mesh-mould: robotically fabricated spatial meshes as reinforced concrete formwork. Archit Des. https://doi.org/10.1002/ad.1753
34. Hack N, Lauer W, Gramazio F, Kohler M (2015) Mesh mould: robotically fabricated metal meshes as concrete formwork and reinforcement. In: Proceedings of the 11th international symposium on ferrocement and 3rd ICTRC international conference on textile reinforced concrete, pp 1–13
35. Graser K, Wang Y, Hoffman M, Bonanomi MM, Kohler M, Hall DM (2019) Social network analysis of DFAB house: a demonstrator of digital fabrication in construction. In: 17th annual engineering project organization conference, edited by Paul Chinowsky and John Taylor. Proceedings of EPOC 2019. Vail, CO. http://hdl.handle.net/20.500.11850/388870
36. The digitally-built DFAB HOUSE by ETH zurich opens in switzerland, https://www.designboom.com/architecture/eth-zurich-dfab-house-dubendorf-switzerland-02-27-2019/. Accessed 12 July 2020
37. THE BOD: Europe's first 3D printed building. https://cobod.com/the-bod/. Accessed 12 Mar 2020
38. Koslow T (2020) The greatest 3D printed houses, buildings & constructions. https://all3dp.com/1/3d-printed-house-building-construction/. Accessed 4 Jan 2020
39. Madrid gets first 3D-printed pedestrian bridge, is 40-feet long and made up of 8 parts https://www.techeblog.com/madrid-gets-first-3d-printed-pedestrian-bridge-is-40-feet-long-and-made-up-of-8-parts/. Accessed 2 Feb 2020
40. Block, India. 2019 "World's largest 3D-printed building completes in Dubai" https://www.dezeen.com/2019/12/22/apis-cor-worlds-largest-3d-printed-building-dubai/. Accessed 12 Mar 2020
41. Affordable Housing: First 3-D printed affordable home in Santa Barbara County, California. https://www.apis-cor.com/affordable-housing. Accessed 23 July 2020

Long Short-Term Memory-Based Deep Learning Algorithm for Damage Detection of Structure

Rounak De, Anirban Kundu, and Subrata Chakraborty

1 Introduction

Structural damage can be considered as intentional or unintentional changes to the internal properties or boundary conditions that reduce the serviceability and life span of a structure. It can happen due to a gradual or sudden change in loading conditions and degradation of material strength and stiffness properties. These damages are often invisible and hidden inside the structure, making them very difficult to detect through visual inspection. Largely used conventional methods of damage identification include periodic visual inspection, localized experimental methods such as acoustic, thermal, magnetic field methods, etc. But the localized nature is the major limitation of such methods. The vicinity of a damaged location should be known beforehand and accessible for physical inspection which makes the process tedious and inefficient. To overcome this, vibration-based damage detection methods have gained large attention from the research community. Unlike the localized approach of the conventional method, the vibration-based approach assesses the overall performance of a structure through a meaningful translation of the vibration response gathered from some selected locations of a structure. The vibration-based method can be classified into two categories: (i) parametric (model-based) and (ii) non-parametric (signal-based). During the last few decades, advancements in computational power, feature extraction techniques, and machine learning algorithms helped in developing efficient parametric methods, where the system identification algorithms are utilized to determine modal parameters such as natural frequencies and mode shapes from the measured responses [1, 2]. The basis of identification is that the commonly measured modal parameters are functions of the physical properties of a structure, such as mass, damping, and stiffness. Any changes in these parameters with respect

R. De (✉) · A. Kundu · S. Chakraborty
Department of Civil Engineering, Indian Institute of Engineering Science and Technology Shibpur, Howrah, West Bengal 711103, India

D. K. Maiti et al. (eds.), *Recent Advances in Computational and Experimental Mechanics, Vol II*, Lecture Notes in Mechanical Engineering,
https://doi.org/10.1007/978-981-16-6490-8_27

to the parameters of the undamaged case are used to recognize the structural damage. However, there are few confounding factors that make the parametric vibration-based damage detection method difficult to implement in practice. First, standard modal properties estimated experimentally from measured response time histories represent a form of data compression, and intuitive information about the state of the structure may be lost during the data reduction and system identification process [3]. The loss of information occurs primarily from the fact that for a linear system the modal properties are independent of the excitation signal characteristics (amplitude and frequency content) and the location of the excitation, whereas the time histories are not. Secondly, damage which typically is a local phenomenon of a structure is captured by higher frequency modes whereas lower frequency modes tend to capture the global response of the structure and are less sensitive to local changes in a structure. From the experimental point of view, more energy is required to excite the structure and produce measurable responses at these higher frequencies than at the lower frequencies. Moreover, small damages that create low-frequency change require very precise measurement [4], whereas a significant amount of damage could also create very less change in frequency in the case of large structures and even change in temperature or humidity could result in a change in frequency [5]. Thus, using the frequency-based vibration methods could lead to unrealistic predictions [6]. Moreover, it is also difficult to choose feature-rich mode shapes for detection purposes [7]. These factors also contribute to the limitation of this technology to the research arena with only limited practice by the engineering community.

To supplement the drawbacks of the parametric method, non-parametric machine-learning-based methods have been explored by the scientific community where signal processing and statistical analysis techniques have been utilized for feature extraction from the response time series in the time domain without loss of any valuable detail. The convolutional neural network-based (CNN) non-parametric approach is explored in the literature [8]. The approach is found to be useful in the field of spatial data handling, e.g., strain fields [9]. On the other hand, the long short-term memory-based (LSTM) recurrent neural network (RNN), a new breakthrough in deep learning algorithm, is quite efficient in sequential data handling. The LSTM network has been used successfully in detecting multiple fatigue damages of aircrafts [10] and analysis of rolling bearing faults of rotating machinery using vibration data [11]. The LSTM-based algorithm to detect faulty sensor [12] and fault diagnosis of a wind turbine [13] have been explored. The present study explores the capability of the LSTM network for damage detection of a structure by analyzing the acceleration response time history. The architecture of the LSTM model consists of a gated operation forming a cell-like structure that can store relevant information of a dynamic sequence. Unrolling the recurrent operation through the temporal dimension, a long interdependent relation between input sequences and target output is established. The sequential application program interface (API) of Keras [14], an open-source deep learning API, written in python, based on TensorFlow [15] is used for this. The entire procedure is performed using 'Google Colaboratory'. The effectiveness of the proposed LSTM algorithm is demonstrated by considering a cantilever beam.

2 LSTM-Based Damage Detection Framework

The LSTM-based RNN was first introduced as an improvement over RNNs and used as a potential solution to vanish and explode the gradient problem of RNNs [16]. The architecture of the LSTM consists of a few gated operations forming a cell-like structure that can store relevant information of a dynamic sequence [16, 17]. Unrolling the recurrent operation through the temporal dimension, a long interdependent relation between input and output sequence can be established. The flow of information is controlled by three primary operations of LSTM cell, i.e., (i) subtraction of old irrelevant information, (ii) selective addition of new information, and (iii) selective reading of the information.

2.1 LSTM Cell

The above-mentioned operations are conducted through point-wise multiplication and addition which is controlled via nonlinear activation functions such as sigmoid and *tanh*, defined as

$$\text{sigmoid}(x) = \frac{1}{1+e^{-x}}, \quad \tanh(x) = \frac{2}{1+e^{-2x}} - 1 \tag{1}$$

The operation of removal of old irrelevant information is done using forget gate that generates f_t as defined in Eq. (2) and forgets the information of the old cell state C_{t-1} which are no longer required.

$$f_t = \sigma\left(W_f \odot \left[h_{t-1}, x_t\right] + b_f\right) \tag{2}$$

where '$\odot$' denotes Hadamard product or element-wise product. The input gate, i_t, selectively adds the new information as shown in Eq. (3) followed by the generation of a temporary cell state, $\hat{C}_t$ as described in Eq. (4).

$$i_t = \sigma\left(W_i \odot \left[h_{t-1}, x_t\right] + b_i\right) \tag{3}$$

$$\check{C}_t = \tanh\left(W_C \odot \left[h_{t-1}, x_t\right] + b_C\right) \tag{4}$$

The output gate produces the output, o_t as follows:

$$o_t = \sigma\left(W_o \odot \left[h_{t-1}, x_t\right] + b_o\right) \tag{5}$$

The cell state for the next time step is produced by adding the point-wise multiplication of the forget gate, previous cell state and input gate, temporary cell state as follows:

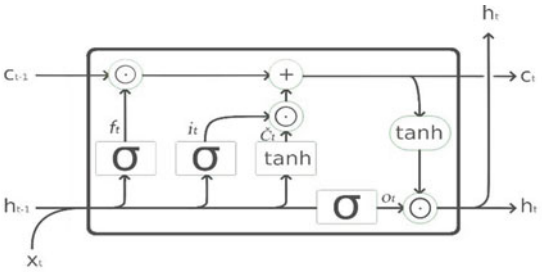

Fig. 1 The LSTM cell, employing the idea of selective forgetting, reading, and writing

$$C_t = f_t \odot C_{t-1} + i_t \odot \check{C}_t \tag{6}$$

The hidden state h_t (Eq. 7) will serve as the output of the current cell, and the input for the cell at the next layer is produced by piece-wise multiplying output gate with newly produced cell state with nonlinearity applied on it.

$$h_t = o_t \odot \tanh(C_t) \tag{7}$$

The overall concept is illustrated in Fig. 1.

2.2 *Simulation of Data Generation of Case Study Problem*

The effectiveness of the proposed LSTM-based deep learning algorithm to predict the change in structural property, e.g., stiffness along with its location and severity utilizing recorded time history at different locations of the structure is elucidated by considering a cantilever beam structure. The beam is 0.04 m wide, 0.01 m depth, and 1 m length and excited with a pulse load applied at the free end. The beam is divided into five finite segments of 0.2 m length as shown in Fig. 2. The response of the beam is simulated in ABAQUS software.

The element type used for meshing is a general-purpose eight-node linear brick element with reduced integration abbreviated in ABAQUS as C3D8R. The size of the block used is 0.01 m × 0.01 m × 0.01 m. The boundary condition is considered as one end fixed with all the translations and rotations restricted. The type of analysis is

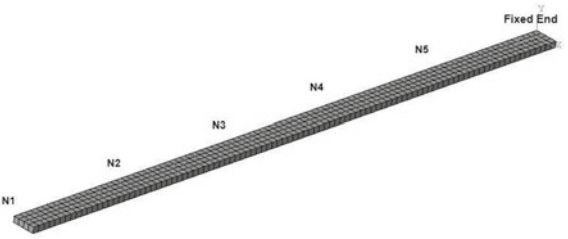

Fig. 2 Beam showing its five finite segments and nodes from where response time history is extracted

taken as 'dynamic implicit' which is generally used in the linear dynamic analysis in ABAQUS. The key intuition is that the change of elastic modulus (E) can trigger the change in stiffness which will cause a change in response acceleration time history of the structure. The undamaged modulus of elasticity (E) of the beam is considered to be $2 \times 10^{11}\text{N/m}^2$.

A design of experiment (DOE) table is created with the help of the Latin hypercube sampling (LHS) [18] method for 75 samples; each comprises five stiffness values for the five finite segments of the beam. The damage is simulated with the help of degradation of the E values limited to 10% of the undamaged structure. So, the DOE table comprises the E values ranging from $2 \times 10^{11}\text{N/m}^2$ to $1.8 \times 10^{11}\text{N/m}^2$ for each five segments mentioned and distributed uniformly. The free end of the beam is excited with a pulse load, for 0.05 s, with peak value of 100 N. The load pattern is shown in Fig. 3.

The response acceleration time history of 10 s duration is recorded at the end of each of the five finite segments, having a time step of 0.01 s. A typical acceleration time history at the first node (N1) is shown in Fig. 4.

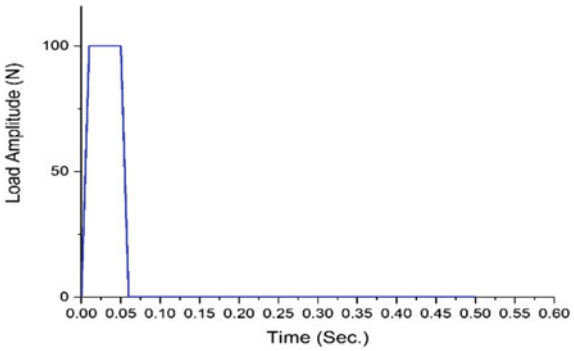

Fig. 3 Impulse load pattern, applied at the free end of the beam

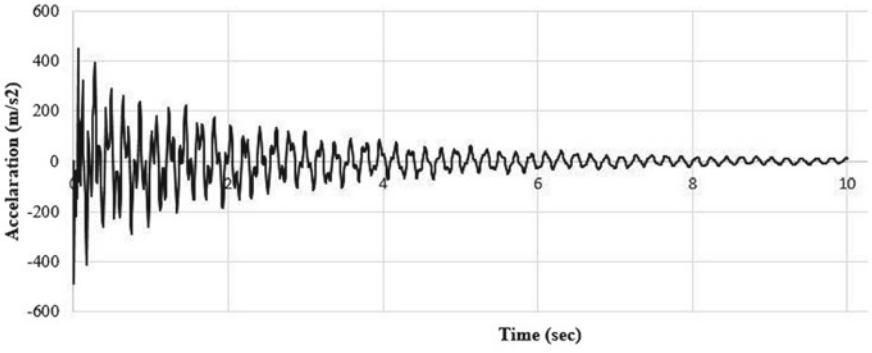

Fig. 4 Response acceleration time history at N1

The data set is divided into training and testing sets. For training purposes, 65 of those 75 sets are used and 10 data sets are kept for testing. The response acceleration time series at the end of five finite segments is prepared as the input data set, whereas the corresponding stiffness values of the five segments are treated as the target in the training phase. The set of the time series from the test set is fed to the trained model and the degraded values of stiffness are predicted.

2.3 Training of the Model

An LSTM architecture is made of one or more LSTM layers, each consisting of LSTM cells, as shown in Fig. 1. The data flow from one layer to another (h_t) as well as within the layer (C_t). The output is generated at the end of the processing of the series. Note that a sequence of outputs can also be generated in the case of sequence to sequence modeling, where output is generated after each time step. But the current study is limited to many-to-one modeling where a single output is generated after processing a sequence of input. Choosing the hyper-parameters such as the number of LSTM layers or the number of LSTM cells in each layer is as tedious as any other neural network problem. There is no definitive rule and is totally dependent on a trial and error basis but a pyramid rule is often followed with the most number of neurons at the start and least at the end [19]. A comparative study with a different combination of layer number and cell number at each layer is performed, each with 1000 epochs. At the end of 1000 epochs, the mean squared error (MSE) for validation is stored. The combination with the least error value is chosen for the training to conduct with 10,000 epochs. It has been assumed that the trend of the decrement of loss (validation error) will be the same for epochs more than 1000. Table 1 shows such a comparative result from where it is clear that the multilayer LSTM performs better than the single-layer configuration.

The best combination is found to be 200/100/50 number of cells at consecutive layers. A full network configuration is shown in Fig. 5. The LSTM layers are then followed by a dense or fully connected layer. A three-dimensional data structure is shown in the input and output of each layer. The first dimension depicts the number of samples put into the training (not fixed at first hand and shown as 'None' in Fig. 5). The second dimension represents the number of features; here five indicates the five E values of five finite segments. And the third dimension represents the sequence length at the input end and a single set of target values at the output end. The name suggests that each neuron is connected to a single output neuron. The piecewise linear, ReLU (Rectilinear Linear Unit) activation function is provided in between the layers.

Adam, a first-order gradient-based optimizer that works based on adaptive estimates of lower-order moments [20] is used. The learning rate is considered as 0.0001. As mentioned earlier, 65 samples of acceleration time history among 75 are used for training. Five acceleration time history from five nodes are considered as the input and a corresponding set of five 'E' values of five segments is considered as the output

Table 1 A study of hyper-parameter optimization

Number of layer	Combination	Validation error
1	50	0.0011
	100	0.00045
	200	0.00032
2	50/50	0.0007
	100/50	0.00042
	100/100	0.00027
	200/50	0.0003
	200/100	0.00027
	200/200	0.00025
3	100/50/50	0.0003
	100/100/50	0.00029
	200/50/50	0.00027
	200/100/50	0.00015
	200/100/100	0.00038
	200/200/50	0.0002
	200/200/100	0.00016

for a single sample. All the data are scaled between a feature range of 0 to 1 before being fed into the model for training with the help of a min–max scaler which is given as: $X_{\text{sc}} = \frac{X - X_{\min}}{X_{\max} - X_{\min}}$. The model is trained with 10,000 epochs where validation loss converges to a satisfactory level. During the training process, 65 training samples are shuffled after each epoch and with 60 samples the training is conducted and the rest of five is used in validation. Batch size is considered as 5. Both the validation and training loss are recorded and shown in Fig. 6. After 10,000 epochs, the validation loss reached 8.78×10^{-10}, and the model is saved as 'the best model'. The entire procedure is performed using 'Google Colaboratory' [21], a free python-based platform where one can use a graphic process unit (GPU) to train a deep neural network.

3 Results and Discussions

The set of response time series from the test set is fed into the trained LSTM model and the degraded '*E*' values are predicted. Figure 7 presents one such case from the test set where percentage reduction of the '*E*' value of the five finite segments is shown. For comparison, both the actual and the prediction values are shown in the plot.

To illustrate the range of errors that occurred at predicting the degraded 'E' values at each segment, a box-whisker plot of normalized error percentage is plotted (Fig. 8).

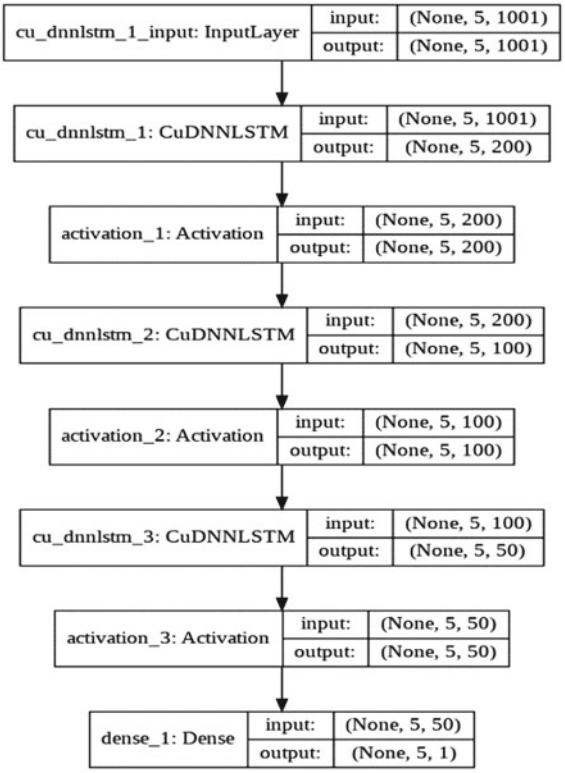

Fig. 5 The LSTM model architecture

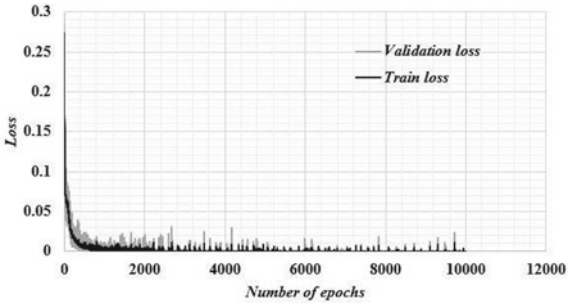

Fig. 6 The training and validation loss with the progress of training

The normalized error at a particular segment among the five segments is defined as $\left|\frac{y_i^{\text{true}} - y_i^{\text{pred}}}{\max(y_i^{\text{true}})}\right| \times 100$, where $i \in \{1, 2, 3 \ldots 10\}$ denotes the 10 prediction data set. And then repeated for the rest of the segments. Then a box-whisker is plotted. Four segments show a median of error below 1% except for the first segment, where a comparatively poor prediction accuracy is noted which is also reflected in Fig. 7. The reason for this needs further study.

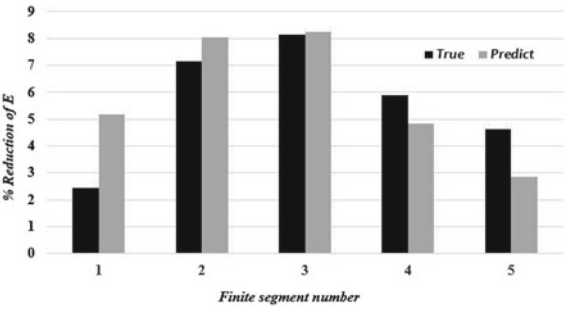

Fig.7 The comparison of the predicted value of the percentage reduction of the E values with the originally simulated one

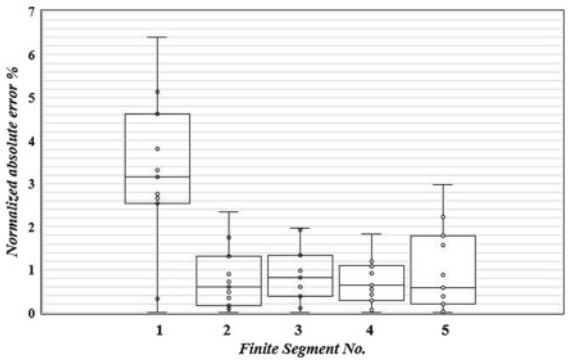

Fig.8 The box-whisker plot of the normalized absolute error in predicting the 'E' values of five segments

The absolute normalized error for the five stiffness values at five segments for 10 prediction set is calculated and then a probability histogram is plotted in Fig. 9. This is zero-mean centric where most of the errors are within ±5% with a sharp peak at 0, indicating a good accuracy.

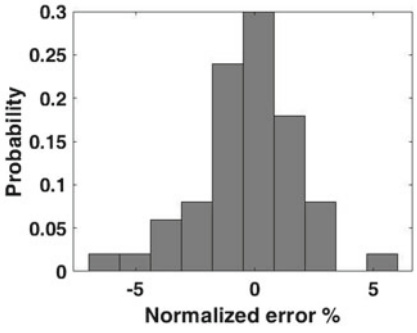

Fig. 9 The probability histogram of the normalized percentage error

4 Conclusions

An LSTM-based deep neural network algorithm for structural damage detection in the time domain using the acceleration time history data is explored in the present study. The proposed approach uses direct time series data and predicts the change in degraded stiffness values which serve as the accurate prediction of location and intensity of damage in the structure. The effectiveness of the proposed LSTM algorithm is demonstrated by considering a cantilever beam structure. The comparison of identified stiffness values with the target stiffness values and statistical error metrics shows the capability of the proposed algorithm. However, an anomaly in the prediction result is found in the first segment where the load is applied at the free end which may be due to stress concentration but it may be for the shortfall of the LSTM model also. Whether it is due to a single factor or several factors that needs further study. Overall, the results can be obtained in an easy, relatable, and understandable way with no pre-processing of data which is a paramount criterion of designing any real-time damage detection method. The study is made on a simple structure and investigations need to be taken up for more complex and real-life structures. The proposed algorithm can be applied for other types of structural components like plate, shell, stiffened panels, etc. Also, the damage is defined by a change in the elastic modulus, and other damage parameters should also be taken into account and the effect of errors in measured responses needs to be studied further.

References

1. Adams RD, Cawley P, Pye CJ, Stone BJ (1978) Vibration technique for non-destructively assessing the integrity of structures. J Mech Eng Sci 20:93–100
2. Salawu OS (1997) Detection of structural damage through changes in frequency: a review. Eng Struct 19:718–723
3. Chance J, Tomlinson G, Worden K (1994) A simplified approach to the numerical and experimental modelling of the dynamics of a cracked beam. In: Proc. 12th int. modal anal. conf., pp. 778–85
4. Doebling SW, Farrar CR, Prime MB (1998) A summary review of vibration-based damage identification methods. Shock Vib Dig 30:91–105
5. Kim JT, Park JH, Lee BJ (2007) Vibration-based damage monitoring in model plate-girder bridges under uncertain temperature conditions. Eng Struct 29:1354–1365
6. Maeck J, De Roeck G (2002) Sdamage assessment of a gradually damaged Rc beam using dynamic system identification. In: Proc IMAC 20, int modal anal conf, pp 1560–1566, Los Angeles, California, USA
7. Salawu OS, Williams C (1995) Bridge assessment using forced-vibration testing. J Struct Eng 121:161–173
8. Abdeljaber O, Avci O, Kiranyaz S, Gabbouj M, Inman DJ (2017) Real-time vibration-based structural damage detection using one-dimensional convolutional neural networks. J Sound Vib 388:154–170
9. Gulgec NS, Takáč M, Pakzad SN (2019) Convolutional neural network approach for robust structural damage detection and localization. J Comput Civ Eng 33:04019005
10. Mas MI, Fanany MI, Devin T, Sutawika LA (2018) An initial exploration of the suitability of long-short-Term-memory networks for multiple site fatigue damage prediction on aircraft lap

joints. In: 2017 int. conf. adv. comput. sci. inf. syst. ICACSIS 2017, vol 2018 Janua, Institute of Electrical and Electronics Engineers Inc., pp 415–21
11. Qiu D, Liu Z, Zhou Y, Shi J (2019) Modified bi-directional LSTM neural networks for rolling bearing fault diagnosis. In: IEEE Int. Conf. Commun., vol. 2019- May, Institute of Electrical and Electronics Engineers Inc.
12. Li L, Liu G, Zhang L, Li Q (2018) Deep learning-based sensor fault detection using S-long short term memory networks. Struct Monit Maint 5:51–65
13. Lei J, Liu C, Jiang D (2019) Fault diagnosis of wind turbine based on Long Short-term memory networks. Renew Energy 133:422–432
14. Chollet FO (2020) Keras: the Python deep learning API. Keras Python Deep Learn API. https://keras.io/. Accessed 13 Nov 2020
15. TensorFlow n.d. https://www.tensorflow.org/. Accessed 13 Nov 2020
16. Hochreiter S, Schmidhuber J (1997) Long short-term memory. Neural Comput 9:1735–1780
17. Gers FA, Schmidhuber J, Cummins F (1999) Learning to forget: continual prediction with LSTM. IEE Conf. Publ., vol 2, IEE, pp 850–5
18. Helton JC, Davis FJ (2003) Latin hypercube sampling and the propagation of uncertainty in analyses of complex systems. Reliab Eng Syst Saf 81:23–69
19. Masters T (1993) Practical neural networks recipes in C++.
20. Kingma DP, Adam Ba JL (2015) A method for stochastic optimization. In: 3rd Int. Conf. Learn. Represent. ICLR 2015 - Conf. Track Proc.
21. Wikipedia contributors. Graphics processing unit. Wikipedia, Free Encycl n.d

Mechanical Properties of Nanocrystalline Copper/CNT Nanocomposites

Avirup Sircar and Puneet Kumar Patra

1 Introduction

High thermal and electrical conductivities, as well as lower thermal expansion coefficient, make copper and its alloys very good materials for many electronic and thermal applications in all length scales. But when it comes to mechanical applications, its poor mechanical properties in comparison to other materials such as iron render it less attractive. Drawing analogy with reinforced concrete, the mechanical properties of copper and its alloys can be improved if it can be reinforced with a suitable agent.

CNT represents such a suitable reinforcement material. After its discovery by Iijima and Ichihashi [1], CNTs have attracted the attention of researchers and have been used in several applications [2, 3] due to their exceptional mechanical and physical properties. In the present context, CNTs have been used for reinforcing several materials: CNT-reinforced polymer [4–6], ceramic-based composites [6–8] and the incorporation of CNTs into metal [9–11] matrices. In view of this, CNT-reinforced copper composites are likely candidates for improving the mechanical response of copper. For example, CNT/copper composites can be used as lighter alternatives to heavy copper electrical and data wiring in automobiles and aircrafts to enhance fuel efficiencies and reduce the cost [12].

Efficient CNT/copper nanocomposites with improved thermal and mechanical properties have been discovered and experimented with since the last decade. Cha et al. [13] and Kim et al. [14] fabricated CNT/copper nanocomposites by the

A. Sircar (✉)
Department of Mechanical Engineering, Indian Institute of Technology Kharagpur, West Bengal, Kharagpur 721302, India

P. K. Patra
Department of Civil Engineering, Indian Institute of Technology Kharagpur, West Bengal, Kharagpur 721302, India
e-mail: puneet.patra@civil.iitkgp.ac.in

D. K. Maiti et al. (eds.), *Recent Advances in Computational and Experimental Mechanics, Vol II*, Lecture Notes in Mechanical Engineering,
https://doi.org/10.1007/978-981-16-6490-8_28

molecular-level mixing process. Chai et al. [15] fabricated the same with the electrochemical co-deposition process. The mechanical strength of Cu/CNT nanocomposites is found to be more than three times greater than that of pure copper. With the reduction in grain size of polycrystalline metals to nanoscales, more precisely less than 100 nm, the mechanical properties like the strength and the hardness also increase [16]. Due to this NC copper has attracted a great deal of attention. But a major problem that still remains is their low ductility. The inclusion of CNT in NC copper can be a solution to the problem. In terms of experiments, Li et al. [17] developed nanostructured CNT-reinforced copper composite of small grain size with high strength and good ductility. Recently, Wang et al. [18] fabricated CNTs-reinforced NC copper matrix composite with high strength and moderate plasticity through the combined use of electroless deposition and spark plasma sintering. The agglomeration and the grain growth problem of NC copper was overcome.

Computational approaches have also been adopted for the theoretical estimation of the strength and to determine the deformation mechanisms. Tensile tests of CNT with single crystal (SC) copper composites have been performed by Yan et al. [19] using molecular dynamics simulations. Different factors like the CNT diameter, presence of multiwalled CNTs, inclusions etc. have been studied. The inclusion of CNTs strongly improves Young's modulus and the yield strength of the copper nanocomposites. Similarly, increasing the number of CNTs and their diameter significantly enhances Young's modulus of the composites. Faria et al. [20] investigated the failure mechanisms of CNT-SC copper nanocomposites by tensile and compressive tests. Their studies show that although the strength and stiffness of the composite may increase due to CNT inclusion, the ductility can decrease fairly. Duan et al. [21] investigated the damping properties and the mechanical strength of Ni-coated CNT-SC copper composites by MD simulations. The strength was greatly seen to improve by nickel coating over the CNT surface.

However, the deformation behavior and mechanism for CNT-reinforced NC copper composites are yet to be studied in atomistic details. These computational studies are necessary for the proper understanding of the interfacial strength of the CNT copper interface and the dislocation mechanisms governing it. The present manuscript tries to address this lacuna in the literature using molecular dynamics simulations. We compute the elastic properties and the failure behavior of NC copper-reinforced with CNTs through a displacement-controlled uniaxial tensile test. With the increase in volume fraction of reinforcement, it is seen that the elastic modulus does not always increase but can decrease due to detachment of CNT with the Cu matrix. Increasing the number of walls of CNT leads to increment of Young's modulus and the tensile strength (Fig. 1).

2 Method and Simulation Details

The simulation domain comprises a box of dimensions $20 \times 20 \times 20$ nm^3. The box is populated with NC copper, created using Voronoi tessellation method through the

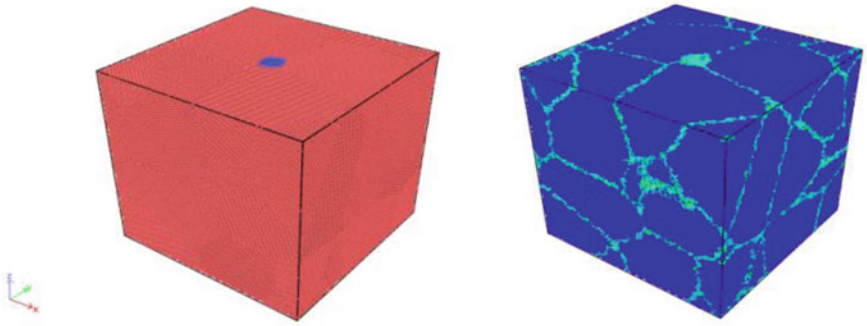

Fig. 1 NC copper with CNT reinforcement

Atomsk software [22]. Armchair single-walled CNTs of different chiralities (and hence, diameters)—(5,5), (15,15), and (25,25)—are placed inside the NC copper block along the Z-direction. For including the CNTs, copper atoms have been removed from the center of the box in a cylindrical manner and replaced with the carbon atoms of the CNT. No copper atoms are present inside the CNT. For understanding the effect of grain size, three different grain sizes are taken into account. Separate simulations with multiwalled CNTs have been performed. Two different temperatures, i.e., at 10 K (low) and 300 K (high) are studied to see the temperature dependence of the mechanical properties.

The interaction between the copper–copper atoms is modeled through the embedded atom potential (EAM) developed by Mendelev and King [23]. The EAM potential can be written as

$$E_i = F_\alpha\left(\sum_{j\neq i}\rho_\beta\left(r_{ij}\right)\right) + \frac{1}{2}\sum_{j\neq i}\sigma_{\alpha\beta}\left(r_{ij}\right) \tag{1}$$

where F_α is the embedding energy, which is a function of the atomic electron density ρ_β, $\sigma_{\alpha\beta}$ is the short-ranged pair potential; and r_{ij} is the distance between the atoms i and j. The two subscripts α and β in $\sigma_{\alpha\beta}$ are the element types of atoms i and j, respectively.

The carbon–carbon interaction within the nanotubes is modeled through the adaptive intermolecular reactive empirical bond order (AIREBO) potential [24]. The AIREBO potential is made of the original reactive empirical bond order (REBO) potential, the Lennard Jones (LJ) potential and the torsional potential term as follows:

$$E = \frac{1}{2}\sum_i\sum_{j\neq i}\left[E_{ij}^{\mathrm{REBO}} + E_{ij}^{\mathrm{LJ}} + \sum_{k\neq i}\sum_{l\neq i,j,k}E_{kijl}^{\mathrm{TORSION}}\right] \tag{2}$$

The three terms describe the covalent bonding forces, the van der Waals forces and the dihedral angle effect. The carbon–carbon interaction between the two layers of CNTs are modeled through the LJ potential similar to that used in graphite:

$$E = 4 \in \left[\left(\frac{\sigma}{r} \right)^{12} - \left(\frac{\sigma}{r} \right)^{6} \right] \tag{3}$$

where ϵ is the depth of the potential well and σ is the distance where the interatomic potential is zero. The parameters for the carbon–carbon LJ interactions are $\epsilon = 0.003$ eV and $\sigma = 3.41$Å. The interatomic potential between carbon and copper is also taken as the LJ potential. The LJ parameters are determined based on the Lorentz-Berthelot mixture rule. The value ϵ_{12} is obtained from the geometric average of ϵ_{11} (copper) and ϵ_{22} (carbon). Similarly, the value σ_{12} is obtained from the geometric average of σ_{11} (copper) and σ_{22} (carbon). With the copper LJ parameters taken as $\epsilon = 0.4150$ eV and $\sigma = 2.28$ Å(20), the carbon/copper LJ parameters become $\in_{12} = 0.0351$ eV and $\sigma_{12} = 2.84$ Å.

The MD simulations are performed using the open-source software LAMMPS [25, 26]. Periodic boundary conditions are used in all three directions to simulate the bulk behavior. The simulations begin with energy minimization using the conjugate gradient method. Subsequently, equilibration is done at 10 K and 300 K using the NPT ensemble for 200,000 timesteps, where each time step corresponds to 1 fs. The model is then subjected to a displacement-controlled uniaxial tensile test in an NVT ensemble at a strain rate of $10^{10}s^{-1}$. The constant temperature is maintained through a Nosé-Hoover thermostat [27]. The strain rate used in MD simulations is very high as compared to the experimental strain rates due to the small timescale of a simulation run.

3 Results

The stress/strain plots of NC copper and NC-CNT-reinforced copper, for three grain sizes and two temperatures, are shown in Figs. 2, 3 and 4. In all of the figures, it is seen that the graph does not pass through the origin, suggesting that there is some residual stress before the deformation run.

The general trend in the plots suggests that, at first, the stress increases linearly with an increase in the strain. A definite yield point is not observed. However, a well-defined ultimate tensile strength (UTS) is observed. Subsequent to reaching the ultimate tensile strength, strain-softening occurs due to defect generation. For most of the plots with reinforced CNTs, we see that at later stages, there is a steep decrease in stress as the strain increases. This occurs because of the fracture of the CNTs. It can be seen that at lower temperatures the CNTs fracture at a higher strain than at higher temperatures.

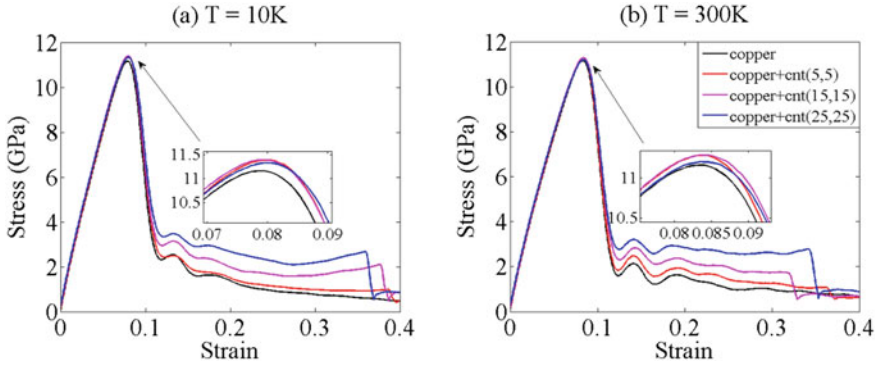

Fig. 2 Properties for grain size 11.7 nm

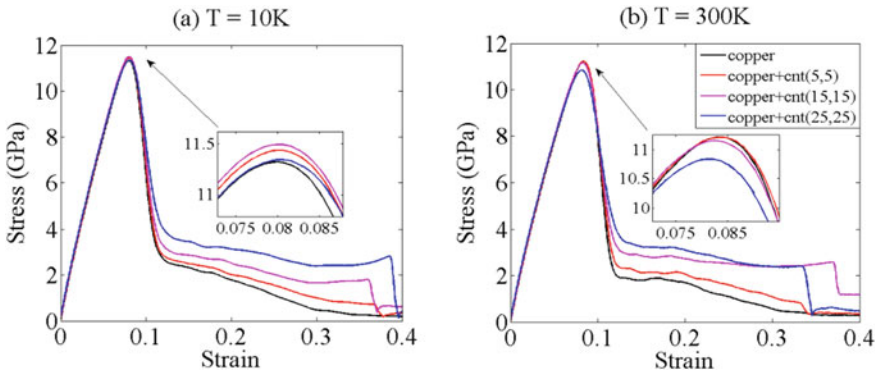

Fig. 3 Properties for grain size 8.7 nm

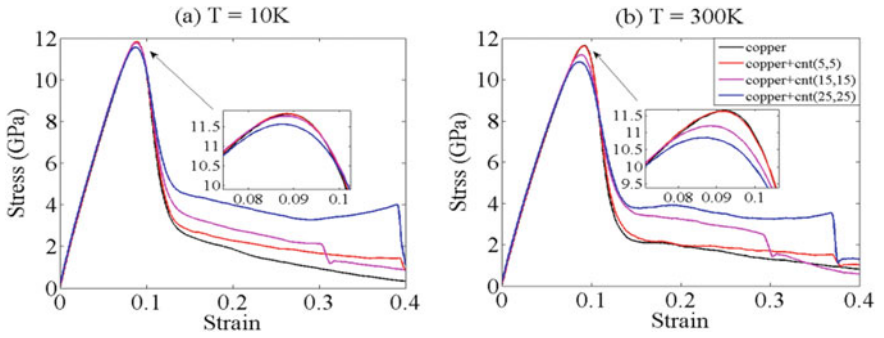

Fig. 4 Properties for grain size 5.7 nm

Table 1, Table 2 and Table 3 show the values of Young's modulus, yield strength and UTS for NC copper and reinforced NC copper for different temperatures and grain sizes. Young's modulus is calculated by a basic fitting curve for data points with a strain less than 0.02. The yield strength is calculated by the 0.2 percent offset method. By comparing Young's modulus at different grain sizes, we can see that the modulus first increases and then decreases with a decrease in grain size. Here for the NC copper, the yield strength does not follow the inverse Hall–Petch relationship which may be due to the high strain rate and the presence of initial residual stress. From the tables, it can be seen that for $T = 10$ K there is an increase of Young's modulus with an increase in the volume fraction of reinforcement initially after which it decreases. Our results indicate that there is an optimum value of reinforcement that maximizes Young's modulus. A similar situation is observed at $T = 300$ K, except the fact that the values are smaller than at $T = 10$ K. The yield strength continuously increases with the increase in volume fraction at all temperatures and grain sizes. For UTS no clear pattern is seen.

Figures 5 and 6 show the centrosymmetry parameter for NC copper and NC copper-reinforced with (25,25) CNT for the grain size of 5.7 nm and temperature

Table 1 Mechanical properties of grain size 11.7 nm

Material	Young's modulus (GPa)		Yield strength (GPa)		UTS (GPa)	
	$T = 10$ K	$T = 300$ K	$T = 10$ K	$T = 300$ K	$T = 10$ K	$T = 300$ K
NC Cu	175.46	172.63	6.727	5.926	11.16	11.16
NC Copper + CNT (5,5)	175.89	173.75	6.985	6.064	11.39	11.28
NC Copper + CNT (15,15)	176.27	174.12	7.682	6.449	11.39	11.28
NC Copper + CNT (25,25)	175.7	172.56	7.906	6.772	11.32	11.20

Table 2 Mechanical properties of grain size 8.7 nm

Material	Young's modulus (GPa)		Yield strength (GPa)		UTS (GPa)	
	$T = 10$ K	$T = 300$ K	$T = 10$ K	$T = 300$ K	$T = 10$ K	$T = 300$ K
NC Cu	176.72	173.65	6.024	5.736	11.32	11.22
NC Copper + CNT (5,5)	177.93	174.62	6.231	5.907	11.44	11.22
NC Copper + CNT (15,15)	178.83	175.35	6.585	6.164	11.49	11.16
NC Copper + CNT (25,25)	177.47	174.18	6.737	6.26	11.34	10.84

Table 3 Mechanical properties of grain size 5.7 nm

Material	Young's modulus (GPa)		Yield strength (GPa)		UTS (GPa)	
	$T = 10$ K	$T = 300$ K	$T = 10$ K	$T = 300$ K	$T = 10$ K	$T = 300$ K
NC Cu	164.44	161.97	6.285	5.962	11.82	11.64
NC Copper + CNT (5,5)	165.57	162.26	6.447	6.228	11.83	11.62
NC Copper + CNT (15,15)	166.34	163.15	6.88	6.528	11.77	11.2
NC Copper + CNT (25,25)	165.38	161.85	6.944	6.772	11.56	10.85

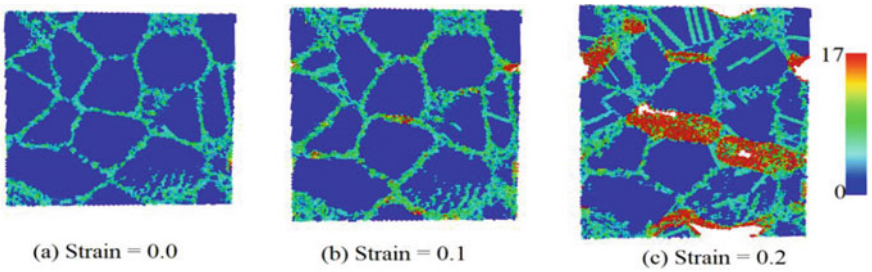

Fig. 5 NC Copper at $T = 10$ K and grain size 5.7 nm

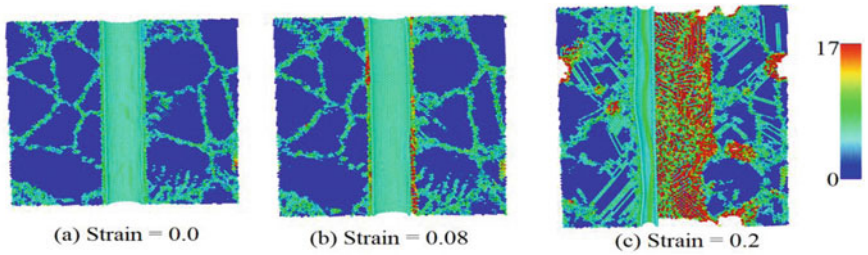

Fig. 6 NC Copper + CNT(25,25) at $T = 10$ K for grain size 5.7 nm

10 K. The figures are obtained by slicing the system at the mid-section. Centrosymmetric parameter sums to zero under a normal single perfect fcc crystal while under any kind of defects the value turns out to be more than zero. In Fig. 5 the NC copper is shown as (a) in the initial state with grain boundaries, (b) at 0.1 strain when the crack starts to develop at the grain boundaries, and (c) the cracks propagation at a strain of 0.2 along the grain boundaries leading to final fracture of the NC copper. From Fig. 6 we see that (a) the initial state is the same as that obtained in the previous figure, except for the inclusion of the reinforcing CNT, (b) the CNT starts to detach from the NC copper along the grain boundaries, and (c) at the strain 0.2 the CNT

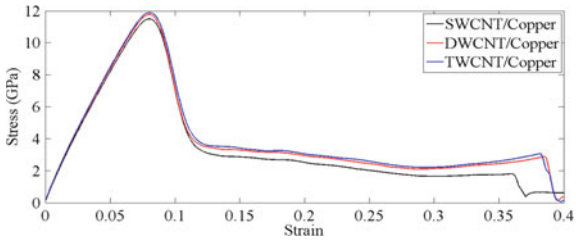

Fig. 7 Mechanical properties of multiwalled CNT composite for $T =$ 10 K and 8.7 nm grain size

Table.4 Properties of multiwalled CNT, grain size 8.7 nm, $T = 10$ K

Material	Young's modulus (GPa)	Yield strength (GPa)	UTS (GPa)
NC Copper + SWCNT	178.83	6.585	11.49
NC Copper + DWCNT	181.62	6.978	11.76
NC Copper + TWCNT	183.24	7.104	11.89

folds up due to tensile deformation and there is an enlargement of the central void along with cracks from the grain boundaries at the sides. At higher strain, in both cases, we can see that the stacking faults develop within the grains. This detachment of CNT causes a decrease in the strength of the material lowering the elastic modulus and the UTS (Fig. 7).

Next, we see the tensile responses of multiwalled CNT-NC copper nanocomposite. Table 4 shows the properties with the effect of single-walled CNT (SWCNT), double-walled CNT (DWCNT) and triple-walled CNT (TWCNT) reinforcement on NC copper with grain size 8.7 nm at $T = 10$ K. With an increasing number of walls of CNT reinforcement, the CNT fracture occurs at a larger strain. Young's modulus and tensile strength also increase.

The centrosymmetric parameters for these cases are now discussed. Figure 8 shows the deformation of the copper reinforced with CNT (15,15), while Fig. 9 shows the deformation of the copper reinforced with CNT (5,5), CNT (10,10) and CNT(15,15). In the former, the deformation is mainly governed by the formation of voids along the CNT/copper surface while in the latter, the deformation initiates in the bulk through void formation at the grain boundary junctions. The van der Waals interaction of the inter-wall nanotubes and nanotube-matrix along with the enhancement of mechanical properties of CNTs with an increasing number of walls significantly affects the properties of multiwalled CNT/NC copper material as compared to the single-walled CNT reinforcement.

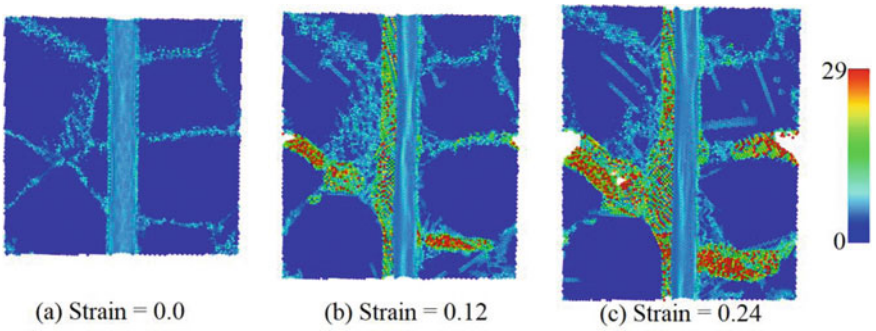

Fig. 8 NC Copper + CNT(15,15) at $T = 10$ K for grain size 8.7 nm

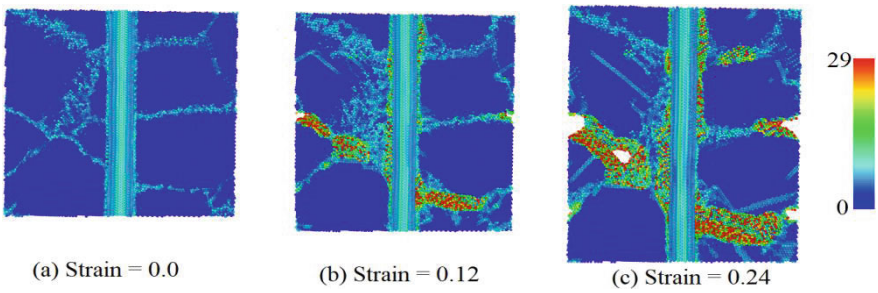

Fig. 9 NC Copper + TWCNT at $T = 10$ K for grain size 8.7 nm

4 Conclusion

By reinforcing NC copper with a single-walled CNT, it is seen that the elastic modulus does not always increase with the increase in volume fraction of the reinforcement, as seen in many other materials such as aluminum [28]. The deviation of the elastic modulus of the composite material from the parent material is not significant, though. The yield strength, on the other hand, has been observed to increase with an increase in the volume fraction of the CNTs. No particular grain dependence of the properties has been found in the composites.

With an increase in strain, NC copper fractures along the grain boundaries. As the strain increases in the NC copper reinforced with a single-walled CNT of chirality (25,25), we observe that the CNTs detach from the parent material. This leads to void formation, crack propagation, and ultimately fracture. All of these result in a decrease in elastic modulus.

With an increase in the number of walls of CNTs, it is seen that both Young's modulus and strength increase. Also due to the interaction of inner CNTs with the matrix and the other layers, there is no CNT detachment, and void formation begins in the grain boundary junction inside the bulk of the material.

Acknowledgements The authors would like to acknowledge the support in part provided by the Indian Institute of Technology through its ISIRD grant number DNI.

References

1. Iijima S, Ichihashi T (1993) Single-shell carbon nanotubes of 1-nm diameter. Nature 363(6430):603–605
2. Calderón-Villajos R, López AJ, Peponi L, Manzano-Santamaría J, Ureña A (2019) 3D-printed self-healing composite polymer reinforced with carbon nanotubes. Mater Lett 249:91–94
3. Muhulet A, Miculescu F, Voicu SI, Schütt F, Thakur VK, Mishra YK (2018) Fundamentals and scopes of doped carbon nanotubes towards energy and biosensing applications. Mater Today Energy [Internet] 9:154–86. https://doi.org/10.1016/j.mtener.2018.05.002
4. Mecklenburg M, Mizushima D, Ohtake N, Bauhofer W, Fiedler B, Schulte K (2015) On the manufacturing and electrical and mechanical properties of ultra-high wt.% fraction aligned MWCNT and randomly oriented CNT epoxy composites. Carbon N Y 91:275–90
5. Cadek M, Coleman JN, Barron V, Hedicke K, Blau WJ (2002) Morphological and mechanical properties of carbon-nanotube-reinforced semicrystalline and amorphous polymer composites. Appl Phys Lett 81(27):5123–5125
6. Athanasiou CE, Zhang H, Ramirez C, Xi J, Baba T, Wang X, et al (2020) High toughness carbon-nanotube-reinforced ceramics via ion-beam engineering of interfaces. Carbon N Y
7. Hwang GL, Hwang KC (2001) Carbon nanotube reinforced ceramics. J Mater Chem 11(6):1722–1725
8. Samal SS, Bal S (2008) Carbon nanotube reinforced ceramic matrix composites-a review
9. Kuzumaki T, Miyazawa K, Ichinose H, Ito K (1998) Processing of carbon nanotube reinforced aluminum composite. J Mater Res 13(9):2445–2449
10. Kim KT, Cha S Il, Hong SH, Hong SH (2006) Microstructures and tensile behavior of carbon nanotube reinforced Cu matrix nanocomposites. Mater Sci Eng A 430(1–2):27–33
11. Bakshi SR, Lahiri D, Agarwal A (2010) Carbon nanotube reinforced metal matrix composites-a review. Int Mater Rev 55(1):41–64
12. Sundaram RM, Sekiguchi A, Sekiya M, Yamada T, Hata K (2018) Copper/carbon nanotube composites: research trends and outlook. R Soc Open Sci 5(11):180814
13. Cha SI, Kim KT, Arshad SN, Mo CB, Hong SH (2005) Extraordinary strengthening effect of carbon nanotubes in metal-matrix nanocomposites processed by molecular-level mixing. Adv Mater 17(11):1377–1381
14. Kim KT, Eckert J, Menzel SB, Gemming T, Hong S-H (2008) Grain refinement assisted strengthening of carbon nanotube reinforced copper matrix nanocomposites. Appl Phys Lett 92(12):121901
15. Chai G, Sun Y, Chen Q, et al (2008) Mechanical properties of carbon nanotube--copper nanocomposites. J Micromechanics Microeng 18(3):35013
16. Lu L, Chen X, Huang X, Lu K (2009) Revealing the maximum strength in nanotwinned copper. Science (80) 323(5914):607–10
17. Li H, Misra A, Horita Z, Koch CC, Mara NA, Dickerson PO et al (2009) Strong and ductile nanostructured Cu-carbon nanotube composite. Appl Phys Lett 95(7):71907
18. Wang H, Zhang Z-H, Hu Z-Y, Wang F-C, Li S-L, Korznikov E et al (2016) Synergistic strengthening effect of nanocrystalline copper reinforced with carbon nanotubes. Sci Rep 6:26258
19. Yan Y, Lei Y, Liu S (2018) Tensile responses of carbon nanotubes-reinforced copper nanocomposites: molecular dynamics simulation. Comput Mater Sci 151:273–277
20. Faria B, Guarda C, Silvestre N, Lopes JNC, Galhofo D (2018) Strength and failure mechanisms of cnt-reinforced copper nanocomposite. Compos Part B Eng 145:108–120

21. Duan K, Li L, Hu Y, Wang X (2017) Damping characteristic of Ni-coated carbon nanotube/copper composite. Mater Des 133:455–463
22. Hirel P (2015) Atomsk: a tool for manipulating and converting atomic data files. Comput Phys Commun 197:212–9
23. Mendelev MI, King AH (2013) The interactions of self-interstitials with twin boundaries. Philos Mag 93(10–12):1268–1278
24. Stuart SJ, Tutein AB, Harrison JA (2000) A reactive potential for hydrocarbons with intermolecular interactions. J Chem Phys 112(14):6472–6486
25. LAMMPS molecular dynamics simulator. https://lammps.sandia.gov/
26. Plimpton S (1995) Fast parallel algorithms for short-range molecular dynamics. J Comput Phys 117(1):1–19
27. Evans DJ, Holian BL (1985) The nose–hoover thermostat. J Chem Phys 83(8):4069–4074
28. Pal S, Babu PN, Gargeya BSK, Becquart CS (2020) Molecular Dynamics simulation based investigation of possible enhancement in strength and ductility of nanocrystalline aluminum by CNT reinforcement. Mater Chem Phys 243 (December 2019)

Support Vector Machines-Based Prediction of Elastic Modulus for Granite Rock

Tammineni Gnananandarao, Rakesh Kumar Dutta, and Vishwas Nandkishor Khatri

1 Introduction

For the construction of any structure on the rock mass, engineering properties (strength and deformation characteristics) of the rock play an important role. These properties are useful in planning and optimizing the utilization of the natural resources of the earth. The design of the structure resting on rock is influenced by the strength and elasticity response under different stress conditions. The major influencing factor is the stress–strain behavior and the elastic modulus (E). These are generally determined by the unconfined compressive strength test. Generally, these properties are dependent on the point load strength index 'Is (50)', rebound number 'Rn', P-wave velocity 'VP', and the porosity 'n' as reported in [1, 2]. It was reported by [3] that the basic rock index tests, such as physical tests, ultrasonic velocity test, point load index test, rebound number test, and Brazilian test, were easy to perform and were economical. In the present study, the elastic modulus (E) of the rock was predicted based on the index properties of the rock.

2 Background

Since the past decade, soft computing techniques have been becoming popular in the field of civil engineering, especially in geotechnical engineering [4–7]. However, the

T. Gnananandarao (✉) · R. K. Dutta
Department of Civil Engineering, National Institute of Technology Hamirpur, Hamirpur, Himachal Pradesh, India

V. N. Khatri
Department of Civil Engineering, Indian Institute of Technology Dhanbad, Dhanbad, Jharkhand, India

D. K. Maiti et al. (eds.), *Recent Advances in Computational and Experimental Mechanics, Vol II*, Lecture Notes in Mechanical Engineering,
https://doi.org/10.1007/978-981-16-6490-8_29

application of artificial neural network (ANN) is one of the most popular research areas in engineering applications due to its diversity. Though, as we know, ANNs have the ability to map the input to the output with the help of the anticipated independent input parameters for the prediction of the desired output parameter. However, the ANN is having the limitations such as the slow learning rate and entrapment of the local minima, as reported by [8, 9]. The support vector machines predict accurately in comparison to the ANN, M5P, and random forest regression [10–14]. Keeping the above in view, the support vector machine with poly kernel and RBF kernel was used in the present study to predict the elastic modulus for granite rock. These techniques (SVM) have been successfully used in the different engineering application areas [15–18]. To achieve the objective of the present study, the input parameters such as porosity '*n*', Schmidt hammer rebound number 'Rn', *P*-wave velocity 'VP', and point load strength index 'Is (50)' were utilized to predict the output (modulus of elasticity 'E').

3 Support Vector Machines

Support vector machines (SVMs) were introduced by [19] with an alternate ε-insensitive loss function. It allows for regression problems to use the definition of margin. However, the boundary is defined as the total of hyperplanes distances from the closest point of two categories. The main aim of the SVM is to find out a function having maximum ε deviation from the real target vectors for all the training data provided and it must be as flat as possible [20]. However, a kernel function concept was introduced by [19] for nonlinear SVM regression. The enthusiastic readers are advised to refer for more descriptions of supporting vector regression [19, 20].

3.1 Details of Kernel

In SVM a kernel function concept was used, where the nonlinear decision surface circumstances occurred [19]. A number of kernel functions are introduced in the past decade, but the literature [21–23] suggests that the polynomial kernel and radial basis kernels (RBF) perform better for geotechnical engineering applications. Hence, in the present article, polynomial kernel $K(x, y) = [(x.y)]^d$ and RBF kernel $e^{-\gamma|x-y|^2}$ were used (where d and γ are the kernel parameters). In order to use SVM, suitable user-defined parameters have to be set first. These used-defined parameters are playing a major role in SVM prediction. The SVM needs kernel-specific parameters in addition to the selection of a kernel. The appropriate values of the regulatory parameter C as well as the size of the error-insensitive zone ε should be determined. A manual procedure was followed to select user-defined parameters (i.e. C, γ, and d), which involves performing a series of trials by means of different combinations of C and d for the polynomial kernel; C and γ for the RBF kernel support vector

Table 1 Range of the parameters used in SVM modeling

Input parameters	Total data set			
	Min	Max	Avg	Standard deviation
Is (50) (MPa)	0.89	7.10	3.34	1.50
Rn	37.00	61.00	49.56	5.96
VP (m/s)	2823.00	7943.00	5580.74	1089.43
n (%)	0.10	0.57	0.37	0.13
E (GPa)	22.00	183.30	88.40	34.93

machines (SVMs). Correspondingly, several trials were conducted in order to find the appropriate value for ε the error-insensitive zone having a fixed value of C and defined kernel parameters. The value of $C = 0.011$ is found to be good for this study. In this article, the radial basis function kernel and the polynomial kernel of the support vector machines are represented as SVM_{RBFK} and $\text{SVM}_{\text{POLYK}}$, respectively.

4 Data Collection

Data used in the present study are taken from an earlier study reported by [24] in which an artificial neural network (ANN) enhanced with the imperialist competitive algorithm (ICA) was used to associate the input index properties of the granite rock to predict the modulus of elasticity (E). To achieve the objective of the present study, a total of 71 data were collected from the literature [24]. It contains the point load strength index 'Is (50)', rebound hammer number 'Rn', P-wave velocity 'VP', porosity 'n', and Young's modulus 'E'. The range of these variables used for the SVM model was shown in Table 1. The input parameters were Is (50), Rn, VP, and n and the output parameter was the modulus of elasticity (E).

5 Statistical Testing Measures

The statistical testing measures (STMs) were used to assess the effectiveness of the poly kernel and the RBF kernel models during the training and the testing phase. The utilized STMs are correlations coefficient (r), coefficient of determination (R^2), mean absolute error (MAE), root mean square error (RMSE), mean absolute error (MAE), and mean absolute percentage error (MAPE). The formulas for the statistical testing measures were reported in [25]. The predictive models with an r and R^2 equal to 1, MAPE less than 20%, and MAE, RMSE, and MAE close to zero indicate a perfect model [5–7, 25].

6 Results and Discussion

The statistical testing measures are the key aspects that were used to assess the performance of the SVM_{POLYK} and SVM_{RBFK} models. The user-defined parameters for the SVM_{POLYK} are C and d; for SVM_{RBFK} C and γ were chosen with different combinations to obtain the best performance of the models. The best user-defined parameters were tabulated in Table 2.

The best statistical testing parameters obtained for both SVM models are presented in Table 3 for the training as well as for the testing. For $SVM_{POLYK,}$ the measured versus predicted plots for the training and the testing were shown in Fig. 1a and b, respectively. Similarly, for the $SVM_{RBFK,}$ the training and the testing were shown in Fig. 2a and b, respectively. From the study of Table 3 and Figs. 1 and 2, it has been revealed that the SVM_{RBFK} is predicting the modulus of elasticity of the granite rock accurately as compared to the SVM_{POLYK}.

Finally, the measured modulus of elasticity and the predicted modulus of elasticity from the SVM_{POLYK} and SVM_{RBFK} were compared for the testing data and presented in Fig. 3. From Fig. 3, the reader can note the difference between the measured versus the predicted variation.

However, the results of the present study were compared with the previous study in terms of the coefficient of determination (R^2) and the comparison is shown in Fig. 4. This figure reveals that the present study models can predict the modulus of the elasticity of the granite rock accurately in comparison to the previously reported models which were developed using soft computing techniques, such as GA-NN, ANFIS, GA, and ICA-NN, and reported in the literature works [24, 26–28] for the rock masses.

Table 2 User-defined parameters

Support vector regression (SVM)			
SVM_{POLYK}		SVM_{RBFK}	
C	*D*	*C*	γ
1.2	5	1.5	7

Table 3 Statistical testing measures for the SVM polynomial kernel and SVM RBF kernel

Performance measures	SVM polynomial kernel		SVM RBF kernel	
	Training	Testing	Training	Testing
R^2	0.95	0.94	0.98	0.97
r	0.95	0.93	0.98	0.97
MAE	389.57	518.02	186.91	265.19
RMSE	19.74	22.76	13.67	16.28
MAE	13.45	16.98	7.27	13.32
MAPE	17.39	24.93	9.85	19.54

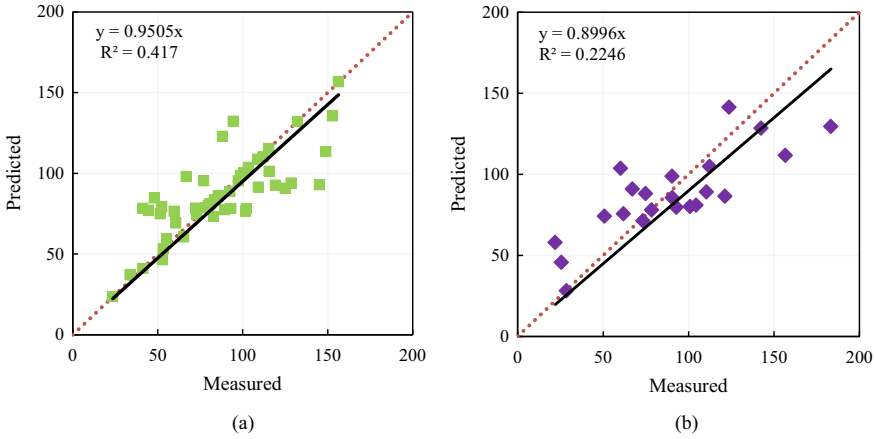

Fig. 1 Scattered plot for the measured versus predicted modulus of elasticity by SVM poly kernel. **a** Training and **b** testing

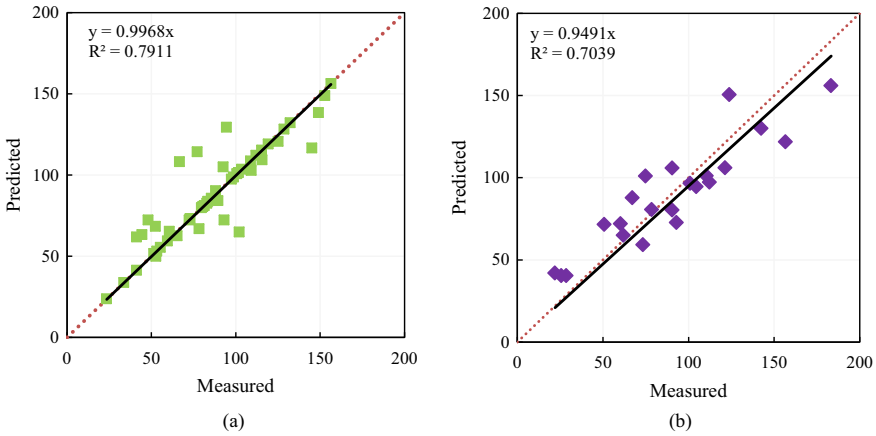

Fig. 2 Scattered plot for the measured versus predicted modulus of elasticity by SVM RBF kernel. **a** Training and **b** testing

6.1 Sensitivity Analysis

Generally, sensitivity analysis is conducted in soft computing techniques to see the influence of each of the input parameters on the output. In the present study, the same was carried out to see the individual input parameter influence on the output parameter prediction. However, the radial basis function kernel model was used in this study. The reason behind choosing the SVM_{RBFK} is that its prediction performance is superior to the polynomial kernel. The results of the sensitivity analysis are presented in Table 4. The study of this table reveals that porosity 'n' and Schmidt hammer rebound number

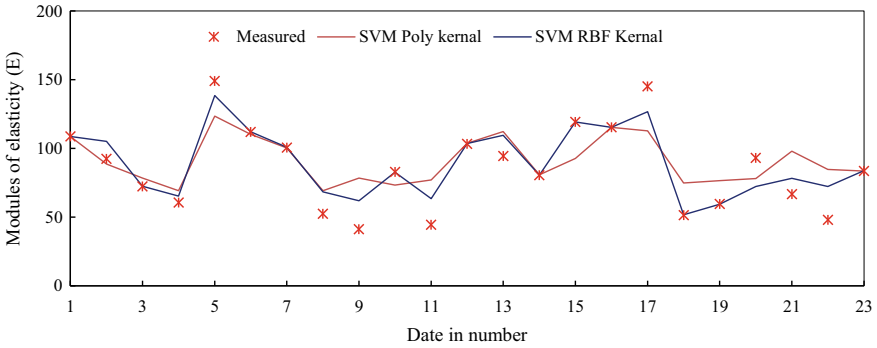

Fig. 3 Plot for the measure, SVM poly kernel and SVM RBF kernel comparison for the testing date of the modulus of elasticity

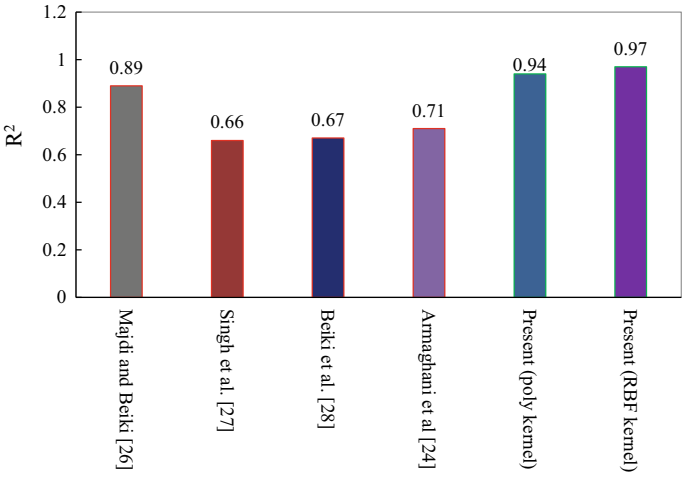

Fig. 4 R^2 for different studies

Table 4 Sensitivity analysis for the SVM_{RBFK}

Input combinations	Input parameter removed	SVM_{RBFK}					
		R^2	r	MAE	RMSE	MAE	MAPE
n, Rn, VP, and Is (50)	–	0.97	0.98	186.91	13.67	7.27	9.85
Rn, VP, and Is (50)	n	0.94	0.97	296.85	17.23	11.55	16.27
n, VP, and Is (50)	Rn	0.94	0.96	341.04	18.47	11.55	16.17
n, Rn, and Is (50)	VP	0.96	0.97	224.36	14.98	8.89	11.61
n, Rn, and VP	Is (50)	0.96	0.97	224.36	14.98	8.89	11.61

'Rn' are the most influencing parameters in comparison to the P-wave velocity 'VP' and point load strength index 'Is (50)'.

7 Conclusions

This study investigates the potential use of SVM polynomial and SVM RBF kernels in predicting the modulus of elasticity of the granite rock masses. The key conclusion that can be drawn from this study is that the SVM RBF kernel model predicted the modulus better than the SVM polynomial kernel. However, both the proposed models in the present study are suitable for predicting modulus of elasticity of granite rock. The results of comparison with the previous studies using soft computing techniques (GA-NN, ANFIS, GA, and ICA-NN) were inferior in comparison to the present techniques (SVM RBF and polynomial kernels). Finally, the sensitivity analysis reveals that the porosity '*n*' and Schmidt hammer rebound number 'Rn' were the most influencing parameters in comparison to the *P*-wave velocity 'VP' and point load strength index 'Is (50)'. The limitation of the present study is that the collected data was limited to one country and the number of the data was also less.

Acknowledgements The authors would like to show gratitude to the anonymous reviewers for reviewing the manuscript carefully and for the suggestions.

References

1. Yilmaz I, Yuksek AG (2008) An example of artificial neural network (ANN) application for indirect estimation of rock parameters. Rock Mech Rock Eng 41(5):781–795
2. Momeni E, Armaghani DJ, Hajihassani M, Amin MFM (2015) Prediction of uniaxial compressive strength of rock samples using hybrid particle swarm optimization-based artificial neural networks. Measurement 60:50–63
3. Singh R, Kainthola A, Singh TN (2012) Estimation of elastic constant of rocks using an ANFIS approach. Appl Soft Comput 12(1):40–45
4. Gnananandarao T, Khatri VN, Dutta RK (2020) Prediction of bearing capacity of H plan shaped skirted footing on sand using soft computing techniques. Arch Mater Sci Eng 103(2):62–74
5. Gnananandarao T, Khatri VN, Dutta RK (2020) Bearing capacity and settlement prediction of multi-edge skirted footings resting on sand. Ing E Investig J (In press)
6. Gnananandarao T, Dutta RK, Khatri VN (2019) Application of artificial neural network to predict the settlement of shallow foundations on cohesionless soils. Geotech Appl, Lect Notes Civ Eng 13:51–58. https://doi.org/10.1007/978-981-13-0368-5_6
7. Dutta RK, Gnananandarao T, Khatri VN (2019) Application of soft computing techniques in predicting the ultimate bearing capacity of strip footing subjected to eccentric inclined load and resting on sand. J Soft Comput Civ Eng 3(2):30–40. https://doi.org/10.22115/SCCE.2019.144535.1088
8. Eberhart RC, Simpson PK, Dobbins RW (1996) Computational intelligence PC tools. Academic Press Professional

9. Adhikari R, Agrawal RK, Kant L (2013) PSO based neural networks vs. traditional statistical models for seasonal time series forecasting. In: Advance computing conference (IACC), IEEE 3rd International, pp 719–725
10. Ahmad S, Kalra A, Stephen H (2010) Estimating soil moisture using remote sensing data: a machine learning approach. Adv Water Resour 33:69–80
11. Puria N, Prasad HD, Jain A (2018) Prediction of geotechnical parameters using machine learning techniques. Procedia Comput Sci 125:509–517
12. Pala M, Singh NK, Tiwari NK (2011) Support vector regression based modeling of pier scour using field data. Eng Appl Artif Intell 24(5):911–916
13. Samui P (2012) Application of statistical learning algorithms to ultimate bearing capacity of shallow foundation on cohesionless soil. Int J Numer Anal Meth Geomech 36:100–110
14. Gill MK, Asefa T, Kemblowski MW, McKee M (2006) Soil moisture prediction using support vector machines. J Am Water Resour Assoc 42(4):1033–1046
15. Singh B, Sihag P, Singh K (2017) Modelling of impact of water quality on infltration rate of soil by random forest regression. Model Earth Syst Environ. https://doi.org/10.1007/s40808-017-0347-3
16. Pal M, Deswal S (2008) Modeling pile capacity using support vector machines and generalized regression neural network. J Geotech Geoenviron Eng 134(7):1021–1024
17. Pal M, Singh NK, Tiwari NK (2011) Support vector regression based modeling of pier scour using field data. Eng Appl Artif Intell 24:911–916
18. Dutta RK, Khatri VN, Gnananandarao T (2019) Soft computing based prediction of ultimate bearing capacity of footings resting on rock masses. Int J Geol Geotech Eng 5(2):1–14
19. Vapnik VN (1995) The nature of statistical learning theory. Springer, New York
20. Smola AJ (1996) Regression estimation with support vector learning machines. Master's Thesis, Technische Universitat München, Germany
21. Pal M, Mather PM (2003) Support vector classifiers for land cover classification. Map India, New Delhi, January 28–31, 2003
22. Pal M, Goel A (2006) Prediction of the end depth ratio and discharge in semi circular and circular shaped channels using support vector machines. Flow Meas Instrum 17:50–57
23. Gill MK, Asefa T, Kemblowski MW, Makee M (2006) Soil moisture prediction using support vector machines. J Am Water Resour Assoc 42:1033–1046
24. Armaghani DJ, Mohamad ET, Momeni E, Monjezi M, Narayanasamy MS (2016) Prediction of the strength and elasticity modulus of granite through an expert artificial neural network. Arab J Geosci 48:1–16
25. Dutta RK, Dutta K, Jeevanandham S (2015) Prediction of deviator stress of sand reinforced with waste plastic strips using neural network. Int J Geosynthatics Ground Eng 1(11):1–12. https://doi.org/10.1007/s40891-015-0013-7
26. Majdi A, Beiki M (2010) Evolving neural network using a genetic algorithm for predicting the deformation modulus of rock masses. Int J Rock Mech Min Sci 47(2):246–253
27. Singh R, Kainthola A, Singh TN (2012) Estimation of elastic constant of rocks using an ANFIS approach. Appl Soft Comput 12(1):40–45
28. Beiki M, Majdi A, Givshad AD (2013) Application of genetic programming to predict the uniaxial compressive strength and elastic modulus of carbonate rocks. Int J Rock Mech Min Sci 63:159–169

Towards Finite Element Modelling of Electrical Activity in Cardiac Tissue Based on Greenstein–Winslow Ventricular Myocyte Model

T. G. Mythri, S. J. Hossain, and Baidurya Bhattacharya

1 Introduction

The heart is a complex electromechanical system. Optimal functioning of the heart depends on Excitation–Contraction Coupling (ECC). ECC is the mechanism responsible for mechanical contraction–relaxation of heart cells. It plays an essential role in controlling the heartbeat. ECC is a multiscale and multiphysics process connecting the whole heart to the cardiac muscle tissue to the single cell, down to the sarcomere.

Ionic currents are the result of the transport of ions across the membranes, mainly through ion channels. These currents play a significant role in shaping the action potential (AP). Complex ionic processes involved at the cellular level determine the arrhythmic behaviour of the heart. Mathematical modelling of the electrical activity of the cardiac tissue gives us a better understanding of the underlying biophysics and helps to study the resulting mechanics of cardiac tissues and mechanisms of arrhythmia.

1.1 Action Potential

Action potential (AP) is caused by the ionic movement across the cell membrane. Ion channels are responsible for ionic currents and transmembrane ion gradients. This is the basis of the physiological processes at the cell level. Typical AP curve of cardiac muscle is shown in Fig. 1. Cardiac AP can be categorized into five phases [1].

- Phase 0: Rapid depolarization caused by a transient increase in Na^+ channel conductance.

T. G. Mythri · S. J. Hossain · B. Bhattacharya (✉)
Department of Civil Engineering, Indian Institute of Technology, Kharagpur, India
e-mail: baidurya@civil.iitkgp.ac.in

D. K. Maiti et al. (eds.), *Recent Advances in Computational and Experimental Mechanics, Vol II*, Lecture Notes in Mechanical Engineering,
https://doi.org/10.1007/978-981-16-6490-8_30

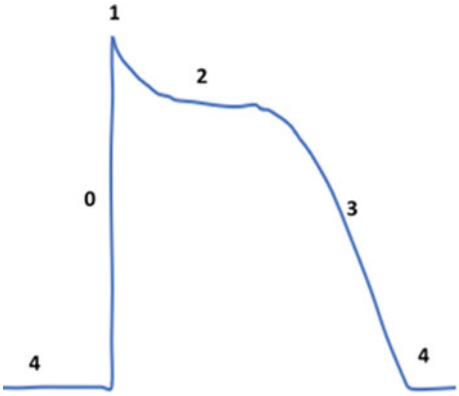

Fig. 1 Cardiac action potential with different phases

- Phase 1: Corresponds to the initial repolarization. It is mainly caused by the opening of transient outward K^+ current.
- Phase 2: Balancing K^+ current with the inward flux of Ca^{2+} current from LCCs results in plateau shaped region
- Phase 3: Repolarization occurs due to increased K^+ rectifier current and inactivation of Ca^{2+} channels.
- Phase 4: Voltage at phase 4 is maintained at its resting value.

In a cardiac muscle, all the cells are linked to each other through structures called gap junctions, which allows the propagation of AP to pass on to the next cell. The AP passes along the cell membrane, causing the cell to contract, thus resulting in contraction and relaxation of cardiac tissue.

1.2 Ion Channels

Ion channels are responsible for ionic currents and transmembrane ionic gradients in the cell. Ion channels are classified based on their nature of gating as, ligand-gated, voltage-gated, mechanosensitive channels. The opening and closing, i.e. gating variable of voltage-gated channels are dependent on the voltage across the membrane. The ion channels driving the ECC process in cardiac myocytes are voltage-gated [1, 2].

Ion channels are proteins, whose gating can be modelled as a series of hypothetical discrete states, where the occurrence of a transition from a state to another depends only on the current state and transition rates to the other states, but not the history of the system3. This property is known as Markovian property. If the state space is discrete, the Markov process is then known as Markov Chain.

Say we have a single ion channel gate with two possible states: O (open), C (closed). The gate can be represented as a Markov model, as shown in Fig. 2. The rates of transition between the states per unit time are given by α, β.

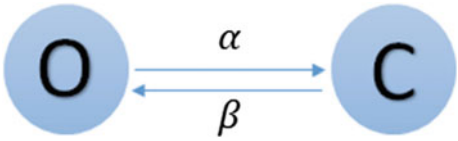

Fig. 2 Two state ion channel gate

The gate can either be closed or open. The probability of the gate being in an open state or closed state, at time t is given by:

$$\frac{d}{dt}P_O(t) = -\alpha P_O(t) + \beta P_C(t) \tag{1}$$

$$\frac{d}{dt}P_C(t) = \alpha P_O(t) - \beta P_C(t) \tag{2}$$

Ion channels can only conduct when they are open. Ionic current for a particular ion x is given as:

$$I = g_x(V - E_x) \tag{3}$$

where g_x is the conductance of membrane to ion x, E_x is Nernst Potential of ion x and V is membrane voltage. When the ion channel is modelled as Markov Model, we have the conductance term as $g_x = \overline{g} \times P_O(t)$. For voltage-gated ion channels, the parameters α, β are dependent on membrane voltage.

1.3 Excitation Contraction Coupling

Excitation Contraction Coupling (ECC) can be termed as the process that is responsible for transforming electrical energy involved in the cardiac myocytes to the mechanical energy, resulting in contraction–relaxation of the tissue [1, 2]. Muscle contraction revolves around the Calcium ion. Schematic diagram of the whole process is given in Fig. 3.

Specialized cells in the heart called Sinoatrial Nodes can spontaneously produce APs. These travel as impulses across the cell membrane, also known as sarcolemma. Propagation of AP from one cell to another happens through channels known as gap junctions. The deep penetrations of sarcolemma into the cell called transverse tubules (t-tubules) allow AP to travel into the cell. L- type calcium channels (LCCs) are voltage-gated ion channels, located on the t-tubule membrane. LCCs open as they get activated by APs and allow transport of calcium ions. Ryanodine Receptors (RyRs) are located on the membrane of structure, called the sarcoplasmic reticulum (SR). With increased Ca^{2+}, RyR gets activated and release more Ca^{2+} into the cell from SR. This process is called calcium-induced calcium release (CICR). These two

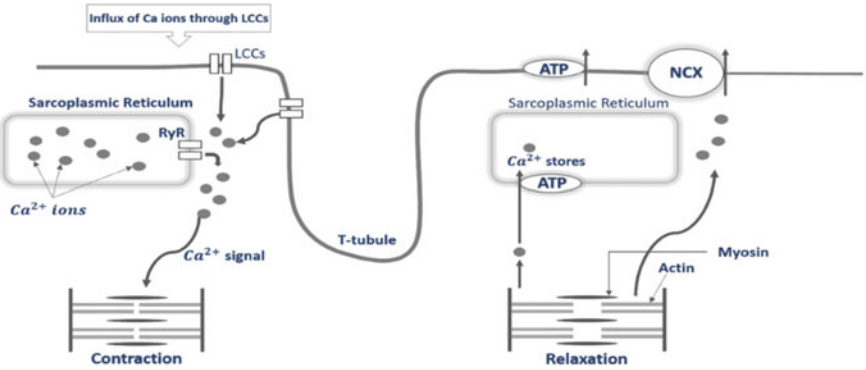

Fig. 3 Schematic diagram of the ECC mechanism

are the sources responsible for Ca^{2+} dynamics inside the cell, leading to muscle contraction. The intracellular Ca^{2+} binds to filaments called actin and myosin and initiates muscle contraction.

1.4 Literature Review

Complex ionic processes underlying the ion transients play a significant role in cardiac cells. Several cardiac models have been developed over time, which are capable of understanding the cardiac electrochemistry. The cell level cardiac models are formulated to include ionic currents, ionic concentrations, voltage and ion channel dynamics, responsible for the electrical activity of the cell. Hodgkin and Huxley [4] (HH-Model) proposed a quantitative model for initiation and propagation of AP for squid axon cells in 1952. The model was described using an analogous electrical circuit where individual ionic currents and capacitive current of membrane contribute to total membrane current I, i.e.

$$I = C_m \frac{dV}{dt} + I_i \tag{4}$$

where V corresponds to membrane voltage and I_i corresponds to the sum of ionic currents of all ions, C_m is membrane capacitance, where ionic current for a specific ion is given by Eq. (4). DiFrancesco and Noble [5] described electrical activity in cardiac cells, including ionic pumps, ionic concentration gradients.

The Beeler-Reuter model [6] (BR-model) developed in 1977 was the first generic ventricular myocyte model. In this model, I_{tot} included four ionic currents, i.e. time-dependent K^+ outward current (I_{K1}), fast inward Na^+ current (I_{Na}), time-dependent outward current (I_{X1}) and an inward current by Ca^{2+} (I_S).

Luo and Rudy's [7] (LR-1 Model, 1991) guinea pig ventricular myocyte model was developed based on BR-model, but, with modified ionic currents description. The ion concentrations inside the cell are unchanged as per this model, and so it can be termed as a passive model. In 1994, the Luo-Rudy dynamic model [8] (LRd-Model) was proposed. This model focused on dynamic intracellular ion concentrations, more detailed intracellular Ca^{2+} processes, detailed Ca^{2+} currents. LRd model was modified to add more details and Faber et al. [9] in 2007 described the more recent version of the LRd model.

Based on the guinea pig ventricular myocyte model by Jafri et al. [10], a canine ventricular myocyte model was proposed by Winslow et al. [11], with modified current descriptions and parameters to represent the canine cells. This model includes detailed Ca^{2+} dynamics by incorporating Markov model-based ion channels for LCCs, RyRs. The model has a total of 13 types of ionic currents. Greenstein et al. [12] studied the effects of transient outward current in shaping the AP, where Markov model-based ion channels were introduced in describing transient outward current. These models are used in modelling the AP in this paper.

Ten Tusscher et al. [13] proposed a human ventricular myocyte model based on LR1 model [7]. Based on the canine myocyte model of Winslow [11], the Iyer–Mazhari–Winslow model [14] was proposed, with 13 ionic currents. This model has around six ionic current descriptions based on Markov chain representations. With more recent experimental data, O'Hara-Rudy [15] dynamic model (ORd Model) was proposed describing un-diseased human ventricular myocyte electrophysiology. Ca^{2+} dynamics play a crucial role in modelling ECC at the cell level. Based on the ORd model [15], Himeno et al. [16] were able to reconstruct membrane potential and critical features of CICR with a new representation of ECC in a human ventricular myocyte model.

The modelling of propagation of AP through the cell membrane has been an exciting and significant problem over the years. Hodgkin and Huxley [4], along with the cell model, proposed propagation of AP in excitable tissue. This is a well-known case of modelling AP propagation in a continuum. The integration algorithm proposed by Rush and Larsen [17] is used in almost all of the propagation models to solve dynamic membrane equations. A finite element model to represent ventricular conduction processes incorporating spatial dispersion, to account for cardiac dysrhythmias was proposed back in the 1980s by Smith and Cohen [18], with a cylindrical model as a first-order approximation of ventricular geometry.

Rogers and McCulloch [19] proposed a computational method involving Galerkin Finite Element model, based on the FitzHugh Nagumo model [20, 21], to solve AP propagation problem on complicated domains. By complexity, we mean both geometric and material complexity.

Among the discretization schemes, finite-difference scheme was used both in spatial and temporal discretization to model cardiac electrical activity. Buist et al. [22] proposed a finite element derived finite difference technique that was used to solve cardiac activation problems over complex geometries with significant deformations. Xie et al. [23] used the LR1 model [7] with modified parameters, and cells are connected through gap junctions, represented as resistive elements. This work

employs conventional Euler method for integration. Cell model proposed by Tusscher and Panfilov [24] focused on formulating efficient human ventricular myocyte models to simulate the whole organ and at the same time detailed enough to capture cell-level dynamics. It was developed based on the Ten Tusscher et al. model [13], but a reduced version to obtain computational efficiency without compromising cellular level responses.

In 2009, Goktepe and Kuhl [25] proposed a novel finite element method to model cardiac electrophysiology by splitting global and local systems. The work was based on Aliev-Panfilov model [26] for cells. Classical Euler backward time integration scheme is used for temporal discretization. Wong, Goktepe and Kuhl [27] proposed a novel finite element approach, which included the LRd model [8] for cellular electrophysiology. The voltage is considered as a global degree of freedom, and all the other equations involving gating variables and ionic concentrations are considered as local degrees of freedom, i.e. at the cellular level. The domain was spatially discretized using finite elements and temporally discretized using a finite difference scheme. Dal et al. [28] extended Goktepe's work to propose a novel finite element algorithm to model cardiac electromechanics using bidomain models.

A discrete mass lattice framework and finite difference method were used to model the electromechanical model of human cardiac tissue by Weise and Panfilov [29] to investigate the effects of stretch conditions on propagation. A continuum approximation of tissue is often used to maintain continuity in computation. To investigate the effects of gap junctions on the electrical behaviour of tissue, Bruce et al. [30] derived a continuum model by introducing gap junctions in the discrete system.

Quarteroni et al. [31] presented a multiscale model of heart, including interactions of electrophysiology with muscle contraction and cell level contraction–relaxation mechanisms. Santiago et al. [32] proposed a model of human heart, incorporating solid mechanics, electrophysiology and fluid mechanics involved in the system. It is a multiphysics model where electrophysiology aspects are modelled based on ORd model [15], blood flow is modelled as incompressible flow, and the mechanical behaviour is modelled using Holzapfel–Ogden material model for cardiac tissue. Bartolucci et al. [33] presented a novel computational model of human ventricular AP, based on the ORd model, with revised calcium handling.

This work aims at proposing a finite element modelling approach for propagation modelling of AP based on Winslow–Greenstein ventricular myocyte model.

2 Technical Approach and Implementation

Multiscale model of whole ventricle can be developed by assembling the model equations of cell level, equations describing the propagation of AP through tissue, and a detailed geometrical model of the heart including the orientation of fibres and shape of ventricles. This work models cardiac AP based on Winslow and Greenstein's cell

model. A finite element approach to model propagation of AP in tissue is described in this work.

2.1 Cell Model

Formulation

At the cell level, the ion channels and transporters present in the cell membrane are responsible for the electrical activity of a cardiac myocyte. Winslow et al. [10–12] ventricular myocyte model has a set of 13 ionic currents, namely, the fast inward Na current (I_{Na}), L-type Ca^{2+} (I_{CaL}), L-type K^+ (I_{CaK}), inward rectifier K^+ (I_{Kr}), delayed rectifier K^+ (I_{Ks}), transient outward (I_{to1}), time-dependent K^+ (I_{K1}), plateau K^+ (I_{Kp}), Na^+–Ca^{2+}exchanger ($I_{Na–Ca}$), Na^+–K^+ pump ($I_{Na–K}$), sarcolemmal Ca^{2+} pump ($I_{p(Ca)}$), background Na^+ ($I_{Na,b}$), background Ca^{2+} ($I_{Ca,b}$) currents. Greenstein et al. [12] implemented a more detailed version of the transient outward (I_{to1}), time-dependent K^+ (I_{K1}) current. Of all these currents, I_{Na}, I_{Kr}, I_{Ks} are obtained from Hodgkin–Huxley gate formulation, I_{CaL}, I_{to1}, I_{CaK} are obtained from Markov model ion channels, and rest are the membrane currents where the conductance does not depend on any gating variables. The cell model consists of 51 dynamic quantities, including voltage, gating parameters and ionic concentrations. The model parameters and equations are taken from Greenstein et al. [12] and Winslow et al. [11]. The master equation describing the membrane voltage is a form of reaction–diffusion equation [24], given by:

$$\frac{\partial V}{\partial t} = \nabla \cdot (D \cdot \nabla V) + \frac{I_{\text{stim}} - I_{\text{ion}}}{C_{\text{m}}} \tag{5}$$

where I_{stim} is the external stimulus current provided to activate the cell, D is diffusivity tensor that describes the diffusion of voltage through the medium. At cellular level $D = 0$, I_{ion} is the total ionic current, which is the sum of all the ionic currents flowing through individual channels described in the model.

Implementation

The 51 dynamic quantities of the cell are state variables. Model is described by a set of differential equations representing the evolution of the state variables. The model has a set of constant parameters called Static Parameters. It also has Dynamic Parameters, which are dependent on other state variables, for example, rate parameters of gating variables are voltage dependent. Thus, all the differential equations are coupled [10, 11] (Fig. 4).

The general form of evolution equation of a state variable can be given as:

$$\frac{dx_i}{dt} = \alpha(V)x_i + \beta(V) \times (1 - x_i) \tag{6}$$

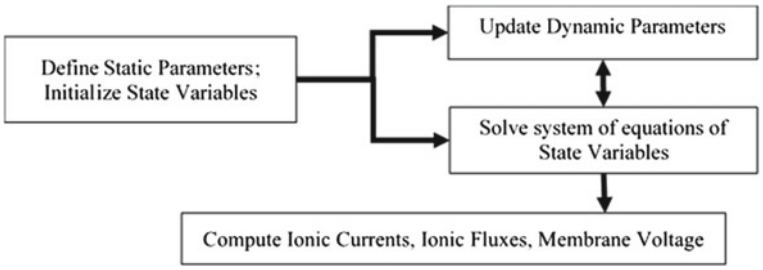

Fig. 4 Cell model computation structure

Fig. 5. 1D fibre discretized using finite linear elements

where $\alpha(V)$, $\beta(V)$ are rate parameter dependent on voltage, which is again one of the state variables.

2.2 Tissue Model Proposed Framework

For the propagation of AP in a 1D fibre, the domain can be discretized into two noded finite elements connected end on end [13–15], as shown in Fig. 5. Each node is considered as a cell, whose voltage evolution can be determined, and each element is a set of cells along which the voltage and effective ionic currents can be interpolated using the nodal values. The nodal values of net membrane currents, i.e. I_{m} are computed using the cell model at each node and are used to obtain nodal voltages at each node. For an n element model, there are ($n_{\mathrm{nodes}} = n_{\mathrm{element}} + 1$) number of nodes, and there are a total of $51 \times n_{\mathrm{nodes}}$ degrees of freedom, considering 51 variables at each node.

A computational framework for the implementation of the tissue model is described in Fig. 6. The cell model is evaluated at each node, and field variables are interpolated across the element and assembled to form the global system.

3 Results

The cell model simulation is performed in MATLAB. The cell model is activated by providing stimulus current and is provided with a delay of 2 ms from the start. The membrane potential at the cell level is obtained, as shown in Fig. 7. The AP curve obtained is similar to the typical cardiac AP curve, as shown in Fig. 1. Rapid

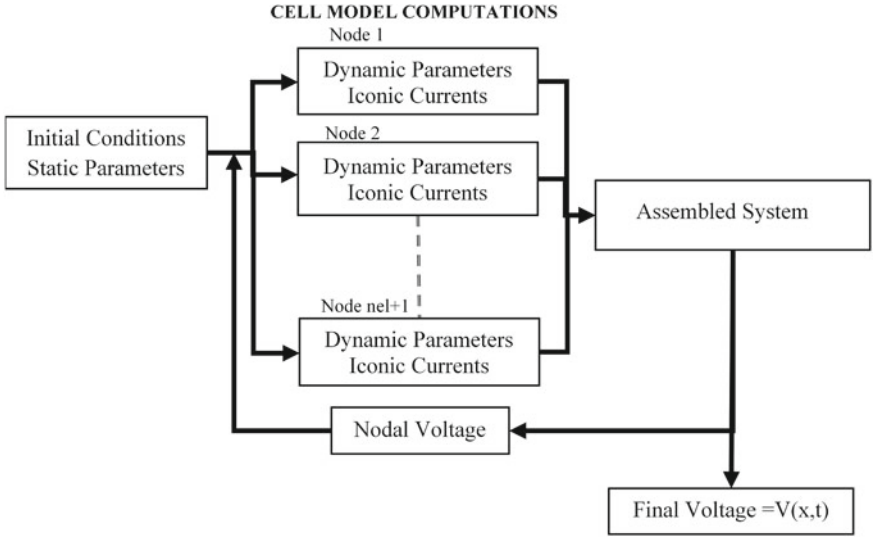

Fig. 6 Flowchart of Implementation of Tissue Model

Fig. 7 Membrane voltage

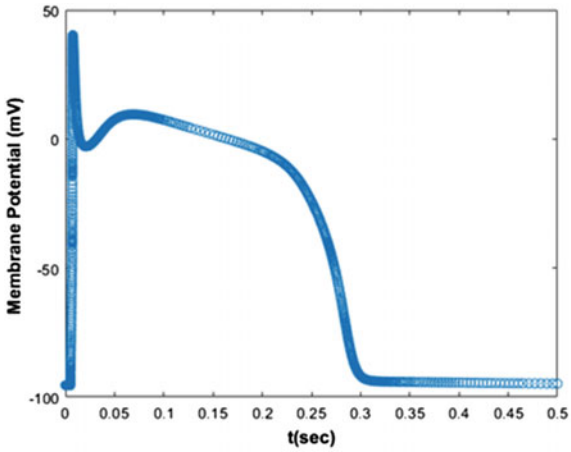

Na current starts immediately after activation and is responsible for the initiation of AP. The rapid depolarising current due to opening of fast Na^+ channels is shown in Fig. 8a.

At phase 1, initial repolarisation is significantly caused by transient outward current, as shown in Fig. 8b. Phase 2 is a plateau phase where the inflow of Ca^{2+} is balanced by slow rectifier K^+ current.

Currents corresponding to phase 2 behaviour of AP, i.e. L-type Ca^{2+} channel current and plateau K^+ current are shown in Fig. 9a, b. The rectifier K^+ currents are

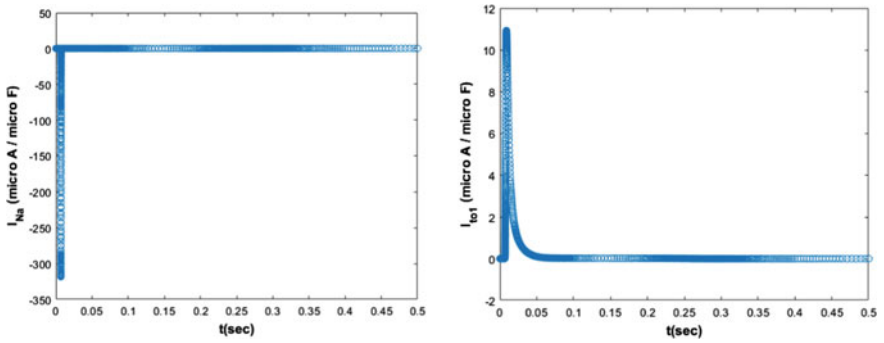

(a) Sodium Current I_{Na} **(b)** Transient Outward K^+ current I_{to1}

Fig. 8 **a** Sodium current I_{Na} **b** Transient outward K^+ current $I_{to\ 1}$

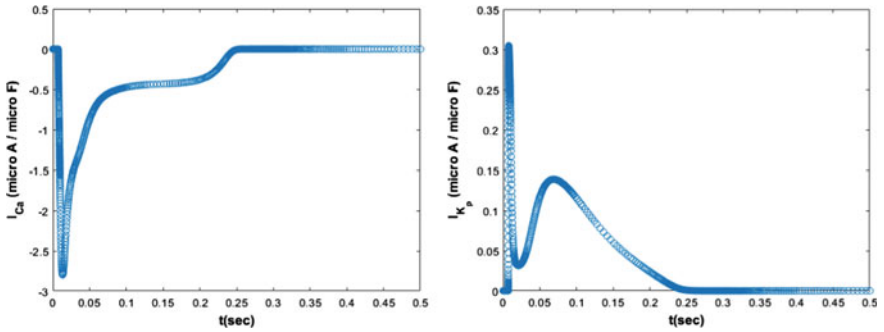

(a) L type Calcium Current I_{CaL} **(b)** Plateau K^+ current IK_p

Fig. 9 **a** L type calcium current I_{CaL} **b** Plateau K^+ current I_{Kp}

shown in Fig. 10a, b.

Phase 4 is the resting phase where outward K^+ channels are deactivated, and inward rectifier continues to take the membrane potential back to its resting value, as of phase 0. The inward rectifier current is shown in Fig. 11.

4 Conclusions

An approach to simulate the propagation of AP in the cardiac tissues based on a reaction–diffusion type model is presented in this work. The ionic currents are expressed by Winslow–Greenstein model. Cell model simulations are in agreement with the literature. Tissue model methodology has been discussed and is yet to be implemented.

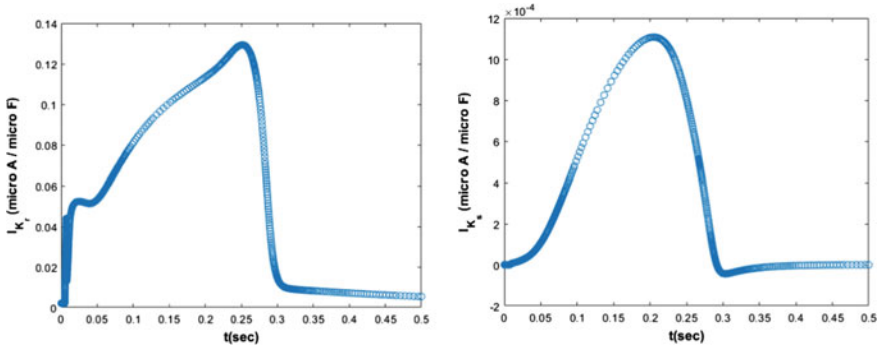

(a) Rapid Rectifier Current I_{Kr} **(b)** Slow Rectifier Current IK_s

Fig. 10 **a** Rapid rectifier current I_{Kr} **b** Slow rectifier current I_{Ks}

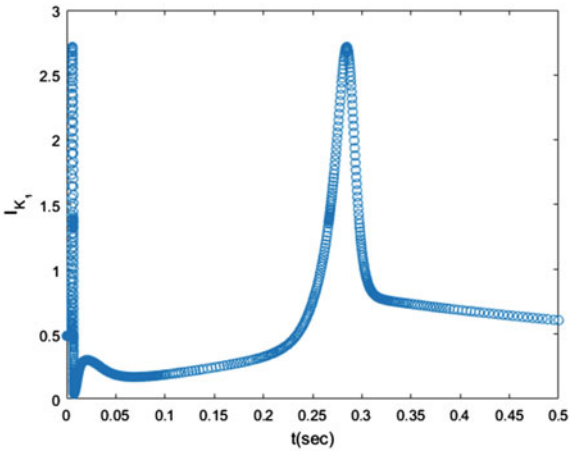

Fig. 11 Inward rectifier current I_{K1}

Future work can be focused on implementing this to a 3D tissue model and further to a geometrically detailed model of a heart including orientation of fibres and shape of ventricles. Furthermore, the model can be extended to implement the mechanical contraction force developed and study the effects in case of arrhythmia.

References

1. Bers DM (2001) Excitation-contraction coupling and cardiac contractile force. Kluwer Academic Publishers, Dordrecht Boston
2. Bertil H (2001) Ion channels of excitable membranes. Sinauer, Sunderland, Mass
3. Sigg D (2014) Modeling ion channels: past, present, and future. J Gen Physiol 144:7–26. https://doi.org/10.1085/jgp.201311130

4. Hodgkin AL, Huxley AF (1952) A quantitative description of membrane current and its application to conduction and excitation in nerve. J Physiol 117:500–544. https://doi.org/10.1113/jphysiol.1952.sp004764
5. DiFrancesco D, Noble D (1985) A model of cardiac electrical activity incorporating ionic pumps and concentration changes. Philos Trans R Soc Lond B, Biol Sci 307:353–398. https://doi.org/10.1098/rstb.1985.0001
6. Beeler GW, Reuter H (1977) Reconstruction of the action potential of ventricular myocardial fibres. J Physiol 268:177–210. https://doi.org/10.1113/jphysiol.1977.sp011853
7. Luo CH, Rudy Y (1991) A model of the ventricular cardiac action potential. Depolarisation, repolarisation, and their interaction. Circ Res 68:1501–1526. https://doi.org/10.1161/01.res.68.6.1501
8. Luo CH, Rudy Y (1994) A dynamic model of the cardiac ventricular action potential. I. Simulations of ionic currents and concentration changes. Circ Res 74:1071–1096. https://doi.org/10.1161/01.res.74.6.1071
9. Faber GM, Silva J, Livshitz L, Rudy Y (2007) Kinetic properties of the cardiac L-type Ca^{2+} channel and its role in myocyte electrophysiology: a theoretical investigation. Biophys J 92:1522–1543. https://doi.org/10.1529/biophysj.106.088807
10. Rice JJ, Saleet Jafri M, Winslow RL (1999) Modeling gain and gradedness of Ca^{2+} release in the functional unit of the cardiac diadic space. Biophys J 77:1871–1884. https://doi.org/10.1016/s0006-3495(99)77030-x
11. Winslow RL, Rice J, Jafri S et al (1999) Mechanisms of altered excitation-contraction coupling in canine tachycardia-induced heart failure, II. Circ Res 84:571–586. https://doi.org/10.1161/01.res.84.5.571
12. Greenstein JL, Wu R, Po S et al (2000) Role of the calcium-independent transient outward current Ito1 in shaping action potential morphology and duration. Circ Res 87:1026–1033. https://doi.org/10.1161/01.res.87.11.1026
13. Ten Tusscher KHWJ, Noble D, Noble PJ, Panfilov AV (2004) A model for human ventricular tissue. Am J Physiol-Hear Circ Physiol 286:H1573–H1589. https://doi.org/10.1152/ajpheart.00794.2003
14. Iyer V, Mazhari R, Winslow RL (2004) A computational model of the human left-ventricular epicardial myocyte. Biophys J 87:1507–1525. https://doi.org/10.1529/biophysj.104.043299
15. O'Hara T, Virág L, Varró A, Rudy Y (2011) Simulation of the undiseased human cardiac ventricular action potential: model formulation and experimental validation. PLoS Comput Biol 7:e1002061. https://doi.org/10.1371/journal.pcbi.1002061
16. Himeno Y, Asakura K, Cha CY et al (2015) A Human Ventricular myocyte model with a refined representation of excitation-contraction coupling. Biophys J 109:415–427. https://doi.org/10.1016/j.bpj.2015.06.017
17. Rush S, Larsen H (1978) A practical algorithm for solving dynamic membrane equations. IEEE Trans Biomed Eng BME 25:389–392. https://doi.org/10.1109/tbme.1978.326270
18. Smith JM, Cohen RJ (1984) Simple finite-element model accounts for wide range of cardiac dysrhythmias. Proc Natl Acad Sci 81:233–237. https://doi.org/10.1073/pnas.81.1.233
19. Rogers JM, McCulloch AD (1994) A collocation-Galerkin finite element model of cardiac action potential propagation. IEEE Trans Biomed Eng 41:743–757. https://doi.org/10.1109/10.310090
20. FitzHugh R (1961) Impulses and physiological states in theoretical models of nerve membrane. Biophys J 1:445–466. https://doi.org/10.1016/S0006-3495(61)86902-6
21. Nagumo J, Arimoto S, Yoshizawa S (1962) An active pulse transmission line simulating nerve axon. Proc IRE 50:2061–2070. https://doi.org/10.1109/JRPROC.1962.288235
22. Buist M, Sands G, Hunter P, Pullan A (2003) A deformable finite element derived finite difference method for cardiac activation problems. Ann Biomed Eng 31:577–588. https://doi.org/10.1114/1.1567283
23. Xie F, Qu Z, Yang J et al (2004) A simulation study of the effects of cardiac anatomy in ventricular fibrillation. J Clin Investig 113:686–693. https://doi.org/10.1172/jci17341

24. Tusscher KHWJT, Panfilov AV (2006) Cell model for efficient simulation of wave propagation in human ventricular tissue under normal and pathological conditions. Phys Med Biol 51:6141–6156. https://doi.org/10.1088/0031-9155/51/23/014
25. Göktepe S, Kuhl E (2009) Computational modeling of cardiac electrophysiology: a novel finite element approach. Int J Numer Meth Eng 79:156–178. https://doi.org/10.1002/nme.2571
26. Aliev RR, Panfilov AV (1996) A simple two-variable model of cardiac excitation. Chaos, Solitons Fractals 7:293–301. https://doi.org/10.1016/0960-0779(95)00089-5
27. Wong J, Göktepe S, Kuhl E (2011) Computational modeling of electrochemical coupling: a novel finite element approach towards ionic models for cardiac electrophysiology. Comput Methods Appl Mech Eng 200:3139–3158. https://doi.org/10.1016/j.cma.2011.07.003
28. Dal H, Göktepe S, Kaliske M, Kuhl E (2013) A fully implicit finite element method for bidomain models of cardiac electromechanics. Comput Methods Appl Mech Eng 253:323–336. https://doi.org/10.1016/j.cma.2012.07.004
29. Weise LD, Panfilov AV (2013) A Discrete electromechanical model for human cardiac tissue: effects of stretch-activated currents and stretch conditions on restitution properties and spiral wave dynamics. PLoS ONE 8:e59317. https://doi.org/10.1371/journal.pone.0059317
30. Bruce D, Pathmanathan P, Whiteley JP (2013) Modelling the effect of gap junctions on tissue-level cardiac electrophysiology. Bull Math Biol 76:431–454. https://doi.org/10.1007/s11538-013-9927-1
31. Quarteroni A, Lassila T, Rossi S, Ruiz-Baier R (2017) Integrated heart—coupling multiscale and multiphysics models for the simulation of the cardiac function. Comput Methods Appl Mech Eng 314:345–407. https://doi.org/10.1016/j.cma.2016.05.031
32. Santiago A, Aguado-Sierra J, Zavala-Aké M et al (2018) Fully coupled fluid-electro-mechanical model of the human heart for supercomputers. Int J Numer Methods Biomed Eng 34:e3140. https://doi.org/10.1002/cnm.3140
33. Bartolucci C, Passini E, Hyttinen J, et al (2020) Simulation of the effects of extracellular calcium changes leads to a novel computational model of human ventricular action potential with a revised calcium handling. Front Physiol 11https://doi.org/10.3389/fphys.2020.00314

Free Vibration Analysis of Isotropic and Laminated Composite Plate on Elastic Point Supports Using Finite Element Method

Sabyasachi Ghosh and Salil Haldar

1 Introduction

Isotropic plates and laminated composite plates resting on elastic point supports have wide engineering applications ranging from aeronautic, automotive, foundation structures to underwater structures and so on. Plates on elastic point supports are also used to approximate conditions of plates on column supports, slabs on beams, aircraft body panels and solar panels on supports. Laminated composites are used in engineering structures because of their favourable properties compared with isotropic materials such as high ratios of stiffness to weight and strength to weight. There are various theories for the analysis of plates like equivalent single layer theory and individual layer theories. Furthermore, equivalent single layer theories are classified into Classical Plate Theory (CPT), First-Order Shear Deformations Theory (FSDT) and Higher Order Shear Deformation Theory (HSDT). Classical Plate Theory is used to study thin plates having side to thickness (a/h $\geq$ 20) as the effect of transverse shear deformation is very less. However, CPT is ineffective for thick plates as the effect of transverse shear deformation cannot be neglected in thick plates, and CPT overestimates the natural frequencies. Extensive study has been done on the vibration of laminated composite plates by various methods, Leissa and Narita [1] conducted vibration analysis of plates using Ritz method for simply supported symmetric plates, Kalita et al. [2] analysed the vibration of plate with nine node isoparametric element. Chow et al. [3] presented the vibrational response of symmetric composite plate using Rayleigh–Ritz method while Reddy [4] used Mindlin's thick plate theory, which considers the shear deformation of plates to analyse free vibration using the finite element method. Aydogdu and Timarci [5] analysed the vibration of cross-ply laminated square plates subjected to different sets of boundary conditions using five degree of freedom shear deformable plate theory and obtained the free vibration

S. Ghosh (✉) · S. Haldar
Indian Institute of Engineering Science and Technology, Shibpur, India

D. K. Maiti et al. (eds.), *Recent Advances in Computational and Experimental Mechanics, Vol II*, Lecture Notes in Mechanical Engineering,
https://doi.org/10.1007/978-981-16-6490-8_31

frequencies by applying the Ritz method. Research work has been carried out on the free vibration analysis of plates on elastic foundations in many studies. For example, Akavci [6] used a hyperbolic displacement model to examine the free vibration of simply supported composite plates on elastic foundations, Barros and Barreiros Martins [7] formulated Mindlin's theory of bending of plates by finite element method to analyse plates resting on elastic foundation and represented the foundation soil with linear elastic behaviour (Winkler's theory). Park and Choi [8] used a simplified first-order shear deformation theory to present an analytical solution for the free vibration analysis of isotropic plates on two-parameter Pasternak elastic foundations. Omurtag and Kadioglu [9] analysed the free vibration of orthotropic plates resting on Pasternak foundation by mixed finite element formulation. Various studies have been conducted for plates on elastic line and point supports using different methods. Pang et al. [10] used an improved Fourier series method to study the transverse vibration of thick plates with elastic point supports at the edges. Li [11] determined the modal characteristics of a rectangular plate with general elastic support along its edges using the Rayleigh–Ritz method. Zietsman et al. [12] considered the vibration of a thin rectangular plate with elastic support at the boundary using the finite element method. Cheung and Zhou [13] analysed the vibrations of orthotropic plates with elastic line supports using the Rayleigh–Ritz method while Huang and Thambiratnam [14] analysed plates resting on elastic supports and elastic foundation using the finite strip method with different boundary conditions. Joseph Watkins and Barton [15] characterised the vibration of an elastic point supported isotropic rectangular plate using Eigen sensitivity analysis. Setoodeh and Karami [16] employed layer-wise finite element method to study the thick composite plates on distributed and point elastic supports.

Limited work has been carried out to analyse free vibration of plates on elastic point supports using First-Order Shear Deformation Theory (FSDT) and isoparametric finite element formulation and previous works have not comprehensively considered the vibration analysis of composite laminated plates on elastic point supports using finite element method. The present work intends to study isotropic and laminated composite plates on point elastic support with different side to thickness ratios, aspect ratios, number of ply layers, fibre angle orientations and boundary conditions using FSDT and finite element formulation.

2 Theoretical Formulations

In the formulation, the effect of shear along the thickness of the plate is incorporated using Mindlin's First-Order Shear Deformation Theory (FSDT), which assumes that the normal to the mid-plane of the plate remains straight, however, it may not be normal to the mid surface and the mid-plane is taken as the reference plane. In FSDT, the displacement along the thickness is assumed to be linear and as the normal strain through the thickness (ε_{zz}) is assumed to be 0, the thickness of the plate does not change after deformation. The shear strain has parabolic variation over the thickness

of the plate in actual; however in this study, it is assumed that the shear strain is constant over the entire thickness of the plate and to incorporate this assumption, a shear correction factor of 5/6 is used.

2.1 Numerical Simulation Procedure

Nine node isoparametric element is used to formulate the current finite element study and any form of plate can be mapped in global coordinate system using an isoparametric element, which is:

$$x = \sum_{r=1}^{9} N_r x_r \text{ and } y = \sum_{r=1}^{9} N_r y_r \tag{1}$$

Here x and y are the global coordinates of a point in the element, N_r is the Lagrange Interpolation Function, while x_r and y_r are the nodal coordinates of the point in the element.

The Lagrange interpolation function (N_r) for a rectangular or square element is derived as the product of Lagrange Interpolation function in x direction and Lagrange Interpolation function in y direction as:

$$N_r = \frac{(x - x_1)(x - x_2)\ldots(x - x_n)}{(x_r - x_1)(x_r - x_2)\ldots(x_r - x_n)} \times \frac{(y - y_1)(y - y_2)\ldots(y - y_n)}{(y_r - y_1)(y_r - y_2)\ldots(y_r - y_n)} \tag{2}$$

In FSDT, the shear rotation $\emptyset_x$ and $\emptyset_y$, which is independent of the total rotation and the bending rotation, is expressed as:

$$\begin{Bmatrix} \emptyset_x \\ \emptyset_y \end{Bmatrix} = \begin{Bmatrix} \theta_x - \frac{dw}{dx} \\ \theta_y - \frac{dw}{dy} \end{Bmatrix} \tag{3}$$

where θ_x and θ_y are the total rotation in x and y directions while dw/dx and dw/dy are the bending rotations in x and y directions, and w is the displacement in transverse direction, while u and v are the in-plane displacement in the x and y directions.

The interpolation function N_r used to represent the global coordinates of an element is also used to represent the displacement field in the element as:

$$u = \sum_{r=1}^{9} N_r u_r;\ v = \sum_{r=1}^{9} N_r v_r;\ w = \sum_{r=1}^{9} N_r w_r;\ \theta_x = \sum_{r=1}^{9} N_r \theta_{xr};\ \theta_y = \sum_{r=1}^{9} N_r \theta_{yr} \tag{4}$$

where u_r, v_r, w_r, θ_{xr}, θ_{yr} are the nodal displacements of a point in the element.

The general stress–strain relation for any elastic material is given by Hooke's law—$\{\sigma\} = [D]\{\epsilon\}$, where $\{\sigma\}$ is the generalised stress resultant vector and $\{\epsilon\}$ is the generalised strain vector.

$$\{\sigma\}^T = \left[N_x N_y N_{xy} M_x M_y M_{xy} Q_x Q_y\right] \tag{5}$$

where N_x, N_y are the in-plane resultant forces in x and y directions: N_{xy} is the resultant shear force in xy plane; M_x, M_y are the effective bending moments in x and y directions; M_{xy} is the resultant twisting moment and Q_x, Q_y are the transverse shear force resultants.

$$\{\varepsilon\}^T = \left\{\left(\frac{du}{dx}\right)\left(\frac{dv}{dy}\right)\left(\frac{du}{dy}+\frac{dv}{dx}\right)\left(-\frac{d\theta_x}{dx}\right)\left(-\frac{d\theta_y}{dy}\right)\left(-\frac{d\theta_x}{dy}-\frac{d\theta_y}{dx}\right)\left(\frac{dw}{dx}-\theta_x\right)\left(\frac{dw}{dy}-\theta_y\right)\right\} \tag{6}$$

The rigidity matrix $[D]$ is given by:

$$[D] = \begin{bmatrix} A_{11} & A_{12} & A_{16} & B_{11} & B_{12} & B_{16} & 0 & 0 \\ A_{12} & A_{22} & A_{26} & B_{12} & B_{22} & B_{26} & 0 & 0 \\ A_{16} & A_{26} & A_{66} & B_{16} & B_{26} & B_{66} & 0 & 0 \\ B_{11} & B_{12} & B_{16} & D_{11} & D_{12} & D_{16} & 0 & 0 \\ B_{12} & B_{22} & B_{26} & D_{12} & D_{22} & D_{26} & 0 & 0 \\ B_{16} & B_{26} & B_{66} & D_{16} & D_{26} & D_{66} & 0 & 0 \\ 0 & 0 & 0 & 0 & 0 & 0 & k_c A_{55} & k_c A_{54} \\ 0 & 0 & 0 & 0 & 0 & 0 & k_c A_{45} & k_c A_{44} \end{bmatrix}$$

where,

$$A_{ij} = \sum_{\mathrm{n}=1}^{m} \left(Q_{ij}\right)_n (Z_{n+1} - Z_n)$$

$$B_{ij} = \frac{1}{2} \sum_{\mathrm{n}=1}^{m} \left(Q_{ij}\right)_n (Z_{\mathrm{n}+1}^2 - Z_n^2)$$

$$D_{ij} = \frac{1}{3} \sum_{\mathrm{n}=1}^{m} \left(Q_{ij}\right)_n (Z_{\mathrm{n}+1}^3 - Z_n^3)$$

are the extensional (A_{ij}), extensional—bending (B_{ij}) and bending stiffness (D_{ij}) coefficients, which are expressed in terms of lamina stiffness coefficients for each layer. Here n represents the nth lamina from the middle lamina and m represents the number of the laminas. $\left(Q_{ij}\right)_n$ terms are the material coefficients for an orthotropic element and they are known in terms of their engineering coefficients of the nth

layer and are given as: $Q_{11}^n = \frac{E_1}{1-\mu_{12}\mu_{21}}$; $Q_{22}^n = \frac{E_2}{1-\mu_{12}\mu_{21}}$; $Q_{12}^n = Q_{21}^n = \frac{\mu_{12}E_2}{1-\mu_{12}\mu_{21}}$; $Q_{44}^n = G_{23}$; $Q_{55}^n = G_{13}$; $Q_{66}^n = G_{12}$

E_1 and E_2 are the elastic modulus in the longitudinal direction and transverse directions, respectively, μ_{12} is the in-plane Poisson's ratio and G_{12}, G_{13}, G_{23} are the shear modulus in the 1–2, 1–3 and 2–3 plane, respectively. From Eqs. (4) and (6), the strain vector may be expressed

$$\{\varepsilon\} = \sum_{r=1}^{9} [B]_r \{\delta_r\}_e \tag{7}$$

where the strain displacement matrix $[B]$ containing interpolation functions and their derivatives is given by:

$$[B] = \begin{bmatrix} \frac{\partial N_r}{\partial x} & 0 & 0 & 0 & 0 \\ 0 & \frac{\partial N_r}{\partial y} & 0 & 0 & 0 \\ \frac{\partial N_r}{\partial y} & \frac{\partial N_r}{\partial x} & 0 & 0 & 0 \\ 0 & 0 & 0 & -\frac{\partial N_r}{\partial x} & 0 \\ 0 & 0 & 0 & 0 & -\frac{\partial N_r}{\partial y} \\ 0 & 0 & 0 & -\frac{\partial N_r}{\partial y} & -\frac{\partial N_r}{\partial x} \\ 0 & 0 & \frac{\partial N_r}{\partial x} & -N_r & 0 \\ 0 & 0 & \frac{\partial N_r}{\partial y} & 0 & -N_r \end{bmatrix}$$

The stiffness matrix is derived using the principle of virtual work,

$$[K] = t \int_{-1}^{1} \int_{-1}^{1} [B]^T [D][B]|J| d\xi d\eta \tag{8}$$

where $|J|$ is the determinant of the Jacobian matrix [J], ξ and η are the local coordinate axis.

In the same way, the element consistent mass matrix is derived as:

$$[M] = \int_{-1}^{1} \int_{-1}^{1} [N]^T [\rho][N]|J| d\xi d\eta \tag{9}$$

The stiffness matrix and mass matrix of individual elements are then assembled to obtain the global stiffness matrix $[K_0]$ and the global mass matrix $[M_0]$ and they are related as:

$$[K_0] = \omega^2 [M_0] \tag{10}$$

Additionally, springs are attached to the plate and the stiffness of the springs at the specified nodes can be added to the global stiffness matrix of the plate as:

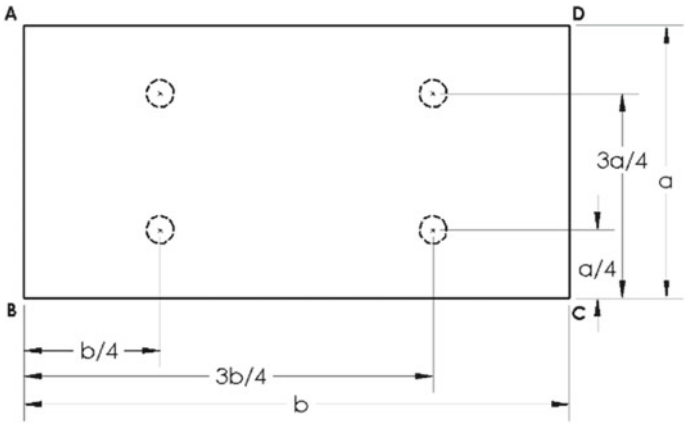

Fig. 1 Composite plate with spring

$$[K_0 + K_S + K_\theta] = \omega^2[M_0] \tag{11}$$

where K_s and K_θ are the transverse stiffness and rotational stiffness of the springs at the specified nodes.

The boundary conditions used are:

a Simply supported (S): $w = u = \theta_x = 0$, at the edges parallel to the y-axis and $w = v = \theta_y = 0$, at the edges parallel to the x-axis.
b Clamped (C): $w = x = y = \theta_x = \theta_y = 0$, along edges parallel to x and y-axis.
c Free Boundary: $u \neq 0$, $v \neq 0$, $w \neq 0$, $\theta_x \neq 0$ and $\theta_y \neq 0$, along edges parallel to x- and y-axis.

The boundary condition of the four edges of a plate is denoted as SCSF where the edges AB, CD, BC and AD of the plate in Fig. 1 are simply supported, clamped, simply supported and free, respectively.

3 Convergence Studies

3.1 Simply Supported Plate with Different Thickness Ratios and Mesh Divisions

A three-layer cross-ply (90°/0°/90°) laminated square plate with simply supported edges is considered. The present non-dimensional frequencies obtained with different plate thickness ratios (a/h) and mesh divisions are given in Table 1 along with the finite element solutions of Aydogdu and Timarci [5]. There is an excellent agreement with the published results. The material properties used in examples 3.1, 3.2 and 3.3

Table 1 Non-dimensional fundamental frequency parameter $\lambda = (\omega a^2)/h \sqrt{(\rho/E_2)}$ of a square simply supported three-layer cross-ply laminate (90°/0°/90°) with varying a/h ratio

Mesh Div.	a/h				
	5	10	20	50	100
Present (4 × 4)	10.20	14.75	17.51	18.64	18.82
Present (8 × 8)	10.23	14.76	17.51	18.64	18.82
Present (12 × 12)	10.28	14.76	17.51	18.64	18.82
Present (16 × 16)	10.28	14.76	17.51	18.64	18.82
Ref.[a]	10.54	14.95	17.59	18.66	18.83

[a] Aydogdu and Timarci [5]

are: $E_1 = 200$ GPa, $E_2 = 5$ GPa, $G_{12} = 3$ GPa, $G_{13} = 3$ GPa, $G_{23} = 2.5$ GPa, $\nu_{12} = 0.25$, $\nu_{21} = 0.00625$

3.2 *Plate with Different Boundary Conditions and Thickness Ratios*

A three-layer square cross-ply (90°/0°/90°) laminated plate having different boundary conditions and thickness ratios, without any springs is considered, and the non-dimensional frequency parameter is given in Table 2 with the results of Aydogdu and Timarci [5] and excellent agreement with the published results is seen.

Table 2 Non-dimensional fundamental frequency parameter $\lambda = (\omega a^2)/h \sqrt{(\rho/E_2)}$ of a three-layer (90°/0°/90°) square composite plate having different thickness ratios (a/h) and boundary conditions

BC[a]		a/h			
		5	20	50	100
SCSC	Present	12.31	24.24	28.08	39.51
	Ref.[b]	12.33	24.89	28.46	40.06
SSSC	Present	10.64	23.62	27.51	28.24
	Ref.[b]	10.98	23.49	27.46	28.23
SSSS	Present	10.28	17.51	18.64	18.82
	Ref.[b]	10.05	17.38	18.62	18.82
SCSF	Present	5.95	7.31	7.41	7.43
	Ref[b]	5.97	7.97	8.21	8.25
SSSF	Present	4.54	5.03	5.06	5.07
	Ref.[b]	4.50	5.03	5.06	5.07

[a] Boundary Condition
[b] Aydogdu and Timarci [5]

Table 3 Non-dimensional fundamental frequency parameter $\lambda = (\omega a^2)/h \sqrt{(\rho/E_2)}$ of a simply supported four-layer anti-symmetric (45°/−45°/45°/−45°) angle ply composite plate having different thickness ratios (a/h) and aspect ratios (a/b)

a/h		a/b				
		1	1.2	1.4	1.6	2.0
10	Present	18.91	21.99	25.19	28.51	35.55
	Ref.[a]	18.60	21.56	24.67	27.95	34.12
20	Present	22.62	26.97	31.65	36.67	47.71
	Ref.[a]	22.58	26.85	31.40	35.56	46.26
30	Present	23.59	28.34	33.51	39.15	51.78
	Ref.[a]	23.67	28.38	33.45	37.82	51.13
40	Present	23.96	28.87	34.25	40.14	53.48
	Ref.[a]	24.11	29.00	34.39	40.07	53.01
50	Present	24.16	29.13	34.61	40.63	54.33
	Ref.[a]	24.34	29.32	34.74	40.65	53.98

[a] Reddy [4]

3.3 Simply Supported Plate with Different Aspect Ratios and Thickness Ratios

The natural frequency of a simply supported four-layer (45°/−45°/45°/−45°) laminated composite plates having different aspect ratios (a/b) and thickness ratios (a/h) is studied.

The present non-dimension frequency is validated with the finite element results obtained by Reddy [4]. From Table 3, it is observed that as the plate thickness decreases and the aspect ratio increases, the frequency increases.

3.4 An Isotropic Rectangular Plate with Elastic Point Support

An isotropic plate with elastic point support and with different boundary conditions is considered. Four springs are attached to the plate at different points (Fig. 1). In the present study, the spring is incorporated in the plate element by adding lumped stiffness to the specified global nodal coordinates of the plate.

The dimensions of the plate are a × b = 76.2 cm × 76.2 cm, h = 1.27 cm. Material properties are E = 68.94 GPa, $\nu = 0.315$, G = 26.21 GPa, and the spring stiffness is K_S = 22,766 N/m. Results are given in Table 4 for various mesh divisions, and it is seen that at 16 × 16 mesh division, the results converge. It can be observed that the present results lie very close to the established results of Watkins and Barton [15], in which eigenvalue sensitivity analysis was used to solve the problem.

Table 4 Non-dimensional frequency parameter $\lambda = (\omega a^2)/2\pi \sqrt{(\rho h/D)}$ of a square isotropic plate having four-point elastic supports

BC	Mesh Div.	λ_1	λ_2	λ_3	λ_4	λ_5
CCSS	4 × 4	4.60	8.68	11.14	15.00	16.42
	8 × 8	4.60	8.68	10.99	14.96	16.19
	12 × 12	4.60	8.69	10.98	14.98	16.17
	16 × 16	4.60	8.69	10.98	15.06	16.17
	Ref.[a]	4.61	8.72	11.21	15.26	16.27
	% Error	0.26	0.37	2.02	1.26	0.58
SSSS	4 × 4	3.15	7.86	7.86	12.49	15.93
	8 × 8	3.15	7.84	7.84	12.52	15.64
	12 × 12	3.15	7.84	7.84	12.53	15.63
	16 × 16	3.15	7.84	7.84	12.53	15.62
	Ref.[a]	3.14	7.85	7.85	12.56	15.71
	% Error	0.22	0.04	0.15	0.24	0.53
CCCC	4 × 4	5.70	11.74	11.74	17.16	22.76
	8 × 8	5.712	11.72	11.72	17.27	20.79
	12 × 12	5.71	11.71	11.71	17.38	20.84
	16 × 16	5.71	11.71	11.71	17.39	20.85
	Ref.[a]	5.73	11.85	11.85	17.58	20.94
	% Error	0.33	1.11	1.11	1.08	0.43

[a] Watkins and Barton [15]

4 Results and Discussions

After sufficient validation of the present finite element formulation in terms of thickness ratios, aspect ratios, different fibre angle orientations and plates with spring attachment, few new examples are presented. The plate vibration is analysed with various aspect ratios, side to thickness ratios, fibre angle and different boundary conditions. Springs are fixed to the plate at different points on the plate, as shown in Fig. 2. The non-dimensional frequency used here is:

$$\lambda = \frac{\omega a^2}{h}\sqrt{\frac{\rho}{E_2}}$$

where a is the shorter in-plane dimension and h is the total thickness of the plate and E_2 is Young's modulus transverse to the fibre direction 16 × 16 mesh division is used for rest of the examples. Material properties used for isotropic plate are $E_1 =$ 200 GPa, $E_2 = 5$ GPa; $G_{12} = G_{13} = 3$ GPa, $G_{23} = 2.5$ GPa; $\mu_{12} = 0.25$, while the material properties for composite plate are $E_1 = 200$ GPa, $E_2 = 5$ GPa, $G_{12} = G_{13}$ $= 3$ GPa, $G_{23} = 2.5$ GPa, $\nu_{12} = 0.25$, $\nu_{21} = 0.00625$.

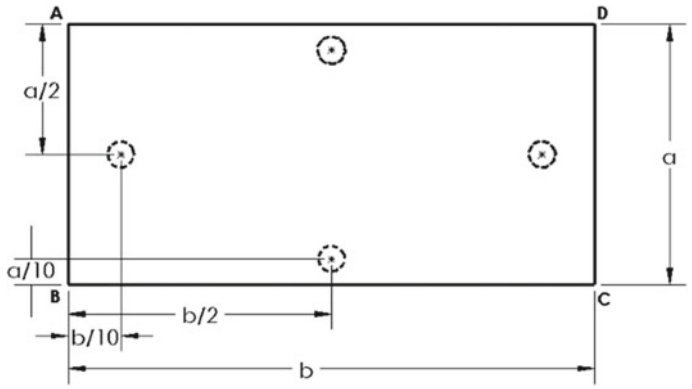

Fig. 2 Plate with four-point springs

Non-dimensional frequencies are obtained for isotropic and laminated composite square plate. The frequencies are obtained for different spring stiffness, and the effect of spring stiffness is studied. In Table 5, results are obtained for isotropic plate and in Table 6, results are obtained for a composite plate, it is observed that as the spring stiffness increases the frequencies increases; spring stiffness of 0 N/m represents a

Table 5 Non-dimensional frequency parameter $\lambda = \frac{\omega a^2}{2\pi}\sqrt{\frac{\rho h}{D}}$ of a clamped square isotropic plate having four elastic point supports, with side to thickness ratio (a/h) = 10 and varying stiffness of spring

K_S (N/m)	λ_1	λ_2	λ_3	λ_4	λ_5
0	5.16	9.84	9.84	13.79	16.24
10^4	5.16	9.84	9.84	13.79	16.24
10^6	5.18	9.85	9.85	13.79	16.26
10^8	5.20	9.89	9.89	13.79	16.36
10^9	5.43	10.17	10.17	13.79	16.58

Table 6 The non-dimensional frequency parameter $\lambda = \frac{\omega a^2}{h}\sqrt{\frac{\rho}{E_2}}$ of a square simply supported four-ply laminate (0°/90°/90°/0°) with spring different spring stiffness and a/h = 5

K_S (N/m)	λ_1	λ_2	λ_3	λ_4	λ_5
0	10.85	19.16	21.22	24.29	24.29
10	10.85	19.16	21.22	24.29	24.29
10^2	10.85	19.16	21.22	24.29	24.29
10^4	10.85	19.16	21.22	24.29	24.29
10^6	10.85	19.16	21.22	24.29	24.29
10^8	11.06	19.37	21.41	24.29	24.30

plate without springs. Frequencies are compared for a composite plate without spring support and with spring of stiffness $K_S = 10^8$ N/m and varying side to thickness ratio with different boundary conditions in Table 7. It is evident from the results that as the side to thickness ratio increases, i.e. as the plate becomes thinner, the frequency of vibration increases.

Frequencies are obtained for a plate resting on springs and varying aspect (a/b) ratio with simply supported boundary conditions. The frequencies are given in Table 8 for isotropic plate and in Table 9 for composite plate and from the table, it can be observed that as the aspect ratio increases, the frequency of vibration increases. Also, we can see the frequency of vibration for clamped plates is maximum.

Variation of non-dimensional frequency of a four-ply (θ/−θ/θ/−θ) simply supported plate with layers having different fibre angle orientations is given in Table 10. Results are shown with spring arrangements as well as without spring. It is seen

Table 7 Comparison of non-dimensional frequency parameter $\lambda = \frac{\omega a^2}{h}\sqrt{\frac{\rho}{E_2}}$ of a four-ply laminate (0°/90°/90°/0°) with aspect ratio a/b = 0.5, with and without four-point elastic supports, with varying side to thickness ratio (a/h) and stiffness of spring $K_S = 10^8$ N/m

B.C	a/h	a/h	λ_1	λ_2	λ_3	λ_4	λ_5
SSSS	5	W/O Spring	9.21	10.85	12.14	14.43	19.16
		With Spring	9.34	11.03	12.14	14.71	19.37
		Change (%)	1.41	1.65	0	1.94	1.09
	20	W/O Spring	15.94	17.66	22.69	31.66	44.00
		With Spring	18.17	20.43	28.51	37.09	48.09
		Change (%)	13.98	15.68	25.65	17.15	9.29
CCCC	5	W/O Spring	10.74	12.62	15.98	20.31	20.68
		With Spring	10.83	12.73	16.22	20.54	20.79
		Change (%)	0.83	0.87	1.50	1.13	0.53
	20	W/O Spring	28.87	30.62	35.22	43.41	54.94
		With Spring	29.60	31.62	38.10	47.32	59.16
		Change (%)	2.52	3.26	8.17	9.00	7.68

Table 8 Non-dimensional frequency parameter $\lambda = \frac{\omega a^2}{2\pi}\sqrt{\frac{\rho h}{D}}$ of a square isotropic plate having four-point elastic supports, with varying aspect (a/b) ratio, a/h = 10 and stiffness of spring $K_S = 10^8$ N/m

a/b	λ_1	λ_2	λ_3	λ_4	λ_5
0.4	1.87	2.61	3.82	5.37	6.13
0.65	2.30	4.14	6.52	7.10	8.14
1.0	3.17	7.32	7.33	11.08	13.53
1.5	4.95	8.99	13.58	15.10	15.93
3.0	13.59	17.06	17.32	20.23	22.40

Table 9 The non-dimensional frequency parameter $\lambda = \frac{\omega a^2}{h}\sqrt{\frac{\rho}{E_2}}$ of a simply supported four-ply laminate (0°/90°/90°/0°) with varying a/b ratio, a/h = 5 and $K_S = 10^8$ N/m

a/b	λ_1	λ_2	λ_3	λ_4	λ_5
1	11.06	19.37	21.41	24.29	24.30
0.5	9.34	11.03	12.18	14.71	19.37
0.2	4.85	9.05	9.17	9.54	9.67
0.1	2.43	4.83	7.11	7.19	7.60

Table 10 The non-dimensional frequency parameter $\lambda = \frac{\omega a^2}{h}\sqrt{\frac{\rho}{E_2}}$ of a simply supported four-ply laminate plate, a/h = 10, a/b = 1.0 and $K_S = 10^8$ N/m

Spring	Fibre Angle β	λ_1	λ_2	λ_3	λ_4	λ_5
W/O Spring	15°/−15°/15°/−15°	15.60	23.00	34.00	34.85	38.03
	30°/−30°/30°/−30°	17.63	29.57	37.75	44.12	48.86
	45°/−45°/45°/−45°	18.46	34.41	34.87	34.87	50.52
	60°/−60°/60°/−60°	17.63	29.57	37.75	44.12	48.86
With Spring	15°/−15°/15°/−15°	16.56	24.10	34.85	35.51	38.71
	30°/−30°/30°/−30°	18.50	30.47	38.46	45.30	48.86
	45°/−45°/45°/−45°	19.30	34.41	35.65	35.65	50.51
	60°/−60°/60°/−60°	18.50	30.47	38.46	45.30	48.86

that frequencies increase up to fibre angle 45° for the first and second modes then decrease because stiffness is maximum for ply angle 45°; also it can be seen that frequencies are same for θ = 30° and θ = 60°. A square simply supported composite plate with side to thickness ratio (a/h) = 10 is considered, and the non-dimensional frequencies are obtained for a different number of layers of laminates and results obtained are given in Table 11, for a plate without any spring, and in Table 12, for a plate with four-point springs.

It is seen that the non-dimensional frequency increases with the number of ply layers for both plates with spring and without spring. However, it is observed that

Table 11 Non-dimensional frequency parameter $\lambda = \frac{\omega a^2}{h}\sqrt{\frac{\rho}{E_2}}$ of a square orthotropic plate with simply supported boundary condition and different number of ply layers, having side to thickness ratio (a/h = 10)

N	Ply Angle ϕ	λ_1	λ_2	λ_3	λ_4	λ_5
2	45°/−45°	15.48	26.89	26.89	34.41	42.92
4	45°/−45°/45°/−45°	18.91	34.41	34.82	34.82	50.68
6	45°/−45°/45°/−45°/45°/−45°	19.28	34.41	35.65	35.65	51.38
8	45°/−45°/45°/−45°/45°/−45°/45°/−45°	19.39	34.41	35.91	35.91	51.60

Table 12 The non-dimensional frequency parameter $\lambda = \frac{\omega a^2}{h}\sqrt{\frac{\rho}{E_2}}$ of a square simply supported laminate having different number of layers, a/h = 10 and $K_S = 10^8$ N/m

N	Ply Angle ϕ	λ_1	λ_2	λ_3	λ_4	λ_5
3	0°/90°/0°	15.78	23.32	38.07	38.30	41.15
5	0°/90°/0°/90°/0°	16.38	30.87	37.57	45.06	48.59
7	0°/90°/0°/90°/0°/90°/0°	16.69	32.74	37.20	45.97	48.61
9	0°/90°/0°/90°/0°/90°/0°/90°/0°	16.77	33.56	36.94	46.31	48.61

frequencies in the fourth mode are equal for plate without spring and frequencies in the third mode are same for plate with spring.

5 Conclusion

A finite element formulation is written in FORTRAN language, which gives an elegant method to study the free vibration of composite plate on elastic point supports including first-order shear deformation theory. Existing studies on the analysis of composite plates on elastic supports using FSDT and isoparametric finite element formulation are very limited. From the study, it is found that the non-dimensional frequency of a composite plate increases with the decrease of thickness ratio of the laminate with and without provision of spring with the plate. As thickness ratio increases, the mass of the plate also increases, which decreases the natural frequencies. Non-dimensional frequency is higher for a plate with elastic supports compared with a plate without elastic supports. It is expected because the attachment of spring increases the overall stiffness of the laminate. Further, non-dimensional frequency increases up to fibre angle direction of 45° after that it decreases. Frequencies increase with an increase in number of layers up to a certain value after that there are no such considerable changes with an increase in the number of layers for plates with and without attachment of spring. As the number of layers increase, the volume of reinforced fibre increases, which increases the stiffness of the plate. Non-dimensional frequencies of the elastically supported laminates depend on the configuration of the springs. The percentage increase of frequencies of a simply supported plate with spring attachment is higher than a clamped plate with elastic support. It means that elastic support is less effective for clamped plates.

References

1. Leissa AW, Narita Y (1989) Vibration studies for simply supported symmetrically laminated rectangular plates. Compos Struct 12:113–132. https://doi.org/10.1016/0263-8223(89)90085-8
2. Kalita K, Ramachandran M, Raichurkar P, Mokal SD, Haldar S (2016) Free vibration analysis

of laminated composites by a nine node isoparametric plate bending element. Adv Compos Lett 25:108–116. https://doi.org/10.1177/096369351602500501
3. Chow ST, Liew KM, Lam KY (1992) Transverse vibration of symmetrically laminated rectangular composite plates. Compos Struct 20:213–226. https://doi.org/10.1016/0263-8223(92)90027-A
4. Reddy JN (1979) Free vibration of antisymmetric, angle-ply laminated plates including transverse shear deformation by the finite element method. J Sound Vib 66:565–576. https://doi.org/10.1016/0022-460X(79)90700-4
5. Aydogdu M, Timarci T (2003) Vibration analysis of cross-ply laminated square plates with general boundary conditions. Compos Sci Technol 63:1061–1070. https://doi.org/10.1016/S0266-3538(03)00016-2
6. Akavci SS (2007) Buckling and free vibration analysis of symmetric and antisymmetric laminated composite plates on an elastic foundation. J Reinf Plast Compos 26:1907–1919. https://doi.org/10.1177/0731684407081766
7. Barros JAO, Barreiros Martins J (1990) Analysis of plates on elastic foundation by the finite elements method. http://hdl.handle.net/1822/12755
8. Park M, Choi DH (2018) A simplified first-order shear deformation theory for bending, buckling and free vibration analyses of isotropic plates on elastic foundations. KSCE J Civ Eng 22:1235–1249. https://doi.org/10.1007/s12205-017-1517-6
9. Omurtag MH, Kadioglu F (1998) Free vibration analysis of orthotropic plates resting on Pasternak foundation by mixed finite element formulation. Comput Struct 67:253–265. https://doi.org/10.1016/S0045-7949(97)00128-4
10. Pang F, Li H, Du Y, Li S, Chen H, Liu N (2018) A series solution for the vibration of Mindlin rectangular plates with elastic point supports around the edges. Shock Vib 2018. https://doi.org/10.1155/2018/8562079
11. Li WL (2004) Vibration analysis of rectangular plates with general elastic boundary supports. J Sound Vib 273:619–635. https://doi.org/10.1016/S0022-460X(03)00562-5
12. Zietsman L, Van Der Merwe AJ, Geldenhuys JJ, Van Rensburg NFJ (2003) Application of the finite-element method to the vibration of a rectangular plate with elastic support at the boundary. Math Comput Model 38:309–322. https://doi.org/10.1016/S0895-7177(03)90089-6
13. Cheung YK, Zhou D (2000) Vibrations of rectangular plates with elastic intermediate line-supports and edge constraints. Thin-Walled Struct 37:305–331. https://doi.org/10.1016/S0263-8231(00)00015-X
14. Huang MH, Thambiratnam DP (2001) Analysis of plate resting on elastic supports and elastic foundation by finite strip method. Comput Struct 79:2547–2557. https://doi.org/10.1016/S0045-7949(01)00134-1
15. Joseph Watkins R, Barton O (2010) Characterizing the vibration of an elastically point supported rectangular plate using eigensensitivity analysis. Thin-Walled Struct 48:327–333. https://doi.org/10.1016/j.tws.2009.11.005
16. Setoodeh AR, Karami G (2004) Static, free vibration and buckling analysis of anisotropic thick laminated composite plates on distributed and point elastic supports using a 3-D layer-wise FEM. Eng Struct. https://doi.org/10.1016/j.engstruct.2003.09.009

Numerical Investigation of Collapse Moment of Deformed Pipe Bends Subjected to Internal Pressure and Bending Moment

Manish Kumar, Pronab Roy, and Kallol Khan

1 Introduction

The pipe bends are the most flexible components used in the piping system. This flexible behavior allows them to undergo large disproportionate deformation. The deformations help them to absorb the higher forces and stresses, which is necessary to maintain the integrity of the piping system. The deformation causes a reduction in stiffness of the pipe bends. Therefore, safety measures must be taken to avoid the undesirable deformation of it.

For the design of pipe bends, an accurate estimation of collapse moment is necessary. The collapse moment is the moment at which large plastic deformation occurred in the cross-section of the pipe bends with a slight increase in applied bending moment. The collapse moment depends on many factors like the size of the pipe bends, loading configurations under which pipe bends are loaded, pipe bend angle and the cross-section of the pipe bend geometry.

The pipe bend cross-section is deformed into an approximate oval shape during the pipe bending process [1–4]. The variation in geometry of pipe bends is measured in ovality and thinning/thickening. The inclusion of ovality and thinning/thickening will result in predicting accurate estimation of collapse moment. Many researchers, assuming the pipe bend geometry to be circular, have carried out the study to determine collapse moment. However, very few works have been carried out for the initially deformed pipe bends. Michael et al. [1] performed the detailed nonlinear finite analysis of 90° pipe bend to investigate the influence of ovality on collapse

M. Kumar · K. Khan
Department of Mechanical Engineering, National Institute of Technology Durgapur, Durgapur, India

P. Roy (✉)
Department of Civil Engineering, National Institute of Technology Durgapur, Durgapur, India
e-mail: pronab.roy@ce.nitdgp.ac.in

D. K. Maiti et al. (eds.), *Recent Advances in Computational and Experimental Mechanics, Vol II*, Lecture Notes in Mechanical Engineering,
https://doi.org/10.1007/978-981-16-6490-8_32

moment under loading condition of in-plane closing moment for different values of pressure. Sorour et al. [5] carried out a limit load study for the pipe bend obtained from pipe bending process using simulation software. The study of initially deformed pipe bend is limited to 90° in literature. This paper investigates the 45°, 90° and 135° pressurized pipe bends with initial deformation subjected to in-plane closing moment. The pipe bends are modeled for 0%, 10% and 20% geometric imperfections. Pipe material is modeled for strain-hardening (SH) and elastic-perfectly plastic (EPP) behaviors.

2 Geometric Imperfection

The pipe bends are manufactured through the pipe bending process. While performing the bending process, the circular cross-section of pipe gets deformed into an approximated oval shape with the variation in thickness, as shown in Fig. 1. The cross-section deformation is measured as ovality, and thickness variation is measured as thickening/thinning. Here, ovality and thickening/thinning collectively are termed as geometry imperfection. Ovality is the ratio of change in diameters to the nominal diameter of the pipe bend, as stated in Eq. (1). The thinning occurs at the extrados of the pipe bend, and it is calculated using Eq. (2). The thickening occurs at intrados of the pipe bend, and it is expressed using Eq. (3).

$$\text{Ovality (in \%)} = \frac{D_{\max} - D_{\min}}{D} \times 100 \tag{1}$$

$$\text{Thinning (in \%)} = \frac{t - t_{\min}}{t} \times 100 \tag{2}$$

$$\text{Thickening (in \%)} = \frac{t_{\max} - t}{t} \times 100 \tag{3}$$

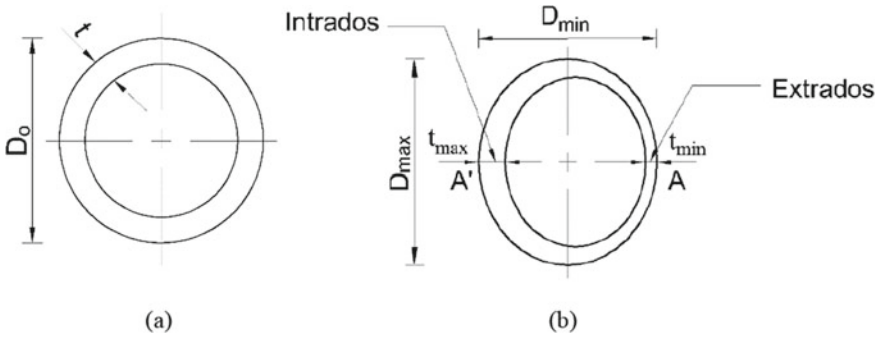

Fig. 1 Pipe bend cross-section **a** before bending, **b** after bending

3 Geometry Modeling and Finite Element Analysis

3.1 Geometry Modeling

In the present finite element analyses, 45°, 90° and 135° pipe bends are considered, and each end of bend is attached with the long straight pipes $L = 5 * D$, as shown in Fig. 2, to avoid the end effects arise because of applied boundary conditions. The modeling parameters selected for the analyses are presented in Table 1. The nominal diameter of the pipe bend is chosen for three different thicknesses to cover the analysis over the wide range of r/t ratio. The pipe bends are modeled for the large bend radius ($R/r > 3$) [6]. The pipe bend is modeled for circular cross-section (0% geometric imperfection) and noncircular cross-section (10% and 20% geometric imperfection) to determine the effect of initial geometric imperfection on the collapse moment. The thinning/thickening has been kept constant equal to 20% (as thinning/thickening effect is insignificant [1]), and ovality has been varied accordingly for 0%, 10% and 20%. The addition of initial imperfection is fulfilled based on the assumptions made in Ref. [2–4]. The pipe bend cross-section of 0%, 10% and 20% initial imperfection is modeled using Python script as it is impossible to generate using the standard toolbox of ABAQUS software [7].

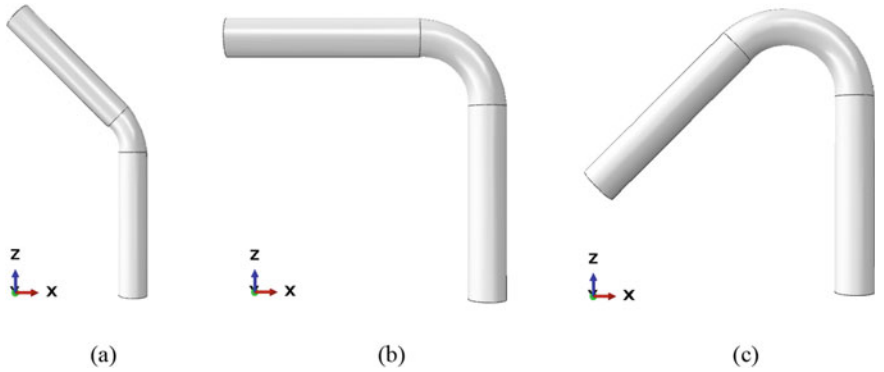

Fig. 2 Pipe bend model of **a** 45° bend angle, **b** 90° bend angle, **c** 135° bend angle

Table 1 Modeling parameters of pipe bends used in the analysis

Modeling parameters	Values
Outside diameter D_o (mm)	168.28
Pipe thickness t (mm)	7.11, 3.40, 2.77
Bend radius R (mm)	298
Bend angle ψ (°)	45°, 90°, 135°
Geometric imperpection K (%)	0, 10, 20

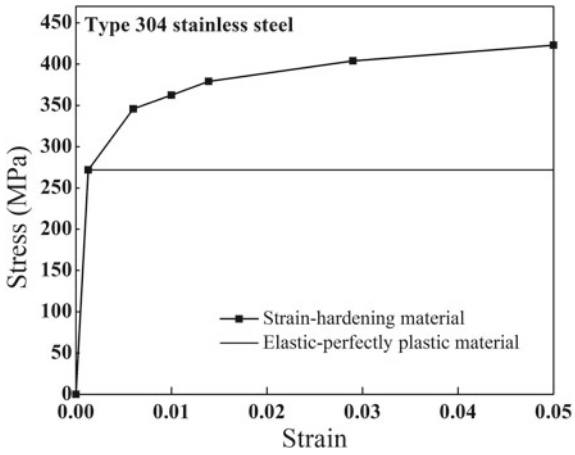

Fig. 3 Type 304 stainless steel stress–strain response for strain-hardening (SH) and elastic-perfectly plastic (EPP) material models

3.2 Finite Element Analysis and Its Validation

Type 304 stainless steel is used for the pipe bend material, which is having corrosion resistance. The material properties adopted for the analysis are Young's modulus (E) = 193.0 GPa, yield stress (σ_1) = 271.9 MPa and Poisson's ratio (υ) = 0.26 [8, 9]. The material is considered as isotropic type and its stress–strain response of SH and EPP material models is shown in Fig. 3.

The three-dimensional finite element analysis is carried out using ABAQUS software. The C3D20R element type, a reduced integration element is used for the analysis to save computation time. The number of elements for all the analysis is kept constant by introducing mapped meshing. Mesh convergence study is carried out for 45° pipe bend of r/t = 24.245, K = 0%, 10% and at p = 0.00, 0.50. The element size in the bend part and along the circumference is varied to determine the number of optimum elements required for the analysis. The number of elements in the connected pipe and across thickness is retained constant as 15 and 3 respectively, as shown in Fig. 4. The total number of elements obtained for the mesh model is varied between 5220 and 9348 and their collapse moment values are determined, as plotted in Fig. 5, and 6912 number of elements are considered as the optimum number for each model of the analysis.

The analysis of pressurized pipe bend is a two-step analysis. In the first step, the internal pressure is applied as the distributed load. For each analysis, the internal pressure is increased by 25% of the design pressure of the straight pipe. The design pressure of the straight pipe (P_s) is determined as per ASME Code NB-3640 [10]. For simulating pipe bend for closed-end conditions, an axial tensile force is applied, as shown in Fig. 6. The axial force is included because internal pressure causes axial thrust in the close piping system. At one end of the attached pipe, all sets of motion are constrained and at the other end, multi-point constraint (MPC) is used for the bending action. In MPC, slave nodes (nodes of the pipe end) are connected

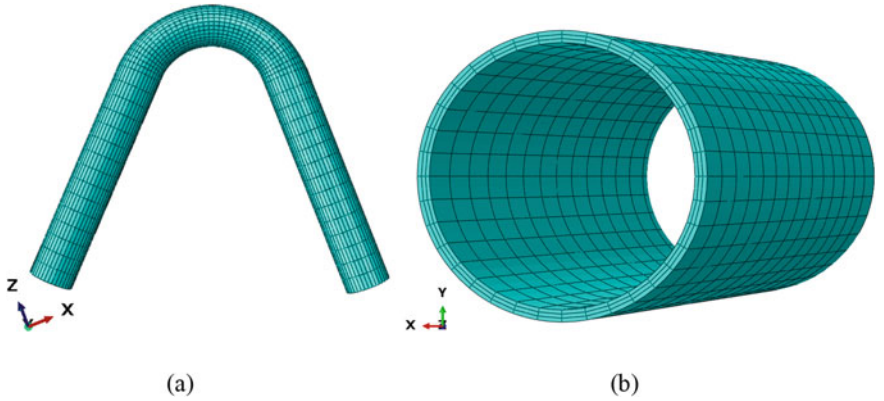

Fig. 4 Mesh model of pipe bend. **a** Whole mesh model of 135° pipe bend, **b** three elements across thickness

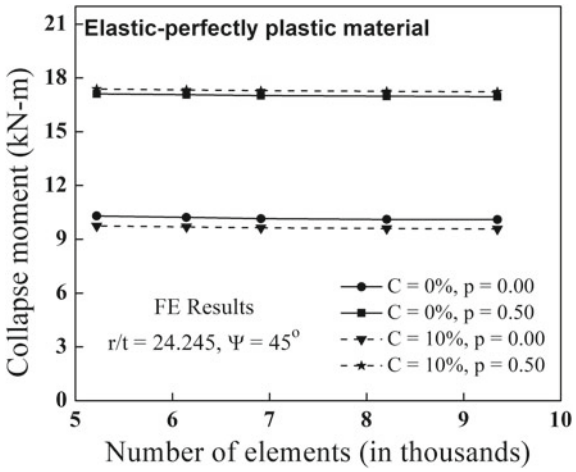

Fig. 5 Mesh convergence study of 45° pipe bend for EPP material

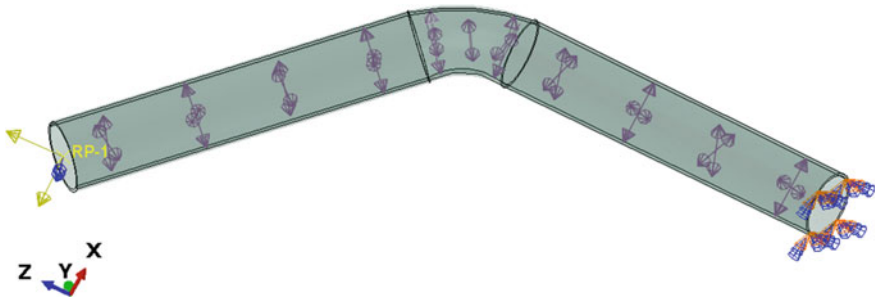

Fig. 6 Pipe bend loading and boundary conditions under internal pressure and in-plane closing moment

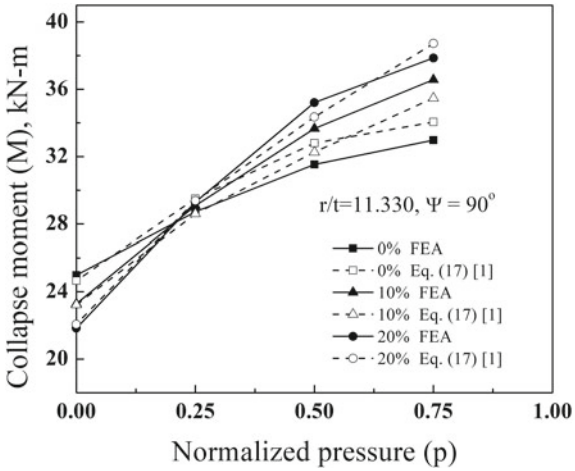

Fig. 7 Comparison of FE results with Eq. (17) proposed by Michael et al. [1]

to the control point (reference point) through beam constrained type. On the control point, closing bending action is applied through rotation boundary conditions in the required direction. The closing bending moment tends to decrease the radius of curvature of the pipe bends. The Static Riks option is invoked in the second step to reach the converged solution for the nonlinear material and geometry properties. The large deformations and displacements in the analysis are included by the Nlgeom option while creating the analysis steps.

The collapse moment for each analysis is determined using the twice-elastic-slope (TES) method [11]. For the validation of the current analysis, the collapse moment of 90° pipe bend is compared with Eq. (17) of Michael et al. [1]. The maximum difference of collapse moment is observed about less than 4%, as shown in Fig. 7. Thus, the analysis of the present study is verified.

4 Results and Discussion

In the present study, the pipe bends of circular and deformed cross-section of three different r/t ratios are analyzed, and their collapse moments are determined for the EPP and SH material models. To understand the influence of internal pressure and initial geometric imperfection on the collapse moment, pipe bends of 45°, 90° and 135° angles are analyzed under the loading condition of in-plane closing moment along with different values of normalized internal pressure (p). The applied pressure (P) is normalized with the design pressure of the straight pipe (P_s).

The presence of initial geometric imperfection in the pipe bend decreases the collapse moment for all considered models applied to in-plane closing moment. It is because imperfection provides initial ovalization in the direction of bending, which helps to develop the collapsing phenomena easily for both material models. Figure 8

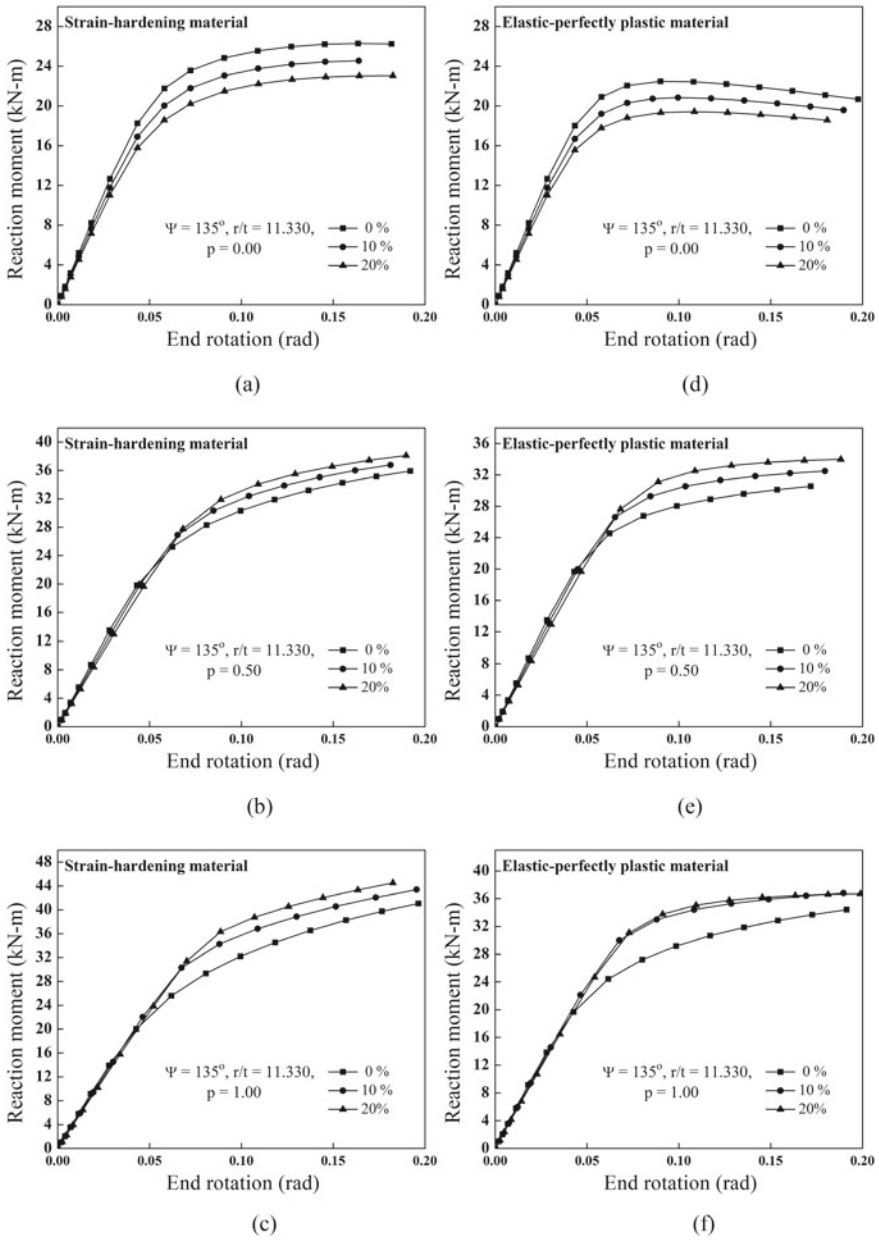

Fig. 8 Moment–end rotation plot of 135° pipe bends with 0%, 10% and 20% imperfection for SH and EPP material

shows the moment versus end rotation plot of the 135° pipe bend for 0%, 10% and 20% imperfections. It is clearly observed from Fig. 8 that the reaction moment decreases with an increase in initial imperfection for $p = 0.00$.

From Figs. 9, 10 and 11, it is observed that the effect of 10% and 20% geometric imperfection is minimum for 45° pipe bend of strain-hardening material as compared with those of 90° and 135° pipe bends. For 45° pipe bend of elastic-perfectly material model, the presence of 10% imperfection increases the collapse moment for the $p \geq 0.50$ as compared with that of circular pipe bend. For 20% imperfection of the same bend, collapse moment reduces due to the generation of hoop stress. Suppose for 45° pipe bend of $r/t = 24.245$, the change in collapse moment due to 10% imperfection is −5.29%, −0.98%, 1.56%, 4.21% and 5.19%, and the change in collapse moment due to 20% imperfection is −9.02%, −2.42%, 2.12%, −11.37% and −28.45% for $p = 0$, 0.25, 0.5, 0.75 and 1, respectively, with compared with the collapse moment of circular pipe bend. Similarly, for strain-hardening material, the difference due to 10% imperfection is −4.89%, −1.09%, 1.03%, 3.12% and 4.01% and for 20% imperfection is −8.92%, −2.13%, 1.80%, 4.31% and 5.33%, respectively. The negative difference shows a decrease in collapse moment and positive difference specifies that the increase in collapse moment due to the presence of initial geometric imperfection.

In Fig. 7, 90° pipe bend shows that imperfection has a negative effect for $p < 0.25$ and with the increase in pressure, the negative effect of imperfection is overcome by the stiffening effect of pressure for both materials except for $p > 0.75$ of elastic-perfectly plastic with 20% imperfection. It is because 20% imperfect pipe bends of elastic-perfectly plastic material collapse early due to the dominating effect of hoop stress at $p > 0.75$. A similar trend is observed for 135° pipe bend for both material models. From the results, it is clear that the collapse moment for the elastic-perfectly plastic material model tends to decrease for 20% imperfection at higher pressure. But for the strain-hardening material model, collapse moment tends to increase and does not decline with an increase in pressure. It is due to the counteracting effect of geometry stiffening of internal pressure along with material-hardening effect.

The collapse moment decreases as the bend angle increases from 45° to 135° for all values of considered r/t, K and p. It is because, 135° pipe bend offers higher end-rotation, which causes larger deformation and greater stress at the mid-section of pipe bends that lead to the early collapsing of it.

Figure 12 compares the strain-hardening and elastic-perfectly plastic materials effect on the 45° pipe bend under pressurized condition. The elastic deformation part of moment versus end rotation curve of both material models shows the same behavior. The plastic deformation shows that due to material stiffening, the collapse moment is higher in strain-hardening material than that of elastic-perfectly plastic part. For the considered case of 45° pipe bend ($r/t = 24.245$, $K = 10\%$ and $p = 0.75$), the collapse moment of strain-hardening is higher by 12.63%, in comparison to that of elastic-perfectly plastic material.

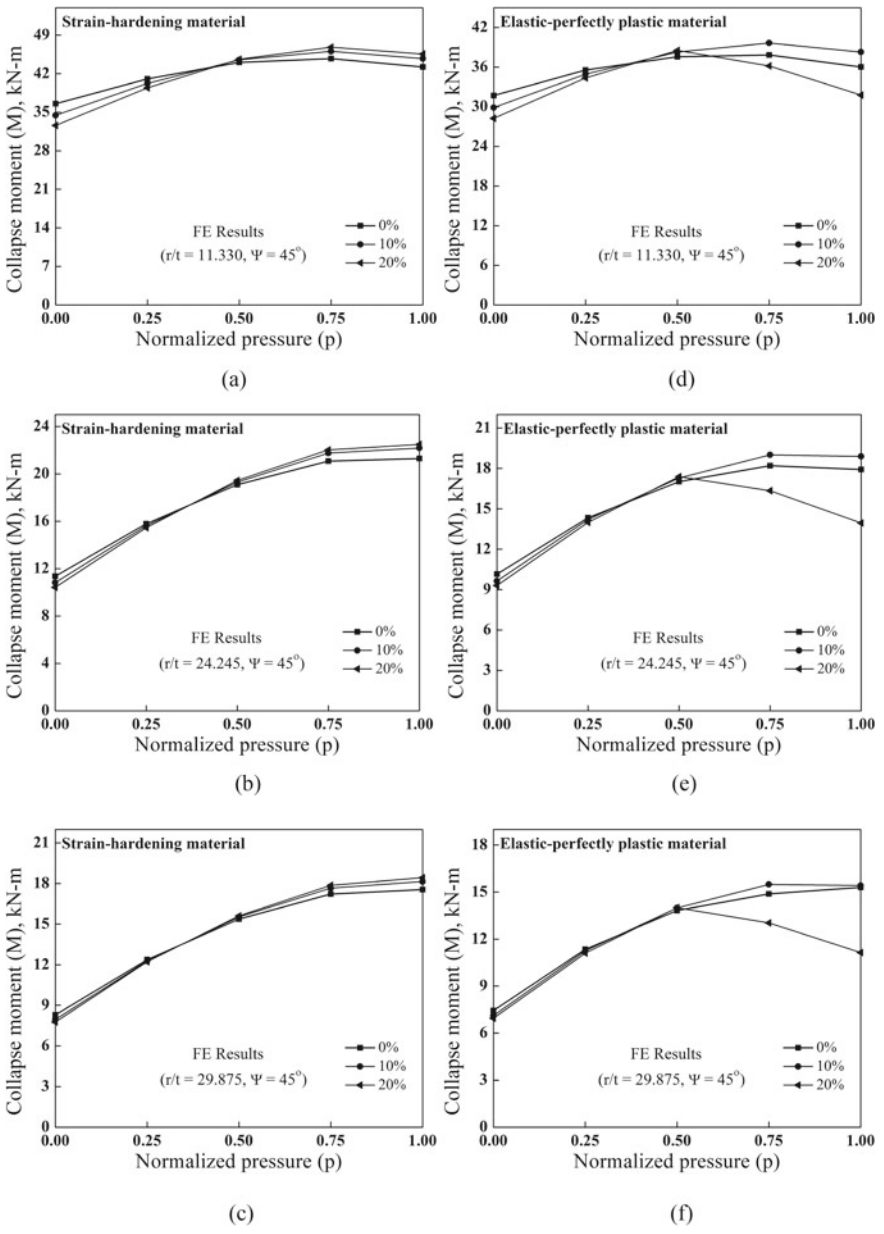

Fig. 9 Collapse moment of 45° pipe bends with 0%, 10% and 20% imperfection for SH and EPP material

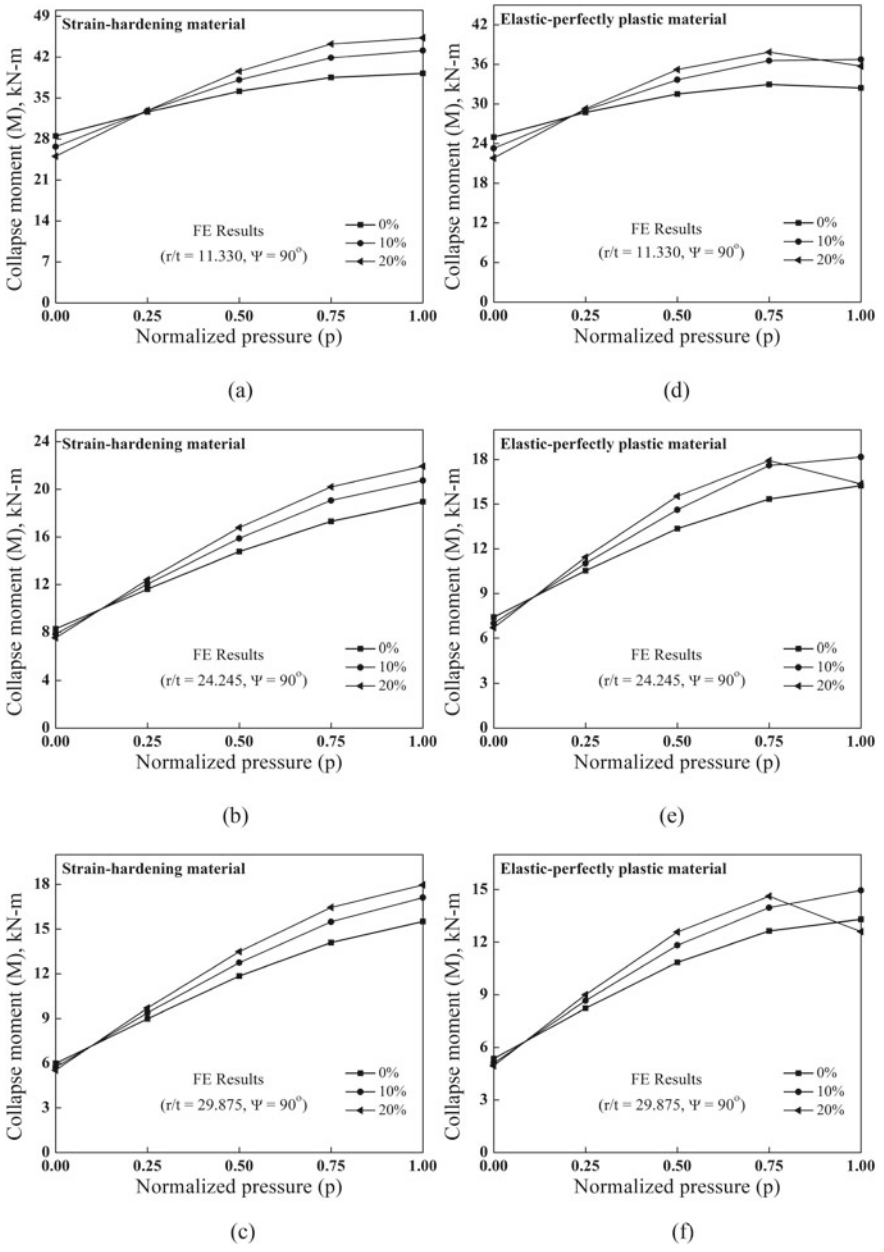

Fig. 10 Collapse moment of 90° pipe bends with 0%, 10% and 20% imperfection for SH and EPP material

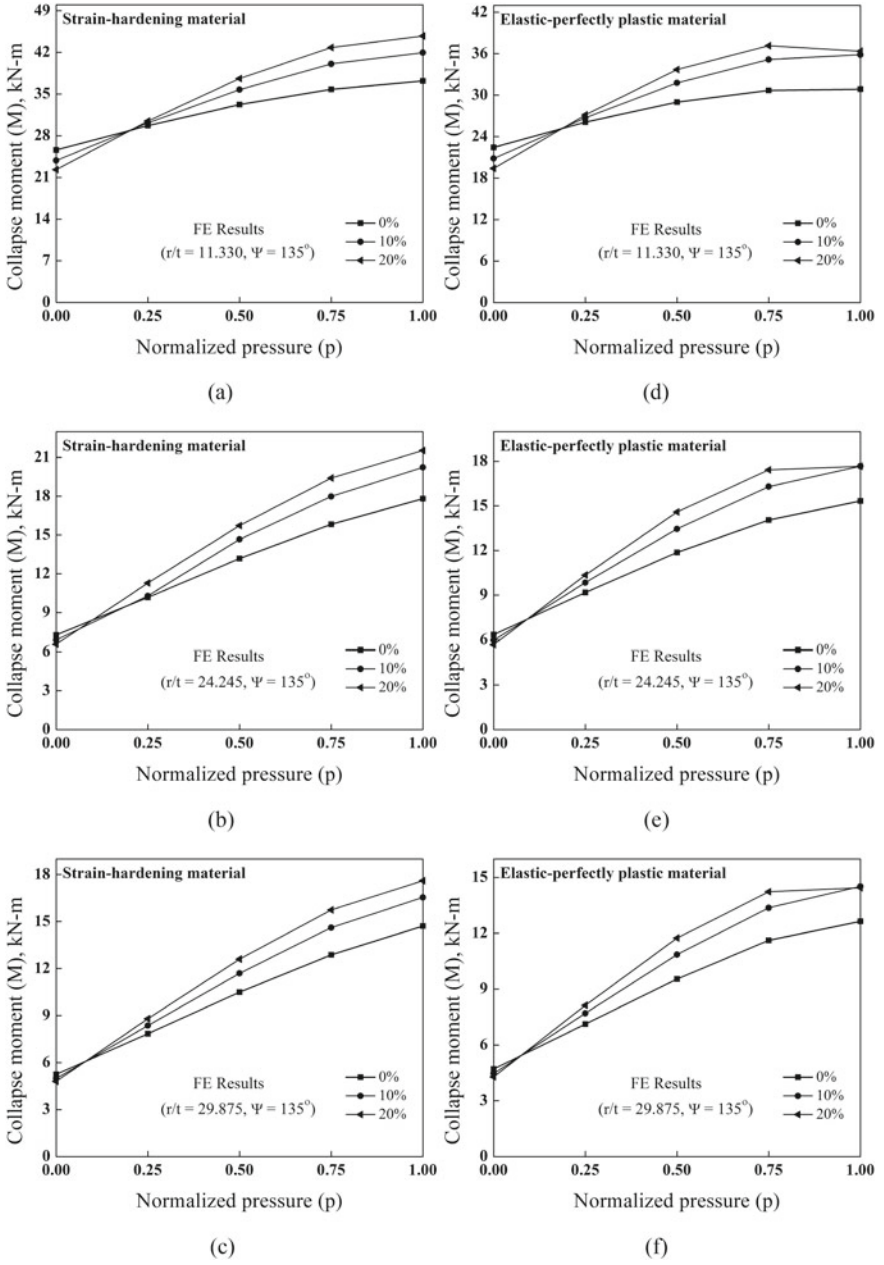

Fig. 11 Collapse moment of 135° pipe bends with 0%, 10% and 20% imperfection for SH and EPP material

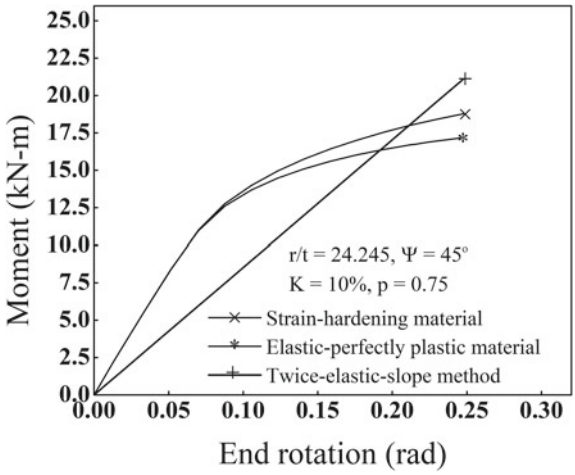

Fig. 12 Moment–end rotation curve for SH and EPP material under pressurized condition

5 Conclusion

The nonlinear FE analysis has been performed to compare the collapse moment of circular and initially deformed pipe bend. The pipe bend has been subjected to closing moment in the presence of internal pressure. The pipe bends of 45°, 90° and 135° angles incorporated with 0%, 10% and 20% initial geometric imperfection are modeled for three different *r/t* ratios.

The application of internal pressure stiffens the pipe bend, which increases the collapse moment of it. There is a significant effect of initial geometric imperfection on the collapse moment. The presence of initial imperfection leads to maximum decrement of 27.19% in case of EPP material and 13.13% in case of SH material. The initial imperfection decreases the collapse moment at lower pressure, and at the higher pressure, the collapse moment increases for 90° and 135° pipe bends. The collapse moment of strain-hardening pressurized pipe bends does not decline with the increase in pressure, on the other hand, in case of elastic-perfectly plastic material, it decreases.

However, the present study is limited to only three bend angles under in-plane closing bending. The present approach can be extended to other pipe bend angles under other modes of bending moments.

References

1. Michael T, Veerappan A, Shanmugan S (2013) Effect of internal pressure and shape imperfections on plastic loads of pipe bends under in-plane closing moment. Eng Fract Mech 105:1–15
2. Pan K, Stelson K (1995) On the plastic deformation of a tube during bending. J Eng Ind 117:494–500

3. Kale A, Thorat H (2009) Effect of precompression on ovality of pipe after bending. J Press Vessel Technol 131:011207-1–7
4. Kale A, Thorat H (2009) Effect of precompression on thickness of pipe during bending. J Press Vessel Technol 131:031201-1–8
5. Sorour S, Shazly M, Megahed M (2019) Limit load analysis of thin-walled as-fabricated pipe bends with low ovality under in-plane moment loading and internal pressure. Thin-Walled Struct 144:106336-1–12
6. Roy P, Ghosh S (2012) Statistical characterisation of B_2 for nuclear pipe bends: In-plane closing moment. Nucl Eng Des 249:268–274
7. Simulia (2014) Abaqus FEA User's Manual. Version 6.14. Dassault Systèmes, USA
8. Mourad H, Younan M (2000) The effect of modeling parameters on the predicted limit loads for pipe bends subjected to out-of-plane bending loading and internal pressure. J Press Vessel Technol 122:450–456
9. Roy P, Ghosh S (2013) Fabrication uncertainty in B_2 for nuclear pipe bends subjected to in-plane opening moment. J Press Vessel Technol 135:011402-1–6
10. The American Society of Mechanical Engineers (2010) ASME boiler and pressure vessel code, Section III, Division I. Rules for construction of nuclear facility components, New York
11. Shalaby M, Younan M (1998) Limit loads for pipe elbows with internal pressure under in-plane closing bending moments. J Press Vessel Technol 120:35–42

Buckling Response of Functionally Graded Material Plates with Cutouts Subjected to Linearly Varying Loads

K. Swaminathan, H. Sachin, and T. Rajanna

1 Introduction

The idea of the Functionally Graded Materials (FGMs) was suggested in 1984 by a group of scientists from Japan working to prepare a material suitable for thermal barrier. FGMs are the advanced heterogeneous type of composite materials in which transition of the material properties takes in continuous or smooth way from one part of the surface to the other part. FGMs, which are commonly prepared of metal and ceramic materials, have two chief properties: toughness and high degree of temperature resistance. FGM plate/shells have a widespread requirement in nuclear, aerospace, civil, automobile, medical, and chemical industries. The wide usage of such materials subjected to various kinds of edge loads in its service life. Usually, the plate is a part of a complicated structure and the stress distribution within that plate is not uniform in nature, but is non-uniform in most of the cases. It is further difficult to find out the exact in-plane load distribution on the plate. Hence, it becomes necessary to consider various types of linearly varying edge loads in order to relate the actual pattern of stress distribution within the plate.

Javaheri and Eslami [1], Hashemi et al. [2], Reddy et al. [3] and Swaminathan and Naveenkumar [4] performed buckling studies on FGM plates exposed to uniform compressive loads. Zhong and Gu [5] obtained buckling response for buckling of rectangular simply supported Ressiner Mindlin plates subjected to linearly varying loads. Panda and Ramachandra [6] using higher order shear deformation theory and obtained buckling loads for isotropic and laminated composites plates subjected to

K. Swaminathan · H. Sachin (✉)
Department of Civil Engineering, National Institute of Technology Karnataka, Mangaluru, India

T. Rajanna
Department of Civil Engineering, B.M.S. College of Engineering, Bengaluru, India

D. K. Maiti et al. (eds.), *Recent Advances in Computational and Experimental Mechanics, Vol II*, Lecture Notes in Mechanical Engineering,
https://doi.org/10.1007/978-981-16-6490-8_33

non-uniform loadings. The authors considered nine different sets of boundary conditions in their work. Bodaghi and Saidi [7] obtained exact analytical solutions for buckling of FGM subjected to nonuniformly distributed edge loads. Levy type solution is adopted to obtain buckling loads for FGM plates supported on two-parameter elastic foundations with different support conditions. Kumar et al. [8] performed analytical studies on dynamic instability analysis of FGM plates subjected to dynamic non-uniform loads using higher order shear deformation theory. Further, Kumar et al. [9] carried out analytical investigation on dynamic stability of FGM skew plates using Rayleigh–Ritz method. Here the analysis is performed considering the neutral plane as reference plane, and the plate is subjected to uniform and linearly varying in-plane loads. Singh and Harsha [10] achieved analytical solution for buckling of FGM plates subjected too uniform, linear and nonlinear type of in-plane loads. In this investigation, Navier technique is adopted, and novel nonlinear in-plane loading pattern based on trigonometric and exponential function are suggested. Adhikari et al. [11] studied buckling characteristics of FGM porous sandwich plates subjected to different types of non-uniform in-planes loads using finite element technique. The authors have considered the effect of porosity and adopted higher order shear deformation theory.

Plates with cutouts are used in rocket engines and exhaust chambers for fuel lines/pipes to pass through. Also, the cutout is introduced in the plate member for several purposes such as offering path for inspections and maintenance, to permit light passage/ventilation, and to have arrangement for establishing connections with different structural members or for the purpose of weight optimization. Many researchers have considered the effect of cutout on buckling of composite plates in their study, and few significant studies are reported. Ghannadpour et al. [12] adopted the finite element technique for prediction of the influence of cutout on buckling behaviour of rectangle-shaped symmetric cross-play laminates. Komur and Sonmez [13] studied elastic buckling of plates with circular cutout by means of the finite element method. Here the effect of variation in position of circular cutout along x-axis on buckling behaviour of plates subjected to in-plane varying load was investigated. Further, Soni et al. [14] incorporated ABAQUS finite element software package to assess the buckling response of laminated composites, with circular and square cutouts, under the number of non-uniform in-plane loads. They studied the influence of plate aspect ratio, location of the cutout and effect of combined non-uniform in-plane and shear load. Rajanna et al. [15] explored the influence of the circular and square cutout on vibration and buckling responses of laminated composite plates exposed to compressive as well as tensile non-uniform in-plane edge load. Recently, Chandra et al. [16] conducted finite element analysis to study the effect of elliptical cutout on buckling behaviour of laminated panels exposed to varying in-planes loadings.

The buckling response studies of FGM plates with a circular cutout under linearly varying in-plane loads have received less attention in the literature, even though it has got significant practical importance. Therefore, through this work, an attempt has been made to investigate the effect of various parameters like cutout sizes and their position, volume fraction index, plate aspect ratio and different linearly varying

edge loads on the buckling behaviour of FGM plates by using FE package ABAQUS [17].

2 Modelling and Physical Description of the Problem

The continuous variation of the constituent material across the specific direction in FGM plates is obtained by varying the volume fraction of materials. The effective Young's modulus material property variation as a function of dimensionless thickness and volume fraction exponent is as plotted in Fig. 1. This variation is mentioned in Eq. (1).

$$E(z) = E_m + (E_c - E_m)V_f^n$$
$$V_f^n = \left(\frac{z}{h} + \frac{1}{2}\right)^n \tag{1}$$

Poisson's ratio $\upsilon = 0.3$ is presumed to be the same throughout the thickness. Geometrical representation of the FGM plates is as shown in Fig. 2. The buckling of the FGM plate subjected to linearly varying load is studied. FGM plates with different volume fraction indexes are considered in this investigation. In-plane linearly varying loads can be represented as:

$$P_x = P_0\left(1 - \frac{\alpha y}{b}\right) \tag{2}$$

where P_x represents the intensity of the compressive forces along the plate edge and α is load parameter, signifying the linear variations of the in-plane load, as represented

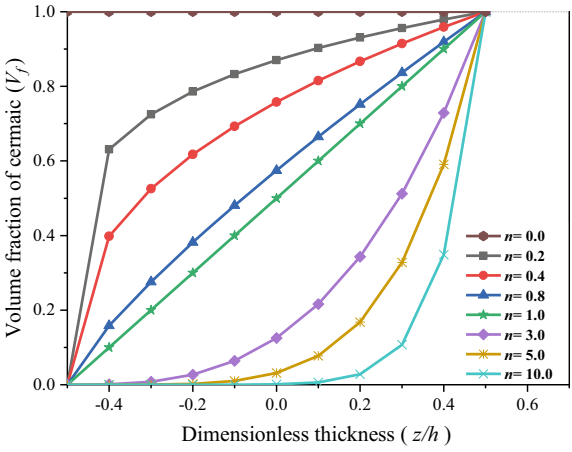

Fig. 1 Volume fraction of ceramic material constituent versus the dimensionless thickness of plate made up of FGM for several volumes fraction index (n)

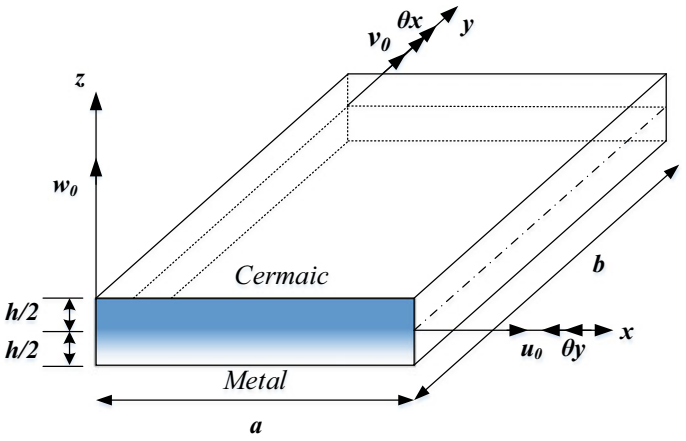

Fig. 2 The geometry of FGM plates with a positive set of plates reference axes and displacements components

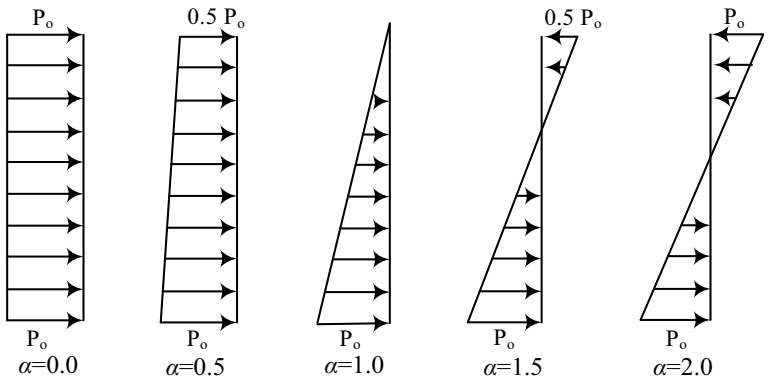

Fig. 3 Examples of linearly varying edge loads

in Fig. 3. The loadings cases with $\alpha = 0.0$, 0.5 and 1.0 are compressive loads, and $\alpha = 1.50$ and 2.0 causes in plane bending.

3 Description of the Finite Elements Model

The robust and multipurpose finite element software package ABAQUS is employed for the purpose of the current investigation. The analysis is carried out using S8R5 element in ABAQUS. Figure 4 shows a schematic representation of the FGM plate with circular cutout and meshing pattern considered for the analysis.

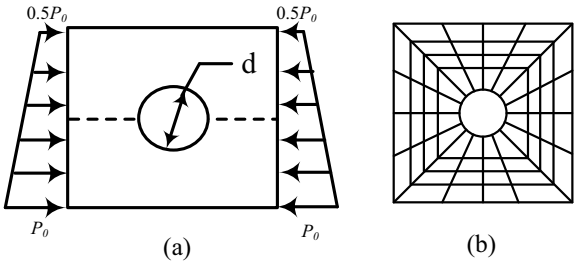

Fig. 4 Schematic representation of FGM plate **a** with circular cutout of diameter (d) and subjected to loading pattern $\alpha = 0.5$, **b** Meshing Pattern considered

3.1 Governing Equation

The governing equations for FGM plates exposed to in plane load is given by

$$M\{\ddot{q}\} + [[K] - P_0[K_G]]\{q\} = \{0\} \tag{3}$$

Ford buckling problem, substitute $\{\ddot{q}\} = 0$ in Eq. (3) to obtain Eq. (4):

$$[[K] - P_0[K_G]]\{q\} = \{0\} \tag{4}$$

4 Result and Discussion

To validate and check the effectiveness of modelling and finite element analysis, results obtained are compared with those existing in the open literatures. The results obtained for buckling load of square FGM plate under the uniform in-plane compression edge loads show a good comparison with results in Reddy et al. [3] as mentioned in Table 2. Furthermore, in Table 3, buckling results for isotropic plates subjected to linearly varying edge load are compared. After validation and establishing accuracy, parametric studies are carried out considering FGM plate with materials properties, as shown in Table 1. The edge condition considered is simply supported on all the sides. Non-dimensional critical load considered is

$$\lambda_{cr} = \frac{P_{cr}b^2}{\pi^2 D};\ D = E_c h^3/12(1-\upsilon^2)$$

Table 1 Materials properties of the FGM for the analysis

Properties	Metals: Aluminium (*Al*)	Ceramics: Tungsten carbide (*WC*)
E (GPa)	70	696
ρ (Kg/m^3)	2700	15,600

Table 2 Comparison of nondimenstional critical buckling load $\left(N_{cr} = \lambda \frac{a^2}{E_m h^3}\right)$ of all sides simply supported square (Al/Al_2O_3) plate under uniaxial compressive in-plane load along the x-axis

a/h	$n = 0.0$	$n = 0.50$	$n = 1.0$	$n = 2.0$	$n = 5.0$	$n = 10.0$
100	19.63	12.86	9.81	7.61	6.31	5.72
	(19.61)	(12.71)	(9.77)	(7.62)	(6.45)	(5.87)
50	19.58	12.84	9.80	7.59	6.36	5.71
	(19.58)	(12.69)	(9.76)	(7.61)	(6.43)	(5.80)
20	19.35	12.70	9.70	7.51	6.26	5.61
	(19.35)	(12.56)	(9.66)	(7.53)	(6.34)	(5.76)

Table 3 Comparisons of non-dimensional critical buckling loads of a simply supported isotropic plates subjected to linearly varying in-planes loads along the x-axis

a/b	α	Present	Literature [5]
1	0.67	5.98	5.96
	0.8	6.60	6.6
	1	7.81	7.81
	1.33	10.95	11.01
	2	25.57	25.53
2	0.67	6.46	6.45
	0.8	7.11	7.11
	1	8.38	8.37
	1.33	11.48	11.48
	2	24.16	24.11

4.1 Influence of Varying Cutouts Sizes and Linearly Varying Loads

The influence of cutout sizes and linearly varying edge loads on buckling of FGM plates are studied in this section by performing parametric studies. The results of cutout size and linearly varying loads on buckling behaviour of FGM plates are as shown in Fig. 5. The critical buckling load is maximum for $\alpha = 2.0$ (pure in-planes loading) and minimum for $\alpha = 0.0$. We can observe that the critical buckling load decreases with an increase in cutout ratio. Critical buckling load is approximately 95% more for $\alpha = 2.0$ in comparison with buckling load for $\alpha = 1.5$ at *d/b* ratio of 0.4. The maximum percentage difference in critical buckling loads between plate without cutout and plate with cutouts ($d/b = 0.6$) is 38.18% for load case of $\alpha = 1.5$. It can also be witnessed that variation in critical buckling load with cutout ratio for plate subjected to uniform compression load ($\alpha = 0.0$) is marginal.

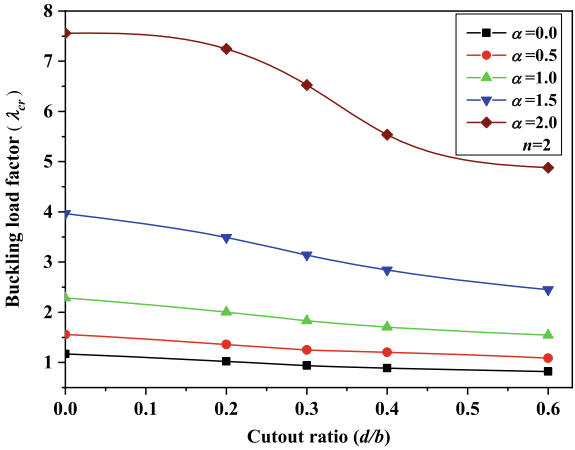

Fig. 5 Buckling load factor versus (λ_{cr}) cutout ratio (*d/b*) for an FGM ($n = 2$) plate with $a/h = 100$ exposed to different linearly varying loadings

4.2 *Effect of Volume Fraction Index*

Figure 6 provides a variation of critical buckling load for FGM plate with cutout ratio (*d/b*) for different volume fraction index (n). In this study, the FGM plate is subjected to load case $\alpha = 1$. The critical buckling load decreases with an increase in cutout ratio irrespective of volume fraction index. The critical buckling load decreases with an increase in volume fraction index and is found to be highest for volume fraction index $n = 0$, i.e., for isotropic plates. The reason for the increase in buckling load with the decrease in volume fraction index is due to the increase in ceramic content (ceramic having higher Young's modulus of Elasticity) and decrease in metal content in the FGM plate.

Values in parenthesis are with respect to Reddy et al. [3]

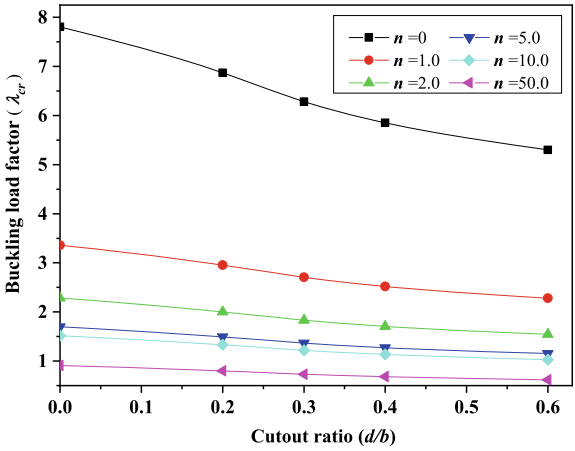

Fig. 6 Buckling load factor (λ_{cr}) versus cutout ratio (*d/b*) for a FGM plate with *a/hi* = 100 subjected too linearly varying loadings ($\alpha = 1$)

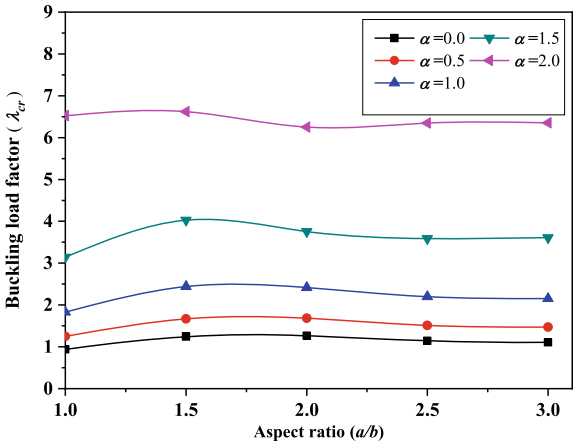

Fig. 7 Variation of the Buckling load factor with aspect ratio for an FGM plate with $n = 2$ and $d/b = 0.3$

4.3 *Effect of Aspect Ratio*

The effect of aspects ratio on the critical buckling loads of the FGM plate subjected to different types of load cases is investigated and is as presented in Fig. 7. The critical buckling load is found to have less variation for FGM plates with aspect ratios 2.5–3.0. The buckling behaviour of FGM plate subjected to load cases with $\alpha = 1.5$, 2, i.e., pure in-plane bending and $\alpha = 1$ case, the critical buckling load increases up to aspect ratio 1.5 and further decreases. This behaviour can be expected due to change buckling mode shapes with an increase in the plate aspect ratios. At the same time, the critical buckling loads increases up to an aspect ratio of 2.0 for FGM plates subjected to load case with $\alpha = 0$ and 0.5.

4.4 *Effect of Cutout Location*

Figure 8 shows the influence of cutout offset ratio (e/b) on buckling response of FGM plate with cutout ($d/b = 0.2$) subjected to linearly varying load. An FGM plate having volume fraction index $n = 2$ is considered for the study. Distance e represents the offset from the centre of the FGM plate to the centre of the circular cutout along the x axis. In this section, the cutout offset ratio is varied from 0 to 0.2. As perceived from Fig. 8 for linearly varying loads, with $\alpha = 0$, 0.5, 1.0 the buckling resistance slightly increases as the cutout position moves towards the edges of the plate. The bending stiffness of middle portion of plate provides larger resistance to buckling. As a result, the presence of a circular cutout in mid portion causes a reduction of the buckling load of plate and hence the buckling increases as the cutout positon is moved away from the centre of the plate. Furthermore, for linearly varying load patterns with $\alpha = 1.5$ and 2.0, the buckling resistance decreases as the cutout moves towards the edges of the plate due to the tensile loads and stress redistribution. The

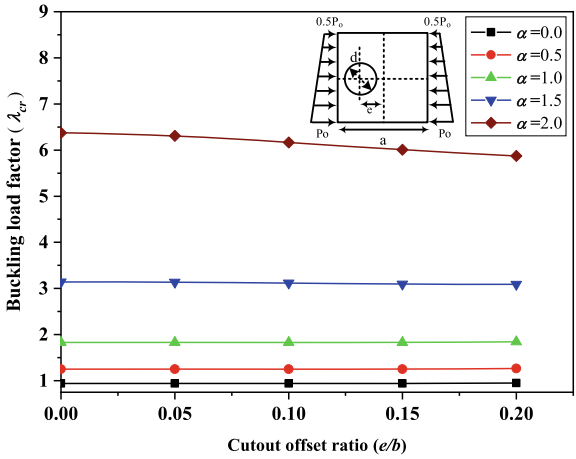

Fig. 8 Variations of the Buckling load factor with cutout offset ratio (*e/b*) for a FGM plate ($n = 2$) exposed to various kinds of linearly varying loads

variation in buckling load is minimum, thus it can be found out that cutout location has a fewer effect on buckling strengths of the FGM plate.

5 Conclusion

1. The buckling strength of FGM plates decreases with an increase in cutout ratio, irrespective of loading conditions. However, the plate with in-plane bending, $\alpha = 1.5$ and 2.0 shows the highest buckling resistance as the tensile stresses restabilize the plates.
2. The buckling resistance increases with the decrease in the volume fraction index.
3. The buckling load demonstrates an increasing trend up to aspect ratio close to 1.5 for $\alpha = 1.0$, 1.5 and 2.0 beyond which the buckling loads displays a decreasing trend. The buckling load variation remains constant for plate aspect ratio 2.5–3.0 irrespective of loading patterns. This behaviour can be expected due to change in buckling mode shapes with an increase in the plate aspect ratios.
4. In case of a linearly varying load pattern with $\alpha = 0$, 0.5, 1.0, the buckling resistance slightly increases as the cutout position move towards the edges of the plate. While for linearly varying load patterns with $\alpha = 1.5$ and 2.0, the buckling resistance decreases as the cutout moves towards the centre of the plate or away from the edges of the plate.

References

1. Javaheri R, Eslami MR (2002) Buckling of functionally graded plates under in-plane compressive loading. ZAMM-J Appl Math Mech (Zeitschrift für Angewandte Mathematik und Mechanik: Applied Mathematics and Mechanics) 82(4):277–283
2. Hosseini-Hashemi S, Khorshidi K, Amabili M (2008) Exact solution for linear buckling of rectangular Mindlin plates. J Sound Vib 315(1–2):318–342
3. Reddy BS, Kumar JS, Reddy CE, Reddy K (2013) Buckling analysis of functionally graded material plates using higher order shear deformation theory. J Compos
4. Swaminathan K, Naveenkumar DT (2014) Higher order refined computational models for the stability analysis of FGM plates–analytical solutions. Eur J Mech-A/Solids 47:349–361
5. Zhong H, Gu C (2006) Buckling of simply supported rectangular Reissner-Mindlin plates subjected to linearly varying in-plane loading. J Eng Mech 132(5):578–581
6. Panda SK, Ramachandra LS (2010) Buckling of rectangular plates with various boundary conditions loaded by non-uniform inplane loads. Int J Mech Sci 52(6):819–828
7. Bodaghi M, Saidi AR (2011) Stability analysis of functionally graded rectangular plates under nonlinearly varying in-plane loading resting on elastic foundation. Arch Appl Mech 81(6):765–780
8. Kumar R, Dutta SC, Panda SK (2016) Linear and non-linear dynamic instability of functionally graded plate subjected to non-uniform loading. Compos Struct 154:219–230
9. Kumar R, Mondal S, Guchhait S, Jamatia R (2017) Analytical approach for dynamic instability analysis of functionally graded skew plate under periodic axial compression. Int J Mech Sci 130:41–51
10. Singh SJ, Harsha SP (2019) Buckling analysis of FGM plates under uniform, linear and non-linear in-plane loading. J Mech Sci Technol 33(4):1761–1767
11. Adhikari B, Dash P, Singh BN (2020) Buckling analysis of porous FGM sandwich plates under various types nonuniform edge compression based on higher order shear deformation theory. Compos Struct 251:112597
12. Ghannadpour SAM, Najafi A, Mohammadi B (2006) On the buckling behavior of cross-ply laminated composite plates due to circular/elliptical cutouts. Compos Struct 75(1–4):3–6
13. Komur MA, Sonmez M (2008) Elastic buckling of rectangular plates under linearly varying in-plane normal load with a circular cutout. Mech Res Commun 35(6):361–371
14. Soni G, Singh R, Mitra M (2013) Buckling behavior of composite laminates (with and without cutouts) subjected to nonuniform in-plane loads. Int J Struct Stab Dyn 13(08):1350044
15. Rajanna T, Banerjee S, Desai YM, Prabhakara DL (2016) Vibration and buckling analyses of laminated panels with and without cutouts under compressive and tensile edge loads. Steel Compos Struct 21(1):37–55
16. Subash Chandra KS, Rajanna T, Rao KV (2020) A parametric study on the effect of elliptical cutouts for buckling behavior of composite plates under non-uniform edge loads. Latin Am J Solids Struct 17(8)
17. Dassault Systemes Simulia Corp., Abaqus Analysis User's Manual, Version 6.9, Providence, RI, USA (2009)

Analysis of a Double Edge Cracked Circular Ring Under Diametrical Compression

K. K. Mohammed Shafeeque and K. V. N. Surendra

1 Introduction

Many fracture specimens are available in the literature for finding the material property of fracture toughness of a material by conducting fracture testing. A review of fracture testing procedures and specimens was given by Zhu and Joyce [1]. Based on the loading, the fracture testing specimens can be broadly divided into compression and tension specimens. Examples for compression specimens include Brazilian disk [2], three-point and four-point bending of edge cracked rectangular beam, semicircular bend (SCB) specimen [3] and compact compression (CC) specimen [4], some of which are shown in Fig. 1. Examples for tension specimens include double cantilever beam (DCB) specimen, single edge notched (SEN) specimen, compact tension (CT) specimen, arch-tension (AT) specimen [5], center-cracked rectangle specimen and diagonally loaded square plate [6]. As the tensile loading requires modification of the specimen and additional fixtures in setup, the compression specimens are more widely used than tension specimens. Few fracture specimens that work under tension are shown in Fig. 2.

Brazilian disk (Fig. 1a) is a widely used compression specimen. There are many experimental/numerical analyses available on the Brazilian disk. Atkinson et al. [2] presented the solution for finding the mixed-mode stress intensity factor (SIF) for any crack orientation in a central cracked Brazilian disk by conducting experiments. Fett [7] computed the stress intensity factor and T-stress solutions for an internally cracked Brazilian disk by using boundary collocation method and weight function.

In some cases, such as thick specimens, the manufacturing of an internal or center crack may become difficult. To overcome this, Chen et al. [8] developed and analyzed double edge cracked Brazilian disk specimen by weight function method. Dong

K. K. Mohammed Shafeeque (✉) · K. V. N. Surendra
IIT Palakkad, Palakkad, India
e-mail: 131814002@smail.iitpkd.ac.in

D. K. Maiti et al. (eds.), *Recent Advances in Computational and Experimental Mechanics, Vol II*, Lecture Notes in Mechanical Engineering,
https://doi.org/10.1007/978-981-16-6490-8_34

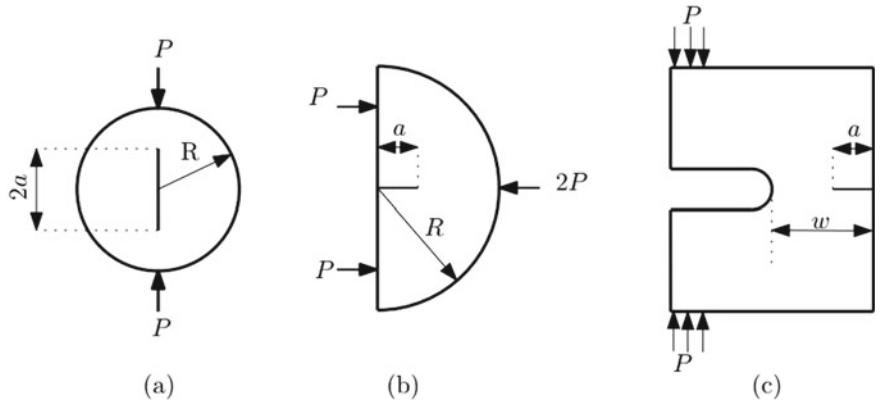

Fig. 1 Compression specimens: **a** Brazilian disk, **b** Semicircular bend specimen, **c** Compact compression specimen

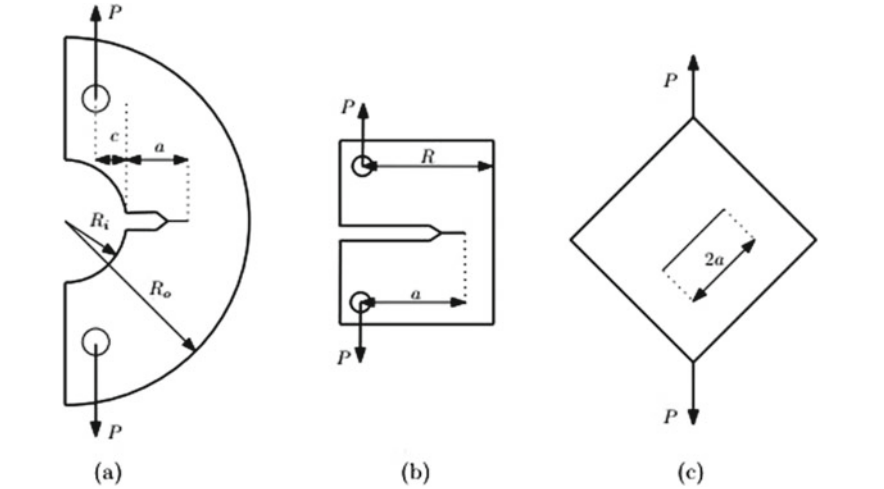

Fig. 2 Tension specimens: **a** Arch-tension specimen, **b** Compact tension specimen, **c** Diagonally loaded square plate

et al. [9] have done a finite element analysis on the Brazilian disk to investigate the dynamic fracture behavior of brittle polymer materials. Ayatollahi and Aliha [10] used a generalized maximum tangential stress criterion for predicting the mixed-mode fracture toughness of rock materials using the Brazilian disk. Tang [11] derived a closed form solution for SIF for center cracked Brazilian disk specimen using the weight function method and also studied the effects of crack length, loading type and friction on the specimen.

A semicircular specimen under three-point bending was experimentally investigated by Lim et al. [3] for fracture testing of rocks and determined the mode I

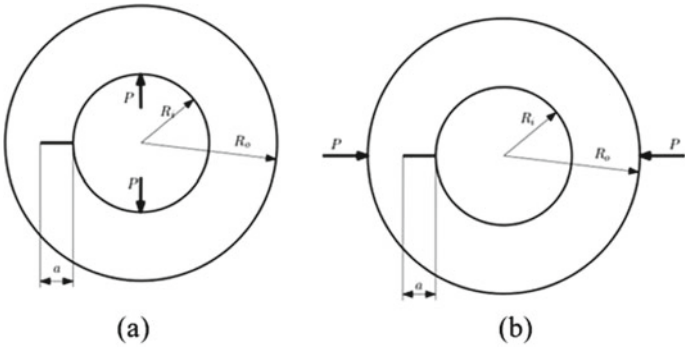

Fig. 3 **a** Circular ring with single radial edge crack opened by loading at inner edge, **b** Circular ring with a radial edge crack opened by loading at outer edge

and mixed-mode I–II fracture toughness of synthetic mud stone. Bui et al. [4] introduced a new approach for experimentally determining the dynamic SIF using a CC specimen and Kolsky bar. Semicircular ring specimen called Arch-Tension specimen with an edge crack is a tension specimen as shown in Fig. 2a, which can be used for mode I fracture testing [5]. Tracy [12] solved the problem of a circular ring segment with radial crack for pure bending and three-point bending loads using the modified collocation technique and partitioning. Bowie et al. also used the modified collocation method for analyzing circular ring with radial crack under uniform external tension [13]. A circular ring with single radial crack under compression and tension as in Fig. 3a, b was analyzed by Ahmed and Ashbough who concluded that such specimens can be used for constant mode I stress intensity factor (K_I) crack propagation tests [14]. A radial crack on a circular ring subjected to crack surface shear stress is analyzed by Leung and Hu by using dislocation solution and singular integral equation techniques for obtaining the mode II stress intensity factor [15].

We introduce a new design of compression fracture specimen, in the form of a double inner/outer edge cracked circular ring as shown in Fig. 4a, b, inspired from Brazilian disk. By modeling a central hole in the Brazilian disk and ensuring that hole diameter is less than center crack length, the new design can be arrived, which magnifies the normal stress distribution on the loading axis thereby increasing the stress intensity factor for a given crack length. Analysis of uncracked circular ring for stresses can provide some hints to reason the corresponding fracture behavior of cracked ring. The new specimen design can be adapted to either pure mode-I (Fig. 4a, b) or mixed-mode I–II loading (Fig. 4c), just by changing the orientation of the axis of cracks with respect to the line of action of loading, similar to the use of Brazilian disk. The pure mode I is obtained by aligning the crack in the direction of line of action for inner edge crack and in the perpendicular to the direction of line of action for outer edge crack. In this paper, only pure mode-I loading is considered for analysis. In the following sections, first, the modeling details of the circular ring specimen are provided followed by results of finite element (FE) modeling.

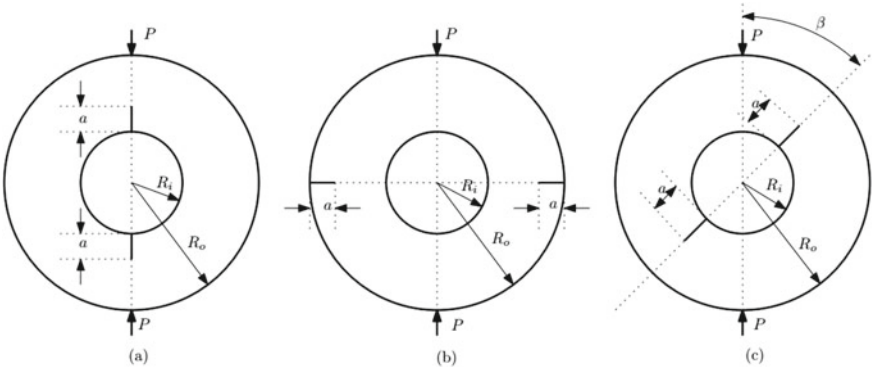

Fig. 4 Double edge cracked circular ring specimen under external diametrical compression. **a** Inner edge cracked (Pure Mode I). **b** Outer edge cracked (Pure Mode I) and **c** Mixed-mode I–II (Inner edge cracked)

2 New Circular Ring Specimen

The geometry and loading configuration of the new circular ring specimen is shown schematically in Fig. 4a, b. This new configuration consists of circular ring of inner radius R_i and outer radius R_o, with edge cracks each of length a situated diametrically opposite at the inner edge. The ring specimen is loaded by two opposite compressive loads (P) on the external boundary. Since it is a compression specimen, it does not require any complicated fixtures for loading, and additional holes do not need to be provided in the geometry. When the crack is oriented along the line of action of loading, the geometry and loading will become symmetric about the common diameter of crack line and loading axis, which makes the configuration a pure mode I case. Note that this configuration also exhibits symmetry about perpendicular diameter. If these two symmetries are made use, then only one-quarter can represent the entire ring. If the specimen is rotated keeping the loading axis in the same direction, then both the symmetries will be lost, thus demanding modeling of full geometry.

Finite element method (FEM) is used to model the fracture problem basically as elasticity problem. Ansys solver was used to solve various cases of new design. As the essential part of post-processing, mode I stress intensity factor (K_I) was found for all the cases modeled, which can be used for parametric analysis of the configuration. Inner radius and length of edge cracks are the chosen parameters to vary and their effect is captured. The details of the FE model and calculations are presented in the next section.

3 Methodology

The pure mode I case of the double inner/outer edge cracked circular ring specimen is symmetric about both vertical and horizontal diametrical axes. Making use of these symmetries, only a quarter of the circular ring is modeled as shown in Figs. 5a and 6a. The commercial software Ansys along with a built-in APDL (Ansys parametric design language) coding option is used for FE modeling and analysis. In the model, the geometry and applied loading conditions were: $R_o = 50\,\text{mm}$, $P/2 = 1000\,\text{N}$ taking unit into-the-plane thickness. Different cases of inner radius: $R_i = 5\,\text{mm}, 10\,\text{mm}, \ldots, 45\,\text{mm}$ were considered keeping the outer radius at the given value, so that $R_i/R_o = 0.1, 0.2, 0.3, \ldots, 0.9$. Independent of R_i/R_o variation, the common length of symmetric pair of edge cracks is varied according to $a/(R_o - R_i) = 0.05, 0.10, 0.15, \ldots, 0.95$ to obtain various crack lengths for a given inner radius value. For the material model, elastic properties of steel were chosen,

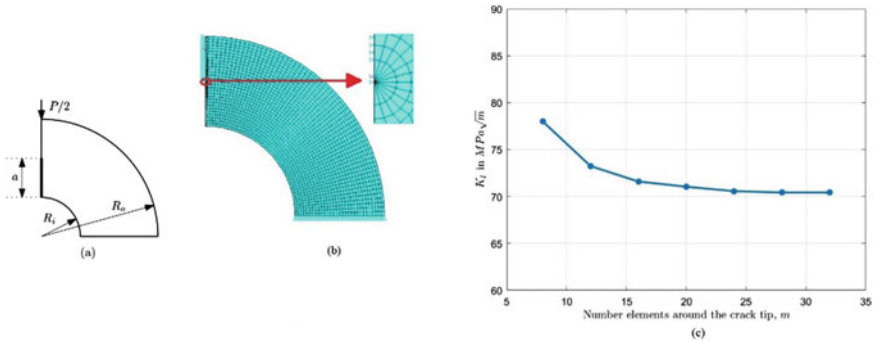

Fig. 5 **a** Quarter-ring modeling of inner edge cracked ring by symmetry, **b** Finite element meshed model of the inner edge cracked circular ring specimen, **c** K_I versus m for the inner edge cracked circular ring specimen with $R_i = 25\,\text{mm}$, $R_o = 50\,\text{mm}$, $a = 12.4\,\text{mm}$ and $s = R_o/400$

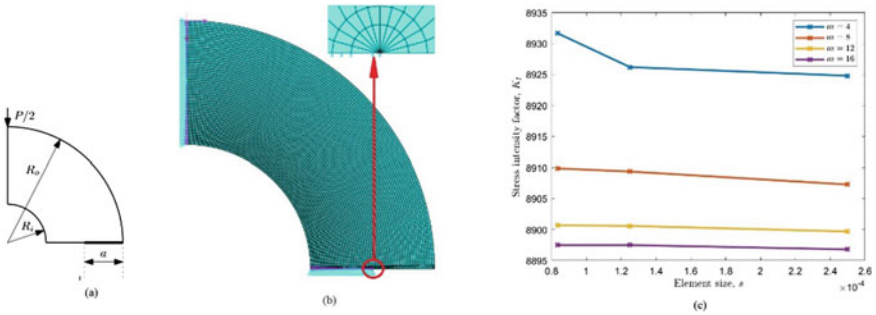

Fig. 6 **a** Quarter-ring modeling of outer edge cracked ring by, **b** Finite element meshed model of the outer edge cracked circular ring specimen, **c** K_I versus s for the outer edge cracked circular ring specimen with $R_i = 25\,\text{mm}$, $R_o = 50\,\text{mm}$, $a = 12.4\,\text{mm}$ for various values of m

which has Young's modulus, $E = 200$ GPa and Poisson's ratio, $\nu = 0.3$. Figure 5b shows a typical mesh pattern generated in Ansys for the case of $R_i = 25$ mm and $a = 12.5$ mm. Eight-node 2D plane elements (PLANE183) were used for meshing of each model of various hole radius, R_i. The inverse square root singularity $\left(1/\sqrt{r}\right)$ of stresses/strains at the crack tip is captured by introducing quarter point elements surrounding the crack tip as shown in Figs. 5b and 6b. The displacement extrapolation method in Ansys was used for finding the stress intensity factors (K_I) for all the cases of crack lengths.

3.1 FE Model of Inner Edge Cracked Specimen

Mesh Insensitivity Analysis

A mesh insensitivity analysis was performed on a typical case of inner radius $R_i = 25$ mm and crack length $a = 12.5$ mm. The analysis was done by varying the number of elements around the crack tip (m) and the size of each element around the crack tip (s). For each case, K_I is found. For testing the convergence, a plot between the K_I and m is shown in Fig. 5c. From the figure, it is observed that the curve is becoming horizontal as the m increases. This shows the convergence of K_I with increasing m. From these results, the value of m is fixed as 20 for all the cases of further analysis of the ring specimen.

3.2 FE Model of Outer Edge Cracked Specimen

Mesh Insensitivity Analysis

As the geometry is different for outer edge cracked specimen, a separate mesh insensitivity analysis was done for this case and also on a particular case of inner radius $R_i = 25$ mm and crack length $a = 12.5$ mm. The number of elements around the crack tip (m) and the size of each element around the crack tip (s) were varied to check the convergence of K_I. A plot between the K_I and s for different values of m is plotted as shown in Fig. 6c for convergence testing. From the figure, it can be observed that K_I value is converging as s decreases. From this, the value of s is taken as $R_o/400$ and m as 12, for all the cases in the analysis of outer edge cracked specimen.

4 Results

4.1 Stress Intensity Factor for Inner Edge Cracked Specimen

The trend of mode I stress intensity factor (K_I), when the crack length (a) is varied, is plotted for the various cases of radii ratio R_i/R_o as shown in Fig. 7. From Fig. 7a, it is observed that for the cases of $R_i/R_o = 0.2, 0.3, 0.4$ and 0.5, the K_I shows a downward trend initially as the crack length increases. After K_I reaches minimum, it rises continuously as the crack length increases further. This regime of small crack length indicates the stable crack propagation. However, for Brazilian disc case, we cannot find such local minimum for K_I. Apparently, there is a concurrent point of all the curves where $a \approx 0.015$ mm and $K_I \approx 120$ MPa $\sqrt{\text{m}}$. This indicates invariance of K_I with R_i/R_o at $a \approx 0.015$ mm. For the case of $R_i/R_o = 0.1$, the initial decreasing trend as in other cases is not clearly visible because the analysis is failed to capture K_I for the smaller crack length, where the decreasing trend should happen for $R_i/R_o = 0.1$. The dashed line shows the variation of K_I for the center cracked Brazilian disk. It can be found that the K_I of the present ring specimen compared with Brazilian disk is significantly higher especially for longer cracks and bigger holes. For the cases of small holes and very short cracks, the K_I for the ring specimen tends to that of Brazilian disk.

The mode I stress intensity factor (K_I) of the specimen can be normalized to get the form factor (F_I), which is expressed as

$$F_I = \frac{K_I}{\sigma^* \sqrt{\pi (R_i + a)}} \tag{1}$$

where $(R_i + a)$ is used in nominal stress intensity factor expression instead of just a to avoid singularity of resulting F_I at $a = 0$.

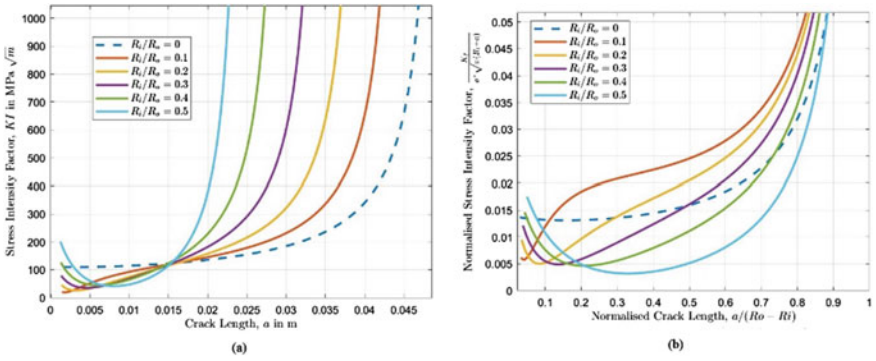

Fig. 7 **a** Variation of mode I stress intensity factor with crack length and **b** variation of normalized K_I with crack length ratio $a/(R_o - R_i)$ for various R_i/R_o values for inner edge cracked specimen

In Eq. (1), σ^* is the characteristic stress and is given by

$$\sigma^* = \frac{P}{(R_o - R_i)h} \tag{2}$$

where h is the specimen thickness and P is the applied load.

The F_I as a function of normalized crack length $a/(R_o - R_i)$ for various R_i/R_o values is shown in Fig. 7b. From the figure, F_I also shows local minima as relative crack length varies. The form factor exhibits singularities at extremities, order of which should be captured by trial and error before fitting an expression for F_I as a function of relative crack length and radii ratio. We will take up this part of work in a future communication as it will be out of scope for this work.

Both the Fig. 7a, b show the curves for the cases of R_i/R_o values up to 0.5. Although we generated the K_I results for higher values of R_i/R_o, we did not show in Fig. 7 to reveal the key aspects of K_I behavior especially at small crack lengths. For $R_i/R_o \gtrsim 0.5$ when the ring becomes thinner, the K_I result shows crack closure effects after some crack length. In such cases, maximum possible crack length is to be identified to ensure the opening of crack in the tests.

4.2 *Stress Intensity Factors for Outer Edge Cracked Specimen*

For outer edge cracked specimen, trend of K_I with a is plotted for various cases of R_i/R_o as shown in Fig. 8a. It can be observed that for all the cases of R_o/R_i K_I shows an increasing trend initially as a increases, reaches a maximum and then continuously decreasing with further increase in crack length. For longer crack lengths,

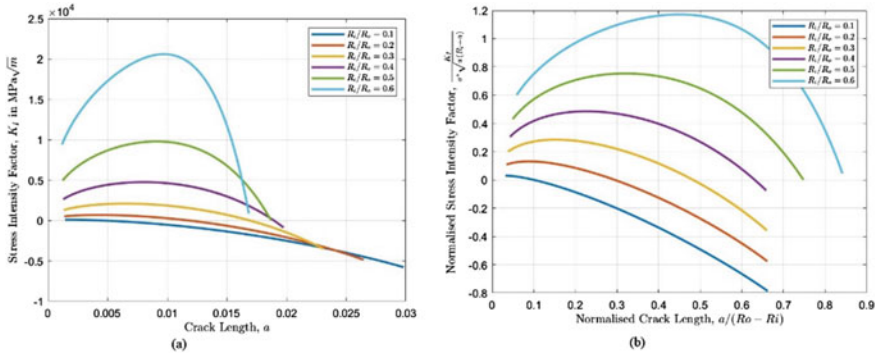

Fig. 8 **a** Variation of mode I stress intensity factor with crack length and **b** variation of normalized K_I with crack length ratio $a/(R_o - R_i)$ for various R_i/R_o values for outer edge cracked specimen

K_I decreases to the negative regime, which indicates the crack closure. This trend indicates the crack arrest behavior of the specimen.

The plot between normalized stress intensity factor and normalized crack length for various R_o/R_i values is shown in Fig. 8b, which also exhibits similar trend as K_I plot. For longer crack length, crack is closed due to the bending effect of the ring.

4.3 Analysis of Uncracked Circular Ring

The fracture behaviors of inner and outer edge cracked circular ring specimens are entirely different as observed from their K_I plots. For further understanding of the specimens, stress analysis was done on the uncracked circular ring under a similar loading condition. A circular ring under diametrical compression was solved by Timoshenko for a special case of $R_i/R_o = 0.5$ [16]. This solution was obtained by superposition of disc under diametrical compression and a circular ring (series solution) whose inner edge is subjected to negative of the traction observed in solid disc case at the corresponding radial distance. The hoop stress $\sigma_{\theta\theta}$ that causes the opening of a probable crack on the vertical and horizontal axes is shown in Fig. 9 for the case of $R_i/R_o = 0.1, 0.2, \ldots 0.5$. From Fig. 9a, on the loading axis, $\sigma_{\theta\theta}$ decreases from tension at inner edge to compression outer edge. As a consequence, an edge crack can initiate at inner edge on the loading axis. From Fig. 9b, on the horizontal axis, $\sigma_{\theta\theta}$ increases from compressive at inner edge to tensile at outer edge, which initiate crack at outer edge in the ring specimen. In both the plots, we can find a concurrent point at $(r - R_i)/(R_o - R_i) \approx 0.5$, indicating normalized hoop stress is independent of R_i/R_o at nearly the mid-point of the width.

The stress distribution in the uncracked circular ring specimen provides some hints to explain the fracture behavior of the double edge cracks circular ring specimens. For an inner edge cracked specimen, the edge crack is on the vertical axis, and the $\sigma_{\theta\theta}$

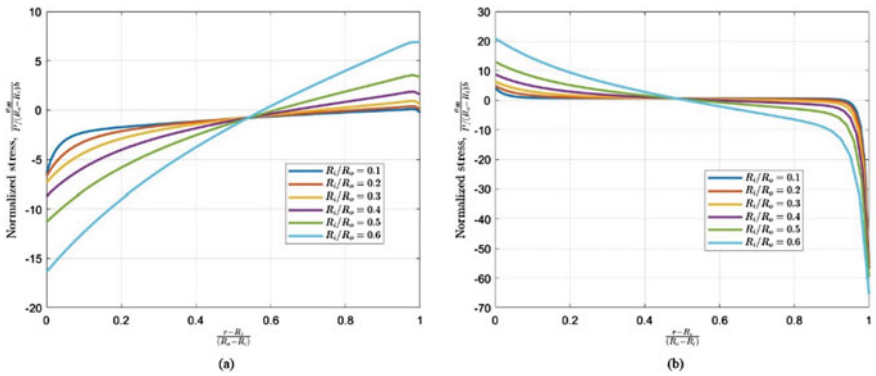

Fig. 9 Distribution of hoop stress along **a** vertical and **b** horizontal axes of an uncracked circular ring under diametrical compression

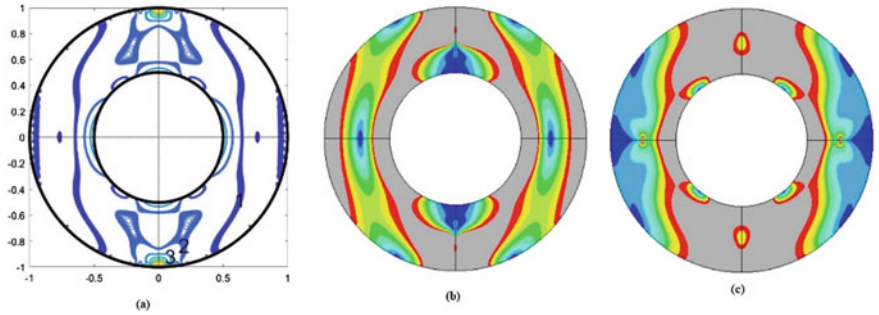

Fig. 10 Isochromatic patterns for **a** Uncracked circular ring, **b** Inner edge cracked ring, **c** outer edge cracked ring

is tensile at the inner edge. As we move away from the inner edge, $\sigma_{\theta\theta}$ decreases to zero and then to compression, which might explain the initial decreasing trend in the K_I versus a plot in Fig. 7a for $R_i/R_o < 0.5$. For higher values of R_i/R_o, this trend is not observed, which may be related to bending of thin rings. On the other hand, for the outer horizontal edge cracked specimen, K_I exhibits completely different behaviors including a crack closure at larger cracks for a similar $\sigma_{\theta\theta}$ distribution. The crack closure may be due to the bending of ring, which is predominant on the horizontal axis even for lower values of R_i/R_o.

The isochromatic patterns of the circular ring specimen for uncracked, inner edge cracked and outer edge cracked cases are plotted in Fig. 10 for the same values of total load applied, inner and outer radii. The contour levels are same for all three plots. Relative crack length is 0.5 for the later two plots. The cracked ring patterns are significantly different from uncracked ring pattern due to the presence of double edge cracks.

5 Discussions

The present analysis was done by modeling the applied load as a concentrated point force on the circular ring in FE. But in reality, the load will get distributed on a finite arc length of the specimen, and hence it is difficult to obtain a point load. This distributed loading can be assumed of uniform distribution or Hertzian distribution. Both of them can be modeled and solved by using the theory of elasticity. The study of stress distribution in the uncracked specimen is useful in determining the behavior of the cracked specimen. This stress distribution along with the weight functions can be used to find the SIF of the cracked ring specimen. The weight function (WF) is independent of the loading configuration but depends on the geometry and the crack configuration. So, by determining the WF of a cracked specimen, K_I can be found for any loading configuration of the specimen by determining the stress distribution in the uncracked specimen under the same loading configuration [17].

6 Conclusion

The new circular ring specimens were analyzed numerically for mode I stress intensity factor. They have the advantages of compressive loading and the enhanced stress intensity factor compared with Brazilian disk specimen. The stress concentration due to the hole at the center of the ring makes it more prone to crack propagation at the stress concentrated region. Inner and outer edge cracked specimens behave differently with the same loading configuration. The hoop stress along the loading and horizontal axes of the uncracked specimen was also different. It decreases from tension at inner edge to compression at outer edge along the loading axis. Along horizontal axis, the hoop stress increases from compression to tension as we move from inner to the outer edge.

References

1. Zhu X-K, Joyce JA (2012) Review of fracture toughness (G, K, J, CTOD, CTOA) testing and standardization. Engng Fract Mech 85:1–46
2. Atkinson C, Smelser RE, Sanchez J (1982) Combined mode fracture via the cracked Brazilian disk test. Int J Fract 18(4):279–291
3. Lim IL, Johnston IW, Choi SK, Boland JN (1994) Fracture testing of a soft rock with semi-circular specimens under three-point bending Part l: Mode-I. Int J Rock Mech Min Sci Geomech Abstr 31(3):185–197
4. Bui HD, Maigre H, Rittel D (1992) A new approach to the experimental determination of the dynamic stress intensity factor. Int J Solids Struct 29(23):2881–2895
5. Underwood JH, Kendall DP (1976) Fracture toughness testing using the C-shaped specimen. Technical Report WVT-TR-76027, Benet weapons laboratory, Rock Island, Illinois-61201, July 1976
6. Ayatollahi MR, Aliha MRM (2009) Analysis of a new specimen for mixed mode fracture tests on brittle materials. Eng Fract Mech 76:1563–1573
7. Fett T (2001) Stress intensity factors and T-stress for internally cracked circular disks under various boundary conditions. Eng Fract Mech 68(9):1119–1136
8. Chen F, Sun Z, Xu J (2001) Mode I fracture analysis of the double edge cracked Brazilian disk using a weight function method. Int J Rock Mech Mining Sci 38:475–479
9. Dong S, Wang Y, Xia Y (2006) A finite element analysis for using Brazilian disk in split Hopkinson pressure bar to investigate dynamic fracture behaviour of brittle polymer materials. Polym Test 25:943–952
10. Ayatollahi MR, Aliha MRM (2008) On the use if Brazilian disc specimen for calculating mixed mode I-II fracture toughness of rock materials. Eng Fract Mech 75:4632–4641
11. Tang SB (2017) Stress intensity factor for a Brazilian disc with a central crack subjected to compression. Int J Rock Mech Mining Sci 93:38–45
12. Tracy PG (1975) Analysis of a radial crack in a circular ring segment. Eng Fract Mech**7**(Mmc):253–260
13. Bowie OL, Freese CE (1972) Elastic analysis for a radial crack in a circular ring. Eng Fract Mech 4(2):315–321

14. Ahmed J, Ashbough NE (1982) Constant K_I crack propagation test specimen. Int J Fract 19:115–129
15. Leung AYT, Hu JD (1997) Mode II stress intensity factors for a circular ring or a hollow cylinder with a radial crack. Int J Press Vessels Piping 72(2):149–156
16. Timoshenko SP, Goodier JN (1970) Theory of elasticity, 3rd ed. McGraw-Hill Book Company
17. Anderson T (2005) Fracture mechanics. Boca Raton. Taylor & Francis, FL

Stress Behavior of an Elasto-Plastic Ellipsoidal Inhomogeneity Embedded in an Elastic Matrix Under Sinusoidal Loading

Suraj K. Jayswal and Prasun Jana

1 Introduction

Inclusions greatly influence the physics and mechanics of materials. Hence, a deeper understanding of inclusions and research in the field of inclusions play a substantial role in the development of cutting-edge materials. Such research is also essential in the enhancement of already existing materials used in aerospace, marine, automotive, and numerous other applications [1]. The study of inclusions and inhomogeneities was pioneered by J. D. Eshelby. The theory of ellipsoidal inclusions has been widely used in homogenization schemes. These schemes, in turn, are utilized to predict failures in composite materials. This theory has also been used to accommodate imperfections and impurities inside material with significant thermal expansion in the detailed design of a machine and its components. Moreover, it has been used in a broad spectrum of research areas such as crack propagation and fatigue initiation from micro defects, semiconductors, biomechanics, and geomechanics. It has also been effectively used in the modeling of nanostructures like Quantum dots (QDs) and Quantum wires (QWRs). A comprehensive review of current studies and researches on this topic can be found in the work by Zhou et al. [1] (Fig. 1).

Eshelby formulated the elastic fields within an ellipsoidal inclusion subjected to some uniform eigenstrain and embedded inside a homogeneous isotropic elastic infinite matrix [2]. The eigenstrain is a non-elastic strain that the inclusion would show if it is not surrounded by the matrix on the outside. It is also called 'strain without stress' or 'zero-stress strain.' The non-elastic strain can be due to misfit, thermal deformation, plastic deformation, and phase transformation. If the elastic modulus

S. K. Jayswal (✉) · P. Jana
Department of Aerospace Engineering, Indian Institute of Technology, Kharagpur 721302, India

P. Jana
e-mail: prasun@aero.iitkgp.ac.in

D. K. Maiti et al. (eds.), *Recent Advances in Computational and Experimental Mechanics, Vol II*, Lecture Notes in Mechanical Engineering,
https://doi.org/10.1007/978-981-16-6490-8_35

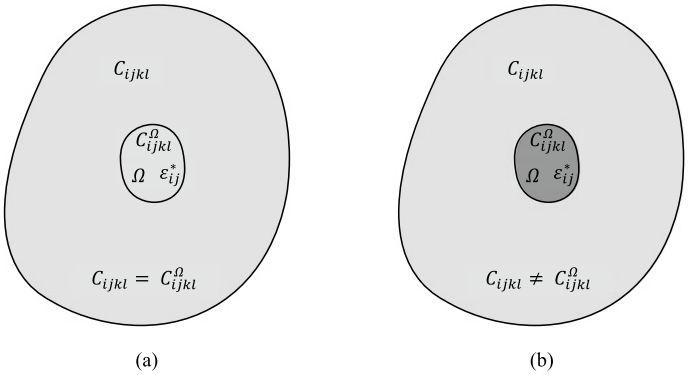

Fig. 1 **a** Homogeneous inclusion (aka inclusion in general): The subregion (Ω) contains an eigenstrain $\left(\varepsilon^{*}_{ij}\right)$ and has the same elastic moduli as the matrix. **b** Inhomogeneous inclusion: The subregion (Ω) contains an eigenstrain $\left(\varepsilon^{*}_{ij}\right)$ and has different elastic moduli than the matrix. For zero eigenstrain, it is known as an *inhomogeneity*

of the subdomain (Ω) is the same as that of the matrix, then it is called a *homogeneous inclusion* or sometimes, *inclusion* in general. And if the elastic modulus of the inclusion is different from that of the matrix, then it is known as an *inhomogeneous inclusion.* When the eigenstrain inside the inhomogeneous inclusion is zero, it is called an *inhomogeneity* [3].

A huge number of studies on ellipsoidal inclusion problems are already done and published. However, a thorough literature review reveals that nearly all the studies deal with elastic inclusions, and semi-analytical methods are also developed for the same. Elasto-plastic inclusions under monotonic loading are discussed in the work by Jana and Chatterjee [4] while such problems under cyclic loading have not received any attention in the research. A potential application of such studies on elasto-plastic inclusions would be modeling of material damping and internal energy dissipation due to elasto-plastic flaws in the material [5].

In this paper, we investigate the stress–strain behavior inside a single elasto-plastic ellipsoidal inhomogeneous inclusion embedded within an infinite isotropic homogeneous elastic matrix under uniform sinusoidal far-field loading using ABAQUS. Two different material models namely elastic/perfectly plastic and elastic/linear isotropic hardening material behavior, along with J_2 flow theory, are considered for the elasto-plastic inclusion in the finite element simulations. Details of the simulations are discussed in the following sections.

2 Finite Element Analysis

It is a fact in the literature that the stress state inside an ellipsoidal inclusion becomes uniform for an infinite unbounded matrix [2]. However, an infinite matrix is an imaginary concept and cannot be thought of in real-world applications. Thus, we work with limits, and hence the size of the inhomogeneity is taken very small such that the matrix behaves as an infinite solid surrounding the inhomogeneity.

For finite element simulations in ABAQUS, the geometric model consists of a cube from the outside that acts as a matrix and an ellipsoid embedded inside the cube that acts as an inhomogeneity. The boundary condition is a uniform state of stress applied on all six faces of the cube on the outside. The nodes at the matrix–inhomogeneity, interface i.e., cube-ellipsoid boundary, are merged for appropriate load transfer. Simulations are carried out for two different aspect ratios of the ellipsoid and two different material models for inhomogeneity. Details of the geometry, finite element mesh, material models, and loading are discussed below. Figure 2 shows a schematic representation of an ellipsoidal inhomogeneity embedded inside a matrix, subjected to uniform far-field stresses.

2.1 Geometry and Mesh Details of the Inhomogeneity

In this article, we have taken two different aspect ratios for the ellipsoidal inhomogeneity. The first one is a general ellipsoidal inhomogeneity while the other one is a spherical inhomogeneity. A cube is taken as the matrix and the size of the cube is taken considerably larger in comparison to that of the inclusion such that the cube behaves as an infinite material body for the inhomogeneity. Details of the geometry and mesh are discussed below.

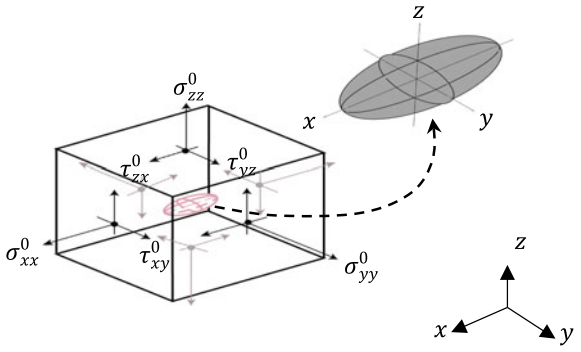

Fig. 2 Schematic of an elasto-plastic ellipsoidal $\left(\frac{x^2}{a_1^2}+\frac{y^2}{a_2^2}+\frac{z^2}{a_3^2}\le 1\right)$ inhomogeneity embedded in an elastic matrix under far-field stresses σ^0_{ij}

2.1.1 Ellipsoidal Inhomogeneity

The first model consists of a general ellipsoidal inhomogeneity, which is an ellipsoid with semi-axes lengths of 1, 0.75, and 0.5 mm, centrally embedded inside the matrix represented by a cube with an edge length of 20 mm. Figure 3a shows a quarter of the full meshed model. The mesh is highly refined near the matrix–inhomogeneity interface to capture the interaction and better the accuracy. The nodes are merged at the matrix–inhomogeneity interface. The complete meshed model consists of 84,032 eight-noded linear brick elements (C3D8R) (see ABAQUS documentation [6] for details). The final mesh with 84,032 elements is arrived at based on a convergence study, which is presented in Sect. 3.

2.1.2 Spherical Inhomogeneity

Similarly, the spherical inhomogeneity is a sphere with a radius of 1 mm, centrally embedded inside the matrix represented by a cube with an edge length of 20 mm. One fourth of the full meshed model for the same is shown in Fig. 3b. The full meshed model consists of a total of 85,440 eight-noded linear brick elements (C3D8R), and high mesh refinement is used for reasons mentioned in the previous subsection. As mentioned earlier, the nodes at the matrix–inhomogeneity interface are merged.

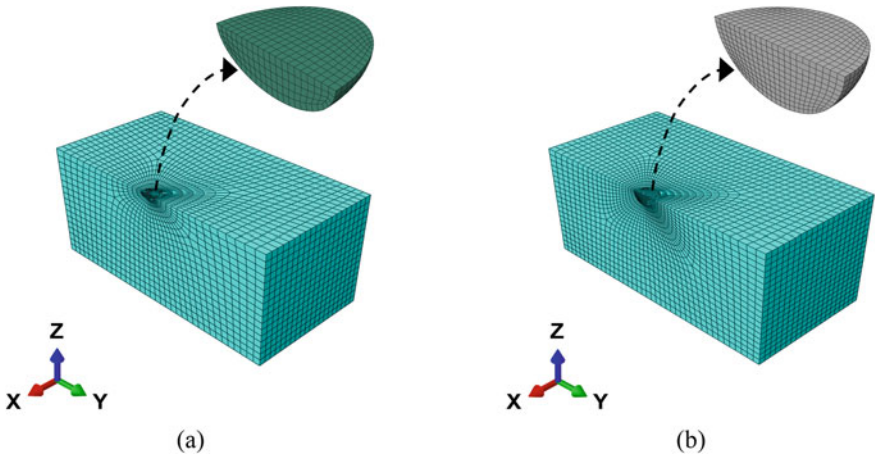

Fig. 3 **a** One quarter of the 3D meshed model consisting of an ellipsoidal inhomogeneity embedded in a matrix. **b** One quarter of the 3D meshed model consisting of a spherical inhomogeneity embedded in a matrix

2.2 *Material Models for the Inhomogeneity*

The matrix and the inhomogeneity are considered to have isotropic material properties. Moreover, the matrix is considered to have purely elastic material behavior while that of the inhomogeneity is considered to have an elastic–plastic behavior. Simulations are carried out for two different elastic–plastic behaviors, viz., elastic/perfectly plastic behavior and elastic/linear isotropic hardening behavior. Schematic representations of both models are shown in Fig. 4a, b.

2.2.1 Elastic/Perfectly Plastic Inhomogeneity

In a material model with elastic/perfectly plastic behavior, the elastic behavior is linear and in the plastic region, the yield stress does not increase with plastic strain but remains constant throughout the loading process [7]. The material properties used for the combination of the elastic matrix and the elastic/perfectly plastic inhomogeneity are given in Table 1. These material properties are chosen from the earlier work by Jana and Chatterjee [4]. Moreover, it is assumed that the inhomogeneity material follows the J_2 flow theory of plasticity.

2.2.2 Elastic/Linear Isotropic Hardening Inhomogeneity

In an elastic/linear isotropic hardening material model, a linear elastic behavior is assumed and in the plastic region, the yield stress increases linearly with increasing

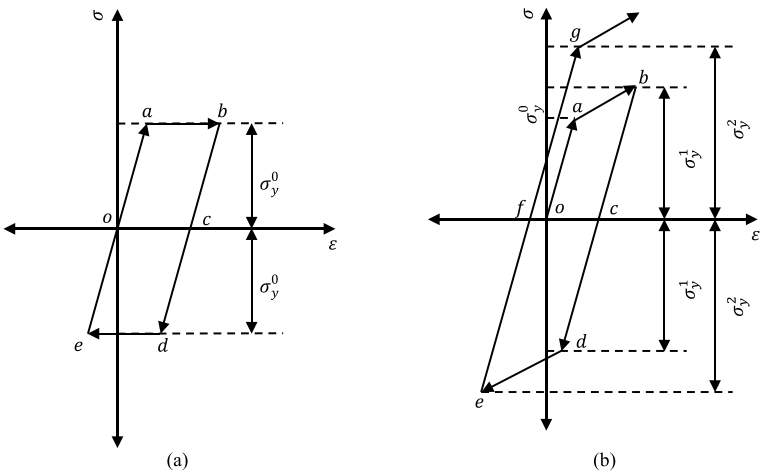

Fig. 4 **a** Schematic representation of an elastic/perfectly plastic material model. **b** Schematic representation of elastic/linear isotropic hardening material model

Table 1 Material properties used in analyses of the elastic/perfectly plastic material model

Elastic matrix material	
Young's modulus	100 GPa
Poisson's ratio	0.3
Elasto-plastic inhomogeneity material	
Young's modulus	50 GPa
Poisson's ratio	0.28
Initial yield strength $\left(\sigma_{yp}^{0}\right)$	25 MPa

Table 2 Material properties used in analyses of the elastic/linear isotropic hardening material model

Elastic matrix material	
Young's modulus	200 GPa
Poisson's ratio	0.3
Elasto-plastic inhomogeneity material	
Young's modulus	120 GPa
Poisson's ratio	0.28
Initial yield strength $\left(\sigma_{yp}^{0}\right)$	40 MPa
Elasto-plastic modulus (H)	10 GPa

plastic strain throughout the loading process [7]. Table 2 shows the material properties used for the combination of the elastic matrix and the elastic/linear isotropic hardening inhomogeneity. These material properties are chosen from the earlier work by Jana [5] and the inhomogeneity material is also assumed to follow the J_2 plasticity flow theory.

2.3 Loading

In ABAQUS, a pseudo-static analysis is carried out for the sinusoidally applied far-field stresses. We have used 200 steps for the sinusoidally applied far-field load in our analyses. The load steps starting from 1 to ending at 200 are represented using an artificial time that ranges from 0 to 1, and this representation of load steps is called a *normalized load step*. The load at a normalized load step depends on the frequency of the sinusoidally applied far-field load $\left(\sigma^{0}\right)$ and amplitude of each component of the far-field load. In this article, we have taken three cycles for the sinusoidally applied far-field stresses. A schematic of the sinusoidally applied far-field load is shown in Fig. 5a. The ordinate shown in the figure shows a multiplication factor k. If σ^{0} is the amplitude of a far-field stress component, then $k\sigma^{0}$ will be the pseudo-statically applied far-field stress. Figure 5b shows the variation of a far-field stress component $\left(k\boldsymbol{\sigma}_{\boldsymbol{xx}}^{0}\right)$ with $\boldsymbol{\sigma}_{\boldsymbol{xx}}^{0} = 75$ MPa used in the analyses.

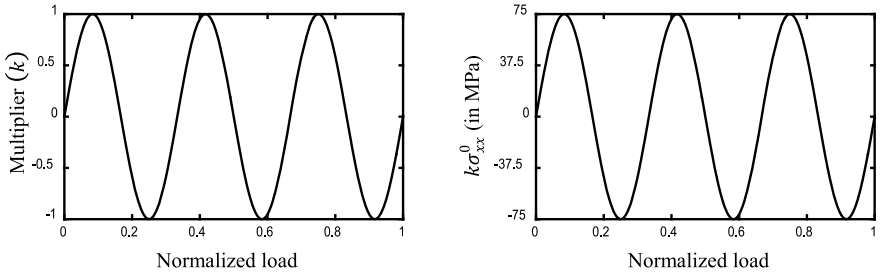

Fig. 5 **a** Schematic of a sinusoidally applied far-field load (three load cycles). **b** Variation of a far-field stress component $(k\sigma^0_{xx})$ with $\sigma^0_{xx} = 75$ MPa

Table 3 Far-field stresses used in analyses of the elastic/perfectly plastic material model

σ^0_{xx}	σ^0_{yy}	σ^0_{zz}	τ^0_{yz}	τ^0_{zx}	τ^0_{xy}
75 MPa	−50 MPa	40 MPa	30 MPa	−25 MPa	65 MPa

Table 4 Far-field stresses used in analyses of the elastic/linear isotropic hardening model

σ^0_{xx}	σ^0_{yy}	σ^0_{zz}	τ^0_{yz}	τ^0_{zx}	τ^0_{xy}
150 MPa	200 MPa	−110 MPa	80 MPa	−150 MPa	−140 MPa

The amplitude of the far-field stresses considered in the analyses for the elastic/perfectly plastic inhomogeneity and elastic/linear isotropic hardening inhomogeneity are given in Table 3 and Table 4, respectively.

3 Results and Discussions

Several cases were simulated and studied for different aspect ratios of ellipsoid geometry, material models, and far-field stresses. Ellipsoidal and spherical elastic/perfectly plastic inhomogeneities were studied for far-field stresses given in Table 3. Ellipsoidal and spherical elastic/linear isotropic hardening inhomogeneities were studied for far-field stresses given in Table 4. The inputs for the material properties and the loadings are motivated and taken from the work done by Jana and Chatterjee [4]. The results from all the analyses reveal that the stress state within the inhomogeneity remains effectively uniform throughout the loading. This is true for both general ellipsoidal and spherical inhomogeneities. The surface plots of different stress components at a given normalized load step are shown in the following figures.

There is a slight non-uniformity in the stress values inside the inhomogeneity, mainly near the matrix–inhomogeneity interface, and this is a consequence of the discretization of the model.

We plot all the stress components in an arbitrarily chosen element near the centroid of the inhomogeneity against the normalized load step. All such plots from the analyses are shown below.

3.1 Elastic/Perfectly Plastic Inhomogeneity

Figures 6b and 7b show that after the transition from the elastic phase to the plastic phase, the normal stresses keep changing but the shear stresses tend to be constant

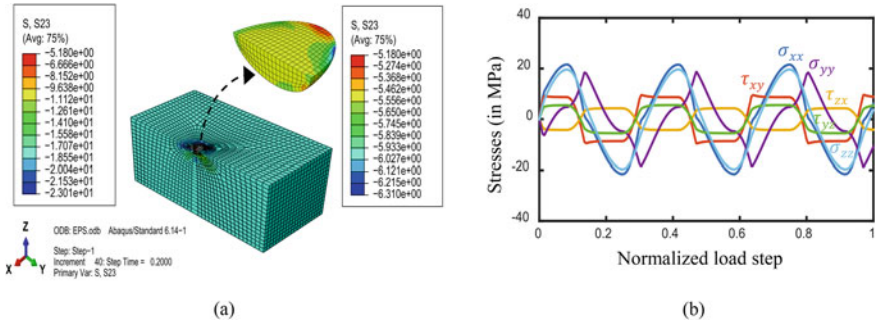

Fig. 6 **a** Surface plot of τ_{yz} in a quarter of the model consisting of the ellipsoidal [1 mm, 0.75 mm, 0.5 mm] elastic/perfectly plastic inhomogeneity embedded in the elastic matrix, at a normalized load step of 0.2. **b** Stress components inside the inhomogeneity for the same model under sinusoidal far-field stresses are in Table 3

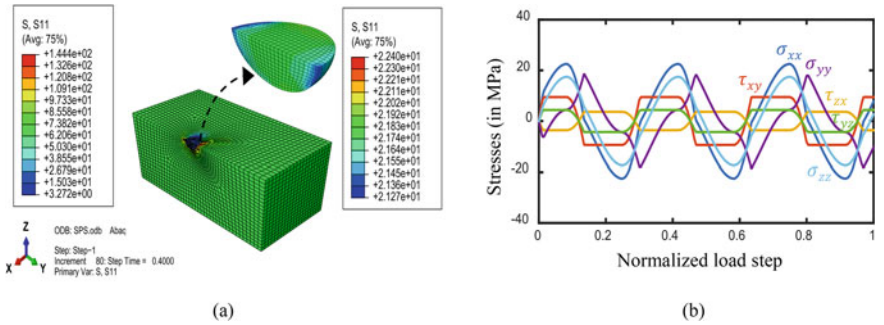

Fig. 7 **a** Surface plot of σ_{xx} in a quarter of the model consisting of the spherical [1 mm] elastic/perfectly plastic inhomogeneity embedded in the elastic matrix, at a normalized load step of 0.4. **b** Stress components inside the inhomogeneity for the same model under sinusoidal far-field stresses are in Table 3

(nearly flat lines). These results are in agreement with the J_2 flow theory because yielding is a result of deviatoric stresses and not hydrostatic stresses. It is also seen that the amplitude of the stress components does not change. This is expected for an elastic/perfectly plastic material.

3.1.1 Ellipsoidal Inhomogeneity

We studied mesh convergence for all the simulations. Table 5 details the mesh convergence study for elastic/perfectly plastic ellipsoidal inhomogeneity embedded inside an elastic matrix at 100th time step of the sinusoidal loading.

An element is chosen near the centroid in each of the coarser and the finer mesh models. The stress values in the element are taken at the 100th time step. It is clear from the table that the results obtained with the finer mesh are closer to those obtained with the coarser mesh. Thus, it is clear that the results have converged. Moreover, the results with finer mesh are shown in this paper.

3.1.2 Spherical Inhomogeneity

See Fig. 7.

3.2 Elastic/Linear Isotropic Hardening Inhomogeneity

Figures 8b and 9b show that even after the transition from the elastic phase to the plastic phase, the stresses behave in a non-linear fashion. It can be noticed that the amplitude of the stress components increases with the normalized load step. This behavior is expected for an elastic/linear isotropic hardening material.

3.2.1 Ellipsoidal Inhomogeneity

See Fig. 8.

3.2.2 Spherical Inhomogeneity

Table 6 details the mesh convergence study for elastic/linear isotropic hardening plastic ellipsoidal inhomogeneity embedded inside an elastic matrix at 150th time step of the sinusoidal loading. An approach similar to the one adopted earlier is used in this case as well. Moreover, the results obtained with the finer mesh are closer to those with the coarser mesh, and hence it can be said that mesh convergence has been achieved.

Table 5 Mesh convergence study of the elastic/perfectly plastic ellipsoidal inhomogeneity at 100th time step

Elements	σ_{xx}	σ_{yy}	σ_{zz}	τ_{yz}	τ_{zx}	τ_{xy}
58,984	−5.8581 MPa	11.0231 MPa	−3.5832 MPa	−5.2842 MPa	4.1646 MPa	−8.8386 MPa
84,032	−6.0163 MPa	10.9146 MPa	−3.6425 MPa	−5.2959 MPa	4.1815 MPa	−8.8751 MPa
%	2.7007	0.9843	1.6516	0.2213	0.4051	0.4129

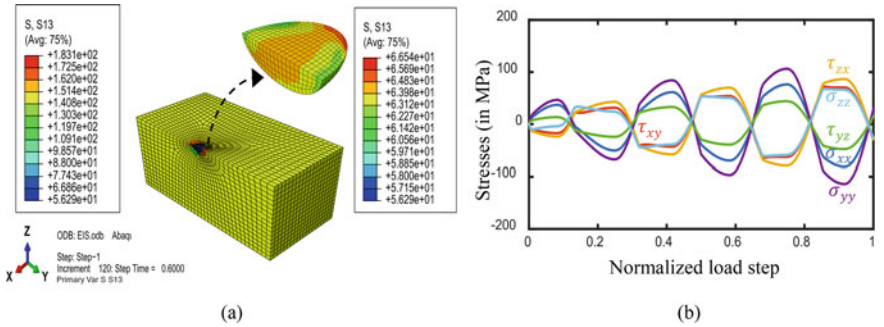

Fig. 8 **a** Surface plot of τ_{zx} in a quarter of the model consisting of the ellipsoidal [1 mm, 0.75 mm, 0.5 mm] elastic/linear isotropic hardening inhomogeneity embedded in the elastic matrix, at a normalized load step of 0.6. **b** Stress components inside the inhomogeneity for the same model under sinusoidal far-field stresses are in Table 4

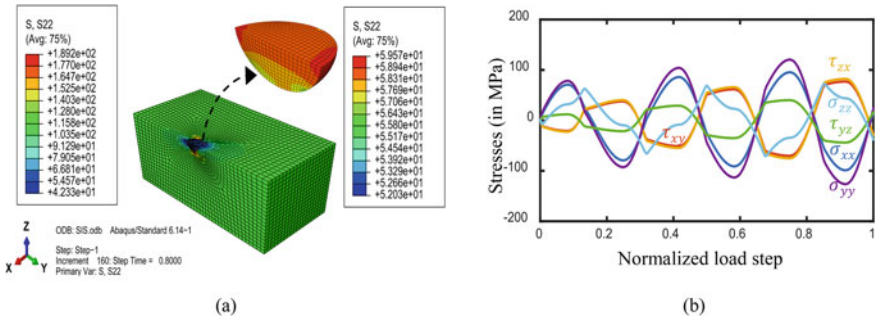

Fig. 9 **a** Surface plot of σ_{yy} in a quarter of the model consisting of the spherical [1 mm] elastic/linear isotropic hardening inhomogeneity embedded in the elastic matrix, at a normalized load step of 0.8. **b** Stress components inside the inhomogeneity for the same model under sinusoidal far-field stresses are in Table 4

4 Conclusions and Future Work

In this paper, the stress–strain behavior in a single elasto-plastic ellipsoidal inhomogeneity embedded inside an infinite isotropic elastic matrix subjected to sinusoidal far-field stresses is investigated using ABAQUS. The study is done for two different material models, viz., elastic/perfectly plastic material model and elastic/linear isotropic hardening material model. The results for both material models are not shown in a single plot because the simulations are done for different loadings in each case, and the reason behind this approach is to validate this work with the work done by Jana and Chatterjee [4]. Nevertheless, this serves its purpose, i.e., we can easily distinguish between the two material behaviors from separate plots.

We also investigated two different shapes of the inhomogeneity namely a general ellipsoid and a sphere, i.e., a special ellipsoid. Moreover, the results for both

Table 6 Mesh convergence study of the elastic/linear isotropic hardening plastic ellipsoidal inhomogeneity at 150th time step

Elements	σ_{xx}	σ_{yy}	σ_{zz}	τ_{yz}	τ_{zx}	τ_{xy}
59,438	96.1036 MPa	119.9842 MPa	−34.5692 MPa	39.6379 MPa	−73.8119 MPa	−70.6183 MPa
85,440	95.4734 MPa	120.4590 MPa	−34.5892 MPa	40.0931 MPa	−75.1702 MPa	−70.1357 MPa
%	0.6557	0.3957	0.0579	1.1482	1.8402	0.6834

geometric models, viz., ellipsoidal and spherical are not shown in the same plot because there is no difference in the mechanics since a sphere is a special case of an ellipsoid. Similar stress behaviors are observed for both geometric models. The major contribution of this work is the preliminary study of stress behavior inside the ellipsoidal inhomogeneity, and this work can be extended to other material models as well. In future, a semi-analytical method, based on Eshelby's approach, can be developed to study the stress behavior, and in that case, this work would be used as validation for the results obtained from the semi-analytical method developed.

References

1. Zhou K, Hoh J, Wang X, Keer L, Pang J, Song B, Wang Q (2013) A review on recent works on inclusions. Mech Mater 60:144–158
2. Eshelby JD (1957) The determination of the elastic field of an ellipsoidal inclusion, and related problems. Proc R Soc Lond A 241:376–396
3. Mura T (1987) Micromechanics of defects in solids. Martinus Nijhoff, Dordrecht
4. Jana P, Chatterjee A (2014) An internal damping formula derived from dispersed elasto-plastic flaws with Weibull-distributed strengths. Int J Mech Sci 87:137–149
5. Jana P (2017) Elastic-plastic behavior of an ellipsoidal inclusion embedded in an elastic matrix. Procedia Engineering, New Delhi
6. ABAQUS Inc. (2014) Analysis user's manual, release 6.14 documentation for ABAQUS
7. Kelly PA (2020) Mechanics lecture notes: introduction to plasticity. University of Auckland, Department of Engineering Science

Effect of Corrections in Smoothed Particle Applied Mechanics and Its Comparison with Molecular Dynamics Simulations for a Parkes Cantilever Beam

Kona Veera Ganesh and Puneet Kumar Patra

1 Introduction

The recent development of micro and nanosystems has been attracting researcher's attention in many different areas. The study of solids at micro and nano scales is complex, and usually, it requires the concepts from multiple scales. The concept of multiple length-scales is especially useful in understanding the problems of fracture mechanics, wherein a crack initiates at atomic scale and propagates to form a macro-sized crack. In this regard, material failure due to impact loading is an even more challenging problem due to high strain rate loading. In this case, material failure involves the formation of crack or deformation at the atomic scale and the behavior of non-linear elasticity and plastic flow at continuum scales. Simulating the whole structural member at the atomic scale is very difficult for researchers, the largest systems solved so far consist of a few billion atoms [1]. In contrast, even a mole of any substance comprises 10^{23} atoms.

The behavior of a projectile-impact loaded cantilever beam is a classical solid mechanics problem [6], and it has been studied for generating valuable results in elasto-plastic structural dynamics. In this problem, a cantilever beam is subjected to a projectile impact at the tip, and is frequently referred to as the Parkes cantilever problem [12]. This problem has been analyzed in details [1, 5] through analytical, numerical, and experimental methods. The Parkes cantilever beam problem is also a prototype for many other structural dynamic-impact problems. The essence of Parkes cantilever problem may be summarized as—the impact created by the projectile load causes a plastic hinge to form at the tip of the beam which then propagates through

Indian Institute of Technology Kharagpur

K. V. Ganesh · P. K. Patra (✉)
Department of Civil Engineering, Indian Institute of Technology Kharagpur, Kharagpur 721302, West Bengal, India
e-mail: puneet.patra@civil.iitkgp.ac.in
URL: http://www.springer.com/gp/computer-science/lncs

D. K. Maiti et al. (eds.), *Recent Advances in Computational and Experimental Mechanics, Vol II*, Lecture Notes in Mechanical Engineering,
https://doi.org/10.1007/978-981-16-6490-8_36

the beam length. The interaction between the projectile and the beam during the impact may lead to the penetration and perforation of the tip. The fracture mechanism of the Parkes cantilever beam was studied by Symonds and Fleming [13] using elasto-plastic large deflection analysis. This problem has been modelled through the finite element method [11, 13], however, mesh based methods suffer from inherent problems of inaccuracy and distortion when there are large local deformations. Consequently, particle based methods, such as Smooth Particle Hydrodynamics (SPH) also known as Smooth Particle Applied Mechanics [4] (SPAM), are more suited for modelling high-velocity impact problems [5].

SPAM is one of the simplest mesh-free methods or particle methods at the continuum scale. It is a grid-less Lagrangian mathematical technique, developed initially for astrophysical and cosmological problems. It is now being widely used in the computational fluid dynamics community and has been extended to solid mechanics problems as well [6]. Recent investigations suggest that the results from SPAM agree with those from experiments as well as other numerical techniques [2, 3, 7]. Due to its particle nature, SPAM is particularly very useful for modeling fragmentation and material separation. These phenomena are typically encountered when cracks form in the material, or the object undergoes large deformations. Molecular Dynamics (MD) simulations solve the Newtonian second law equations of motion for each particle. The interaction potential is used for deriving the forces acting on the particles, and the accuracy of the results depends on the selected interaction potential. Using MD, one can check the processes explaining the mechanism of deformation during atomic impact scales. Researchers [4, 10] have utilized the one-one interaction between MD and SPAM to explain the nature of the post-impact reaction. Travis and Hiddleston [14] compared a goal impacted by a rigid ball post-impact reaction and showed that MD and SPAM yielded results.

2 Molecular Simulations for Modeling Impact

In this section, we describe the methodology adopted for simulating the Parkes cantilever problem at atomistic scale. The geometrical details of the model are shown in Fig. 1. Our modelling of the problem closely follows that by Hiddleston [14] and Travis and Hoover and Hoover [4] for a free-free beam impacted by a rigid ball. In classical MD simulations, the equations of motion are developed through the Hamiltonian approach. Consider an isolated 2-dimensional system, that comprises N particles, and is governed by a Hamiltonian $\mathcal{H}$:

$$\mathcal{H} = \sum_{i=1}^{N} \frac{||\mathbf{p}_i||^2}{2m} + \Phi\left(\mathbf{r_1}, \mathbf{r_2}, \mathbf{r_3}, \ldots, \mathbf{r_N}\right), \tag{1}$$

where, $\mathbf{r}_i \equiv (x_i, y_i)$ and $\mathbf{p}_i \equiv (p_{xi}, p_{yi})$ denote the position and the momentum of the ith particle in the domain, and $\Phi\left(\mathbf{r_1}, \mathbf{r_2}, \mathbf{r_3}, \ldots, \mathbf{r_N}\right)$ denotes the potential energy

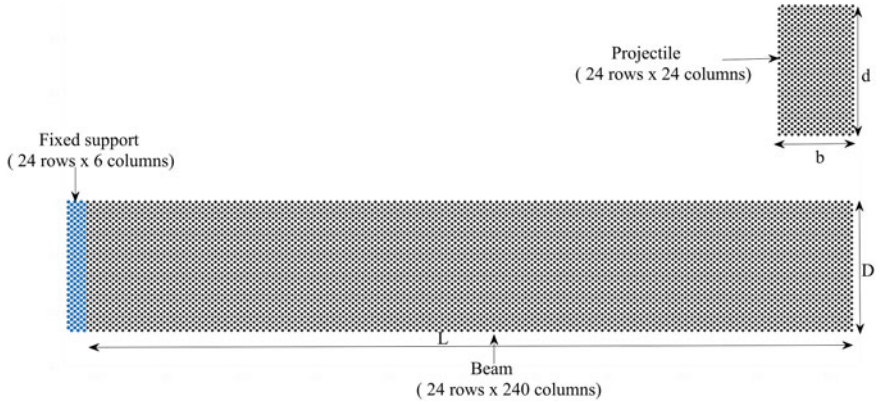

Fig. 1 The pre-deformed geometry of the Parkes cantilever beam and the projectile

of the system. Each particle has a mass m_i. The two $4N$ first-order equations of motion, therefore, become:

$$\frac{d\mathbf{r}_i}{dt} = \frac{\partial \mathcal{H}}{\partial \mathbf{p}_i} = \frac{\mathbf{p}_i}{m_i}, \quad \frac{d\mathbf{p}_i}{dt} = -\frac{\partial \mathcal{H}}{\partial \mathbf{r}_i} = -\frac{\partial \Phi}{\partial \mathbf{r}_i}. \tag{2}$$

The model is a 2-dimensional problem, so that we have to integrate the $4N$ ordinary differential equations that will obtain from the system at the microstate. In MD simulations, the most popular technique integrate these equations of motion can be integrated using the Velocity-Verlet algorithm [10], an accuracy of second order. Using this time-integration method, the updated position and the momentum of each particle can be obtained as follows,

$$\begin{aligned} \mathbf{r}_i(t + \Delta t) &= \mathbf{r}_i(t) + \frac{\mathbf{p}_i(t)}{m_i}\Delta t + \frac{1}{2}\frac{\mathbf{F}_i(t)}{m}\Delta t^2, \\ \mathbf{p}_i(t + \Delta t) &= \mathbf{p}_i(t) + \frac{1}{2}\left[\mathbf{F}_i(t) + \mathbf{F}_i(t + \Delta t)\right]\Delta t. \end{aligned} \tag{3}$$

In MD simulations, an interaction potential is used for deriving the forces acting on the particles, and the accuracy of the results depends on the selected interaction potential. In this work, we use the simple (m, n) potential of the system as follows,

$$\Phi_{m,n} = \frac{m}{n-m}\left(2 - r_{ij}^2\right)^n - \frac{n}{n-m}\left(2 - r_{ij}^2\right)^m \tag{4}$$

This potential is used for modelling the intra-particle interaction of the beam and the projectile particles. The parameters m and n represent positive integer constants that define the material strength are taken as 2 and 4, respectively. The cross-interactions between the particles of the beam and the projectile are modeled through a potential of the form:

$$\Phi_{b,p} = \omega \left[1 - \left(\frac{r_{ij} - R}{\sigma} \right)^2 \right]^4 \tag{5}$$

where r_{ij} is the distance between the i and j particles, $\omega = 100$ denotes the interaction strength between the particles, R is a distance parameter which allows soft-sphere collision between the beam and the projectile particles, is taken as 6 units and $\sigma = 0.80$ is the length scale parameter. Previously, similar potentials have been used by other researchers [3, 5] for studying multiscale phenomena. The particles of the projectile are initialized at a specific velocity v.

3 Smooth Particle Applied Mechanics with Impact Modeling

In the Smooth Particle Applied Mechanics (SPAM), the entire domain is discretized into a set of particles with continuum properties. These particles interact through the kernel function, such that every particle in the domain satisfies the fundamental conservation equations. For more information, the readers are recommended to refer to the work by Hiddleston and Travis [14] and other references therein.

3.1 Basic Conservation Equations

The basic conservation equations in continuum mechanics are,

$$\begin{aligned} \frac{d\rho}{dt} &= -\rho \frac{\partial v^\beta}{\partial x^\beta}, \\ \frac{dv^\alpha}{dt} &= -\frac{1}{\rho} \frac{\partial \sigma^{\alpha\beta}}{\partial x^\beta}, \\ \frac{de}{dt} &= -\frac{\sigma^{\alpha\beta}}{\rho} \frac{\partial v^\alpha}{\partial x^\beta}, \text{ and} \\ \frac{dx^\alpha}{dt} &= v^\alpha. \end{aligned} \tag{6}$$

For any material point of view, ρ denotes its mass density of the material, e is the specific internal energy, v^α and $\sigma^{\alpha\beta}$ are respectively the elements of velocity and Cauchy stress tensor, x^α is the spatial coordinate and d/dt is the time derivative taken in the moving Lagrangian frame. In a 2D problem, the indices of α and β take the values $1-3$, which represent the X, Y, and Z-directions. For our case, the Parkes cantilever problem is modeled as a plane strain problem, where the dimension along the Z-direction is taken to be unity. As the stresses developed in the Z-direction are small when compared to the other two directions, we neglect them in the further

analysis. In SPAM, kernel functions are used to approximate the field variable in the domain. We use Lucy's 2-dimensional kernel function in the present work:

$$w(r_{ij} \leq h) = \frac{5}{\pi h^2}\left[1 + 3\left(\frac{r_{ij}}{h}\right)\right]\left[1 - \left(\frac{r_{ij}}{h}\right)\right]^3. \tag{7}$$

where r_{ij} is the distance between the ith and jth particles, and h represents the smoothening length of the kernel function, taken as 3 units here. The discretized form of the above basic conservation equations can be written as:

$$\begin{aligned}
\frac{d\rho_i}{dt} &= \sum_j m_j v_{ij}^{\beta} w_{ij,\beta}, \\
\frac{dv_i^{\alpha}}{dt} &= \sum_j m_j \left(\frac{\sigma_i^{\alpha\beta}}{\rho_i^2} + \frac{\sigma_j^{\alpha\beta}}{\rho_j^2}\right) w_{ij,\beta}, \\
\frac{de_i}{dt} &= -\frac{1}{2}\sum_j m_j v_{ij}^{\alpha} \left(\frac{\sigma_i^{\alpha\beta}}{\rho_i^2} + \frac{\sigma_j^{\alpha\beta}}{\rho_j^2}\right) w_{ij,\beta}, \text{ and} \\
\frac{dx_i^{\alpha}}{dt} &= v_i^{\alpha}.
\end{aligned} \tag{8}$$

where, $v_{ij} = v_i - v_j$ is the relative velocity between ith and jth particles and the summation over j indicates that summation over the particles that lie within the support of kernel function, and $w_{ij,\beta} = \partial w_{ij}/\partial \mathbf{x}^{\beta}$. The stress tensor $\sigma^{\alpha\beta}$ divided into its hydrostatic (P_i) and deviatoric stress ($s^{\alpha\beta}$) components:

$$\sigma_i^{\alpha\beta} = P_i \delta^{\alpha\beta} - S_i^{\alpha\beta}. \tag{9}$$

The hydrostatic pressure P_i may be obtained from the above mentioned variables, such as e_i and ρ_i from the mechanical equation of state (EoS). The EoS used in this simulation analysis is taken as:

$$P_i = -12\rho_{i,0}\left[\left(2 - \frac{\rho_{i,0}}{\rho_i}\right)^3 - \left(2 - \frac{\rho_{i,0}}{\rho_i}\right)\right]. \tag{10}$$

The deviatoric stress rate may be derived from its rate equation, which is mathematically represented by:

$$\dot{S}_i^{\alpha\beta} = 2\mu\left(\dot{\epsilon}_i^{\alpha\beta} - \frac{1}{3}\delta^{\alpha\beta}\dot{\epsilon}_i^{\gamma\gamma}\right), \tag{11}$$

Here $\epsilon^{\alpha\beta}$ is the component of the strain rate tensor, and is given by:

$$\dot{\epsilon}_i^{\alpha\beta} = \frac{1}{2}\left(\frac{\partial v^{\alpha}}{\partial x^{\beta}} + \frac{\partial v^{\beta}}{\partial x^{\alpha}}\right), \tag{12}$$

Table 1 The various material properties used in the SPAM simulations. Readers are directed to Travis and Hiddleston's work [14] to consider how such properties can be derived from MD simulations

Parameter	Value
Bulk modulus (B)	27.713
The velocity of sound (c)	5.657
Shear modulus (μ)	13.856
Elastic modulus (E)	36.950
Yield stress (σ_y)	1.360
Ultimate stress (σ_u)	4.270

To account for material yielding in SPAM simulations, we use the simplest model of the Von-Mises failure theory. The yielding and plastic behavior is brought into the model through the radial-return plasticity algorithm [2]. Whenever the second invariant of the deviatoric stress tensor for each particle $J_{2,i} = \frac{1}{2}\epsilon^{\alpha\beta}\epsilon^{\alpha\beta}$ exceeds the value of $\frac{\sigma_y^2}{3}$ (where σ_y is uniaxial yield stress), the particle yields. Upon yielding, the individual deviatoric stress components are brought back to the yield plane using:

$$S_i^{\alpha\beta} \rightarrow f \times S_i^{\alpha\beta} = \frac{\sigma_y}{\sqrt{3J_{2,i}}} \times S_i^{\alpha\beta}, \tag{13}$$

Here we assume that, the beam material failure occurs when the maximum shear stress exceeds the ultimate strength of the material (σ_u):

$$\frac{1}{2}\left(\sigma_i^{xx} + \sigma_i^{yy}\right) \geq \sigma_u, \tag{14}$$

then the Eq. 14 is satisfied, the deviatoric stresses of the system are zeroed, and the density is reset to the stress- free density of material $\rho_{i,0}$. The continuum scale properties used in the SPAM simulations are listed in Table 1.

3.2 Adding of All Corrections into the SPAM Equations

Jaumann Stress Rate Correction In this correction, the deviatoric stress tensor is obtained through the frame invariant Jaumann stress rate. The deviatoric stress rate components of Eq. 11 are as follows:

$$\dot{S}_i^{\alpha\beta} = 2\mu\left(\dot{\epsilon}_i^{\alpha\beta} - \frac{1}{3}\delta^{\alpha\beta}\dot{\epsilon}_i^{\gamma\gamma}\right) + S_i^{\alpha\gamma}\Omega_i^{\beta\gamma} + S_i^{\gamma\beta}\Omega_i^{\alpha\gamma}. \tag{15}$$

where $\Omega^{\alpha\beta}$ denotes a spin tensor, and it mathematically represents as follows:

$$\Omega_i^{\alpha\beta} = \frac{1}{2}\left(\frac{\partial v^\alpha}{\partial x^\beta} - \frac{\partial v^\beta}{\partial x^\alpha}\right). \tag{16}$$

The velocity gradient of each particle can be computed as:

$$\frac{\partial v^\alpha}{\partial x^\beta} = -\sum_j v_{ij}^\alpha w_{ij,\beta}\frac{m_j}{\rho_j}. \tag{17}$$

Artificial viscosity correction Monaghan and Gingold [3, 8] developed the artificial viscosity correction to solve the problem of sudden shocks in the computational domain [9]. In this approach, artificial viscosity terms are used in the momentum and the energy conservation equations. The artificial viscosity converts the part of the kinetic energy to internal energy and removes the discontinuities in the computational domain. The discontinuous of the field variables are replaced by rapidly changing continuous field variables at every time step in the simulation. The forms of artificial viscosity correction in the momentum and energy equations are as follows,

$$\begin{aligned}\frac{dv_i^\alpha}{dt} &= \sum_j m_j\left(\frac{\sigma_i^{\alpha\beta}}{\rho_i^2} + \frac{\sigma_j^{\alpha\beta}}{\rho_j^2} - \pi_{ij}\delta^{\alpha\beta}\right)w_{ij,\beta},\\ \frac{de_i}{dt} &= -\frac{1}{2}\sum_j m_j v_{ij}^\alpha\left(\frac{\sigma_i^{\alpha\beta}}{\rho_i^2} + \frac{\sigma_j^{\alpha\beta}}{\rho_j^2} - \pi_{ij}\delta^{\alpha\beta}\right)w_{ij,\beta}.\end{aligned} \tag{18}$$

where π_{ij} denotes the artificial viscosity, whose mathematical representation is as follows:

$$\pi_{ij} = \left\{\begin{array}{ll}\dfrac{-\alpha_1\bar{C}_{ij}\mu_{ij} + \beta_1\mu_{ij}^2}{\bar{\rho}_{ij}}, & \text{if}\sum_\alpha v_{ij}^\alpha x_{ij}^\alpha \le 0\\ 0, & \text{otherwise}\end{array}\right\} \tag{19}$$

Here α_1 and β_1 are the strength controlling parameters of artificial viscosity, $\mu_{ij} = \frac{\sum_\alpha h v_{ij}^\alpha x_{ij}^\alpha}{\sum_\alpha x_{ij}^\alpha x_{ij}^\alpha + 0.01h^2}$, $\bar{C}_{ij} = \frac{1}{2}(C_i + C_j)$, $C_i = \sqrt{E/\rho_i}$ and $\bar{\rho}_{ij} = \frac{1}{2}(\rho_i + \rho_j)$.

XSPH correction This correction is adopted to prevent large scale particle penetrations between the impacting bodies. It is also known as the XSPH correction [7]. This correction modifies the actual velocity of the particles through a weighted averages of the surrounding particles, and allows the particles to exhibit an averaged velocity that can be mathematically expressed as:

$$\frac{dx_i^\alpha}{dt} = v_i^\alpha - \eta\sum_j \frac{m_j v_{ij}^\alpha}{\bar{\rho}_{ij}}w_{ij}, \tag{20}$$

where, η denotes a dimensionless constant, is taken as 0.05.

4 Results from MD and SPAM Simulations

4.1 Comparison of Kinetic Energy

For problems involving impact loading, the kinetic energy of the projectile is transferred to the object. Depending on the initial kinetic energy of the projectile, different post-impact responses are observed at both scales. However, a direct quantitative comparison of the kinetic energy obtained from the MD simulations cannot be compared with those from SPAM simulations, except perhaps at the initial time-stages of the models. Figure 2 shows the comparison of the kinetic energy obtained from MD simulations and those from SPAM with different corrections. For all cases, the velocity of the projectile is chosen as 1.5 units downwards. In MD, the kinetic energy of the system decreases rapidly at the initial stages. During these stages, the kinetic energy of the system is converted to the potential energy. After this initial decrease, the kinetic energy of the system remains fairly constant. The vibrational component of the kinetic energy dominates over the translation part. As the simulations have been performed at constant energy ensemble, there is no provision for energy taken out of the system, and hence the total kinetic energy remains fairly constant. Note that the MD results may change for simulations at a constant temperature ensemble. In the SPAM simulations, the situation is completely different. Here the kinetic energy of the system continues to decrease until the entire kinetic energy is converted completely to the internal energy of the system. While generating the kinetic energy plots for both simulations, the best agreement was found that when there are no corrections applied in the SPAM model—SPAM with artificial viscosity correction comes very close, but the agreement is limited up to the initial time-stages. Interest-

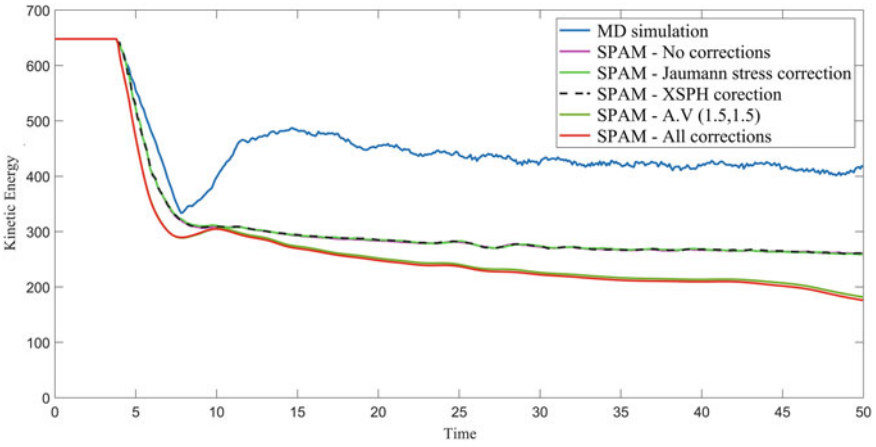

Fig. 2 Comparison of the kinetic energy of the system obtained from SPAM and MD simulations. The initial velocity of the projectile is 1.5 units

ingly, SPAM with all corrections is qualitatively able to describe the dip and increase of kinetic energy observed in the MD simulations around 7.5 time units. However, SPAM being continuum scale model does not allow particle vibrations, and hence, a fair comparison of kinetic energy between the SPAM and MD models cannot be made.

4.2 Comparison of the Deformation Profile

Possibly the best way of comparing the MD results with those from SPAM is by looking at the deformation profiles. The deformation profile of the beam and the projectile post-impact are shown in Figs. 3 and 4. Even though both the methods are particle-based, as they solve different differential equations at different scales, one cannot expect exactly the same response from them. However, as unlike SPAM, MD simulations are free from any assumptions, one can use MD results to improve upon the SPAM modelling. We play around with the parameters of SPAM corrections so that the deformation profile of the beam after 50-time units nearly matches with the MD simulation. Notice that the deformation profile of the beam and projectile, which are developed post impact is different for MD and SPAM simulations without any corrections. Moreover, one can observe the separation of particles at the top surface of the beam after impact. Such kind of separation happens due to the tensile instability in the SPAM simulations. The effects of tensile instability can be observed when only

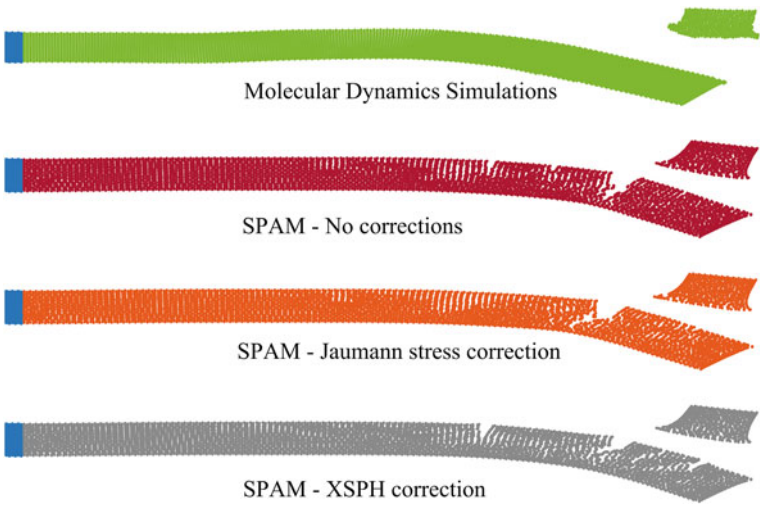

Fig. 3 The response for the different cases after 50 time units (light green shows the results of MD simulations, red highlights SPAM results without any corrections, brown shows that SPAM with Jaumann stress correction, and black is for SPAM with XSPH correction at the same time)

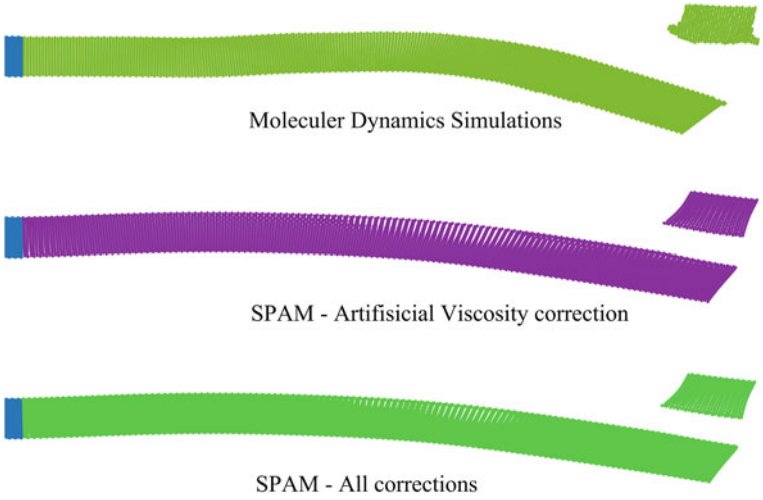

Fig. 4 The response of remaining cases after 50 time units (light green shows the results of MD simulations, purple highlights SPAM results with artificial viscosity correction, and green shows that SPAM with all correction at the same time)

the XSPH correction and the Jaumann stress rate correction are applied to the SPAM modelling. The unphysical surface cracks reduce somewhat when Jaumann stress rate correction is adopted. However, using XSPH correction worsens the situation. The deformation profile slightly changes from that due to SPAM without any corrections. However, no significant agreement with MD results is obtained due to these two corrections applied standalone. The results tend to change significantly once the artificial viscosity corrections (coefficients equal to 1.5 and 1.5) are implemented as can be seen from Fig. 4 (purple). The deformation profile of the beam model starts to look similar to that obtained from the MD simulations, and there are no visible cracks on either the top surface of the beam or the point of impact. This, though, comes at a cost—employing artificial viscosity means an unphysical transfer of the kinetic energy to the viscous energy.

Lastly, the deformed shape shown in green color of Fig. 4 indicates SPAM results with all corrections. If all the corrections described in the SPAM simulations are included in the modelling, the post-impact deformation profile of the beam and projectile looks very similar to the MD simulations deformation profile. We see that although specific corrections do not contribute to significant changes, all corrections converge to get the closest results to the MD simulations. Similar to that in the SPAM model, a kink is observed in the MD results. However, a qualitative agreement between the two is not obtained. This could be because of the way the plasticity is incorporated in the SPAM model—as the shear stress exceeds the yield strength, all stresses are brought back to the yield plane. Such simplified assumption is not there in MD simulations.

4.3 Centrosymmetry Parameter and Radial Distribution Function

The Centrosymmetry parameter (CSP) [10] of system lattices can be used to distinguish them from other structures such as crystal defects where the local bond symmetry is broken, etc. It is quantifies that the local loss of centrosymmetry at every particle site, which is characteristic for most crystal defects. The CSP value of a particle having N nearest neighbors is defined as,

$$CS(i) = \sum_{j=1}^{N/2} |r_{i,j} - r_{i,j+N/2}|^2 \tag{21}$$

where $r_{i,j}$ denotes the relative position vector of the jth nearest neighbor of the ith particle, and the sum is carried over half the nearest neighbor particles $(N/2)$. For our case, the closest neighbors are six because the particles are arranged on a triangular lattice. CSP for each atom (except those at surfaces of the beam) would be 0 in a perfectly symmetrical arrangement. So we use CSP to determine if the triangular lattice structure stays as it is with time. These findings are presented in the following Fig. 5. Now we compare the radial distribution function (RDF) obtained from MD simulations and those obtained from SPAM without any corrections and with all corrections. RDF is used to describe the particle distribution with respect to

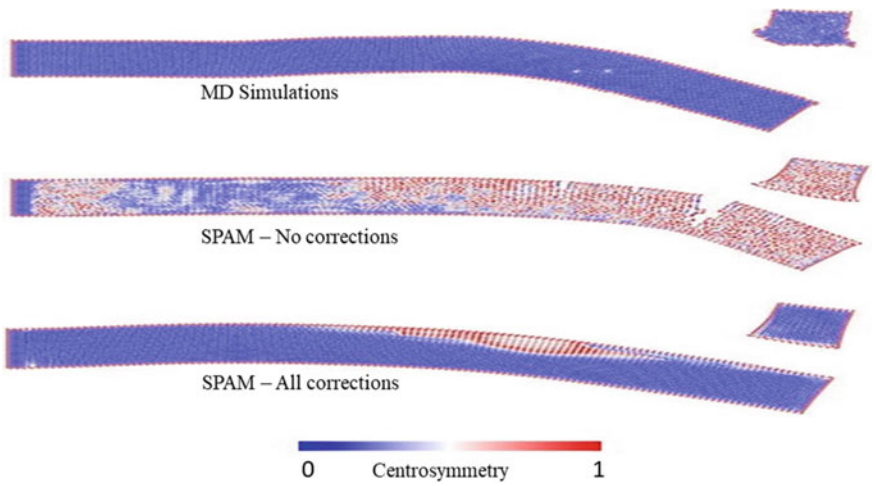

Fig. 5 Comparison of parameter centrosymmetry shows that Shift in the partition distribution from the original triangular lattice. The triangular lattice remains in MD except on the surface of the beam. Without any In SPAM Corrections, all over the triangular lattice is missed. A better lattice structure developed after Many corrections are used in SPAM. These Results Were obtained from Ovito software

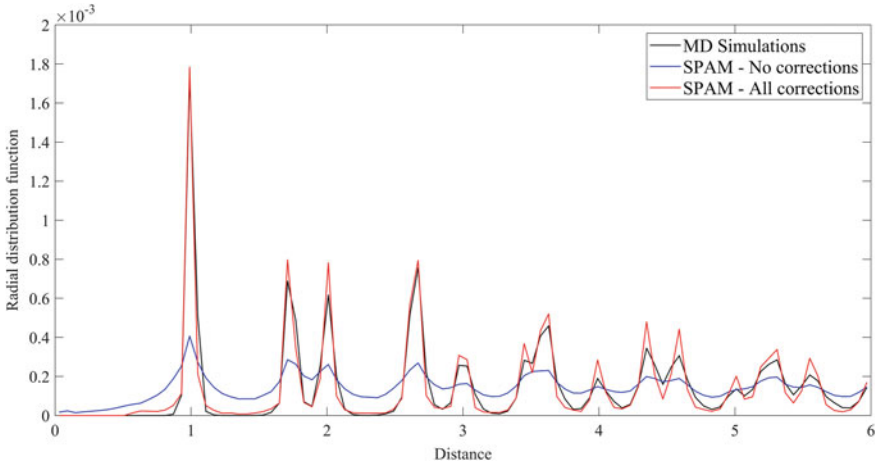

Fig. 6 Comparison of RDF obtained from MD simulations, SPAM without corrections, and SPAM with all corrections

any reference particle in the system. RDF has been calculated as a similar way given in the book [10], and the values of RDF parameters are chosen as, max $\Delta R = 0.01$, $R = 6.0$. Our purpose of comparing RDFs of MD with SPAM is simply to understand the particle distribution, particularly when the various corrections are placed on the SPAM equations. These results are shown in Fig. 6 As is evident from Fig. 6, SPAM correctly describes the RDF peaks obtained from MD simulations with all the corrections. But the peaks are not as sharp, and the main peaks are surrounded by smaller peaks. This occurs predominantly due to tensile instability.

5 Conclusion

MD and SPAM simulations are important particle-based methods to study the impact mechanics at atomistic and continuum scales, respectively. Our goal in this problem is to carefully match the SPAM (or SPH) simulations using the failure behavior of the Parkes cantilever beam to that obtained from MD simulations. This has been achieved by adding various corrections to the classical SPAM simulations—artificial viscosity corrections, XSPH corrections, and Jaumann stress corrections. A qualitative comparison indicates that while individual corrections do not result in improved agreement of SPAM with MD, all corrections put together provide results of SPAM that agree fairly well with MD. As is evident from the simulations, spurious cracks arising due to tensile instability still exist even when all corrections are imposed on SPAM. There are two ways in which tensile instability may be tackled—(i) inclusion of short-ranged artificial pressure correction and (ii) moving the analysis from Eulerian framework to Total Lagrangian framework. In the first approach, a short-

ranged repulsive pressure acts whenever two particles come closer than a predefined distance. In the second approach, the conservation equations are written in the undeformed reference configurations. However, in the present work, we do not explore this line of investigation.

Acknowledgements The authors acknowledge the support in part provided by the Indian Institute of Technology Kharagpur through its Institute Challenge Grant number MDE-ICG-2017.

References

1. Abraham FF, Walkup R, Gao H, Duchaineau M, De La Rubia TD, Seager M (2002) Simulating materials failure by using up to one billion atoms and the world's fastest computer: work-hardening. Proc Natl Acad Sci 99(9):5783–5787
2. Bednarcyk BA, Aboudi J, Arnold SM (2008) The equivalence of the radial return and Mendelson methods for integrating the classical plasticity equations. Comput Mech 41(5):733–737
3. Gingold RA, Monaghan JJ (1977) Smoothed particle hydrodynamics: theory and application to non-spherical stars. Mon Not R Astron Soc 181(3):375–389
4. Hoover WG (2006) Smooth particle applied mechanics: the state of the art
5. Johnson GR, Stryk RA, Beissel SR (1996) SPH for high velocity impact computations. Comput Methods Appl Mech Eng 139(1–4):347–373
6. Libersky LD, Petschek AG (1991) Smooth particle hydrodynamics with strength of materials. In: Advances in the free-Lagrange method including contributions on adaptive gridding and the smooth particle hydrodynamics method. Springer, pp 248–257
7. Monaghan JJ (2005) Smoothed particle hydrodynamics. Rep Prog Phys 68(8):1703
8. Monaghan JJ, Gingold RA (1983) Shock simulation by the particle method SPH. J Comput Phys 52(2):374–389
9. Parshikov AN, Medin SA (2002) Smoothed particle hydrodynamics using interparticle contact algorithms. J Comput Phys 180(1):358–382
10. Rapaport DC (2004) The art of molecular dynamics simulation. Cambridge University Press
11. Reid S, Gui X (1987) On the elastic-plastic deformation of cantilever beams subjected to tip impact. Int J Impact Eng 6(2):109–127
12. Shaw A, Reid S, Roy D, Chakraborty S (2015) Beyond classical dynamic structural plasticity using mesh-free modelling techniques. Int J Impact Eng 75:268–278
13. Symonds PS, Fleming W Jr (1984) Parkes revisited: on rigid-plastic and elastic-plastic dynamic structural analysis. Int J Impact Eng 2(1):1–36
14. Travis KP, Hiddleston T (2014) Multiscale modelling of material failure using particles. Mol Simul 40(1–3):141–153

Prediction of Elastic Constants of Spiral MWCNT-Reinforced Nanocomposites by Finite Element Analysis

Krishnendu Bhowmik, Hela Ambati, Niloy Khutia, and Amit Roy Chowdhury

1 Introduction

The discovery of carbon nanotube (CNT) along with the characterization of its synthesis by Iijima [1] enthused many researchers to examine its potential when reinforced in composites due to its spectacular mechanical properties such as ultra-high Young's modulus and tensile strength. The impact of waviness and agglomeration of CNTs on the effective stiffness is studied theoretically using micromechanics model [2] having a helical shape along with Eshelby's inclusion model. The spiral carbon nanotubes are used as a great alternative to enhance the fracture toughness of the composites [3]. It is observed by the characterization of nanomechanical properties of spiral CNT-reinforced epoxy composites using nanoindentation tests [4] that these CNTs scattered well and strongly bind with the epoxy matrix, which led to the enhancement of mechanical and thermal properties. A detailed study on various possible geometries of spiral CNTs to obtain from torus CNTs is conducted [5] specifying the skewness of corresponding spiral CNTs. Using classical molecular dynamics (MD) simulations, the mechanical properties of spiral CNTs and a single-walled carbon nanotubes (SWCNTs) are compared indicating spiral CNT is much less stiff and has a much larger pull-out force than SWCNT in a polyethylene matrix [6]. Multidimensional force spectroscopy technique is applied to spiral CNT under compression, buckling and bending to record frictional phenomena of CNTs [7]. The essential considerations deciding the physical properties of spiral CNTs are to verify whether the core is amorphous or with MWCNTs. Tian and Guo [8] reported the mechanical properties of carbon nano coils (CNCs) using MD method based on four types of nano coil models with heptagon defects. They observed that

K. Bhowmik (✉) · H. Ambati · N. Khutia · A. R. Chowdhury
Department of Aerospace Engineering and Applied Mechanics, Indian Institute of Engineering Science and Technology, Shibpur, Howrah 711103, India
e-mail: krishnendub@aero.iiests.ac.in

D. K. Maiti et al. (eds.), *Recent Advances in Computational and Experimental Mechanics, Vol II*, Lecture Notes in Mechanical Engineering,
https://doi.org/10.1007/978-981-16-6490-8_37

the tensile behaviour of the CNCs is dependent on the orientation of the defects. The vibration analysis of various hybrid composite beams using CNT as nanofiller shows that the stiffness and damping ratio can be improved due to frictional jerk between nanofillers and the matrix [9]. Using the molecular structural mechanics method, the mechanical properties of spiral SWCNTs are examined and the results show that the spring constant and the shear moduli of spiral CNTs increases as the tube diameter enlarges [10]. An MD finite element (FE) method is adopted for complex three-dimensional (3-D) structure of spiral defective CNTs and explored the effect of the dimensions of spiral CNTs on their mechanical properties [11]. The structural variations at different strains of double-walled carbon nano coils during the tension process are investigated showing that the nano coils have maximum stress and super-elastic characteristics similar to that of CNT with the same chirality [12]. The approach of engineering interphase at the molecular level is noteworthy to tackle the theoretical limits of mechanical properties [13]. The mechanical properties of interphase and its effects on elastic properties of composites are studied using various approaches [13–15]. It is reported by Pérez and Avilés [15] that interphase thickness has significant impact on the overall elastic properties and stress distribution of nanocomposite under loading when the modulus of matrix is low compared with the reinforcement (CNT). A Representative Volume Element (RVE)-based finite element (FE) analyses including various types of nanofillers have been carried out by developing a customized algorithm or by running python code to predict the elastic properties of spiral CNT nanocomposites [16–18]. The mechanical properties in axial and transverse directions are varied with the spiral width [16–18]. Khani et al. [16] demonstrated that effective Young's modulus and shear modulus of nanocomposite decreased with no. of coils of coiled carbon nanotube (CCNT). Yousefi et al. [17] also reported that overall Young's modulus of nanocomposite are reduced with no. of coils of CCNT. The nanomechanical properties of graphene spirals are investigated for various spiral inner and outer radii using molecular dynamics simulations [18]. Tserpes and Chanteli [19] show that effective axial modulus and Poisson's ratios are greatly dependent on height fraction (ratio of CNT height and RVE length). When height fraction is increased, the CNT ends become closer to the RVE, where loads are being applied. This leads to the fact that CNT behave like comparatively more stiff and more percentage of applied loads will be carried by the CNT and hence an increase in axial modulus. The extreme case, where CNT is continuous in RVE, the height fraction is 1 and maximum axial modulus is expected.

This article demonstrates the prediction of elastic constants for spiral MWCNT-reinforced nanocomposites in view of a square-based RVE using three-dimensional (3-D) finite element analyses for different height fractions (ratio of CNT height and RVE length), interphase properties and thickness, number of coils and volume fraction of MWCNTs.

2 Methodology

The effective elastic modulus of CNT-reinforced composite greatly depends upon modulus ratio, λ_1 (Young's modulus ratio of CNT and matrix); CNT aspect ratio, λ_2 (CNT height and diameter ratio); CNT height fraction, λ_3 (CNT height and RVE length ratio); CNT volume fraction, V_f (volume ratio of CNT and RVE) [20]. When CNT is reinforced with matrix, a layer of interphase exists between CNT and matrix [14, 15, 19]. The elastic modulus of interphase (E_{int}) have a crucial role in the overall elastic response of the composites. In this study, the variation of Young's modulus of interphase (E_{int}) is considered as an exponential function between E_p and E_m [15] as follows:

$$(E_{int})_{exp} = E_p e^{-(\frac{1}{t_i} ln \frac{E_p}{E_m})\Delta t_k} \tag{1}$$

where, E_p and E_m are the Young's modulus of particle (CNT) and matrix, respectively; t_i and Δt_k are interphase thickness and distance from the outer surface of CNT to mid-point of interphase. Further, the influence of imperfection in bonding between CNT and interphase is considered and represented by adhesion coefficient (K) as reported by Giannopoulos and Kallivokas [21] for calculation of interphase property. Giannopoulos and Kallivokas [21] demonstrated that the effective modulus of nanocomposite is influenced by the adhesion coefficient (K). The limiting case, $K = 1$ and 0, represent perfect bonding and complete de-bonding between CNT and interphase. In this present study, the values of K are considered as 1.0, 0.666 and 0.333 [21].

3 Finite Element Analysis

In this current study, MWCNTs are considered as solid annular tubes in square-based prismatic Representative Volume Element (RVE) [20, 22]. The length of the MWCNT, outer and inner diameter are taken as 350 nm, 7 nm and 2.24 nm, respectively. Young's modulus and Poisson's ratio of MWCNT are considered as 1000 GPa and 0.3, respectively [19]. The corresponding values for epoxy matrix are 3.5 GPa and 0.3, respectively [19]. Hence, λ_1 and λ_2 values are taken as 285.71 and 50, respectively, for all analyses. The nominal diameter of coils is taken as 17.5 nm. The interphase thicknesses are varied from 0 to 2.72 nm [19]. The interphase thickness is assumed as thickness of 0/2/4/6/8 layers of SWCNT thickness of 0.34 nm (0, 0.68, 1.36, 2.04 and 2.72 nm). The interactions between CNT/interphase and interphase/matrix are assumed to be glued together and represented by shared nodes between them [15–17, 19, 21] for simplicity. The Young's moduli of interphase considered in FE analysis are extracted from Eq. (1) for different interphase thickness and are presented in Table 1. Typical RVE with mesh and CNT with different number of coils (N) are presented in Figs. 1a and 1b, respectively. To demonstrate

Table 1 Young's modulus of interphase (GPa) considered in analysis

K	Interphase thickness	0.68 nm	1.36 nm	2.04 nm	2.72 nm
1.00	No. of Layer = 1	59.161	–	–	–
1.00	No. of Layers = 2	243.230	14.390	–	–
1.00	No. of Layers = 3	389.653	59.161	8.982	–
1.00	No. of Layers = 4	493.183	119.957	29.177	7.097
0.66	No. of Layers = 4	345.580	93.046	25.052	6.745
0.33	No. of Layers = 4	188.429	60.333	19.318	6.185

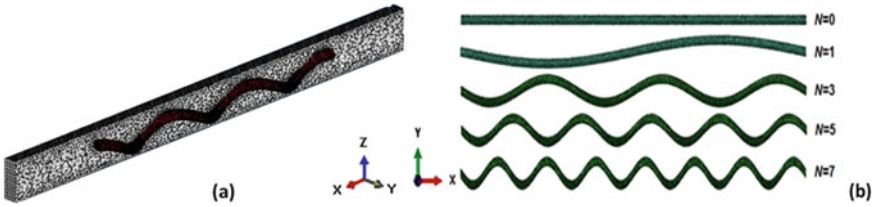

Fig. 1 Typical representation of **a** spiral CNT inside RVE (some portion of RVE is not shown) and **b** CNT with different number of coils (N)

the effect of coils, straight CNTs are also considered ($N = 0$). The typical mesh sizes for CNT, interphase and matrix are taken as 0.34 nm, 0.6 nm and 4 nm, respectively. The final mesh sizes are obtained after mesh sensitivity studies. For example, the number of nodes and elements (Abaqus 6.14, linear tetrahedral elements) are 97,307 and 502,332, respectively, for $N = 4$, t = 2.72 nm, $\lambda_3 = 0.8$ and $V_f = 1.0\%$. The linear elastic static analyses are considered in present study. The elastic properties are extracted by using Abaqus EasyPBC plugin tool [23] where periodic RVE homogenization method is used. The meshes are created in FE models in such a way that, periodic boundary constitutions of all faces can be applied. This EasyPBC tool creates required node sets, constraint equations and boundary conditions to calculate the overall elastic properties of the nanocomposites. The theory and algorithm used in EasyPBC plugin tool are outlined in Ref. [24].

4 Results and Discussions

4.1 Effect of Number of CNT Coils

The effect of the number of CNT coils with nominal diameter of 17.5 nm on elastic properties under specific considerations is shown in Figs. 2 and 3. The variation of Young's modulus of composite along the longitudinal axis (E_{11}) versus the number of coils for different volume fractions (0.5%, 1% and 1.5%) of CNT with height

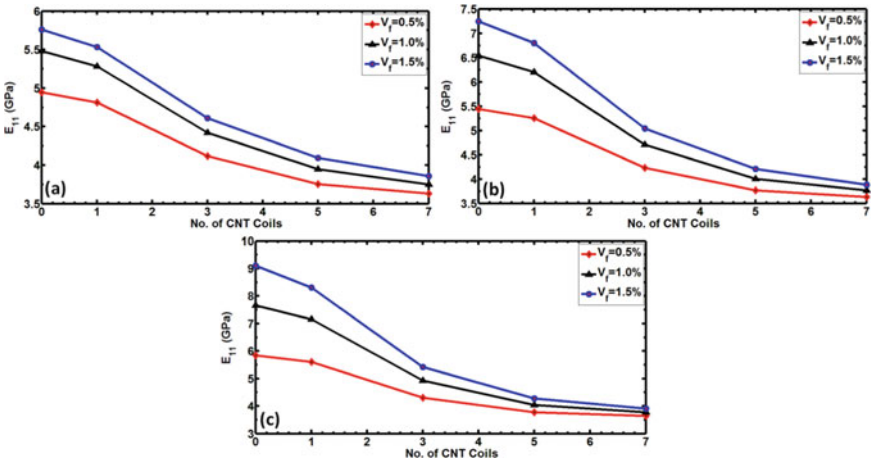

Fig. 2 Young's modulus (E_{11}) versus number of CNT coils for **a** $\lambda_3 = 0.4$, **b** $\lambda_3 = 0.6$ and **c** $\lambda_3 = 0.8$

fractions (λ_3) of 0.4, 0.6 and 0. 8 are shown in Figs. 2a, 2b and 2c, respectively. The numbers of coils of CNT (N) are taken as 0, 1, 3, 5 and 7 (Fig. 1b). Figure 2 indicates that Young's modulus (E_{11}) increases with the increase in CNT volume fraction (V_f) for the same number of coils and constant height fractions. Figure 2 also illustrates that with the increase in the number of coils, Young's modulus gradually decreases. The most extreme and least estimations of Young's modulus are 9.104 GPa (for $N = 0$, $\lambda_3 = 0.8$ and $V_f = 1.5\%$) and 3.6323 GPa (for $N = 7$, $\lambda_3 = 0.4$ and $V_f = 0.5\%$), respectively. The values of normalized axial Young's modulus (E_{11}/E_m) for straight CNT ($N = 0$) are compared with the values extracted from Extended rule of Mixtures (ERM) [20] and are presented in Table 2. A good agreement is found between results obtained by ERM and FE analysis for straight CNTs.

Figures 3a, 3b and 3c show the variations of E_{11}, E_{22} and E_{33} with the number of MWCNT coils (N), respectively, for $V_f = 1\%$. It is seen from the graphs that E_{11}, E_{22} and E_{33} values are higher for higher value of λ_3. E_{11} value reduces with an increase in the number of CNT coils (N). In Figs. 3b and 3c, the values of E_{22} and E_{33} are almost equal and decrease up to $N = 5$ and then increase till $N = 7$. The effects of number of coils on shear moduli (G_{12}, G_{13} and G_{23}) are explained in Figs. 3d, 3e and 3f, respectively. The plots 3(d) and 3(e) show similar variations in the results. The values of G_{12}, G_{13} are slightly varying for higher values of height fraction (λ_3). Figure 3f illustrates that for $V_f = 1\%$, there is very slight variation of values of G_{23} concerning the number of coils for $\lambda_3 = 0.4$, 0.6 and 0.8. The G_{23} values increase with the increase in the number of coils. The maximum and minimum values of G_{23} are 1.4025 GPa for $\lambda_3 = 0.8$ and 1.3709 GPa for $\lambda_3 = 0.4$, respectively. The variations of Poisson's ratio for $\lambda_3 = 0.4$, 0.6 and 0.8 are illustrated in Figs. 3g, 3h and 3i. The values of ν_{12}, ν_{13} increase up to $N = 3$ and then gradually decrease till $N = 7$ as depicted in Figs. 3g and 3h. In the case of Fig. 3i, the ν_{23} values decrease

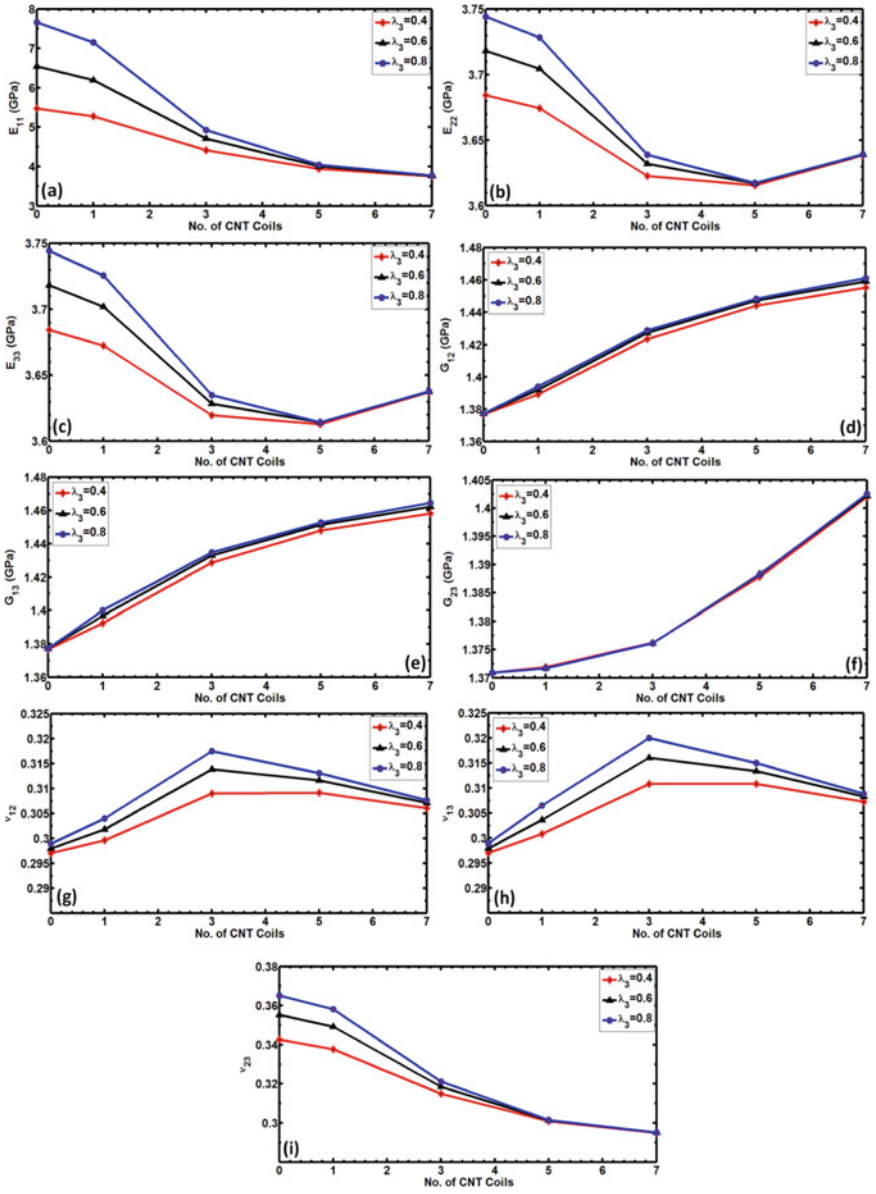

Fig. 3 Elastic properties versus number of CNT coils with $V_f = 1.0\%$ for **a** E_{11} **b** E_{22} **c** E_{33} **d** G_{12} **e** G_{13} **f** G_{23} **g** ν_{12} **h** ν_{13} and **i** ν_{23}

Table 2 Comparison of results obtained from FE analysis and ERM (for $N = 0$)

V_f	E_{11} (GPa) (FE)	E_{11}/E_m (FE)	E_{11} (GPa) (ERM)	E_{11}/E_m (ERM)	Error (%)
0.5%	4.9477	1.4136	5.0800	1.4514	2.6740
1.0%	5.4797	1.5656	5.3937	1.5410	–1.5713
1.5%	5.7626	1.6464	5.5160	1.5760	–4.2760

with the increase in the number of coils. The maximum values of ν_{12}, ν_{13} and ν_{23} are 0.3175 (for $N = 3$), 0.3200 (for $N = 3$) and 0.3651 (for $N = 0$), respectively. Similar trends of elastic properties variations with helix angle are observed by Khani et al. [16].

4.2 *Effect of Interphase Thickness*

The effect of thickness and adhesion coefficient of interphase on elastic properties against height fractions (λ_3) for $V_f = 1.0\%$ is outlined in Figs. 4 and 5. Figure 4 illustrates the variation of E_{11} and E_{22} with regard to height fraction (λ_3) for different values of the interphase thickness ($t = 0$, 0.68 nm, 1.36 nm, 2.04 nm and 2.72 nm) with $N = 3$. The value of E_{11} and E_{22} increases with the increase in thickness

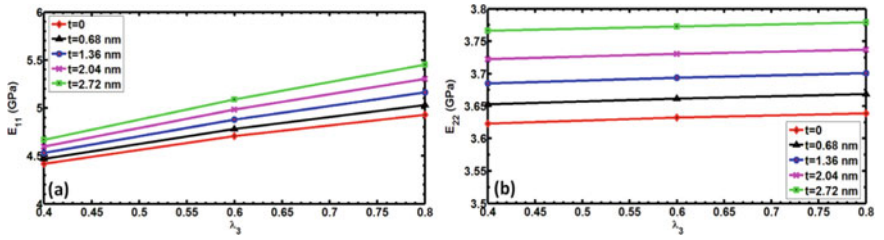

Fig. 4 **a** E_{11} and **b** E_{22} versus CNT height fraction (λ_3) for different interphase thickness with $V_f = 1.0\%$ and $N = 3$

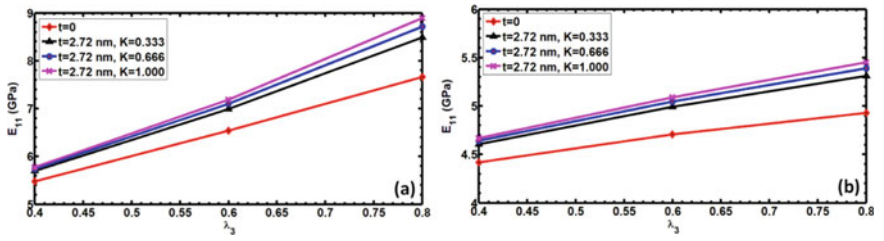

Fig. 5 E_{11} versus CNT height fraction (λ_3) with $V_f = 1.0\%$ for different values of K **a** $N = 0$ and **b** $N = 3$

of interphase for the same values of λ_3. A significant variation of E_{11} with height fraction (λ_3) is observed (Fig. 4a) and corresponding variations of E_{22} is relatively less (Fig. 4b). The maximum and minimum values of E_{11} are 5.4530 GPa (for $\lambda_3 = 0.8$ and $t = 2.72$ nm) and 4.4195 GPa (for $\lambda_3 = 0.4$ and $t = 0$), respectively. In Fig. 5, the variations of E_{11} against height fraction (λ_3) are shown with $N = 0$ and $N = 3$ for different values of adhesion coefficient K (0.333, 0.666 and 1.0 with $t = 2.72$ nm). Further, results are compared with that of $t = 0$. With the increase in the values of K, there is notable improvement seen in E_{11} values for a constant λ_3. The maximum and minimum values of E_{11} are 8.8928 GPa (for $\lambda_3 = 0.8$, $t = 2.72$ nm and $K = 1.0$) and 5.4797 GPa (for $\lambda_3 = 0.4$ and $t = 0$), respectively. Thus, there is a significant influence of the interphase on Young's modulus, especially in the longitudinal direction. The similar behaviour of interface effect is reported by Tserpes et al. [19] for straight CNT-reinforced nanocomposites.

5 Conclusions

In this paper, the homogenized elastic properties of the MWCNT have been extracted for square-based RVE using finite element analysis. The parameters considered in the study are the CNT volume fraction, height fraction, number of coils, the interphase adhesion coefficient and interphase thickness. The following concluding remarks can be drawn from the present study:

- The axial Young's modulus (E_{11}) values are higher for higher volume fraction (V_f) and height fraction (λ_3) of CNT. The extreme case where CNT is continuous in RVE ($\lambda_3 = 1$), the maximum E_{11} value is expected. The variation of E_{11} with height fraction (λ_3) is more compared with E_{22} or E_{33}.
- Increasing the number of coils leads to the reduction of effective axial Young's modulus (E_{11}) and enhancement of shear modulus. The E_{22} and E_{33} values reduce with no. of coils up to $N = 5$ and then slightly increase for $N = 7$. This may be due to the fact that the configuration of coiled CNT structure for $N = 7$, exhibit slightly more stiff behaviour in 2 and 3 directions and hence slight enhancement of E_{22} and E_{33}.
- Interphase plays a key role in enhancing elastic properties. The thickness of the interphase strongly influences Young's modulus (E_{11}) of the nanocomposite. Higher interphase thickness exhibits higher Young's modulus of composite.
- Interphase adhesion coefficient affects the directional Young's modulus especially in axial direction.

References

1. Iijima S (1991) Helical microtubules of graphitic carbon. Nature 354:56–58
2. Shi DL, Feng XQ, Huang YGY, Hwang KC, Gao HJ (2004) The effect of nanotube waviness and agglomeration on the elastic property of carbon nanotube-reinforced composites. J Eng Mater Tech 126(3):250–257
3. Lau KT, Lu M, Hui D (2006) Coiled carbon nanotubes: synthesis and their potential applications in advanced composite structures. Compos Part B 37(6):437–448
4. Li X-F, Lau K-T, Yin Y-S (2008) Mechanical properties of epoxy-based composites using coiled carbon nanotubes. Compos Sci Technol 68:2876–2881
5. Chuang C, Fan Y-C, Jin B-Y (2012) On the structural rules of helically coiled carbon nanotubes. J Mol Struct 1008:1–7. https://doi.org/10.1016/j.molstruc.2011.10.048
6. Wang J, Kemper T, Liang T, Sinnott SB (2012) Predicted mechanical properties of a coiled carbon nanotube. Carbon 50(3):968–976
7. Barber JR, Boyles JS, Ferri AA, Bottomley LA (2014) Empirical correlation of the morphology of coiled carbon nanotubes with their response to axial compression. J Nanotechnol. https://doi.org/10.1155/2014/616240
8. Tian L, Guo X (2015) Fracture and defect evolution in carbon nanocoil—a molecular dynamics study. Comput Mater Sci 103:126–133
9. Farrash SMH, Shariati M, Rezaeepazhand J (2017) The effect of carbon nanotube dispersion on the dynamic characteristics of unidirectional hybrid composites: an experimental approach. Compos B 122:1–8
10. Ghaderi SH, Hajiesmaili E (2012) Molecular structural mechanics applied to coiled carbon nanotubes. Comput Mater Sci 55:344–349
11. Ghaderi SH, Hajiesmaili E (2013) Nonlinear analysis of coiled carbon nanotubes using the molecular dynamics finite element method. Mater Sci Eng A 582:225–234
12. Ju S-P, Lin J-S, Chen H-L, Hsieh J-Y, Chen H-T, Weng M-H, Zhao J-J, Liu L-Z, Chen M-C (2014) A molecular dynamics study of the mechanical properties of a double-walled carbon nanocoil. Comput Mater Sci 82:92–99
13. Pramanik C, Nepal D, Nathanson M, Gissinger JR, Garley A, Berry RJ, Davijani A, Kumar S, Heinz H (2018) Molecular engineering of interphases in polymer/carbon nanotube composites to reach the limits of mechanical performance. Compos Sci Technol 166:86–94
14. Saber-Samandari S, Khatibi AA (2006) The effect of interphase on the elastic modulus of polymer based nanocomposites. Key Eng Mater 312:199–204
15. Hernández-Pérez A, Avilés F (2010) Modeling the influence of interphase on the elastic properties of carbon nanotube composites. Comput Mater Sci 47:926–933
16. Khani N, Yildiz M, Koc B (2016) Elastic properties of coiled carbon nanotube reinforced nanocomposite: a finite element study. Mater Des 109:123–132
17. Yousefi E, Sheidaei A, Mahdavi M, Baniassadi M, Baghani M, Faraji G (2017) Effect of nanofiller geometry on the energy absorption capability of coiled carbon nanotube composite material. Compos Sci Technol 153:222–231
18. Norouzi S, Kianfar A, Fakhrabadi MMS (2020) Multiscale simulation study of anisotropic nanomechanical properties of graphene spirals and their polymer nanocomposites. Mech Mater 103376. https://doi.org/10.1016/j.mechmat.2020.103376.
19. Tserpes KI, Chanteli A (2013) Parametric numerical evaluation of the effective elastic properties of carbon nanotube-reinforced polymers. Compos Struct 99:366–374
20. Bhowmik K, Kumar P, Khutia N, Chowdhury AR (2018) Evaluation of directional strength of SWCNT reinforced nanocomposites: a finite element study. Mater Today Proc 5:20528–20534
21. Giannopoulos GI, Kallivokas IG (2014) Mechanical properties of graphene based nanocomposites incorporating a hybrid interphase. Finite Elem Anal Des 90:31–40

22. Chen XL, Liu YJ (2004) Square representative volume elements for evaluating the effective material properties of carbon nanotube-based composites. Comput Mater Sci 29:1–11
23. Abaqus/CAE, Simulia. http://www.3ds.com/products/simulia/portfolio/abaqus. Accessed 18 May 2018
24. Omairey SL, Dunning PD, Sriramula S (2018) Development of an ABAQUS plugin tool for periodic RVE homogenization. Eng Comput 35:567–577

Transient Response Analysis in a Cylindrical Viscoelastic Waveguide Using a Nonlinear Model

Jothi Saravanan Thiyagarajan

1 Introduction

The guided ultrasonic wave propagation-based acoustic emission (AE) monitoring has broad application for nondestructive evaluation and structural health monitoring of cables in bridges and overhead transmission line conductors. It has the characteristics of propagating long distances along the waveguide [1–4]. The guided wave propagation and its dispersion characteristics are studied in the past for many decades. The classical wave equations in linear elastic and viscoelastic cylindrical waveguide materials are derived using the Pochhammar-Chree equation [5, 6]. In pioneering research carried out by outstanding researchers, the finite element method (FEM) and spectral FEM are utilized to study elastic stress wave propagation computation in a detailed manner [7–11]. The formulation using the semi-analytical finite element (SAFE) method is developed to reduce the computation cost and improve the guided ultrasonic wave mode propagation efficiency. Many scholars have made contributions for analyzing elastic and viscoelastic waveguides in the SAFE method, namely, laminated circular cylinders [12–15], hollow cylinders [16], plate laminates [17], rails [18], helical structure [19–21]. Due to the damping of material and the wave dispersion, the signal's energy or amplitude will decrease. The exciting research on transient ultrasonic guided wave propagation is studied for layered plates [22] and damped cylinders [23] using the SAFE method. They considered narrowband excitation as a time-dependent load. Other parameters, like preload effects are considered on the elastic and damped cylindrical waveguide using the SAFE method, are discussed in a detailed manner for understanding the dispersion features [24].

J. S. Thiyagarajan (✉)
School of Infrastructure, Indian Institute of Technology Bhubaneswar, Bhubaneswar, Odisha, India
e-mail: tjs@iitbbs.ac.in

D. K. Maiti et al. (eds.), *Recent Advances in Computational and Experimental Mechanics, Vol II*, Lecture Notes in Mechanical Engineering,
https://doi.org/10.1007/978-981-16-6490-8_38

In this paper, firstly, the time-transient response, including wave scattering phenomenon, caused by the tone burst excitation in the axisymmetric viscoelastic cylindrical waveguide at a specific position in its longitudinal direction is studied in a detailed manner. Based on the axisymmetric SAFE method, the time-transient response simulation of a steel wire under the narrowband excitation is considered for numerical investigation. The frequency response is calculated using frequency-domain analysis combined with the Cauchy residue theorem and modal superposition principle. As the contact state determines the contact and friction forces between the steel wires, it has a nonlinear characteristic. A nonlinear simplified model considering the contact and friction effects of the surrounding steel wires in a multi-wire environment is proposed. Also, an analysis framework of single steel wire wave scattering is further developed in the present work. For the nonlinear model, the contact and friction effects of the surrounding steel wire are reduced to contact springs and friction dampers, and only the propagation of longitudinal waves is considered. The effects of different spring stiffness and preload conditions on the steel wire transient response are analyzed.

2 Governing Equation for Axisymmetric Waveguide Media

Consider an axisymmetric waveguide medium with a constant cross-section and material properties divided into finite elements in its radial direction, as shown in Fig. 1. The semi-analytical method follows a cylindrical coordinate system with the cross-section lying in the $r - \theta$ plane. The displacement field vector is given as

$$\boldsymbol{u} = \left[u_r \; u_\theta \; u_z \right]^T, \tag{1}$$

where r, θ, z represents the radial, circumferential, and axial directions of the axisymmetric cross-section, respectively. The strain and stress vectors are expressed as

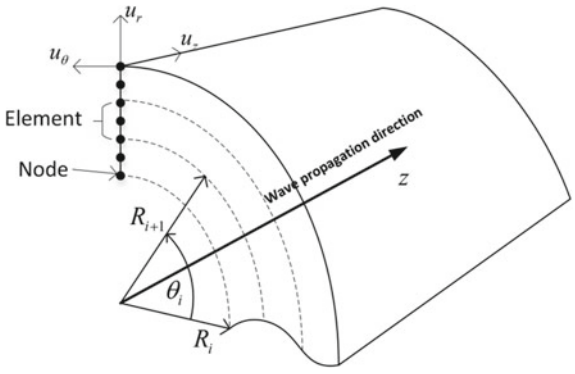

Fig. 1 Representation of the SAFE model and its nodal degree of freedom

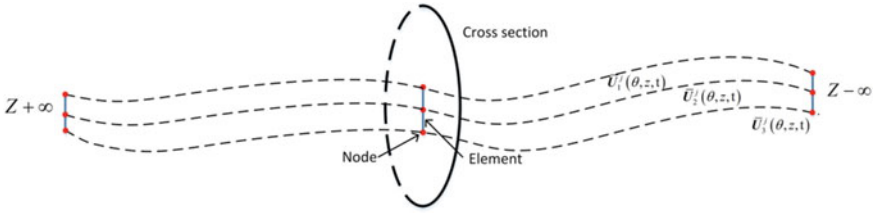

Fig. 2 Displacement field function

$$\begin{aligned}\boldsymbol{\varepsilon} &= \left[\varepsilon_r\ \varepsilon_\theta\ \varepsilon_z\ \gamma_{r\theta}\ \gamma_{\theta z}\ \gamma_{zr}\right]^T \\ \boldsymbol{\sigma} &= \left[\sigma_r\ \sigma_\theta\ \sigma_z\ \tau_{r\theta}\ \tau_{\theta z}\ \tau_{zr}\right]^T.\end{aligned} \tag{2}$$

By using a one-dimensional three-node element, the displacement field function at any point in the *j*th element is represented in the finite element format as

$$\boldsymbol{u}^j(r,\theta,z,t) = \boldsymbol{N}(r)\overline{\boldsymbol{U}}^j(\theta,z,t). \tag{3}$$

The cylindrical waveguide medium is composed of a limited number of layers fluctuating longitudinally in infinite space, as shown in Fig. 2. An interpolation function $\boldsymbol{N}(r)$ approximates the fluctuation.

The governing balancing equation that can be established using the virtual work equation is [5]

$$\int_V \delta u^T\, \rho \ddot{u} dV + \int_V \delta \varepsilon^T\, \sigma dV = \int_\Gamma \delta u^T\, t dS, \tag{4}$$

where V represents the volume of the waveguide medium, and it is infinitely long in the z-direction; Γ is the surface area of the medium acting with the surface force $\boldsymbol{t}$. Using the standard unit set procedure and considering the arbitrariness of the differential terms, the governing equation of the discrete system with variables θ and z, as follows:

$$\int_z \int_\theta \left(\boldsymbol{M}\ddot{\overline{\boldsymbol{U}}} + \boldsymbol{K}_{11}\overline{\boldsymbol{U}} + \boldsymbol{K}_{12}\overline{\boldsymbol{U}}_{,\theta} - \boldsymbol{K}_{13}\overline{\boldsymbol{U}}_{,\theta\theta} + \boldsymbol{K}_{21}\overline{\boldsymbol{U}}_{,z} - \boldsymbol{K}_{22}\overline{\boldsymbol{U}}_{,\theta z} - \boldsymbol{K}_3\overline{\boldsymbol{U}}_{,zz} - \boldsymbol{F}\right) d\theta dz = 0, \tag{5}$$

where $\overline{\boldsymbol{U}} = \overline{\boldsymbol{U}}(\theta,z,t)$ and $\boldsymbol{F} = \boldsymbol{F}(\theta,z,t)$ are the nodal displacement and equivalent nodal force vectors, respectively; $\boldsymbol{M}$ and $\boldsymbol{K}$ are the overall mass matrix and overall stiffness matrix.

For a simple harmonic load with frequency ω acting on any point on the waveguide medium, the response of the waveguide medium must also have the same frequency [6]. From Eq. (5), nodal displacement and force vectors are converted into continuous Fourier transform (CFT) into,

$$\begin{aligned} \boldsymbol{F}^{\omega}(\theta, z) &= \int_{-\infty}^{+\infty} \boldsymbol{F}(\theta, z, t) e^{i\omega t} dt \;\; \boldsymbol{F}(\theta, z, t) = \tfrac{1}{2\pi} \int_{-\infty}^{+\infty} \boldsymbol{F}^{\omega}(\theta, z) e^{-i\omega t} d\omega \\ \overline{\boldsymbol{U}}^{\omega}(\theta, z) &= \int_{-\infty}^{+\infty} \overline{\boldsymbol{U}}(\theta, z, t) e^{i\omega t} dt \;\; \overline{\boldsymbol{U}}(\theta, z, t) = \tfrac{1}{2\pi} \int_{-\infty}^{+\infty} \overline{\boldsymbol{U}}^{\omega}(\theta, z) e^{-i\omega t} d\omega \,, \end{aligned} \tag{6}$$

where $\boldsymbol{F}^{\omega}(\theta, z)$ and $\overline{\boldsymbol{U}}^{\omega}(\theta, z)$ are the CFT coefficients of $\boldsymbol{F}(\theta, z, t)$ and $\overline{\boldsymbol{U}}(\theta, z, t)$ with respect to time t, respectively, representing harmonic loads or responses with complex-valued amplitudes. For a given excitation frequency ω, the forced vibration response $\boldsymbol{Q}_n^{\omega,k}$ with a circumferential order n is formed by the summation of mutually orthogonal right eigenvectors through the modal expansion method [18],

$$\boldsymbol{Q}_n^{\omega,k} = \sum_{m=1}^{2M} \alpha_{nm} \boldsymbol{Q}_{n,R}^{\omega,k_m}, \tag{7}$$

where $\boldsymbol{Q}_{n,R}^{\omega,k_m} = \begin{bmatrix} \boldsymbol{U}_{n,R}^{\omega,k_m} & k_m \boldsymbol{U}_{n,R}^{\omega,k_m} \end{bmatrix}^T$. The displacement response of all DOF at the steady-state frequency ω for a circumferential order n at an axial coordinate z_R away from the wave source kept at z_S is represented as

$$\boldsymbol{U}_n^{\omega}(z_R) = -i \sum_{m=1}^{M} \frac{\begin{bmatrix} \boldsymbol{Q}_{n,R}^{\omega,k_m} \end{bmatrix}^T \boldsymbol{P}_n^{\omega,k}(\theta)}{\begin{bmatrix} \boldsymbol{Q}_{n,R}^{\omega,k_m} \end{bmatrix}^T \boldsymbol{B}\, \boldsymbol{Q}_{n,R}^{\omega,k_m}} \boldsymbol{U}_{n,R}^{\omega,k_m} e^{ik_m(z_R - z_S)}. \tag{8}$$

The time–space domain displacement response of a certain point in the waveguide medium can be obtained by taking the time IFT of the global frequency response as follows:

$$\boldsymbol{U}(\theta_R, z_R, t) = \frac{1}{2\pi} \int_{-\infty}^{+\infty} \boldsymbol{U}^{\omega}(\theta_R, z_R) e^{-i\omega t} d\omega, \tag{9}$$

where $\boldsymbol{U}(\theta_R, z_R, t)$ represents the displacement response vector of the DOFs of each node at $z = z_R, \theta = \theta_R$. It can be observed that $\boldsymbol{U}^{\omega}(\theta_R, z_R)$ should include the frequency-domain response superposition of M wave modes, where M is the system's total number of DOF. According to the distance between the calculated response point and excitation point on the z-axis, the threshold $(z_R - z_S)\mathrm{Im}(k_m) < \gamma_{\max}$ of

the attenuation can be set to filter out the part that contributes little to the overall composite response.

3 Numerical Investigation

3.1 Response Under Narrowband Excitation

Consider 5 mm diameter high-strength steel wire with material characteristics as illustrated in Table 1 for the case study to calculate its displacement response under a narrowband external force excitation. The external excitation unit force load is acting on the radial center node ($r_S = 2.5/2$ mm, $\theta_S = 0$, $z_S = 0$) of the cross-section along the z-direction, as shown in Fig. 3a. The narrowband excitation force with a center frequency of 0.2 MHz and sub-plot, illustrating the tone burst excitation, is shown in Fig. 3b. To accurately calculate the displacement response, the meshing criterion [12] needs to be satisfied to obtain the exact wavenumber solution at the specified

Table 1 Material characteristics of high-strength steel wire

Young's Modulus, E (MPa)	Density, ρ (kg/m^3)	Poisson's ratio, ν	Diameter, d (mm)	Longitudinal wave velocity, C_L(m/s)	Shear wave velocity, C_S (m/s)
2×10^5	7850	0.3	5	5856.4	3130.4

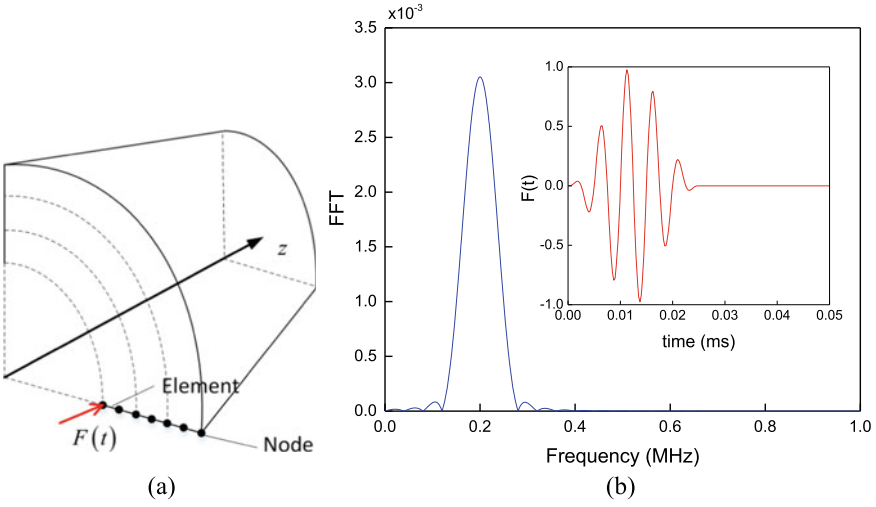

Fig. 3 Representation of narrowband excitation in the spatial domain

frequency. In this example, the maximum calculation frequency is 0.4 MHz, and the maximum element length is $l_{\max} = 1.6$ mm, and the finite elements required is $n_{el} = 2$. Due to the low computational cost of the axisymmetric SAFE method for an elastic material, six nodes are distributed in the radial direction with the total sampling and calculation time as 2 ms. The sampling frequency is 4 MHz. If the waveguide medium's material is considered viscoelastic, then change the material stiffness matrix to the corresponding complex stiffness matrix. For high-strength steel wire, attenuation factors of longitudinal body wave, κ_L=$0.003Np/\lambda$ and transverse body wave, κ_T=$0.008Np/\lambda$, respectively. Figure 4 shows the displacement responses of the damped waveguide at $r_R = 2.5$ mm, $\theta_R = 0$ and distance $z_R - z_S$ equal to 1, 3, and 5 m, respectively. It can be seen that the vibration amplitude decreases rapidly with the increase of the propagation distance, as $F(1, 1)$ a mode with a small amplitude disappears after 5 m. This trend is due to the combined effect of wave dispersion and damping. Among them, the damping effect is dominant.

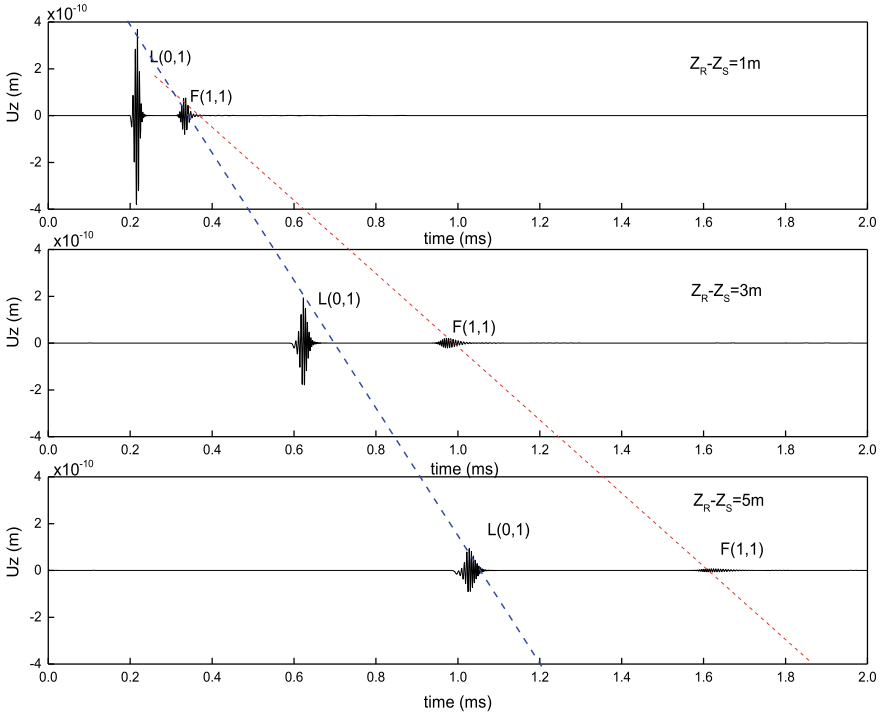

Fig. 4 Longitudinal and flexural modes in a damped steel wire representing axial displacement response U_z at a distance $z_R - z_S$ equal to 1, 3, and 5 m

4 Nonlinear Simplified Model

In practical scenarios, the bridge cable or overhead transmission line conductors contains multiple-wire steel strands. The process of the AE signal propagating through the steel wires is bound to be affected by the contact and friction of the surrounding wires. The wire where the initial AE source is located is called the active wire, surrounded by passive steel wires, as illustrated in Fig. 5. The objective is to establish a simple method for calculating the active steel wire's nonlinear response considering external contact and friction. Consider only the longitudinal wave component in the AE signal, which can further simplify the existing nonlinear model. The corresponding contact springs and friction dampers need to be considered only in radial and longitudinal directions. Under the simplified conditions, the longitudinal wave 1D SAFE method is used for analysis, which has low calculation cost, high efficiency, and accuracy. At present, each set of contact springs and friction dampers in Fig. 5 has the same response in the circumferential direction. The solution of the external excitation time history on the contact spring and friction damper is the solution of the roots of a nonlinear equation system, expressed as

$$K(G(NonlinF)) = NonlinF, \tag{10}$$

where $NonlinF$ is the nonlinear external excitation caused by the contact spring and friction damper.

The function $G(\bullet)$ is the mapping relationship between the nonlinear external excitation and the response at the corresponding point. This function contains the incident wave and the FRF information of the single wire linear system by default. The function $K(\bullet)$ is the mapping relationship between the response at the application

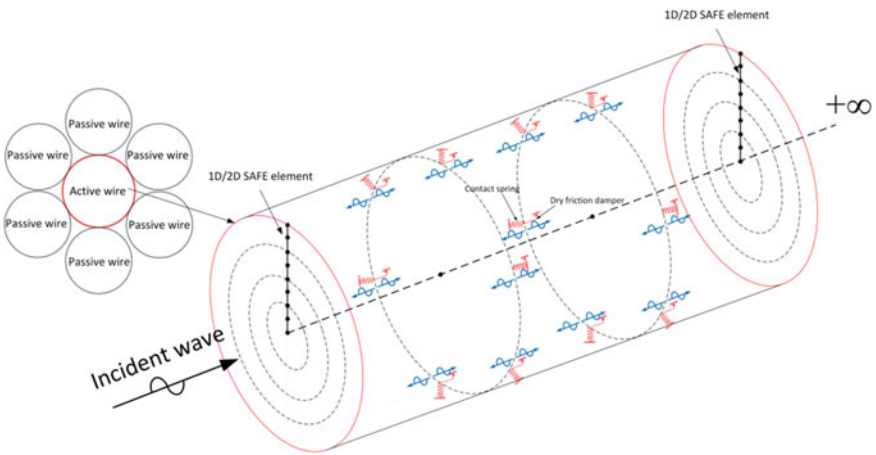

Fig. 5 A nonlinear simplified model of active steel wire

point of the nonlinear device and its corresponding nonlinear excitation. This function includes the properties of the nonlinear device itself, such as stiffness and damping. Consider an external input in one-set of the nonlinear device, and then the FRF is a scalar value at each discrete frequency point. Assume that there are multiple sets of nonlinear devices interacting or multiple incident waves in the nonlinear system. The FRF forms a compliance matrix, δ_{ij} at each discrete frequency point, where i is the sum of DOF corresponding to the nonlinear device, and j is the sum of DOF corresponding to the incident wave. Figure 5 shows that when the incident wave passes through the first set of nonlinear devices, it transfers the nonlinear external excitation. Both the external excitation and the incident wave together affect the first set of nonlinear DOF responses. Subsequently, the first set of nonlinear external excitations will cause secondary waves to propagate in both directions.

4.1 Transient Response of a Single Set of Nonlinear Devices

The nonlinear simplified model and calculation framework considers a single 5 mm diameter high-strength steel wire with a single set of nonlinear devices for numerical investigations. The external excitation is given at Z = 0, and one-set of nonlinear devices is kept at Z = 0.5 m. The longitudinal and radial response at the steel wire's outer surface is obtained at Z = 1 m. The external excitation in a time–space domain is a point load acting on the center of the cross-section, as shown in Fig. 6. In this numerical investigation, the total calculation time is 1 ms, the sampling frequency is 4 MHz, and the model is divided into 20 one-dimensional semi-analytical units radially. The material is considered to be viscoelastic. The ultimate tensile stress of the high-strength steel wire used in actual engineering is 1860 MPa. Considering the tensile stress of seven steel strands is 0.4 times the ultimate stress, the stiffness of the distributed contact spring is calculated to be about 2.5×10^9 N/m^2. According

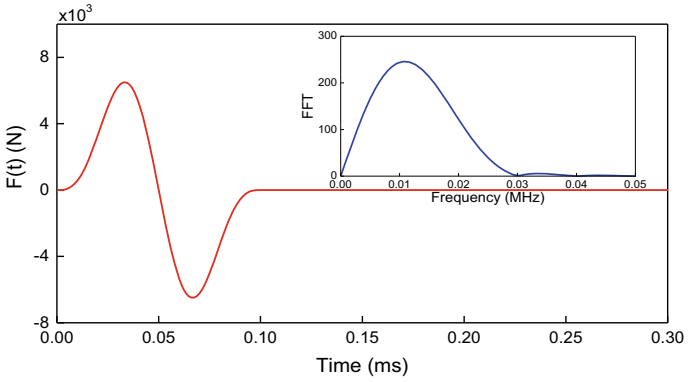

Fig. 6 External excitation in time and frequency domain

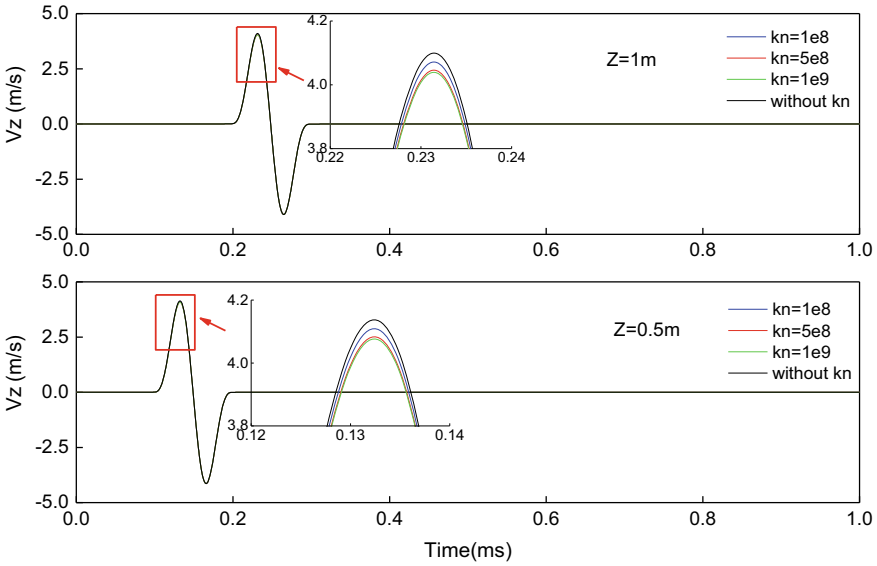

Fig. 7 Longitudinal velocity response for one-set of nonlinear devices under various spring stiffness

to the different longitudinal lengths, the stiffness of the concentrated contact spring is added.

For comparative analysis, three different stiffness (k_n) values are utilized: 1×10^8 N/m, 5×10^8 N/m, and 1×10^9 N/m, respectively, by ignoring the preloading factor. The stiffness value here refers to the stiffness of each spring in a set. The calculation also considers the combined effect of all six spring stiffness in a set. Figure 7 and Fig. 8 show the longitudinal and radial velocity response on the wire's outer surface at Z = 1 m and Z = 0.5 m, respectively. The different colored lines in the figure represent the stiffness of different contact springs. The overall longitudinal waveform has not changed significantly at $Z = 1$ m and 0.5 m, as observed in Fig. 7. For radial velocity, at $Z = 1$ m, the waveform has not changed significantly, as shown in Fig. 8. The high-frequency signal is generated by the high-frequency component of the nonlinear external excitation. Moreover, the velocity of the high-frequency component group of the first-order longitudinal wave is slightly lower than that of the low-frequency component. The radial velocity signal at $Z = 0.5$ m is severely distorted by the contact spring, as shown in Fig. 8. It is observed that the amplitude of the first half of the waveform decreases rapidly as the spring stiffness increases by comparing the results. Figure 9 shows the preload effect of longitudinal velocity response at $Z = 1$ m and 0.5 m, respectively, but its overall effect on the waveform is minimal. For the radial velocity, in the second half of the waveform at Z = 1 m, compared to the linear or no preload condition, some high-frequency components are mixed, and its amplitude increases with the increase of preloads, as observed from Fig. 10. Like zero preload, a high-frequency component signal appears at the

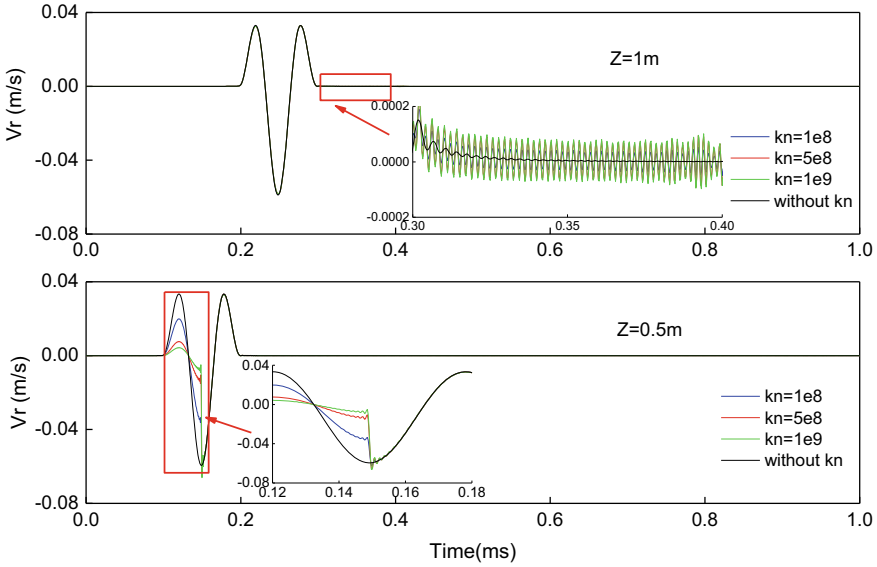

Fig. 8 Radial velocity response for one-set of nonlinear devices under various spring stiffness

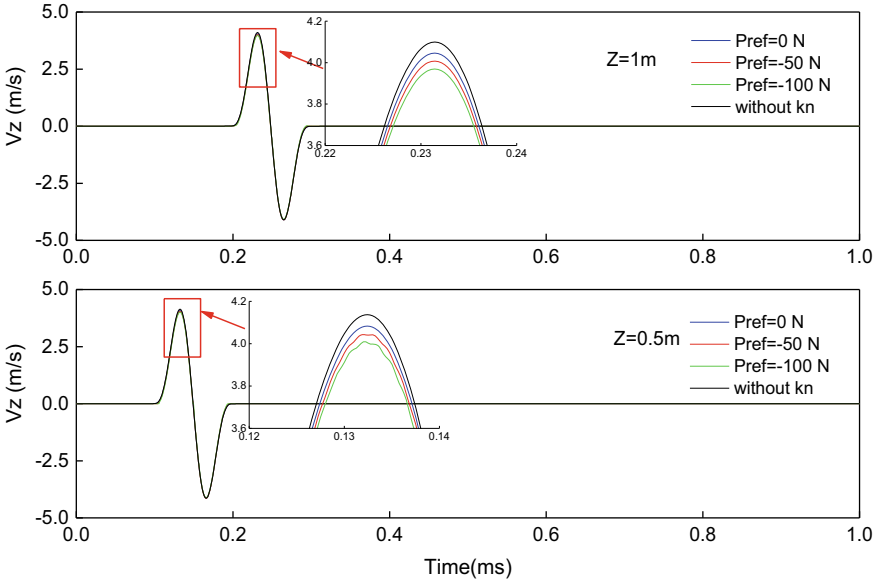

Fig. 9 Longitudinal velocity response for one-set of nonlinear devices under various preloads

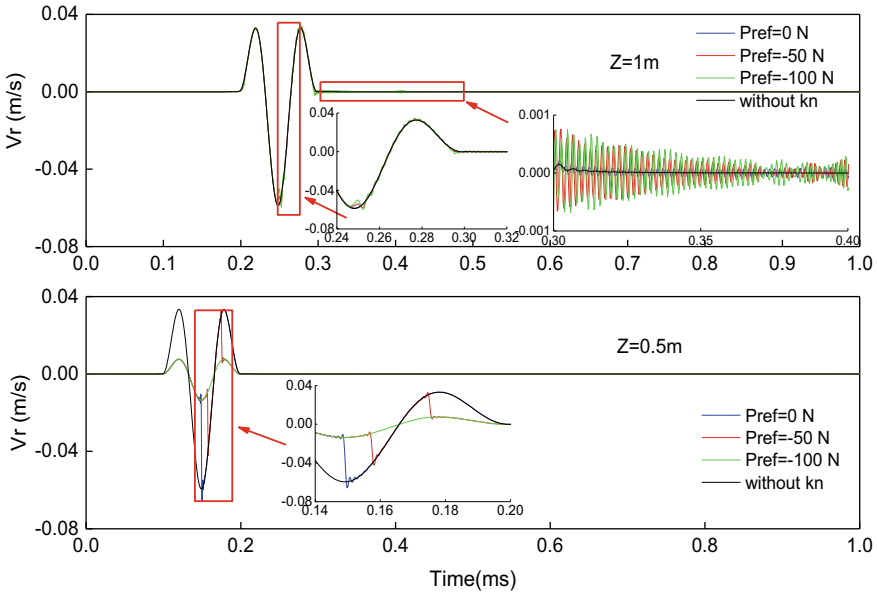

Fig. 10 Radial velocity response for one-set of nonlinear devices under various preloads

waveform's tail, increasing as the preload increases. The sudden change of radial velocity at $Z = 0.5$ m has a different form than the case without preload.

5 Conclusions

In this paper, the axisymmetric SAFE method is used to understand the time-transient response in an axisymmetric viscoelastic cylindrical waveguide, particularly for a high-strength steel wire. The frequency-domain analysis is performed by a combination of FT and Cauchy residue theorem. The modal superposition method is then used to calculate the frequency response at each point for an applied time-dependent excitation. The novelty of the present work is to propose a simplified nonlinear model with contact spring and friction damper. Based on the Hertz contact width calculation between the steel wires, the stiffness of the distributed contact spring is calculated. Under various stiffness values in one-set of the nonlinear device, the overall longitudinal velocity waveform has not changed considerably. Still, it is observed to have a slight downward trend as the spring stiffness increases. This is due to the indirect increase in friction caused by the increase in spring stiffness. From the radial velocity signal, it is observed that the amplitude of the first half of the waveform decreases rapidly as the spring stiffness increases. Compared to longitudinal velocity, the radial velocity does not reflect the effect of friction damping. The damping force is always perpendicular to the radial velocity, and the work done is

zero. Under various preloads in one-set of the nonlinear device, the damping effect on the longitudinal velocity response is minimal. Some high-frequency components are mixed for the radial velocity, and its amplitude increases as the preload increases. A high-frequency component appears at the tail of the waveform, which increases as the preload increases. As the acoustic emission signal propagating through the steel wires is bound to be affected by the contact and friction of the surrounding wires, the proposed model will account for the nonlinear characteristics.

References

1. Laura PA, Vanderveldt H, Gaffney P (1969) Acoustic detection of structural failure of mechanical cables. J Acoust Soc Am 45(3):791–793
2. Nair A, Cai CS (2010) Acoustic emission monitoring of bridges: review and case studies. Eng Struct 32(6):1704–1714
3. Saravanan TJ, Gopalakrishnan N, Rao NP (2015) Damage detection in structural element through propagating waves using radially weighted and factored RMS. Measurement 73:520–538
4. Saravanan TJ (2020) Non-destructive testing mechanism for pre-stressed steel wire using acoustic emission monitoring. Materials 13(21):5029
5. Charlier JP, Crowet F (1986) Wave equations in linear viscoelastic materials. J Acoust Soc Am 79(4):895–900
6. Saravanan TJ (2020) Investigation of guided wave dispersion characteristics for fundamental modes in an axisymmetric cylindrical waveguide using rooting strategy approach. Mech Adv Mater Struct: 1–11
7. Gavrić L (1995) Computation of propagative waves in free rail using a finite element technique. J Sound Vib 185(3):531–543
8. Moser F, Jacobs LJ, Qu J (1999) Modeling elastic wave propagation in waveguides with the finite element method. NDT and E Int 32(4):225–234
9. Saravanan TJ, Gopalakrishnan N, Rao NP (2017) Detection of damage through coupled axial–flexural wave interactions in a sagged rod using the spectral finite element method. J Vib Control 23(20):3345–3364
10. Kumar KV, Saravanan TJ, Sreekala R, Gopalakrishnan N, Mini KM (2017) Structural damage detection through longitudinal wave propagation using spectral finite element method. Geomech Eng 12(1):161–183
11. Saravanan TJ, Gopalakrishnan N, Rao NP (2018) Experiments on coupled axial–flexural wave propagation in a sagged rod with structural discontinuity using piezoelectric transducers. J Vib Control 24(13):2717–2731
12. Bartoli I, Di Scalea FL, Fateh M, Viola E (2005) Modeling guided wave propagation with application to the long-range defect detection in railroad tracks. NDT and E Int 38(5):325–334
13. Bartoli I, Marzani A, Di Scalea FL, Viola E (2006) Modeling wave propagation in damped waveguides of arbitrary cross-section. J Sound Vib 295(3–5):685–707
14. Marzani A, Viola E, Bartoli I, Di Scalea FL, Rizzo P (2008) A semi-analytical finite element formulation for modeling stress wave propagation in axisymmetric damped waveguides. J Sound Vib 318(3):488–505
15. Saravanan TJ (2020) Convergence study on ultrasonic guided wave propagation modes in an axisymmetric cylindrical waveguide. Mech Adv Mater Struct: 1–18
16. Mu J, Rose JL (2008) Guided wave propagation and mode differentiation in hollow cylinders with viscoelastic coatings. J Acoust Soc Am 124(2):866–874
17. Galán JM, Abascal R (2002) Numerical simulation of Lamb wave scattering in semi-infinite plates. Int J Numer Meth Eng 53(5):1145–1173

18. Hayashi T, Song WJ, Rose JL (2003) Guided wave dispersion curves for a bar with an arbitrary cross-section, a rod and rail example. Ultrasonics 41(3):175–183
19. Treyssède F (2007) Numerical investigation of elastic modes of propagation in helical waveguides. J Acoust Soc Am 121(6):3398–3408
20. Treyssède F, Laguerre L (2013) Numerical and analytical calculation of modal excitability for elastic wave generation in lossy waveguides. J Acoust Soc Am 133(6):3827–3837
21. Treyssède F (2019) Free and forced response of three-dimensional waveguides with rotationally symmetric cross-sections. Wave Motion 87:75–91
22. Mazzotti M, Marzani A, Bartoli I, Viola E (2012) Guided waves dispersion analysis for prestressed viscoelastic waveguides by means of the SAFE method. Int J Solids Struct 49(18):2359–2372
23. Marzani A (2008) Time–transient response for ultrasonic guided waves propagating in damped cylinders. Int J Solids Struct 45(25–26):6347–6368
24. Mukdadi OM, Datta SK (2003) Transient ultrasonic guided waves in layered plates with rectangular cross section. J Appl Phys 93(11):9360–9370

A Numerical Approach to Model Heterogeneity of Concrete in RC Beam Subjected to Impact Loading

Abhinov Bharadwaj and Sukanta Chakraborty

1 Introduction

Concrete is one of the most extensively used materials in the world. Over the ages, concrete structures have been analysed for both static and dynamic loading. Impact loading is a dynamic loading characterized by the application of enormous intensity of load within a short span of time. Impact loading is most likely a type of accidental loading, as such, many structures can undergo impact loading during their service life. Recently, many studies have been performed for low-velocity impacts such as falling of rocks in hilly areas, falling of tree branches during a storm, dropping of heavy loads in factories because of accidents, etc. [1–3]. Therefore, some essential structures must be designed for impact resistance. In recent times, numerical simulation has been widely used since it is economical and requires less time than the cost-exhaustive, prolonged real-life experiments [4, 5].

Whenever this impact event is simulated numerically, the target material of the system is generally assigned homogenous (isotropic/orthotropic/functionally graded) strength parameters [6, 7] irrespective of its material characteristics. Reinforced concrete is a multiphase system comprised of cement, fine aggregate, coarse aggregate, water voids, reinforcing rebar, and sometimes with added admixtures. Although the reinforcing rebars have been modelled as separate elements in earlier studies to accommodate the ductility and tensile strengthening in flexure, seldom the concrete is focused upon. However, it is well established that concrete constituent materials contain distinct properties, particularly the aggregates acquiring most of the volumes providing major load-carrying capacity and the cement mortar proving the transition zone and binding. And specifically in damage (cracks) propagation studies, this heterogeneity plays a vital role in yielding dynamic crack kinking from the

A. Bharadwaj (✉) · S. Chakraborty
Department of Civil Engg, Indian Institute of Technology (ISM) Dhanbad, Dhanbad, India
e-mail: abhinov.17dr000453@cve.ism.ac.in

D. K. Maiti et al. (eds.), *Recent Advances in Computational and Experimental Mechanics, Vol II*, Lecture Notes in Mechanical Engineering,
https://doi.org/10.1007/978-981-16-6490-8_39

aggregate-mortar interfaces. This crack deflection may significantly alter the global failure patterns of the target specimen. So it is imperative to study the effect of this heterogeneity considering the aggregates and the mortar as separate phases.

Due to the scarce literature available in the modelling of heterogeneity of concrete, insights were given into the field of rock mechanics. Concrete and rock are somewhat comparable in nature [8]**.** Benz and Asphaug [9] using Smoothed Particle Hydrodynamics modelled brittle solid (rock) by the inclusion of randomly distributed flaws, the strength of which is dependent upon the activation and propagation of flaws which has been assigned randomly across the volume by using Weibull Distribution [10]. Researchers used Weibull statistics to characterize different material parameters of brittle solids. Angulo et al. [11] proposed a methodology for the selection of natural aggregates for high strength concrete based on the probability distribution (Weibull) of strength, elastic modulus, and water absorption for granite and limestone aggregates effectively. Weibull statistics have been effectively applied to quantify the strengths of railway ballast [12]. So from the above literature, it is evident that Weibull distribution theory can help to quantify various parameters in a particular volume of rock. Concrete is a substantially heterogeneous material having random placement of aggregate with varying size and strength. So, Weibull theory is being incorporated in concrete by randomly assigning the strength parameter (Elastic Modulus). Henceforth, numerical simulation is conducted by assigning the material model of Concrete Damage Plasticity (CDP) for the target material. The current objective is to investigate the effect on the global impact response when randomly shaped aggregates in the form of randomly assigned stronger inclusions are incorporated in a simply supported RC beam. To this end, the major influencing energy quantities such as damage dissipation energy (DDE) and plastic dissipation energy (PDE) are obtained for both homogeneous and heterogeneous target. And their effect on the failure pattern and the ballistic performance is investigated.

2 Numerical Simulation of RC Beam

Numerical simulation for impact test is being exercised in the finite element software, Abaqus/CAE [13] in the dynamic explicit package. As impact phenomenon is indulged in high strain rate, so dynamic explicit is an essential tool to simulate these kinds of dynamic problems. For the validation purpose, the geometry, material parameters, and impact severance are benchmarked as per the specification given by Fujikake et al. [1]. The drop height of 150 mm is considered in this study.

The details of the beam modelled initially as homogenous, solid, and deformable specimen are shown in Fig. 1. The main and shear reinforcement is designed as a deformable truss member. The impactor is a solid rigid member with an inertial mass of 400 kg is assigned at a reference point on top of the impactor (assuming insignificant nose-shape sensitivity for brittle yet hard concrete in line with literature). The material properties of the beam are shown in Table 1. The compressive strength

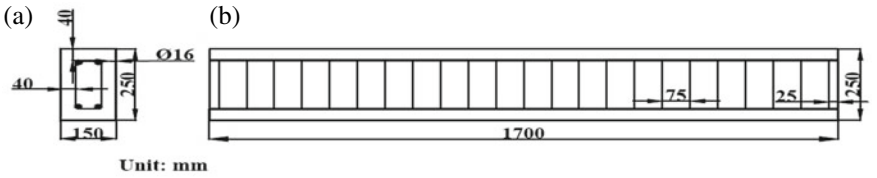

Fig. 1 Reinforcement details **a** cross sectional view, **b** front view

Table 1 Material Properties of different parts

Properties	Concrete	Main reinforcement	Shear reinforcement
Density, ρ	2400 kg/m^3	8000 kg/m^3	8000 kg/m^3
Modulus of elasticity, E	27,874.62 MPa	210,000 MPa	210,000 MPa
Poisson's ratio, μ	0.15	0.3	0.3
Yield stress	Defined by the CDP model	426 MPa	295 MPa

Table 2 Element types used in the simulation

Beam	C3D8R-eight node linear brick element reduced integration with hourglass control
Impactor	R3D4-four node rigid element with quad–dominated element
Reinforcement (Main and shear)	T3D2-two node linear truss element

of 42 MPa is used in the beam as to validate the problem with that of Fujikake et al. [1]. Different kinds of elements used in this study are mentioned in Table 2.

As for the contact algorithm, kinematic contact method is applied in surface to surface contact (Explicit). The impactor surface was treated as master surface and beam surface as a slave. Hard contact was applied during the interaction. The reinforcement, both main and shear are inserted in the beam using embedded constraint as the perfect bond is assumed to exist between the concrete and reinforcement.

2.1 Constitutive Model

Concrete is a quasi-brittle material [14]. To accommodate the response of concrete subjected to dynamic loading, Concrete Damage Plasticity (CDP) model is used. This model elucidates the main failure pattern in concrete which is cracking in tension and crushing in compression. So, the stress–strain curves for the particular grade of concrete (in tension and compression) need to be inserted in the CDP model. Also CDP model needs the values of inelastic strain and cracking strain and thereby checks

the accuracy of the stress–strain curve from the plastic strain and damage values. All the equations required in the CDP model are discussed briefly in Appendix A.

2.2 Mess Convergence and Validation

The Peak impact load and maximum deflection of Fujikake et al. [1] are taken as reference cases to carry out the mess convergence study, which will also facilitate the validation of the current model. The mesh sizes taken under consideration are 18.75, 15, 12.5, 10, 7.5, and 5 mm (Fig. 2). In the present study, 150 mm drop height and 400 kg impactor were selected for the validation purpose in which the peak load and maximum deflection were obtained from Fujikake et al. [1]. From the peak load versus mesh size (Fig. 2a), it can be seen that at 5 mm seed size, the peak load calculated from the numerical simulation was lesser than that of the experiment conducted by Fujikake et al. [1]. From Table 3, it can be deduced that at 7.5 mm seed size, the percentage change from the experimental result is only –3.28% which is

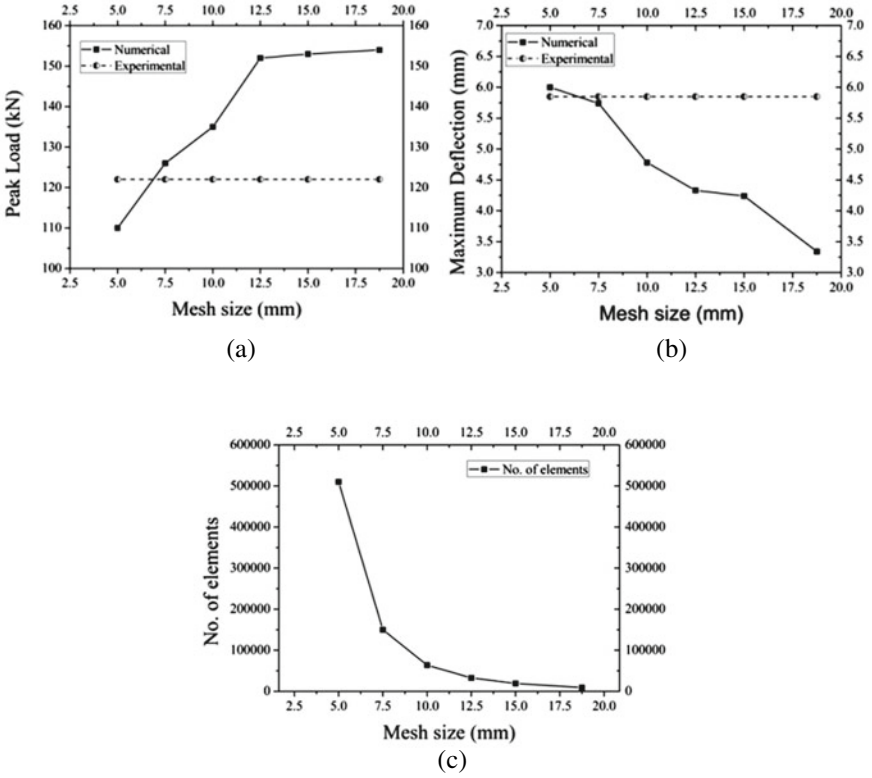

Fig. 2 Mesh size versus **a** peak load, **b** maximum deflection, and **c** number of elements

Table 3 Comparative data for percentage change of peak load and maximum deflection

Mesh size (mm)	Peak load (kN)			Maximum deflection (mm)		
	Experimental [1]	Numerical current study	Percentage change	Experimental [1]	Numerical current study	Percentage change
18.75	122	154	−26.2	5.85	3.34	42.9
15	122	153	−25.4	5.85	4.24	27.5
12.5	122	152	−24.6	5.85	4.33	26
10	122	135	−10.6	5.85	4.78	18.9
7.5	122	126	−3.28	5.85	5.74	1.9
5	122	110	9.8	5.85	6	2.56

comparatively lesser than the other seed sizes. Also, from Fig. 2b, it is clear that, at 5 mm mesh size, the maximum mid-span deflection from the numerical analysis was over-estimated. Table 3 shows that for maximum deflection, percentage change is least in case of 7.5 mm seed size which is 1.9%. The computational cost at 5 mm seed size (almost 3.4 times that of 7.5 mm) was exorbitant, Fig. 2c. So, it can be concluded that 7.5 mm mesh size is ideal for conducting the numerical simulation as it has an optimum number of elements, and its peak load and maximum deflection are in good agreement with that of the experimental results. Further the mid-span permanent deformation and impact force as obtained from the present model is validated by comparing with analytical and experimental evidences from literature.

3 Methodology to Incorporate Heterogeneity

Selecting the elements from the input file randomly in MATLAB [15], it is ensured that selected elements are roughly equal to the total number of course aggregates in the beam. While selecting the random elements, the elements that are in the outer surface were excluded. Now small perturbation was assigned in the coordinates of the nodes of those randomly chosen elements. Now those newly generated nodes were used to generate the randomly sized and shaped aggregates which were replaced with the old regular aggregates. Thus the random inclusion having the arbitrary shape was obtained. Zhang et al. [16] have considered the three-dimensional shape of aggregate as approximated to be hexahedron, tetrahedron, and pentahedron. In this study, we consider only the hexahedron as the aggregate shape. As C3D8R (brick) element is used for the target material (beam), so it is convenient to use hexahedron as the aggregate. The typical view of the aggregate is shown in Fig. 3.

As for the material properties of the aggregates, only elastic properties were given to the aggregates in which, keeping the density and Poisson's ratio same only Elastic Modulus is allowed to vary using Weibull Probability distribution which will define the strength parameters per unit volume. The major reason for choosing Elastic

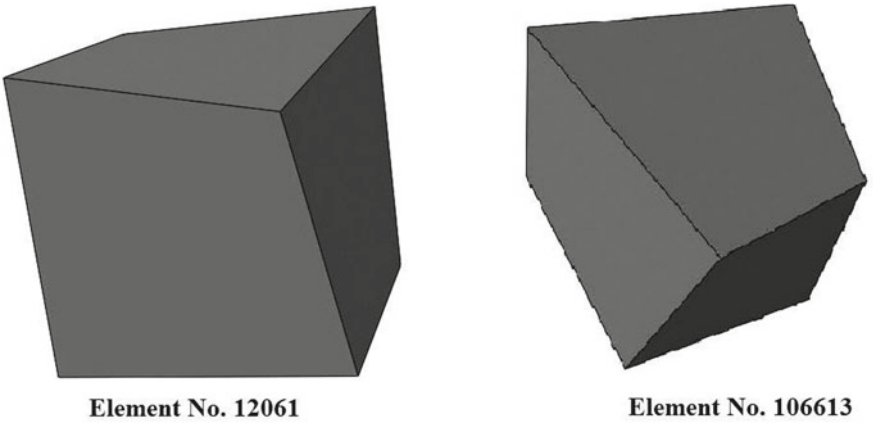

Fig. 3 Typical 3D view of the element used as aggregate

Modulus is that upon the development of the crack in the Beam, the E becomes zero which indicates element deletion as the crack propagates through it.

The Weibull distribution function can be expressed as

$$P_s(V_0) = \exp[-(X/X_0)^m], \tag{1}$$

where P_s describes the probability of survival for a volume V_0 for a particular parameter X.

X_0 represents a scale parameter such that the probability of survival is 37% (63% failure rate) and m is the shape parameter or Weibull modulus which represents the degree of dispersion in the data which increases as the dispersion decreases. The above function can be linearized as

$$\ln\left[\ln\left(\frac{1}{P_S}\right)\right] = m[\ln(X) - \ln(X_0)]. \tag{2}$$

In the present study, the parameter X is taken as E (Elastic Modulus). Now to calculate P_s, all the distributed Elastic modulus values are arranged in ascending order and given a rank accordingly. Then from the following formula, P_S is determined.

$$P_S = \frac{n - 0.5}{N}, \tag{3}$$

where n is the rank for a particular value of X and N is the total distributed numbers. The Weibull parameters are determined by fitting a straight line to $\mathrm{Ln}[\mathrm{Ln}(1/P_s)]$ against Ln(E). E_0 represents the 37% survival probability for the Elastic Modulus. So the values below E_0 will have lesser strength. In this study, the size parameter ($E_0 = 55{,}746$ MPa) and shape parameter ($m = 5.15$) were taken from Angulo

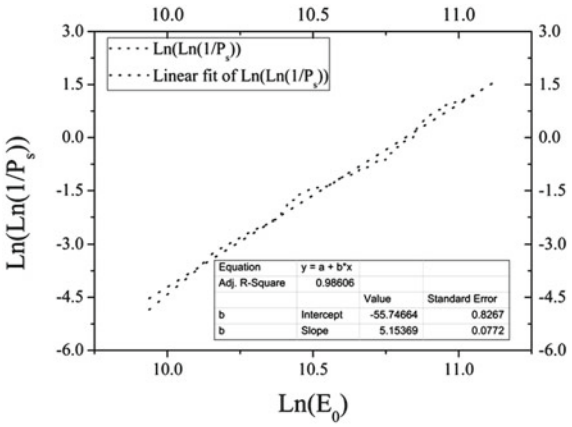

Fig. 4 Survival probability of elastic modulus

et al.2019[11]. From the random numbers generated, we find the probability of survival and Ln[Ln(1/P_s)] against Ln(E_0) which is plotted using linear fit as shown in Fig. 4. It can be seen that 61% lie below E_0 which is close to the theoretical value (63%). So this methodology is used here, and if desired, the strength and Elastic Modulus of each aggregate (in groups) can be determined experimentally.

4 Results and Discussion

To check the efficacy of the current model, the impact loading is applied in an unreinforced beam in two cases ~ (a) on a plain concrete beam without any inclusion and (b) on a beam with added inclusions, having identical strength and "E" varying randomly with respect to the Elastic Modulus of Concrete. Since it is a plain concrete beam, crack originates from the tension side below the point of impact and as there is no reinforcement to encounter, the crack propagates perpendicular to the span of the beam as shown Fig. 5. And no other crack has been seen to emanate except for those in the supports. Now the same plain concrete beam has been modelled, but the inclusion has been added only in two sections. Upon impact loading, it was seen that the first crack propagates from the centre and then two cracks start simultaneously at the location of the inclusion and propagate perpendicularly to the span of the beam. This study gives an imperative idea that, when there is a weaker inclusion in the structure, stress nucleation occurs in that concerned area, which in turn commences the crack to propagate. Hence, the current approach shows positive insights on the effect of heterogeneity.

Energy variation for both heterogeneous and homogeneous model is plotted in Fig. 6a and 6b, respectively. In both cases, the total energy (TE) of the system remains constant with a slight variation of less than 1%. After the impact, Kinetic Energy (KE) of the system drops sharply as the velocity of the impactor decreases, hits zero

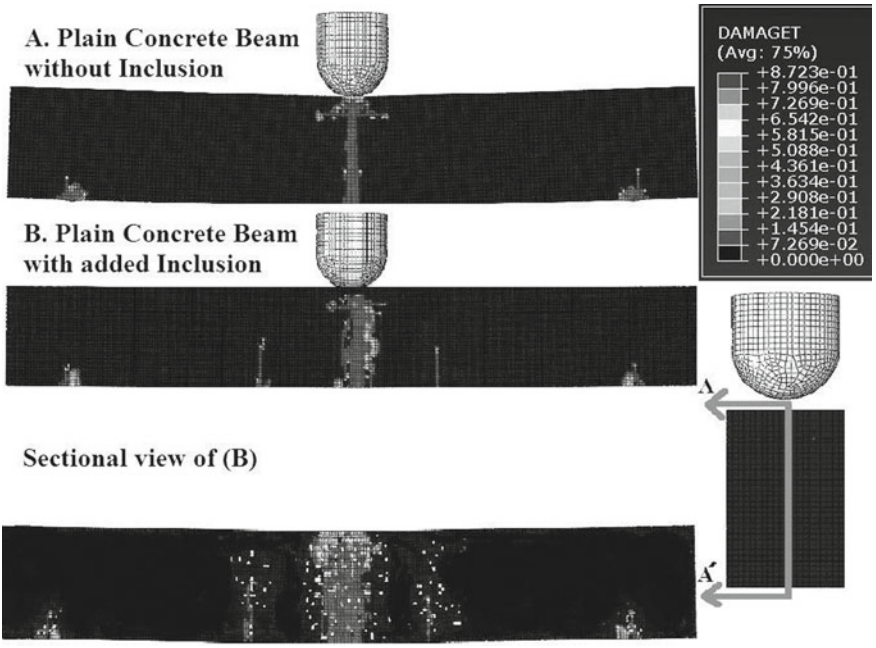

Fig. 5 Comparison of propagation of cracks in the plain concrete beam without and with the weaker inclusion

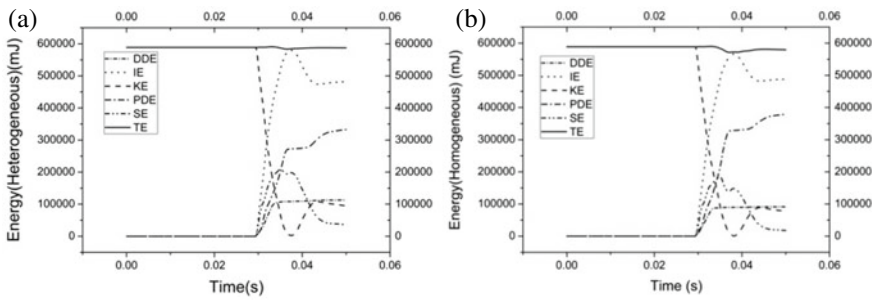

Fig. 6 Time-history of energies for **a** heterogeneous concrete model; **b** homogeneous concrete model

and rebound back by gaining some energy, and finally remains constant. However, in the case of Internal energy, which is the sum of recoverable strain energy (SE), plastic dissipation energy (PDE) and damage dissipation energy (DDE) depicts that after impact, it rises with a steep slope to a certain value close to total energy and after rebounding it drops and remains constant afterwards. Thus it can be interpreted that by adding the random inclusions and giving them varying material properties, the energy of the system is still conserved. The increase in mid-span deflection

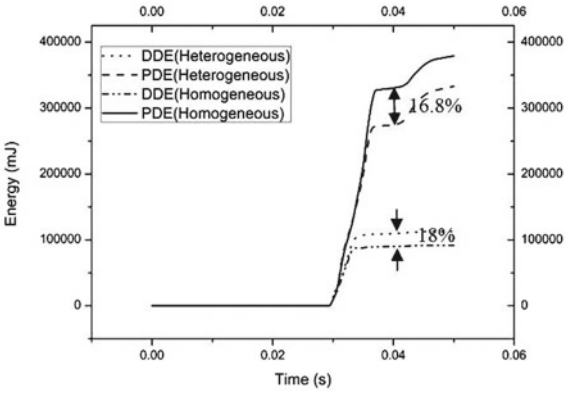

Fig. 7 Comparison of DDE and PDE for the heterogeneous and homogeneous model

with increase in momentum transferred and energy imparted for varying impact severance was also observed in line with intuitive conclusions as well as evidences from literature.

Now DDE and PDE of the whole target are extracted for a particular impact event for both the cases (with and without proposed heterogeneity modelling) as shown in Fig. 7. Firstly, PDE is found to be higher and extending over longer time duration as compared to DDE. It is evidently because of the fact that damage dissipation is comparatively a localized phenomenon, whereas plastic dissipation occurs over a larger region and for a longer period. Now, as shown in Fig. 7, the heterogeneous model depicted ~16.8% drop in PDE probably because of enhanced load-carrying capacity offered by the exclusively modelled aggregates. It is worthwhile to mention that total mid-span deflections obtained from both the models are comparable, indicating similar elastic work done. However, investigation of DDE denoted ~18% increase in case of heterogeneous modelling probably because of more damage concentration for impendence incongruity at the interfaces.

Although generally mid-span deformation patterns and crack-patterns are investigated to estimate the impact response of plain or reinforced concrete sub-structural elements, the present heterogeneity modelling may depict further insight on that behaviour. As heterogeneous model depicted lower PDE accumulation, it is perceived that the permanent plastic deformation may be lower keeping the total deformation comparable as that of homogenous model. Keeping in view that there is scope of improving the present heterogeneity modelling, the current result at its present form also dictates a requirement of measuring the final plastic deformation experimentally filtering out the initial transient oscillations. Now this deformation profile is meaningful as long as the specimen remains un-cracked at least up to a reasonable limit. However when dealt with high-intensity pulse loading such as impact, limiting the damage extent may be a defining design criteria. And there lies the importance of the present consideration of modelling the heterogeneous aggregate-mortar assembly explicitly. As shown in the present investigation, the DDE and hence the subsequent damage accumulation may be higher for accounting the inherent heterogeneity owing

to material impedance mismatch at the aggregate-mortar interfaces. Although it is accepted that the interface property may play a key role in enhancing or diminishing the overall damage behaviour, the present investigation yields the interesting phenomenon of increasing damage accumulation at local level despite of decreasing plastic work done on a more extensive area. The details of simultaneous failure mechanisms and the contributory energy associated in the total DDE may exhibit more insight to this end.

Further details of the failure behaviour may be derived if quantification of cracks generated may be compared for homogeneous and heterogeneous models by methods such as identifying number density within a representative volume element along with length scale of individual cracks, crack-tip velocity, etc. That study is under investigation and may constitute a future communication.

5 Conclusion

In closure, it can be concluded that the proposed methodology can be used to counter the complex heterogeneity involved in a material model. As it has been shown that it can be used in conjunction with the Concrete Damage Plasticity model, so nonlinearity associated with the material has been taken care of. It can be seen that the crack propagation can be predicted in this system in a way where weaker inclusions are stationed. This is an indication of the efficacy of the present model. The interpretation of the energy variation is a clear indication that the energy of the system is being conserved and no severe distortion is seen. Further from the PDE and DDE comparison, there have been increase in DDE and decrease in PDE in case of heterogeneous model delineate that with having inclusion, more localized damage has been observed which is congruous with the real-life experiments. This model exhibits a basic structure of incorporating the heterogeneity in numerical simulation, hence it has a viable prospect of tuning up to acquire greater degree of coherence with the real-life phenomenon.

Appendix A

The stress–strain curve for concrete in compression is deduced from the following empirical equations given by Hsu and Hsu [17]

$$\eta = \frac{n\beta x}{n\beta - 1 + x^{n\beta}} \tag{4}$$

$$\eta = \frac{f_c}{f_c'} \tag{5}$$

$$x = \frac{\varepsilon_c}{\varepsilon_0} \tag{6}$$

$$\beta = \left(\frac{f_c'}{9.46}\right)^3 + 2.59, \tag{7}$$

where n = 1 ($f_c' < 62$ MPa), 2 (62 MPa < f_c' < 76 MPa), 3 (76 MPa < f_c' < 90 MPa) and 5 ($f_c' > 90$ MPa).

$f_c^{/}$ = Compressive strength of the concrete (kip/in^2); f_c = Compressive Stress in general (kip/in^2).

ε_0 = strain corresponding to the peak stress; ε_c = strain corresponding to f_c

$$\varepsilon_0 = 8.9 * 10^{-5} * f_c' + 2.114 * 10^{-3} \tag{8}$$

$$E = 1.2431 * 10^2 * f_c' + 3.28312 * 10^3. \tag{9}$$

And stress–strain curve for concrete in tension is drawn by using the equation given by Aslani [18] as

$$f_t = f_t'\left(\frac{\varepsilon_{ct}'}{\varepsilon_t}\right)^{0.85} \tag{10}$$

$$f_t' = 0.1 * f_c', \tag{11}$$

where, f_t' = tensile strength of concrete (MPa); f_t = Tensile stress in general (MPa).

ε_{ct}' = critical strain at maximum tensile stress; ε_t = Strain corresponding to f_t.

The CDP model needed the values of inelastic strain in compression and cracking strain in tension. This can be calculated from ABAQUS 6.13 user's guide [13] as

$$\text{For compression, } \varepsilon_c^{in} = \varepsilon_c - \varepsilon_0^{el}. \tag{12}$$

$$\text{For tension, } \varepsilon_t^{ck} = \varepsilon_t - \varepsilon_0^{el}. \tag{13}$$

ABAQUS checks the accuracy of the stress–strain curve by considering the plastic strain values.

$$\text{For Compression, } \varepsilon_c^{pl} = \varepsilon_c^{in} - \frac{d_c}{1 - d_c} * \frac{f_c}{E}. \tag{14}$$

$$\text{For Tension, } \varepsilon_t^{pl} = \varepsilon_t^{ck} - \frac{d_t}{1 - d_t} * \frac{f_t}{E}. \tag{15}$$

Damage parameters are calculated by using linear damage rule ABAQUS 6.13 user's guide [13] as

$$\text{For compression, } d_c = 1 - \frac{f_c}{f_c'} \tag{16}$$

where ε_c^{in} = Inelastic strain; ε_0^{el} = Elastic strain corresponding to undamaged material.

ε_t^{ck} = Cracking strain; ε_c^{pl} = Plastic strain in compression; ε_t^{pl} = Plastic strain in tension.

d_c = Damage parameter in compression; d_t = Damage in tension.

References

1. Fujikake K, Li B, Soeun S (2009) Impact response of reinforced concrete beam and its analytical evaluation. J Struct Eng 135:938–950. https://doi.org/10.1061/(asce)st.1943-541x.0000039
2. Farnam Y, Mohammadi S, Shekarchi M (2010) Experimental and numerical investigations of low velocity impact behavior of high-performance fiber-reinforced cement based composite. Int J Impact Eng 37(220–229). https://doi.org/10.1016/j.ijimpeng.2009.08.006
3. Mindess S, Yan C (1993) Perforation of plain and fibre reinforced concretes subjected to low-velocity impact loading. Cem Concr Res 23:83–92. https://doi.org/10.1016/0008-8846(93)90138-Y
4. Jiang H, Wang X, He S (2012) Numerical simulation of impact tests on reinforced concrete beams. Mater Des 39:111–120. https://doi.org/10.1016/j.matdes.2012.02.018
5. Liao W, Li M, Zhang W, Tian Z (2017) Experimental studies and numerical simulation of behavior of RC beams retrofitted with HSSWM-HPM under impact loading. Eng Struct 149:131–146. https://doi.org/10.1016/j.engstruct.2016.07.040
6. Iqbal MA, Gupta PK, Deore VS, Tak SK, Tiwari G, Gupta NK (2012) Effect of target span and configuration on the ballistic limit. Int J Impact Eng 42:11–24. https://doi.org/10.1016/j.ijimpeng.2011.10.004
7. Radnić J, Matešan D, Grgić N, Baloević G (2015) Impact testing of RC slabs strengthened with CFRP strips. Compos Struct 121:90–103. https://doi.org/10.1016/j.compstruct.2014.10.033
8. Anderson TL (2005) Fracture mechanics: fundamentals and applications. CRC Press, Boca Raton
9. Benz W, Asphaug E (1995) Simulations of brittle solids using smooth particle hydrodynamics. Comput Phys Commun 87:253–265. https://doi.org/10.1016/0010-4655(94)00176-3
10. Weibull W (1939) A statistical theory of the strength of materials. http://www.barringer1.com/wa_files/Weibull-1939-Strength-of-Materials.pdf
11. Angulo SC, Silva NV, Lange DA, Tavares LM (2020) Probability distributions of mechanical properties of natural aggregates using a simple method. Constr Build Mater 233. https://doi.org/10.1016/j.conbuildmat.2019.117269
12. Lim WL, McDowell GR, Collop AC (2004) The application of Weibull statistics to the strength of railway ballast. Granul Matter 6:229–237. https://doi.org/10.1007/s10035-004-0180-z
13. Dassault systems: Abaqus/CAE user manual. 1051 (2010)
14. De Borst R (2001) Fracture in quasi-brittle materials: a review of continuum damage-based approaches. Eng Fract Mech 69:95–112. https://doi.org/10.1016/S0013-7944(01)00082-0
15. MatLab: programming fundamentals R 2014 b. Manual. 1–1050 (2014)

16. Zhang D, Huang X, Zhao Y (2012) Investigation of the shape, size, angularity and surface texture properties of coarse aggregates. Constr Build Mater 34:330–336. https://doi.org/10.1016/j.conbuildmat.2012.02.096
17. Hsu LS, Hsu CTT (1994) Complete stress—strain behaviour of high-strength concrete under compression. Mag Concr Res 46:301–312. https://doi.org/10.1680/macr.1994.46.169.301
18. Aslani F, Jowkarmeimandi R (2012) Stress-strain model for concrete under cyclic loading. Mag Concr Res 64:673–685. https://doi.org/10.1680/macr.11.001202010

Analytical Solution for Buckling of Rectangular Plate Subjected to Non-uniform Uniaxial Compression Using FSDT

Sushree Das and Prasun Jana

1 Introduction

Complex structural systems are often built by making plate as one of its constituting elements. In practical applications, plates are idealization of segment of larger stiffened and built-up structures like a wing of aircraft or the stiffened plate in the ship structure. In most of the cases, the loads causing buckling are exerted by the adjoining structural constituents. Hence, mathematical modeling of real load distribution on the extremity of small rectangular portion under study is not an easy task. In actual practice, the elastic forces between the adjoining elements are dependent on their relative stiffness. In general, such internal elastic force distributions can be assumed to be varied from structure to structure and it may not be possible to determine this force distribution without an intricate investigation of the whole structure. So, it remains to be an important task to examine the impact of several non-uniform simple edge load distributions and to analyze their impact on buckling behavior of the plate both qualitatively and quantitatively.

Literature on buckling response of isotropic rectangular plate under the influence of different types of loading and boundary conditions is rich. For example, Wang et al. [1] incorporated Galerkin's method along with Legendre's polynomials as shape functions. They inspected the buckling aspect of rectangular plates under the effect of different in-plane edge compressive load which are linearly varying in nature. Authors verified the same with two loaded edges having simply supported boundary condition and the other two sides are either of simply supported or clamped. Buckling of moderately thick plate was analyzed by Sundaresan et al. [2] in the framework of finite element model. In the same research article, geometric stiffness matrix

S. Das (✉) · P. Jana
Department of Aerospace Engineering, Indian Institute of Technology Kharagpur, Kharagpur 721302, India

D. K. Maiti et al. (eds.), *Recent Advances in Computational and Experimental Mechanics, Vol II*, Lecture Notes in Mechanical Engineering,
https://doi.org/10.1007/978-981-16-6490-8_40

followed by stress distribution within the plate was figured out by solving the pre-buckling equations. Exact solutions have been presented by Leissa and Kang [3] for the buckling and free vibration analysis of rectangular plates subjected to in-plane loading which are linearly varying in nature. The configuration of the plate considered was two opposite edges having simply supported and the rest of the two were clamped along with simply supported boundary condition. Frobenius power series method has been used here. Jana and Bhaskar [4] performed an in-depth assessment of plane stress analysis by adopting rigorous superposition approach by considering a comprehensive set of loads and it was observed that the critical load changed by significant amount with slight differences in the characteristic of load distribution. Wang and Lee [5] examined the buckling response of the orthotropic plates applied to in-plane non-uniform load with distinguishable set of boundary conditions. Kalyan and Bhaskar [6] presented convergent studies on buckling analysis of rectangular orthotropic plate subjected to different uniaxial load distribution implementing first-order shear deformation theory (FSDT). In their work, Galerkin's method and principle of super position for two-dimensional in-plane stress analysis played the key role for the determination of critical buckling load. In the research article Nguyen et al. [7], the shear correction co-efficient for FSDT was highlighted and applications were presented for a sandwich plate with simply supported boundary condition clamped at both the ends. In addition to this, the effect of this shear correction factor on the static response had been studied. Shufrin et al. [8] inspected the buckling behavior by taking symmetrically laminated rectangular plate and adopted a semi-analytical multi-term extended Kantrovich method with a set of general boundary conditions thereby eliminating the limitation of single-term extended Kantrovich method. Ramachandra and Panda [9] evaluated the buckling behavior of rectangular composite plate with nine sets of boundary conditions applied to non-uniform in-plane loading as well as he discussed about buckling mode shapes. Bodaghi and Saidi [10] developed an appropriate solution for buckling of functionally graded rectangular plate resting on Pasternak foundation where there is a distribution of non-uniform in-plane load acting at two simply opposite edges.

Levy type buckling equation and method of Frobenius for exact solution was adopted in their work. Accurate buckling of rectangular plate under uni-axial and bi-axial compressive load by differential quadrature method was analyzed by Wang and Wang [11]. The author demonstrated the computational efficiency of DQM in solving partial differential equation with boundary conditions using Dirac delta function. An analytical procedure was developed by Mijušković et al. [12] for critical load of plates with various types of boundary condition under arbitrary in-plane compressive loads. Singh and Harsha [13] implemented non-polynomial based HSDT and found the buckling response of FGM subjected to uniform, linear and non-linear in-plane loads. Various parametric studies had been carried out to find out its effect on deflection, stress and critical buckling loads.

It is imperative to mention here that very few studies have been focused on the influence of non-uniform compressive loads on the plate. Additionally, the analytical solution corresponding to the buckling of isotropic plate subjected to non-uniform compressive edge load distributions using first-order shear deformation theories

(FSDT) has received very little attention. By the implementation of FSDT, the solution will be applicable to thicker plates. Therefore, the objective of this work is to develop an analytical solution corresponding to the buckling behavior of simply supported rectangular plate subjected to various non-uniform edge load distributions by using FSDT. In the initial stage, in-plane stress field is determined. For the in-plane stress, the solution procedure is adopted from Jana and Bhaskar [4]. The approach includes the superposition of three Airy's stress function which are to be suitably obtained for each non-uniform uniaxial compression applied at the opposite edges (as shown in Fig. 1). The stress solutions are taken in appropriate Fourier series terms so that boundary conditions and all the field equations are satisfied. After obtaining the stress field within the plate, the same has been used in the computation of the buckling load by the implementation of Galerkin's method with a definite set of permissible functions thereby ensuring convergence.

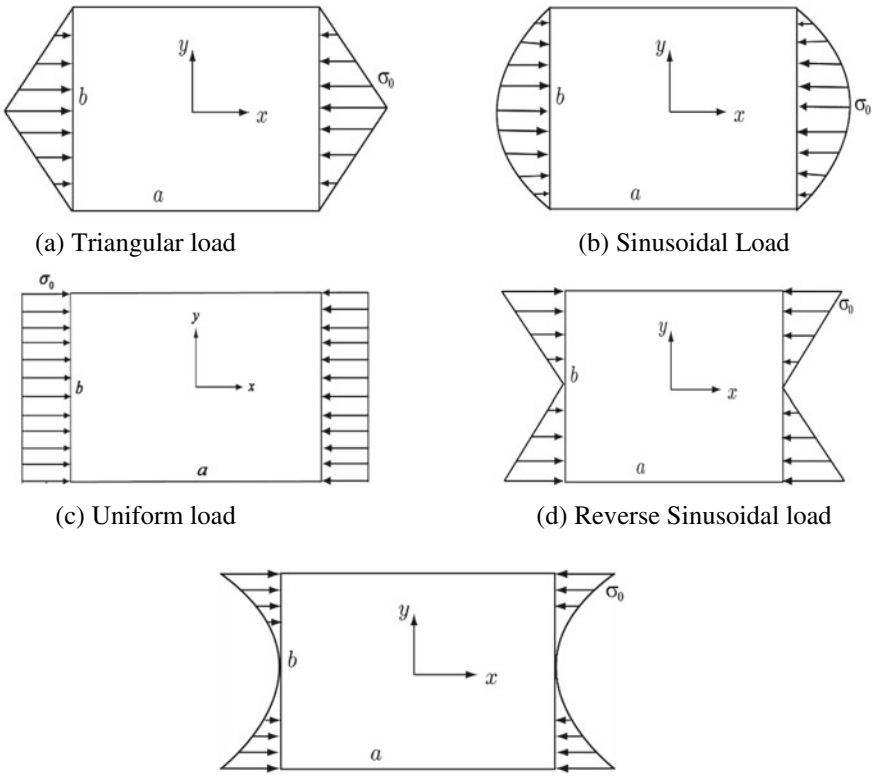

(a) Triangular load (b) Sinusoidal Load

(c) Uniform load (d) Reverse Sinusoidal load

(e) Reverse sinusoidal load

Fig. 1 Various non-uniform uniaxial compressive load cases considered in the analysis

2 Mathematical Modeling and Formulation

2.1 Plane Stress Solution

Superposition of Airy's stress function, assumed in the form of Fourier series, has been adopted here as a solution strategy. Each of the uniaxial compressive loads is expressed in terms of Fourier series in an effort to satisfy the boundary conditions at each of loading edges.

2.1.1 Building Block 1

The solution procedures for in-plane stress field have been taken from Jana and Bhaskar [4]. A uniaxial load symmetric about x-axis is applied on the rectangular plate

$(-a/2 \leq x \leq a/2, -b/2 \leq y \leq b/2)$ in the present study (see Fig. 1). The loads are represented by taking an appropriate series and are expressed in the form

$$\sigma_x = \sum_{p=1,3,5}^{\infty} \sigma_p \cos(p\pi\lambda), \lambda = \frac{y}{b} \tag{1}$$

An admissible Airy's stress function ϕ_1 is given by

$$\phi_1 = \sum_{p=1,3,5} f(x) \cos(p\pi\lambda). \tag{2}$$

Substituting the above Airy's stress function in the governing partial differential equation $\nabla^4\phi = 0$, the general solution for the function $f(x)$ is found to be

$$f(x) = \sum_{p=1,3,5} C_{1p} \cosh(p\pi\alpha) + C_{2p} \sinh(p\pi\alpha) + C_{3p}x \cosh(p\pi\alpha) + C_{4p}x \sinh(p\pi\alpha) \tag{3}$$

where $\alpha = \frac{x}{a}$.

In which constants $C_{1p}, C_{2p}, C_{3p}, C_{4p}$ are to be computed by applying the suitable boundary conditions.

It is important to emphasize that this stress function comes with a solution with zero normal stress at $\lambda = \pm 1/2$. Imposition of zero shear stress and normal stress, as stated in Eq. (1), at $\eta = \pm 1/2$ yields

$$\phi_1 = \sum_{p=1,3,5} \cos(p\pi\lambda)\left[C_{1p} \cosh(p\pi\alpha) + C_{4p}x \sinh(p\pi\alpha)\right]. \tag{4}$$

The mathematical expressions of C_{1p} and C_{4p} are provided in appendix A.

Regardless of the appropriate application of boundary conditions, the in-plane stress solution produces residual stress (τ_1) at the edges $\lambda = \pm 1/2$ given by

$$\tau_1 = \pm \sum_{p=1,3,5} \frac{p\pi}{b} \sin\left(\frac{p\pi}{2}\right)\left[\left(C_{1p}\frac{p\pi}{b} + C_{4p}\right)\sinh(p\pi\alpha) + C_{4p}\frac{p\pi}{b}x\cosh(p\pi\alpha)\right] \tag{5}$$

To nullify the effect of these above obtained residual shear stresses, superposition of two additional stress functions is done on the first solution which promotes two additional building blocks.

2.1.2 Building Block 2

The additional building block is emerged as a consequence of applying shear stresses at $\lambda = \pm 1/2$ and this applied shear stress is expressed by the Fourier sine series

$$\tau_{xy2} = \pm \sum_{s=1,3,5} A_s \sin(s\pi\alpha), \tag{6}$$

where A_s are the co-efficients to be determined.

The above procedure as described in building block 1 is followed here. Applying zero normal stress and enforced shear stress boundary conditions at $\lambda = \pm 1/2$, another stress function ϕ_2 for this case can be represented as

$$\phi_2 = \sum_{s=1,3,5} \cos(s\pi\alpha)[C_{1s}\cosh(s\pi\beta) + C_{4s}y\sinh(s\pi\beta)],\ \beta = \frac{y}{a} \tag{7}$$

The co-efficients C_{1s} and C_{4s} are mentioned in Appendix A.

As described in the building block 1, this solution also gives rise to a residual stress (τ_2) at $\eta = \pm 1/2$ which is given by

$$\tau_2 = \sum_{s=1,3,5} \frac{s\pi}{a} \sin\left(\frac{s\pi}{2}\right)\left[\left(C_{1s}\frac{n\pi}{a} + C_{4s}\right)\sinh(s\pi\beta) + C_{4s}\frac{s\pi}{a}y\cosh(s\pi\beta)\right] \tag{8}$$

2.1.3 Building Block 3

To eliminate the residual shear stress arising at $\eta = \pm 1/2$, there is a requirement of third building block. Here, shear stresses at $\eta = \pm 1/2$ have been imposed and expressed by the Fourier sine series

$$\tau_{xy3} = \pm \sum_{q=1,3,5} B_q \sin(q\pi\lambda), \tag{9}$$

with B_q as the undetermined co-efficients.

The stress function in case of third building block has similarities as that of first building block. Again, enforcing applied shear stress at $\eta = \pm 1/2$ and zero normal stress, the stress solution yields

$$\phi_3 = \sum_{q=1,3,5} \cos(q\pi\lambda)\left[C_{1q}\cosh(q\pi\alpha) + C_{4q}x\sinh(q\pi\alpha)\right], \tag{10}$$

where the co-efficients C_{1q} and C_{4q} are described in Appendix A.

This stress solution again comes up with a residual solution (τ_3) at the edge $\lambda = \pm 1/2$ and given by

$$\tau_3 = \pm \sum_{q=1,3,5} \frac{q\pi}{b} \sin\left(\frac{q\pi}{2}\right)\left[\left(C_{1q}\frac{q\pi}{b} + C_{4q}\right)\sinh(q\pi\alpha) + C_{4q}\frac{q\pi}{b}x\cosh(q\pi\alpha)\right] \tag{11}$$

2.2 Superposition

In order to determine the stress field within the plate accurately, all the three building blocks are superimposed and zero shear boundary condition is applied. This leads to the following equations

$$\tau_1 + \tau_3 + \tau_{xy2} = 0 \text{ at } \lambda = \pm 1/2. \tag{12}$$

$$\tau_2 + \tau_{xy3} = 0 \text{ at } \eta = \pm 1/2. \tag{13}$$

It is worth mentioning that the solution of Eqs. (12) and (13) implicates the expansion of τ_1,τ_2,τ_3 into a Fourier sine series and yields as many as number of equation required for the unknown co-efficients A_s and B_q.

After getting all the unknown co-efficients, the final in-plane stress fields are calculated as follows:

$$\phi = \phi_1 + \phi_2 + \phi_3 \tag{14}$$

And

$$\sigma_x = \frac{\partial^2 \phi}{\partial y^2}, \sigma y = \frac{\partial^2 \phi}{\partial x^2}, \tau_{xy} = -\frac{\partial^2 \phi}{\partial y \partial x}. \tag{15}$$

2.3 Results and Discussions

Results are obtained for the load cases presented in Fig. 1. For each of the load cases, satisfactory number of terms are taken (in Eqs. (1), (4), (7) and (10)) to make sure that the final in-plane stress solutions are converged up to first four digits. An effort has been made to fulfill the requirement of zero shear boundary conditions, and to accomplish this, superposition of three stress functions is implied at the edges of the plate. The final superposed value of shear stress is found to be converged and it is observed that the value shifts towards zero as the number of terms are increased considered in ϕ_2 and ϕ_3 (i.e., $s_{\max}$ and $q_{\max}$). $s_{\max}$ and $q_{\max}$ are considered equal on the grounds of convenience. Similar kind of study has been conducted for each load case for assurance of the numerical fulfillment of zero shear boundaries always. The maximum value of σ_y and τ_{xy} is not insignificant as compared to σ_x in load cases except uniform load case which gives trivial solutions and the effect of these stresses (i.e., σ_y and τ_{xy}) on buckling cannot be neglected.

3 Buckling Analysis and Results

The governing differential equations corresponding to the buckling of rectangular plate based on FSDT are given below [14]:

$$k_s A_{55}(w_{0,xx} + \phi_{x,x}) + k_s A_{44}(w_{0,yy} + \phi_{y,y}) + N_{xx} w_{0,xx} + 2N_{xy} w_{0,xy} + N_{yy} w_{0,yy} = 0 \tag{16}$$

$$D_{11}\phi_{x,xx} + D_{12}\phi_{y,xy} + D_{66}\left(\phi_{x,yy} + \phi_{y,xy}\right) - k_s A_{55}\left(w_{0,x} + \phi_x\right) = 0 \tag{17}$$

$$D_{66}\left(\phi_{x,xy} + \phi_{y,xx}\right) + D_{12}\phi_{x,xy} + D_{22}\phi_{y,yy} - k_s A_{44}\left(w_{0,y} + \phi_y\right) = 0 \tag{18}$$

Exact analytical solution is quite complex to obtain as in-plane stress is a function of both x and y. Therefore, Galerkin's method is implemented to find out the buckling solution for the case of simply supported boundary condition case. An admissible function for w, ϕ_x and ϕ_y has been taken and is given below:

$$w(x, y) = \sum_{m=1,2,3} \sum_{n=1,2,3} w_{mn} \sin\left[m\left(\frac{\pi}{2} - \pi\eta\right)\right] \sin\left[n\left(\frac{\pi}{2} - \pi\lambda\right)\right]$$

Table 1 Total buckling load (non-dimensional values for K in $P_{cr} = K\pi^2 D/b$) for five different load cases. b/h = 10,$k_s = 5/6$

Load cases	Square plate		Rectangular plate ($a/b = 2$)	
	Ref. [4] (CPT)	Present (FSDT)	Ref. [4] (CPT)	Present (FSDT)
Triangular load	3.339	3.157	3.576	3.442
Sinusoidal load	3.450	3.263	3.656	3.503
Uniform load	4.000	3.800	4.000	3.800
Reverse triangular load	4.934	4.663	4.350	4.207
Reverse sinusoidal load	5.438	5.131	4.456	4.411

$$\phi_x(x, y) = \sum_{m=1,2,3} \sum_{n=1,2,3} \phi_{xmn} \cos\left[m\left(\frac{\pi}{2} - \pi\eta\right)\right] \sin\left[n\left(\frac{\pi}{2} - \pi\lambda\right)\right]$$

$$\phi_y(x, y) = \sum_{m=1,2,3} \sum_{n=1,2,3} \phi_{ymn} \sin\left[m\left(\frac{\pi}{2} - \pi\eta\right)\right] \cos\left[n\left(\frac{\pi}{2} - \pi\lambda\right)\right]$$

where α, β, λ are already mentioned and $\eta = \frac{x}{a}$.

The buckling loads for rectangular plate have been achieved based on the superposition approach for two-dimensional in-plane stress analysis and by implementing Galerkin's method for stability analysis subjected to various uniaxial compressive edge load distributions. The convergent buckling results have been presented in tabular form below. A comparison of non-dimensional buckling load based on CPT and FSDT has been presented in Table 1.

In Table 1, the non-dimensional critical buckling load for the rectangular plate for different load cases along with two different aspect ratios has been presented. From the results presented in Table 1, it is observed that the plate aspect ratio plays an important role during the estimation of critical buckling load. It can be said that critical buckling load varies with both plate aspect ratio and type of loading applied. For the first two load cases, the critical buckling load increases with increase in the plate aspect ratio, whereas for uniform load cases, its value remains constant. Considering the last two load cases, it can be stated that the critical buckling load decreases with increase in the aspect ratios of the plate.

Additionally, it is observed that in all the load cases presented in Table 1, non-dimensional critical buckling load computed based on FSDT is less than that of the value calculated using CPT. Therefore, it can be concluded that CPT over predicts the critical buckling load. Hence, FSDT theory is more successful in evaluating buckling load in comparison to CPT.

4 Conclusion

Buckling analysis for a number of non-uniform uniaxial load distributions for isotropic plate using first-order shear deformation theory (FSDT) has been presented here for the first time. At first, plane stress solution is obtained using superposition of Airy's stress functions. Based on the plane stress solution, Galerkin's methodology has been implemented where a sufficient number of trial functions are taken to ensure convergence. It is expected that these converged critical buckling load values can be treated as a benchmark for comparing the accuracies involved in various approximate methods such as finite element method.

The dependency of buckling load on aspect ratio has been shown in tabular form and compared with that of the published result based on classical plate theory (CPT). It is shown that the buckling load has great dependency on the aspect ratio of the plate. This tendency is observed from the analysis based on both FSDT and CPT. Estimated value of buckling load for first two load cases increases with higher respect ratio while it shows a decreasing tendency for the last two load cases. For uniform load, it remains constant. It can be noted that the present approach can be applied for thicker plate as FSDT has been used in the analysis. In the future, the present work will be extended for buckling analysis of orthotropic and functionally graded plate subjected to non-uniform compressive edge loads.

Appendix A

$$C_{1p} = -\frac{\sigma_p b^2\left[ap\pi\cosh\left(\frac{ap\pi}{2b}\right) + 2b\sinh\left(\frac{ap\pi}{2b}\right)\right]}{p^2\pi^2\left[ap\pi + b\sinh\left(\frac{ap\pi}{b}\right)\right]}$$

$$C_{4p} = \frac{2\sigma_p b^2\sinh\left(\frac{ap\pi}{2b}\right)}{p\pi\left[ap\pi + b\sinh\left(\frac{ap\pi}{b}\right)\right]}$$

$$C_{1s} = -\frac{a^2 bA_s\sinh\left(\frac{s\pi b}{2a}\right)}{bs^2\pi^2 + (as\pi)\sinh\left(\frac{bs\pi}{a}\right)}$$

$$C_{4s} = \frac{2a^2 A_s\cosh\left(\frac{s\pi b}{2a}\right)}{bs^2\pi^2 + (as\pi)\sinh\left(\frac{bs\pi}{a}\right)}$$

$$C_{1q} = -\frac{ab^2 B_q\sinh\left(\frac{q\pi a}{2b}\right)}{aq^2\pi^2 + bq\pi\sinh\left(\frac{aq\pi}{b}\right)}$$

$$C_{4q} = \frac{2b^2 B_q\cosh\left(\frac{q\pi a}{2b}\right)}{aq^2\pi^2 + bq\pi\sinh\left(\frac{aq\pi}{b}\right)}$$

References

1. Wang J, Biggers SB, Dickson JN (1984) Buckling of composite plates with a free edge in edgewise bending and compression. AIAA J 22:394–402
2. Sundaresan P, Singh G, Rao GV (1998) Buckling of moderately thick rectangular composite plates subjected to partial edge compression. Int J Mech Sci 40:1105–1117
3. Leissa A, Kang J (2002) Exact solutions for vibration and buckling of an SS-C-SS-C rectangular plate loaded by linearly varying in-plane stresses. Int J Mech Sci 44:1925–1945
4. Jana P, Bhaskar K (2006) Stability analysis of simply-supported rectangular plates under non-uniform uniaxial compression using rigorous and approximate plane stress solutions. Thin-Walled Struct. 44:507–516
5. Wang IH, Lee JS (2006) Buckling of orthotropic plates under various in plane loads. KSCE J Civ Eng 10:349–356
6. Kalyan JB, Bhaskar K (2008) An analytical parametric study on buckling of non-uniformly compressed orthotropic rectangular plates. Compos Struct 82:10–18
7. Nguyen TK, Sab K, Bonnet G (2008) First-order shear deformation plate models for functionally graded materials. Compos Struct 83:25–36
8. Shufrin I, Rabinovitch O, Eisenberger M (2008) Buckling of symmetrically laminated rectangular plates with general boundary conditions—a semi analytical approach. Compos Struct 82:521–531
9. Panda SK, Ramachandra LS (2010) Buckling of rectangular plates with various boundary conditions loaded by non-uniform in plane loads. Int J Mech Sci 52:819–828
10. Bodaghi M, Saidi AR (2011) Stability analysis of functionally graded rectangular plates under nonlinearly varying in-plane loading resting on elastic foundation. Arch Appl Mech 81:765–780
11. Wang X, Wang Y (2015) Buckling analysis of thin rectangular plates under uniaxial or biaxial compressive point loads by the differential quadrature method. Int J Mech Sci 101–102:38–48
12. Mijušković O, Ćorić B, Šćepanović B (2015) Accurate buckling loads of plates with different boundary conditions under arbitrary edge compression. Int J Mech Sci 101–102:309–323
13. Singh SJ, Harsha SP (2019) Buckling analysis of FGM plates under uniform, linear and non-linear in-plane loading. J Mech Sci Technol 33:1761–1767
14. Reddy JN (2006) Theory and analysis of elastic plates and shells, 2nd edn. CRC Press

Dynamic Stresses in Bridge Girder Caused by the Randomly Moving Loads

Anjaly J. Pillai and Sudip Talukdar

1 Introduction

Analysis of dynamic response of bridges subject to moving vehicles has been an area of major research for several decades [1] because of its several practical applications which includes structural health monitoring of bridges, vibration control in real time and prediction of fatigue life of the bridges. In recent times, design span of the bridges has been increased whereas traffic also keeps growing day by day due to increase of socio-economic activities. Considering various innovative design of bridges and heavy truck movement, analysis of bridge vibration to obtain dynamic amplification factor induced by vehicles has been reported by various researchers and codified for practice [2, 3].

The problem of dynamic response of the bridge due to moving loads has been studied in a deterministic manner [4, 5]. Since the vehicular loads arrive on the bridge at random times having random magnitude, it is necessary to study the transverse vibration of the bridge considering the arrival time of the vehicle as a random variable. The vibration of a beam due to random moving force has been studied [6, 7]. The vibration of the beam due to the random stream of moving forces assuming that the bridge response follows a filtered renewal process has been studied [8]. The dynamic response assuming that the interarrival time of the vehicle as a random variable was evaluated [9, 10]. The traffic excitation model, assuming that the vehicle arrival follows Poisson process was developed [11].

Several authors have considered the effect of road surface conditions and used coupled bridge-vehicle equations to study the dynamic response of the structure. The dynamic interaction between vehicles and structures was analysed [2, 12–14]. The dynamic response of the bridge under suspended moving loads considering the

A. J. Pillai (✉) · S. Talukdar
Department of Civil Engineering, Indian Institute of Technology, Guwahati, Assam 781039, India
e-mail: anjalypillai@iitg.ac.in

D. K. Maiti et al. (eds.), *Recent Advances in Computational and Experimental Mechanics, Vol II*, Lecture Notes in Mechanical Engineering,
https://doi.org/10.1007/978-981-16-6490-8_41

effects of random surface irregularities was analysed [15]. Vehicle model to estimate the impact in highway bridge was developed wherein the vehicular load was assumed to be a constant load with a sinusoidally varying component [16].

There is scanty of literatures reported on the dynamic response of bridge considering the stream of vehicles arriving on bridge at random rate, which actually happens in real scenario. The present study is thus focused on the dynamics of bridge subject to randomly moving load over uneven pavement. An orthogonal polynomial-based method has been used to obtain the statistics of the bridge response. Effects of vehicle speed, vehicle arrival time and road roughness on the amplification of dynamic stress have been studied.

2 Methodology

The bridge-vehicle couple dynamic equations for the mathematical model of single span bridge and multiple quarter car vehicle model is shown in Fig. 1. The variables appearing in model are sprung mass m_s; unsprung mass m_w; suspension stiffness k_s; suspension damping c_s; tyre stiffness k_w; tyre damping c_w; sprung mass displacement z_1; unsprung mass displacement z_2. The displacement of bridge is y at time instant t at location x. All the vehicles are assumed to travel with same velocity, however, their arrival time are treated as random variable, which follows Poisson process. The governing differential equations can be written after expanding damping matrix C, stiffness matrix K and force vector F using Taylor series about the mean and retaining only first terms as [17],

$$\begin{aligned} \boldsymbol{M}\ddot{\boldsymbol{x}} + \left[\boldsymbol{C_m} + \boldsymbol{C}_{\lambda t_n}\{\lambda t_n - \mu(\lambda t_n)\}\right]\dot{x} + \left[\boldsymbol{K_m} + \boldsymbol{K}_{\lambda t_n}\{\lambda t_n - \mu(\lambda t_n)\}\right]\boldsymbol{x} \\ = \boldsymbol{F_m}(\boldsymbol{t}) + \boldsymbol{F}_{\lambda t_n}\{\lambda t_n - \mu(\lambda t_n)\} \end{aligned} \tag{1}$$

in which $\boldsymbol{M}$ is mass matrix, $\boldsymbol{C_m}$, $\boldsymbol{K_m}$ and $\boldsymbol{F_m}$ are the mean values of damping, stiffness matrix and force vector, respectively, λ is the mean arrival rate of the vehicles and t_n is the arrival time of the vehicles on the bridge, $\mu(\lambda t_n)$ is the mean arrival time. The terms $\boldsymbol{C}$, $\boldsymbol{K}$ and $\boldsymbol{F}$ with subscript λt_n denote first-order differential coefficient of the corresponding variable with respect to λt_n, evaluated at $t = \lambda t_n$.

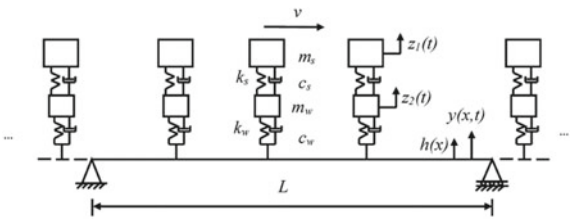

Fig. 1 Vehicle movement on bridge

The mass matrix consists of vehicle mass and bridge mass. The damping and stiffness matrices comprise of vehicle damping and stiffness and bridge damping and stiffness. The element X_i of the array x (response vector) is expressed as the summation of the product of transformed time co-ordinate and orthogonal polynomial function as,

$$X_i(t) = \sum_{l=0}^{N_1} Q_{il}(t) L_l^n(\lambda t_n);\ i = 1,\ 2,\ ...,\ n_d \tag{2}$$

where, n is analogous to the shape parameter of Gamma distribution which is the number of vehicle arrivals in the present study, n_d is the number of degrees of freedom considered, N_1 is the number of basic functions with respect to λt_n, $L_l^n(\lambda t_n)$ is the orthogonal function considered and $Q_{il}(t)$ is the time variation of displacement. Since, the arrival time of the vehicle follows Poisson process, the distribution of arrival time is Gamma distribution given by,

$$p_{t_n}(t) = \frac{\lambda^n t^{n-1} \exp(-\lambda t)}{\Gamma(n)} \tag{3}$$

where, $pt_n(t)$ is the probability density function of the arrival time, and Γ is the gamma function. Using the property of function of random variable [18], the probability density function of λt_n is given as,

$$p_{\lambda t_n}(\lambda t) = \frac{t^{n-1} \exp(-t)}{\Gamma(n)} \tag{4}$$

In the present study, orthogonal polynomial function considered to be Associated Laguerre Polynomial [19] is found to satisfy orthogonality condition as shown below,

$$\int_0^{\lambda t} p_{\lambda t_n}(\lambda t) L_l^n(\lambda t_n) L_k^n(\lambda t_n)\, d\lambda t_n = d_l^2 \delta_{lk};\ l,\ k = 0,\ 1,\ 2,\ ...,\ N_1 \tag{5}$$

The following recurrence relationships derived will be utilized in present formulation to find the expected value of response quantities [20].

$$\begin{aligned}
&\lambda t_n L_l^n(\lambda t_n) = \alpha_{l-1} L_l^n(\lambda t_n) + \beta_l L_l^n(\lambda t_n) + \\
&\gamma_{l+1} L_l^n(\lambda t_n) \\
&\alpha_{l-1} = -(l - 1 + n) \\
&\gamma_{l+1} = -(l + 1 + 1) \\
&\beta_l = (2l) + n + 1
\end{aligned} \tag{6}$$

Let the response vector be expressed as

$$\boldsymbol{X}(t) = \sum_{l=0}^{N_1} \boldsymbol{Q}_l(t)\, L_l^n(\lambda t_n) \tag{7}$$

Now substitute Eq. (7) in Eq. (1),

$$\boldsymbol{M} \sum_{l=0}^{N_1} \ddot{\boldsymbol{Q}}_l(t) L_l^n(\lambda t_n) + \left(\boldsymbol{C}_m + \boldsymbol{C}_{\lambda t_n}\{\lambda t_n - \mu(\lambda t_n)\}\right) \sum_{l=0}^{N_1} \dot{\boldsymbol{Q}}_l(t) L_l^n(\lambda t_n)$$
$$+ \left(\boldsymbol{K}_m + \boldsymbol{K}_{\lambda t_n}\{\lambda t_n - \mu(\lambda t_n)\}\right) \sum_{l=0}^{N_1} \boldsymbol{Q}_l(t) L_l^n(\lambda t_n) = \boldsymbol{F}(t)_m + \boldsymbol{F}(t)_{\lambda t_n}\{\lambda t_n - \mu(\lambda t_n)\} \tag{8}$$

The steps adopted now are to (i) multiply Eq. (8) by $L_k^n(\lambda t_n)$ and utilize the recurrence relation for terms $\lambda t_n L_l^n(\lambda t_n)$ as in Eq. (6), (ii) multiply again the resulting equation by probability density function $p_{\lambda tn}(\lambda t)$ and (iii) finally integrate in the domain of random variable using orthogonal property of polynomial mentioned earlier. The resulting equation is obtained as

$$\boldsymbol{M} \sum_{l=0}^{N_1} \ddot{\boldsymbol{Q}}_l(t) d_l^2 \delta_{lk} +$$
$$\sum_{l=0}^{N_1} \dot{\boldsymbol{Q}}_l(t) \Big[\boldsymbol{C}_m\, d_l^2 \delta_{lk} + \boldsymbol{C}_{\lambda t_n}\left(\alpha_{l-1} d_{l-1}^2 \delta_{l-1k} + \beta_l\, d_l^2 \delta_{lk} + \gamma_{l+1} d_{l+1}^2 \delta_{l+1k}\right) - \boldsymbol{C}_{\lambda t_n} \mu(\lambda t_n) d_l^2 \delta_{lk}\Big] +$$
$$\sum_{l=0}^{N_1} \boldsymbol{Q}_l(t) \Big[\boldsymbol{K}_m\, d_l^2 \delta_{lk} + \boldsymbol{K}_{\lambda t_n}\left(\alpha_{l-1} d_{l-1}^2 \delta_{l-1k} + \beta_l\, d_l^2 \delta_{lk} + \gamma_{l+1} d_{l+1}^2 \delta_{l+1k}\right) - \boldsymbol{K}_{\lambda t_n} \mu(\lambda t_n) d_l^2 \delta_{lk}\Big] =$$
$$\boldsymbol{F}(t)_m d_0^2 \delta_{0k} + \boldsymbol{F}(t)_{\lambda t_n}\left(\alpha_{k-1} d_0^2 \delta_{0k-1} + \beta_0\, d_0^2 \delta_{0k} + \gamma_{0+1} d_{0+1}^2 \delta_{0+1k}\right) - \boldsymbol{F}(t)_{\lambda t_n} \mu(\lambda t_n) d_0^2 \delta_{0k} \tag{9}$$

where, δ_{lk} is Kronecker delta and

$$d_l^2 = \frac{\Gamma(l+n+1)}{\Gamma(l+1)\Gamma(n+1)} \tag{10}$$

In Eq. (9), the value of k changes from 0 to N_1. Equation (9) is solved using Newmark's Method [20] to obtain the time variation of displacement $\boldsymbol{Q}$. The evaluation of expectation of the response using the properties of orthogonal polynomial functions is shown below,

$$\boldsymbol{X}(t) = \sum_{l=0}^{N_1} \boldsymbol{Q}_l(t) L_l^n(\lambda t_n) \tag{11}$$

Multiplying Eq. (11) by $L_0^n(\lambda t_n)$ such that the value of $L_0^n(\lambda t_n)$ is 1, one obtains

$$\boldsymbol{X}(t)L_0^n(\lambda t_n) = \sum_{l=0}^{N_1} \boldsymbol{Q}_l(t)L_l^n(\lambda t_n)L_0^n(\lambda t_n) \tag{12}$$

Applying the expectation operator on both sides of Eq. (12) and using the property of orthogonal polynomials, the expectation of the response is obtained as

$$E[X_i(t)] = Q_{i0}(t)d_0^2\,;\; i = 1,\ 2,\ \ldots,\ n_d \tag{13}$$

3 Comparison of Present Method with Published Work

The present method is compared with State-space representation of system equations [18]. In state-space representation, second-order coupled system equations are converted to $2n$ dimensional first-order differential equations. The flexural stresses obtained at mid span of the bridge for single vehicle traversing the bridge from the two methods for 20 km/h vehicle velocity and for good and very poor road surface conditions are shown in Figs. 2 and 3.

The comparison as shown in Figs. 2 and 3 shows that present orthogonal polynomial expansion method closely agrees with the conventional state-space approach as outlined in Nigam (1983) [18].

The DAF obtained from the present method for single vehicle traversing on the bridge has been compared with the empirical relation which is shown below [21].

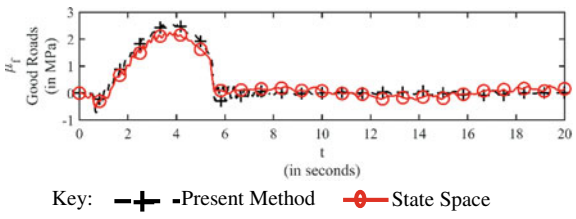

Fig. 2 Comparison of flexural stresses at mid span of the bridge obtained from present method and State-space representation for good roads

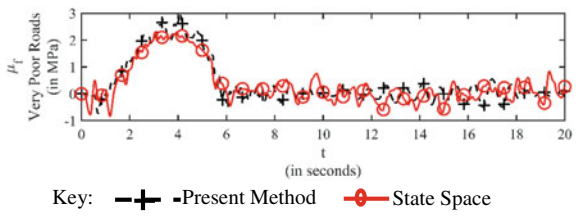

Fig. 3 Comparison of flexural stresses at mid span of the bridge obtained from present method and State-space representation for very poor roads

Table 1 Comparison of DAF obtained from present method and using empirical relation [21]

Vehicle velocity (km/h)	DAF			
	Good		Very poor	
	Present method	Chang and Lee (1994) [21]	Present method	Chang and Lee (1994) [21]
60	1.37	1.29	1.43	1.37
70	1.38	1.34	1.47	1.41
80	1.43	1.39	1.53	1.5

$$i = \frac{-202}{10^4} + \frac{898}{10^7}L + \frac{441}{10^5}V + \frac{748}{10^2}R \tag{14}$$

In Eq. (13), i, L, V, R represent impact factor, span length (metres), vehicle speed (km/h) and maximum magnitude of surface roughness (metres), respectively. DAF is given by Chang and Lee, 1994 [21]

$$DAF = 1 + i \tag{14}$$

The vehicle velocity considered is from to 80 km/h, bridge natural frequency is 2.027 Hz, mass per unit length is 14,900 kg/m, moment of inertia is 4.94 m^4 and span length is 50 m [21]. The total vehicle weight is 210 kN and suspension/tyre stiffness ratio is 2.8. The comparison of DAF for single vehicle traversing the bridge obtained from the present method and using the empirical relation in Eq. (13) is shown in Table 1 for good roads and very poor roads.

It is observed from Table 1 that the DAF obtained from the present method and that from the empirical relation [21] agrees with each other showing slightly conservative value in the present method.

4 Results and Discussion

The present method has been illustrated with an example of single span box girder bridge of twin cell cross section and is of span 30 m. The vehicle total weight is 400 kN, suspension/tyre stiffness ratio = 4.0; Fundamental natural frequency of the bridge = 4.5 Hz. The influence of vehicle speed, arrival rate and pavement roughness on dynamic stresses is shown below. The peak observed in mean time history of flexural stresses at mid span of the bridge are compared for different time windows, as shown in Table 2.

It is observed from Table 2, that the peak flexural stresses at mid span of the bridge increase for time windows varying from 10 s to 20 s and the variation from 20 s to 25 s is not much significant. The optimal time window considered is 20 s for calculating the mean flexural stresses at mid span of the bridge.

Table 2 Peak flexural stresses at mid span of the bridge for different time windows for varying velocity for very poor road

Velocity (km/h)	Peak flexural stresses (MPa) for different time windows			
	10 s	15 s	20 s	25 s
20	18	23	28	28.9
40	11	16	18.2	18.4
60	9	9.2	9.6	10

In bridge design, complete dynamic analysis for vehicle live load is not usually required as various codes suggested Dynamic Amplification Factor (DAF) to magnify the static effect. The DAF is evaluated as shown below

$$DAF = \frac{f_{dyn}}{f_{stat}} \tag{15}$$

where, f_{dyn} and f_{stat} is the maximum dynamic flexural stress and maximum static flexural stress, respectively. Past study has shown that DAF depends on vehicle speed, road surface condition, arrival rate of the vehicle in addition to bridge characteristics. In the present study, DAF has been evaluated for different vehicle speeds, road surface conditions, arrival rate of the vehicles and time windows taking into account multiple vehicles traversing the bridge.

4.1 Effect of Vehicle Velocity

The velocity of the vehicle is varied from 20 km/h to 60 km/h with an increment of 20 km/h. The mean arrival rate considered is two vehicles per second. The variation of mean flexural stresses at mid span of the bridge for 20 s time window for good and very poor road case are shown in Figs. 4 and 5, respectively.

It is observed that for a 20 s time window, the mean flexural stresses evaluated at mid span of the bridge decrease with increase in vehicle velocity when the arrival time of the vehicle is considered as a random variable as shown in Figs. 4 and 5. This is because the number of vehicles crossing the bridge decreases with increasing the vehicle velocity as the duration of loading decreases.

The f_{dyn} for different time windows for good road and very poor road for velocities 20 km/h, 40 km/h and 60 km/h are shown in Table 3. f_{stat} is calculated using Influence Line Diagram when the vehicle is at the centre of the span for multiple vehicles on the bridge as shown in Table 3.

It is observed from Table 3, that the static flexural stresses and dynamic flexural stresses vary for different time windows. The DAF calculated is shown in Table 4.

It has been observed from Figs. 4 and 5 that for higher vehicle velocity, the dynamic flexural stress decreases. The static stresses for higher velocity also decreases due to

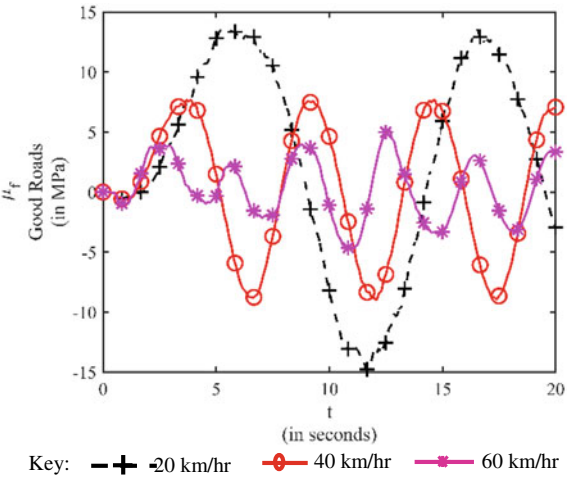

Fig. 4 Mean flexural stress at mid-span of the bridge for different vehicle velocity for 20 s time window for good road ($S_{GG}(\Omega_0) = 32 \times 10^{-6}$ m^2/cycle/m)

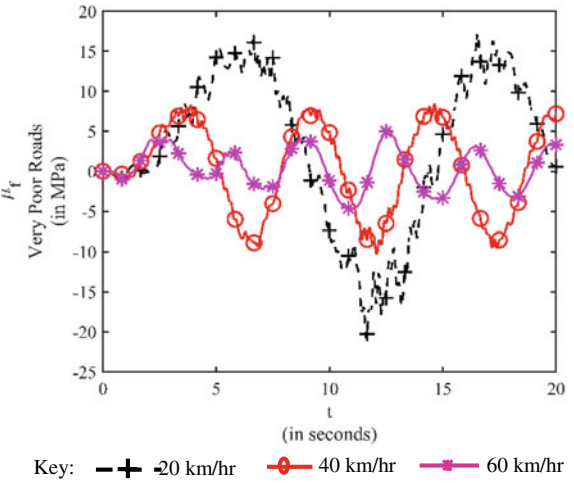

Fig. 5 Mean flexural stress at mid-span of the bridge for different vehicle velocity for 20 s time window for very poor road ($S_{GG}(\Omega_0) = 1024 \times 10^{-6}$ m^2/cycle/m)

decrease in the duration of loading. It is observed from Table 4, that the DAF decreases as the vehicle velocity increases. The decrease in DAF for increase in vehicle velocity is because of lower duration of loading leading to lower dynamic stresses and lower static stresses. It is also observed that as the time window increases, the duration of loading increases leading to increase in static stresses thereby reducing the DAF. This can be due to the suppression effect of multiple vehicles acting simultaneously on the bridge.

Table 3 f_{dyn} and f_{stat} for good road and very poor road by varying the vehicle velocity for different time windows

Time window (s)	f_{stat} (MPa)			f_{dyn} (MPa)					
	Multiple vehicles traversing bridge for each duration of loading based on vehicle velocity			20 km/h		40 km/h		60 km/h	
	20 km/h	40 km/h	60 km/h	Good	Very poor	Good	Very poor	Good	Very poor
10	7.14	7.82	5.78	11.2	18	8.2	11	6.8	9
15	11.05	8.66	6.46	14.6	23	8.8	16	6.9	9.1
20	14.96	9.865	6.63	15.8	28	10	18.2	6.9	9.3
25	16.3	10.54	7.3	16.5	28	10	18.2	7	9.5

Table 4 DAF for good road and very poor road by varying the vehicle velocity for different time windows

Time window (s)	DAF					
	20 km/h		40 km/h		60 km/h	
	Good	Very poor	Good	Very poor	Good	Very poor
10	1.56	2.52	1.04	1.4	1.17	1.56
15	1.32	2.08	1.02	1.85	1.06	1.4
20	1.05	1.88	1.01	1.84	1.04	1.4
25	1.01	1.72	0.95	1.73	0.95	1.3

4.2 Effect of Road Surface Roughness

It is also observed that the mean flexural stress at mid span of the bridge increases with the increase in road roughness coefficient. This is because the dynamic stresses increase with deteriorating road conditions which can be observed from Figs. 4 and 5. As can be observed from Table 4, the DAF is more for very poor category of road surface.

4.3 Effect of Arrival Rate

The dynamic flexural stresses at mid span of the bridge for vehicle velocity 20 km/h and 60 km/h for very poor category of road surface and varying the arrival rate 1 vehicle/s, 2 vehicles/s and 3 vehicles/s are shown in Figs. 6 and 7, respectively. The arrival rates imply the traffic loading on the bridge, i.e., lowest traffic on the bridge and highest traffic on the bridge.

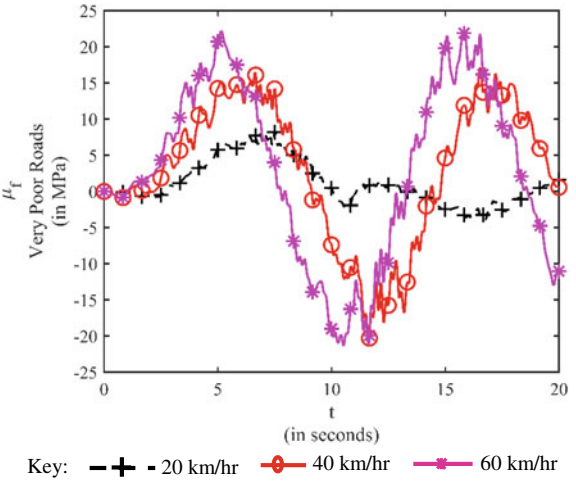

Fig. 6 Mean flexural stress at mid-span of the bridge for different vehicle arrival rate for 20 s time window for very poor road ($S_{GG}(\Omega_0) = 1024 \times 10^{-6}$ m^2/cycle/m) and for vehicle velocity 20 km/h

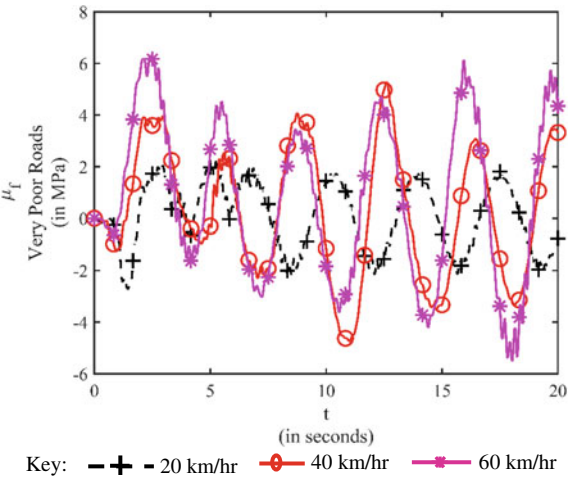

Fig. 7 Mean flexural stress at mid-span of the bridge for different vehicle arrival rate for 20 s time window for very poor road ($S_{GG}(\Omega_0) = 1024 \times 10^{-6}$ m^2/cycle/m) and for vehicle velocity 60 km/h

Higher arrival rate leads to higher dynamic stresses as number of vehicles present on the bridge increases which is observed from Figs. 6 and 7. The DAF for vehicle velocity 20 km/h and 60 km/h for different arrival rates and for very poor road surface condition is shown in Table 5.

Table 5 DAF for 20 km/h and 60 km/h by varying the arrival rate for very poor road surface

Arrival rate	DAF (20 km/h)	DAF (60 km/h)
1 Vehicle (s)	1.00	1.28
2 Vehicles (s)	1.88	1.4
3 Vehicles (s)	2.2	1.44

As can be observed from Table 5, the DAF increases with increase in arrival rate due to increase in dynamic force on the bridge.

5 Conclusions

The present study outlines an analytical approach to find the first-order response statistics for sequence of moving vehicles randomly arriving on the bridge. The orthogonal polynomial functions have been used to solve the problems. The results reflect the effect of multiple vehicles in different time windows at different arrival rate which is a unique feature of the study. Although, a Quarter car model has been assumed, but the method can be easily extended to multiple axles loading only by modification of vehicle equation of motion. This method ignores the pavement irregularity in transverse direction. Based on the results obtained from the study, the main conclusions are as follows:

- Flexural stresses obtained from the orthogonal polynomial expansion method and State-space approach closely agree with each other.
- The DAF obtained from the orthogonal polynomial expansion method and that from the empirical relation are approximately same.
- With the increase in vehicle velocity, the mean flexural stress of the bridge decreases when the arrival time of the vehicle is considered as a random variable. But with the increase in road roughness coefficient, the mean flexural stress of the bridge increases due to increase in the dynamic stresses with deteriorating road conditions.
- The DAF decreases with increase in vehicle velocity from 20 km/h to 60 km/h for arrival rate 2 vehicles/s for a given time window and it also increases for very poor road surface.
- DAF decreases with increase in time window.
- DAF increases with increase in arrival rate of the vehicle.
- The most unfavourable response is found in very poor category of road surface. However, it has been also observed that a stream of vehicles at low speed increases bridge-vehicle-interaction time in which static response also increases. However, since amplification factor being a fraction of static live load effect, at low speed, dynamic effect in some category of pavement surface is not much prominent.

References

1. Fryba L (1996) Dynamics of railway bridges. Thomas Telford, London
2. GreenMF, Cebon D (1997) Dynamic interaction between heavy vehicles and highway bridges. Comput Struct 62(2):253–264
3. IRC 6 (2019) Standard specifications and code of practice for road bridges, section-II loads and stresses. Indian Road Congress, New Delhi

4. Frýba L (1972) Vibration of solids and structures under moving loads. Thomas Telford Ltd., London
5. PesterevAV, BergmanLA, Tan CA (2003) On asymptotics of the solution of the moving oscillator problem. J Sound Vib 260:519–536
6. Sniady P (1984) Vibration of of a beam due to a random stream of moving forces with random velocity. J Sound Vib 97:23–33
7. Turner JD, Pretlove AJ (1988) A study of the spectrum of traffic-induced bridge vibration. J Sound Vib 122:31–42
8. Tung CC (1969) Response of highway bridges to renewal traffic loads. J Eng Mech Div 95:41–58
9. Śniady P, Biernat S, Sieniawska R, Zukowski S (2001) Vibrations of the beam due to a load moving with stochastic velocity. Probab Eng Mech 16:53–59
10. Shinozuka M, Kobori T (1972) Fatigue analysis of highway bridges. In: Proceedings of JSCE, pp 137–148
11. Chen Y, Feng MQ, Tan C-A (2009) Bridge structural condition assessment based on vibration and traffic monitoring. J Eng Mech 8(135):747–758
12. Blejwas TE, Feng CC, Ayre RS (1979) Dynamic interaction of moving vehicles and structures. J Sound Vib 67:513–521
13. Akin JE, Mofid M (1989) Numerical solution for response of beams with moving mass. J Struct Eng 1(115):120–131
14. Yang Y-B, Lin B-H (1995) Vehicle-bridge interaction analysis by dynamic condensation method. J Struct Eng 11(121):1636–1643
15. Coussy O, Said M, van Hoove J-P (1989) The influence of random surface irregularities on the dynamic response of bridges under suspended moving loads. J Sound Vib 130:313–320
16. Tin THT, O'Connor C (1990) Vehicle model for highway bridge impact. J Struct Eng 7(116):1772–1793
17. Li J, Chen J (2009) Stochastic dynamics of structures. John Wiley and Sons (Asia) Pte Ltd, Clementi Loop, Singapore
18. Nigam NC (1983) Introduction to random vibrations. The MIT Press Cambridge, Masachusetts, London, England
19. Schoutens W (2000) Lecture notes in statistics. In: Bickel P, Diggle P, Fienberg S et al (eds) Stochastic processes and orthogonal polynomials. Springer
20. Chopra AK (2011) Dynamic of structures theory and applications to earthquake engineering. Fourth. Prentice Hall
21. Chang D, Lee H (1994) Impact factors for simple-span highway bridge girders. J Struct Eng 120:704–715

Model-Based Study of Coupled Plate-String Vibration Related to Stringed Musical Instruments

Soumyabrata Mukherjee, Suvadeep Patra, and Santanu Das

1 Introduction

Musical instruments have been known since thousands of years. Although their working has long been known, exact rigorous analysis of physics of musical instruments started relatively recently in the nineteenth century [1, 2]. All the higher natural frequencies are integer multiples of the fundamental frequency for a string with both the ends fixed [3, 4]. In case of a stringed instrument, the strings cannot be considered to be fixed at both the ends as the wooden plate also vibrates along with the strings [5]. The objective of this study is to understand the effect of plate vibration on the natural frequencies of the string. In the recent times, there has been a lot of study that are going on to understand the effect of curved bridge on the natural frequencies of the Indian stringed musical instruments [6–8]. These studies have found that musical instruments exhibit extremely complex dynamics. A sound becomes a musical sound when the containing higher frequencies are integer multiples of the lowest (fundamental) frequency, i.e., harmonic in nature [7, 9]. The main source of inharmonicity in a string is its bending rigidity which is generally neglected to obtain the wave equation [9]. The other important source of inharmonicity is the coupling between the plate and the string [7, 9]. In this study, the guitar is considered to be the musical instrument of interest. The bridge in case of guitar is sharp as opposed to many Indian stringed musical instruments (see Figs. 1 and 2). The models considered in this study are devoid of the complexities that the curved bridge possess. The equations of motion are derived for these models and the corresponding solutions are also obtained. With the help of those solutions, the sources of inharmonicity are pointed out.

S. Mukherjee · S. Patra · S. Das (✉)
Department of Mechanical Engineering, Indian Institute of Engineering Science and Technology (Shibpur), Howrah 711103, India
e-mail: sdas@mech.iiests.ac.in

D. K. Maiti et al. (eds.), *Recent Advances in Computational and Experimental Mechanics, Vol II*, Lecture Notes in Mechanical Engineering,
https://doi.org/10.1007/978-981-16-6490-8_42

Fig. 1 Guitar bridge (*Source* Internet)

Fig. 2 Sitar bridge (*Source* Internet)

2 Mathematical Models

In the first model, the string is fixed at one end and the other end of the string vibrates according to a single degree of freedom (SDOF) spring mass system (see Fig. 4). The vibration of the plate is modeled as the spring mass system. This is to note that as the boundary conditions at the left end has changed, the natural frequencies of the system will also change. The second model consists of two parallel strings of equal length, both fixed at one end and their other ends are connected via a rigid bar which is supported by a torsional and a linear spring at the middle (see Fig. 5). The bar with two springs acts as a 2DOF system. Weinreich [10] studied coupled two string vibration for piano, but the current model was not considered (Fig. 3).

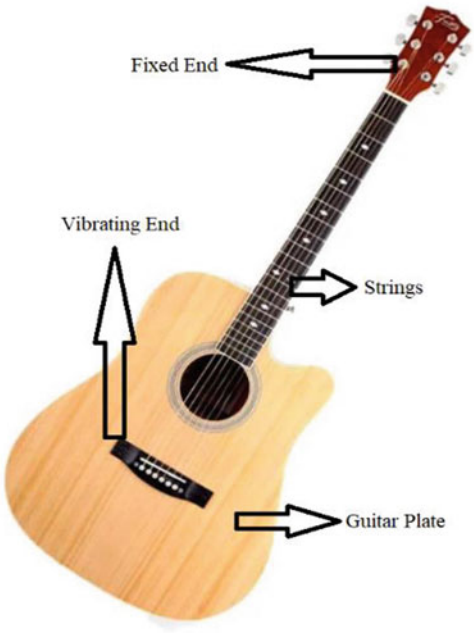

Fig. 3 Guitar (*Source* Internet)

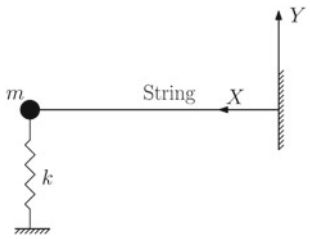

Fig. 4 The most simplified model of coupled plate-string vibration (Single string model)

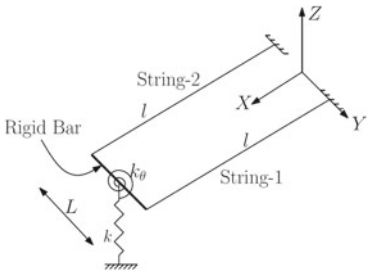

Fig. 5 Model of coupled plate-string vibration (Two string model)

2.1 Derivation of Equations for the First Model

In order to derive the equation of motion, Hamilton's principle is used. The total kinetic energy of the system is

$$KE = \frac{1}{2}\int_0^l \rho A w_t^2(x,t)dx + \frac{1}{2}m w_t^2(l,t),$$

where $\boldsymbol{\rho}$ is the density of the material of the string, $\boldsymbol{A}$ is the cross-sectional area of the string, $\boldsymbol{l}$ is the length of the string, $\boldsymbol{m}$ is the mass attached with spring, and $\boldsymbol{w(x,t)}$ is the transverse displacement of the string at any time instant $\boldsymbol{t}$ and position $\boldsymbol{x}$. The total potential energy of the system is (Fig. 4)

$$PE = \frac{1}{2}\int_0^l T w_x^2(x,t)dx + \frac{1}{2}k w_x^2(l,t),$$

where T is the tension (taken to be constant) in the string and k is the stiffness of the spring and $w_x = \frac{\partial w}{\partial x}$,$w_t = \frac{\partial w}{\partial t}$.

The Lagrangian ($\mathcal{L}$) is obtained as

$$\mathcal{L} = KE - PE = \frac{1}{2}\int_0^l \left[\rho A w_t^2 - T w_x^2\right] + \frac{1}{2}m w_t^2(l,t) - \frac{1}{2}k w^2(l,t).$$

From Hamilton's principle ($\delta\int_{t_1}^{t_2}\mathcal{L}dt = 0$), the equation of motion is obtained as

$$\rho A w_{tt} - T w_{xx} = 0 \tag{1}$$

where $w_{xx} = \frac{\partial^2 w}{\partial x^2}$,$w_{tt} = \frac{\partial^2 w}{\partial t^2}$. The boundary conditions are

$$w(0,t) = 0 \text{ at } x = 0 \text{ and } T w_x(l,t) + m w_{tt}(l,t) + k w(l,t) = 0 \text{ at } x = l. \tag{2}$$

For $m = 0$ and $k = \infty$, the string with both ends fixed is obtained.

2.2 Derivation of Equations for the Second Model

Similar to the first model, the equations of motion are derived by using Hamilton's principle in this model. Let $w_1(x,t)$ and $w_2(x,t)$ be the displacements of string-1 and string-2, respectively (both in the Z direction). The linear displacement of middle

point of the bar is given by $z = \frac{w_1(l,t)+w_2(l,t)}{2}$ and the angular displacement of the bar is given by $\theta = \frac{w_1(l,t)-w_2(l,t)}{L}$, where $\boldsymbol{L}$ is length of the bar (Fig. 5).

The total kinetic and potential energy of the system are given by

$$KE = \frac{1}{2}\int_0^l \rho_1 A_1 w_{1t}^2(x,t) + \frac{1}{2}\int_0^l \rho_2 A_2 w_{2t}^2(x,t) + \frac{1}{2}m\dot{z}^2 + \frac{1}{2}I\dot{\theta}^2$$

$$PE = \frac{1}{2}\int_0^l T_1 w_{1x}^2(x,t) + \frac{1}{2}\int_0^l T_2 w_{2x}^2(x,t) + \frac{1}{2}kz^2 + \frac{1}{2}k_\theta\theta^2,$$

where ρ_1, ρ_2 are the densities of the material of the string-1 and string-2, A_1, A_2 are the cross-sectional areas of the string-1 and string-2,l is the length of the strings, m is the mass of the bar and I is the mass moment of inertia of the bar about the center of mass (middle point), T_1, T_2 are the constant tensions in the string-1 and string-2, k and k_θ are the stiffness of linear and torsional springs.

The equations of motions for both strings are obtained as

$$\rho_1 A_1 w_{1tt}(x,t) - T_1 w_{1xx}(x,t) = 0 \text{ and} \tag{3}$$

$$\rho_2 A_2 w_{2tt}(x,t) - T_2 w_{2xx}(x,t) = 0. \tag{4}$$

The corresponding displacement boundary conditions are $w_1(x,t) = w_2(x,t) = 0$ at $x = 0$. The other two boundary conditions at $x = l$ are given by

$$T_1 \frac{\partial w_1(x,t)}{\partial x}|_{x=l} + T_2 \frac{\partial w_2(x,t)}{\partial x}|_{x=l} + \frac{m(\ddot{w}_1 + \ddot{w}_2)}{2}|_{x=l} + \frac{k(w_1+w_2)}{2}|_{x=l} = 0 \text{ and} \tag{5}$$

$$T_1 \frac{\partial w_1(x,t)}{\partial x}|_{x=l} - T_2 \frac{\partial w_2(x,t)}{\partial x}|_{x=l} + \frac{2I(\ddot{w}_1 - \ddot{w}_2)}{L^2}|_{x=l} + \frac{2k_\theta(w_1-w_2)}{L^2}|_{x=l} = 0. \tag{6}$$

3 Analytical Solutions

The two models discussed in the previous sections are linear in nature and the boundary conditions are homogeneous. Separation of variables method is used to obtain the solutions for these models.

3.1 Solution for the First Model

The equation Eq. (1) can be written in the following way

$$W_{tt} - c^2 W_{xx} = 0, \text{ where } c^2 = \frac{T}{\rho A}.$$

Using the boundary condition Eq. (2), the characteristic equation is obtained for the first model. The characteristic equation is given by

$$\left[\frac{T\omega}{c}\cos\frac{\omega l}{c} + \left(k - m\omega^2\right)sin\frac{\omega l}{c}\right] = 0. \tag{7}$$

This is a transcendental equation. Upon solving this equation, all the natural frequencies (ω) of the system can be obtained. The solution corresponding to displacement function of the system is given by

$$w(x,t) = \sum_{j=1}^{\infty}\left(U_j cos\omega_j t + V_j sin\omega_j t\right)sin\frac{\omega_j x}{c} \tag{8}$$

where, U_j and V_j are the unknown constants corresponding to jth mode to be determined by initial shape of the string. For this purpose, the following orthogonality condition will be used

$$m w_j(l) w_k(l) + \frac{T}{c^2}\int_0^l w_j w_k \, dx = 0, \text{ for } j \neq k \tag{9}$$

where $w_j = sin\frac{\omega_j x}{c}$ is the jth modeshape.

3.2 Solution for the Second Model

The boundary conditions Eqs. (5) and (6) along with the equations of motions Eqs. (3) and (4) lead to the characteristic Eq. (10). The characteristic Eq. (10) is written in a determinant form. This is also a transcendental equation which needs to be solved numerically for the natural frequencies.

$$\begin{vmatrix} 2\frac{T_1\omega}{c_1}\cos\left(\frac{\omega l}{c_1}\right) + \left(k - m\omega^2\right)\sin\left(\frac{\omega l}{c_1}\right) & 2\frac{T_2\omega}{c_2}\cos\left(\frac{\omega l}{c_2}\right) + \left(k - m\omega^2\right)\sin\left(\frac{\omega l}{c_2}\right) \\ \frac{T_1\omega}{c_1}\cos\left(\frac{\omega l}{c_1}\right) + \frac{2}{L^2}\left(k_\theta - I\omega^2\right)\sin\left(\frac{\omega l}{c_1}\right) & -\frac{T_2\omega}{c_2}\cos\left(\frac{\omega l}{c_2}\right) - \frac{2}{L^2}\left(k_\theta - I\omega^2\right)\sin\left(\frac{\omega l}{c_2}\right) \end{vmatrix} = 0, \tag{10}$$

where $c_1^2 = \frac{T_1}{\rho_1 A_1}$ and $c_2^2 = \frac{T_2}{\rho_2 A_2}$. The solution corresponding to displacement function of the system is given by

$$w_1(x,t) = \sum_{j=1}^{\infty} P_{1j}\left(U_j cos\omega_j t + V_j sin\omega_j t\right) sin\frac{\omega_j x}{c_1} \text{ and} \tag{11}$$

$$w_2(x,t) = \sum_{j=1}^{\infty} P_{2j}\left(U_j cos\omega_j t + V_j sin\omega_j t\right) sin\frac{\omega_j x}{c_2} \tag{12}$$

where P_{1j} and P_{2j} will be found using the following equation

$$\begin{bmatrix} 2\frac{T_1\omega}{c_1}\cos\left(\frac{\omega l}{c_1}\right) + \left(k - m\omega^2\right)\sin\left(\frac{\omega l}{c_1}\right) & 2\frac{T_2\omega}{c_2}\cos\left(\frac{\omega l}{c_2}\right) + \left(k - m\omega^2\right)\sin\left(\frac{\omega l}{c_2}\right) \\ \frac{T_1\omega}{c_1}\cos\left(\frac{\omega l}{c_1}\right) + \frac{2}{L^2}\left(k_\theta - I\omega^2\right)\sin\left(\frac{\omega l}{c_1}\right) & -\frac{T_2\omega}{c_2}\cos\left(\frac{\omega l}{c_2}\right) - \frac{2}{L^2}\left(k_\theta - I\omega^2\right)\sin\left(\frac{\omega l}{c_2}\right) \end{bmatrix}_{\omega=\omega_j} \begin{bmatrix} P_{1j} \\ P_{2j} \end{bmatrix} = 0 \tag{13}$$

and U_j and V_j are obtained using the following orthogonality condition

$$\left(\frac{m}{4} + \frac{I}{L^2}\right)\left(w_{1j}w_{1k} + w_{2j}w_{2k}\right) + \left(\frac{m}{4} - \frac{I}{L^2}\right)\left(w_{1k}w_{2j} - w_{1j}w_{2k}\right) + \frac{T_1}{c_1^2}\int_0^l w_{1j}w_{1k}dx + \frac{T_2}{c_2^2}\int_0^l w_{2j}w_{2k}dx = 0 \text{ for } j \neq k. \tag{14}$$

4 Results

4.1 Results for the First Model

Equation (7) can be written as $tan\Omega + \frac{\alpha\Omega}{(1-\alpha\beta\Omega^2)} = 0$, where $\Omega = \frac{\omega l}{c}$, $\alpha = \frac{T}{kl}$, and $\beta = \frac{m}{\rho A l}$. If the string parameters are kept fixed, α represents the inverse of the stiffness of the spring and β represents the mass attached to the spring for the first model.

From Figs. 6 and 7, as α is increased (decrease of stiffness) and β is increased (increase of mass), the first natural frequency decreases. The trend is similar for the other natural frequencies. For a single string fixed on both the sides, the other higher natural frequencies are integer multiple of the fundamental natural frequency. Since for this model the plate vibration is coupled with string vibration, this property vanishes (see Figs. 8 and 9). It is also evident from Figs. 8 and 9 that at first the ratio decreases from the integer value as α is increased from $\alpha = 0$, after that the ratio increases. This non-monotonous nature of the graph points out the possibility of guitar design in such a way that the frequency ratios become almost integer values.

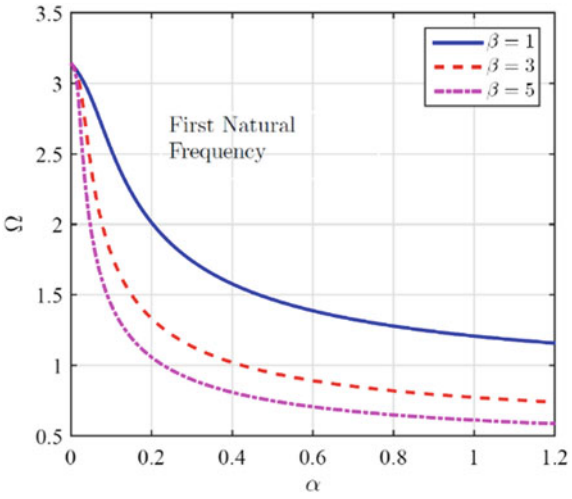

Fig. 6 Variation of first natural frequency w.r.t. α. (First model)

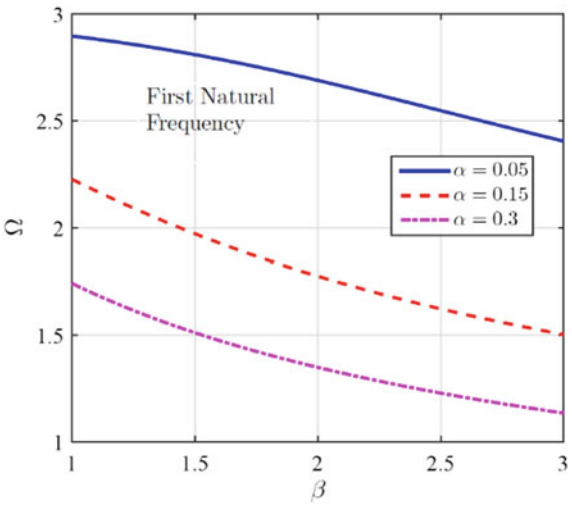

Fig. 7 Variation of first natural frequency w.r.t. β. (First model)

4.2 Results for Second Model

After non-dimensionalization, Eq. (10) becomes

$$F(\Omega) = \left(2\alpha_1\Omega cos\Omega + \left(1-\alpha_1\beta_1\Omega^2\right)sin\Omega\right)$$
$$\left(\alpha_{2\theta}\left(\Omega\frac{c_1}{c_2}\right)\mathbf{cos}\left(\Omega\frac{c_1}{c_2}\right) + 2\left(1-\alpha_{1\theta}\beta_{1\theta}\Omega^2\right)\mathbf{sin}\left(\Omega\frac{c_1}{c_2}\right)\right)$$
$$+ \left(\alpha_{1\theta}\Omega\mathbf{cos}\Omega + 2\left(1-\alpha_{1\theta}\beta_{1\theta}\Omega^2\right)\mathbf{sin}\Omega\right)$$

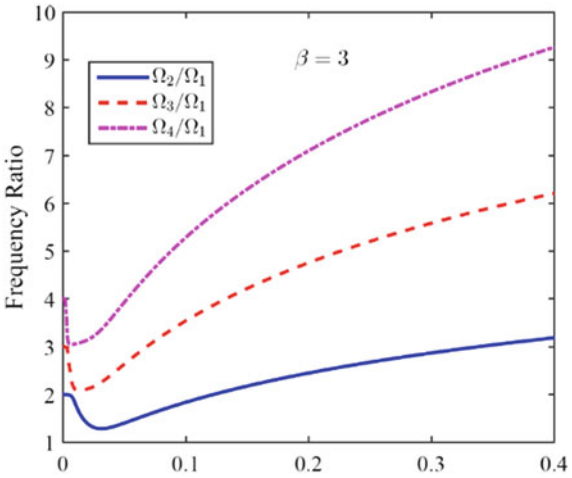

Fig. 8 Frequency ratio as a function of α.(First model)

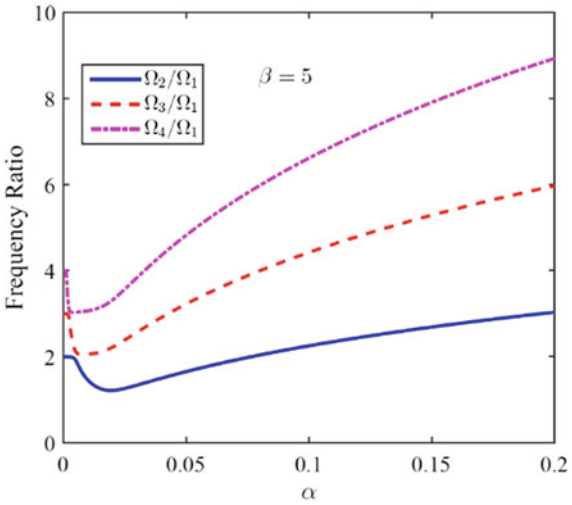

Fig. 9 Frequency ratio as a function of α. (First model)

$$\left(2\alpha_2\left(\Omega\frac{c_1}{c_2}\right)\mathbf{cos}\left(\Omega\frac{c_1}{c_2}\right)+\left(1-\alpha_1\beta_1\Omega^2\right)\mathbf{sin}\left(\Omega\frac{c_1}{c_2}\right)\right)=0, \tag{15}$$

where $\Omega = \frac{\omega l}{c_1}$, $\alpha_1 = \frac{T_1}{kl}$, $\beta_1 = \frac{m}{\rho_1 A_1 l}$, $\alpha_2 = \frac{T_2}{kl}$, $\alpha_{1\theta} = \frac{T_1 L^2}{k_\theta l}$, $\beta_{1\theta} = \frac{I}{\rho_1 A_1 L^2 l}$, and $\alpha_{2\theta} = \frac{T_2 L^2}{k_\theta l}$.

Pure Translational and Torsional Modes

Taking $T_1 = T_2 = 60N, \rho_1 = \rho_2 = 8000\,\mathrm{Kg/m^3}, A_1 = A_2 = 0.25{\cdot}\pi{\cdot}(0.0015)^2\,\mathrm{m^2}$, $m = 0.06\,\mathrm{Kg}$, $l = 1\,\mathrm{m}$, $L = 0.1\,\mathrm{m}$, $I = \frac{1}{12}\,\mathrm{mL^2\,Kg-m^2}$, $k = 600\,\mathrm{N/m}$, $k_\theta =$

$0.8\,\mathrm{N}-\mathrm{m}$, $F(\Omega)$ is plotted as function of Ω (see Fig. 10). Figure 10 shows that many two roots come in 'almost pair'. They correspond to translational and torsional modes (see Table 1 for the values). For the two identical strings, the torsional and the translational modes are close to each other. Due to this closeness of torsional and translational frequencies, the beat phenomenon occurs. For the identical strings (all parameters being same), the translational modes do not depend on k_θ and torsional mode do not depend on k. For non-identical strings, these two properties cease to exist (see Fig. 11 and Table 2). Each mode then becomes a combination of both translational and torsional modes. For identical strings, the odd numbered modes (in Table 1) are corresponding to the pure translational ($P_{1j} : P_{2j} = 1 : 1$) and even numbered modes are corresponding to pure torsional ($P_{1j} : P_{2j} = 1 : -1$) modes (of the bar). Table 1 shows that the higher modes are not integer multiples of the fundamental frequency. The inharmonicity exists due to coupled plate-string vibration.

Torsional stiffness (k_θ) and the distance between two parallel strings (L) influence the torsional frequencies only as all the other parameters are fixed. This is evident from Figs. 12 and 13. For $L = 1$ cm, it can be seen that 2nd and 3rd natural frequencies come close to each other, thereby leading to a different beating. Similarly, the linear spring stiffness (k) only influences the translational modes. The corresponding results are not shown here.

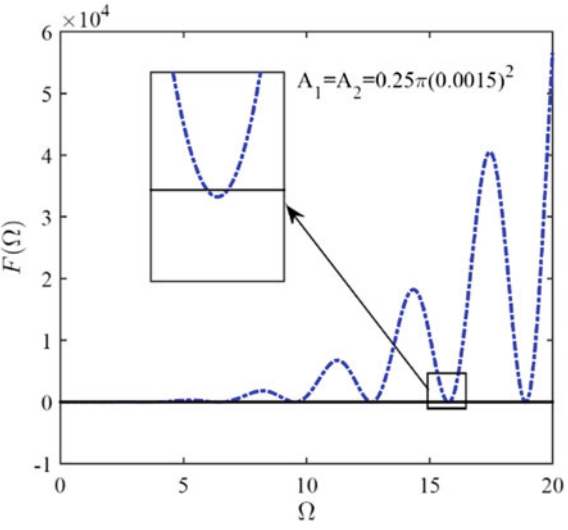

Fig. 10 $F(\Omega)$ as function of Ω (Second model)

Table 1 First ten frequencies corresponding to Fig. 10

Ω_1	Ω_2	Ω_3	Ω_4	Ω_5	Ω_6	Ω_7	Ω_8	Ω_9	Ω_{10}
1.5418	1.7903	3.3202	3.6391	6.3617	6.5169	9.4758	9.5775	12.6043	12.6800

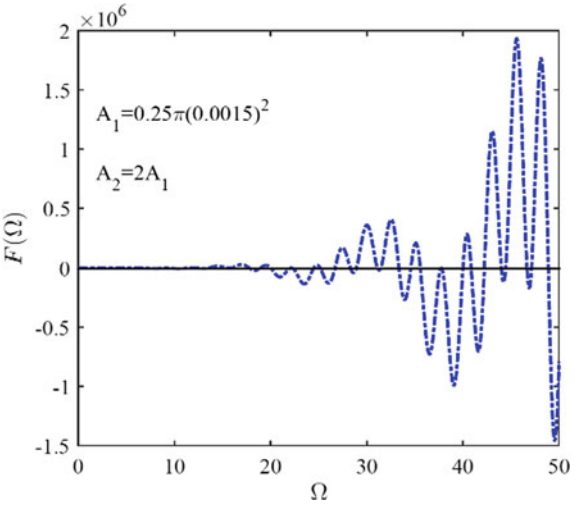

Fig. 11 $F(\Omega)$ as function of Ω. Except cross-sectional area of the 2nd string, all the other parameters are fixed corresponding to Fig. 10 (Second model)

Table 2 First ten frequencies corresponding to Fig. 11

Ω_1	Ω_2	Ω_3	Ω_4	Ω_5	Ω_6	Ω_7	Ω_8	Ω_9	Ω_{10}
1.4184	1.6671	2.6791	3.4909	4.6742	6.4256	6.8236	8.9891	9.5305	11.1930

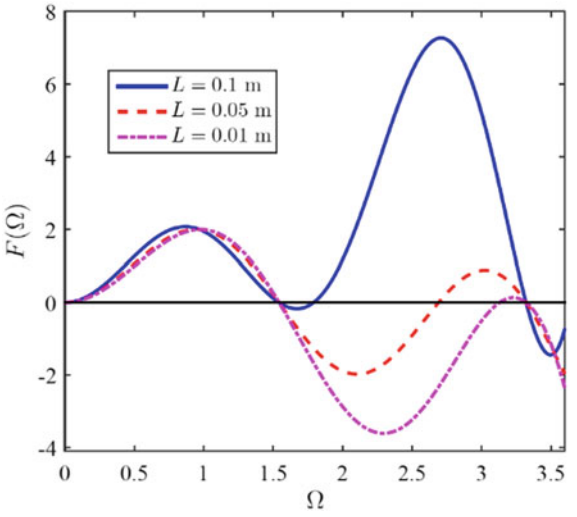

Fig. 12 $F(\Omega)$ as function of Ω. Except the distance between two strings, all the other parameters are fixed corresponding to Fig. 10 (Second model)

Combined Modes

When different parameters are taken for two different strings, the strings become non-identical. For non-identical strings, the torsional and translational modes do not

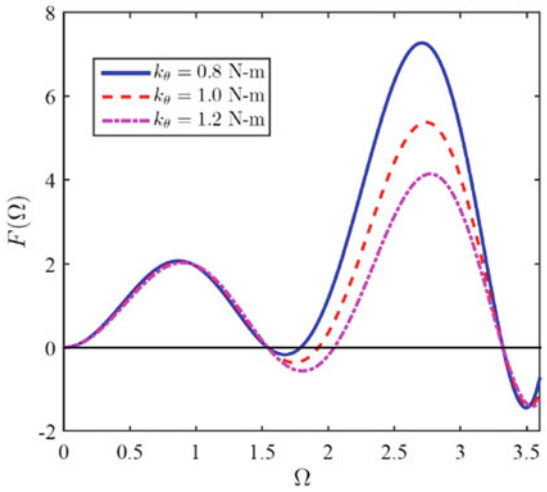

Fig. 13 $F(\Omega)$ as function of Ω. Except the torsional stiffness, all the other parameters are fixed corresponding to Fig. 10 (Second model)

remain pure in nature rather they become combined ($P_{1j} : P_{2j} \neq 1 : \pm 1$). Figure 11 and Table 2 show the natural frequencies corresponding to two coupled non-identical strings.

Table 2 shows that 4th, 5th frequencies and 8th, 9th frequencies are coming close to each other, respectively. This implies that with different sets of parameters, different beating phenomena can be achieved.

The area and tension of the 2nd string are varied to obtain the frequency ratios with respect to the first frequency, respectively (see Figs. 14 and 15). Clearly, the frequencies are not harmonic. But the frequency ratios for different frequencies show different trends. These trends are non-unique and do not tell a lot about the

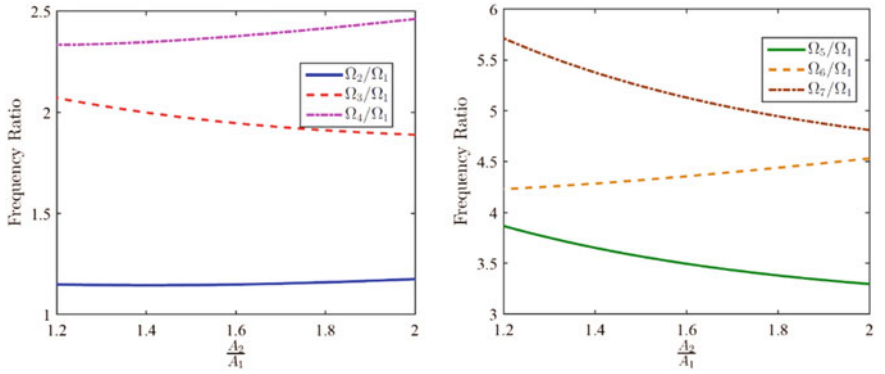

Fig. 14 Frequency ratio as a function of ratio of the cross-sectional areas ($A_1 = \frac{\pi}{4} \cdot (0.0015)^2$ m^2). Except the area of the 2nd string, all the other parameters are fixed corresponding to Fig. 10 (Second model)

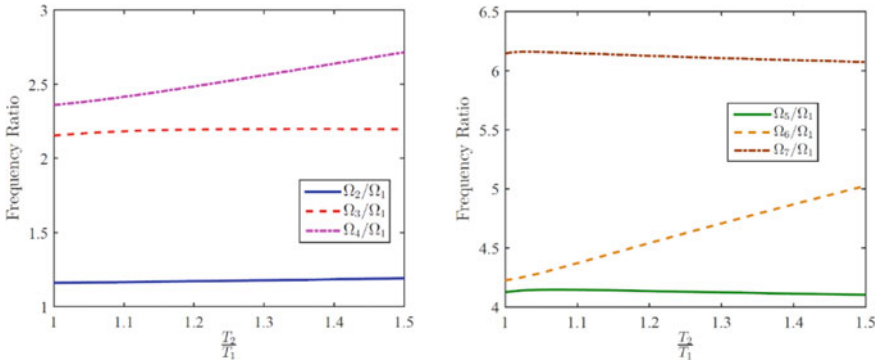

Fig. 15 Frequency ratio as a function of the ratio of the string tensions ($T_1 = 60N$). Except the tension of the second string, all the other parameters are fixed corresponding to Fig. 10 (Second model)

inharmonicity of the frequencies. A detailed parametric study will reveal more about the harmonicity of the frequencies.

5 Conclusion

In this study, two mathematical models of coupled plate-string vibrations have been considered.

The first model (single string) itself shows that the introduction of coupling between the string and the plate destroys the harmonicity of the natural frequencies that are found in a simple string fixed on both the ends. Variation of different parameters (mass and stiffness of the plate) show that the musical instrument can be designed in such a way that the frequencies become nearly harmonic.

In the second model, two parallel strings both fixed on one end and the other ends of the string coupled through a rigid bar supported on a translational and torsional springs have been considered. The equations of motion and boundary conditions have been systematically derived. The complete solution of the system has also been obtained. To ascertain the uniqueness of the initial conditions corresponding to each mode, the orthogonality conditions have been derived. For identical strings, the existence of pure torsional and translational modes is shown. By varying torsional stiffness and distance between the strings, it has been shown that the torsional modes can be shifted, and different beating frequencies can be obtained. For the non-identical strings, modes become a combination of torsional and translational modes. The inharmonicity of the modes are pointed. On varying two parameters (tension and cross-sectional area) of the second string, it was found out that the frequency ratios vary non-uniquely for different frequency.

This study corresponding to second model (two strings) can be extended in future. A rigorous parametric study is required to understand the dependency of the frequencies on different parameters. The two strings model can be extended to six strings (for guitar). The models that are studied here are linear in nature. For this reason, the modal interaction cannot be studied. Experiment-based corrections to the models are required for better understanding the dynamics of the guitar. These are some of the studies that can be carried out in the future.

References

1. Raman CV (1935) The Indian musical drums. Proc Indian Acad Sci A1:179–188
2. Raman CV (1921) On some Indian stringed instruments. Proc Indian Assoc Cultiv Sci 7:29–33
3. Hagedorn P, DasGupta A (2007) Vibrations and waves in continuous mechanical systems. Wiley
4. Perov P, Johnson W, Perova-Mello N (2016) The physics of guitar string vibrations. Am J Phys 84:38–43
5. Giordano N, Gould H, Tobochnik J (1998) The physics of vibrating strings. Comput Phys 12:138–145
6. Vyasarayani CP, Birkett S, McPhee J (2009) Modeling the dynamics of a vibrating string with finite distributed unilateral constraint: application to the sitar. J Acoust Soc Am 125(6):3673–3682
7. Mandal AK, Wahi P (2015) Natural frequencies, mode shapes and modal interactions for strings vibrating against an obstacle: relevance to sitar and veena. J Sound Vib 338:42–59
8. Mandal AK, Wahi P (2019) Coupled plate-string vibrations in the presence of a finite bridge: effect on natural frequencies and harmonicity. J Acoust Soc Am 146(5):3362–3372
9. Mandal AK (2016) Vibration characteristics of strings against smooth boundary obstacle: relevance to musical instruments. PhD dissertation, Indian Institute of Technology Kanpur, Kanpur, India
10. Weinreich G (1977) Coupled piano strings. J Acoust Soc Am 62(6):1474–1484

Detection and Identification of a Crack in a Rod Based on Changes in Its Natural Frequencies

Pratibha Patel, Akhilendu Roy, Deepankar Kumar, and Nirmal Kumar

1 Introduction

Mechanical components such as bars are important structural elements which are used to transmit high loads. These machine components are often subjected to cyclic loading conditions which can eventually lead to crack initiation in the component. Cracks are considered as a major cause of catastrophic failure of machine components [1, 2]. The initiation and propagation of a crack are required to be monitored to avoid failure without warning [3, 4]. Several methods have been used in the past by the researchers to detect the presence of a crack and its severity [5]. One of these methods is the use of vibration measurement shown in the research of Ismail et al. [6] which also serves the purpose of non-destructive testing. Morassi [7, 8] has conducted various researches and concluded that crack propagation leads to a drop in the natural frequency of the system. A similar study on the crack detection problem has been done by Lee [9]. In addition to these works, in several studies [7–16], it has been observed that the drop of natural frequency of a system is a very effective diagnostic tool for damage detection under running conditions. Our focus in this work is to use the changes in the natural frequency of the system to estimate the severity of a single crack. A mathematical formulation has been derived to theoretically determine the position of crack initiation and its propagation in an undamaged component which

P. Patel (✉) · A. Roy · D. Kumar · N. Kumar
Department of Mechanical Engineering, Birla Institute of Technology Ranchi, Ranchi 835215, India
e-mail: ppatel15111998@gmail.com

A. Roy
e-mail: r.akhil7777@gmail.com

D. Kumar
e-mail: deepankarkumar07@gmail.com

N. Kumar
e-mail: nirmal@bitmesra.ac.in

D. K. Maiti et al. (eds.), *Recent Advances in Computational and Experimental Mechanics, Vol II*, Lecture Notes in Mechanical Engineering,
https://doi.org/10.1007/978-981-16-6490-8_43

has been further validated experimentally. An Electromagnetic Resonance High-Frequency Fatigue Testing Machine has been employed for testing the components at the resonant frequencies of the system. In order to estimate the effect of corners and flaws, we have taken three specimens such as cylindrical and flat specimens which are without flaws and another specimen with a flaw in the middle. The specimens are subjected to a range of frequency and the machine checks for the frequency at which maximum displacement at any section occurs, which corresponds to the resonant frequency of the system. We have determined empirical relations between frequency drop and the number of cycles. The constants in the relations (coefficients and exponents) provide the effect of the presence of corners and flaws.

2 Problem Formulation

We begin with considering a bar (specimen) as a continuous body. In general, fatigue crack in a material body without flaw initiates from the surface. Unlike static loading, the longitudinal stress in a bar subjected to cyclic loading is not the same at all planes. Apart from that, the machine detects the natural frequency of the system which consists of the specimen and an adjustable lumped mass (see Fig. 4) set in the machine. Therefore, we have modeled the machine separately to determine the position of maximum stress and to predict the natural frequency of vibration in the following subsections.

2.1 Derivation of the Boundary Value Problem

Here, we first determine the position of maximum stress. For this purpose, the experimental setup has been modeled as shown in Fig. 1. In Fig. 1a, a lumped mass M is attached at the end of the bar which is subjected to an oscillating force. Consider the mass per unit length of the rod is m, damping force per unit length is $f(x,t)$ (see Fig. 1b), and the displacement of material points of the rod in axial direction is $u(x,t)$.
The equation of motion of the bar is written as

$$EA\frac{\partial^2 u(x,t)}{\partial x^2} - c\frac{\partial u(x,t)}{\partial t} + (F_0 \cos \Omega t)\delta(x-L) = m\frac{\partial^2 u(x,t)}{\partial t^2} \tag{1}$$

where E is Young's modulus of elasticity, A is the cross-sectional area, and c is the damping coefficient of the specimen. The internal damping $f(x,t)$ has been replaced by $-c\partial u(x,t)/\partial t$. The boundary conditions for the equation of motion are as follows: at $x = 0$ (fixed end), $u(x,t) = 0$ and at $x = L$ (free end), $EA\partial u(x,t)/\partial x = F_0 \cos \Omega t$. The qualitative plot of the solution of the equation of motion, i.e., Eq. (1), is shown in Fig. 2. The amplitude of vibrating force F_0 is considered 0.6–0.7 times

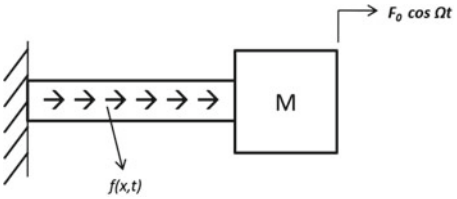

(a) Free body diagram of the lumped mass and the bar.

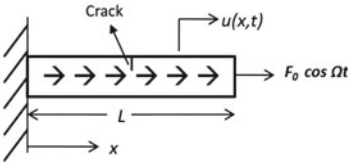

(b) Free body diagram of the bar.

Fig. 1 Mathematical model of the experimental setup

Fig. 2 Qualitative plot of the solution of the equation of motion

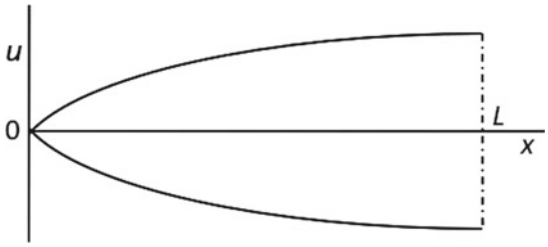

Fig. 3 Equivalent setup

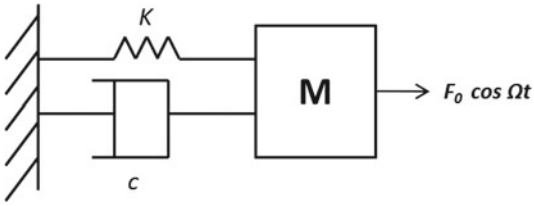

of the ultimate tensile strength of the specimen, as microplasticity develops in the specimen in this range of stress [17]. The displacement profile of axial displacement of material points ($u(x, t)$) is shown in Fig. 2. In this figure, we see the temporal strain in the axial direction ($\partial u(x, t)/\partial x$) is maximum at the root of the specimen, and therefore, the stress will be maximum at the root for a homogeneous and isotropic material. Hence, in a flawless material, the surface crack will start at the root (fixed end) of the specimen.

In order to predict resonance frequency, the experimental setup has been modeled as a spring-mass-damper system as shown in Fig. 3. The vibrating frequency is determined as $\Omega = \sqrt{\frac{K}{M}(1 - \zeta^2)}$ where $\zeta = c/2\sqrt{KM}$ and stiffness as K.

3 Experimental Setup

The Electromagnetic Resonance High-Frequency Fatigue Testing Machine has two gripping heads which are provided to hold the test component (with the help of grips and fixtures) and fatigue load is applied by vibrating one end with the help of a transducer and a large mass, keeping the other end fixed. A load cell is applied on the machine table at the fixed end to measure the loads and forces acting on the specimen under test. The vibrations are produced by a transducer present in the oscillating head of the machine at the resonant frequency of the test specimen setup. A large mass is attached at the oscillating head to control the operating frequency of the machine.

4 Experimental Procedure

We have conducted multiple experiments, and a few of them are discussed in this paper. It is assumed that the components taken for experimentation are homogeneous with no pre-crack or initial flaw. The crack developed in the course of loading is the outcome of the fatigue load applied. The machine, with loaded specimen between the grips and lumped mass of 100 Kg attached at the top of the setup, is shown in Fig. 4.

For crack detection, different shaped (cylindrical and flat) specimens, with and without flaw, have been considered. The same procedure for testing has been used for all the specimens.

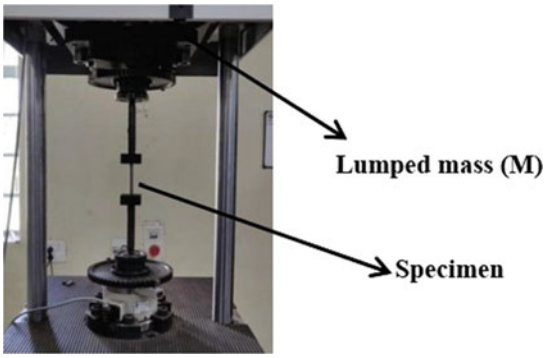

Fig. 4 Sample between two grips of the machine

Fig. 5 Cylindrical sample of 10 mm diameter, and the grip distance is 40 mm. The ends of the specimen have been flattened to fit in the hydraulic gripper. The length along the axial direction of the specimen is 25 mm and the width is 1.5 times of the diameter of the specimen

Table 1 Relation between crack growth and drop in natural frequency

Condition of crack	No. of cycles required for 0.001 Hz drop in natural frequency (cycles)
Crack Initiation at surface	5000–8000
Crack Growth/up to critical length	11000–25000
Crack at critical length	28000–20000
Crack growth after critical length	5000–1500

4.1 Cylindrical Specimen

A cylindrical mild steel specimen has been taken (see Fig. 5). The diameter of the cylindrical part is 10 mm, the distance between grips is 40 mm, and the overall length is 100 mm.

The sample has been gripped between the two grips of the setup and a fatigue load with dynamic stress of 120 MPa peak to peak has been applied. The force causing this stress is 9.425 kN tensile and compressive. The natural frequency determined by the machine is 93.333 Hz. The sample is under longitudinal vibration with one end fixed and the other end being forced by the oscillating head. The drop in frequency, along with the number of load cycles and the corresponding loads, has been recorded. A decrease in the value of the natural frequency of the system is noted which corresponds to the reduction in the stiffness of the component. This implies that the crack has initiated and is growing in the component. The observed drop in the frequency of the system relates to the three stages—crack initiation, crack growth, and critical crack growth phase. The crack initiation is the first phase where the number of cycles required for drop-in frequency kept on increasing up to a certain limit. This limit remains unchanged for some amount of cycles, which can be said as the growth phase, after which the number of cycles required for the same drop in frequency started to decrease, which can be said as the critical crack growth phase and leads to component failure. This has been shown in Table 1.

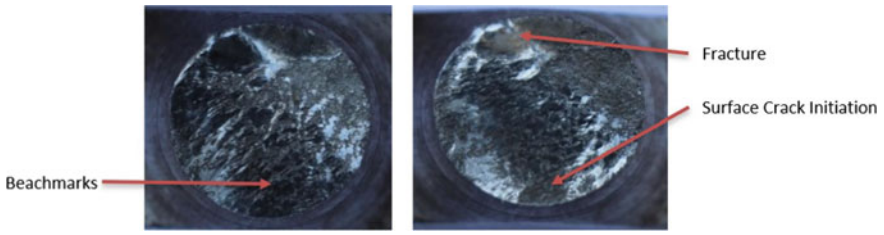

Fig. 6 Fractured surface in which beach marks and dimples are visible

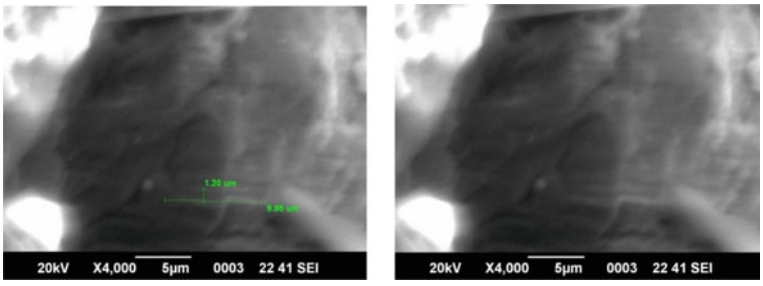

Fig. 7 Striation and the crack length detected in SEM

4.1.1 Fractured Surface Analysis

In fatigue fracture, the two zones that can be detected from naked eyes are the beach mark zone and the sudden fracture zone. The machine ran on a daily basis for a fixed number of hours and beach marks developed on the surface on stopping the machine. The number of cycles has been noted after each day's operation which corresponds to the beach marks developed on the surface. This process of the daily operation of the machine has been continued till the day when the sample failed. The beach mark area (fatigue zone) has a smooth texture and is visible to the naked eye. Striations produced on the surface are not visible to the naked eye. Hence, the cracked surface has been viewed under a Scanning Electron Microscope (SEM).

The cracked surface as viewed under the microscope is shown in Fig. 6, and the snaps of striations and beach marks have been taken. Dimples, which occurred at the moment of catastrophic failure, i.e., at the end of the experiment as shown in Fig. 7, have been viewed at 4000× zoom. Striations have been observed at 1000× and 2000× zoom and are of the order of 20–30 μm.

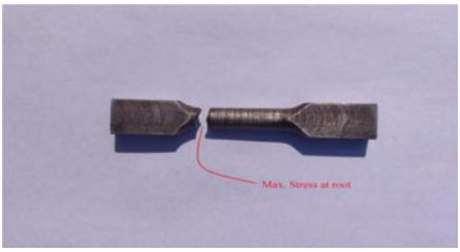

Fig. 8 Failure at the root of the specimen

4.1.2 Location of Crack and Failure

After running several cycles, the specimen failed at the root which belongs to the fixed end, as shown in Fig. 8. The static longitudinal/axial stress is the same throughout the specimen. However, in dynamic conditions, due to wave propagation, the maximum stress develops at the fixed end. This stress caused the inception of surface crack at the location of failure. Hence, it is evident that failure occurs at the root of a homogeneous rod with no flaws present in it.

4.1.3 Relation Between Frequency Drop and Crack Propagation

According to the data obtained from the fatigue testing machine, a graph is plotted between the ratio of change in natural frequency ($d\Omega$) to the crack length (da), i.e., the frequency drop rate and the number of cycles (N). From Fig. 9, it has been observed that there is a sudden drop in ($d\Omega/da$) after 20000 cycles and goes on decreasing continuously. The empirical relationship shown in Eq. (2) between $d\Omega/da$ and N is obtained using MS-Excel (produced in the computer attached to the machine). This sudden drop in frequency depicts that the crack initiated after this point and further propagated in the component up to its failure.

$$\frac{d\Omega}{da} = 3.892\, N^{-0.79} \tag{2}$$

4.2 Flat Specimen

To understand the effects of corners in a body, we have chosen a flat specimen for our experiment. Figure 10a shows that the flat mild steel specimen has been taken for testing, where the distance between the grips is 40 mm and the overall length is 100 mm. The width of the test section is 10 mm and thickness is 4 mm.

The sample has been gripped between the grips of the setup and a fatigue load with dynamic stress of 300 MPa peak to peak has been applied. The corresponding

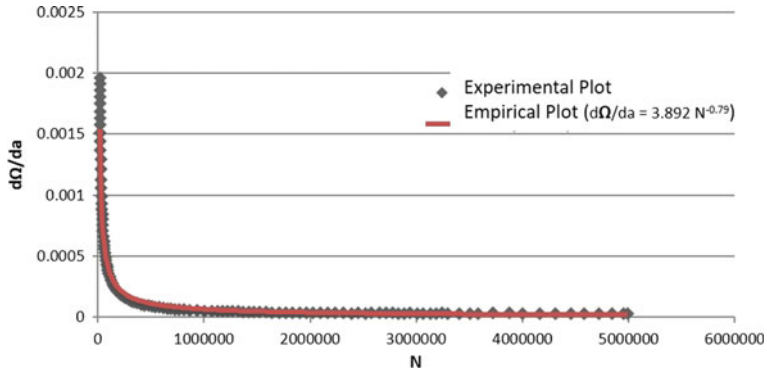

Fig. 9 Cylindrical mild steel specimen plot

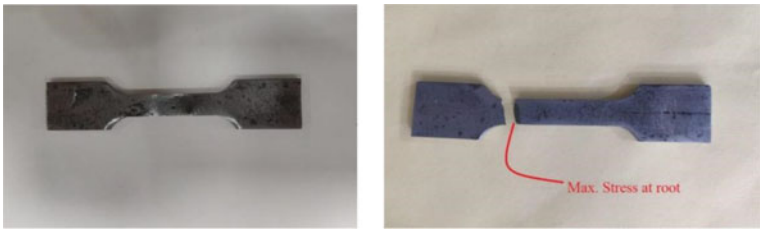

(a) Before failure. (b) After failure.

Fig. 10 Flat mild steel specimen

force is 10.8 kN tensile and compressive. The natural frequency determined by the machine is 79.88 Hz. The machine ran until the sample failed. In this case also, the crack occurred at the root due to the same reason explained in Sect. 2.

From Fig. 10b, it is noted that whatever be the shape, if the component is homogeneous and free from flaws/discontinuities, then the crack initiates from the surface and causes failure at the root. The cracked surface of the flat specimen has been observed (Fig. 11) under the Scanning Electron Microscope and the snaps of the striations and beach marks have been taken.

4.2.1 Relation Between Frequency Drop and Crack Propagation

The fatigue test data from the setup has been observed and upon analysis, a relationship has been developed between $(d\Omega/da)$ and the number of cycles, which when plotted showed that after nearly 5000 cycles, the crack initiates as there is a sudden drop in the graph of Fig. 12, after which there is a gradual decrease in the slope of the graph, which further confirms about the propagation of the crack during the running conditions of the setup. The empirical relationship shown in Eq. (3) between $d\Omega/da$

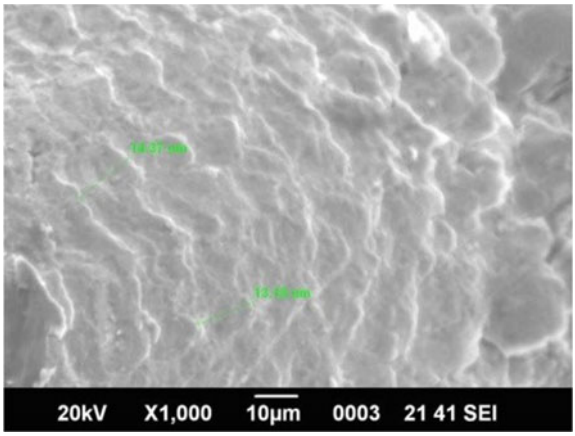

Fig. 11 Crack propagation and striations in the direction of propagation

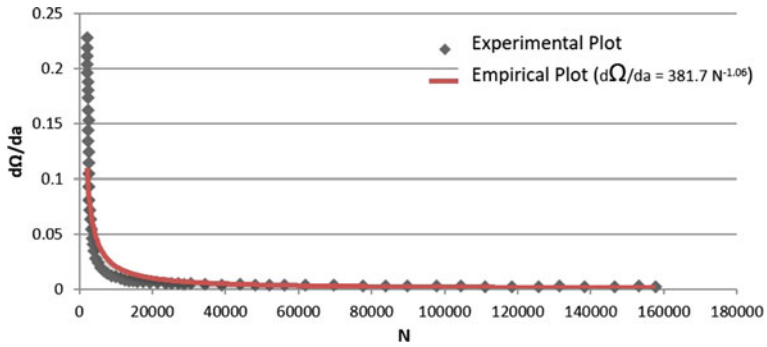

Fig. 12 Flat mild steel specimen plot

and N is obtained using MS-Excel.

$$\frac{d\Omega}{da} = 381.7\, N^{-1.06} \tag{3}$$

4.3 Flat Specimen with a Flaw

A flat specimen made of aluminum of thickness 6 mm has been taken as shown in Fig. 13a. The distance between the grips is 57 mm and the total length is 136 mm. The width of the test section is 12 mm.

The sample has a flaw in the middle of its test section as shown in Fig. 13. The flaw has been created by friction welding. The sample has been gripped between the

(a) Before failure. (b) After failure.

Fig. 13 Flat aluminum specimen

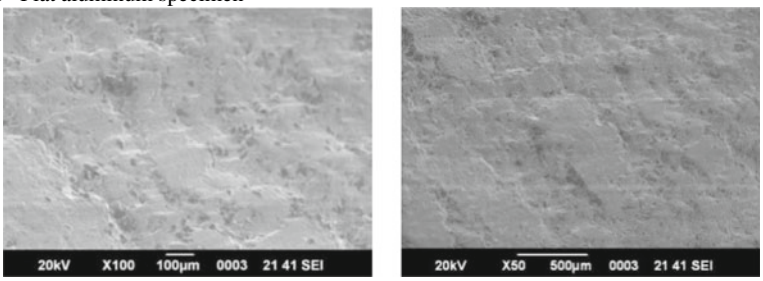

(a) (b)

Fig. 14 Visible beach marks at the crack surface

two grips of the testing machine and a fatigue load with dynamic stress of 45 MPa peak to peak has been applied. The force is 3.33 kN tensile and compressive. The natural frequency is 69.81 Hz. The machine has been set up in the same manner and is kept running until the sample fails.

In contrast to previous findings, the sample fails in the middle of the test section (see Fig. 13b). The reason is the lower stiffness/Young's Modulus at that section, which reduces the crack resistance of the material. The fatigue cracks appear at the middle section and failure occurs at this point. The cracked surface of the specimen has been observed under Scanning Electron Microscope and snaps have been taken.

The cracked surface of the aluminum sample has been studied under the Scanning Electron Microscope and some nice visible beach marks have been spotted on the cracked surface. The beach marks are at a distance of 180–250 µm. These are visible at 50× zoom of the microscope. The snaps of the cracked surface are shown in Fig. 14a, b.

4.3.1 Relation Between Frequency Drop and Crack Propagation

The fatigue test data from the setup has been observed and upon investigation and analysis, a relationship has been developed between $(d\Omega/da)$ and the number of cycles. This relationship has been plotted in the form of a graph (Fig. 15) and is

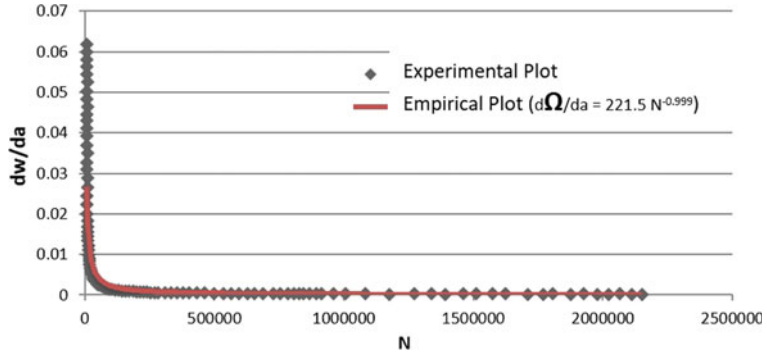

Fig. 15 Flat aluminum specimen (with flaw) plot

similar to that obtained in the case of a cylindrical specimen. It has been observed that nearly after 5000 cycles, the crack initiates as there is a sudden drop in the graph, after which there is a gradual decrease in the slope of the graph, which further confirms the propagation of the crack during the running conditions of the setup. The empirical relationship shown in Eq. (4) between $d\Omega/da$ and N is obtained using MS-Excel. Even though the specimen used in this case has a flaw present in it, the crack propagation is quite similar to the previous cases.

$$d\Omega/da = 221.2\, N^{-0.99} \tag{4}$$

5 Results

Considering the effects of corners and flaws, the empirical relationship shown in Eqs. (2–4) of the three specimens has been determined and it has been observed that the exponent value of flat specimen with and without flaw is approximately similar, i.e., 1.06 and 0.99 while the exponent of the cylindrical specimen is 0.79.

6 Conclusion

In this work, crack detection and propagation in cylindrical and rectangular cross-sectional specimens of mild steel and aluminum have been studied to include the effect of corners and flaws with the help of a fatigue testing machine. The specimens have been gripped in the machine and subjected to an oscillating load at one end keeping the other end fixed. We have mathematically formulated the system and determined the location of maximum stress in the specimen. It has been noticed

that the crack initiation occurs at the root of the specimen with no flaws, and for the specimen with a flaw, the crack initiates at the discontinuity. The severity of crack has been determined by the drop in the natural frequency of the system. Crack propagation with respect to natural frequency drop has been observed and plotted for the specimens, and an empirical relationship has been obtained for the same. The empirical relationships for the various specimens reveal that the rate of frequency drop of the system is inversely proportional to an approximately similar power of the number of cycles for the flat specimens in both the cases, i.e., with and without flaws, respectively. However, the value of the exponent is significantly different in the case of the cylindrical specimen as compared to that of the flat specimens.

References

1. Jack A, Paterson A (1977) Cracking in 500 mw IP rotor shafts, The Influence of Environ Fatigue 75–83
2. Greco J, Agnew J, Erhardt K, Bertilsson J, Stys Z (1978) Cumberland steam plant: cracked IP rotor coupling of unit 2. In: Proceedings of the American power conference (United States), vol 40
3. Campbell G, Lahey R (1984) A survey of serious aircraft accidents involving fatigue fracture. Int J Fatigue 6(1):25–30
4. Bhaumik S, Sujata M, Venkataswamy M (2008) Fatigue failure of aircraft components. Eng Fail Anal 15(6):675–694
5. Il'gamov M (2017) Longitudinal vibrations of a bar with incipient transverse cracks. Mech Solids 52(1):18–24
6. Ismail F, Ibrahim A, Martin H (1990) Identification of fatigue cracks from vibration testing. J Sound Vib 140(2):305–317
7. Dilena M, Morassi A (2011) Dynamic testing of a damaged bridge. Mech Syst Signal Process 25(5):1485–1507
8. Morassi A (2001) Identification of a crack in a rod based on changes in a pair of natural frequencies. J Sound Vib 242(4):577–596
9. Lee Y-S, Chung M-J (2000) A study on crack detection using eigenfrequency test data. Comput Struct 77(3):327–342
10. Dimarogonas A, Papadopoulos C (1983) Vibration of cracked shafts in bending. J Sound Vib 91(4):583–593
11. Chondros T, Dimarogonas A, Yao J (1998) Longitudinal vibration of a continuous cracked bar. Eng Fract Mech 61(5–6):593–606
12. Dimarogonas AD (1996) Vibration of cracked structures: a state of the art review. Eng Fract Mech 55(5):831–857
13. Chondros T, Dimarogonas A, Yao J (1998) A continuous cracked beam vibration theory. J Sound Vib 215(1):17–34
14. Morassi A (1997) A uniqueness result on crack location in vibrating rods. Inverse Problems Eng 4(3):231–254
15. Loya J, Rubio L, Fernández-Sáez J (2006) Natural frequencies for bending vibrations of timoshenko cracked beams. J Sound Vib 290(3–5):640–653
16. Karthikeyan M, Tiwari R, Talukdar S, Development of a novel algorithm for a crack detection, localization, and sizing in a beam based on forced response measurements. J Vib Acoust 130(2)
17. Mozafari F, Thamburaja P, Srinivasa A, Moslemi N (2019) A rate independent inelasticity model with smooth transition for unifying low-cycle to high-cycle fatigue life prediction. Int J Mech Sci 159:325–335

Baseline Free Damage Localization in Beam-Like Structures Using Teager–Kaiser Energy Operator

P. Madankumar, J. Prawin, and Glory Joseph

1 Introduction

The structural damage diagnosis method based on vibration theory has the advantage of non-destructivity, and it can carry out effective damage identification for varied engineering applications such as fault diagnosis of wind turbine gearbox, bridge scours detection, etc. The vibration-based techniques are preferred for damage diagnosis as they are global methods and it does not need a priori information about the damage including its spatial location [1–4]. Generally, the process of vibration-based structural damage detection consists of recording structural vibration, extracting modal properties, and identifying damages based on changes in structural dynamic properties. In vibration data recording, the source of excitation can be generated from a specific vibrating machine, ambient loading, or operational loading [5]. At present, identification methods based on vibration characteristics can be divided into natural frequency, mode shape and its curvature, residual force vector flexibility matrix, transfer function/frequency response function, and modal strain energy. These features are directly related to changes in mass, stiffness, and damping matrices associated with physics-based models (correlated with the original system). A comparison of the features extracted from the modal parameters of the structure in a pristine state to the features obtained from the current data provides information about the presence of damage, its corresponding spatial location, and severity [6]. The change of structural vibration mode contains more damage information, which has a significant advantage in determining crack location. However, the traditional damage localization index based on the mode shape difference approach between the measurements of the healthy and damaged structure gives false results

P. Madankumar · G. Joseph
Cochin University of Science and Technology, Kochi, Kerala, India

J. Prawin (✉)
CSIR-Structural Engineering Research Center, CSIR Campus, Chennai, Tamil Nadu, India

D. K. Maiti et al. (eds.), *Recent Advances in Computational and Experimental Mechanics, Vol II*, Lecture Notes in Mechanical Engineering,
https://doi.org/10.1007/978-981-16-6490-8_44

by showing more than one peak apart from the damage location due to its sensitivity to noise, difficulty in identifying subtle cracks, and crack location coinciding with the zero node of the corresponding selected mode. This paper presents a robust Teager–Kaiser Energy Operator (TKEO)-based baseline free damage localization approach for beam-like structures overcoming the above-said limitations. Numerical studies and experimental validation have been performed for the proposed approach.

2 Proposed Strategy

Damage diagnosis basically involves obtaining acceleration time history response at "N" locations spatially across the structure with sampling frequency $f_{s.}$ Then the modal features like natural frequencies and mode shapes will be extracted from each sensor measurements using the well-established operational modal analysis technique. The obtained mode shapes of the structure with localized damage is integrated with Teager Kaiser Energy Operator (TKEO) for damage diagnosis of the target structure. Section 3 presents the modeling details related to beam-like structures for vibration analysis. The present work employs Frequency-Domain Decomposition (FDD) method for modal features extraction, described later in Sect. 4. The details related to TKEO are presented in Sect. 5.

3 Modeling for Vibration Analysis

The beam is modeled using one-dimensional Euler–Bernoulli elements. Several modeling techniques are available in the literature to simulate crack in the beam-type structure, and the present work uses the popular Sinha damage model. The Sinha damage-related modeling is only briefly reported, and more details can be found in [7]. The flexural rigidity at each section "x" through Sinha damage modeling is given by

$$EI(x) = \frac{EI_0}{1 + C\exp(-2\alpha|x - x_j|/d')}; C = \frac{(I_0 - I_{cj})}{I_{cj}} \tag{1}$$

where I_0 and I_{cj} indicate the moment of inertia of the beam without and with crack. Similarly, d, d_{cj} indicates the depth of the beam without and with crack at the section "X" (particular element of the finite element model). The parameters x_j and d represent the position and depth of the crack. The coefficient α is a constant and l_c is the effective length. The crack length lc is taken as 1.5d.

4 Frequency-Domain Decomposition (FDD)

In the FDD technique, the basic step is the estimation of the Power Spectral Density (PSD) $G_{yy}(j\omega)$ observed at discrete frequencies ω-ω_i and then decomposing the PSD matrix using singular value decomposition [8]:

$$G_{yy}(jw) = U_i S_i U_i^H \tag{2}$$

The power spectral density of the response is related to modal parameters by

$$G_{yy}(j\omega) = \sum_{k\in\omega} \frac{d_k \phi_k \phi_k^T}{j\omega - \lambda_k} + \frac{\overline{d}_k \overline{\phi}_k \overline{\phi}_k^T}{j\omega - \overline{\lambda}_k} \tag{3}$$

where ϕ indicates the "kth" mode shape and λ_k refers to the "kth" mode contribution amplitude.

The natural frequencies and mode shapes are computed respectively from the singular values and singular vectors of the power spectral density. The mode is chosen by the identification of the singular vector having a modal assurance criterion value greater than the threshold. On the other hand, if none of the singular vectors have a MAC larger than a threshold, the search for matching parts of the autospectral density is terminated.

5 Teager–Kaiser Energy Operator

Teager–Kaiser Energy Operator (TKEO) is a nonlinear and energy-tracking operator estimated based on the instantaneous energy of the signal [9–12]. TKEO is popularly used in Structural Health Monitoring (SHM) in identifying instantaneous frequency and phase for both time-invariant and time-varying linear and nonlinear systems. Due to its advantages of high resolution (time and frequency resolution), simplicity, and efficiency, TKEO is used to analyze demodulation signals and to identify discontinuities in the data.

The continuous and discrete Teager–Kaiser Energy Operator $\Psi[.]$ is given by

$$\psi_c[\phi] = \left[\dot{\phi}\right]^2 - \phi\ddot{\phi} \tag{4}$$

$$\psi_d[\phi] = \phi_n^2 - \phi_{n+1}\phi_{n-1} \tag{5}$$

where ϕ refers to the mode shape of the target structure and the superscripts single dot and double dot indicate the first and second derivative of the mode shape.

Instead of the traditional mode shape difference, the proposed work uses the mode shape of the structure with damage integrated with TKEO to exactly identify the geometrical position of the damage.

The proposed Damage Localization Index (DLI) is defined as

$$\mathrm{DLI} = \mathrm{TKEO}\left(\ddot{\phi}_i^{\mathrm{damaged}}\right) \tag{6}$$

The position of the highest value of DLI gives the position of the damage. The magnitude of the DLI at the identified damage location quantifies the severity of the damage. The two damage localization indices DLI1 and DLI2 involve computation of TKEO using Eqs. 4 and 5.

It should be mentioned here that Teager–Kaiser Energy Operator (TKEO) as a damage localization index provides better estimate of the location of damage as compared to traditional methods because it is basically a signal discontinuity magnifier. Besides, TKEO offers distinct capabilities of suppressing noise, cancelling global fluctuation trends and intensify of the local singularity caused by a damage for a measured mode shape involving noise. These property and characteristic features maximize the sensitivity to damage and accuracy of damage localization.

6 Numerical Investigations

A numerical example of a 25 m RCC simply supported beam having a cross-section of 0.6 × 1.2 m as illustrated in Fig. 1 is considered. The considered 1D Euler beam is discretized using 25 elements. Sinha crack model [11] is used for simulation of damage. Newmark time integration technique is used to compute vibration measurements (acceleration time history) at varied locations on the simply supported beam. The measurements are corrupted with 5% noise prior to modal parameter estimation.

FDD [6] technique is used to estimate modal parameters. The first few natural frequencies of the healthy (undamaged) structure are computed as 2.7546, 11.0182, 24.7910, and 44.0728 Hz.

To verify and validate the TKEO-based damage identification technique, the following three damage scenarios are considered:

D1—6 m (element affected is 6) from left-hand support with a 10% reduction in moment of inertia;

Fig. 1 Simply supported RCC beam

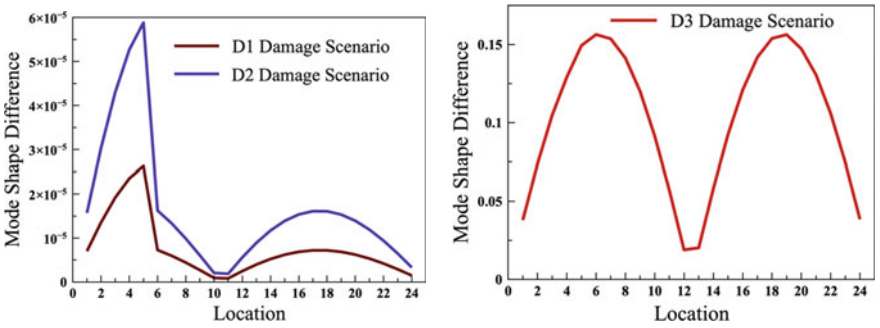

a) Damage Scenarios D1 and D2 b) Damage Scenario D3

Fig. 2 Mode 2 difference of undamaged and damaged beams

D2—6 m (elements affected is 6) from left-hand support with a 20% reduction in moment of inertia; and

D3 multiple damages—5 m and 20 m (elements affected are 5 and 20) from left-hand support with a 20% reduction in moment of inertia.

The traditional damage localization index based on the difference of mode shapes of the structure with and without damage for different damage scenarios D1 and D2 is presented in Fig. 2a corresponding to the second mode. In addition, similar result for damage scenario D3 is presented in Fig. 2b. It should be mentioned here that the proposed algorithm works effectively irrespective of the selected mode, and the related results are presented later in this paper.

It can be observed from Fig. 2, even though peaks occur at the location of the damage, there exist other peaks at other locations. This results in misinterpretation of the damage. This is due to measurement noise, zero nodes of the selected mode, and low intensity of the damage. Hence, the mode shape difference between the two states of the structure cannot be employed for locating the damage.

Therefore, the proposed work uses the mode shape of the structure with damage integrated with the Teager–Kaiser energy operator as a damage localization index to find the position of damage located anywhere in the structure. The results of three damage scenarios corresponding to damages at 6 m with 10 and 20% stiffness reduction and another scenario of multiple damages at 5, 20 m with stiffness reduction of 20% each are presented in Fig. 3. The continuous and discrete TKEO results are presented in Fig. 3a, b, respectively.

Figure 3 illustrates that the damage localization index based on either continuous or discrete TKEO shows peak only at the damage location. The proposed DLI increases with an increase in stiffness reduction. The proposed approach can identify a minimum stiffness reduction of about 10%. Apart from this, the proposed approach is capable of identifying multiple damages and is also insensitive to noise.

The results of the continuous and discrete Teager–Kaiser energy operator-based damage localization index corresponding to damage scenario D1 estimated for Mode 1–2 are presented in Figs. 4a and 5a, respectively. Similarly, the results for Mode 3–4 are presented in Figs. 4b and 5b.

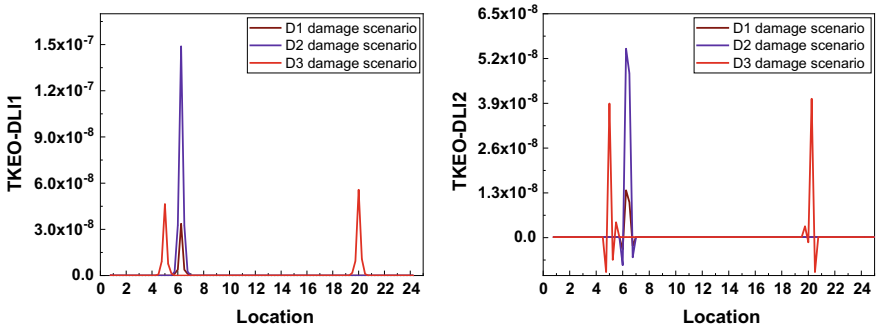

a) TKEO Continuous Operator b) TKEO Discrete Operator

Fig. 3 Mode 2 damage localization index

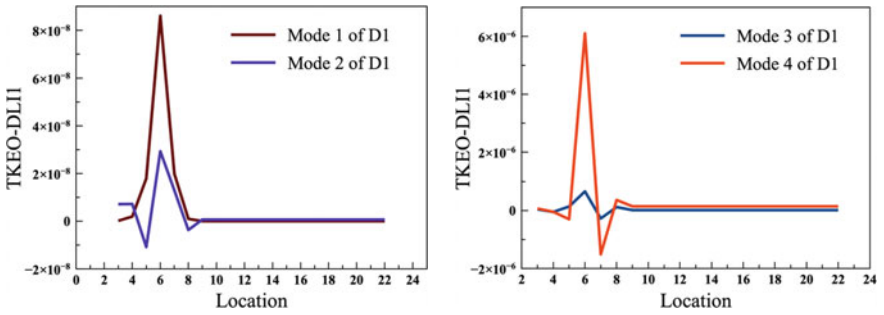

a) Mode 1 and Mode 2 of Damage Scenario D1 b) Mode 3 and Mode 4 of Damage Scenario D1

Fig. 4 Damage localization index 1—TKEO continuous operator

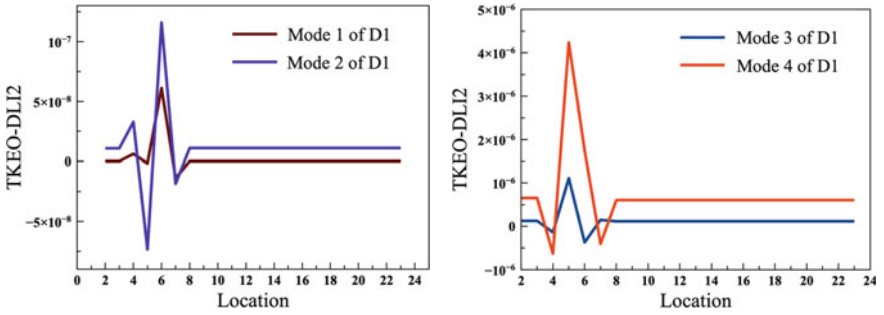

a) Mode 1 and Mode 2 of Damage Scenario D1 b) Mode 3 and Mode 4 of Damage Scenario D1

Fig. 5 Damage localization index 2—TKEO discrete operator

Figures 4 and 5 depict that the proposed TKEO approach can localize irrespective of the chosen mode. Apart from this, it is very much evident from the numerical investigation that the proposed TKEO-based localization index does not require any reference measurement or the measurement corresponding to the underlying healthy structure.

7 Experimental Validation

Experimental investigations at the laboratory have been performed on steel simply supported ISMB 100 beam of length 3 m for validation. The properties are depth—100 mm; width of flange—60 mm; flange thickness—7.2 mm; web thickness—4 mm; area—14.6 cm^2; moment of inertia Ixx—257.5 cm^4; and Iyy—40.8 cm^4. The experimental setup for the beam is shown in Fig. 6. The first few natural frequencies of the healthy structure are found to be 36.28,145.42, 327.52, and 579.88 Hz. The beam is instrumented with 15 PZT accelerometers and the traditional modal shaker, and the data acquisition system is used. The sampling frequency is 2400 Hz and each realization is measured for about 5 s. A total of 100 realizations of the healthy beam encompassing varied environmental and operational conditions are obtained.

To demonstrate the TKEO-based algorithm for identifying single as well as multiple damages and also smaller damages, two different damage scenarios furnished in Table 1 are simulated. Either one or two holes at each location are considered for simulation of damage with different intensities. The natural frequencies corresponding to damage scenarios D1 and D2 are also presented in Table 1. Table 1 illustrates that the variations of natural frequency are due to its sensitivity to damage. However, only specific modes are sensitive and dependent on both the position of the damage and the severity of the damage.

The traditional damage localization index based on the difference of mode shapes of the beam with and without damage estimated for damage scenarios D1 and D2 is presented in Fig. 7a, b corresponding to the third mode. Similar to numerical

Fig. 6 Lab-level test setup—simply supported steel beam

Table 1 Experimental specimens

Damage scenario	Damage location	Sensor location	Natural frequency (in Hz)
D1	A single hole near the bottom flange at 0.76 m from the left support	Near sensor 4	35.86,143.23,323.21,578.62
D2	Two holes–one hole @0.76 m from the left support and another one hole @1.82 m from the left support	Near sensor 4 and sensor 10	36.01,144.96,323.82,579.65

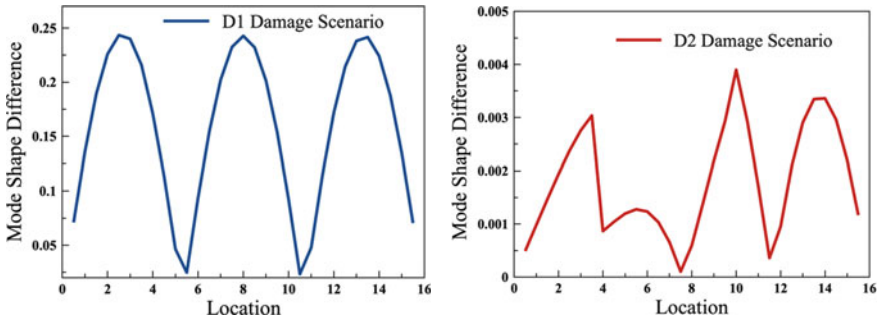

(a) Damage Scenarios D1 (b) Damage Scenario D2

Fig. 7 Mode 3 difference of undamaged and damaged beams

observation it can be concluded from Fig. 7 that the mode shape difference fails to locate the damage.

The results of the Teager–Kaiser energy operator-based damage index for the varied damage scenarios, i.e., D1 and D2 of the lab-level specimen are presented in Figs. 8 and 9. It can be observed from Fig. 8a, b corresponding to TKEO continuous and discrete operator results that the maximum value of the damage localization index for the damage scenario D1 is at the sensor node 4. This coincides with the geometric location of the damage.

Similarly, the damage localization index presented in Fig. 9a, b for scenario D2 shows a peak at both sensor 4 and sensor 10 due to the presence of two damages at two different spatial locations. Therefore, it can be observed from this investigation that the proposed algorithm can locate multiple damages present anywhere in the structure. It can be observed from Fig. 9 that even though for the damage scenario D2, the stiffness reduction is same at both the spatial locations of the damage (i.e., at sensor nodes 4 and 10), the TKEO magnitude is different at two locations due to the sensitivity of each mode to the spatial location of the damage and TKEO being a nonlinear operator. In other words, any localized damage would affect each mode differently, depending on the particular location and severity of the damage. Therefore, the comparison of TKEO results at the same spatial location of the damage

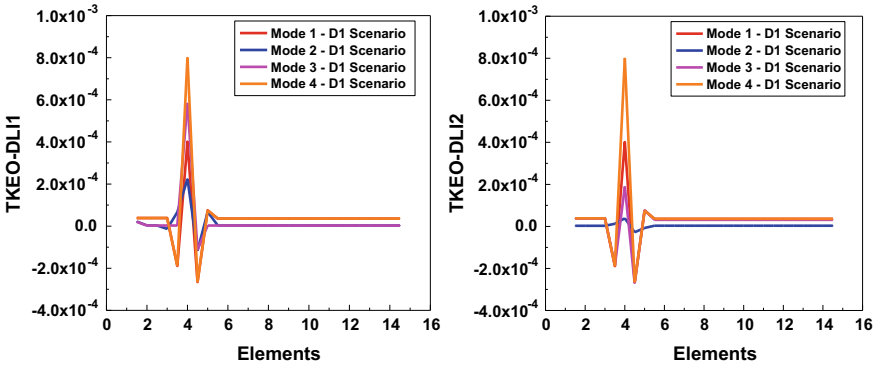

a) TKEO Continuous Operator b) TKEO Discrete Operator

Fig. 8 Damage localization index–experimental specimen–damage scenario D1

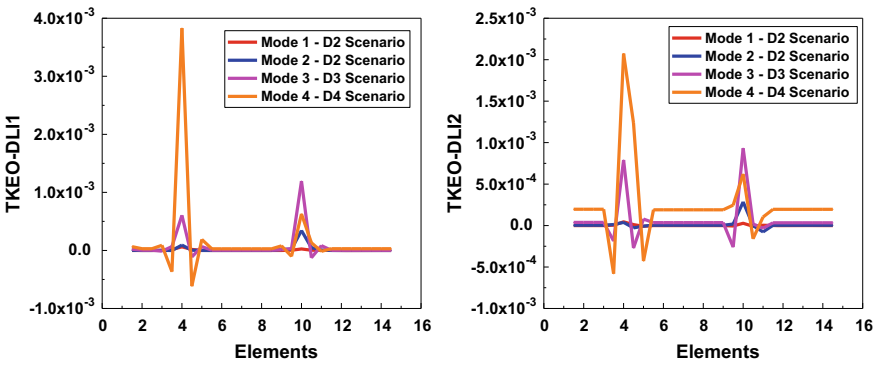

a) TKEO Continuous Operator b) TKEO Discrete Operator

Fig. 9 Damage localization index–experimental specimen–damage scenario 2

and the same selected mode only gives relative quantification of severity of the damage. This is also evident from the numerical investigation presented in earlier Sect. 6.

8 Conclusion

The proposed work uses the mode shape of the structure with damage integrated with the Teager–Kaiser energy operator as a damage localization index to find the geometric location of damage located anywhere in the structure. From the numerical and experimental investigations carried out in this paper, it is clear that the damage location can be identified at the sensor node corresponding to the maximum DLI

value. The proposed TKEO-based technique can locate multiple damages present at any geometric location in the structure. TKEO-based technique is baseline free and can identify very subtle cracks even using polluted measurements. However, it should be mentioned here that the proposed TKEO approach is baseline free with the assumption that the system has uniform stiffness. The proposed approach is applicable to systems with non-uniform stiffness, but in that case, TKEO needs to be applied on the difference of the mode shape between the reference (i.e., healthy state) and current (i.e., damaged state) state measurements of the structure under consideration. Therefore, for systems with non-uniform stiffness, the proposed TKEO approach is not baseline free.

Acknowledgements The first and third authors acknowledge the support of professional and technical help received including lab-level experiment from SERC-CSIR, Chennai.

References

1. Prawin J, Lakshmi K, Rama Mohan Rao A (2020) Structural damage diagnosis under varying environmental conditions with very limited measurements. J Intell Mater Syst Struct 31(5):665–686
2. Farahani RV, Penumadu D (2016) Damage identification of a full-scale five-girder bridge using time-series analysis of vibration data. Eng Struct 115:129–139
3. Husain NA, Ouyang H (2011) Detection of damage in welded structure using experimental modal data. J Phys-Conf Ser 305(1):012120
4. Shabbir F, Khan MI, Ahmad N, Tahir MF, Ejaz N, Hussain J (2017) Structural damage detection with different objective functions in noisy conditions using an evolutionary algorithm. Appl Sci 7(12):1245
5. Prawin J, Rama Mohan Rao A (2019) A method for detecting damage-induced nonlinearity in structures using weighting function augmented curvature approach. Struct Health Monitor 18(4):1154–1167
6. Prawin J, Rama Mohan Rao A (2019) Reference-free breathing crack identification of beam-like structures using an enhanced spatial Fourier power spectrum with exponential weighting functions. Int J Struct Stab Dyn 19(02):1950017
7. Sinha JK, Friswell MI, Edwards S (2002) Simplified models for the location of cracks in beam structures using measured vibration data. J Sound Vib 251(1):13–38
8. Brincker R, Zhang L, Andersen P (2001) Modal identification of output-only systems using frequency domain decomposition. Smart Mater Struct 10(3):441–451
9. Antoniadou I, Manson G, Dervilis N, Barszcz T, Staszewski WJ, Worden K (2012) Use of the Teager-Kaiser energy operator for condition monitoring of a wind turbine gearbox. In: International conference on noise and vibration engineering, pp 4255–4268
10. Feng Z, Wang T, Zuo MJ, Chu F, Yan S (2011) Teager energy spectrum for fault diagnosis of rolling element bearings. J Phys-Conf Ser 305(1):012129
11. Kaiser JF (1990) On a simple algorithm to calculate the'energy' of a signal. In: International conference on acoustics, speech, and signal processing. IEEE, pp 381–384
12. Vakman D (1996) On the analytic signal, the Teager-Kaiser energy algorithm, and other methods for defining amplitude and frequency. IEEE Trans Signal Process 44(4):791–797

Seismic Assessment of RC Structure with and Without Lateral Load Resisting Members

Shubham Chandra, B. K. Singh, and Anshu Tomar

1 Introduction

The role of science and engineering in reducing the effects of natural disasters like earthquake is the most debatable topic in earthquake. RC structures are gaining recognition in providing a sustainable, energy efficient, durable, affordable, and resilient response to increasing demand for residential and commercial multi-story buildings. Large lateral acceleration has been reported during earthquakes in buildings. Acceleration assessments are encountering an increasing impact in earthquake engineering as a reliable method for seismic building evaluation, such accelerations have been held responsible for inertia force induced by infrastructure failure and are a major factor for structural deterioration and also for the failure of structures [1]. Diaphragm is one of the most important elements and plays a crucial function as a lateral load transferring to vertical load resistant elements [2]. Lateral load-resistant components in multi-story buildings, which typically transfer gravity loads to the vertical element, are also needed for the transmission of lateral inertial force to the vertical structural element. For the designing of earthquake-resistant structure, floor accelerations are needed to evaluate in-plane diaphragm forces.

Less or no research has been done to consider both the constraint parameters of the RD or horizontal X-BE, and their effect on the lateral distribution forces in the reinforced concrete frame structure. In fact, no diaphragm is either completely rigid or perfectly flexible; however, to simplify the analysis, diaphragms can be assumed as rigid or flexible. In terms of displacement, the linear response of a structure with different floor diaphragm [3] or diaphragm discontinuity [4] is explored extensively under seismic actions. Some of the seismic standards used in India are Indian Standard Code [6], FEMA 440 [7], and ASCE 7–10 Code [8], which are considered in the use of different analytical approaches that can provide a simple indication of the seismic

S. Chandra (✉) · B. K. Singh · A. Tomar
DIT University, Dehradun 248009, India

D. K. Maiti et al. (eds.), *Recent Advances in Computational and Experimental Mechanics, Vol II*, Lecture Notes in Mechanical Engineering,
https://doi.org/10.1007/978-981-16-6490-8_45

behavior of the structure to resolve these disadvantages. The results of maximum displacement, maximum drift, max story stiffness presented in this study are related to improved understanding of the RC structure incorporated with Rigid diaphragm or Horizontal X-bracing, and performance point and ductility ratio are also illustrated.

2 Literature Review

Kehila Fouad et al. [9] explore the deformity of the floor in their layout under the influence of horizontal seismic behavior and the finding obtained such as seismic response with different parameters and indicate the difference in the supposed form of diaphragm floor [9]. Francesca Barbagallo et al. [10] studied to resolve this downside by adding a simple additional element, called axial buffer element, at one end of each beam and the effect of the influence of the axial buffer element on the seismic response of a collection of RC buildings representing real structures. Incremental nonlinear dynamic analysis and nonlinear static analysis have been performed for that purpose [10]. Rodriguez et al. [11] discuss an experimental evaluation of an empirical method that was previously suggested for the evaluation of the horizontal floor accelerations caused by earthquake in symmetrical buildings constructed with rigid diaphragms. Horizontal floor accelerations obtained from shake table tests were collected from four small-scale structures representing multi-story reinforced concrete buildings with frame and frame-wall. In the time 1979–1989, these buildings were checked on the shaking table at the University of Illinois Urbana-Champaign [11]. Ju et al. [12] paper's main aim is to determine the disparity among both rigid-floor and flexible-floor analyses of buildings with and without shear walls and the analysis is done by finite-element method. This research shows that the rigid-floor model is as reliable as the flexible model, even for non-standard flooring systems. This is concluded since the slab's in-plane rigidity is much greater than the stiffness of the out of plane column. Because of the very large lateral rigidity of the shear wall system, the rigid-floor and flexible-floor analyses can differ greatly for the buildings with shear walls [12]. Sadek Bahar et al. [13] study the in-plane deformation of rectangular floors of single-story structures under the influence of horizontal seismic behavior. Furthermore, the impact of parameters affecting floor behavior such as size opening and distance, shear wall location, span-to-depth ratio, and floor-constituent materials have been studied. Results imply that a diaphragm, whether marked as rigid or flexible, should act in a flexible manner. A small opening in the floor, however, can alter the actions of an assumed rigid diaphragm, and make it function like a flexible diaphragm [13]. Mustafa's [14] numerical analysis is studied in this research for a twelve-story structure with dual reinforced concrete column and wall structure. On RC walls, the seismic efficiency of the two structures tested was measured with different parameters. Generally, Rigid Diaphragm produce results relatively similar to those of Semi-Rigid Diaphragm for base shear, story displacements, and inter-story drifts as the slab is thick enough and membrane deformation is negligible due to lateral load [14]. Francesco Porco et al. [15] explain the seismic response

of the structure of reinforced concrete with special emphasis on the importance the floor system plays. The rigid-floor concept is also used for vulnerability evaluation of existing buildings by RC, to simplify the analysis of their structural response with different seismic codes. Generalized from actual RC existing structures using numerical methods, with and without the assumption of a rigid floor [15]. The aim of Raffaele NUDO et al.'s [16] investigation is to evaluate the beam-floor connection's effect on the absorption of seismic behavior in RC structural systems and, in specific, to estimate the decrement in internal forces encountered by beams as a result of the intervention of elements relating to floor structures. A parametric analysis has been established for this objective; it has defined the position of floor joists parallel to the beam as the most significant consideration factor [16]. The aim of Bhuiyan et al.'s [17] study is to analyze the effects of the flexibility of the diaphragm on the structural behavior of a 64-story global model high-rise structure. The study concluded that structures modelled with flexible diaphragms can report greater accelerations and displacements than rigid diaphragm-modelled structures, and their fundamental vibrational periods can be significantly greater [17]. Elsa Thomas et al.'s [18] research examines the condition of the diaphragm for the various types of office building flooring systems. Also calculated is the effect of aspect ratio and height of the building on the diaphragm behavior. To help enhance clinical practice and help minimize the vulnerability, the analysis of diaphragm condition is important [18]. In the analysis by Md Aziz Ur Rahman et al. [19], seismic response of high-rise RC building frames was conducted considering the use of two separate types of floor diaphragm, i.e., semi-rigid diaphragm and rigid diaphragm, and ETABS 2016 software was used for analysis. Results are obtained according to various parameters [19]. Using a performance-based approach, J.M. Barron et al.'s [20] study focuses on evaluating the influence of diaphragm flexibility on the structural behavior of typical RC rectangular construction structure. 3-story and 5-story RC structure with 2:1 and 3:1 aspect ratio end shear wall was built and constructed as per the current code procedure considering rigid diaphragm behavior [20].

Based on the above review on floor diaphragms, it can be seen that researchers have worked on either taking different diaphragm system or diaphragm discontinuity. In the present work, both geometrical constraints as well as constraints regarding losses have been considered. The purpose of the analysis is to examine the effects of the study of different lateral load resisting member in G + 5 frames by comparing the three models BF, RD, X-BE with same structural configuration and the results shown are of different parameters.

3 Methodology

Different type of diaphragms could influence the value of internal force acting on reinforced concrete structure, so it is necessary to improve the resisting response from changing lateral load resisting horizontal member from Rigid diaphragm (RD) to X-brace element (X-BE). Since most of the designed multi-story structures are based

solely on static seismic loads. Floor diaphragm is one of the prominent methods to reduce the floor accelerations. For a better comparison of the diaphragm effects on the internal forces of the RC structure, all structural configuration (IS 456:2000) and seismic configuration (IS 1893:2016) of the structure have been fixed, keeping the lateral load-resistant elements (RD and X-BE) varying. Three G + 5 story structure with regular shape configuration has been designed as per Indian standard code, and the seismic analysis of a structure shall be performed according to nonlinear static pushover method with FEMA 440EL and ASCE 7–10 code considering DDBD (direct displacement-based) approach. The primary objective of selected structure with regular shapes both in plan and elevation provides a good result as inertia force is transmitted without trying to bend due to the geometry of structure [21]. All the 3-building model has been created in the building analysis and design software ETABS 18.0.2. All the parameters are shown in PO-X (i.e., target displacement in X-direction.) and PO-Y (i.e., target displacement in Y-direction) viz. performance point, maximum story displacement, maximum story drift, base shear, and story stiffness (shown in EQ-X an EQ-Y) obtained from the analysis, and the results were compared.

3.1 Structural Configuration

In this study, three rectangular G + 5 story RC frame structures with different types of lateral load-resistant elements were chosen for static nonlinear pushover analysis. All RC frame structures are integrated lateral load resisting elements having same length, height, and thickness (total length of 16 m, height of each floor 4.5 m, and thickness of RD is 125 mm and for X-BE 125 × 125 mm). For all buildings, the columns size was 400 × 400 mm, the size of the beams was 300 × 350 mm. For analytic evaluation of the structures considered, the structural software, ETABS 18.0.2 was used. The floor was assumed as either RD or X-BE. The seismic loads subjected to the structure are provided according to Indian standard seismic code 2016 [6].

The material properties are taken from IS 456:2000 like Concrete grade (M30) and Grade of steel (Fe 415) [5], and mechanical property taken from ETABS 18.0.2 in Table 1.

For this analysis, the considered static loads are as follows: vertically imposed dead load of wall 18.63 and 4.14 kN/m^2 as parapet wall load and a constant value of 3 kN/m^2 for live loads.

Seismic characteristic is defined as per IS 1893 (Part 1): 2016 [6]. Importance factor is a measure that indicates seismic structural forces, depending on the practical

Table 1 Mechanical specification

Modulus of elasticity E	27,386.13 MPa
Poisson's ratio U	0.2
Shear modulus G	11,410.89 MPa

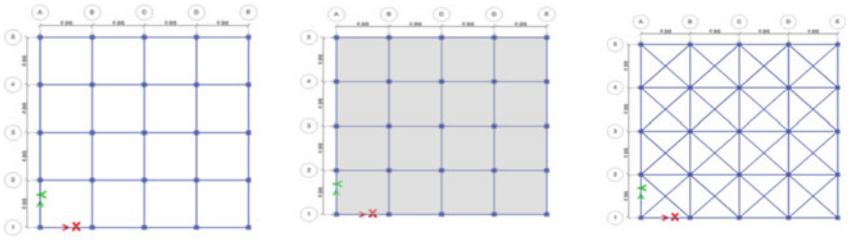

a) BF b) RD c) X-BE

Fig. 1 ETABS model for the structure plan

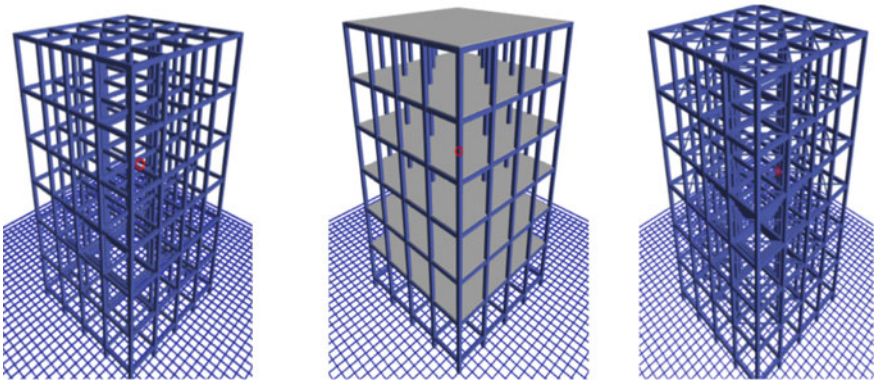

a) BF b) RD c) X-BE

Fig. 2 ETABS model for the structure 3D view for this study

application of a structure characterized by its historical or economic importance and significance, functional need post-earthquake, or failure outcome. Seismic zone factor is the peak ground acceleration value used to design structures located within each seismic zone. Zone IV was selected because of the maximum seismicity, and the seismic criteria were selected as follows: zone factor (z) is 0.24 (ANNEX E), Response Reduction Factor (R) of 5 (clause 7.2.6), Importance Factor (I) of 1 (clause 7.2.3), soil type 2, and Damping ratio of 0.05 (Figs. 1 and 2).

4 Results and Discussions

Extensive analysis and systematic study have been conducted to establish how deformation of lateral load-resistant elements (RD and X-BE) play an important role in the design of RC structures for seismic resistance. A comparative study conducted on three frame model with same configuration, i.e., regular configuration of both plan

Table 2 Performance results for the three building cases

	BF	RD	X-BE
Shear	1148.2002 kN	3088.6479 kN	1420.0234 kN
Displacement	−217.68 mm	−208.904 mm	−205.431 mm
Sa	0.056281	0.127243	0.080766
Sd	175.95 mm	169.379 mm	165.449 mm
T secant	3.527 s	2.315 s	2.812 s
T effective	3.457 s	2.669 s	2.941 s
Ductility Ratio	4.98044	3.191968	5.542999
Effective Damping	0.1992	0.1696	0.1899
Modification Factor	0.9633	1.329837	1.085633

and elevation, structural configuration, and seismic configuration with and without lateral resisting member has been studied through DDBA approach.

Seismic response assessment is conducted using capacity spectrum curve under conditions of repeated earthquake and extreme earthquake, and efficient Pushover analysis measures the capacity spectrum curve in the form of base shear force and top displacement. The iterative method used to calculate G + 5 story RC frame structure performance points with and without the lateral load resisting factor is illustrated in Table 2. Performance point shows the ductility behavior of the structure. The performance points have been taken as per FEMA 440EL and response spectrum data taken as per ASCE 7–10 for site A with 1000 mm target displacement considered.

Results of an assessment of seismic performance are shown in Table 2. On the basis of ductility ratio as seen in Table 2, in comparison with RD, BF and X-BE show better result (FIgs. 3, 4 and 5).

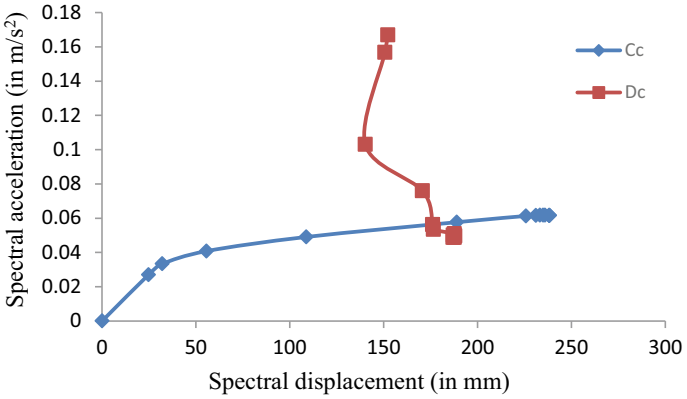

Fig. 3 Performance point of BF

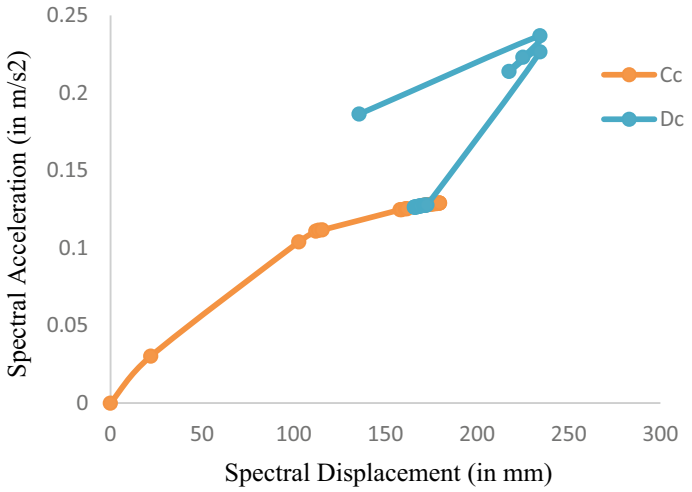

Fig. 4 Performance point of RD

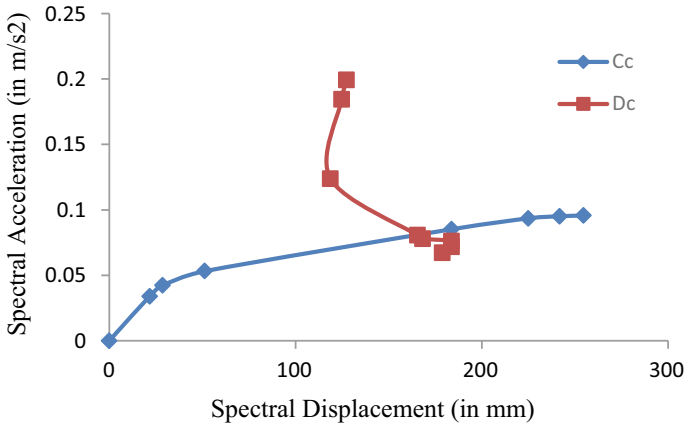

Fig. 5 Performance point of X-BE

The nonlinear static pushover analysis of the three reinforced concrete building cases (incorporating RD and X-BE) showed that the buildings provided almost identical results as demonstrated for the seismic parameters in Table 3. The maximum story displacement and story drift values in both PO-X and PO-Y increase when we move toward the top with each story in each case, and same trend in story stiffness in both EQ-X AND EQ-Y has also been observed.

As we have seen in Table 3, in maximum story displacement, as we move toward the top, displacement increases with each story. The difference of displacement between base and story 1 is least as compared to other story because of the difference

Table 3 Three structure cases seismic result

	Max displacement (in mm)		Max drift (unitless)		Max Story stiffness (in kN/m)	
	PO-X	PO-Y	PO-X	PO-Y	PO-X	PO-Y
BF	31.654	31.651	0.001812	0.001812	772,467.587	772,690.619
RD	27.858	30.89	0.001612	0.001788	922,249.582	922,249.264
X-BE	27.717	27.725	0.001591	0.001592	857,200.423	857,514.694

of heights, i.e., from story 1 to story 7 the height is kept constant at 4.5 m whereas the height from base to story 1 is only 1.5 m. For all the values observed in PO-X and PO-Y direction, the max value seen in BF is 31.654 and 31.651 mm, for RD the value is 27.858 and 30.89 mm, and for X-BE the max value is 27.717 and 27.725 mm (Fig. 6).

Major difference in inter-story drift is noticed along the X-direction and Y-direction, respectively, presented in Fig. 5. It has been observed that moving from base to story 3, the inter-story drift increases linearly and moving towards the top from story 3, again the story drift decreases. The max value seen for BF is 0.001812 and 0.001812, for RD the value is 0.001612 and 0.001788, and for X-BE the max value is 0.001591 and 0.001592 (Fig. 7).

The result shows that with the increase in height, the story stiffness increases; hence, the max value obtained for BF is 772467.587 and 772,690.619 N/m, for

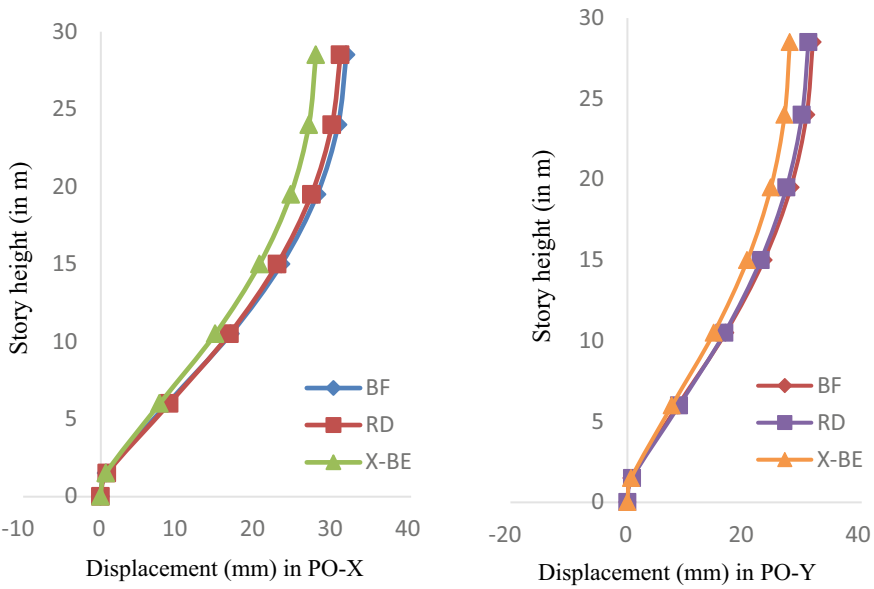

Fig. 6 Max story displacement in PO-X and PO-Y

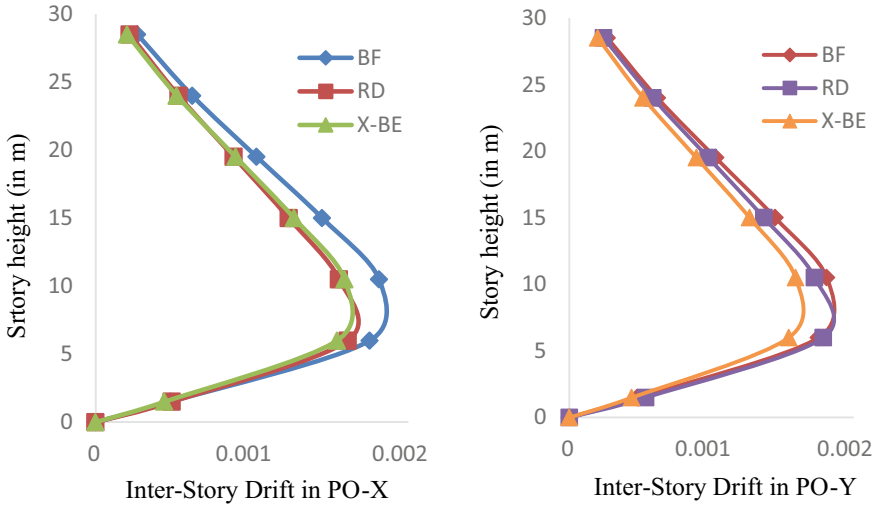

Fig. 7 Max story drift in PO-X and PO-Y

RD the value is 922249.582 and 922,249.264 N/m, and for X-BE the max value is 857200.423 and 857,514.694 N/m (Fig. 8).

Comparing the BF, RD, and X-BE analytical results for maximum story displacement, story drift, and story stiffness, there is a slight difference in the transfer of

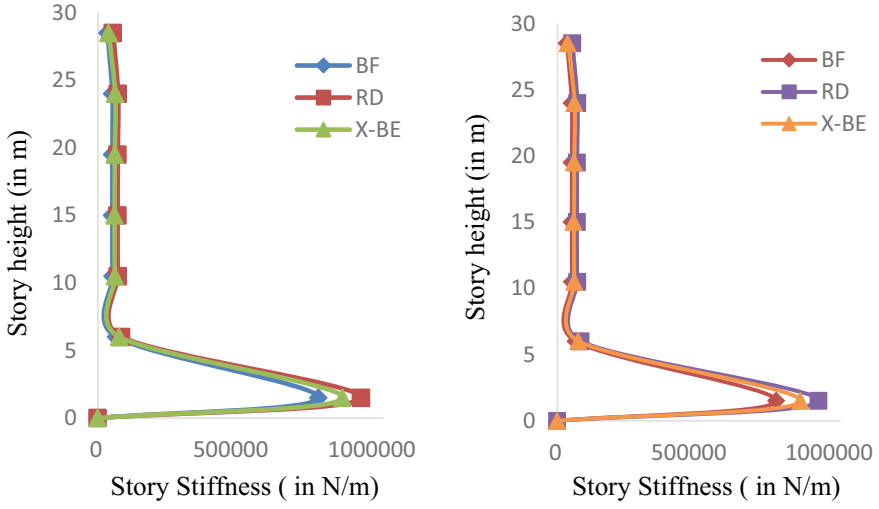

Fig. 8 Max story stiffness in EQ-X and EQ-Y

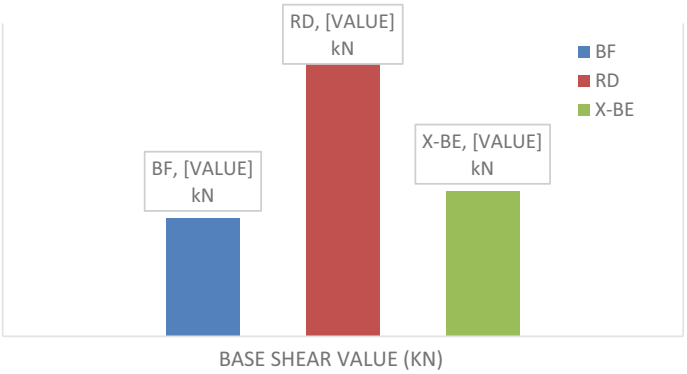

Fig. 9 Base shear value of three building cases

forces. The resulting vertical forces from the lateral seismic load (PO-X) and (PO-Y) are approximately identical and no substantial difference can be identified for all three cases BF, RD, and X-BE (Fig. 9).

Base shear is the force produced at the ground story due to lateral loads. In other two models except BF, the base shear has been increased due to the stiffness and mass provided by the RD and horizontal X-BE, the maximum value of base shear has been obtained in frame with RD which is 684.1247 kN.

5 Conclusion

The performance point shows the ductility behavior of structure. In BF, RD, and X-BE by using FEMA 440EL and design spectrum ASCE 7–10. In X-BE, the ductility ratio is 5.542999 which means the ductility is a better result in X-BE as compared to the rest of two models. From Table 3 in both X and Y directions, the three building cases showed very similar results of the maximum story displacement, maximum story drift, and story stiffness values. In addition, for the story drifts, no significant difference was seen. Bare frame structure possesses maximum displacement during earthquake as compared to rigid diaphragm and horizontal X-bracing. The bare frame showed more displacement which is 31.654 mm in PO-X and 31.651 mm in PO-Y and in comparison, of bare frame, the rigid diaphragm and horizontal X-bracing show 12 and 12.43% less displacement, respectively.

Maximum story drift is characterized as the lateral change of one stage relative to another level. The peak drift value of the story is seen in BF at story 3 because BF has least lateral stiffness as compared to RD and X-BE because of the presence of rigid diaphragm and X-bracing, respectively. The stiffness of the story 1 is higher in RD which is 922249.582 kN/m as compared to the rest of two models.

References

1. Rodriguez ME, Restrepo JI, Carr AJ (2002) Earthquake-induced floor horizontal accelerations in buildings. Earthquake Eng Struct Dyn 31:693–718
2. Nagpure A, Sanghai SS (2019) Effect of floor diaphragms on seismic response of RCC framed building—a review. Springer Nature, Singapore
3. Nandeesh NH, Ghule SC, Ravikiran R (2018) Comparative study of rigid and flexible floor diaphragm. Int Res J Eng Technol 05:01
4. Md Shehzad C, Arfath S, Md Ahmed M, Pasha N (2018) Comparative study on seismic analysis of multi storey building having diaphragm discontinuity using Etabs. Int J Res Advent Technol 6
5. IS 456:2000 (2000) Plain and reinforcement concrete-code of practice (fourth revision). Bureau of Indian Standards, New Delhi
6. IS-1893:2016 (2016) Criteria for earthquake resistant design of structures, part 1 general provisions and buildings (sixth revision). Bureau of Indian Standards, New Delhi
7. FEMA 440 (2005) Improvement of nonlinear static seismic analysis procedures. Washington, D.C
8. ASCE (2013) Minimum design loads for buildings and other structures. American Society of Civil Engineers, Reston, Virginia
9. Fouad F, Ali Z, Mustafa R (2012) Structural analyses with flexibility effect of the floor slab. In: 15th World conference on earthquake engineering
10. Barbagallo F, Bosco M, Marino EM, Rossi PP (2019) On the fiber modelling of beams in RC framed buildings with rigid diaphragm. Springer Nature
11. Rodriguez ME, Restrepo JI, Blandón JJ (2007) Seismic design forces for rigid floor diaphragms in precast concrete building structures. J Struct Eng
12. Ju SH, Lin MC (1999) Comparison of building analyses assuming rigid or flexible floors. J Struct Eng 125
13. Bahar S, Benanane A, Belarbi ADJ (2019) The influence of deformability of horizontal diaphragms in the distribution of seismic loads to bracing elements in rectangular buildings. J Mater Eng Struct
14. Mustafa TS (2019) Comparative study for the effect of rigid and semirigid diaphragms on reinforced Concrete walls. J Eng Res Rep 1–8:Article no. JERR.52447
15. Porco F, Ruggieri S, Raffaele D (2017) Influence of rigid floor assumption in seismic analysis of RC existing building. In: 6th ECCOMAS thematic conference on computational methods in structural dynamics and earthquake engineering
16. Nudo R, Sara G, Viti S (2004) Influence of floor structures on seismic performance of RC frames. In: 13th world conference on earthquake engineering. Vancouver
17. Bhuiyan MT, Leon RT (2013) Effect of Diaphragm flexibility on tall building responses. Structures Congress ASCE
18. Thomas E, George J, Paulose D (2017) Assessment of the diaphragm condition for the floor systems. Int Res J Eng Technol 04(06)
19. Rahman MAU, Jamshetty N (2019) Seismic effect of rigid floor diaphragm. Int Res J Eng Technol 06(08)
20. Barron JM, Hueste MD (2004) Diaphragm effects in rectangular reinforced concrete buildings. ACI Struct J 101(5):615–624
21. Murty CVR, Goswami R, Vijayanarayanan AR, Mehta VV (2012) Some concepts in earthquake behavior of buildings. Gujarat State Disaster Management Authority, Gandhinagar

System Identification of Two Wheelers Using a Smartphone

Nishant Rana, Amirth Varshan, and Arpan Gupta

1 Introduction

The field of system identification and parameters estimation has developed rapidly in the last few years. The idea of system identification originally began in the field of Electrical Engineering and has extended to the other fields like control and mechanical engineering. The main work of system identification is to study the existing system through its output response to the provided input.

1.1 System

This study involves the identification of system parameters for the lumped analysis model of a two-wheeler—Honda Activa scooter with a single rider. Professional tools are accurate and reliable [1, 2] but are often expensive and inaccessible to many researchers. Thus, this work emphasizes on the use of easily available means such as smartphones and android applications to identify a real system and its parameters. Two different quarter car models are used to solve the problem mathematically. The first model has only a single degree of freedom, and the second model has two degrees of freedom. A quarter car model is used for modeling the suspension system of a vehicle to simplify the calculations involved in the problem [2]. The vertical vibrations of vehicles may be modeled by a Two-Degree of Freedom linear system and used for simulation and analysis. As suggested by its name, a quarter car comprises of the quarter portion of a car/vehicle. It includes mass, spring, and damper required for the appropriate modeling of the system [3]. For this analysis, a Honda Activa scooter is used to record the vibrations over a speed hump at a constant

N. Rana (✉) · A. Varshan · A. Gupta
Acoustics and Vibration Lab, School of Engineering, IIT Mandi, Mandi, Himachal Pradesh, India

D. K. Maiti et al. (eds.), *Recent Advances in Computational and Experimental Mechanics, Vol II*, Lecture Notes in Mechanical Engineering,
https://doi.org/10.1007/978-981-16-6490-8_46

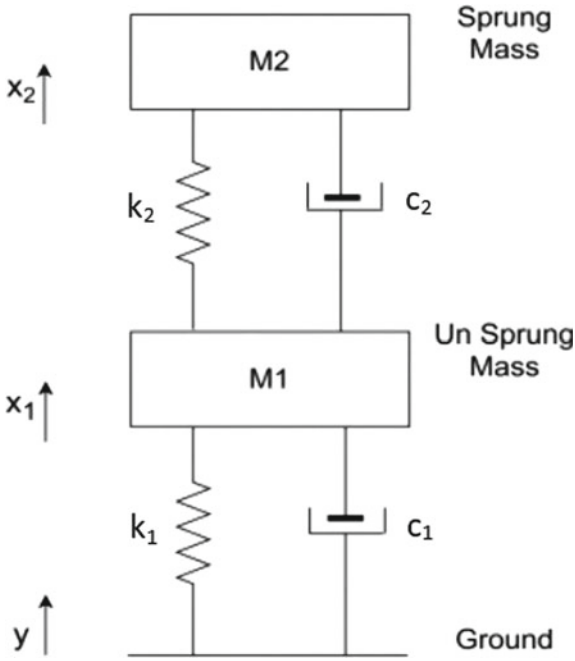

Fig. 1 Model used for the analysis (half-bike model)

velocity. The smartphone is mounted near the rear suspension and under the driver's seat [4, 5]. Thus, it is more accurate to consider only the rear half of the scooter (called Half-Bike model) for mathematical modeling of the problem. In other words, this study identifies the parameters of the rear suspension of the motorcycle. As shown in Fig. 1, the un-sprung mass includes the mass of suspension and wheel assembly. k_1 and c_1 represent the stiffness and damping of the tire, respectively. The sprung mass includes all the mass supported by the suspension such as the mass of other parts (body) of two-wheeler and rider. k_2 and c_2 represent the stiffness and damping characteristics of the rear suspension system.

1.2 Motivation

The motivation behind writing this paper and to work on the project was to make use of the acceleration sensors available in the smartphones and to utilize it for the system identification of the vibration systems. The work done will also make way for the development of vibration identification systems which could be developed using the basic sensors and hence, at an economic price with easy availability.

2 Methodology

2.1 Experiment

A Honda Activa scooter is used to conduct the experiment. The vehicle was driven over a speed hump on the road at 10 km/hr. The vibrations in the vertical direction were recorded in a smartphone using a mobile application named "Bosch iNVH". The android application exported data in CSV (comma-separated values) format. After exporting the data to Matlab, a curve was plotted that reveals the response of the vehicle (discussed in Sect. 3).

Experimental Setup. The mobile phone was mounted firmly inside the storage compartment of the motorcycle (see Fig. 2). Strong industrial double-sided tape (refer Fig. 3) was used to fix the smartphone on the vertical walls of the storage compartment.

Experimental Parameters. Table 1 shows the parameters used for the experiment. The android application started to record just before the speed hump and stopped right after that to keep the unnecessary vibrations minimal. Note that the mass of the setup is only half (approximately) of the motorcycle.

Data Recorded. Figure 4 shows the response of the sprung mass acceleration recorded by smartphone in the vertical direction. The vibration response recorded from "Bosch iNVH" app was in CSV format. The data collected from the app was transferred to Matlab and used to plot the following graph. The application started recording a few seconds before the vehicle drove over the hump. Thus, the time in Fig. 4 starts at 3.7 s (the response before 3.7 s was not caused by the hump).

Fig. 2 Smartphone mounted in the storage compartment of Activa scooter

Fig. 3 Industrial standard double-sided tape used for attaching the smartphone on the body of the bike

Table 1 Experimental parameters

Parameters	Values
Hump Height in meters	0.1
Hump Width in meters	0.8
Vehicle Velocity	10
Driver Mass	65
Mass of Half-bike Setup	55
Mobile App Used	Bosch iNVH

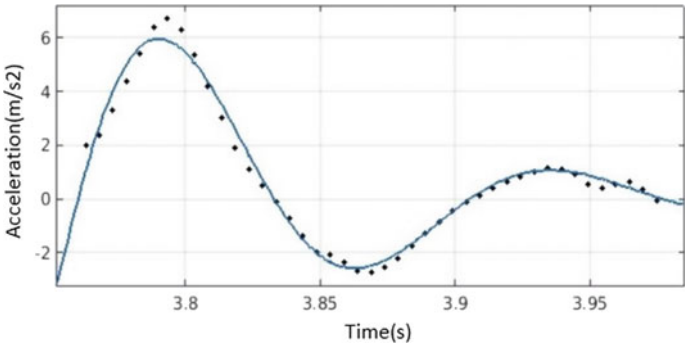

Fig. 4 Transient response of vehicle after crossing the hump

2.2 Mathematical Solution

The experimental problem is solved mathematically in two ways. Two methods will ensure the validity of the simulations. The values obtained from both the approaches are compared with the actual suspension parameters (Discussed in Sect. 3).

Method I: Single Degree of Freedom Model. Figure 5 shows a quarter car model that is used to solve the experimental problem mathematically. This model represents the whole motorcycle [6]. The sprung mass depicts everything above the suspension system (rear and front). The parameters k and c are stiffness and damping of the suspensions, vehicle body, and tires combined.

Logarithmic decrement method is used to solve for the required parameters [7, 8]. The peak acceleration of the two sequential Maximas from Fig. 4 can be noted as:

$\ddot{\mathbf{X}}_1 =$ 6.736 at t_2=3.793 s.

$\ddot{\mathbf{X}}_2 =$ 1.15 at t_1=3.934 s.

From logarithmic decrement method, $\delta = \ln \frac{\ddot{X}_1}{\ddot{X}_2}$

$$\Rightarrow \delta = 1.767$$

$$Also,\ \delta = \frac{2\pi}{\sqrt{1-\zeta^2}}$$

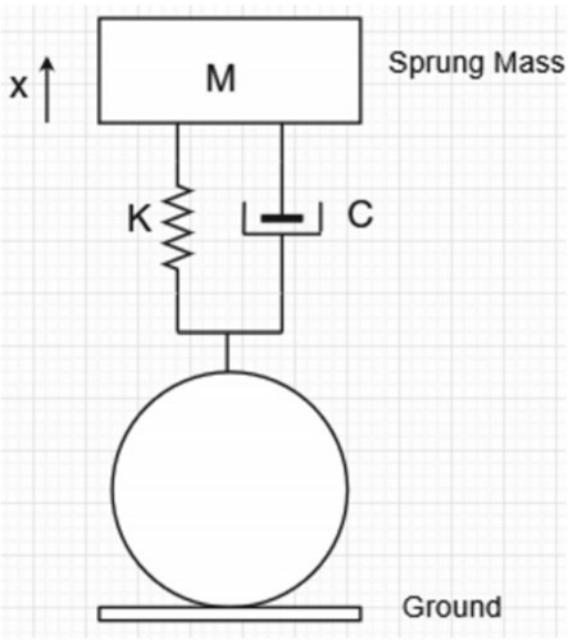

Fig. 5 Single DOF model

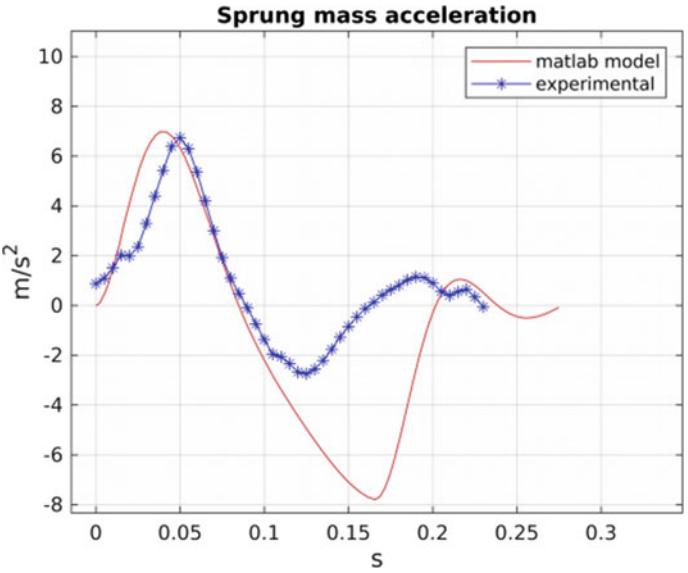

Fig. 6 Matlab simulation model response and experimental response analysis

$$\Rightarrow \zeta = \frac{\delta}{\sqrt{4\pi^2 + \delta^2}}$$

$\therefore$ Damping Ratio, $\zeta = .176$
From Fig. 3:

$$Time\ Period,\ t_d = t_2 - t_1 = 3.394 - 3.793 = 0.141\,s$$

$$Damped Frequency, \omega_d = \frac{2\pi}{t_d} = 44.54Hz$$

$$Natural Frequency, \omega_n = \frac{\omega_d}{\sqrt{1-\zeta^2}} = 45.96Hz$$

From Fig. 5:

$$m = 120Kg$$

$$Natural Frequency, \omega_n = \sqrt{\frac{k}{m}}$$

$$\Rightarrow k = m{\omega_n}^2$$

$\therefore$ Spring Stiffness, $k = 253478N/m$

$$Critical Damping Coefficient, C_c = 2m\omega_n = 11030Ns/m$$

$$Damping Coefficient, C = \zeta C_c = .176 * 11030 = 1941Ns/m$$

Method II: Two Degrees of Freedom Model. In this case, the quarter car model that represents the vehicle has two degrees of freedom as depicted by the model in figure. The force "y" is given at the base. Force balance equations are listed below. ODE 45 method [9, 10] is used in Matlab to solve the differential Eqs. 1 and 2 (solving for $\times$ 1 and $\times$ 2).

$$\ddot{x}_1 = \frac{(k_1 y - k_1 x_1 + c_1 \dot{y} - c_1 \dot{x_1} - k_2 x_1 + k_2 x_2 - c_2 \dot{x_1} + c_2 \dot{x_2})}{m_1} \tag{1}$$

$$\ddot{x}_2 = \frac{(k_2 x_1 - k_2 x_2 + c_2 \dot{x_1} - c_2 \dot{x_2})}{m_2} \tag{2}$$

For the simulation purpose, the speed control hump is approximated to be of a half sine wave. The amplitude of the sine wave taken for simulation is equal to the height of the actual (experimental) hump. The wavelength depends on the time "T" taken by the motorcycle to cross the hump. It is calculated from this expression;

$$T = \frac{3.6 * L}{V}$$

where L is the width of the hump and V is vehicle velocity. The frequency of input sine wave is written as; $\omega = \frac{\pi}{T}$. Thus, the forcing function becomes $y = H\sin(\omega t)$ where, H is the height of the speed bump. As per the experimental data, L = 0.1 m and H = 0.8 m. The second method to identify the system parameters is to align the curve obtained from ODE 45 solver to the curve extracted from the BOSCH iNVH application (Fig. 4). Curve fitting tool from Matlab is used to achieve this. Hit and Trial method is used to fit the Matlab curve approximately to the actual vehicle response. The values of rest of the parameters, namely, m1, m2, c_1, c_2, k_1, and k_2 are taken in such a way that the resulting simulation curve is close to the experimental response (see Fig. 6). The final values obtained from this method are listed in Sect. 3.

Table 2 Parameters identified for single DOF model

Parameters	Values
Damping Ratio	0.176
Damped Frequency	44.54
Natural Frequency	45.96
Stiffness (N/m)	253,478
Damping Coefficient (N s/m)	

3 Results

3.1 Method I (Single Degree of Freedom)

Table 2 shows the values obtained by using the method I as discussed in Sect. 2.2. The values in Table 2 depict the whole system's (vehicle body + suspension + driver) characteristics. For example, the stiffness mentioned in the below table is the combined stiffness of both front and rear suspension and the tires. Thus, these values could not be compared directly with real-world figures.

3.2 Actual Data

The approximate (real-world) values of the parameters of Honda Activa scooter is listed below [11, 12].

4 Conclusion

The numbers from Table 2 suggest that it is possible to simplify a complex vibration problem to a simplistic mathematical model with a Single Degree of Freedom. However, this model cannot be used for detailed analysis. The results from tables 3 and 4 show that the actual parameters of the vehicle's suspension and the values obtained by the second (two-DOF) mathematical model are of the same order. The second model is more involved to solve but quite accurate to represent the real experimental setup. As the results suggest that the mathematical values are close to the actual values of the motorcycle used in the experiment, it can be concluded that using smartphone sensors and android applications can be handy to identify a simple vibrational system and its parameters. From this study, it can also be derived that the above two mathematical approaches can be used to verify the simulations before proceeding to work on them.

Table 3 Actual parameters of the vehicle

Parameters	Values
Tire stiffness: k_1 (N/m)	(1 to 3) $\times$ 10^5
Tire damping coefficient: c_1 (Ns/m)	5 to 15
Suspension stiffness: k_2 (N/m)	(1 to 4) $\times$ 10^4
Suspension damping coefficient: c_2 (Ns/m)	(1 to 9) $\times$ 10^3
Sprung mass (Rear half of the vehicle + driver): m2 (kg)	65 + 45 = 110
Un-sprung mass (wheel assembly): m1 (kg)	5–12

Acknowledgements The authors would like to thank Dr. Arpan Gupta, Associate Professor, Indian Institute of Technology, Mandi (School of Engineering) for allowing them to work on the project "Modeling and Analysis of Active Suspension System" and providing his able guidance and support to complete this study. The authors.

References

1. Ghafooripour, Amin & Aghakoochak, A.A. & Kiamehr, H.. (2000). "An Overview of System Identification Methods And Applications Part Ii: Theory, Type Of Tested Structures, History and Prospective of System Identification."
2. Kamalakannan, K & Elayaperumal, Ayyasamy & Mangalaramanan, Sathya Prasad & Kandavel, Arunachalam. (2011). "Performance Analysis And Behaviour Characteristics Of CVD (Semi Active) In Quarter Car Model". i-manager's Journal on Future Engineering and Technology. 5. https://doi.org/10.26634/jfet.5.4.1287.
3. Jazar R.N. (2014) "Quarter Car Model. In: Vehicle Dynamisc." SPringer,NewYork,NY. https://doi.org/10.1007/978-1-4614-8544-5_15
4. Chen H-C, Chen W-C, Liu Y-P, Chen C-Y, Pan Y-T (2009) Whole-body vibration exposure experienced by motorcycle riders –An evaluation according to ISO 2631–1 and ISO 2631–5 standards. Int J Ind Ergon 39:708–718. https://doi.org/10.1016/j.ergon.2009.05.002
5. Philip & Stannard, Stephen. (2014). "Transference of 3D accelerations during cross country mountain biking" Journal of Biomechanics. 47.https://doi.org/10.1016/j.jbiomech.2014.03.024
6. Singiresu S. Rao , Addison-Wesley World Student Series, 1995, Mechanical Vibrations, 5thedition, ch 3, section 3.6, ISBN0201526867, 9780201526868
7. Montenegro Joo, Javier. (2016). "Use of the Logarithmic Decrement to Assess the Damping in Oscillations." RIF: Revista de Investigación de Física. 19. 161901551.
8. Cooper JE (1996) EXTENDING THE LOGARITHMIC DECREMENT METHOD TO ANALYSE TWO DEGREE OF FREEDOM TRANSIENT RESPONSES. Mechanical Systems and Signal Processing 10(4):497–500. https://doi.org/10.1006/mssp.1996.0034
9. Ahmed W (2012) MATLAB/ode45 for Differential Equations and Engineering Applications: Advantages and Disadvantages. International Journal of Engineering (IJE). 7:27

10. R. Ashino, M. Nagase, R. Vaillancourt. " Behind and beyond the Matlab ODE suite, Computers & Mathematics with Applications," Volume 40, Issues 4–5, 2000, Pages 491–512, ISSN 08981221,https://doi.org/10.1016/S0898-1221(00)00175-9
11. Lozoya-Santos J, de-J., Cervantes-Muñoz, D., Tudón-Martínez, J. C., & Ramírez-Mendoza, R. A. (2015) Off-Road Motorbike Performance Analysis Using a Rear Semiactive EH Suspension. Shock and Vibration 2015:1–13. https://doi.org/10.1155/2015/291089
12. Chiara A, Stefano B. "Motorcycle Progressive Suspensions." multibody.ne

Modeling and Analysis of Active Suspension System

Amirth Varshan, Nishant Rana, and Arpan Gupta

1 Introduction

The road conditions in India pose many challenges for people [1]. Studies [2–4] have shown that recurring exposure to body vibrations can cause long-term health issues. Moreover, several accidents take place because vehicles lose control at high speed when passing over the bumpy roads [5]. The frequent uncomfortable rides have serious health challenges in the long run and hamper the working capabilities as well as affect the movement of goods [6–8].

1.1 Significance of the Study

The above challenge can be tackled by improving the existing suspension system in vehicles, which in the current form is not efficient enough to provide the most comfortable ride possible. In an active suspension system, the suspension will be adjusting itself to mitigate the effect of bumpy roads and provide a comfortable experience. To get the most comfortable ride, the damping and stiffness coefficients should be tailored to specific road conditions, and this is used in active suspension systems. This study gives knowledge of how to obtain those tailored values for a sinusoidal road profile. In simple terms, solving the following mathematical model for a certain road profile could be the computation done by the on-board computer in the vehicle before riding over irregularities.

A. Varshan (✉) · N. Rana · A. Gupta
Acoustics and Vibration Lab, School of Engineering, IIT Mandi, Mandi, India

D. K. Maiti et al. (eds.), *Recent Advances in Computational and Experimental Mechanics, Vol II*, Lecture Notes in Mechanical Engineering,
https://doi.org/10.1007/978-981-16-6490-8_47

1.2 Quarter Car Model

The rear suspension of a motor-cycle supports the majority of the weight as the center of mass is closer to the rear end, and for the same reason using an active suspension for the rear would be more effective. Thus, the model used for the following analysis only depicts the rear-half of the motor-cycle and is called a half-bike model (Driver + rear half of the motor-cycle). Figure 1 represents the model (Two-Degrees of freedom) and its parameters. The sprung mass (driver and rear half of the bike) being m2 and the vehicle's suspension stiffness and damping coefficient being k2 and c2, respectively. The unsprung mass is m1 (tire and wheel assembly). The parameters k1 and c1 represent the tire's stiffness and damping coefficient, respectively. The variable 'y' in the equations denotes forcing function (road profile/hump) which is approximated to a sine wave and '$\dot{y}$' is its first derivative. The variables $\times$ 2 and $\ddot{x}_2$ denote the sprung mass displacement and acceleration in the vertical direction, respectively. The variable $\times$ 1 is the displacement of the unsprung mass.

2 Methodology

The force 'y' is given at the base. Force balance equations are listed below. ODE 45 method [9, 10] is used in Matlab to solve the differential Eqs. 1 and 2 (solving for

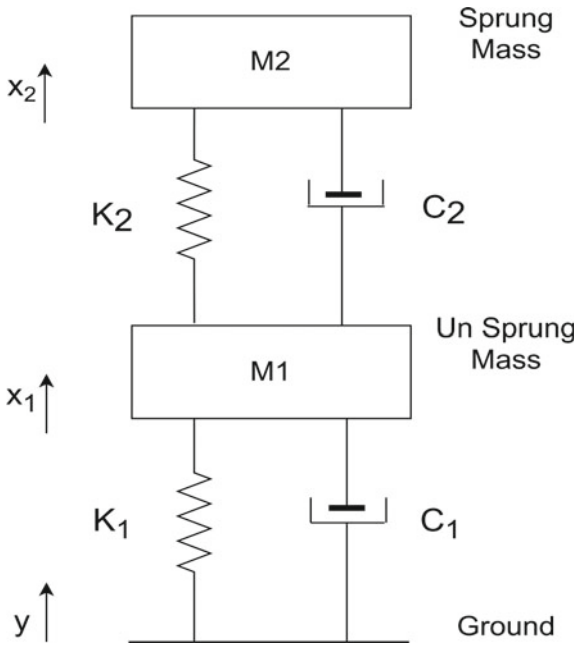

Fig. 1 Model used for the analysis (half-bike model)

Table 1 Values of the parameters

Parameters	Values
m1(tire + wheel) in Kg	8
m2 (Driver + rear half of Activa scooter) in Kg	65 + 55 = 120
c1(Tire's damping coefficient) in Ns/m	5
c2 (Rear suspension's damping coefficient) in Ns/m	2000
k1 (Tire's stiffness) in N/m	2×10^5
k2 (Rear suspension's stiffness) in N/m	14,000
L (Hump width) in meters	0.1
H (Hump height) in meters	0.8

x_1 and x_2).

$$\ddot{x}_1 = (1/m_1) \times (k_1 y - k_1 x_1 + c_1 \dot{y} - c_1 \dot{x}_1 - k_2 x_1 + k_2 x_2 - c_2 \dot{x}_1 + c_2 \dot{x}_2) \quad (1)$$

$$\ddot{x}_2 = (1/m_2) \times (k_2 x_1 - k_2 x_2 + c_2 \dot{x}_1 - c_2 \dot{x}_2) \quad (2)$$

For the simulation purpose, the hump on the road is approximated to be of a half-sine wave. Although, the response of the model from a full-sine wave has been done, considering some humps and irregularities can be approximated as full-sine waves. The amplitude of the sine wave taken for simulation is equal to the height of the actual (experimental) hump. The wavelength depends on the time taken by the vehicle to cross the hump. The time 'T' taken by the vehicle to cross the hump is calculated by T = L × 3.6/V (horizontal acceleration is neglected). Where, L is the width of the hump and V is vehicle velocity. The frequency of input sine wave is calculated as ω = π/T. Thus, the forcing function becomes y = H × Sin (ω × t). Where, H is the height of the speed bump. Table 1 shows the values of the parameters considered for the simulations. The values of k2 and c2 are fixed for a passive suspension but will change during the simulation of the active suspension system.

2.1 Model Validity

Limiting values have been used to ensure that the model responds rationally. Assigning k2 = c2 = infinity implies that the two masses would behave as a single rigid object. In other words, degrees of freedom of the system have been reduced from two to one; this means that the response of both the masses should be the same (see Fig. 2). As the value of c1 is minuscule, the damping in the following response is minimal. Thus, the amplitude of the response does not diminish immediately.

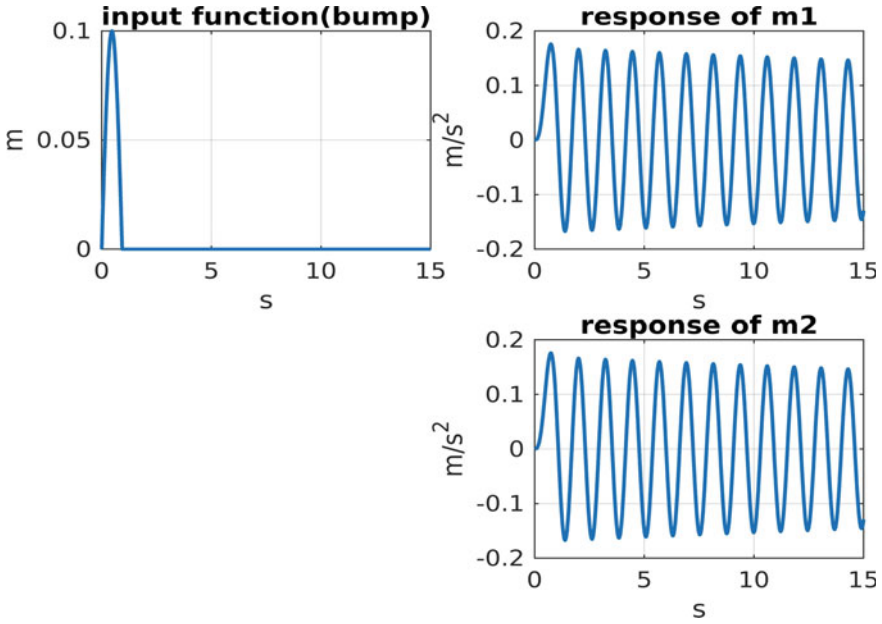

Fig. 2 Response of both the masses when c2 = k2 = infinity

2.2 Passive Model Response

For a passive suspension, the values of k2 and c2 are kept constant. A passive suspension system has fixed values of parameters. The dampers and springs used in such a suspension system do not allow altering the stiffness (k2) or the damping coefficient (c2) in real-time. Thus, the vehicle may or may not provide the most comfortable ride possible for various road conditions. The below-given plots depict the sprung mass' acceleration, velocity, and displacement along with the given input. Figure 3 shows a basic response of the system when a full-sine input is given at V = 10 km/hr. Figure 4 represents the scenario when the vehicle drives over a speed control hump (here approximated to a half-sine input) at V = 10 km/hr.

3 Results and Discussion

Evaluating an active suspension system requires understanding the response of the system under various road conditions, vehicle speed, and using different values of the suspension parameters, namely, k2 and c2. The acceleration of the sprung mass is directly proportional to the force experienced by the driver and passengers during the ride. Moreover, several comfort parameters like Vibration Dose Values (VDV) [11, 12] and Spine acceleration response [11, 12] are directly dependent on the sprung

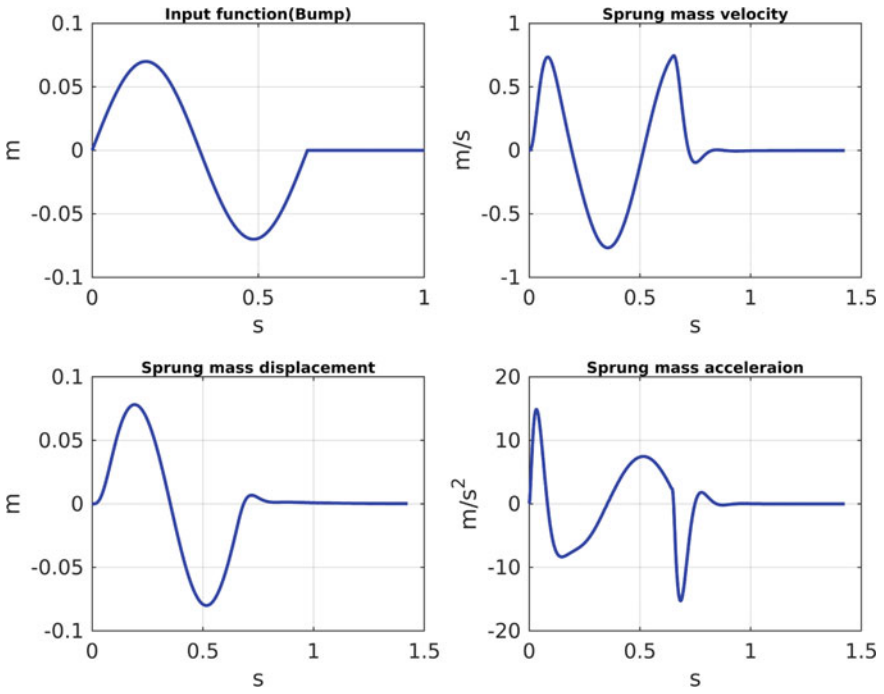

Fig. 3 Passive model response at V = 10 km/hr with a full-sine input

mass acceleration. Thus, the results of this study focus on the acceleration (vertical direction only) response of the model for a given input.

3.1 Active Model Response

Variable Damping. The following simulations depict the response of the system when the value of the damping coefficient (c2) is varied from 1000 Ns/m to 3000 Ns/m (see Fig. 5). The range has been kept short so that the plot is clear. Later, it has been varied from 1000 Ns/m to 6000 Ns/m (Figs. 6 and 7). The damping coefficient range has been selected by considering that a typical commercial vehicle may have damping coefficient values anywhere from 1000 Ns/m to 3000 Ns/m, depending upon the vehicle type. Other specialized (racing) vehicles can have higher (4000–6000 Ns/m) damping values to improve driving dynamics [13, 14]. Figure 5 shows clearly, as the damping decreases, the motion of the sprung mass increases. The relation between acceleration and damping is much complex. Thus, Figs. 6 and 7 show only the absolute maximum values of acceleration/displacement corresponding to a particular value of the damping coefficient (c2). From Fig. 6 (blue curve), it can be observed that the displacement of the sprung mass can be minimized by increasing

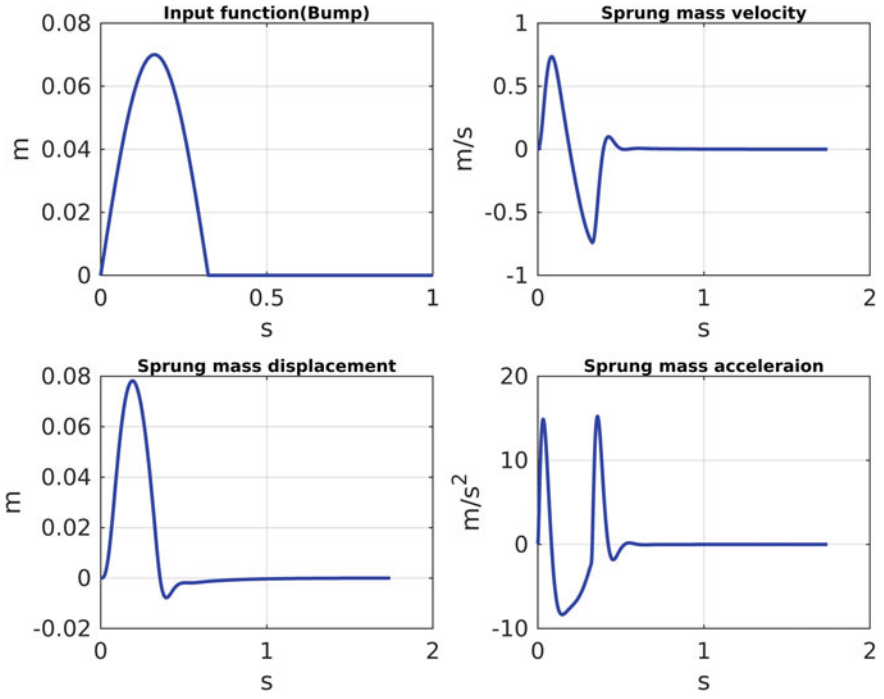

Fig. 4 Passive model response at V = 10 km/hr with a half-sine input

the damping coefficient. Reduced movement of the sprung mass can result in a sportier ride. But, increasing the damping coefficient too much would also cause higher sprung mass acceleration. Higher accelerations mean that the passenger would experience a higher force, hence an uncomfortable ride [15, 16]. The performance of the model changes significantly once the velocity or the input changes. At v = 20 km/hr (Fig. 7), the curve for maximum acceleration almost remains the same, but now the maximum displacement curve has a minima. The minimas indicate that the active suspension system can get the best values for a stiffer (sportier) or looser (comfortable) ride quality at a particular velocity of the vehicle for a given road condition.

The response of the model varies drastically as the input is changed from a half-sine to a full-sine wave. The behavior of the displacement curve remains similar, but the velocity and acceleration curves have changed (see Fig. 8). Figures 9 and 10 show the plot of maximum acceleration/displacement values against the damping coefficient. Figures 9 and 10; both the acceleration curves (red) have a minima that indicate the benefits of an active suspension system. Figure 9 (V = 10 km/hr) suggests that the value of c2 should be from 1500–2000 Ns/m to keep the ride comfortable. At V = 20 km.hr (Fig. 10), the red curve implies that c2 should be close to 2000Ns/m to attain the most comfortable ride. Refer to the blue curves from Figs. 9 and 10, to achieve a sportier (lower sprung mass displacement) ride; c2 has to be higher in value

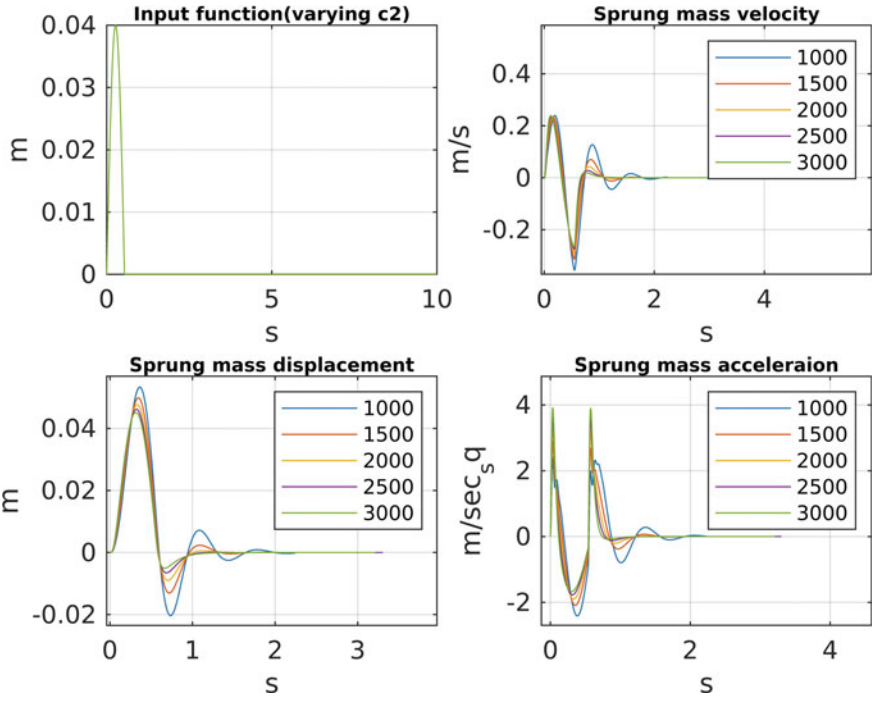

Fig. 5 Response of the model with variable damping; C2 varied from 1000-3000Ns/m. The input given is a half-sine wave at V = 10 km/hr

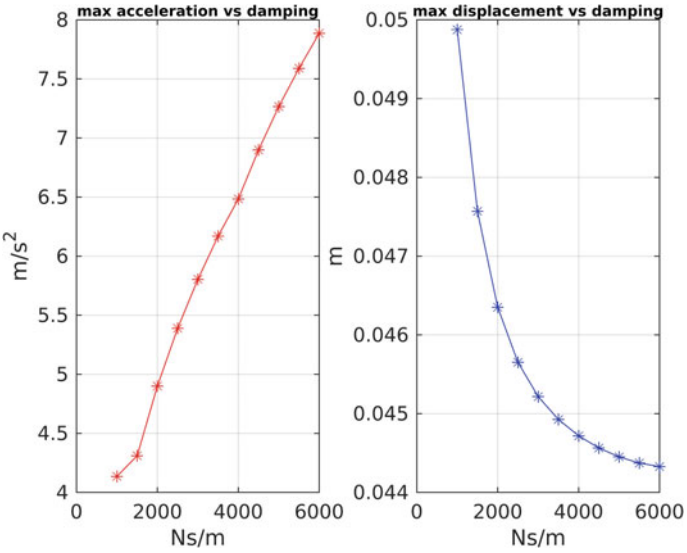

Fig. 6 Plot of maximum acceleration and displacement against varying damping (c2) for a half-sine input at V = 10 km/hr

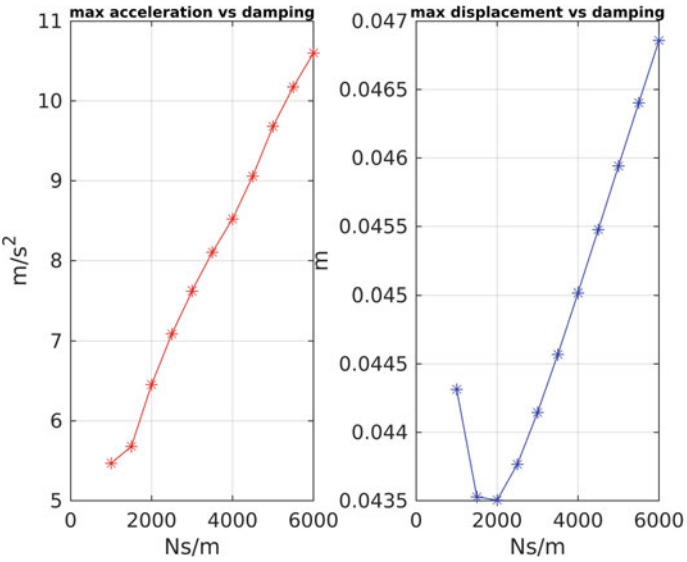

Fig. 7 Plot of maximum acceleration and displacement against varying damping (c2) for a half-sine input at V = 20 km/hr

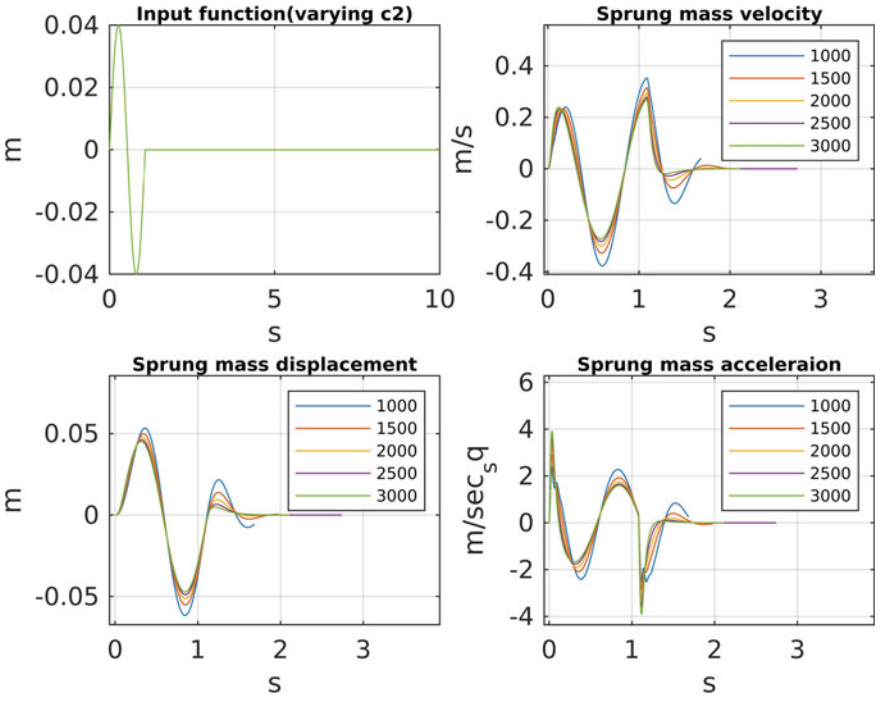

Fig. 8 Response of the model with variable damping; C2 varied from 1000-3000Ns/m. The input given is a full-sine wave at V = 10 km/hr

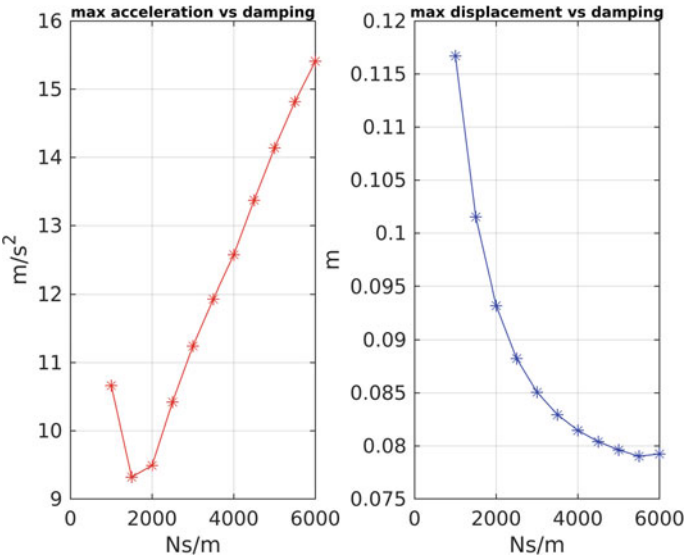

Fig. 9 Plot of maximum acceleration and displacement against varying damping (c2) for a full-sine input at V = 10 km/hr

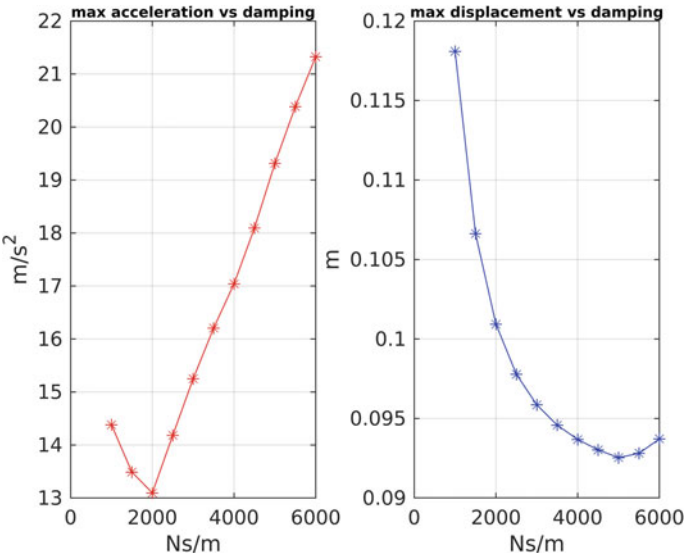

Fig. 10 Plot of maximum acceleration and displacement against varying damping (c2) for a full-sine input at V = 20 km/hr

(5000–6000 Ns/m). Such a response is produced because a full-sine wave input is more complex (higher irregularities), and the sprung mass motion gets significantly increased compared to a half-sine input. Thus, the absolute values of the sprung mass acceleration and displacement also get higher. However, the responses in Figs. 9 and 10 have sharper corners/minimas (due to the nature of the differential equations representing this model) than the plots for the half-sine input (Figs. 5, 6 and 7), which indicates that active suspension systems may function better for complex road profiles than simpler ones. The above analysis reflects that producing both a sportier and a comfortable ride is challenging.

Variable Stiffness. The next simulations show the response of the model when the stiffness is varied. Varying the stiffness of the suspension in real-time is challenging [17, 18]. Nonetheless, the study has been done to understand the impact of such variation. Figure 11 depicts the model behavior against the various values of suspension stiffness (k2). The range of k2 has been kept from 12,500 N/m to 22,500 N/m to retain clarity in the plot. Later, the range is extended from 12,500 N/m to 40,000 N/m (Figs. 12 and 13). Figure 11 reveals that there is only minimal change in the behavior of the displacement, acceleration, and velocity of the sprung mass throughout the

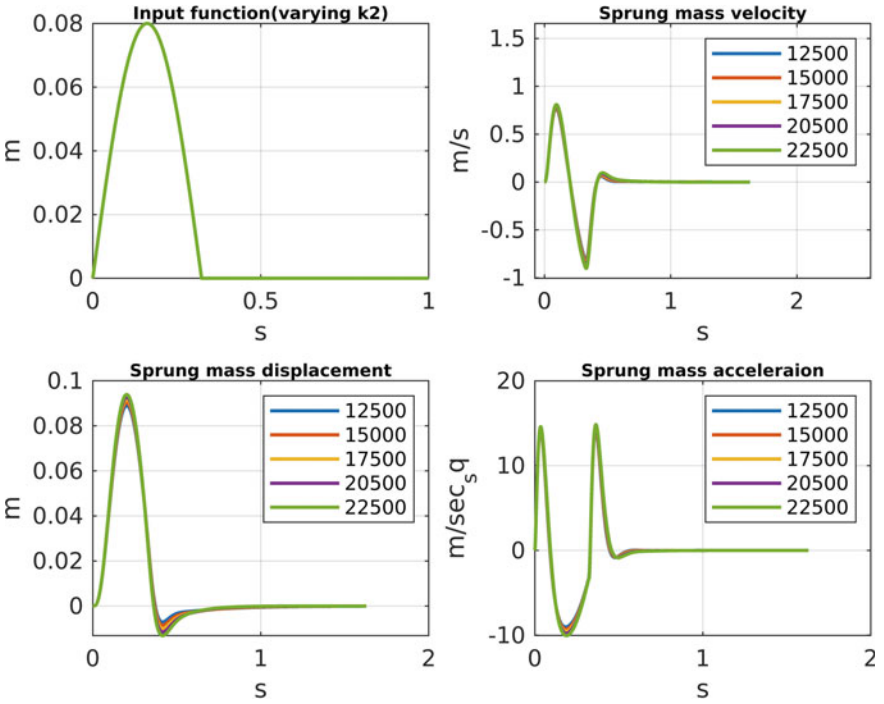

Fig. 11 Response of the model with variable stiffness; k2 varied from 12,500–22500 N/m. The input given is a half-sine wave at V = 10 km/hr

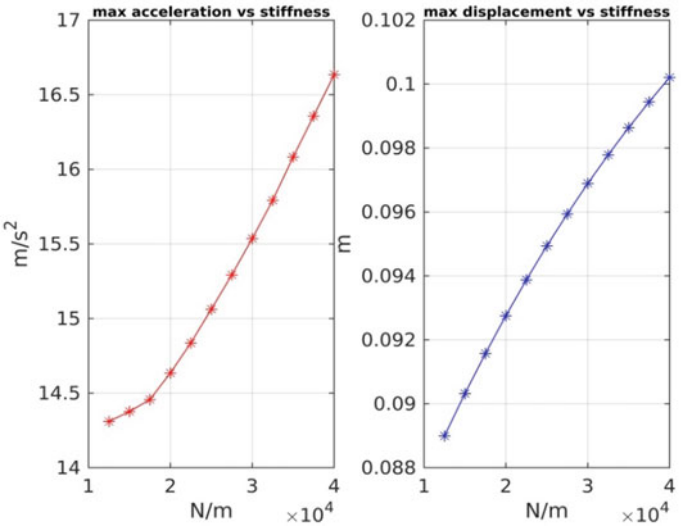

Fig. 12 Plot of maximum acceleration and displacement against varying stiffness (k2) for a half-sine input at V = 10 km/hr

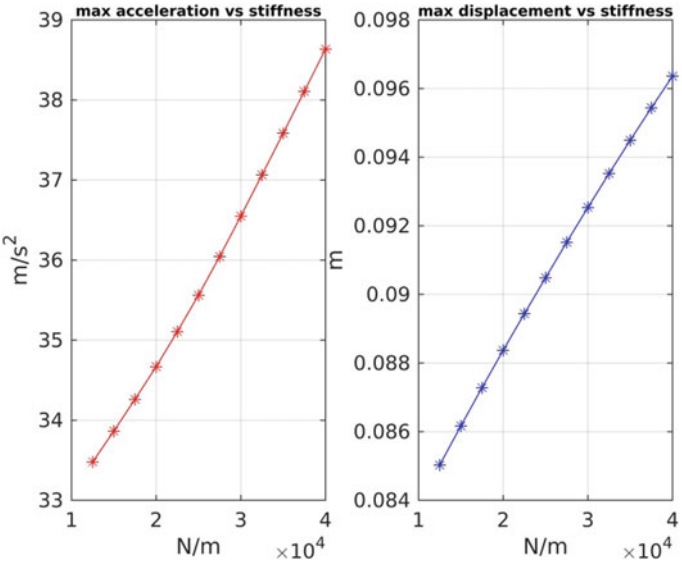

Fig. 13 Plot of maximum acceleration and displacement against varying stiffness (k2) for a half-sine input at V = 20 km/hr

varying stiffness values. From Figs. 12 and 13, it can be noticed that the relationship between maximum acceleration/displacement with k2 is almost linear and thus, predictable.

For a better understanding of an active suspension system, both the suspension stiffness (k2) and damping (c2) are varied simultaneously. Figures 14 and 15 are 3D plots that show the sprung mass acceleration when both k2 and c2 are varied together. The surface plot depicts that the optimum value of suspension stiffness should be 10,000–20,000 N/m, and the damping coefficient should be 1000–2000 Ns/m to keep the sprung mass acceleration minimal.

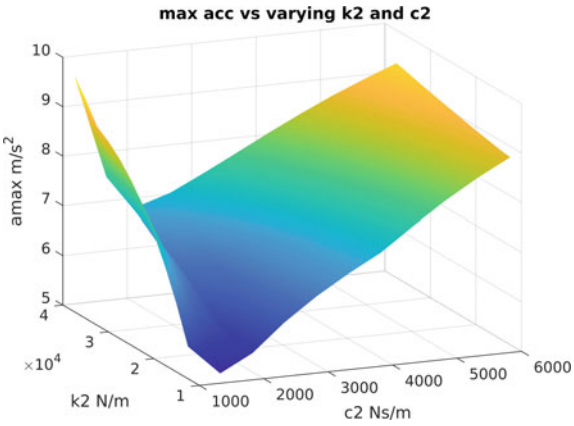

Fig. 14 3D plot of maximum acceleration of the sprung mass vs. damping and stiffness with full-sine input at v = 10 km/hr

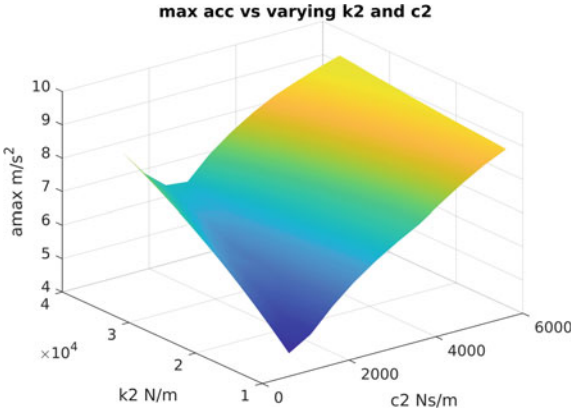

Fig. 15 3D plot of maximum acceleration of the sprung mass vs. damping and stiffness with a half-sine input at v = 10 km/hr

3.2 Discussion

As mentioned in Sect. 3.1, the technology to vary the stiffness of a suspension system in real-time is sophisticated to implement. Thus, this study is directed to understand mostly the effects of variable damping. An active suspension system can work by communicating with the external sensors (cameras, Infra-Red, accelerometers) and the on-board computer system. The computer would adjust the damping value of the suspension as per the road conditions and vehicle velocity [19, 20]. This system can become more robust by considering more inputs such as steering angle, ground clearance, vehicle roll, and pitch angles. Such a versatile system can offer more safety in extreme off-road conditions and day-to-day commutes.

4 Conclusion

From the above analysis of the results, it can be observed that the response of the vehicle acceleration and displacement depends on several parameters like vehicle velocity, road conditions (hump type and irregularities), stiffness and damping of the suspension, and the stiffness and damping of the tires as well. From the plots, it can be inferred that the behavior of the curve is not always predictable when the above-mentioned parameters are varied. Thus, the concept of an active suspension system that can alter at least the damping value of the suspension in real-time can be beneficial for a desirable driving experience. One key observation made from this study is that the damping value of a two-wheeler suspension (rear) should be around 1500–2500 Ns/m to drive over a speed control hump safely and comfortably at low speeds (10–20 km/hr). Most of the vehicles have a passive suspension system (fixed values of stiffness and damping coefficients). Due to this restriction, they are unable to get a suitable ride for different road conditions [21, 22]. But, from the above results, it is clear that an active suspension system can provide the optimum values of suspension parameters to obtain the desired ride quality. Thus, such a system can be valuable to make rides more comfortable.

Acknowledgements The authors would like to thank Dr. Arpan Gupta, Associate Professor, Indian Institute of Technology, Mandi (School of Engineering) for allowing them to work on the project 'Modelling and Analysis of Active Suspension System' and providing his able guidance and support to complete this study. The authors would also like to mention Indian Institute of Technology, Mandi for the necessary funding.

References

1. Nallathiga R (2019) Highways and road development in india: progress and prospects. MEDC Economic Digest II(4):13–17
2. Singh LP (2019) Musculoskeletal disorders and whole body vibration exposure among auto-rickshaw (three wheelers) drivers: a case study in Northern India. Ergon Int J 3. https://doi.org/10.23880/EOIJ-16000206
3. Borse PA, Desale PS (2017) Effect of motor vehicle structural vibration on human body—review. Int Adv Res J Sci, Eng Technol 4(7). IARJSET ISSN (Online) 2393–8021 ISSN (Print) 2394–1588, ISO 3297:2007
4. Quadros G, Suhas P, Vaishak NL (2016) A numerical study for determining the ideal operating speed for a two-wheeler rider on varying terrain amplitudes. J Mech Sci Technol 30:2435–2442. https://doi.org/10.1007/s12206-016-0503-0
5. Rajput K, Sharma MR, Shinde Y, Khachane D (2020) A Review on Evaluation of Speed Breakers in India. SSRG Int J Civ Eng 7(7):1–6. https://doi.org/10.14445/23488352/IJCE-V7I7P101
6. Mishra N (2013). Bumpy ride on roads has a bad impact on human body. Times of India. https://timesofindia.indiatimes.com
7. Seidel H, Heide R (1986) Long-term effects of while-body vibration: a critical survey of the literarure. Int Arch Occup Environ Health 58(1):1–26. https://doi.org/10.1007/BF00378536
8. Mansfield NJ, Mackrill J, Rimwell AN, MacMull SJ (2014) Combined effects of long-term sitting and whole-body vibration on discomfort onset for vehicle occupants. Hindawi Publishing Corporation ISRN Automot Eng. https://doi.org/10.1155/2014/852607
9. Ahmed W (2013) Advantages and disadvantages of using MATLAB/ode45 for solving differential equations in engineering applications. Int J Eng (IJE). 7;27. Author, F.: Contribution title. In: 9th International Proceedings on Proceedings, pp 1–2. Publisher, Location (2010)
10. Ashino R, Nagase M, Vaillancourt R (2000) Behind and beyond the Matlab ODE suite. Comput Math Appl—Int J 40(4–5):491–512. ISSN 08981221, https://doi.org/10.1016/S0898-1221(00)00175-9
11. Khorshid E, Alkalby F, Kamal H (2007) Measurement of whole-body vibration exposure from speed control humps. J Sound Vib 304:640–659. https://doi.org/10.1016/j.jsv.2007.03.013
12. Duarte MLM, de Araújo PA, Horta FC, Vecchio SD, de Carvalho LAP (2018) Correlation between weighted acceleration, vibration dose value and exposure time on whole body vibration comfort levels evaluation. Saf Sci 103:218–224. https://doi.org/10.1016/j.ssci.2017.11.008
13. Smith MC, Swift SJ (2016) Design of passive vehicle suspensions for maximal least damping ratio, vehicle system dynamics. Int J Veh Mech Mobility 54(5):568–584. https://doi.org/10.1080/00423114.2016.1145242
14. Tare HK, Dharankar CS (2016) Determination of damping coefficient of automotive hydraulic damper using sinusoidal testing. Int J Curr Eng Sci Res (IJCESR) 3(7). ISSN (print): 2393–8374, (online): 2394–0697
15. Dixon JC (2007) The shock absorber handbook, chapter 2, 2nd edn. Wiley, Chichester, pp 71–80
16. Jugulkar L, Singh S, Sawant S (2016) Analysis of suspension with variable stiffness and variable damping force for automotive applications. Adv Mech Eng 8.https://doi.org/10.1177/1687814016648638
17. Anubi O, Patel D, Iii C (2013) A new variable stiffness suspension system: passive case. Mech Sci 4:139–151. https://doi.org/10.5194/ms-4-139-2013
18. Doulatani VK, Chaitanya SV (2014) A review on technologies of passive suspension system with variable stiffness. Int J Eng Res Technol (IJERT) 03(06). IJERTV3IS061155.ISSN: 2278–0181
19. Leegwater MSP, An active suspension system capable of economically leveling a car during cornering. Section 3 & 5, Eindhoven University of Technology (TU/e), The Netherlands Department of Mechanical Engineering, DCT 2007.087, S010527 (TU/e)

20. Riduan M, Fahmi A, Tamaldin N, Sudrajat A, Ahmad F (2018) Review on active suspension system. SHS Web of Conf 49:02008. https://doi.org/10.1051/shsconf/20184902008
21. Abdolvahab A, Sabet GS, Barouz A (2012) Simulation and analysis of passive and active suspension system using quarter car model for different road profile. Int J Eng Trends Technol 3(5). ISSN: 2231–5381
22. Rao T, Venkata Rao G, Purushottam A, Sreenivasa K (2010) Analysis of passive and semi active controlled suspension systems for ride comfort in an omnibus passing over a speed bump. Int J Res Rev Appl Sci 5

Structural Damage Identification in GFRP Composite Plates Using TLBO Algorithm

Suryamani Behera, Mayank Mishra, and Subhajit Mondal

1 Introduction

In recent years, the construction fields prefer the use of composite materials because of their lightweight and elevated strength and stiffness. The composite structures are susceptible to damages because of their prolonged uses. Health monitoring of the composite structures is a matter of concern. The damage detection techniques based on the dynamic responses are favourable for composite structures in which damage locations or loss of materials are mostly within layers. In most of the cases, it is difficult to access the location of damage as well as to measure the damage severity. The modal data obtained can be used to detect the damages and their severity. Recently, metaheuristic-based algorithms have gained popularity for monitoring of structures. Health monitoring of composite structures, using vibration data with a combination of such metaheuristic algorithms is quite effective. These techniques are based on minimizing an objective function, which can be stated as the difference between the eigenvalues obtained from the structure with damage experimentally and eigenvalues extracted using the finite element method. The Teacher–Learning-based Optimization (TLBO) algorithm focuses on the phenomena of the teaching–learning in a classroom which describes the impact of the teacher on learners. The algorithm is described in two basic ways of learning. In the first phase, the teacher teaches to the learners and in the second phase, the learners interact with each other to learn.

Recently, metaheuristic-based optimization algorithms are in demand for the detection of damage in structures. Structural health monitoring of composite structures can be achieved using vibrational responses in combination with metaheuristic

S. Behera · S. Mondal (✉)
Department of Civil Engineering, NIT Rourkela, Rourkela, India
e-mail: mondalsubhajit@nitrkl.ac.in

M. Mishra
School of Infrastructure, IIT Bhubaneswar, Bhubaneswar, India

D. K. Maiti et al. (eds.), *Recent Advances in Computational and Experimental Mechanics, Vol II*, Lecture Notes in Mechanical Engineering,
https://doi.org/10.1007/978-981-16-6490-8_48

algorithms considering the difference in the dynamic responses. There are many optimization algorithms available in the literature which tries to attempt the damage detection in composite structures.

Kogiso et al. [1] implemented the Genetic Algorithm (GA) for designing composite laminates under external loading and buckling. Abachizadeh and Tahani [2] developed the ant colony optimization (ACO) algorithm to design composite laminates. Roseiro et al. [3] investigated a laminate composite plate for locating the damage as well as for determining the extent of damage by the use of a free forward type neural network combined with the Levenberg–Marquardt algorithm utilizing experimental data. Ding et al. [4] and Sun et al. [5] implemented the artificial bee colony (ABC) algorithm for damage detection using a hybrid search strategy based on vibrational responses and to estimate parameters in the system of a structure, respectively, and the outcome was compared with GA. Vosoughi et al. [6] implemented PSO along with continuous genetic algorithm (CGA) and Behtani et al. [7] used GA to find damage in composite structures. Luh and Lin [8] performed PSO to solve the truss problems to determine the minimum weight of truss considering stress and deflection. Mishra et al. [9] performed the ant lion optimization (ALO) for damage detection in different truss structures. The results showed that the ALO algorithm requires fewer parameters for damage detection in comparison to the other algorithms. Shyamala et al. [10] used the support vector machine (SVM) algorithm by introducing frequency data to identify damage in a GFRP composite plate.

Rao et al. [11] optimized the mechanically designed problems by proposing the Teaching–learning-based optimization (TLBO) algorithm. Various mechanically designed problems were solved using the algorithm and its efficiency was studied by comparing its outcome with other optimization algorithms. Das et al. [12] implemented the TLBO algorithm to identify damage location and severity for truss, beam, and frame problems. A better outcome from the TLBO algorithm implementation is observed for damage detection using the modal data, i.e. natural frequencies. Khatir et al. [13] carried out isogeometric analysis and used the finite element method to obtain the damage in beam structures. The local frequencies change ratio indicator was used to locate the damage in the beams. Mishra et al. [14, 15] performed ten metaheuristic-based algorithms for identification of damage location as well as severity in large-scale truss structures. Better accuracy and precision of the TLBO algorithm was observed in damage detection [14] and identifying the lowest factor of safety along the critical slip surface of soil slope [15].

It has been observed that there are a few kinds of literature on TLBO for damage detection in composite structures. Moreover, the health monitoring of composite structures using vibration data in combination with TLBO is very limited. In the present study, a metaheuristic-based optimizer TLBO is used for identifying the damage in composite plates. The vibrational responses of the composite plate are determined using FEM software. The error function is then formulated based on the difference between the eigenvalues of the baseline plate model and the same obtained from the Eigen Solver which varies in each iteration. The TLBO algorithm minimizes the error function to identify the damage and its extent. The algorithm is

found to be satisfactory to locate the damage and the severity of the damage of the composite plate.

The organization of the remaining of the paper is described as follows: Sect. 2 describes the FE modelling and analysis of the FRP composite plate to obtain the eigenvalues and eigenvectors; Sect. 3 explains the working steps of the metaheuristic TLBO algorithm. Section 4 describes the damage detection in a composite plate using the TLBO algorithm, and finally, Sect. 5 gives the concluding remarks.

2 Finite Element Analysis of Composite Structures

For modelling a composite laminate, the equivalent single layer theory (ESL) is used which states that the laminated composite structures or plates are treated as a statically equivalent single layer. Strains do not vary within a layer, the mass and stiffness matrices of the laminated composite are acquired considering the geometrical mid-plane as the reference plane. After contributions of mass and stiffness are acquired, an eight-noded isoparametric shell element is used for the modelling of the composite plate. In order to model the composite structure, general-purpose computer software ABAQUS v6.13–4 [16] is used.

2.1 Free Vibration of Composite Laminate

The equations of equilibrium for the composite laminated structures can be written as

$$[M]\{\ddot{x}\} + [C]\{\dot{x}\} + [K]\{x\} = \{F(t)\} \tag{1}$$

The undamped equation of motion as in Eq. (2) is solved to obtain the eigenvalues and eigenvectors using suitable Eigen solver within the ABAQUS environment.

$$\left\{ [K] - \omega_i^2 [M] \right\} \{ \phi_i \} = \{0\} \tag{2}$$

Here, ${\omega_i}^2$ is the ith eigenvalue and ϕ_i is the mode shape. Convergence studies were then carried out to get the accurate model and then the TLBO algorithm is developed in MATLAB [17] to identify both damaged location and the severity of the damage.

3 Teacher–Learning-Based Optimization

The TLBO algorithm is an algorithm, based on various populations, which mimics phenomena of the teaching and learning in a classroom and models the impact of

the teacher on learners. The algorithm is described in two basic phases of learning: (a) learners learning from teacher, i.e. teacher phase and (b) learners learning by communicating with each other which is learner phase. The population is represented by a group of learners, and design variables are represented by subjects and learners' result give the fitness value. The best solution is the teacher of the whole population. The two basic phases of the algorithm are as follows.

3.1 Teacher Phase

The mean result of the learners in a particular subject is increased by the teacher in this phase. Assume that the number of subjects provided to learners is s, the number of learners is l, and the learners' mean result in subject j is $MR_{j,I}$, where i is the iteration count. The result of the best learner kb is $R_{t,kb,i}$ considering all the subjects in the whole population. However, the algorithm identifies the teacher as the best learner as the teacher is considered best above learners. The difference between the learners' mean result and the teacher's result in each subject can be defined as:

$$DM_{j,k,i} = q_i\left(R_{j,kb,i} - T \times MR_{j,i}\right) \tag{3}$$

where, $R_{j,kb,i}$ is the best learner's result in subject j, q_i is the number ranging from 0 to 1. Range and the value of mean is decided by teaching factor T which can be defined as

$$T = round[1 + rand(0, 1)\{2 - 1\}] \tag{4}$$

Based on the difference of results of teacher and learner, $DM_{j,k,i}$ is updated as per the Eq. (5).

$$R'_{j,kb,i} = R_{j,kb,i} + DM_{j,k,i} \tag{5}$$

where, $R'_{j,kb,i}$ is the updated value of $R_{j,kb,i}$. If the function has encouraging value than the existing one, $R'_{j,kb,i}$ is accepted. These function values are the inputs for the learner phase.

3.2 Learner Phase

In the learner phase, the learners share their knowledge with each other to acquire new things. The phase of learning is explained as follows. Y and Z are two random learners such that $R'_{j,Y,i} \neq R''_{j,Z,i,}$. If $R"_{j,Y,i}$ gives a promising value of the function, it is accepted and is defined as below.

$$R''_{j,Y,i} = R'_{j,Y,i} + q_i\left(R'_{j,Y,i} - R'_{j,Z,i}\right), \text{ if } R'_{j,Y,i} < R'_{j,Z,i} \tag{6}$$

$$R''_{j,Y,i} = R'_{j,Y,i} + q_i\left(R'_{j,Z,i} - R'_{j,Y,i}\right), \text{ if } R'_{j,Z,i} < R'_{j,Y,i} \tag{7}$$

3.3 Formulation of the Error Function

The error function '*EF*' is formulated for the optimization through TLBO algorithm based on the eigenvalues of the composite plate and can be defined as follows:

$$EF = \sqrt{\frac{1}{N}\sum_{i=1}^{N}(ev_i^{bsm} - ev_i^{fem})^2} \tag{8}$$

Here, N represents the number of modes considered. The superscript ev_i^{bsm} represents ith eigenvalue of the baseline composite beam model and ev_i^{fem} is the corresponding eigenvalue of the finite element model through eigenvalue solver. The damage in the composite plate results in the natural frequencies reduction. The error function given by Eq. (8) is minimized using the TLBO algorithm. A stepwise working of the TLBO algorithm is explained in a flowchart as shown in Fig. 1.

4 Damage Identification Using TLBO Algorithm

In this section, a numerical simulation of the composite plate is explained for the analysis of applications of the TLBO algorithm for structural damage detection. The dynamic response of a structure can be demonstrated in terms of vibrational responses. It is assumed that the mass and stiffness properties of the undamaged structure are known before the damage detection using TLBO is implemented. The basic steps in this method are preparing a FE model, forming the error function, and finally, implementing TLBO for identification of damage location and extent of the damage in the composite plate using parameter estimation as a damage indicator.

4.1 Numerical Simulation

The GFRP composite plates of size 400 mm by 300 mm were modelled using finite element method-based software ABAQUS, and the natural frequencies and corresponding mode shapes were obtained. At least 300 'S8R' elements were generated by dividing the plate into small elements of 20 × 20 mm size. Reduction in the

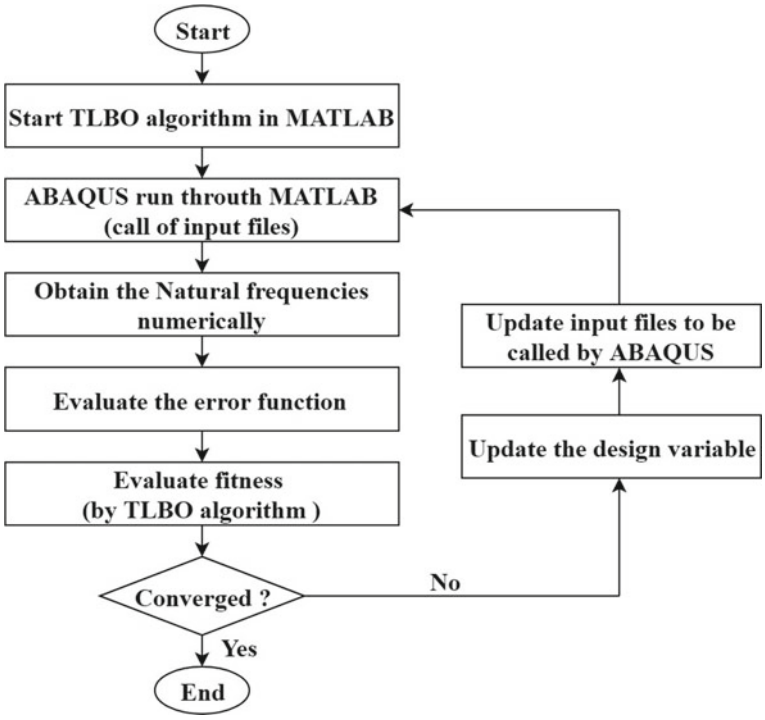

Fig. 1 Working of TLBO algorithm

frequency of the plate indicates the presence of damage in the plate and frequencies are considered as the damage indicator. The plate model was simulated as equivalent single layer theory, and the material properties considered for the numerical simulation are presented in Table 1. Here, E_x is the modulus of elasticity along x direction. E_y is the modulus of elasticity in y direction, G_{xy} is the shear modulus in xy plane, G_{xz} is the shear modulus in xz plane, G_{xz} is the shear modulus in xz, G_{yz} is the shear modulus in yz, υ_{xy} is the Poisson ratio in xy plane.

Table 1 Material properties of the GFRP plate

Material property	Values
Density	1960 kg/m^3
E_x	32.1 GPa
E_y	29.1 GPa
G_{xy}	6.55 GPa
G_{xz}	5 GPa
G_{yz}	5 GPa
υ_{xy}	0.2

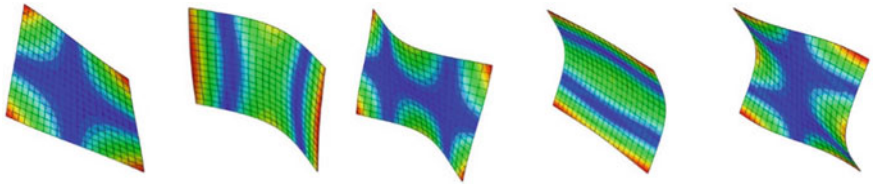

Fig. 2 First five-mode shapes of undamaged GFRP plate model

Table 2 Frequencies of the undamaged GFRP composite plate

Mode	Corresponding frequencies (Cycles/time)
1	159.21
2	259.60
3	414.07
4	447.90
5	542.11

Here, x and y are the longitudinal and transverse directions of the plate, respectively. The first five-modes are shown in Fig. 2 and the corresponding frequencies for undamaged FRP plate modelled considering the above properties are presented in Table 2.

In the present study, the damage is induced at a location of the plate by reducing thickness through half of it. The damage size for all the cases was fixed to 40 mm with variation in the number of elements. The damage cases considered are S1 (single element damaged), S2 (two elements damaged), and S3 (four elements damaged). The damage locations for the cases are shown in Fig. 3. The first five frequencies and mode shapes for the damaged plate are shown in Fig. 4. The TLBO algorithm aims to recognize such damage through the detection of material loss or the reduced thickness at a specific location.

4.2 Outcome of TLBO Algorithm

The TLBO algorithm aims to recognize such damage through the detection of material loss or the reduced damaged thickness at the damaged location. In the present study, the damage is induced in the plate models by reducing thickness at specified locations leading to reduced natural frequencies. The TLBO algorithm is performed for identification of the location and severity of damage by identifying the damage thickness. The algorithm minimizes the eigenvalue-based error function to identify the damage and its extent. The population size for each iteration was kept constant. The iteration count was observed to be increasing when the number of elements

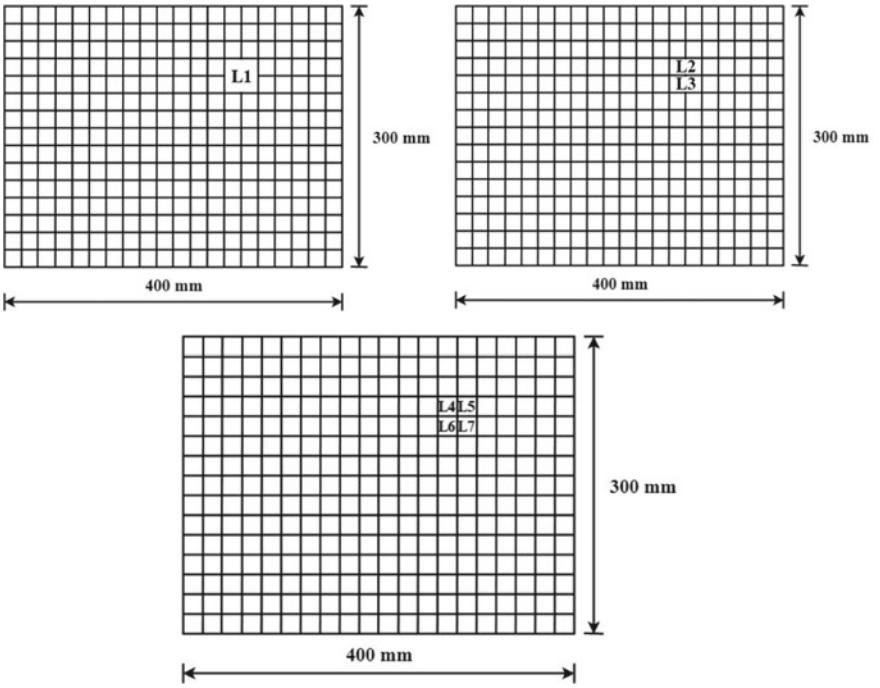

Fig. 3 Locations of damage in the composite plate

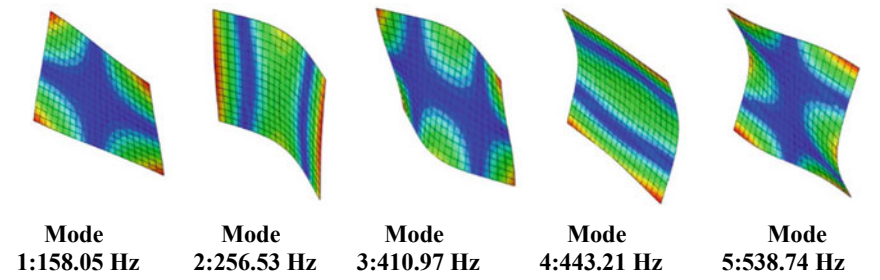

Fig. 4 First five-mode shapes and corresponding frequencies (cycles/time) of the damaged composite plate

increased. The details about the number of iteration until the convergence is achieved is presented in Table 3.

The damage identification for the cases S1, S2, and S3, where the damage size for all the cases was fixed at 40 mm, is illustrated in Table 4. The outcome from the algorithm is found to be effective for the detection of the damage in the composite plate. It is noticed that TLBO is capable of identifying both the location of damage as well as the damage severity effectively.

Table 3 No. of iteration required for each case

Case	S1	S2	S3
Population size	20	20	20
No. of elements damaged	1	2	4
No. of iteration	18	41	64

Table 4 Damage estimation in the GFRP plate using TLBO algorithm

Damage cases	Damage induced (in m)	Damaged element location	Detected damage (in m)	Remarks
S1	0.005	L1	0.0047–0.0052	Detecting damage correctly
S2	0.005	L2, L3	0.0044–0.0055	Detecting damage correctly
S3	0.005	L4, L5, L6, and L7	0.0040–0.0056	Detecting damage correctly

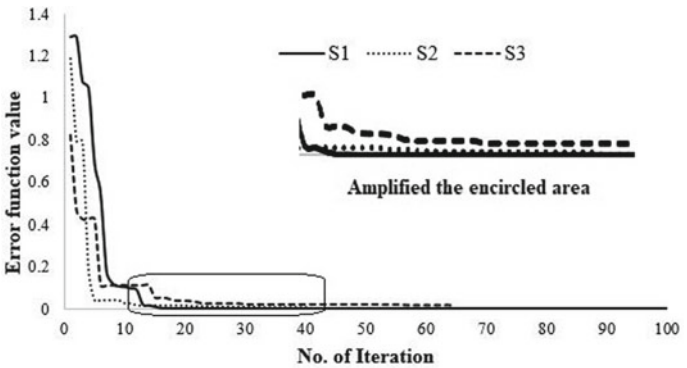

Fig. 5 Comparison of convergence curves for cases S1, S2, and S3

It is also observed that the error function considered converges effectively. The convergence curves for the cases S1, S2, and S3 are compared a delayed convergence is noticed at an increased number of elements which is explained in Fig. 5.

5 Conclusions

In the present study, metaheuristic-based algorithm inspired by the teaching–learning process, i.e. TLBO algorithm is implemented to locate the damage as well as the extent of damage in a fibre-reinforced plastic composite plate. The numerical simulation of the plate is accomplished by the finite element method. The TLBO algorithm

is implemented in the MATLAB environment considering the baseline model as well as damaged models where the error function is minimized. It is noticed that the TLBO algorithm is able to identify the damage location and severity of the damage in the plates with single as well as multiple damage locations. Additionally, the primary objective of the research is to employ TLBO, which is independent of algorithmic specific parameters such that the chances of getting struck in local minima are low. A good convergence of the error function is observed from the implementation of the present approach. With the number of elements or the damage locations increasing, an increasing number of iterations for the convergence is noticed. It is also found that the TLBO algorithm is efficient to detect damage in composite structures because of its accuracy and consistency.

In future studies, the current study can be expanded by comparison with different optimization algorithms and their efficacy in damage detection. Furthermore, experimental data can be obtained to simulate the actual damaged conditions and could be used for validating the model, which in current study is limited to numerically simulated damage cases only.

References

1. Kogiso N, Watson LT, Gurdal Z, Haftka RT, Nagendra S (1994) Design of composite laminates by a genetic algorithm with memory. Mech Compos Mater Struct 1(1):95–117
2. Abachizadeh M, Tahani M (2011) Optimizing laminated composites using ant colony algorithms. In: Ostfeld A (ed) Ant colony optimization—methods and applications. InTech
3. Roseiro L, Ramos U, Leal RP (2015) Neural networks in damage detection of composite laminated plates. In: Proceedings of the 6th WSEAS international conference on neural networks. Lisbon, Portugal, June 16–18, pp 115–119
4. Ding ZH, Huang M, Lu ZR (2016) Structural damage detection using artificial bee colony algorithm with hybrid search strategy. Swarm Evol Comput 28:1–13
5. Sun H, Lus H, Betti R (2013) Identification of structural models using a modified artificial bee colony algorithm. Comput Struct 116:59–74
6. Vosoughi AR, Gerist S (2014) New hybrid FE-PSO-CGAs sensitivity base technique for damage detection of laminated composite beams. Compos Struct 118:68–73
7. Behtani A, Bouazzouni A, Khatir S, Tiachacht S, Zhou YL, Wahab MA (2017) Damage localization and quantification of composite beam structures using residual force and optimization. J Vibro Eng 19(7):4977–4988
8. Luh GC, Lin CY (2011) Optimal design of truss-structures using particle swarm optimization. Comput Struct 89:2221–2232
9. Mishra M, Barman SK, Maity D, Maiti DK (2018) Ant lion optimisation algorithm for structural damage detection using vibration data. J Civ Struct Health Monit. ISSN 2190–5452
10. Shyamala P, Mondal S, Chakraborty S (2018) Numerical and experimental investigation for damage detection in FRP composite plates using support vector machine algorithm. Struct Monit Maintenance 5(2):243–260
11. Rao RV, Savsani VJ, Vakharia DP (2011) Teaching–learning-based optimization: a novel method for constrained mechanical design optimization problems. Comput Aided Des 43(3):303–315
12. Das S, Dhang N (2018) Structural damage detection using modal data employing teaching learning based optimization. Int J Civ Environ Eng 12(5). Berlin, Germany. May 21–22

13. Khatir S, Wahab MA, Boutchicha D, Khatir T (2019) Structural health monitoring using modal strain energy damage indicator coupled with teaching-learning-based optimization algorithm and isogoemetric analysis. J Sound Vib 448:230–246
14. Mishra M, Barman SK, Maity D, Maiti DK (2020) Performance studies of 10 metaheuristic techniques in determination of damages for large-scale spatial trusses from changes in vibration responses. J Comput Civ Eng 34(2):04019052
15. Mishra M, Gunturi VR, Maity D (2020) Teaching–learning-based optimisation algorithm and its application in capturing critical slip surface in slope stability analysis. Soft Comput 24:2969–2982
16. ABAQUS v6.13–4, Dassault Systemes Simulia Corp
17. MATLAB 2018a. MATLAB Simulink- Mathworks

Experimental Modal Analysis of Carbon Nanotubes-Reinforced Composite Plates

Asha Patel and Shishir Kumar Sahu

1 Introduction

Carbon nanotube-reinforced polymer composite (CNTRC) is an important discovery in the area of nanocomposites. The requirement of good performance material in marine, aerospace, automobile industries felicitate its wide application; owing to its specific properties like low-density, high strength, and stiffness. Because of lightweight, CNTRC structures are susceptible to resonance failure; hence, modal analysis of CNTRC elements is an important research area. The modal analysis evaluates natural frequency, damping characteristics, and mode shapes of elements. In recent times, due to development in vibration measurement systems, experimental modal analysis has become possible and became an important tool to study the real-time dynamic behavior of elements.

Systematic analysis of laminated plates starts with the formulation developed by Reissoner and Stavsky [1] by extending Kirchhoff's theory. Rock and Hinton [2] modified the formulation for free vibration analysis of composite plates by incorporating transverse shear deformation. Reddy [3] further developed different shear deformation theories applicable to the analysis of composite elements. After the discovery of CNT by Iijima and Ichihashi [4] as a prospective reinforcement of composites, various theoretical studies are made on CNTRC elements by many researchers. The same laminated plate theories were being extended via methods like the Rule of mixture, H-T model, Mori–Tanaka model, etc., to evaluate the effective properties and to model CNTRC composites.

A. Patel (✉) · S. K. Sahu
Civil Engineering Department, National Institute of Technology, Rourkela, India
e-mail: apatel@nitrkl.ac.in

S. K. Sahu
e-mail: sksahu@nitrkl.ac.in

D. K. Maiti et al. (eds.), *Recent Advances in Computational and Experimental Mechanics, Vol II*, Lecture Notes in Mechanical Engineering,
https://doi.org/10.1007/978-981-16-6490-8_49

Some recent works on vibration analysis of CNTRC elements include, Formica et al. [5] studied the effects of CNT alignment, volume percentages, types of hosting matrix on dynamic behavior of CNTRC plates involving Eshelby–Mori–Tanaka method. Zhu et al. [6] examined the vibration of Functionally Graded-CNTRC (FG-CNTRC) plates considering the different distribution of CNT and by using FEM based on First Order Shear Deformation (FSDT). Lin and Xiang [7] executed a parametric study of vibration analysis of FG-CNTRC beams based on first-order and third-order shear deformation theories by using the meshless p-Ritz method. Zhang et al. [8] performed bending and dynamic analysis of CNTRC cylindrical panels adopting the kp-Ritz method. Most of the works available in the open literature are theoretical investigation involving analytical, 2D/3D FEM, meshfree FEM, etc.

The experimental modal analysis is an efficient tool of dynamic analysis. Cawley and Adams [9] attempted experimental modal analysis on composite plates. Experimental studies were made by Chakraborty et al. [10], Mishra and Sahu [11] on FRP composites considering delamination and Panda et al. [12] with the hygrothermal environment and compared with predicted results obtained by using FEM. However, experimental studies dealing with composites with CNT are scarce in the literature except by the authors [13] using ABAQUS software.

The current work presents a detailed study on modal testing of CNTRC plates of different thickness (b/h = 40, 60, 80, and 100), aspect ratios (a/b = 1, 2, 3, 4, 5), CNT weight percentage (0.1, 0.3, and 0.5%), under clamped (CCCC) and cantilever (CFFF) boundary conditions. The material properties of CNTRC with different wt. % are determined experimentally and used in numerical analysis. A FEM code based on FSDT in MATLAB is developed using eight noded isoparametric plate bending element for experimental validation.

2 Experimental Programme

The experimental programme comprises of fabrication of MWCNT-reinforced composite plates, tensile test to assess Young's modulus, and free vibration test or modal tests to determine natural frequencies.

2.1 Fabrication of CNT-Reinforced Composites

The CNTRC mixes are prepared by using K-6 hardener and Lapox L-12 in 1: 10 proportion as hosting matrix and MWCNT in a weight proportion of 0.1, 0.2, 0.3, 0.4, and 0.5% as reinforcing fiber.

The CNTRC mix is prepared by mixing MWCNT in the required wt. proportion and 100 ml of acetone and placed in sonicator to stir for 30 min to avoid agglomeration. The preheated epoxy is then added to this mixture. The epoxy/CNT combination is stimulated on a magnetic stirrer at 120 °C for 3 to 4 h till acetone evaporates

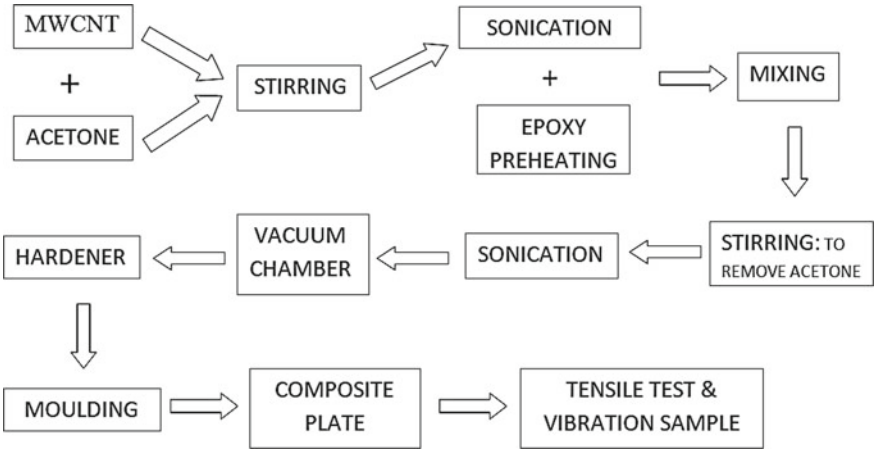

Fig. 1 Representation of CNTRC fabrication process

from the mixture and again put in a sonicator for deagglomeration of CNT. Next, it is kept in a degassed chamber for removing entrapped air. Just before the casting of composite, hardener is added to CNT/epoxy mixture and mixed vigorously and poured into molds for casting plates of desired size and thickness, then left to be cured for 3–4 days. The images of the fabrication process are presented in Fig. 1 and the instruments used are shown in Fig. 2. The cured plates are cut to the desired size by a diamond cutter for further testings.

This procedure is used to prepare 15 CNTRC plates of different thickness and aspect ratios with different percentages of CNT. The thickness and density of plates are measured. These plates are used to conduct tensile strength tests and modal tests.

2.2 Tensile Test

To determine Young's modulus of CNTRC mix, tensile tests are conducted by using UTM (INSTRON 8862) as per ASTM (D-3039). The test is conducted on epoxy and CNTRC samples containing five different wt. % (0.1, 0.2, 0.3, 0.4, 0.5%) of MWCNT. Five samples of standard dimensions 250 × 25 × 2.5 mm are fabricated for each mix. The tensile test set up with the samples is given in Fig. 3. Figure 4 presents experimentally obtained stress–strain diagrams of CNTRC mix containing 0.1, 0.3, and 0.5% of MWCNT.

The effect of CNT wt.% on Young's modulus is presented in Fig. 5. Compared to neat epoxy, addition of 0.1, 0.2, 0.3, 0.4, and 0.5% MWCNT wt. % to the mixes are found to enhance the elastic modulus by 15.45, 27.62, 55.38, 37.21, and 3.13%, respectively. An increase is observed up to 0.3% and thereafter decrease in Young's

Fig. 2 CNTRC fabrication setup

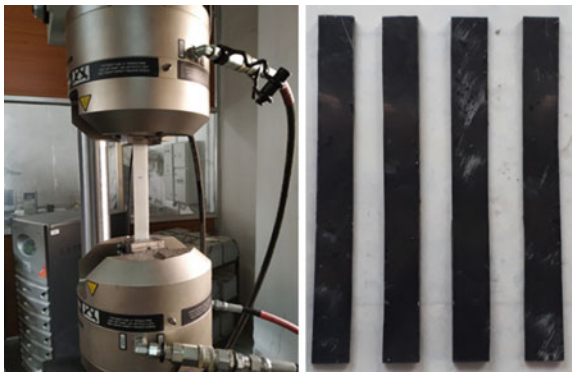

Fig. 3 INSTRON 8862 UTM and CNTRC specimens

modulus is detected apparently due to agglomeration of CNTs in the mix. Agglomeration of CNT in the mix with higher wt. percentage (>0.3%) destroy the bond between the CNT and epoxy and affects the interfacial stress transfer causing a decrease in tensile strength and Young's modulus.

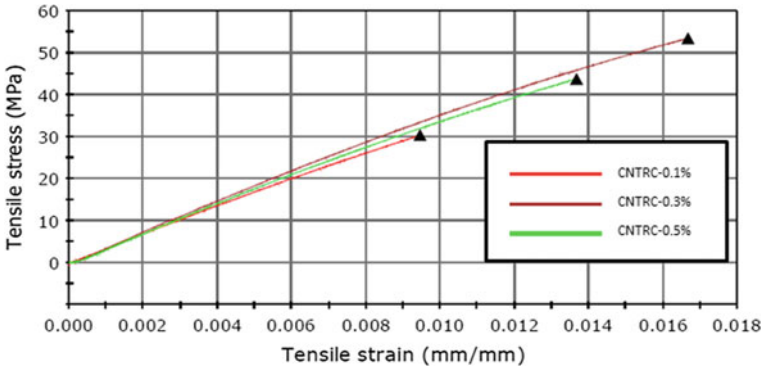

Fig. 4 Tensile stress–strain curves

Fig. 5 Young's Modulus versus CNT wt.%

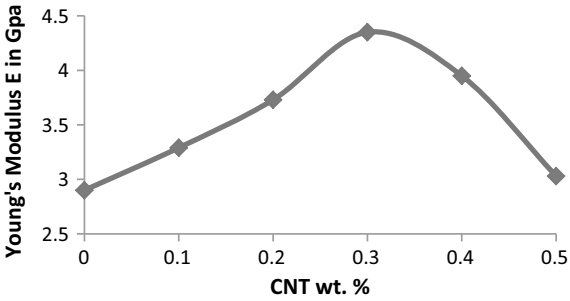

2.3 *Free Vibration Test*

The experimental free vibration tests on CNTRC plates are accomplished using the setup shown in Fig. 6. The setup consists of a modal impact hammer (model B&K 2302–5), transducer (model B&K 4507), and FFT analyzer (B&K 3560 C)

Fig. 6 The test set up for vibration measurement

supporting Pulse software. The tests are conducted on lab fabricated square CNTRC plates of size 235 mm for three weight percentages (0.1, 0.3, and 0.5) of MWCNT, aspect ratios (a/b = 1,2,3,4, and 5), side-to-thickness ratio 20 to 100 under cantilever (CFFF) and all clamped (CCCC) boundary conditions.

Modal frequencies of CNTRC plates are measured in the form of frequency response functions (FRFs) (Acceleration per force vs. Frequency graphs), auto-spectrums graphs (amplitude vs. frequency graphs), and coherence graphs representing the accuracy of measurements for each case.

3 Numerical Analysis

To validate the experimental results, numerical vibration analysis of CNTRC panels is performed using FEM. A MATLAB code is developed for numerical computation.

3.1 Finite Element Formulation

An 8-node with five degrees of freedom per node isoparametric plate element is employed to discretize the plate as shown in Fig. 7. The FSDT is implemented to incorporate transverse shear deformation in the analysis [4].

The CNTRC is obtained by mixing the polymer and randomly oriented MWCNT and assumed to be distributed uniformly throughout the body. In numerical analysis, the material properties of CNTRC are determined following the extended rule of mixture as proposed by Shen [14]. The displacement field following Mindlin plate theory is given by

$$\begin{aligned} u &= u_0 + z\phi_{0x} \\ v &= v_0 + z\phi_{0y} \\ w &= w_0 \end{aligned} \tag{1}$$

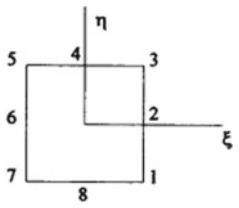

Fig. 7 8-node Serendipity plate element

Using an 8-noded serendipity plate element, the displacement field is written as

$$u = \sum_{i=1}^{8} N_i(\xi, \eta)u_{0i} + z\sum_{i=1}^{8} N_i(\xi, \eta)\phi_{0xi}$$
$$v = \sum_{i=1}^{8} N_i(\xi, \eta)v_{0i} + z\sum_{i=1}^{8} N_i(\xi, \eta)\phi_{0yi} \quad (2)$$
$$w = \sum_{i=1}^{8} N_i w_{0i}$$

where u_0, v_0, w_0 are nodal translation and ϕ_{0x}, ϕ_{0y} are nodal rotations, N_i (i = 1,8) are shape functions for serendipity plate element, and ξ, η are natural coordinates of the plate. The x,y coordinates can be expressed as

$$x = \sum_{i=1}^{8} N_i(\xi, \eta)x_i$$
$$y = \sum_{i=1}^{8} N_i(\xi, \eta)y_i \quad (3)$$

The strain–displacement equations are given by

$$\{\varepsilon\} = [B]\{\delta\} \quad (4)$$

where

$$\{\varepsilon\} = \left\{\epsilon_x \epsilon_x \gamma_{xy} \gamma_{yz} \gamma_{zx}\right\}^T$$

$$[B] = [B_1 B_2 B_3 B_4 B_5 B_6 B_7 B_8]$$

$$\{\delta\} = \{\delta_1 \delta_2 \delta_3 \delta_4 \delta_5 \delta_6 \delta_7 \delta_8\} \quad (5)$$

with

$$\{\delta_i\} = \left\{u_{0i} v_{0i} w_{0i} \phi_{0xi} \phi_{0yi}\right\}^T (i = 1 - 8)$$

$$[B_i] = \begin{bmatrix} \frac{\partial N_i}{\partial x} & 0 & 0 & 0 & 0 \\ 0 & \frac{\partial N_i}{\partial y} & 0 & 0 & 0 \\ \frac{\partial N_i}{\partial y} & \frac{\partial N_i}{\partial x} & 0 & 0 & 0 \\ 0 & 0 & \frac{\partial N_i}{\partial x} & 0 & 0 \\ 0 & 0 & 0 & 0 & \frac{\partial N_i}{\partial y} \\ 0 & 0 & 0 & 0 & \frac{\partial N_i}{\partial x} \\ 0 & 0 & \frac{\partial N_i}{\partial x} & N_i & 0 \\ 0 & 0 & \frac{\partial N_i}{\partial y} & 0 & N_i \end{bmatrix} (i = 1 - 8) \tag{6}$$

The stress–strain relation for k-th layer is written as.

$$\{\sigma\} = [Q]^k \{\epsilon\} \tag{7}$$

where $\{\sigma\} = \left\{\sigma_x \sigma_y \tau_{xy} \tau_{yz} \tau_{zx}\right\}^T$

$$\left[Q^k{}_{ij}\right] = \begin{bmatrix} Q^k{}_{11} & Q^k{}_{12} & & 0\,0\,0 & \\ Q^k{}_{12} & Q^k{}_{22} & & 0\,0\,0 & \\ 0 & 0 & Q^k{}_{66} & 0 & 0 \\ 0 & 0 & 0 & Q^k{}_{55} & 0 \\ 0 & 0 & 0 & 0 & Q^k{}_{44} \end{bmatrix} \tag{8}$$

where Q_{ij} represents stiffness coefficients of composite plate [15].

The strain energy U is calculated as

$$U = \frac{1}{2} \iint \left(\int_{-h/2}^{+h/2} \{\varepsilon\}^T \{\sigma\} dz \right) dx dy \tag{9}$$

Using Eq. (7)

$$\mathrm{U} = \frac{1}{2} \iint \{\epsilon\}^{\mathrm{T}} [\mathrm{D}] \{\epsilon\} \mathrm{dxdy} \tag{10}$$

$$.[D] = \int_{-h/2}^{+h/2} [T]^T [Q_{ij}][T] dz \tag{11}$$

$$[\mathrm{T}] = \begin{bmatrix} \cos^2\theta & \sin^2\theta & \sin\theta\cos\theta \\ \sin^2\theta & \cos^2\theta & -\sin\theta\cos\theta \\ -2\sin\theta\cos\theta & 2\sin\theta\cos\theta & \cos^2\theta - \sin^2\theta \end{bmatrix} (\mathrm{i, j} = 1, 2, 6) \tag{12}$$

$$[\mathrm{T}] = \begin{bmatrix} \cos\theta & \sin\theta \\ -\sin\theta & \cos\theta \end{bmatrix} (\mathrm{i, j} = 4, 5)$$

where D is rigidity and T is transformation matrix, respectively.

3.2 Computation of Modal Parameters

The governing equation of dynamics of composite plates are:

$$[M]\{\ddot{\delta}\} + [C]\{\dot{\delta}\} + [K]\{\delta\} = \{F(t)\} \tag{13}$$

where [M] is mass matrix, [C] is damping matrix, [K] is stiffness matrix, and $\{\delta\}$ is nodal displacement.

For free undamped vibration, the equation reduces to

$$[M]\{\ddot{\delta}\} + [K]\{\delta\} = \{0\} \tag{14}$$

Using modal coordinates, the equation becomes

$$\{[K] - \omega^2[M]\}\{\varphi\} = \{0\} \tag{15}$$

where $\{\varphi\}$ is modal displacement vector and ω is the natural frequency in radian per second.

The element stiffness matrix can be written as

$$[k]_e = \int_{-1}^{+1}\int_{-1}^{+1} [B]^T[D][B]|J|d\xi d\eta \tag{16}$$

Similarly, the consistent element mass matrix can be written as

$$[m]_e = \int_{-1}^{+1}\int_{-!}^{+1} [N]^T[\rho][N]|J|d\xi d\eta \tag{17}$$

where [ρ] is density matrix and $|J|$ is determinant of jacobian matrix.

The Gaussian Quadrature formula is used for numerical integration. Reduced integration practice is used to escape shear locking. The global stiffness matrix [K] and global mass matrix [M] are found by assembling the respective element matrices.

The solution procedure involves solving Eq. (15) to get 'ω,' the natural frequencies. A code is written in MATLAB to solve the generalized eigenvalue problem to find natural frequency ω and mode shapes. The experimentally obtained material constants are used in numerical analysis. The addition of a very small weight percentage of randomly oriented CNT will not disturb the isotropic behavior of the resulting CNTRC mix. Therefore in the current numerical investigation, the modulus of CNTRC plates are taken the same in all directions, i.e., $E_{11} = E_{22}$ and shear

Table 1 Convergence study for non-dimensional frequencies ϖ for first four modes of clamped square CNTRC with Vcnt = 0.14%, b/h = 10

Mesh Size	Non-dimensional frequency ϖ in Hz for			
	mode 1	mode 2	mode 3	mode 4
4 × 4	20.20	28.77	39.57	43.43
8 × 8	18.76	25.81	37.68	38.08
10 × 10	18.17	24.52	35.34	35.65
12 × 12	18.17	24.08	35.02	35.23

modulus G is calculated by using the relationship $G_{12} = G_{21} = E_{11}/\ 2(1 + \upsilon)$. Poisson's ratio of epoxy is taken as 0.3 and for MWCNT is taken as 0.28 following the [16].

4 Results and Discussions

4.1 Convergence Study

As discussed earlier, the convergence study is performed by using FEM via MATLAB coding to get the natural frequency in non-dimensional form $\varpi = \omega(a^2/h)\sqrt{\rho^m/E^m}$ for square CNTRC plate having b/h = 10 for all clamped condition, using different mesh sizes.

The results are tabulated in Table 1. The lower modes are observed to converge faster than higher modes. The modes are found to converge at 10 × 10 mesh size, hence adopted for subsequent numerical analysis.

4.2 Comparison with the Previous Study

For the validity of the current numerical model, the example of square CNTRC plate of b/h ratio = 10 with 0.11, 0.14, and 0.17% volume fraction of CNTs under CCCC condition is solved and results are compared with the published results by Zhu et al. [6] in Table 2. The results are compared and discrepancies are found negligible.

4.3 Experimental Validation

Experimentally, the response frequency spectrums, i.e., FRFs and auto-spectrums are obtained by using an FFT analyzer with the Pulse platform for each case. The accuracy of measurement is predicted by approaching coherence closer to unity.

Table 2 Comparison study for non-dimensional natural frequency ϖ of all clamped CNTRC square plates with $V_{cnt} = 0.11$, 0.14, and 0.17%, $\upsilon_m = 0.34$, $\rho_m = 1.15$ g/cm^3, $E^m = 2.1$GPa, and $\varpi = \omega(a^2/h)\sqrt{\rho^m/E^m}$

b/h ratio	CNT volume fraction					
	$V_{CNT} = 0.11\%$		$V_{CNT} = 0.14\%$		$V_{CNT} = 0.17\%$	
	Present FEM	Zhu et al	Present FEM	Zhu et al	Present FEM	Zhu et al
10	17.48	17.62	18.17	18.12	21.74	22.01
20	27.78	28.4	29.12	29.91	34.72	35.31
50	40.26	39.73	43.85	43.58	49.82	49.07

The frequencies are obtained by selecting the peak points of the spectrum. Figure 8 represents distinctive FRF, auto-spectrum, and coherence graphs for square cantilever CNTRC plate having 0.3% CNT and b/h ratio = 100. The FRF and auto-spectrum graphs gave the same values of natural frequencies. The modal tests are conducted for all CNTRC plates and natural frequencies are determined. The experimental results are compared with numerical results as obtained by the present FEM formulation. The effect of various parameters on fundamental frequencies of CNTRC plates are studied as follows.

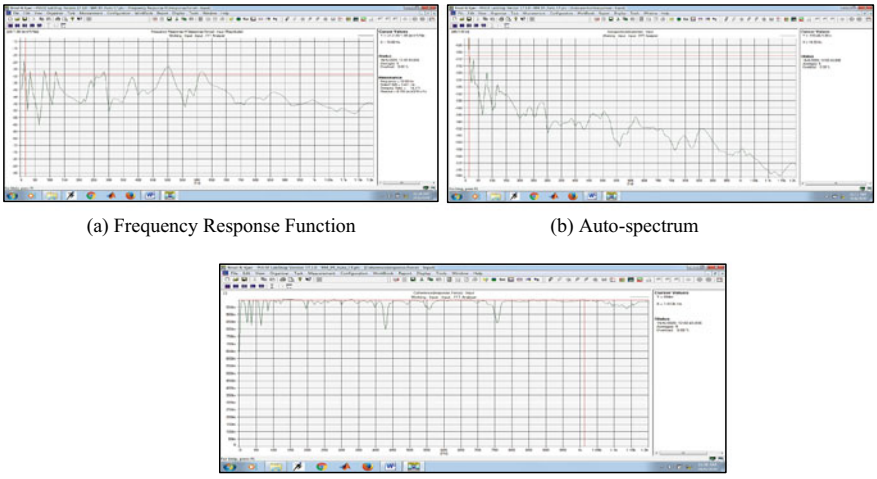

(a) Frequency Response Function (b) Auto-spectrum

(c) Coherence

Fig. 8 Response spectrums of Cantilever CNTRC square plate (235 mm) having 0.3% CNT, b/h = 100

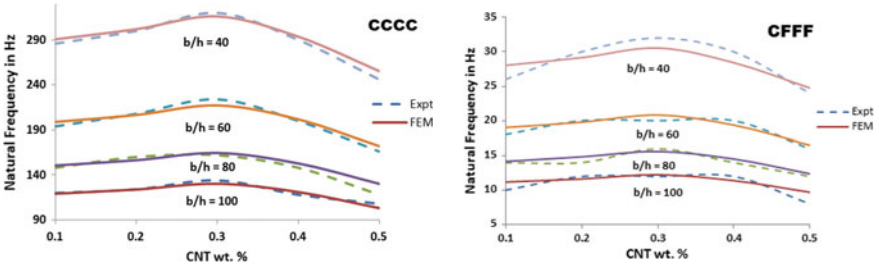

Fig. 9 Natural frequency versus wt. % of CNT for CCCC and CFFF boundary conditions

4.3.1 Effect of Wt. % of CNTs on Frequencies of CNTRC Plates

The variation of experimentally and numerically obtained natural frequency of vibration of square clamped and cantilever plates having different wt.% of CNT are shown in Fig. 9 for b/h = 40, 60, 80, and 100.

Natural frequencies are found to increase with wt % of CNT and observed to be maximum for CNTRC with 0.3% of CNT for plates of all thickness (b/h ratio) under both CCCC and CFFF conditions as shown in Fig. 9. Related to the frequency of plate having 0.1% CNT, an increase of 11.34% and 19.27% are witnessed for a plate having 0.3% CNT under CCCC and CFFF conditions, respectively. The increase is caused by rise in stiffness due to enhanced Young's modulus as determined experimentally (ref. Fig. 5).

4.3.2 Effect of Side-To-Thickness Ratios (b/h) on Natural Frequencies of CNTRC Plates

Effect of thickness of CNTRC square plates on natural frequency under CCCC and CFFF condition is presented in Fig. 10 for a plate having 0.3% of CNT. Since thicker plates have higher stiffness, hence higher natural frequencies are obtained for thicker plates.

4.3.3 Effect of Aspect Ratios (a/b) on Frequencies of CNTRC Plates

The natural frequencies of plates with 0.1, 0.3, and 0.5 wt.% of CNT are observed experimentally for aspect ratios = 1, 2, 3, 4, and 5 for cantilever (CFFF) condition only and variation is presented in Fig. 11. The frequencies are found to be increasing exponentially with increasing aspect ratios.

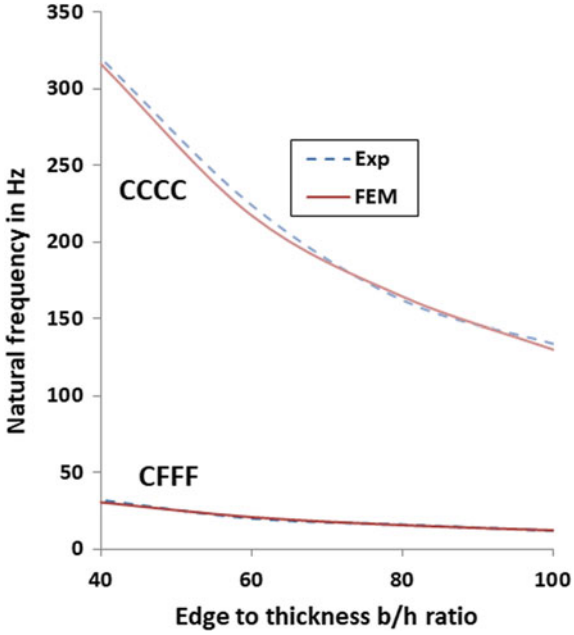

Fig. 10 Frequency versus b/h ratio

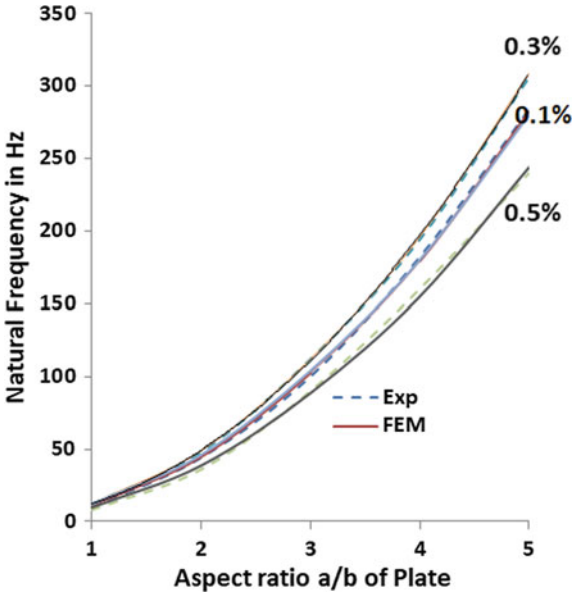

Fig. 11 Frequency versus aspect a/b ratio

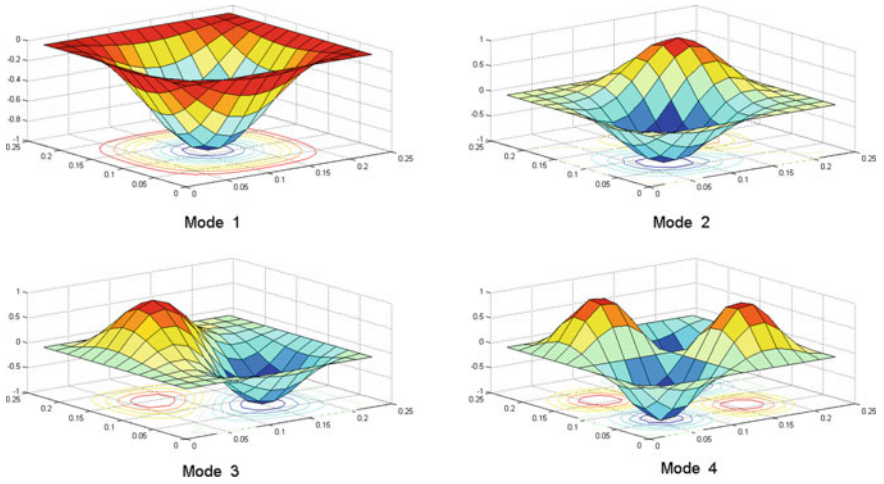

Fig. 12 Mode shapes of Clamped CNTRC Plate

4.3.4 Effect of Boundary Conditions on Frequencies of CNTRC Plates

Since clamped (CCCC) condition imparts more stiffness than the cantilever (CFFF) to the plate, hence natural frequency observed under the CCCC condition is more than the natural frequency observed by CFFF boundary conditions as shown in Figs. 8 and 9.

4.4 Mode Shapes

Mode shapes are also an important inherent dynamic property of a structure. First four mode shapes of the plate under CCCC and CFFF boundary conditions as computed using present codes are presented in Figs. 12 and 13, respectively.

5 Conclusions

The study describes an investigation on the natural frequency of clamped and cantilever CNTRC plates of different thickness, aspect ratio, and reinforced with different wt. percentage of CNT. The natural frequencies of CNTRC plates are determined experimentally from measured frequency response functions, auto-spectrums by modal testing.

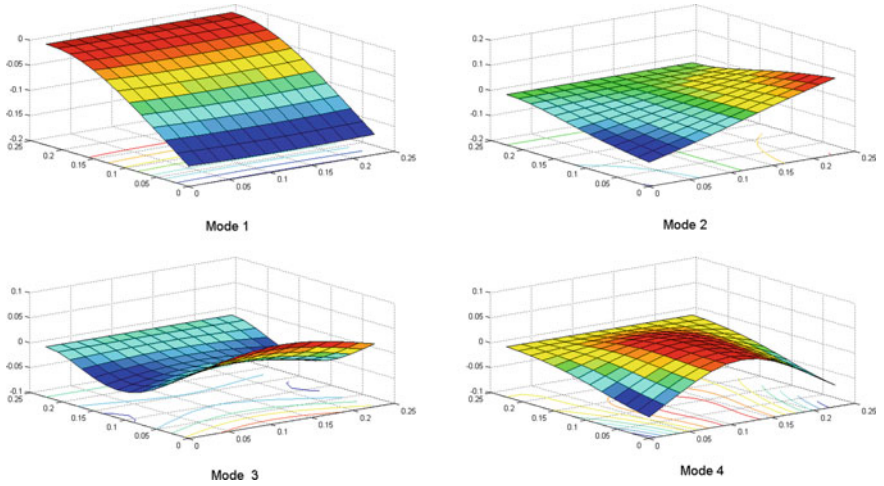

Fig. 13 Mode shapes of Cantilever CNTRC Plate

- The study revealed that small percentages of CNTs to polymer significantly enhance elastic properties and frequencies of vibration of CNTRC panels of any side-to- thickness ratios, aspect ratios, and boundary conditions.
- Young's modulus and natural frequency are increasing to 0.3% of the weight of CNT and reducing further, primarily owing to clustering of CNT in the mix.
- The frequencies of CNTRC plates are found to increase with the decrease in b/h ratios.
- The frequency of CNTRC plates varies parabolically with the side-to-thickness ratio for all boundary conditions.
- The frequency of vibration is significantly affected by the aspect ratio a/b of CNTRC panels.
- Higher natural frequencies are observed for clamped than cantilever CNTRC plates.
- Frequencies and mode shapes are also computed numerically by using the Finite element method based on FSDT and an 8-noded isoparametric element.
- The numerically computed frequencies are found to match closely with the frequencies measured from modal tests.

References

1. Reissner E, Stavsky Y (1961) Bending and stretching of certain types of heterogeneous aelotropic elastic plates. Appl Mech Trans ASME 28:402–408
2. Rock TA, Hinton E (1976) A finite element method for the free vibration of plates allowing for transverse shear deformation. Comput Struct 6:37–44

3. Reddy JN, Ochoa O (1987) Finite element analysis of composite laminates. Technomic Publishing Company, US
4. Iijima S, Ichihashi T (1993) Single shell carbon Nano-tube of 1-nm diameter. Nature 363:603–605
5. Formica G, Lacarbonara W, Alessi R (2010) Vibrations of carbon nanotube-reinforced composites. J Sound Vib 329:1875–1889
6. Zhu P, Lei ZX, Liew KM (2012) Static and free vibration analyses of carbon nanotube reinforced composite plates using finite element method with first order shear deformation platetheory. Composit Struct 94(4):1450–1460
7. Lin F, Xiang Y (2014) Vibration of carbon nanotube reinforced composite beams based on the first and third order shear theories. Appl Math Modell 38:3741–3754
8. Zhang LW, Lei ZX, Liew KM, Yu JL (2014) Static and dynamic of carbon nanotube reinforced functionally graded cylindrical panels. Compos Struct 111:205–212
9. Cawley P, Adams RD (1978) The predicted and experimental natural modes for free-free CFRP plates. J Compos Mater 12:336–347
10. Chakraborty S, Mukhopadhyay M, Mohanty AR (2000) Response of FRP composite plates: experimental and numerical studies. J Reinforc Plast Comp 19(7):535–551
11. Mishra I, Sahu SK (2015) Modal analysis of woven fiber composite plates with different boundary conditions. Int J Struct Stab Dyn 15(01):1540001
12. Panda HS, Sahu SK, Parhi PK (2014) Effects of moisture on the frequencies of vibration of woven fibre composite doubly curved panels with strip delaminations. Thin Walled Struct 78:79–86
13. Patel A, Das R, Sahu SK (2020) Experimental and numerical study on free vibration of multiwall carbon nanotube reinforced composite plates. Int J Struct Stab Dyn 20(12):2050129
14. Shen SH (2009) Nonlinear bending of functionally graded carbon nanotube reinforced composite plates in thermal environments. Compos Struct 91:9–19
15. Jones RM (1975) Mechanics of composite materials. McGraw-Hill, New York
16. Lu JP (1997) Elastic properties of single and multilayered nanotubes. J Phys Chem Solids 158(11):1649–1652

System Reliability and New Measure of Robustness of Truss Structure in Progressive Collapse

Minangshu Baidya and Baidurya Bhattacharya

1 Introduction

Structures are generally designed for normal loads. It has been estimated that approximately 15–20% of building failures are due to progressive collapse [8]. Ellingwood et al. [5] proposed to design buildings for abnormal loads. Abnormal loads include vehicular collision, gas explosion, bomb explosion, etc. Code (ASCE 07) defines progressive collapse as an extent of damage or collapse that is disproportionate to the magnitude of the initiating event. In Euro code, engineers provide tying the system together or designing the system to tolerate accidental removal of an element. General service administration [3] codes specified threat-independent approach of alternate load path method for progressive collapse analysis. GSA guidelines permit nonlinear dynamic analysis for progressive collapse analysis. Principal action–comparison action load combination format is found, in one form or another, in all modern probability-based design codes including ASCE07 (cl. 4 in, ASCE standard 07), Eurocode (EN 1990:2002). It specifies three methods of design approaches: (1) Indirect approach, (2) Specific local resistance method, and (3) Alternate load path method. (Part 1 in JCSS 2002) provides probabilistic design approach for robustness analysis. During the last decades' different structures have been analyzed for reliability computation using mostly linear elastic methods [6–8]. Geometric nonlinearities were considered in a few cases (e.g., Imai and Frangopol [9] part 1 and 2).

Various researchers proposed different robustness measure of structures. Baker et al. [10] proposed a risk-oriented conceptual model that relates robustness to both direct and indirect risks. Nafday [11] proposed a static stiffness-based approach where the author carried out a linear elastic analysis of a truss model and defined an index based on normalized determinant of the elastic static stiffness matrix. Brett

M. Baidya (✉) · B. Bhattacharya
Indian Institute of Technology, Kharagpur, India

D. K. Maiti et al. (eds.), *Recent Advances in Computational and Experimental Mechanics, Vol II*, Lecture Notes in Mechanical Engineering,
https://doi.org/10.1007/978-981-16-6490-8_50

et al. [12] proposed a conceptual generic model of robustness. Starossek et al. [13] proposed energy-based measure of robustness. Frangopol and Curley [14] and Fu and Frangopol [15] proposed some probabilistic measure based on structural redundancy. Maes [16] proposed three methods of robustness where one method is based on system reliability. Čizmar et al. [7] worked on reliability-based index of structural robustness based on Danish code. Most of the existing robustness approaches are not probability based. Existing reliability-based indices are not bounded between 0 and 1. There is no such repair strategy based on robustness and system reliability. Repair strategy should be based on robustness. This paper implements a new measure of robustness including uncertainties in model and geometric nonlinear dynamic analysis is performed [7].

2 Approach

In progressive collapse analysis, intact structure is analyzed first. Depending on the failure criteria, members are removed one by one and the analysis is carried out toward global collapse of the structure. In different failure sequences, the structure can reach collapse. Sudden removal of the members causes dynamic amplification of response of the structure. Therefore, geometric nonlinear dynamics analysis is performed. Material behavior may be ductile or brittle or semi-brittle. In this paper, material behavior is taken to be brittle. Member removal criteria may be based on permissible stress or strain. Here, it is based on yield stress. Identification of collapse is defined as follows:

- For 2D truss, global static degree of indeterminacy or instability: $(2 \times No.of joints) - No.of members - No.of reactions > 0$
- Condition number of the global stiffness matrix becomes exceedingly large due to member failure(s).

2.1 Implementing Geometric Nonlinear Dynamic Analysis

Basic finite element analysis is performed for this process. Equation of motion for the structure is:

$$M\ddot{u} + C\dot{u} + Ku = F(t) \tag{1}$$

where M is the global mass matrix, C is the global damping matrix, K is the global stiffness matrix, and F(t) is the force vector at time t. Removal of the members is processed by element stiffness corresponding to the element is equal to zero. For the time integration, Newmark's family of methods can be used. Here, Newmark's average acceleration method is used [18].

2.1.1 Geometric Nonlinearity

In progressive collapse analysis, deformation of the structure may not be negligible. Therefore, equilibrium should be satisfied in deformed configuration. Finite deformation analysis is more accurate than small deformation analysis where strains are large. Tension force developed in the elements depends on large strain:

$$\epsilon = \frac{du}{dx} + \frac{1}{2}\left(\frac{dw}{dx}\right)^2 \tag{2}$$

where u is the axial deformation and w is the = plane deformation orthogonal to the axial deformation. Here, the element stiffness matrix has two parts: (1) elastic part, (Element stiffness matrix (k_E) + (2) Geometric part, (k_G). Each time step equilibrium should be satisfied. Therefore, the stiffness matrix will be updated as Fig. 1.

$$k_E = \frac{EA}{L_0}\begin{bmatrix} 1 & 0 & -1 & 0 \\ 0 & 0 & 0 & 0 \\ -1 & 0 & 1 & 0 \\ 0 & 0 & 0 & 0 \end{bmatrix} \quad k_G = \frac{T}{L}\begin{bmatrix} 0 & 0 & 0 & 0 \\ 0 & 1 & 0 & -1 \\ 0 & 0 & 0 & 0 \\ 0 & -1 & 0 & 1 \end{bmatrix} \tag{3}$$

where E is the elastic modulus, A is the cross-sectional area, L is the length of the member, and member tension T can be calculated as

$$T \approx \frac{EA}{L_0}\left[(u_3 - u_1) + \frac{1}{2L_0}(u_4 - u_2)^2\right] \tag{4}$$

Each time step equilibrium should be satisfied. Therefore, the stiffness matrix will be updated as Fig. 1.

2.2 System Reliability Analysis

The random variables are load and strength of the members. Load and strength can follow any distribution. Load random variables are generated by Latin hypercube sampling (Melchers and Beck 1987). Member strengths are independent and identically distributed. All failure sequences are analyzed for each generated load vector and system failure probability is computed. Then the average of system failure probability for all generated loads is the actual system failure probability. The process is given in Fig. 2.

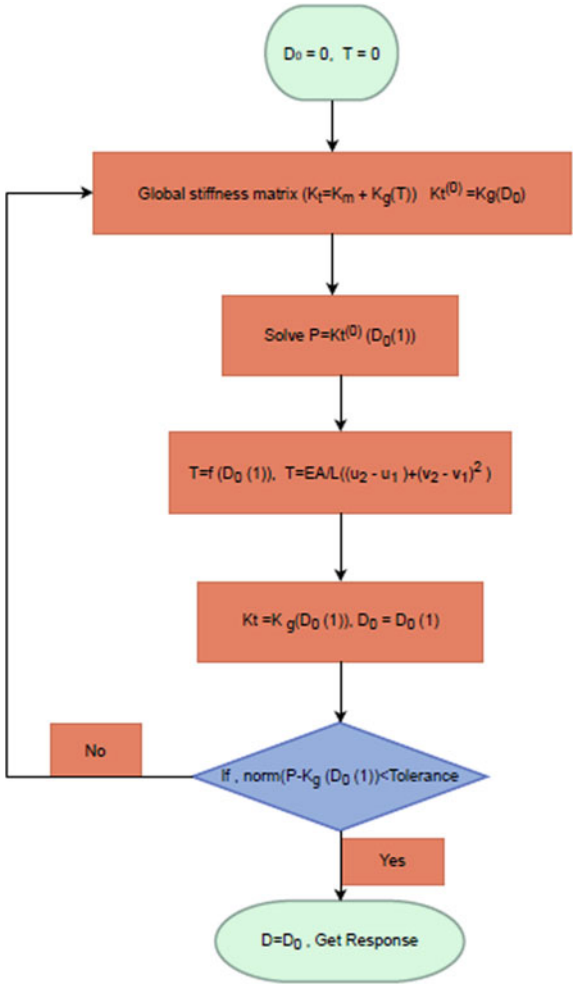

Fig. 1 Geometric nonlinear flow chart for the stiffness matrix update

2.2.1 Reliability Formulation

Let F_0^K denotes the failure of the Kth member in an originally intact structure. Given F_0^K as the initial damage, the system failure probability can be written in terms of the complete collection of cut sets S_i as $P[F_{sys}|F_0^K] = \sum_{i=1}^{n_c} P[S_i|F_0^K]$. Cut sets are the unique combinations of component failures that can cause system failure. Specifically, a cut set is said to be a minimal cut set if, when any basic event is removed from the set, the remaining events collectively are no longer a cut set. Now, if each cut set is minimal, and if each minimal cut set is defined in terms of a sequence of member failures, the conditional system failure probability can be written as the sum: $P[F_{sys}|F_0^k] = \sum_{i=1}^{n_c} P[S_i|F_0^k]$. The Ith minimal cut set, $S_I = \{F_K^{n_I^1, n_I^2, \ldots, n_I^{m(I)}}\}$,

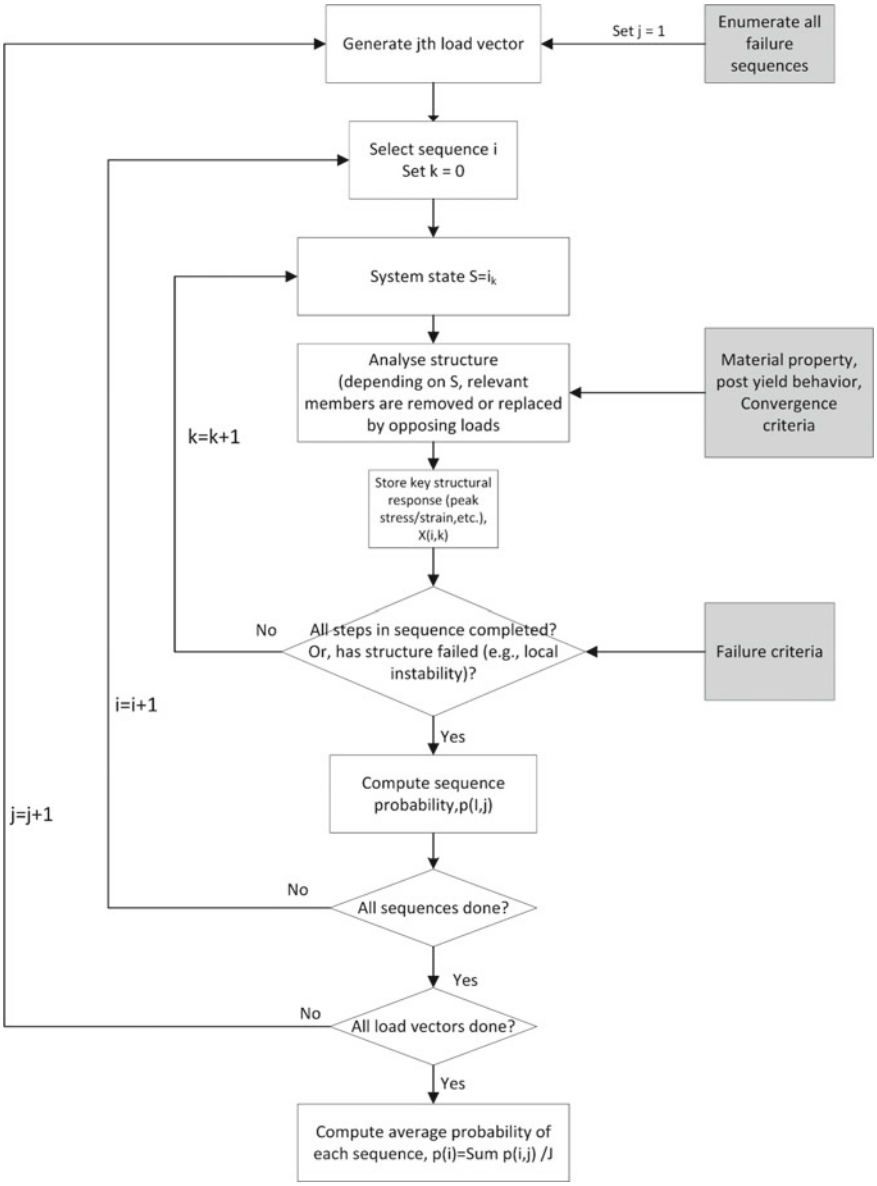

Fig. 2 System failure probability computation flow chart

signifies the sequence of member failures from left to write given that member K has already failed:

n_I^1 is the ID of the first member to fail, n_I^2 is the ID of the second member to fail, and so on up to $n_I^{m(I)}$, where $m(I)$ is the total number of members in the Ith cut set. Defined this way, it is easy to see that any two minimal cut sets S_i and S_j are disjoint ($i \neq j$). Let the random capacity (strength) of the Ith member be C_i. The event S_I is the intersection of a sequence of member level limit states:

$$
\begin{aligned}
S_I = \{F_K^{n_I^1, n_I^2, \ldots, n_I^{m(I)}}\} &= \{C_{n_I^1} < \sigma_{n_I^1}^K(\underline{L}), C_{n_I^2} > \sigma_{n_I^2}^K(\underline{L}), C_{n_I^3} \\
&> \sigma_{n_I^3}^K(\underline{L}), \ldots, C_{n_I^{m(I)}} > \sigma_{n_I^{m(I)}}^K(\underline{L})\} \\
&\cap \{C_{n_I^2} < \sigma_{n_I^2}^{K,n_I^1}(\underline{L}), C_{n_I^3} > \sigma_{n_I^3}^{K,n_I^1}(\underline{L}), \ldots, C_{n_I^{m(I)}} > \sigma_{n_I^{m(I)}}^{K,n_I^1}(\underline{L})\} \\
&\cap \{C_{n_I^2} < \sigma_{n_I^2}^{K,n_I^1}(\underline{L}), C_{n_I^3} > \sigma_{n_I^3}^{K,n_I^1}(\underline{L}), \ldots, C_{n_I^{m(I)}} > \sigma_{n_I^{m(I)}}^{K,n_I^1}(\underline{L})\} \\
&\ldots. \cap \{C_{n_I^{m(I)}} < \sigma_{n_I^{m(I)}}^{K,n_I^1,n_I^2,\ldots,n_I^{m(I)-1}}(\underline{L})\}
\end{aligned} \tag{5}
$$

where $C_{n_I^1} < \sigma_{n_I^1}^K(\underline{L})$ denotes the failure of the first member in cut set I, $C_{n_I^2} > \sigma_{n_I^2}^K(\underline{L})$ denotes the survival of the second member in cut set I, and so on. It is emphasized that the load effect in each member is a function of the applied random load vector $\underline{L}$. We compute the system failure probability by generating the load vector $\underline{L}$ repeatedly through Latin hypercube sampling:

$$
P[F_{sys}|F_0^K] = \int_{all\,\underline{l}} \sum_{i=1}^{n_C} P[S_i|F_0^K, \underline{L} = \underline{l}] f_{\underline{L}}(\underline{l}) d\underline{l} \tag{6}
$$

Similarly, system failure probability of intact structure is complete collection of all sequences where no initial damage is considered.

2.3 Robustness Measure

Robustness measure can be defined as a measure of structure that have ability to absorb initial damage. The measure of structural robustness against progressive collapse must have the following properties: it must be monotonically increasing with increasing size or intensity of the initial damage; for the same initial damage. Here, the robustness will be measured by index based on reliability index of damage as well as intact structure [20].

$$
R_b = \exp\left(\frac{\beta' - \beta}{\beta}\right) \tag{7}
$$

where R_b is the Robustness index, $\beta^{'}$ = Reliability index of damaged structure, and β = Reliability index of intact structure. The Robustness index value is bounded between 0 and 1, where 0 defines the collapse of the structure and 1 defines fully robust.

3 Results

Here, two-bay redundant truss is analyzed for the existing loads. The boundary conditions are as per Fig. 3. Left support is hinged and right support is roller. One horizontal load (40kN) and one vertical load (235kN) is applied at the center bottom node of the truss.

Geometric properties are given in the Table 1. Degree of indeterminacy (D.O.I) of the truss is (m + r-2j) = 2. Hence, three members' removal will cause collapse of the structure. Besides, exceedingly large condition number of global stiffness matrix will also be defined as collapse of the structure (as an example, two diagonal members' removal). Due to sudden removal of members, the load redistribution occurs (Fig. 4).

Reaction forces change due to the removal of members, but steady-state response remains indifferent. Removal of the members causes dynamic amplification of the

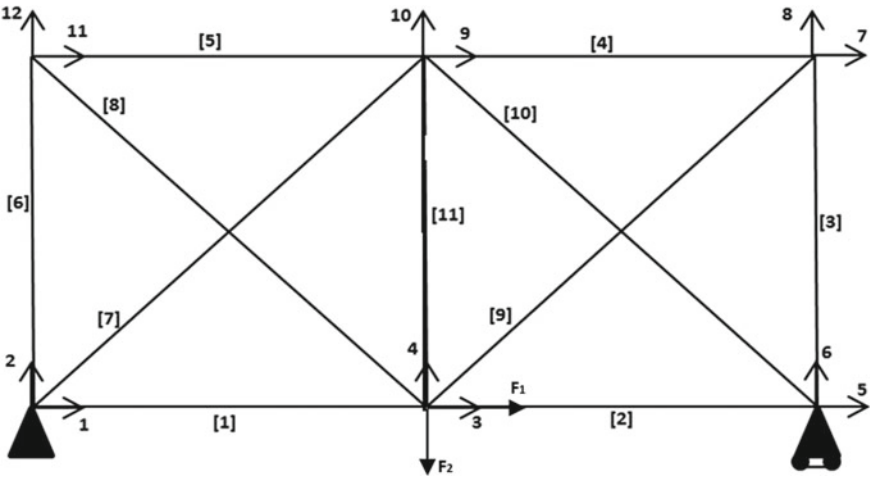

Fig. 3 Two-bay truss

Table 1 Geometric properties of the truss

Members	Length (Meter)	Elastic modulus (N/m^2)	Area (cm^2)	Density (Kg/m^3)
1, 2, 3, 4, 5, 6, 11	2	2×10^{11}	6.77	8050
7, 8, 9, 10	2.8284	2×10^{11}	6.77	8050

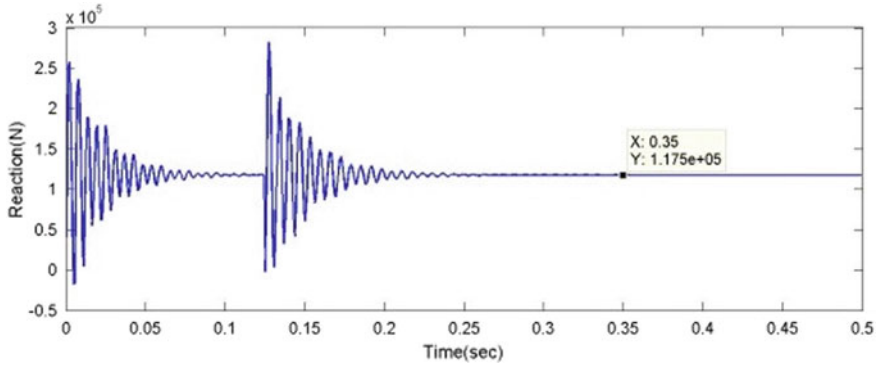

Fig. 4 Reaction time history before and after removal of the member 11

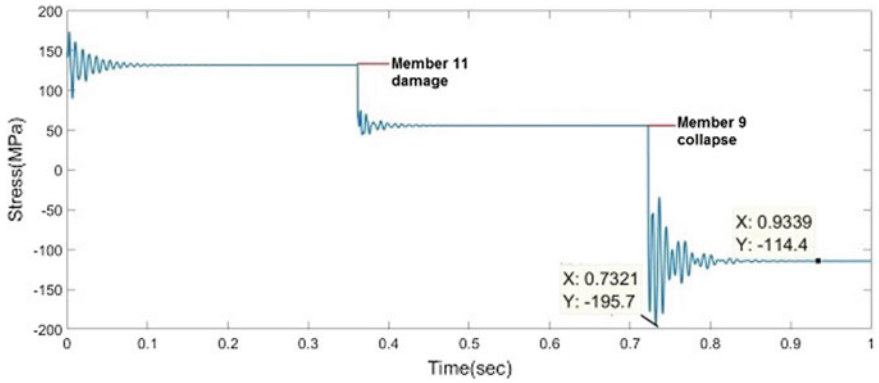

Fig. 5 Stress time history of member 1

member stresses which may cause failure of the members. Figures 5 and 6 are the nonlinear stress time history of the members 1 and 4, respectively, at removal of member 11 and 9 and Fig. 7 is the nonlinear stress time history of member 9 at removal of members 11 and 8. The member stress histories are dramatic in nature because it may be low or high due to different removal of the member. Therefore, it is unpredictable which member will fail next. So, all possible sequences are analyzed to predict system failure probability.

3.1 Reliability Computation

In reliability analysis, applied load follows Gumbel distribution with mean 40kN and 235kN and C.O.V 20 and 25%, respectively. All member strengths are identically and independently distributed and follow Normal distribution with mean 410 MPa and

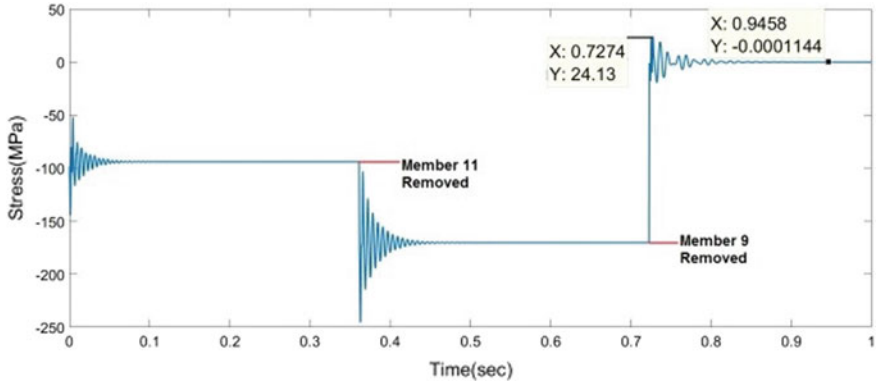

Fig. 6 Stress time history of member 4

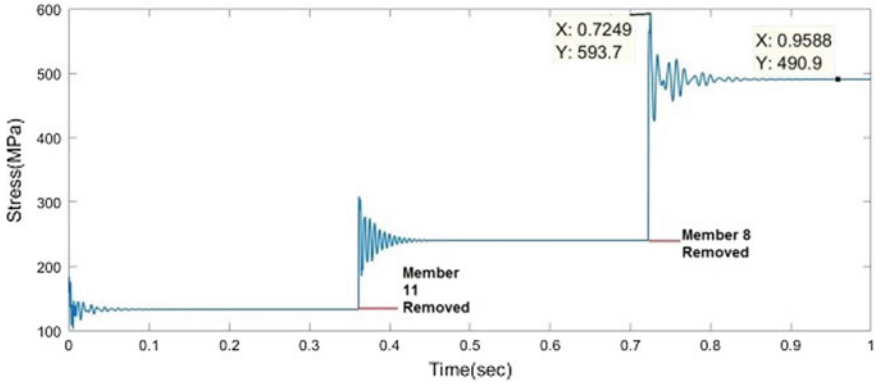

Fig. 7 Stress time history of member 9

COV 20% for both tension and compression. First, the structure is analyzed for mean load. Damaged structure is considered as member 11 is removed. In the damaged truss, ten members are there. Therefore, two members' removal will cause collapse of the structure. For the damaged truss, the number of all possible sequences are $({}^{10}P_2)90$ wherein local instability due to exceedingly large condition number is included as there is no such case. The probability of occurrences of sequence $\boldsymbol{F}_{11}^{8-9}$ and $\boldsymbol{F}_{11}^{9-8}$ are 0.01344 and 0.00939, respectively (detailed calculation is shown in appendix). For intact structure, all possible sequences are $({}^{11}P_3 = 990)$ where local instability is not considered. After analyzing all possible sequences, it is found that most of them are zero and considering local instability, system failure probability is 0.00171. Next, ten sets of load random variables are generated by Latin hypercube sampling (Table 2). All possible sequences of damaged as well as intact truss are computed for the generated load. The bar diagram of the actual probability of occurrences of damaged and intact truss are given in the Figs. 8 and 9 Considering load uncertainty,

Table 2 Load random variables generated by LHS

F_1 (kN)	F_2 (kN)
38.670	446.542
46.093	405.386
36.468	209.177
50.781	310.755
40.871	281.217
56.120	259.235
67.490	567.872
97.664	349.114
73.709	302.007
47.418	224.374

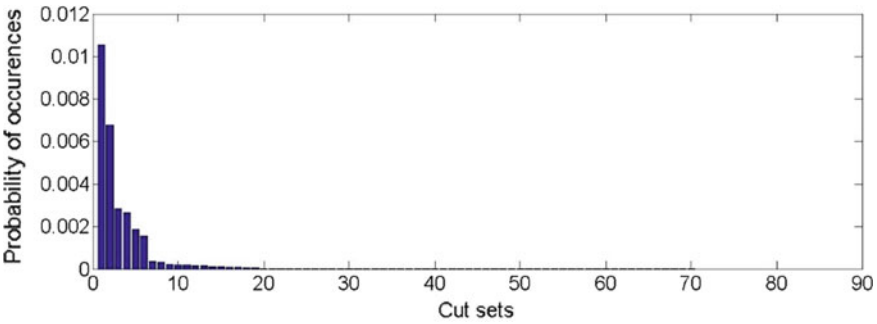

Fig. 8 Failure sequences of total cut sets for removal of member 11

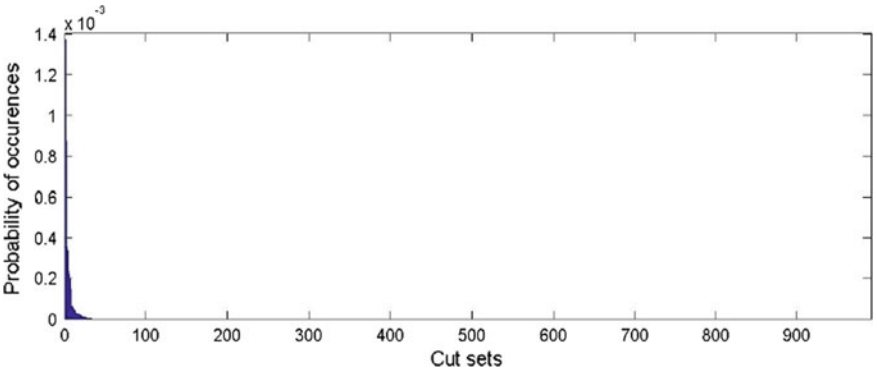

Fig. 9 Failure sequences of total cut sets for intact structure

Table 3 Robustness for different damage scenarios

Damage scenarios (Member removed first)	Robustness	Damage scenarios (Member removed first)	Robustness	Damage scenarios (Member removed first)	Robustness
1	0.4736	5	0.576	9	0.588
2	0.507	6	0.584	10	0.478
3	0.646	7	0.464	11	0.7603
4	0.582	8	0.5899		

actual probability of system failure of damaged structure is 0.0286 and system failure probability of intact structure is 0.00435. Other damage scenarios are done.

3.2 Computation of Robustness Index

Robustness is depending on system failure probability of intact and damaged structure. Robustness is measured based on the reliability index of damaged as well as intact structure. Reliability index of intact structure is 2.6197. If the robustness value is high after this damage, then the damage is not very important to cause collapse of the structure. If the robustness value is very low due to any damage, then the damage is very likely to cause system failure in progressive mode. Therefore, this particular member needs to retrofit or repair so that it should not fail to prevent progressive collapse. Ten damage scenarios are adopted next. Same as member 11, the rest of the 10 members are removed first and system failure probability is computed. From the system failure probability of corresponding damage, robustness is measured in Table 3. Among the 11 damage scenarios, the robustness values fall below 0.5 in damage cases 1, 7, and 10. That means when members 1, 7, and 10 are removed first, the system is highly prone to collapse compared with other damage cases. Therefore, members 1, 7, and 10 should be repaired so that it should prevent progressive collapse. Repairing or strengthening the members will improve the system reliability of the system.

4 Conclusion

Steady-state values are well matched with the quasi-static results of each response. Steady-state reaction is different before and after the removal; therefore, the truss can be said to be load path redundant. Dynamic peaks are very high with respect to steady-state value for the time step of time integration close to fundamental period. Failure criteria is based on stress reached at its maximum peak. For intact or damaged

structure, the common feature is a very few sequences are dominant among all failure sequences to compute system failure probability. Efficient methods are required to identify the probabilistically dominant sequences. The system failure probability of damaged and intact structure is consistent for mean load as well as considering load uncertainty. From the result, it is more reasonable that intact structure is more reliable in comparison with damaged structure. The measured robustness values are in the scale of 0–1. Among the all damage scenarios the truss has moderately high robustness against failure of members 3 or 11. Robustness after damages 1, 7, and 10 is falling below 0.5. In this way, we can identify the member(s) needs to strengthen or repair to improve system reliability of the system.

Appendices

C_i: Strength of the ith member, σ_i^j: Stress of the i-th member after j-th member failure. Now the sequence

$$F_{11}^{9-8} = \{Member\ 8\ fails\ 2nd \cap 9\ fails\ 1st \mid Member\ 11\ has\ failed\}$$

$$\{(C_1 > \sigma_1^{11-9},\ C_2 > \sigma_2^{11-9},\ C_3 > \sigma_3^{11-9},\ C_4 > \sigma_4^{11-9},\ C_5 > \sigma_5^{11-9},\ C_6 > \sigma_6^{11-9},\ C_7 > \sigma_7^{11-9},\ C_8 > \sigma_8^{11-9},\ C_{10} > \sigma_{10}^{11-9})$$
$$\cap\ (C_1 > \sigma_1^{11},\ C_2 > \sigma_2^{11},\ C_3 > \sigma_3^{11},\ C_4 > \sigma_4^{11},\ C_5 > \sigma_5^{11},\ C6 > \sigma_6^{11},\ C_7 > \sigma_7^{11},\ C_8 > \sigma_8^{11},\ C_9 < \sigma_9^{11},\ C_{10} > \sigma_{10}^{11})\}$$

$$= \{(C_1 > \max(\sigma_1^{11-9},\ \sigma_1^{11})),\ (C_2 > \max(\sigma_2^{11-9},\ \sigma_2^{11})),$$
$$(C_3 > \max(\sigma_3^{11-9},\ \sigma_3^{11})), (C_4 > \max(\sigma_4^{11-9},\ \sigma_4^{11})),$$
$$(C_5 > \max(\sigma_5^{11-9},\ \sigma_5^{11})),\ (C_6 > \max(\sigma_6^{11-9},\ \sigma_3^{11})),$$
$$(C_7 > \max(\sigma_7^{11-9},\ \sigma_7^{11})),\ (\sigma_8^{11} < C_8 < \sigma_8^{11-9}),$$
$$(C_9 < \sigma_9^{11}),\ (C_{10} > \max(\sigma_{1o}^{11-9},\ \sigma_{10}^{11}))\}$$

$$= P\{(C_1 > \max(\sigma_1^{11-9},\ \sigma_1^{11})),\ (C_2 > \max(\sigma_2^{11-9},\ \sigma_2^{11})),$$
$$(C_3 > \max(\sigma_3^{11-9},\ \sigma_3^{11})), (C_4 > \max(\sigma_4^{11-9},\ \sigma_4^{11})),$$
$$(C_5 > \max(\sigma_5^{11-9},\ \sigma_5^{11})),\ (C_6 > \max(\sigma_6^{11-9},\ \sigma_3^{11})),$$
$$(C_7 > \max(\sigma_7^{11-9},\ \sigma_7^{11})),\ (\sigma_8^{11} < C_8 < \sigma_8^{11-9}),$$
$$(C_9 < \sigma_9^{11}),\ (C_{10} > \max(\sigma_{1o}^{11-9},\ \sigma_{10}^{11}))\}$$

References

1. ASCE Standard 7–16 Minimum Design Loads and Associated criteria for Buildings and Other Structures (2017)
2. Baker JW, Schubert M, Faber MH (2008) On the assessment of robustness. Struct Saf 30:253–267
3. Bennett RM (1985) Reliability analysis of frame structure with brittle components. Struct Saf 2:281–290
4. Brett C, Young L (2013) Assessment of robustness of structures: Current state of research. Front Struct Civ Eng 7(4):356–368
5. Bhattacharya B (2020) A reliability based measure of structural robustness for coherent systems. Structural Safety 89(2021):102050
6. Chopra K (2019) Dynamics of structure
7. Čizmar a D, Kirkegaardb PH, Sørensenb JD, Rajčić V (2011) Reliability based robustness analysis for a Croatian sports hall. Eng Struct 33:3118–3124
8. Edgar V Leyendecker, Eric FP Burnett (1976) The incidence of abnormal loading in residential buildings. Washington DC, 20234
9. Ellingwood B, Leyendecker EV, Yao JT (1983) Probability of failure from abnormal load. J Struct Eng 109(4):875–890
10. Frangopol DM, Curley JP (1987) Effects of damage and redundancy on structural reliability. J Struct Eng 113(7):1533–1549
11. Fu G, Frangopol DM (1990) Balancing weight, system reliability and redundancy in a multiobjetive optimization framework. Structural Safety 7:165–175
12. GSA Alternate Path Analysis and Design Guidelines for Progressive Collapse Resistance (2013)
13. Imai DM Frangopol (2000) Geometrically nonlinear finite element reliability analysis of structural systems. Computers and Structures, pp. 677–691
14. Joint Committee on Structural Safety, Probabilistic model code (2000)
15. Karamchandani, Structural system reliability analysis methods, Department of civil and environment engineering Standford University (1987)
16. Lee YJ, Song J. Risk analysis of fatigue induced sequential failures by branch and bound method employing system reliability bounds. J Eng Mech 137(12):807–821
17. Maes MA, Fritzsons KE, Glowienka S (2006) Risk-based indicators of structural system robustness. Struct Eng Int 6(2):101–107
18. Melchers RE, Beck AT (2017) Structural reliability analysis and prediction
19. Nafday AM (2008) System safety performance metrics for skeletal structures. J Struct Eng 134(3):499–504
20. Starossek U, Haberland M (2011) Approaches to measure of structural robustness. Struct Infrastruct Eng 7:625–631

Stochastic Frequency Analysis of Variable Stiffness Laminated Composite Beam

Narayan Sharma and Dipak Kumar Maiti

1 Introduction

The use of laminated composite structure has been increased in the modern structural application due to high specific stiffness and excellent corrosion resistance. From the past few decades, the use of straight fibers has been widely adopted in composite structures. Such laminates are known as constant stiffness composite laminates (CSCL) because the stiffness of the lamina doesn't vary in their plane. With the help of tow-placement technology, the manufacturing of curved fiber laminates has been possible. The laminate made of curved fibers is generally known as variable stiffness composite laminates (VSCL). In the recent study, researchers have been showing their interest to improve the mechanical properties of the composite structures [1]. With the use of VSCL plate, the load-carrying capacity of the structures can be improved [2]. The fundamental linear and non-linear natural frequency of symmetric laminates are slightly higher than the anti-symmetric laminates [3]. Sharma and Maiti [4] performed a comparative study of free vibration for composite laminates using constant fibers and the curvilinear fibers.

There are well-established techniques available to manufacture the laminate with curvilinear fibers. However, the uncertainty associated with the material properties and the fiber orientations cannot be ignored. There are abundant pieces of literature available which deal with the frequency analysis of a laminated plate with straight fibers, considering the uncertainty in the properties of the material. Considering the random material properties, Singh et al. [5] performed the stochastic analysis of the composite plate. In the recent study, Swain et al. [6] carried out the aeroelastic analysis considering the uncertainty in the material properties. A study is conducted to perform the layup optimization for the calculation of maximum fundamental frequency for symmetric and anti-symmetric variable stiffness laminated composite

N. Sharma (✉) · D. K. Maiti
Department of Aerospace Engineering, IIT, Kharagpur, India

D. K. Maiti et al. (eds.), *Recent Advances in Computational and Experimental Mechanics, Vol II*, Lecture Notes in Mechanical Engineering,
https://doi.org/10.1007/978-981-16-6490-8_51

plates with various boundary conditions [7]. Some researchers investigated [3, 8] the free vibration analysis of laminated plate with curved fibers considering the effect of geometric non-linearity. In ref [3], the presented results show that the fundamental linear and non-linear frequencies of symmetric laminates are slightly higher than those of anti-symmetric laminates. The flutter and divergence characteristics are analyzed by Akhavan and Ribeiro [9]. The effect of skew angle of variable stiffness laminates is performed by Houmat [10] and he found the change in curvature of normal modes and degree of hardening due to change in skew angle. S. Dey et al. [11] employed PNN model to investigate the effect of material randomness on the free vibration. A comparative study is performed by S. Dey et al. [12] on various surrogate models for the stochastic frequency analysis based on the computational efficiency and accuracy. In a recent study, Sharma et al. [13] performed the stochastic frequency analysis of variable stiffness laminated composite plate. They found that the fiber orientation is the most sensitive parameter for the fundamental frequency cantilever plate, while for other boundary conditions, such as simply supported and clamped, density showed the maximum contribution to the fundamental frequency. As far as the author's knowledge, no work has been reported so far on stochastic natural frequencies analysis of laminated beam with curvilinear fibers due to the uncertain material properties and the fiber orientations. As it is known that uncertainties within the composite structures cannot be avoided, so the study of uncertainty quantification is very important. This study explains the difference between the desired response and the actual response of the structural system. To find the influence of each input parameter on the global response of the system, sensitivity analysis is performed.

In this paper, the randomness of material properties such as $E_{11}, E_{22}, G_{12}, G_{13}, G_{23}$, υ, ρ, and the fiber orientations θ_0, θ_1 are considered. First-order shear deformation theory (FSDT) is adopted to construct a finite element model (FEM) in MATLAB environment. Variance-based global sensitivity analysis is used to describe the sensitive patterns of each input variable for the free vibration through various parametric studies. The conventionally used MCS is a cumbersome method to study the effect of randomness in the material properties on the natural frequencies, due to the requirement of large sample size. Thus, stochastic frequency analysis of VSCL beam is carried out using a polynomial neural network (PNN). The efficiency and accuracy of the PNN model are compared with those of MCS.

2 Mathematical Formulation

The path of fiber orientation of variable stiffness laminates varies linearly with x from θ_0 at the center to θ_1 at the distance a/2 from the origin as shown in Fig. 1. The orientations of the lamina are expressed as $< \theta_0 / \theta_1 >$. The path followed by the fiber 'y' and the orientation of fiber in the plane of the lamina is given as [3]

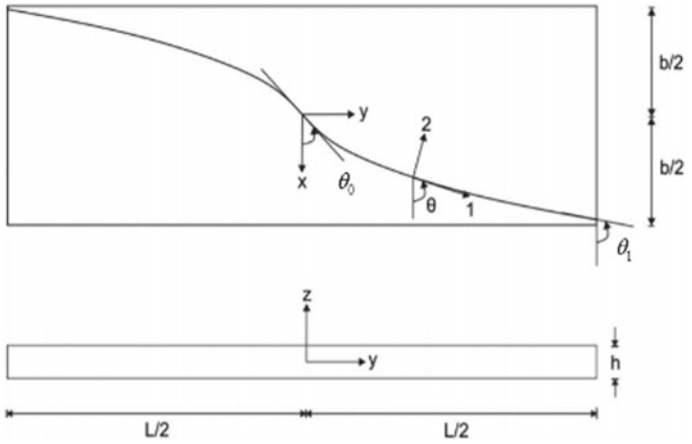

Fig. 1 Reference fiber and orientation of laminated beam with curved fiber [14]

$$y(x) = \left\{ \begin{array}{l} \frac{a}{2(\theta_1-\theta_0)}\left\{-\ln[\cos(\theta_0)] + \ln\left[\cos\left(\theta_0 - \frac{2(\theta_1-\theta_0)}{a}x\right)\right]\right\} \quad for \quad \frac{-a}{2} \le x \le 0 \\ \frac{a}{2(\theta_1-\theta_0)}\left\{-\ln[\cos(\theta_0)] - \ln\left[\cos\left(\theta_0 + \frac{2(\theta_1-\theta_0)}{a}x\right)\right]\right\} \quad for \quad 0 \le x \le \frac{a}{2} \end{array} \right\}$$

$$\theta(x) = \left\{ \begin{array}{l} \frac{-2}{a}(\theta_1 - \theta_0)x + \theta_0 \quad for \quad \frac{-a}{2} \le x \le 0 \\ \frac{2}{a}(\theta_1 - \theta_0)x + \theta_0 \quad for \quad 0 \le x \le \frac{a}{2} \end{array} \right\}$$

2.1 Free Vibration

The first-order shear deformation laminated plate theory (FSDT) is adopted to define the displacement field.

$$\begin{aligned} u(x, y, z, t) &= u_0(x, y, t) + z\theta_x(x, y, t) \\ v(x, y, z, t) &= v_0(x, y, t) + z\theta_y(x, y, t) \\ w(x, y, z, t) &= w_0(x, y, t) \end{aligned}$$

where (u_0, v_0, w_0) are the mid-plane displacements along (x, y, z) coordinate directions and θ_x, θ_y are the rotations about y- and x-axes, respectively.

The governing equation for the free vibration is obtained as

$$[M]\{\ddot{u}\} + [K]\{u\} = 0$$

where [M], [K], and {u} are the global mass matrix, stiffness matrix, and displacement vector, respectively.

2.2 Polynomial Neural Network (PNN)

The algorithm uses linear, quadratic, or any higher order polynomial. It uses the complex hidden pattern to construct the optimal structure of the network. The partial descriptive of the data is constructed which is the input of the layers. The complex pattern of layers is constructed until the optimized performance is achieved as depicted in Fig. 2. To build the optimal PNN structure, the optimal order of the polynomial is selected. The selected polynomial is a relation between the input and output data of the model and can be represented as $(x_i, y_i) = \left(x_{i1}, x_{i2}, ..., x_{im,}\ y_i\right)$.

where m denotes the number of input variables. The first layer uses all the combinations of the input parameters and creates the data of PDs. The regression coefficient of the polynomial equation is solved using the least-square method. For the computation of the second layer, the output generated from the previous layer is selected as the input variable for the next layer. The termination process is provided by the user or it stops when the model starts over-fitting the data.

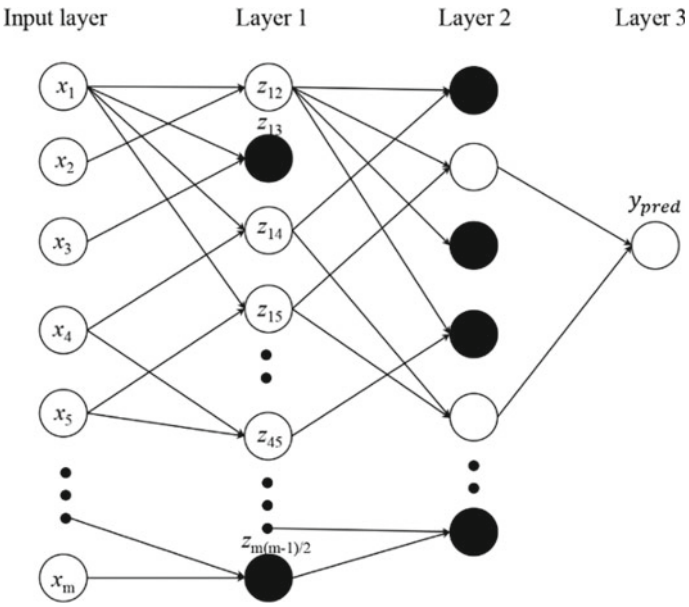

Fig. 2 Structure of polynomial neural network

Table 1 Frequency parameter $\left(\Omega = \omega L^2\sqrt{\rho h/D_0}\right)$ of beam with curvilinear fibers

Mode	BC	Layup	Ω(Present)	Ω ([12])
1	CF	$[< 90/90 >, < 90/90 >]_s$	3.436	3.510
	CC	$[< 90/90 >, < 90/90 >]_s$	20.89	22.335
	CS	$[< 90/90 >, < 90/90 >]_s$	14.696	15.392
2	CF	$[- < 90/90 >, - < 45/60 >]_s$	19.982	20.811
	CC	$[- < 85/80 >, < 65/50 >]_s$	51.373	51.881
	CS	$[- < 90/80 >, < 65/60 >]_s$	43.526	45.024

3 Results and Discussion

The finite element model is developed using eight-noded isoparametric elements in the MATLAB environment. In the case of curved fiber laminate, the stiffness coefficients are calculated at each gauss points because the stiffness coefficients vary over the surface due to fiber orientation.

3.1 Validation

A four-layered composite laminated beam with curved fiber is considered as per ref [14]. The dimensions of the beam are as follows: h/L = 0.02 and b/L = 0.1. The optimum fundamental frequency parameter of a four-layered laminated beam is calculated for various boundary conditions, such as cantilever (CF), clamped (CC), and clamped-hinged (CS). The results obtained by the developed FEM model are well matched with the published literature as shown in Table 1.

3.2 Numerical Results

A three-layered laminated beam with curvilinear fiber is considered for the free vibrational analysis. The material properties and the dimensions of the beam are as follows: b/L = 0.1, h/L = 0.01; E_{11} = 138GPa, E_{22} = 8.96GPa, G_{12} = 7.1GPa, G_{13} = 7.1GPa, G_{23} = 2.84GPa, υ_{12} = 0.3, ρ = 1600 kg/m^3. The coordinate system of a beam is taken as per ref [12]. The non-dimensional frequency $\overline{\omega} = \left(\omega L^2/h\right)\sqrt{\rho/E_2}$ of the VSCL beam for various boundary conditions is shown in Table 2.

The randomness in material properties and the fiber orientation is considered as 5% (standard deviation/mean). For the stochastic frequency analysis, the widely used Monte Carlo simulation required a large number of samples and computational cost. So, a polynomial neural network is adopted here. Firstly, the convergence of the

Table 2 Non dimensional fundamental frequency $\overline{\omega} = \left(\omega L^2/h\right)\sqrt{\rho/E_2}$ of beam with curvilinear fibers

BC	[<15/45 > , < 15/45 > , < 15/45 >]	[<30/45 > , < 30/45 > , < 30/45 >]	[<60/45 > , < 60/45 > , < 60/45 >]
CC	9.5309	11.3581	16.6553
CS	6.5437	7.8085	11.4752
CF	1.4931	1.7822	2.6211
SS	6.1291	7.1676	9.9099

Table 3 Comparison of stochastic results obtained using PNN with MCS for [<15/45 > ,- < 15/45 > , < 15/45 >] laminates

Methods	Samples	CC		CS	
		μ	σ	μ	σ
PNN	256	35.9612	1.6018	24.6784	1.0648
	512	35.9521	1.5880	24.6840	1.0641
	1024	35.9691	1.5841	24.6874	1.0710
MCS	10,000	35.9592	1.5741	24.6887	1.0782

Note μ denotes the mean and σ is the standard deviation

Table 4 Comparison of stochastic results obtained using PNN with MCS for [<15/45 > ,- < 15/45 > , < 15/45 >] laminates

Methods	Samples	CF		SS	
		μ	σ	μ	σ
PNN	256	5.6012	0.2601	23.1401	1.0745
	512	5.6324	0.2584	23.1242	1.0454
	1024	5.6326	0.2492	23.1541	1.0322
MCS	10,000	5.6334	0.2454	23.1199	1.0147

Note μ denotes the mean and σ is the standard deviation

sample for the PNN is investigated and that sample is used for further stochastic frequency and the sensitivity analysis.

From Tables 3 and 4, it is observed that PNN with 512 samples is giving efficient results compared to the MCS with 10,000 samples. A converged PNN model is used for the further analysis, which is more efficient and required less computational cost. The accuracy of the PNN model (512 samples) compared to MCS (10,000) can be seen in Fig. 3. The sensitivity of input parameters for fundamental frequency is given in Table 5. Sensitivity analysis showed that the effect of G_{13},G_{23}, and υ on natural frequency is almost negligible. So, these parameters are not considered for the pdf plot, at which the effect of individual random parameters to the fundamental natural frequency is shown in Figs. 4 and 5.

From the results, it is observed that fiber orientation is the most sensitive parameter for the fundamental natural frequency of the laminated beam with curved fibers. The second most sensitive parameter is the density of a material. This analysis is helpful to minimize the variability within the material. In the manufacturing process more care is taken for those parameters which have high sensitivity value. The difference between the desired response and the actual response can be reduced with the sensitivity analysis.

For a given lamination sequence of VSCL beam, the sensitivity of input parameters to fundamental natural frequency is showing a similar pattern for all four boundary

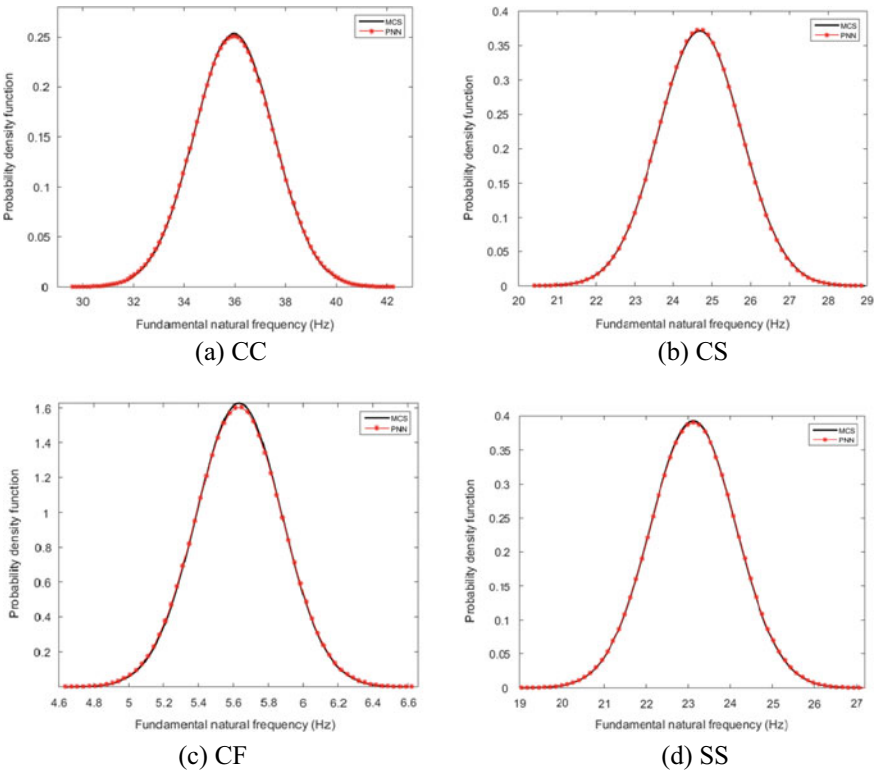

Fig. 3 Comparison of distribution curve of fundamental frequency obtained using PNN and MCS for [<15/45 > ,- < 15/45 > , < 15/45 >] lamination sequence with various boundary conditions

Table 5 Sensitivity (%) of input parameters of [<15/45 > ,- < 15/45 > , < 15/45 >] laminated beam for fundamental natural frequency

Parameters	CC	CS	CF	SS
E_{11}	3.8824	3.7798	3.7881	4.6461
E_{22}	3.8219	3.9501	3.9494	3.1708
G_{12}	2.0397	2.0890	2.0911	1.7979
G_{13}	0.0475	0.0492	0.0477	0.0773
G_{23}	0.0229	0.0239	0.0226	0.0246
υ	0.0861	0.0870	0.0871	0.075
ρ	33.7942	34.1564	34.1018	33.659
θ_0	2.9599	3.0388	3.0422	2.4465
θ_1	53.3454	52.8258	52.87	54.1028

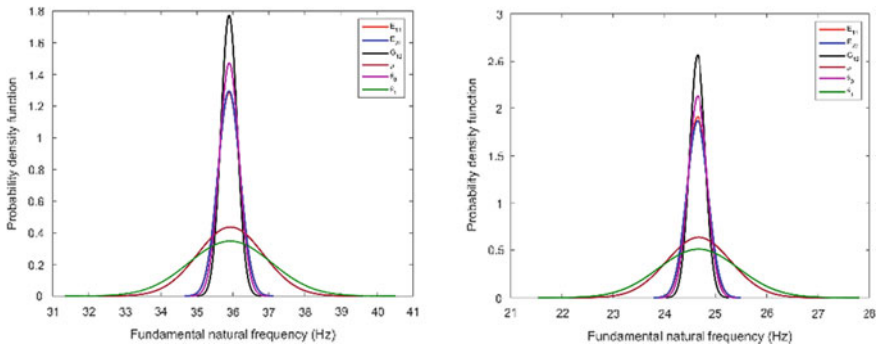

(a) CC (b) CS

Fig. 4 PDF plot of stochastic input parameters of [<15/45 > ,- < 15/45 > , < 15/45 >] laminated beam for fundamental natural frequency

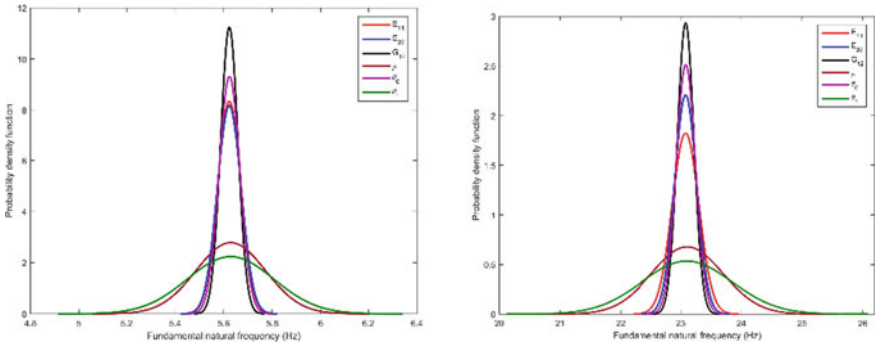

(a) CF (b) SS

Fig. 5 PDF plot of stochastic input parameters of [<15/45 > ,- < 15/45 > , < 15/45 >] laminated beam for fundamental natural frequency

conditions. The sensitivity analysis are extended for two more lamination sequences as shown in Tables 6 and 7.

The obtained results reveal that the sensitivity of input parameters is significantly changed with the lamination sequences as presented in Figs. 5, 6, and 7. From Table 8, it is observed that, for the same randomness in material properties and the fiber orientations, the lamination sequence [<60/45 > ,- < 60/45 > , < 60/45 >] is having a greater effect on fundamental natural frequency than other two lamination sequences.

Table 6 Sensitivity (%) of input parameters of [<30/45 > ,- < 30/45 > , < 30/45 >] laminated beam for fundamental natural frequency

Parameters	CC	CS	CF	SS
E_{11}	7.5213	7.4522	7.4738	8.4571
E_{22}	1.1303	1.1587	1.1579	0.9381
G_{12}	1.5519	1.5764	1.5772	1.3454
G_{13}	0.0412	0.042	0.0399	0.075
G_{23}	0.0123	0.0124	0.0114	0.0151
υ	0.0709	0.0713	0.0713	0.0611
ρ	28.8349	28.9738	28.9077	29.5791
θ_0	17.2104	17.5338	17.5561	13.5147
θ_1	43.6268	43.1795	43.2047	46.0145

Table 7 Sensitivity (%) of input parameters of [<60/45 > ,- < 60/45 > , < 60/45 >] laminated beam for fundamental natural frequency

Parameters	CC	CS	CF	SS
E_{11}	14.771	14.7544	14.8233	16.2314
E_{22}	0.0812	0.0825	0.0823	0.0755
G_{12}	0.3006	0.3016	0.301	0.2938
G_{13}	0.0289	0.0275	0.0242	0.0714
G_{23}	0.0055	0.0052	0.0043	0.012
υ	0.0216	0.0215	0.0216	0.0204
ρ	25.2997	25.2418	25.1595	28.4851
θ_0	42.5027	42.8202	42.848	32.5971
θ_1	16.9887	16.7452	16.7358	22.2134

4 Conclusion

The following conclusions are drawn from this research work:

- The use of VSCL beam is very helpful to adjust the natural frequencies and the mode shape of the beam.
- For the stochastic and sensitivity analysis, the PNN method is more efficient than MCS.
- Fiber orientation is the most sensitive parameter for the fundamental natural frequency.
- For a given lamination sequence, the sensitivity patterns of the input parameters to the fundamental natural frequency are almost the same for all boundary conditions.

The use of curvilinear fibers in a laminated beam provides more flexibility to adjust the natural frequencies and difference between the two modes of frequency. These

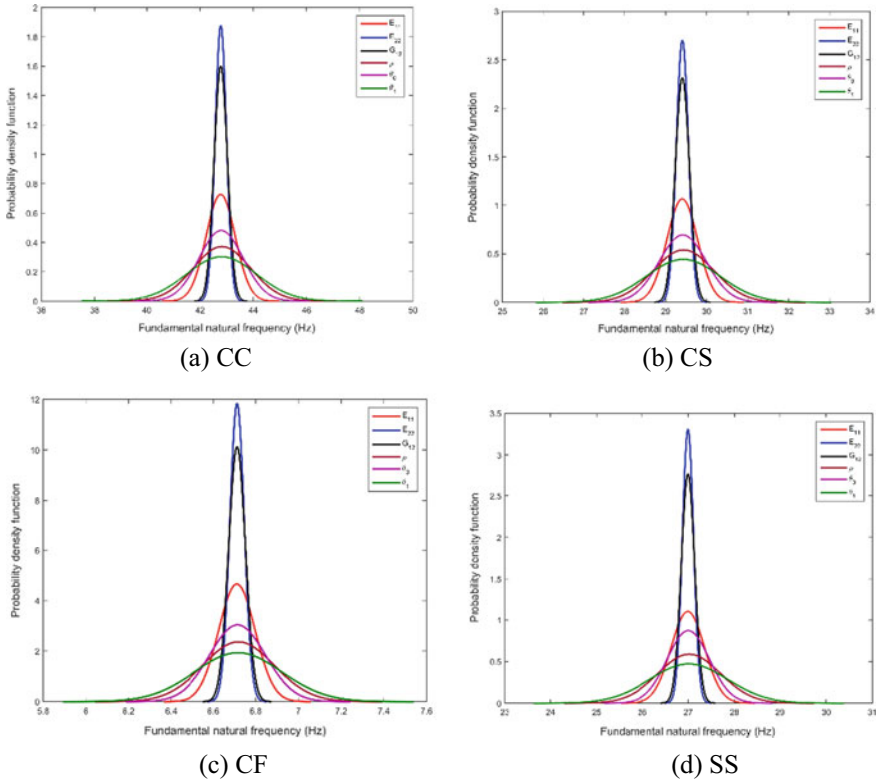

Fig. 6 PDF plot of stochastic input parameters of [<30/45 > ,- < 30/45 > , < 30/45 >] laminated beam for fundamental natural frequency

benefits are enhancing the use of curved fiber in many structural applications. This can also be useful to alter the mode shapes of the beam in a favorable manner. Mode shape adjustment can be very beneficial in the aerospace industry for the dynamic aeroelasticity problems where the mode shape are the important factors.

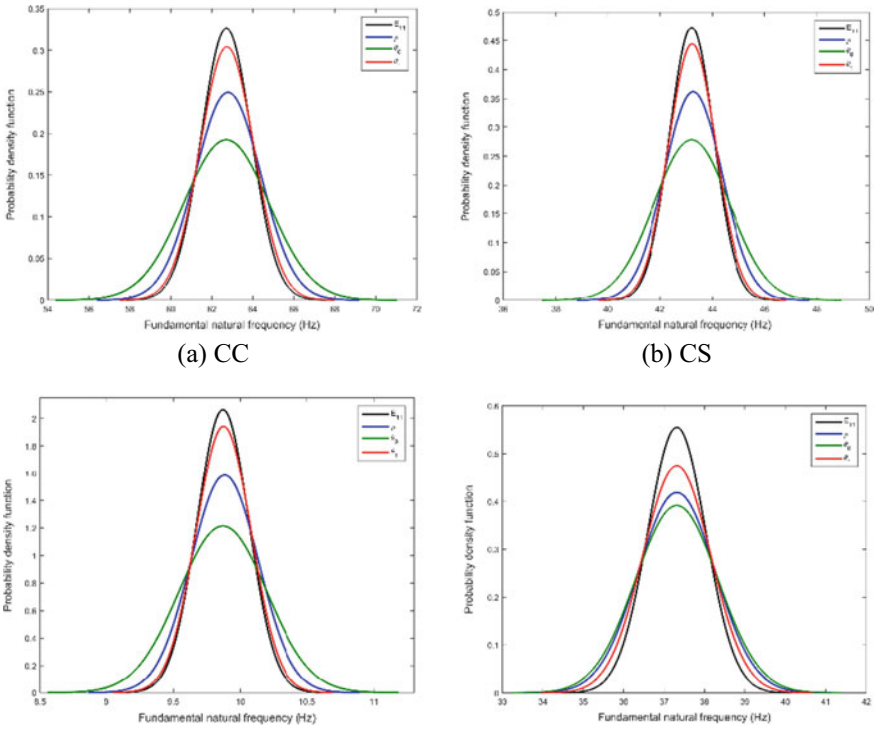

Fig. 7 PDF plot of stochastic input parameters of [<60/45 > ,- < 60/45 > , < 60/45 >] laminated beam for fundamental natural frequency

Table 8 Stochastic fundamental frequency of laminated beam for fundamental natural frequency

BC	[<30/45 > ,- < 30/45 > , < 30/45 >]		[<60/45 > ,- < 60/45 > , < 60/45 >]	
	μ	σ	μ	σ
CC	42.8482	2.0373	62.7654	3.1727
CS	29.4576	1.3975	43.2441	2.1887
CF	6.7234	0.3193	9.8777	0.5008
SS	27.032	1.2671	37.336	1.7731

References

1. Ribeiro P, Akhavan H, Teter A, Warmiński J (2014) A review on the mechanical behaviour of curvilinear fibre composite laminated panels. J Compos Mater 48(22):2761–2777
2. Hyer MW, Charette RF (1991) Use of curvilinear fiber format in composite structure design. AIAA J 29(6):1011–1015
3. Houmat A (2013) Nonlinear free vibration of laminated composite rectangular plates with curvilinear fibers. Compos Struct 106:211–224

4. Narayan Sharma, Dipak Kumar Maiti (2020) A comparative study of stochastic frequency analysis of variable stiffness and constant stiffness laminated composite plate. Proceedings of International conference, AeSI-2020 on Aviation Technology-current scenario
5. Singh BN, Yadav D, Iyengar NGR (2001) Natural frequencies of composite plates with random material properties using higher-order shear deformation theory. Int J Mech Sci 43(10):2193–2214
6. Swain PK, Sharma N, Maiti DK, Singh BN (2020) Aeroelastic analysis of laminated composite plate with material uncertainty. J Aerosp Eng 33(1):04019111
7. Houmat A (2018) Optimal lay-up design of variable stiffness laminated composite plates by a layer-wise optimization technique. Eng Optim 50(2):205–217
8. Ribeiro P (2015) Non-linear modes of vibration of thin cylindrical shells in composite laminates with curvilinear fibres. Compos Struct 122:184–197
9. Ganapathi M, Venkatachari A, Haboussi M, Mathew AT (2018) Nonlinear free flexural vibration of curvilinear fibre composite laminates using a higher-order element. Int J Struct Stab Dyn 18(12):1850147
10. Akhavan H, Ribeiro P (2018) Aeroelasticity of composite plates with curvilinear fibres in supersonic flow. Compos Struct 194:335–344
11. Houmat A (2015) Nonlinear free vibration analysis of variable stiffness symmetric skew laminates. Eur J Mechan A/Sol 50:70–75
12. Dey S, Naskar S, Mukhopadhyay T, Gohs U, Spickenheuer A, Bittrich L, Sriramula S, Adhikari S, Heinrich G (2016) Uncertain natural frequency analysis of composite plates including effect of noise–A polynomial neural network approach. Compos Struct 143:130–142
13. Dey S, Mukhopadhyay T, Adhikari S (2017) Metamodel based high-fidelity stochastic analysis of composite laminates: a concise review with critical comparative assessment. Compos Struct 171:227–250
14. Sharma N, Swain PK, Maiti DK, Singh BN (2020) Stochastic frequency analysis of laminated composite plate with curvilinear fiber. Mechanics of Advanced Materials and Structures, pp.1–16
15. Meskine A, Houmat A, Guenanou A (2020) A layer-wise optimization method for the optimal stacking sequence design of symmetric VSCL beams in air and in water. Mechanics of Advanced Materials and Structures, pp.1–12

Vibration Control of Duffing Oscillator by Passive and Active Control with Time-Delayed Linear and Nonlinear Acceleration Feedback

Saikat Suvra Mondal, Ranjan Kumar Mitra, and Atul Krishna Banik

1 Introduction

Harmonically forced Duffing oscillator exhibits complex behavior of quasi-periodic responses, bifurcations, jump phenomena, chaos, and also nonlinear resonances. The primary resonance of an externally excited nonlinear dynamic system occurs when the forcing frequency is in the neighborhood of the linearized natural frequency. Linear vibration absorber can suppress the large-amplitude resonant vibrations of the primary system by shifting its resonating frequency [1] and makes the system as a two-degree-of-freedom system with two resonant frequencies. Several researchers [2, 3] studied the effect of linear vibration absorber in suppression of the primary resonance vibrations of the weakly nonlinear system under harmonic excitation. The nonlinear vibration absorber may introduce dynamic instabilities and other complex dynamical phenomena, including much higher amplitudes, one-to-two internal resonance conditions [4]. In the recent past, time-delayed linear and nonlinear feedback control has been successfully used to suppress the nonlinear resonant vibrations of the external excited weakly nonlinear systems [5]. Mitra et al. [6] investigated the effect of time-delayed linear and nonlinear acceleration feedback on the Duffing oscillator under mono-harmonic excitation. Eissa and Sayed [7] controlled the response of a nonlinear pendulum in both longitudinal and transverse directions by using tuned absorber and negative velocity feedback.

S. S. Mondal (✉) · A. K. Banik
Department of Civil Engineering, NIT, Durgapur, India

A. K. Banik
e-mail: atul.banik@ce.nitdgp.ac.in

R. K. Mitra
Department of Mechanical Engineering, NIT, Durgapur, India
e-mail: ranjankumar.mitra@me.nitdgp.ac.in

D. K. Maiti et al. (eds.), *Recent Advances in Computational and Experimental Mechanics, Vol II*, Lecture Notes in Mechanical Engineering,
https://doi.org/10.1007/978-981-16-6490-8_52

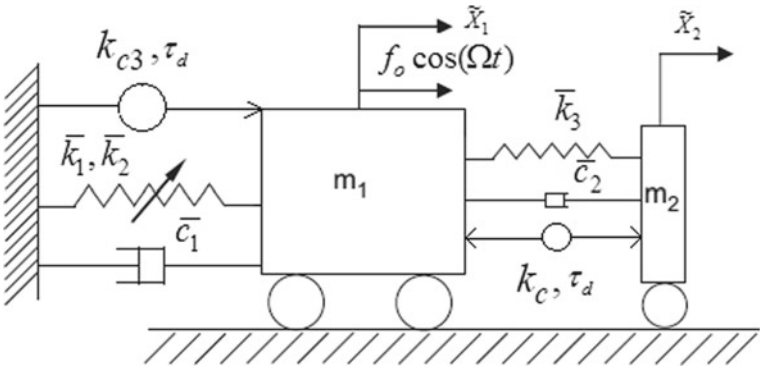

Fig. 1 Duffing oscillator under passive and active control

In the present study, the nonlinear vibrations of a mono-harmonically forced Duffing oscillator is considered for vibration control under passive and active control schemes. The passive controller attached with the primary system acts as secondary system and linear in nature, whereas the active control technique employs both linear and nonlinear time-delayed acceleration feedback with the primary system and linear acceleration feedback scheme with the absorber system. Figure 1 represents the schematic diagram of the control techniques.

Method of slowly varying parameter (SVP) is employed to draw the complete period-1 frequency response graphs both for uncontrolled and controlled systems. The stability of solutions is examined by using Routh–Hurwitz criterion. Appropriate sets of control parameters are chosen from the linear stability study of the oscillator. Some of the results obtained by SVP method are compared with Runge–Kutta fourth-order numerical integration method (NI) in Matlab/Simulink environment.

2 Mathematical Model and Equation of Motion

The mathematical model of the mono-harmonically forced Duffing oscillator under passive and active control techniques is shown in Fig. 1. The dimensional equation of motion of the said system is expressed by Eq. 2.1.$\bar{k}_1, \bar{k}_2$, and $\bar{c}_1$ denote the linear, nonlinear spring stiffness, and damping coefficient, respectively, for the primary system of mass m_1. The periodic excitation force $f_0 \cos(\Omega t)$ is acting on the primary system. f_0 and Ω are the forcing amplitude and forcing frequency, respectively. The absorber system consists of mass m_2, linear stiffness $\bar{k}_3$, and damping coefficient $\bar{c}_2$. $\tilde{X}_1$ and $\tilde{X}_2$ denote the displacement responses of the primary and absorber system, respectively. An over dot indicates the differentiation with respect to time t. $\ddot{\tilde{x}}_1(t-\tau_d)$ and $\ddot{\tilde{x}}_1^3(t-\tau_d)$ represent the active control signal due to linear and nonlinear time-delayed acceleration feedback, respectively; k_{c3} and k_c are corresponding dimensional control gains. The dimensional time-delay is represented by

τ_d.

$$
\begin{aligned}
&m_1\ddot{\tilde{X}}_1 + \bar{k}_1\tilde{X}_1 + \bar{k}_2\tilde{X}_1^3 + \bar{c}_1\dot{\tilde{X}}_1 + \bar{k}_3(\tilde{X}_1 - \tilde{X}_2) + \bar{c}_2(\dot{\tilde{X}}_1 - \dot{\tilde{X}}_2) = \\
&f_o\cos(\Omega t) + k_c\ddot{\tilde{X}}_1(t-\tau_d) + k_{c3}\ddot{\tilde{X}}_1^3(t-\tau_d) \\
&m_2\ddot{\tilde{X}}_2 + \bar{k}_3(\tilde{X}_2 - \tilde{X}_1) + \bar{c}_2(\dot{\tilde{X}}_2 - \dot{\tilde{X}}_1) = -k_c\ddot{\tilde{X}}_1(t-\tau_d)
\end{aligned} \tag{2.1}
$$

The non-dimensional form of Eq. (2.1) is recast as

$$
\begin{aligned}
&\ddot{x}_1 + \omega_1^2 x_1 + \alpha x_1^3 + \mu_1\dot{x}_1 - m\omega_2^2 x_2 - m\mu_2\dot{x}_2 \\
&= f\cos(\Omega t) + g\ddot{x}_1(t-\tau) + g_3\ddot{x}_1^3(t-\tau) \\
&\ddot{x}_2 + \omega_2^2(x_2 - x_1) + \mu_2(\dot{x}_2 - \dot{x}_1) = -g\ddot{x}_1(t-\tau)
\end{aligned} \tag{2.2}
$$

where $m = m_2/m_1, \mu_1 = (\bar{c}_1 + \bar{c}_2)/m_1 = \mu_{10} + m\mu_2, \omega_1^2 = (\bar{k}_1 + \bar{k}_3)/m_1 = \omega_{10}^2 + m\omega_2^2\,\omega_2^2 = \bar{k}_3/m_2, \alpha = \bar{k}_2/m_1$, $f = f_0/m_1$, $\mu_{10} = \bar{c}_1/m_1$, $\omega_{10}^2 = \bar{k}_1/m_1$, $g = k_c/m_1$, $g_3 = k_{c3}/m_1$. Here, parameters μ_{10} and ω_{10} denote the damping coefficient and linearized natural frequency of the weakly nonlinear oscillator alone. m represents the mass ratio. $\ddot{x}_1(t-\tau)$ and $\ddot{x}_1^3(t-\tau)$ are the dimensionless control singles due to time-delayed linear and nonlinear acceleration feedback, respectively; g and g_3 are the corresponding gains.τ is the non-dimensional time-delay parameter.

3 Frequency Response Analysis

The steady-state frequency responses of the proposed system under primary resonance condition are obtained by employing the slowly varying parameter (SVP) method. The first-order approximation for the steady-state solutions of Eq. (2.2) is assumed as

$$
x_j = c_j(t)\cos(\Omega t) + d_j(t)\sin(\Omega t) \qquad j = 1, 2 \tag{3.1}
$$

where $c_j(t)$ and $d_j(t)$ are the slowly varying function of time t such that one can neglect the terms: $\ddot{c}_j, \ddot{d}_j, \dot{c}_j\dot{d}_j$. Differentiating Eq. (3.1) with respect to t, yield.

$$
\dot{x}_j = (\dot{c}_j + \Omega d_j)\cos(\Omega t) + (\dot{d}_j - \Omega c_j)\sin(\Omega t) \tag{3.2}
$$

Differentiating Eq. (3.2) with respect t yields the acceleration as

$$
\ddot{x}_j = (-\Omega^2 c_j + 2\Omega\dot{d}_j)\cos(\Omega t) - (\Omega^2 d_j + 2\Omega\dot{c}_j)\sin(\Omega t) \tag{3.3}
$$

From Eq. (3.1), x_1^3 is calculates as

$$x_1^3 = \frac{3}{4}c_1(c_1^2 + d_1^2)\cos(\Omega t) + \frac{3}{4}d_1(c_1^2 + d_1^2)\sin(\Omega t) \tag{3.4}$$

Next, the time-delay term reduces to

$$\ddot{x}_1(t-\tau) = \{(2\Omega\dot{c}_1 + \Omega^2 d_1)\sin(\Omega\tau) + (2\dot{d}_1\Omega - \Omega^2 c_1)\cos(\Omega\tau)\}\cos(\Omega t) + \{(2\dot{d}_1\Omega - c_1\Omega^2)\sin(\Omega\tau) - (2\dot{c}_1 + d_1\Omega)\cos(\Omega\tau)\}\sin(\Omega t) \tag{3.5}$$

Let P and Q represent the coefficient of $\cos(\Omega t)$ and $\sin(\Omega t)$, respectively. Hence,$\ddot{x}_1^3(t-\tau)$ reduces to,

$\ddot{x}_1^3(t-\tau) = \frac{3}{4}(PQ^2 + P^3)\cos(\Omega t) + \frac{3}{4}(Q^3 + P^2 Q)\sin(\Omega t) +$ higher harmonic (3.6).

Substituting the Eqns. (3.1–3.6) in Eq. (2.2) and ignoring the higher order harmonic terms, the coefficients of $\sin(\Omega t)$ and $\cos(\Omega t)$ are separately matched, one can obtained the following equation, written in matrix form:

$$\begin{bmatrix} L_{11} & \cdots & L_{14} \\ \vdots & \ddots & \vdots \\ L_{41} & \cdots & L_{44} \end{bmatrix}_{(4\times4)} \begin{bmatrix} \dot{c}_1 & \dot{d}_1 & \dot{c}_2 & \dot{d}_2 \end{bmatrix}^T_{(1\times4)} = \begin{bmatrix} R_{11} & R_{21} & R_{31} & R_{41} \end{bmatrix}^T_{(1\times4)} \tag{3.7}$$

where L_{n1}, L_{n2}, L_{n3}, L_{n4}, and R_{n1} ($n \subset 1...4$) are all functions of c_1, d_1, c_2, d_2 and system parameters. Their expression are not shown to maintain brevity.

$A_1(=\sqrt{c_1^2 + d_1^2})$ and $A_2(=\sqrt{c_2^2 + d_2^2})$ denote the amplitude of primary system and absorber, respectively. The steady-state solutions of the slow-flow equations are obtained by setting $\dot{c}_1 = \dot{d}_1 = \dot{c}_2 = \dot{d}_2 = 0$ in the Eq. (3.7). The steady-state solutions obtained from Eq. (3.7), are solved simultaneously to obtain the closed-form solutions of steady-state amplitude of vibration A_1 and A_2. Hence, for $R_{31} = 0$ and $R_{41} = 0$, the amplitude of the absorber can be expressed by the following equation:

$$A_2^2 = ((\omega_2^2 + \Omega^2 g\cos(\omega\tau))^2 + (\Omega\mu_2 - \Omega^2 g\sin(\omega\tau))^2 / ((\Omega^2 - \omega_2^2)^2 + (\mu_2\Omega)^2)A_1^2 \tag{3.8}$$

Substituting the Eq. (3.8) to the expression of $R_{11} = 0$ and $R_{21} = 0$ and performing some mathematical operations yields

$$C_1 A_1^{10} + C_2 A_1^8 + C_3 A_1^6 + C_4 A_1^4 + C_5 A_1^2 + C_6 = 0 \tag{3.9}$$

Here,C_1–C_6 all are constant and calculated from the system parameters (not shown here). The real roots of the A_1 give the amplitude of the primary system. After solving A_1 and A_2, the Jacobian of the functions $\dot{c}_1$, $\dot{d}_1$, $\dot{c}_2$, and $\dot{d}_2$ at a solution points (a_{10}, b_{10}, a_{20}, b_{20}) are evaluated. When all the real parts of eigenvalues of the Jacobian

matrix are positive, then the respective solution become unstable; otherwise, the solution become stable.

4 Linear Stability Analysis

In a close-loop control system, instability of the system may occur due to improper selection of control gain and delay. By the linear stability analysis, appropriate gain and delay values are selected from the primary stability zone of the linear stability chart under time-delayed acceleration feedback. The Laplace transform of the linear part of Eq. (2.2) yields the following characteristic equation:

$$\hat{U}(s) + \hat{V}(s)e^{-s\tau} = 0 \tag{4.1}$$

where both $\hat{U}(s)$ and $\hat{V}(s)$ are polynomial equation of complex variable s and also function of system parameters and g. Their expression are not shown here to maintain brevity. The Hopf bifurcation occurs for the critical values of control parameters, and the roots of the Eq. (4.1) become a pair of pure imaginary quantity. Substituting $s = i\varpi$ into characteristic Eq. (4.1) and separating real and imaginary part yields

$$A_0 \cos(\varpi\tau) + B_0 \sin(\varpi\tau) = C_0 \tag{4.2}$$

$$B_0 \cos(\varpi\tau) - A_0 \sin(\varpi\tau) = D_0 \tag{4.3}$$

where A_0, B_0, C_0, and D_0 all are the function of g, ϖ and all other system parameters. Eliminating τ from Eqs. (4.2) and (4.3), the following polynomial equation of ϖ can be obtained:

$$P_1\varpi^8 + P_2\varpi^6 + P_3\varpi^4 + P_4\varpi^2 + P_5 = 0 \tag{4.4}$$

where P_1–P_5 are functions of system and absorber parameters and their expression are not shown here shown to maintain brevity. Substituting the real positive or trivial roots (ϖ_c) of Eq. (4.4) into Eqs. (4.2) and (4.3), the critical values of the time-delay τ_c are obtained as

$$\begin{aligned} \tau_c = &\left(2n\pi + \tan^{-1}((A_0C_0 + B_0D_0)/(A_0D_0 + B_0C_0))\right) \\ &/\varpi_c, \forall n = 0, 1, 2, ..., \infty \end{aligned} \tag{4.5}$$

The crossing velocity of the complex conjugate eigenvalues at the stability boundary at (ϖ_c, τ_c) is computed as

$$\overline{V}(\varpi_c, \tau_c) = \mathrm{Re}\left(ds/d\tau \big|_{s=i\varpi_c, \tau=\tau_c} \right) \tag{4.6}$$

The stability characteristic of the equilibrium switches from stable to unstable if $\overline{V}(\varpi_c, \tau_c) > 0$ and vice versa, when τ increases to past τ_c. When $\overline{V} = 0$, the eigenvalues cannot cross the imaginary axis and the corresponding critical values are ignored for the computation of the stability boundaries. Using Eqs. (4.4)–(4.6), the local stability boundaries can be computed for any value of system and absorber parameters.

5 Results and Discussion

The efficacy of the passive and active techniques for suppressing the nonlinear vibrations of the mono-harmonically forced Duffing oscillator under primary resonance conditions is studied by employing SVP method. The passive absorber is first employed to study the role of absorber stiffness and damping coefficient for suppressing the primary system responses. The set of absorber parameters that produces maximum suppression of peak response of the primary system are considered for further study under combined proposed active control techniques. Numerical investigations are performed for: $\mu_{10} = 0.1$, $\omega_{10} = 1.0$, $\alpha = 0.05$, and $f = 1.0$, unless otherwise specified.

5.1 Uncontrolled Response

Frequency–response plot of the uncontrolled primary system for the primary resonance condition is shown in Fig. 2. The horizontal axis represents the interval of forcing frequency $\Omega \in [0, 2.5]$ rad/s. It is seen that stiffness nonlinearity is responsible for the skewness of response graph. Multiple solutions exists toward a higher frequency range. The dotted lines represent the stable solutions, whereas the unstable solutions are represented by 'o' marks. The peak amplitude is 6.32 m and it occurs at $\Omega = 1.58$ rad/s. In this frequency–response curve, the unstable branch of solutions exist in between the forcing frequency range 1.27 rad/s and 1.58 rad/s. The stable solutions obtained from numerical integration (NI) are shown by ' + ' marks. A good agreement of results obtained by SVP and NI are observed.

5.2 Controlled Response

In this section, at first, the uncontrolled frequency responses shown in Fig. 2 are investigated for vibration control.

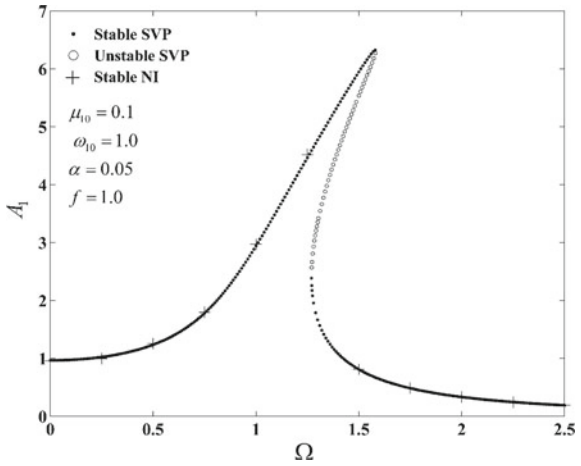

Fig. 2 The frequency–response plots for primary resonance response of the nonlinear primary system

Effect of passive Control. The role of absorber stiffness and damping parameters in suppressing the period-1 frequency–response of the primary system is depicted in Fig. 3a–d. Figure 3a, b, c show the controlled responses with damping coefficient

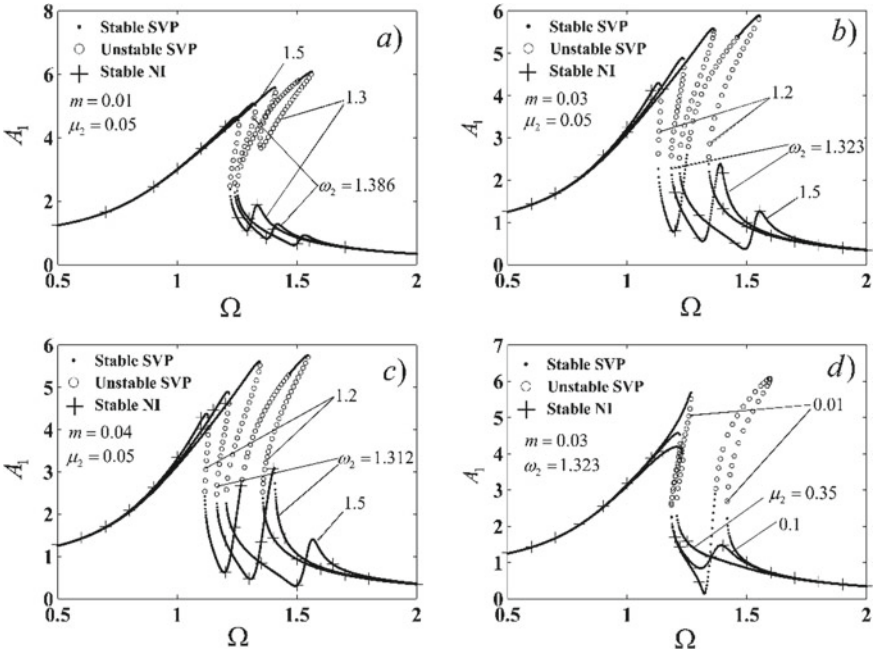

Fig. 3 The controlled period-1 frequency–response plots of the primary system with attached absorber under different ω_2 for mass ratio **a** $m = 0.01$, **b** $m = 0.03$, **c** $m = 0.04$; **d** different values of μ_2

$\mu_2 = 0.05$ Ns/m and varying absorber stiffness in terms of natural frequency ω_2 for the mass ratio $m = 0.01$, 0.03 and 0.04, respectively. In Fig. 3a, it is observed that a limit cycle oscillation has started at $\Omega = 1.345$ rad/s for $\omega_2 = 1.3$ rad/s and it disappeared at $\omega_2 = 1.386$ rad/s. Further, from Fig. 3a, it is seen that the maximum suppression amplitude of the nonlinear primary system has occurred at $\omega_2 = 1.386$ red/s and further an increase in ω_2 will increase the peak amplitude response plot. Comparing Fig. 3a to c, it is seen that for the primary system, the maximum suppression of the peak amplitude occurs with $m = 0.03$ and $\omega_2 = 1.323$ red/s. This set of system parameters indicates that the mass ratio m is 3% only and the coupling stiffness is approximately 5.25% of the linear stiffness of the nonlinear primary system.

After the attachment of the passive absorber with parameters $m = 0.03$ and $\omega_2 = 1.323$ rad/s, the linearized natural frequency of the primary system is found to be $\omega_1 = 1.025$ rad/s, which indicate a slight changes in ω_{10}, only at approximately 2.43%. Figure 3d shows the frequency–response curves of the primary system with attached absorber parameters $m = 0.03$,$\omega_2 = 1.323$ rad/s and varying damping coefficient. Frequency–response of the primary system are obtained for $m = 0.03$,$\omega_2 = 1.323$ rad/s and different values of μ_2 and are shown in Fig. 3d. An increase of μ_2 values leads to a considerable reduction of the maximum responses of the primary system at its resonant frequencies.

Effect of Active and Passive Control. In this section, the effects of linear and nonlinear acceleration feedback on the system response (both the primary system and the absorber) are discussed. The frequency–response curve of the primary system (shown in Fig. 3d) controlled by using an absorber with absorber mass ratio $m = 0.03$, natural frequency $\omega_2 = 1.323$, and damping coefficient $\mu_2 = 0.1$, is considered for active vibration control. Appropriate values of gain and delay parameters are chosen from the *'primary stability zone'* of linear stability chart, shown in Fig. 4. Time-

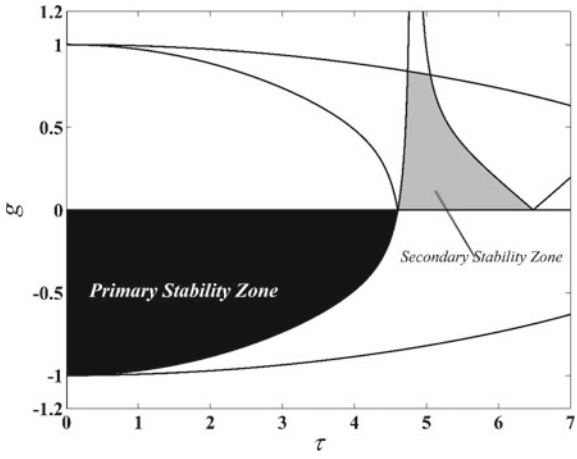

Fig. 4 Linear stability charts under time-delayed acceleration feedback

delayed negative acceleration feedback is observed to be most effective in amplitude suppression.

Following two cases are consider separately for describing the effect of active vibration control, i.e., linear acceleration feedback ($g \neq 0$, $g_3 = 0$) and linear plus nonlinear acceleration feedback ($g \neq 0$, $g_3 \neq 0$).

Linear feedback control ($g \neq 0$, $g_3 = 0$). The effect of variation in g at $g_3 = 0$ with $\tau = 1.5$ on the responses of the primary system and the absorber system are depicted in Fig. 5a and b, respectively. The previously controlled peak response of the primary system has been suppressed to 2.457 m at 1.00 rad/s, whereas for the absorber the maximum peak amplitude become 9.848 m at 1.32 rad/s on selecting $g = -0.3$ and $\tau = 1.5$, respectively. Higher values of g results in entrainments of higher amplitude but the attenuation of the second peak of the absorber amplitude is slightly affected by the linear acceleration feedback. Further, from Figs. 5a and b, it is seen that the branch of unstable solution can be eliminated on selecting $g = -0.3$ and $\tau = 1.5$.

Linear plus nonlinear feedback control ($g \neq 0$, $g_3 \neq 0$).The effect of variation in g_3 at $g = -0.05$ with $\tau = 1.5$ on the frequency–response of the primary and absorber system are shown in Fig. 6a and b, respectively. From Fig. 6a and b, it is observed that by the application of a very small value of g_3 ($= -0.005$) with $g = -0.05$, a better stability condition of the (primary and absorber) system response can be achieved throughout the entire frequency range. Further, it is seen that on selecting both g and g_3 equal to -0.05 and $\tau = 1.5$ the response amplitude of the absorber and primary system has been suppressed 11.02 m at 1.33 rad/s and to 2.514 m at 0.959 rad/s, respectively. From Fig. 6b, it is observed that with increase in g_3 values, the response of the absorber at the first peak is reduced rapidly but corresponding response in the second peak reduced with very slow rate. The second peak of the absorber can be suppressed by increasing the damping coefficient of the absorber as shown in Fig. 3d.

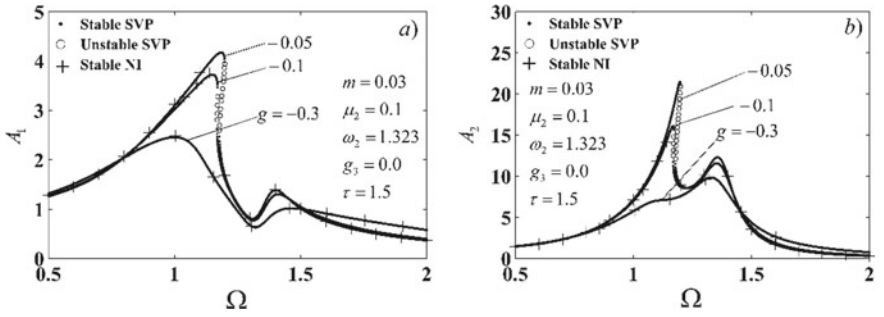

Fig. 5 The controlled period-1 frequency–response plots of the **a** primary system and **b** absorber under different values of g

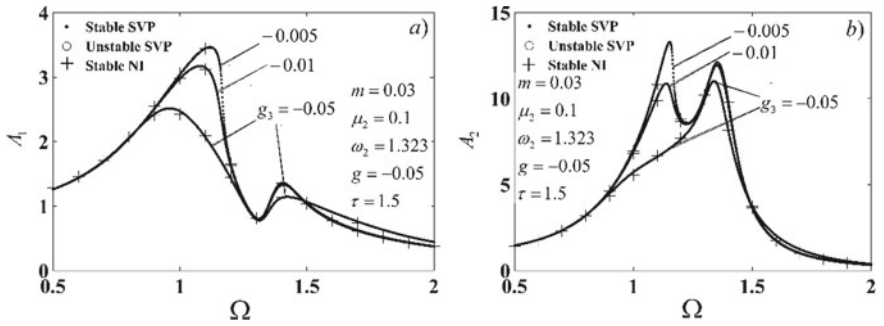

Fig. 6 The controlled frequency–response plots for primary resonance response of **a** the nonlinear primary system and **b** absorber under different values of g_3

Table 1 Comparison of amplitudes calculated by NS and SVP with system parameters $\mu_{10} = 0.1$, $\omega_{10} = 1.0$, $\alpha = 0.05$, and $f = 1.0$

Control Parameters		Ω rad/s	Amplitude (A_1) in m		% error
Passive	Active		SVP	NI	
$m = 0.03, \omega_2 = 1.323, \mu_2 = 0.05$	$g = 0, g_3 = 0, \tau = 1.5$	1.178	4.4880	4.5512	1.388
		1.322	0.57640	0.57658	0.031
$m = 0.03, \omega_2 = 1.323, \mu_2 = 0.1$	$g = -0.3, g_3 = 0, \tau = 1.5$	1.023	2.4450	2.46756	0.914
		1.333	0.6461	0.64743	0.205
	$g = -0.05, g_3 = -0.05, \tau = 1.5$	0.964	2.514	2.45599	2.361
		1.312	0.7774	0.77690	0.064

5.3 Comparison of Results

Uncontrolled and controlled amplitudes obtained by SVP and NI method at some discrete frequency are compared in Table 1. From Table 1, it is seen that a good agreement exists in between results obtained by SVP and NI.

6 Conclusion

The mono-harmonically forced Duffing oscillator with passive and active vibration absorbers is investigated in the frequency domain by SVP method. The active control technique utilizes both the linear and nonlinear time-delayed acceleration feedback. The effect of passive and active control parameters on vibration control are examined.

Following are the conclusions of the study:

- The SVP method efficiently traces the entire frequency response graphs of all possible stable and unstable solutions for both the uncontrolled and controlled

oscillator. Comparison of results obtained by SVP and NI methods reveals that they are in good agreement.

- The primary system attached with passive absorber exhibits entrainment phenomena for $m = 0.01$ and $\omega_2 = 1.3$ rad/s (Fig. 3a), which indicates the existence of limit cycles in the corresponding free oscillation.
- A considerable suppression of peak amplitude of the primary system attached with passive absorber occurs for the absorber parameters $m = 0.03$, $\omega_2 = 1.323$ rad/s, and $\mu_2 = 0.05$ Ns/m (Fig. 3b).
- An increase of the absorber damping leads to a considerable reduction of the maximum responses of both systems at their resonant frequencies but has a greater signification on the reduction of the second peak amplitude of the absorber.
- Time-delayed negative acceleration feedback is observed to be the most effective in amplitude suppression and also it is easier to implement.
- A considerable reduction in the peak value of the responses of both the primary and the absorber system can be achieved by using linear time-delayed acceleration feedback. It also reduces the unstable branches of solution.
- In the case of nonlinear acceleration feedback along with the linear one, a batter suppression of the peak value of the responses can be achieved by keeping small values of the control gain (g and g_3).
- A good agreement exists between the SVP method's solutions and numerical integration (NI). For the primary resonance response, the first-order approximation made in the SVP method is sufficient. An additional term of the second-order or higher order should include the approximate solution for a more accurate result.

References

1. Den Hartog JP (1985) Mechanical Vibrations, Dover publications
2. Ji JC, Zhang N (2010) Suppression of the primary resonance vibrations of a forced nonlinear system using a dynamic vibrationa absorber. J Sound Vib 329:2044–2056
3. Korenev BG, Reznikov LM (1993) Dynamic vibration absorbers. Wiley, NewYork
4. Djemal F, Chaari F, Dion J-L, Renaud F, Tawfiq I, Haddar M (2014) Performance of a non linear dynamic vibration absorbers. J Mech 31(03):345–353
5. Ji JC (2001) Local bifurcation control of a forced single-degree-of-freedom nonlinear system: saddle-node bifurcation. Nonlinear Dyn 25:369–382
6. Ranjan Kumar Mitra, Atul Krishna Banik, Shymal Chatterjee (2014) Vibration control by time delayed linear and non-linear acceleration feedback. Appl Mechan Mater 592–594:2107–2111
7. Eissa M, Sayed M (2006) A comparison between active and passive vibration control of nonlinear simple pendulum, part I: transversally tuned absorber and negative feedback. Math Comput Appl 11(2):137–149

A Comparative Study on the Vibration Control of a Bridge Under Moving Springing Mass by TMD and TMDI

Anirban Bhattacharjee and Aparna Dey Ghosh

1 Introduction

Recent technological advancements have enabled engineers to develop new design methods, advanced materials, and advanced construction equipment to build lighter and more slender structures. Consequently, structures are becoming prone to dynamic loads, especially moving loads. Deflection and vibration induced by heavy and high-speed vehicles affect the safety and serviceability of bridges. Vibration control using mechanical control devices like a tuned mass damper and a fluid viscous damper is very effective to suppress the response of bridges to ensure safety and serviceability of the structure.

A Tuned Mass Damper (TMD) is a simple and effective device; hence, one of the most widely adopted vibration control devices. The TMD is tuned to the fundamental vibration frequency of the primary structure in such a way so that it resonates out of phase with the original structure to dissipate vibration energy. There are mainly two challenges in the implementation of this system in a bridge deck. One of the most critical challenges arises from considerable static stretching of the spring connected between the bridge deck and TMD mass due to gravity. Lower the frequency of the TMD (which is close to the fundamental frequency of the structure), more will be the static stretching of the TMD. Also, the vibrational energy of the primary structure is transferred to the TMD mass, which is responsible for large stroke of TMD. Streamlined bridge decks have very little space to accommodate this damper displacement. In recent times, a device named inerter, developed for the suspension system of Formula-1 racing cars, is found to be effective in controlling vibration of structures. It is used to amplify the physical mass of the system by transforming

A. Bhattacharjee (✉) · A. D. Ghosh
Department of Civil Engineering, IIEST, Shibpur, Howrah, India

A. D. Ghosh
e-mail: aparna@civil.iiests.ac.in

D. K. Maiti et al. (eds.), *Recent Advances in Computational and Experimental Mechanics, Vol II*, Lecture Notes in Mechanical Engineering,
https://doi.org/10.1007/978-981-16-6490-8_53

linear motion into high-speed rotational motion. Thus, it can generate an inertial force which is similar to force generated by inertia of physical mass.

To understand the bridge behavioural characteristics under moving loads, Biggs [1] derived the equations of motion of a simply supported bridge under a moving vehicle where the vehicle is modelled as a springing mass having one degree of freedom supported by a spring and a dashpot. Using this bridge vehicle model, Humar and Kashif [2] numerically analysed different bridges that consist of one or multiple simply supported spans and identified the influencing parameters for their response. Wang et al. [3] modelled the car-body as a flexible multi-body system and the bridge as a Euler Beam. They identified that though the car-body acceleration produces peak responses at certain speeds, the flexibility of the car-body does not significantly affect the bridge response. Salcher and Adam [4] considered the effect of rail irregularities during modal analysis of a train–bridge model and simulated the interaction between both subsystems. Paultre et al. [5] have given prime concern to the vertical acceleration of the bridge deck under pedestrian load to ensure structural safety and serviceability.

Extensive research has been conducted to control moving load-induced bridge vibrations and different solutions have been proposed for different situations. Kwon et al. [6] studied the vibration response of a three-span bridge induced by high-speed trains, considering the vehicle to be modelled as a moving mass model, which consists of the vehicle body and wheel, and designed a TMD to suppress the bridge vibrations. Sadek et al. [7] reviewed existing literature on the topic and suggested that in the choice of TMD parameters, large mass ratios must be used for heavy damping in the first two modes. Marian and Giaralis [8] used TMDI as a passive vibration control and energy harvesting device in a harmonically excited structure. Optimal TMDI parameters were obtained using Den Hartog's [9] tuning approach. This system was reported to be more robust than the traditional TMD to detuning effects. Xu et al. [10] studied the reduction of undesirable vortex-induced vibrations that influences the fatigue life and serviceability of the bridge structure using the TMDI. Papageorgiou and Smith [11] presented experimental results on inerters and proposed a methodology for testing inerters as well.

In this paper, the focus is on controlling the vibration of a bridge deck produced by moving vehicles using TMD and TMDI. The work aims to present a comparison of the performances of the two devices and to highlight the greater practical applicability of the TMDI system in the bridge deck from the viewpoint of the limited space available to accommodate the stroke of the damper mass. In what follows, first, the working principle of the TMDI is discussed. Next, the modelling of the bridge–vehicle damper system is presented for various cases of the TMD and TMDI. This is followed by a numerical study into the performance of the damper systems in mitigating the bridge vibrations and the stroke lengths of the damper mass is carried out under different speed and frequency parameters of the moving vehicle and bridge systems.

2 Working Principle of the TMDI

Smith [7] developed the concept of the inerter. It is a linear two-terminal device with negligible physical mass which produces internal (resisting) force F, proportional to the relative acceleration between its two terminals. That is,

$$F = b(\ddot{u}_1 - \ddot{u}_2) \tag{1}$$

where, u_1 and u_2= the displacement coordinates of the inerter terminals,

$\ddot{u}_1 - \ddot{u}_2$= relative acceleration between the two terminals of the inerter,

b = constant of proportionality (inertance).

Figure 1 shows a device consisting of a flywheel linked to a rack-and-pinion via n gears (here $n = 4$) called inerter. The inertance of this device is given by

$$b = m_f \frac{\gamma_f^2}{r_{fp}^2} \left(\prod_{k=1}^{n} \frac{r_k^2}{r_{kp}^2} \right) \tag{2}$$

where m_f = mass of the flywheel; γ_f = radius of gyration of the flywheel; r_{fp} = radius of flywheel pinion; r_k = radii of the kth gear; and r_{kp} = radii of the kth gear pinion (Fig. 2).

Let $\ddot{d}$ be the acceleration of the TMD and α_1 and M_1 be the angular acceleration and torque at the centre of the gear; $\alpha_1 = \frac{\ddot{d}}{r_{1p}}$.

Let α_f be the angular acceleration of the flywheel

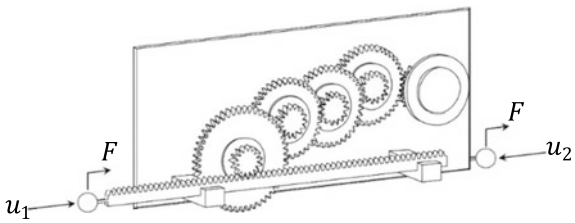

Fig. 1 Rack-pinion-flywheel based inerter device with four gear

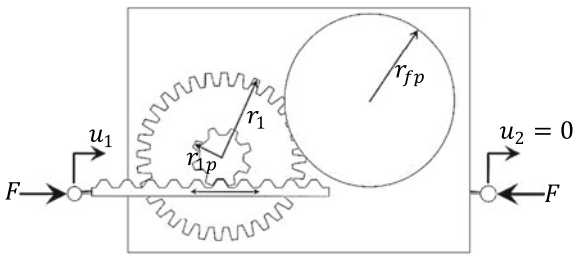

Fig. 2 Single gear inerter

$$\alpha_f \cdot r_{fp} = \alpha_1 \cdot r_1 \tag{3}$$

or

$$\alpha_f = \frac{\alpha_1 \cdot r_1}{r_{fp}} = \frac{\ddot{d}}{r_{fp}} \cdot \frac{r_1}{r_{fp}}$$

Now, torque at the centre of the flywheel

$$M_f = I \cdot \alpha_f \tag{4}$$

where I = Moment of inertia of the flywheel and α_f = angular acceleration of the flywheel.

Now,

$$\alpha_f = \alpha_1$$

Or

$$\frac{M_f}{r_f} = \frac{M_1}{r_1}$$

Or

$$M_1 = M_f \cdot \frac{r_1}{r_f} \tag{5}$$

The amount of force generated by the inerter due to acceleration of the TMD is then given by

$$F = \frac{M_1}{r_1} = \frac{M_f}{r_{fp}} \cdot \frac{r_1}{r_{1p}} = \frac{I \cdot \alpha_f}{r_{fp}} \cdot \frac{r_1}{r_{1p}} = \frac{I}{r_{fp}} \cdot \frac{\ddot{d}}{r_{fp}} \cdot \frac{r_1}{r_{fp}} \cdot \frac{r_1}{r_{1p}}$$

Or

$$F = m_f \cdot \frac{\gamma_f^2}{r_{fp}^2} \left(\frac{r_1^2}{r_{fp}^2} \right) \cdot \ddot{d} \tag{6}$$

3 Modelling of Bridge–Vehicle Damper System

3.1 Modelling of the Bridge and the Vehicle

In Fig. 3, the bridge is modelled [1] as a uniform prismatic isotropic beam. Here, a simplified analytical technique is used to model the complex dynamic behaviour of a bridge to identify the response governing characteristics, which may help develop rational design procedures. The vehicle body is supported by a spring of stiffnessk_v. m_b is the mass per unit length of the bridge. The wheel load, damping of the vehicle body and damping of the bridge deck are ignored. The vehicle, as it rolls along, is assumed to be always in contact with the surface of the deck. In the beam and vehicle model of Fig. 3, the displacement of the sprung mass relative to its absolute position before deflection under self-weight is represented byu_v. $u_b = z(t)\sin\frac{\pi x}{l}$, represents the displacement of the sprung mass, that models the vehicle body, relative to its position of equilibrium when moving, where $\sin\frac{\pi x}{l}$ is the first mode shape of the beam. Assuming the vehicle is moving at a constant speed$v$, Biggs [2] derived the equation of motion of the position of the vehicle body along with the bridge deck, reproduced as follows:

$$\begin{bmatrix} m_v & 0 \\ 0 & \frac{m_b l}{2} \end{bmatrix}\begin{bmatrix} \ddot{u}_v \\ \ddot{z}_c \end{bmatrix} + \begin{bmatrix} k_v & -k_v \sin\frac{\pi vt}{l} \\ -k_v \sin\frac{\pi vt}{l} & k_v \sin^2\frac{\pi vt}{l} + \frac{\pi^4 EI}{2l^3} \end{bmatrix}\begin{bmatrix} u_v \\ z_c \end{bmatrix} = g\begin{bmatrix} 0 \\ m_v \sin\frac{\pi vt}{l} \end{bmatrix} \quad (7)$$

We now define $\chi = \frac{m_v}{m_b}$= mass ratio, ω_v= bounce frequency of the vehicle, ω_b = frequency of the bridge model, $\phi = \frac{\omega_v}{\omega_b}$= frequency ratio, and $\alpha = \frac{vT_b}{2L}$ as the speed parameter. Further, the following coordinates are defined.

$$\tilde{u}_v = \frac{u_v}{\delta} = \frac{u_v \omega_v^2}{g} \quad (8)$$

$$\tilde{z_c} = \frac{z_c}{\Delta_{st}} = \frac{z\omega_b^2}{2\chi g} \quad (9)$$

$\tilde{z_c}$ = dynamic amplification factor.

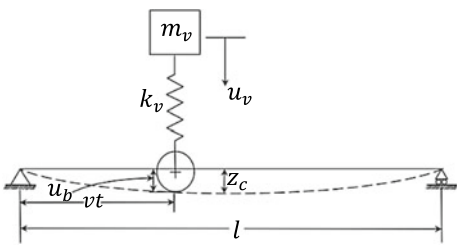

Fig. 3 Modelling of bridge vehicle system

Transforming coordinates to a non-dimensional system, $\tilde{u}_v$ and $\widetilde{z_c}$, the equations reduce to

$$\begin{bmatrix} \frac{1}{\omega_v^2} & 0 \\ 0 & \frac{2\phi^4\chi}{\omega_v^2} \end{bmatrix} \begin{bmatrix} \ddot{\tilde{u}}_v \\ \ddot{\tilde{z}}_c \end{bmatrix} + \begin{bmatrix} 1 & -2\chi\phi^2 \sin\frac{\alpha}{\phi}\omega_v t \\ -2\chi\phi^2 \sin\frac{\alpha}{\phi}\omega_v t & 4\chi^2\phi^4 \sin^2\frac{\alpha}{\phi}\omega_v t + 2\chi\phi^2 \end{bmatrix} \begin{bmatrix} \tilde{u}_v \\ \tilde{z}_c \end{bmatrix} = \begin{bmatrix} 0 \\ 2\chi\phi^2 \sin\frac{\alpha}{\phi}\omega_v t \end{bmatrix} \tag{10}$$

Equation 10 thereby represents a set of non-dimensional equations that are solved by the ode45 solver in MATLAB R2018b.

It is evident from Eq. 10 that the response of the bridge is controlled by the following four parameters, ω_v, χ, ϕ *and* α.

After introducing a new time variable $\bar{t} = \omega_v t$, we obtain

$$\frac{\partial^2 \tilde{u}_v}{\partial t^2} = \omega_v^2 \frac{\partial^2 \tilde{u}_v}{\partial \bar{t}^2}$$

and

$$\frac{\partial^2 \tilde{z}_c}{\partial t^2} = \omega_v^2 \frac{\partial^2 \tilde{z}_c}{\partial \bar{t}^2}$$

It can be concluded from the above equations that the response is independent of ω_v.

3.2 *Modelling of the Bridge–Vehicle System with TMD*

In Fig. 4, m_d is the mass of TMD, k_d is the stiffness of the spring of TMD and d is the relative displacement of the mass of TMD. Figure 4 shows the vehicle and bridge

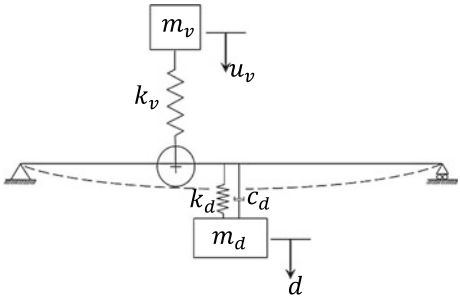

Fig. 4 Modelling of vehicle bridge system with TMD

interaction with TMD at the mid-span of the bridge, can be derived as follows:

$$\begin{bmatrix} m_v & 0 & 0 \\ 0 & \frac{m_b l}{2} & 0 \\ 0 & 0 & m_d \end{bmatrix} \begin{bmatrix} \ddot{u}_v \\ \ddot{z}_c \\ \ddot{d} \end{bmatrix} + \begin{bmatrix} c_v & -c_v sin\frac{\pi vt}{l} & 0 \\ 0 & c_b + c_d & -c_d \\ 0 & -c_d & c_d \end{bmatrix} \begin{bmatrix} \dot{u}_v \\ \dot{z}_c \\ \dot{d} \end{bmatrix}$$
$$+ \begin{bmatrix} k_v & -k_v sin\frac{\pi vt}{l} & 0 \\ -k_v sin\frac{\pi vt}{l} & k_v sin^2\frac{\pi vt}{l} + \frac{\pi^4 EI}{2l^3} & -k_d \\ 0 & -k_d & k_d \end{bmatrix} \begin{bmatrix} u_v \\ z_c \\ d \end{bmatrix} = g \begin{bmatrix} 0 \\ m_v sin\frac{\pi vt}{l} \\ 0 \end{bmatrix} \quad (11)$$

3.3 Modelling of the Bridge–Vehicle System with TMDI (When an Inerter Device is Connected Between TMD Mass and a Fixed Support/pier)

The second terminal of the inerter device is here considered fixed so that the maximum inertance effect can be achieved. The force generated by the inerter is given by $F = b(\ddot{d} - 0) = b\ddot{d}$. Figure 5 shows the vehicle and bridge interaction with a TMDI instead of a TMD at the mid-span of the bridge, represented in Eq. 12 can thus be derived.

$$\begin{bmatrix} m_v & 0 & 0 \\ 0 & \frac{m_b l}{2} & 0 \\ 0 & 0 & m_d + b \end{bmatrix} \begin{bmatrix} \ddot{u}_v \\ \ddot{z}_c \\ \ddot{d} \end{bmatrix} + \begin{bmatrix} c_v & -c_v sin\frac{\pi vt}{l} & 0 \\ 0 & c_b + c_d & -c_d \\ 0 & -c_d & c_d \end{bmatrix} \begin{bmatrix} \dot{u}_v \\ \dot{z}_c \\ \dot{d} \end{bmatrix}$$
$$+ \begin{bmatrix} k_v & -k_v sin\frac{\pi vt}{l} & 0 \\ -k_v sin\frac{\pi vt}{l} & k_v sin^2\frac{\pi vt}{l} + \frac{\pi^4 EI}{2l^3} & -k_d \\ 0 & -k_d & k_d \end{bmatrix} \begin{bmatrix} u_v \\ z_c \\ d \end{bmatrix} = g \begin{bmatrix} 0 \\ m_v sin\frac{\pi vt}{l} \\ 0 \end{bmatrix} \quad (12)$$

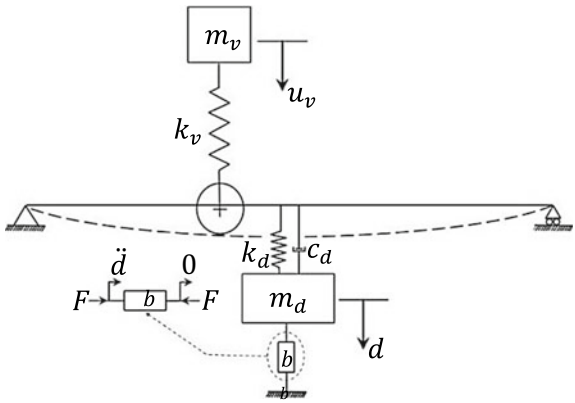

Fig. 5 Modelling of vehicle bridge system with TMDI (when an inerter device is connected between TMD mass and a fixed support/pier)

3.4 *Modelling of the Bridge–Vehicle System with TMDI (When an Inerter Device is Connected Between TMD Mass and the Bridge Deck)*

There is a practical limitation in attaching the inerter between TMD mass and fixed support/pier, but it is easier to attach the second terminal to the bridge deck. As there is a large difference between the acceleration of the TMD mass and the mid-span of the bridge deck, we can make use of this relative acceleration to generate force in the inerter, though it will be lower than that in the case of attaching the inerter is connected between TMD mass and fixed support/pier. The force generated here is $F = b(\ddot{d} - \ddot{z}_c)$. Figure 6 shows the vehicle and bridge interaction with a TMDI when the inerter is connected between TMD mass and bridge deck at the mid-span of the bridge, which are represented by Eq. 13.

$$\begin{bmatrix} m_v & 0 & 0 \\ 0 & \frac{m_b l}{2} & -b \\ 0 & -b & m_d + b \end{bmatrix} \begin{bmatrix} \ddot{u}_v \\ \ddot{z}_c \\ \ddot{d} \end{bmatrix} + \begin{bmatrix} c_v & -c_v \sin\frac{\pi v t}{l} & 0 \\ 0 & c_b + c_d & -c_d \\ 0 & -c_d & c_d \end{bmatrix} \begin{bmatrix} \dot{u}_v \\ \dot{z}_c \\ \dot{d} \end{bmatrix}$$
$$+ \begin{bmatrix} k_v & -k_v \sin\frac{\pi v t}{l} & 0 \\ -k_v \sin\frac{\pi v t}{l} & k_v \sin^2\frac{\pi v t}{l} + \frac{\pi^4 EI}{2l^3} & -k_d \\ 0 & -k_d & k_d \end{bmatrix} \begin{bmatrix} u_v \\ z_c \\ d \end{bmatrix} = g \begin{bmatrix} 0 \\ m_v \sin\frac{\pi v t}{l} \\ 0 \end{bmatrix} \tag{13}$$

4 Performance of TMDI Compared to the Classical TMD in Vibration Suppression

For reduction of the bridge deck response subjected to a moving springing mass, closed-form expressions for optimum tuning parameters of the TMD are given in

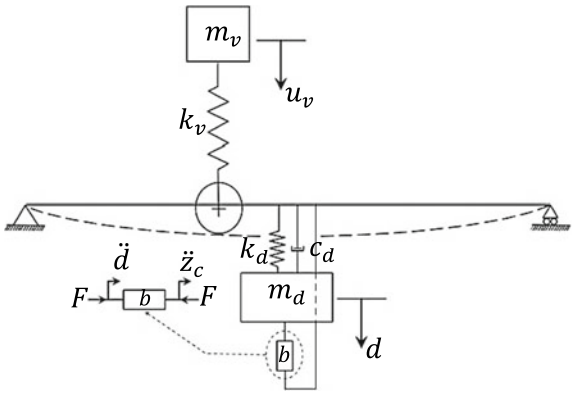

Fig. 6 Modelling of vehicle–bridge system with TMDI (when an inerter device is connected between TMD mass and the bridge deck)

Table 1, as suggested by Den Hartog [6] for harmonically excited structures. By replacing μ with $\mu + \beta$ as suggested by Marian and Giaralis [4], the expressions for the TMDI are derived.

An example bridge [2] is now taken, that is a half through truss with following properties: weight = 1031.936 kN; length = 24.384 m; natural frequency of the bridge, f_b= 3.95 Hz; the ratio of vehicle mass to bridge mass per unit length, $\chi = m_v/m_b = 0.517$; frequency ratio, $\phi=\omega_v/\omega_b = 0.7$. The variation of maximum mid-span acceleration of bridge deck with speed ratio, α, (a) with TMD (b) with TMDI when the inerter is connected between TMD mass and fixed support/pier and (c) with TMDI when the inerter is connected between TMD mass and bridge deck, for different values of damper mass ratio, μ, are presented in Fig. 7.

It can be seen from Fig. 7 that the peak acceleration of the bridge deck at mid-span is almost linearly increasing with the speed ratio, α. Further, increasing the mass of the TMD always achieves greater efficiency in the reduction of the mid-span acceleration response though the maximum mid-span acceleration does not improve much at $\mu = 10\%$ from $\mu = 5\%$. In the case of the TMDI, when the second terminal of the inerter is grounded, it achieves higher efficiency at the same mass ratio as the TMD. However, if inerter is connected between TMD mass and bridge deck, the TMDI efficiency is lower than that in the case of the TMD.

At a higher mass ratio, μ, the dynamic displacement of the mass of TMD is smaller, but for lower μ, the stroke of the TMD is significant. When the TMDI is used, and the inerter is connected between TMD mass and fixed support/pier, the maximum displacement of the mass of TMDI is reduced. It may, however, be difficult to ground the second terminal of the inerter. Instead, if the inerter is connected between TMD mass and bridge deck, the stroke of the damper mass is substantially reduced, and this configuration would be easy to install within the bridge deck.

The variation of relative maximum stroke of the mass of TMDI to that of the TMD with inertance, β (a) when inerter is connected between TMD mass and fixed support/pier and (b) when inerter is connected between TMD mass and bridge deck, for different values of mass ratio, μ is studied. It is observed from Fig. 8a that for very low mass ratios, such as $\mu = 0.5\%$, the effectiveness of the inerter in reducing the stroke of the TMDI with a grounded terminal as compared to the TMD at the same mass ratio is up to 23%. With increasing mass ratio, μ, the effect of inertance in reducing the stroke of the TMDI reduces and is hardly 2.5% for $\mu = 10\%$. However, it is seen from Fig. 8b that when inerter is connected between TMD mass and bridge deck, for mass ratio $\mu = 0.5\%$, the effectiveness of the inerter in reducing the stroke of the TMDI as compared to the TMD is up to 69% at same mass ratio; which is

Table 1 Optimum frequency ratio (ν) and Optimum damping ratio (ζ) for TMD and TMDI

	Optimum frequency ratio (ν)	Optimum damping ratio (ζ)
TMD	$\frac{1}{1+\mu}$	$\sqrt{\frac{3\mu}{8(1+\mu)}}$
TMDI	$\frac{1}{1+\mu+\beta}$	$\sqrt{\frac{3(\mu+\beta)}{8(1+\mu+\beta)}}$

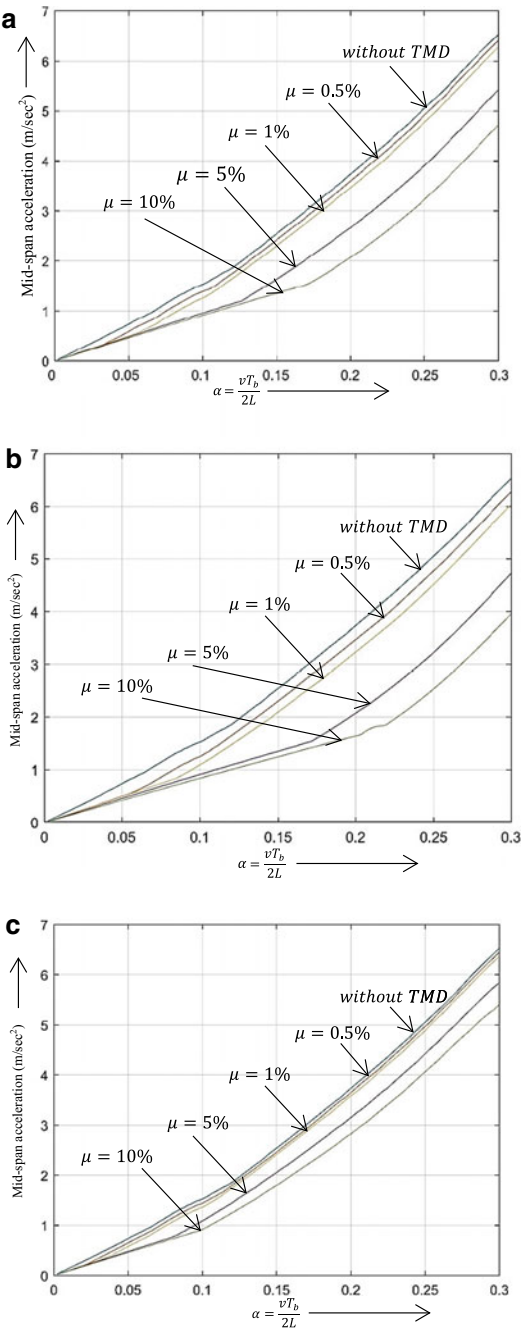

Fig. 7 **a** Mid-span acceleration of bridge with and without TMD. **b** Mid-span acceleration of bridge with and without TMDI when the inerter is connected between TMD mass and fixed support/pier. **c** Mid-span acceleration of bridge with and without TMDI when the inerter is connected between TMD mass and pier bridge deck

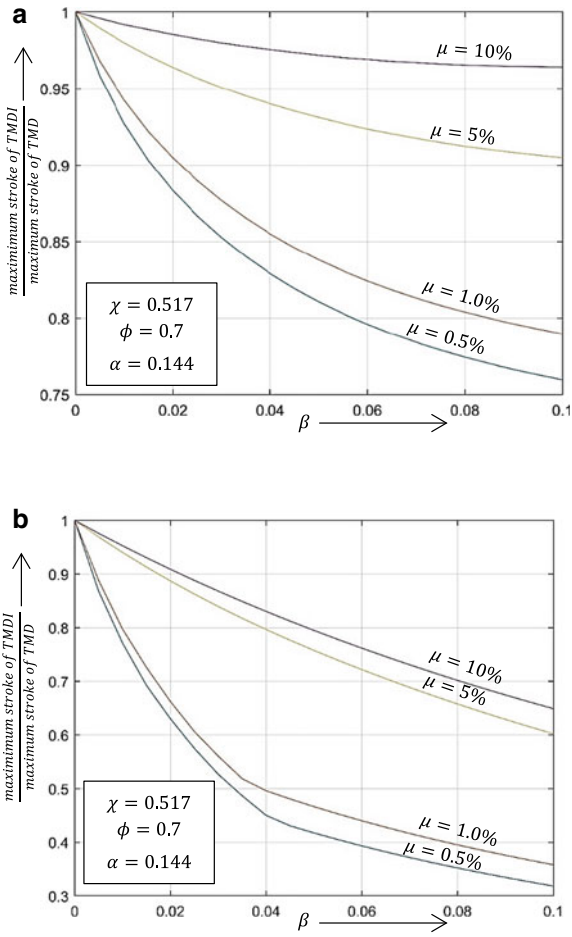

Fig. 8 **a** Maximum stroke of the mass of the TMDI (inerter is connected between TMD mass and fixed support/pier) normalised by the maximum stroke of the TMD at same mass ratio. **b** Maximum stroke of the mass of the TMDI (inerter is connected between TMD mass and bridge deck) normalised by the maximum stroke of the TMD at same mass ratio

much higher as compared to the previous case. With increasing mass ratio, μ, the effect of inertance in reducing the stroke of the TMDI reduces. However, it is still as high as 35% for the case of $\mu = 10\%$. Thus, this system is highly effective in reducing the stroke of the damper mass while mitigating the bridge deck vibrations. Moreover, this system can be easily installed within a bridge deck, both for new as well as for existing structures.

5 Conclusions

A TMD, which is very effective in controlling structural vibrations, has applicability in mitigating bridge deck vibrations induced by the moving vehicle. Increasing the

mass of the TMD generally increases the efficiency of the TMD. However, the mass cannot be increased indiscriminately as the static deflection of the TMD also increases with the increase in mass and imposes a practical limitation on the installation of the TMD in bridge decks. Further, the large stroke of the TMD compounds the problem. In such cases, the TMDI configuration resolves these problems. The effectiveness of the TMDI compared to the TMD system when the inerter is connected between damper mass and fixed support/pier is significant. The following conclusions are drawn for this case.

I. At the same mass ratio, this system is very effective in reducing the mid-span acceleration of the bridge as compared to the TMD. The inertance of the system acts as a virtual mass without adding additional static deflection to the system.
II. For lower mass ratio ($\mu = 0.5\%$), the effectiveness of the inerter in reducing the stroke of the TMDI as compared to the TMD at the same mass ratio is up to 23%. The effect of the inertance with increasing mass ratio in reducing the stroke of the TMDI reduces and is hardly 2.5% for $\mu = 10\%$.

When the inerter is connected between TMD mass and bridge deck, the following conclusions are obtained from the study.

I. In this configuration of the inerter, the efficiency of TMDI system is lower as compared to the TMD system. However, installing TMDI would be more feasible since the static deflection of the damper mass is drastically reduced.
II. For lower mass ratio ($\mu = 0.5\%$), the effectiveness of the inerter in reducing the stroke of the damper mass as compared to the TMD is up to 69% at the same mass ratio; which is much higher as compared to the previous case of TMDI configuration. With increasing mass ratio, the effect of inertance in reducing the stroke of the TMDI reduces. However, it is as high as 35% for the case of $\mu = 10\%$.

Overall, the TMDI system is very effective in reducing the stroke of the damper mass. Though this system is less effective than the TMD in reducing the mid-span response of the bridge, it can be installed easily inside a bride deck. Further, another advantage of the proposed system is that it can be applied to new and existing bridge structures.

References

1. Biggs JM (1964) Introduction to structural dynamics. McGraw-Hill book company, ISBN 07-005255-7
2. Humar JL, Kashif AM (1992) Dynamic response of bridges under travelling loads. Canadian J Civil Eng 20:287–298. April 1993, doi:https://doi.org/10.1139/l93-033
3. Wang K, Xia H, Xu M, Guo W (2015) Dynamic analysis of train-bridge interaction system with flexible car-body. J Mech Sci Technol 29(9):3571–3580. https://doi.org/10.1007/s12206-015-0801-y
4. Salcher P, Adam C (2015) Modelling of dynamic train–bridge interaction in highspeed railways. Acta Mech 226(10):3561–3561. https://doi.org/10.1007/s00707-015-1449-5

5. Paultre P, Proulx J, Légeron F, Le Moine M, Roy N (2000) Dynamic testing of the sherbrooke pedestrian bridge. IABSE Congress Report 16(9):1254–1261. https://doi.org/10.2749/222137900796313889
6. Kwon H-C, Kim M-C, Lee I-W (1998) Vibration control of bridges under moving loads. Comput Struct. https://doi.org/10.1016/S0045-7949(97)00087-4,66,4,(473-480)
7. Sadek F, Mohraz B, Taylor AW, Chung RM (1997) A method of estimating the parameters of tuned mass dampers for seismic applications. Earthquake Eng Struct Dyn 26(6):617–635. doi:https://doi.org/10.1002/(sici)1096-9845(199706)26:6<617::aid-eqe664>3.0.co;2-z
8. Marian L, Giaralis A (2017) The tuned mass-damper-inerter for harmonic vibrations suppression, attached mass reduction, and energy harvesting. Smart Struct Syst 19(6):665–678. https://doi.org/10.12989/sss.2017.19.6.665
9. Xu K, Bi K, Han Q, Li X, Du X (2019) Using tuned mass damper inerter to mitigate vortex-induced vibration of long-span bridges: Analytical Study. Eng Struct 182:101–111. https://doi.org/10.1016/j.engstruct.2018.12.067
10. Den Hartog JP (1956) Mechanical vibrations. McGraw-Hill (4th ed.), New York, NY, USA
11. Papageorgiou C, Smith MC (2005) Laboratory experimental testing of inerters. IEEE Conference on Decision and Control, Seville, Spain, December, 44, 3351–3356. doi:https://doi.org/10.1109/cdc.2005.1582679

Design of Overhead Water Tank with Floating Base for Utilization as Tuned Liquid Damper Against Lateral Excitation

Tanmoy Konar and Aparna Dey Ghosh

1 Introduction

Over the last one and half centuries, researchers have worked on the development of techniques to protect building structures against lateral excitations induced by hostile environmental conditions, such as earthquake, storm, ocean wave, etc. [1]. Among the available options of structural vibration control, passive energy dissipation devices are reliable and cost-effective. Ease of installation, maintenance, operation, and design amenability provide the tuned liquid dampers (TLDs) with distinct advantages over other passive energy dissipation devices. The term TLD refers to the family of dampers in which liquid is used as the inertial mass and energy dissipation takes place due to movement of liquid. TLDs are broadly divided into two groups, namely, (a) tuned liquid column damper (TLCD) and its variations such as complaint TLCD [2], liquid column vibration absorber (LCVA) [3, 4], (b) tank damper. Conventionally, the term TLD refers to the tank damper, wherein energy dissipation takes place due to sloshing of the contained liquid. The vibrational energy is absorbed by the damper from the primary structure when the liquid sloshing frequency is tuned to the dominant structural frequency. The applicability of TLDs in controlling structural vibrations due to strong wind [5] as well as earthquake [6] has been well documented.

It is common for the building structures to have overhead water tanks (OWTs) installed for storage and distribution of water. However, despite the proven effectiveness of the TLD as a vibration control device, there are very limited attempts to design OWTs as TLD. There are chiefly two reasons behind this. Firstly, the fluctuation in water level due to functional requirements in conventional circular or

T. Konar (✉) · A. D. Ghosh
Department of Civil Engineering, IIEST, Shibpur, Howrah, India

A. D. Ghosh
e-mail: aparna@civil.iiests.ac.in

D. K. Maiti et al. (eds.), *Recent Advances in Computational and Experimental Mechanics, Vol II*, Lecture Notes in Mechanical Engineering,
https://doi.org/10.1007/978-981-16-6490-8_54

rectangular OWTs causes a continual change in the liquid sloshing frequency. Thus, if the sloshing frequency at a particular tank-full condition is designed to be tuned to the structural frequency, the fluctuating water level would lead to mistuning of the damper [7]. Secondly, in the conventional TLD, the ratio of the liquid height to the base dimension of the damper, along the direction of expected vibration, is kept shallow (to about 0.1). This enhances the sloshing phenomenon and consequently the energy dissipation [8]. However, from functional considerations, this would be impossible to maintain in case of the OWT.

Very few research works are available which have attempted to address the aforementioned issues. Bandyopadhyay et al. [7] presented a particular profile of the OWT for which the liquid sloshing frequency becomes independent of the water level. However, the profile is different from the conventional circular or rectangular shapes of OWT and would be required to be constructed specifically for a particular building structure. Rai et al. [9] proposed compartmentalization of OWT into many small parts to transform it into multiple shallow TLDs. However, this approach would interfere with the basic functionality of the OWT.

The current paper proposes a novel design of the OWT with floating base (FB) and henceforth the combined system is designated as the OWT-FB. The OWT-FB can eliminate the aforementioned hindrances to effectively utilize the OWT as a dynamic vibration absorber, without hampering its basic functioning of water storage and supply. In the succeeding sections, a description of the proposed OWT-FB is presented along with its working principle. Next, a numerical study is presented to illustrate the effectiveness of the design using an example building structure with OWT-FB, by subjecting it to recorded seismic base excitation.

2 Description and Working Principle of OWT-FB

The OWT-FB consists of a conventional OWT of circular or rectangular shape and a floating container inserted in it (see Fig. 1a). The dimensions of the floating container are so chosen so that it can just be accommodated in the OWT and its free movement in the vertical direction within the OWT is not restricted. The bottom of the floating container acts as the FB. The desired water height, determined from the tuning requirement, is always maintained above the FB irrespective of the water level in the OWT. To achieve this, the floating container is provided with a hole at the center of its base and with annular floaters below its base. If the water depth in the OWT varies, the floating container adjusts its position automatically through vertical movement to maintain a constant water level above the FB [10].

When the building supporting the OWT-FB is subjected to lateral excitation, the building transfers a portion of the vibrational energy to the OWT. In turn, the energy passes on from the OWT to the floating container and lastly from the container to the water within it. This leads to sloshing of the water above the FB and ultimately to dissipation of the vibrational energy (see Fig. 1b). For the present study, both the OWT and the floating container are assumed to be rigid. The wall of the floating

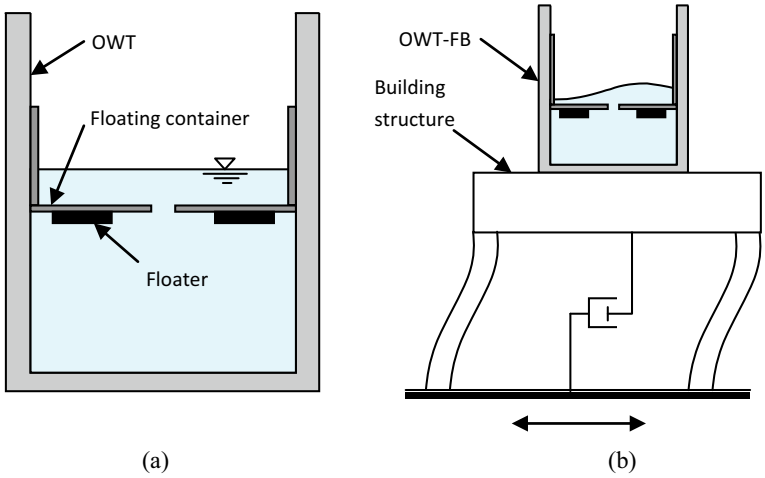

Fig. 1 **a** OWT-FB, **b** Simplified model of laterally excited building structure-OWT-FB system

container thereby denies any relative motion (translational or rotational) between the FB and the OWT when the OWT-FB system is laterally excited. With this design, the portion of the OWT above the FB functions as an independent conventional TLD maintaining the sloshing frequency required for the tuning with the frequency of the building structure, even though the water level in the OWT fluctuates. The experimental validation of the proposed system is available in [10].

3 Numerical Study

3.1 Example Building Structure

A 12-storied building with reinforced concrete-framed (RC-framed) structure and aerated concrete (AC) block walls is considered as the example structure for the numerical study. The schematic drawing of a typical floor plan and elevation of the building frame is shown in Fig. 2. The important parameters of the building structure are given in Table 1.

The building frame is analyzed using STAAD.Pro V8i software. The natural period of the building is determined to be 3.0 s and the modal mass corresponding to the fundamental mode is 1614302 kg. The damping ratio of the building structure is taken as 1%. The OWT-FB is designed to control the fundamental mode of vibration of the building structure. The building structure is henceforth denoted as an equivalent single degree of freedom (SDOF) system. The natural period (T_s) and mass (M_s)

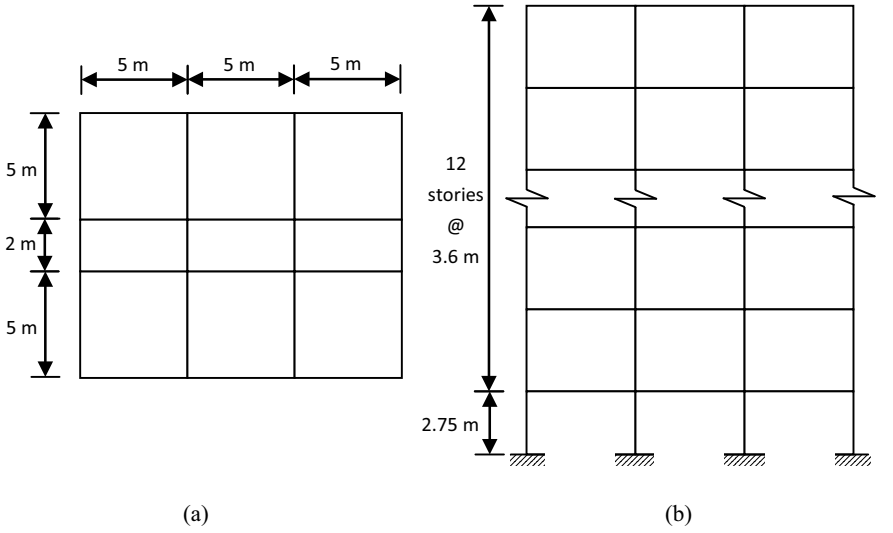

Fig. 2 Schematic drawing of example building frame **a** typical floor plan and **b** elevation

Table 1 Parameters of example building structure

Sl. No	Building parameters	Value
1	Grade of concrete	M25
2	Grade of steel	Fe500
3	Size of column	400 mm × 400 mm
4	Size of beam	250 mm × 400 mm
5	Slab thickness	135 mm
6	Thickness of external wall (30% open for doors and window)	250 mm
7	Thickness of internal wall (30% open for doors and window)	100 mm
8	Density of AC block	6.5 kN/m^3

of this SDOF system are equal to the period and modal mass corresponding to the fundamental mode of the building.

3.2 Design of OWT-FB

The floating container of the OWT-FB is assumed to be made of steel and thermocol is used as the floater. The density of steel, thermocol, and water are taken as 7850 kg/m^3, 30 kg/m^3, and 1000 kg/m^3, respectively. Let the OWT-FB system consist of ten numbers of interconnected circular tanks of 2.0 m diameter. The maximum allowable height of water in each OWT is assumed to be 1.8 m. The thickness of the wall and

the base of the floating containers is considered as 8 mm. A clearance of 2 mm is provided between the internal surface of the wall of the OWT and the external surface of the wall of the floating container. Thus, the floating container has the internal diameter of 1.98 m. A hole is made in the middle of the FB to make sure that water moves freely between the upper and lower part of the OWT separated by the FB and a constant water height is maintained above the FB. Based on the required liquid sloshing frequency (ω), the height of water (H) above the FB is calculated using Eq. (1) [11].

$$\omega = \left[\frac{3.682g}{D}\tanh\left(\frac{3.682H}{D}\right)\right]^{1/2} \tag{1}$$

Here, D and g, respectively, denote the internal diameter of the floating container and the acceleration due to gravity.

Assuming the tuning ratio equal to unity for simplicity, the height of water required above the FB is calculated as 0.132 m. The vertical wall of the floating containers is considered to be 0.3 m high. Thus each floating container weighs 309.5 kg. To make the container float in equilibrium maintaining the desired water height above the FB, annular floaters made of thermocol, each having external diameter, internal diameter, and thickness equal to 1.6 m, 0.4 m, and 0.152 m, respectively, are fixed below the base of the floating containers. Thus, the designed OWT-FB system would be able to maintain tuning of frequencies with the primary structure, if water levels in the OWT units remain at 0.292 m above their bases. Hence, for the ten tanks of the OWT-FB system, 47,368 L of water, which is about 83% of the maximum storage capacity of the OWTs, could be used to meet the water demand of the residence of the building. Thus, the proposed design effectively utilizes the OWT system of a building as passive vibration control device with nominal interference.

The extent of detuning that can occur due to water level fluctuation in the OWT system if FBs are not used is also studied. Three particular tank-full conditions, namely, tank 1/6th full, tank 1/3rd full, and tank 2/3rd full, are considered, for which the fundamental period of liquid sloshing is evaluated as 2.09 s, 1.65 s, and 1.49 s, respectively. These clearly do not meet the tuning requirement. Figure 3 indicates the variation of the fundamental period of liquid sloshing with the variation of liquid level in the OWT without FB and in the OWT-FB. The advantage of the OWT-FB regarding maintenance of tuning with the primary structure is evident from Fig. 3.

3.3 Peformance of OWT-FB Under Seismic Base Excitation

The performance of the designed OWT-FB system under lateral excitation is illustrated considering the structure-damper to be subjected to the N08W component of the 1979 Imperial Valley earthquake (station Delta) with peak ground acceleration of 0.350 g. The equation of motion of the equivalent SDOF structure–damper system

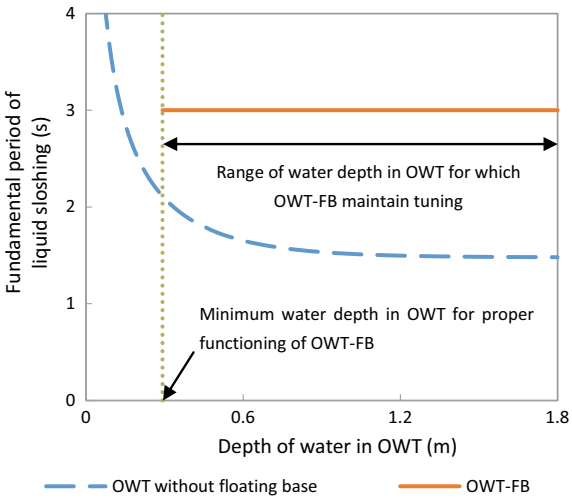

Fig. 3 Variation of the fundamental period of liquid sloshing with the variation of liquid level in OWT without FB and WT-FB

is given in Eq. (2).

$$\begin{bmatrix} M_s & 0 \\ 0 & nM_d \end{bmatrix}\begin{Bmatrix} \ddot{x} \\ \ddot{y} \end{Bmatrix} + \begin{bmatrix} C_s + nC_d & -nC_d \\ -nC_d & nC_d \end{bmatrix}\begin{Bmatrix} \dot{x} \\ \dot{y} \end{Bmatrix} + \begin{bmatrix} K_s + nK_d & -nK_d \\ -nK_d & nK_d \end{bmatrix}\begin{Bmatrix} x \\ y \end{Bmatrix} = \begin{Bmatrix} -M_s\ddot{z}(t) \\ 0 \end{Bmatrix} \tag{2}$$

Here, K_s and C_s are the stiffness and damping, respectively, of the equivalent SDOF structure. M_d, K_d and C_d, respectively, denote the equivalent lumped mass, stiffness, and damping corresponding to the sloshing water in a single OWT-FB. The number of tanks in the OWT-FB system is n. The horizontal displacement of the SDOF structural system and the equivalent lumped mass representing the sloshing water of the OWT-FB are, respectively, given by x and y. The seismic base acceleration is represented by $\ddot{z}(t)$.

The M_d, K_d, and C_d are determined using Eqs. (3)–(5) [11, 12].

$$M_d = \frac{\pi\rho D^3}{17.6}\tanh\left(\frac{3.682H}{D}\right) \tag{3}$$

$$K_d = M_d\omega^2 \tag{4}$$

$$C_d = 3.094\frac{\nu^{1/2}}{D^{3/4}g^{1/4}}\left[\frac{0.318}{\sinh(3.68H/D)}\left(\frac{1-2H/D}{\cosh(3.68H/D)}+1\right)+1\right]{M_d}^{1/2}{K_d}^{1/2} \tag{5}$$

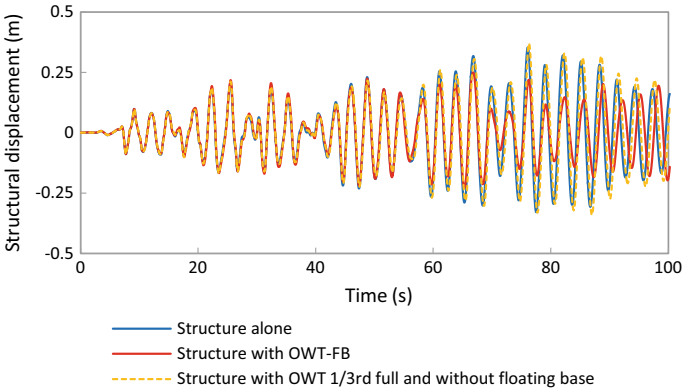

Fig. 4 Displacement time history of **a** structure alone, **b** structure with OWT-FB, and **c** structure with OWT 1/3rd full and without FB

Here, ν represents the kinematic viscosity of water and its value is considered as 10^{-6} m^2/s.

Now, for the example structure–damper system and the considered base excitation, Eq. (2) is solved using the 'ode45' solver of MATLAB and the displacement time history of the structure is evaluated. The performance of the OWT-FB system is assessed by the achieved response reduction of the equivalent SDOF structure, expressed as a percentage of the uncontrolled response. The OWT-FB system is able to achieve 30 and 24% reductions, respectively, in peak and root mean square (rms) displacement response of the structure, which are substantial for passive dampers (see Fig. 4). This is compared with the response of the structure with OWT 1/3rd full and without FB. The peak and rms displacement responses of the structure are found to have increased by 5% and 3%, respectively, as compared to the uncontrolled structural response (see Fig. 4). This kind of result is expected due to lack of tuning.

4 Conclusions

Overall, it may be stated that, in a conventional OWT, it is practically infeasible to maintain the desired tuning of the sloshing frequency with the dominant frequency of the building structure so that passive energy dissipation may take place. With the introduction of the FB in the OWT, a constant tuning is maintained even if the water depth in the main tank fluctuates. The proposed design is economic with the requirement of very low capital and maintenance costs. The FB can be incorporated easily into an existing OWT without any modification in the original tank structure. The numerical study shows significant structural response reduction under the considered seismic base excitation. Thus, the OWT-FB system can be effectively designed to

serve as a dynamic vibration absorber against lateral excitation, in addition to its primary function of water storage and supply.

Acknowledgements This research did not receive any specific grant from funding agencies in the public, commercial, or not-for-profit sectors.

References

1. Touaillon J (1870) Improvement in buildings
2. Ghosh A, Basu B (2004) Seismic vibration control of short period structures using the liquid column damper. Eng Struct 26:1905–1913
3. Hitchcock PA, Kwok KCS, Watkins RD, Samali B (1997) Characteristics of liquid column vibration absorbers (LCVA) I. Eng Struct 19:126–134
4. Konar T, Ghosh AD (2010) Passive control of seismically excited structures by the liquid column vibration absorber. Struct Eng Mech 36:561–573
5. Konar T, Ghosh AD (2020) Flow damping devices in tuned liquid damper for structural vibration control: a review. Arch Comput Methods Eng. https://doi.org/10.1007/s11831-020-09450-0
6. Parulekar YM, Reddy GR (2009) Passive response control systems for seismic response reduction: a state-of-the -art review. Int J Struct Stab Dyn 9:151–177
7. Bandyopadhyay R, Maiti S, Ghosh AD, Chatterjee A (2018) Overhead water tank shapes with depth-independent sloshing frequencies for use as TLDs in buildings. Struct Control Heal Monit 25:1–13
8. Fujino Y, Pacheco BM, Chaiseri P, Sun LM (1988) Parametric study on tuned liquid damper (TLD) using circular containers by free oscillation experiment. Struct Engg Earthq Eng 5:177–187
9. Rai NK, Reddy GR, Venkatraj V (2011) Effectiveness of multiple TSWDs for seismic response control of masonry-infilled RC framed structures. ISET J Earthq Technol 48:85–101
10. Konar T, Ghosh AD (2021) Development of a novel tuned liquid damper with floating base for converting deep tanks into effective vibration control devices. Adv Struct Eng 24:401–407
11. Abramson HN, Chu WH, Ransleben GE Jr (1961) Representation of fuel sloshing in cylindrical tanks by an equivalent mechanical model. Am Rocket Soc J 31:1697–1705
12. Mikishev GN, Dorozhkin NY (1961) An experimental investigation of free oscillations of a liquid in containers (in Russian). Izv. Akad. Nauk SSSR, Otd. Tekhnicheskikh Nauk. Mekhanika i Mashinostr 4:48–83

Comparative Study on the Effectiveness Between Shear Wall and Bracing Systems on High-Rise Structures

Piash Ghosh, Saurabh Kumar Singh, Mainak Mallik, and Damodar Maity

1 Introduction

High-rise structures are often constructed throughout the metro cities due to space or architectural constraints, though the asymmetricity of the plan of some buildings cannot be avoided. This is evident that the high-rise building with asymmetric plan is highly susceptible to damage due to seismic forces and high wind pressure. The existence of the shear walls plays an important role in arresting the deformation of the adjacent parts of the buildings, by providing an ample amount of stiffness to the building. Elevator core panels are the natural location of shear walls in a building. RCC bracings can also be provided instead of providing shear walls in the panels. Shear walls and bracings both provide stiffness efficiently.

Bhojkar and Bagade [1] have found that the X type of steel bracings significantly contributes to the structural stiffness and reduces the maximum inter-storey drift of the frames of a G+9 (ten storied) building. Alashkar et al. [2] have observed that for a G+7 building shear walls reduce a significant amount of lateral displacement, bending moment, and shear forces in the frame members when the shear walls are suitably placed. Azad and Gani [3] concluded that the usage of vertical bracings is more important than the floor bracings for a symmetric G+8 building. A parametric study has been performed by Thapa and Sarkar [4] to compare the dynamic responses of frame structure with and without the shear wall.

From the above discussions, it is evident that till date, no significant studies have been performed on the performance evaluation of high-rise structures with the comparison of shear walls and RCC bracings under seismic and wind loading. In this context, this paper is an attempt to perform a comparative study between the

P. Ghosh (Deceased) · S. K. Singh (✉) · D. Maity
Department of Civil Engineering, IIT, Kharagpur, India

M. Mallik
Department of Civil Engineering, NIT, Nirjuli, Arunachal Pradesh, India

D. K. Maiti et al. (eds.), *Recent Advances in Computational and Experimental Mechanics, Vol II*, Lecture Notes in Mechanical Engineering,
https://doi.org/10.1007/978-981-16-6490-8_55

effectiveness of RC shear wall and X-type of concrete bracing system of high-rise structure having an asymmetric plan. For understanding the effect of the shear wall and bracing system in the buildings having asymmetric plan in a better manner, a building having symmetric plan of the same height has also been incorporated in this study. In the present work, two different types of G+25 building of asymmetric plan and one G+25 building of symmetric plan of the same height have been modelled and analyzed using finite element software STAAD.Pro. The maximum base shear, storey drift, and maximum base moment under seismic and wind forces are calculated for the buildings with shear wall and concrete bracing systems.

2 Finite Element Formulation

2.1 Formulation for Frame

The stiffness matrix $[K]$ for a beam element may be expressed as

$$[K] = \int_0^L [B]^T E I [B] \mathrm{d}x \tag{1}$$

where E is the modulus of elasticity, I is the second moment of area and $[B]$ is the curvature displacement relationship matrix which may be expressed as

$$[B] = \left[\frac{\partial^2 N_1}{\partial x^2} \;\; \frac{\partial^2 N_2}{\partial x^2} \;\; \frac{\partial^2 N_3}{\partial x^2} \;\; \frac{\partial^2 N_4}{\partial x^2} \right] \tag{2}$$

The stiffness matrix for a truss element may be expressed as

$$[K] = \int_0^L [B]^T E [B] A \mathrm{d}x \tag{3}$$

where E is the modulus of elasticity, A is the area of the element and the strain–displacement matrix is

$$[B] = \left[\frac{\partial N_1}{\partial x} \;\; \frac{\partial N_2}{\partial x} \right] \tag{4}$$

In the present case, the structures have been analyzed as a planar frame model using two-dimensional beam element with three degrees of freedom at each node. By superimposing the stiffness matrix of a truss element corresponding to Eq. (3) and the stiffness matrix of a beam element corresponding to Eq. (1) after expanding to 6×6 stiffness matrix individually, the desired stiffness matrix can be obtained. The corresponding element stiffness matrix is

$$[K] = \begin{bmatrix} H_1 & 0 & 0 & -H_1 & 0 & 0 \\ 0 & 12H_2 & 6H_2L & 0 & -12H_2 & 6H_2L \\ 0 & 6H_2L & 4H_2L^2 & 0 & -6H_2L & 2H_2L^2 \\ -H_1 & 0 & 0 & H_1 & 0 & 0 \\ 0 & -12H_2 & -6H_2L & 0 & 12H_2 & -6H_2L \\ 0 & 6H_2L & 2H_2L^2 & 0 & -6H_2L & 4H_2L^2 \end{bmatrix} \quad (5)$$

where $H_1 = AE/L$, $H_2 = EI_z/L^3$, where I_z is the second moment of area about the z-axis, L is the length of the element, A is the cross-sectional area and E is the modulus of elasticity.

2.2 Formulation for Shear Wall

The finite element formulation of shear wall has been explained by Sepehrnia et al. [5]. They have presented the shear wall panel as shown in Fig. 1.

The degrees of freedom of the panel element (PE) is considered to be eight. Here, the degrees of freedom indicates the lateral and vertical movements associated with two in-plane rotational deformations, which are u_1, $-\delta u_1/\delta y$ corresponding to ω_1, v_1, v_2 and u_2, $-\delta u_2/\delta y$ corresponding to ω_3, v_3, v_4. They have been considered at the lower chord and the upper chord of the panel element, respectively. The analytical relation between strain vector $\{\varepsilon\}$, displacement vector $\{D\}$ and strain–displacement matrix $[B]$ is

$$\left[\varepsilon_x \ \varepsilon_y \ \gamma_{xy}\right]^T = [B].\{D\} \quad (6)$$

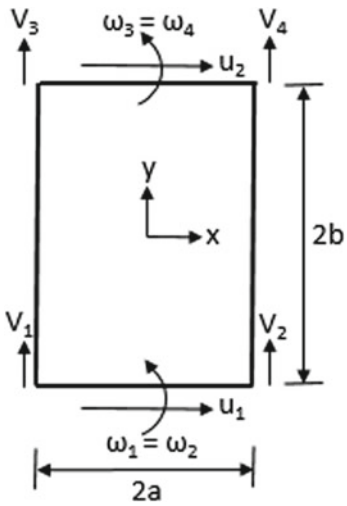

Fig. 1 Panel element of shear wall

where ε_x is the horizontal strain, ε_y is flexural strain and γ_{xy} is the shear strain.

$$\{D\}_{\mathrm{PE}} = \left\{ u_1 \ \omega_1 \ v_1 \ v_2 \ u_2 \ \omega_3 \ v_3 \ v_4 \right\}^T \tag{7}$$

As per the assessment made by Taranath [6], in the modelling process of tall buildings, the horizontal strain is assumed to be negligible, for this type of element. The shear wall panel is considered to act as a deep beam and ε_y along Y-direction is considered to study the flexural behaviour of the panel. The stiffness matrix of the element is evaluated by standard expression as

$$[K] = t \int_A [B]^T [D_m][B] \mathrm{d}A \tag{8}$$

where $[D_m] = diag\left[E \ E \ G \right]$, G and E are shear and elasticity modulus, respectively, t is the thickness of the element. The element stiffness matrix (Sepehrnia et al. [5]) has been given as follows:

$$[K] = [K_{\mathrm{F}}] + [K_{\mathrm{S}}] \tag{9}$$

where $[K_{\mathrm{F}}]$ and $[K_{\mathrm{S}}]$ are flexural and shear stiffness matrices, respectively.

$$[K_{\mathrm{F}}] = \begin{bmatrix} \frac{25a^3}{21b^3} & & & S & & & \\ -\frac{25a^3}{21b^2} & \frac{25a^3}{21b} & & & Y & & \\ 0 & 0 & \frac{a}{3b} & & & M & \\ 0 & 0 & \frac{a}{6b} & \frac{a}{3b} & & & M \\ -\frac{25a^3}{21b^3} & \frac{25a^3}{21b^2} & 0 & 0 & \frac{25a^3}{21b^3} & & \\ -\frac{25a^3}{21b^2} & \frac{25a^3}{21b} & 0 & 0 & \frac{25a^3}{21b^2} & \frac{25a^3}{21b} & \\ 0 & 0 & -\frac{a}{3b} & -\frac{a}{6b} & 0 & 0 & \frac{a}{3b} \\ 0 & 0 & -\frac{a}{6b} & -\frac{a}{3b} & 0 & 0 & \frac{a}{6b} \ \frac{a}{3b} \end{bmatrix} \tag{10}$$

$$[K_{\mathrm{S}}] = \begin{bmatrix} 0 & & & S & & & \\ 0 & \frac{8ab}{7} & & & Y & & \\ 0 & \frac{4b}{7} & \frac{2b}{7a} & & & M & \\ 0 & -\frac{4b}{7} & -\frac{2b}{7a} & \frac{2b}{7a} & & & M \\ 0 & 0 & 0 & 0 & 0 & & \\ 0 & \frac{6ab}{7} & \frac{3b}{7} & -\frac{3b}{7} & 0 & \frac{8ab}{7} & \\ 0 & \frac{3b}{7} & \frac{3b}{14a} & -\frac{3b}{14a} & 0 & \frac{4b}{7} & \frac{2b}{7a} \\ 0 & -\frac{3b}{7} & -\frac{3b}{14a} & \frac{3b}{14a} & 0 & -\frac{4b}{7} & -\frac{2b}{7a} \ \frac{2b}{7a} \end{bmatrix} \tag{11}$$

The strain–displacement matrix $[B]$ of the proposed panel element (Sepehrnia et al. [5]) is

$$[B] = \begin{bmatrix} 0 & -\frac{5xy^3}{2b^5} & 0 \\ 0 & \frac{5xy^3}{2b^4} & \frac{y^3}{2b^3} - \frac{1}{2} \\ 0 & \frac{x}{4ab} - \frac{1}{4b} & \frac{y^3}{4ab^3} - \frac{1}{4a} \\ 0 & -\frac{x}{4ab} - \frac{1}{4b} & -\frac{y^3}{4ab^3} + \frac{1}{4a} \\ 0 & \frac{5xy^3}{2b^5} & 0 \\ 0 & \frac{5xy^3}{2b^4} & -\frac{y^3}{2b^3} - \frac{1}{2} \\ 0 & -\frac{x}{4ab} + \frac{1}{4b} & -\frac{y^3}{4ab^3} - \frac{1}{4a} \\ 0 & \frac{x}{4ab} + \frac{1}{4b} & \frac{y^3}{4ab^3} + \frac{1}{4a} \end{bmatrix}^T \tag{12}$$

3 Numerical Modelling of the Buildings

The numerical modelling and analysis of the buildings have been performed by finite element software STAAD.Pro. The model of Building 1 (B1) is shown in Fig. 2.

The specification of the model of the buildings is shown in Table 1.

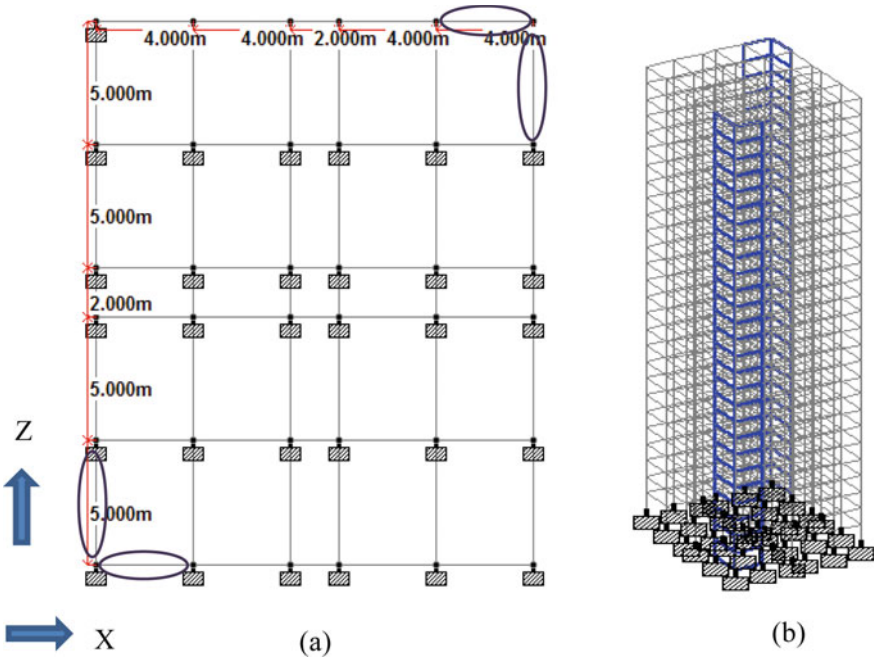

Fig. 2 **a** Top view of the model of B1 with positions indicating shear wall and bracings and **b** isometric view of B1 with bracings

Table 1 Specification of model

Specification	Building 1 (B1)	Building 2 (B2)	Building 3 (B3)
No. of storeys	G+25	G+25	G+25
Height of building in m	81.00	81.00	81.00
Size of the beam in mm × mm (width × depth)	300 × 400	300 × 400	300 × 400
Size of the column in mm × mm	800 × 800 (B+G+8th)	800 × 800 (B+G+8th)	800 × 800 (B+G+8th)
	600 × 600 (9–18th)	600 × 600 (9–18th)	600 × 600 (9–18th)
	500 × 500 (19–25th)	500 × 500 (19–25th)	500 × 500 (19–25th)
Thickness of shear wall in mm	150	150	150
Size of RCC bracings in m × m (width × depth)	0.42 × 0.42	0.43 × 0.43	0.42 × 0.42
	0.44 × 0.44	0.45 × 0.45	0.43 × 0.43
Frame configuration	Moment resisting RC frame	Moment resisting RC frame	Moment resisting RC frame
Plan type	Symmetric	Asymmetric	Asymmetric

3.1 Building Model Configuration

Bracings of different dimensions have been provided at different locations of the buildings so that the volume of concrete in the shear wall provided in each panel should be equal to the volume of concrete in bracings in each panel. The purpose of this study is to compare the effectiveness between the shear wall and bracings of each individual building only and not among the buildings. So, the comparison has been restricted to each individual building only. Models of Building 2 and Building 3 are shown in Figs. 3 and 4, respectively.

From Fig. 2, it can be seen that, the shear walls and bracing systems in the symmetric building have been provided at the diagonal positions. From the study of Thapa and Sarkar [4], it has been found that shear wall at corners (i.e. at diagonal positions of the building) reduce displacement of the building along with height significantly.

3.2 Loading Configuration

Dead Load and Live Load. Dead load and live load have been assigned as per IS 875 (Part 1) [7] and IS 875 (Part 2) [8], respectively. For the load calculation, the thickness of the wall has been considered 250 mm, the height of the parapet wall has been considered 1.20 m. The unit weight of brick masonry is 20 kN/m^3. Except

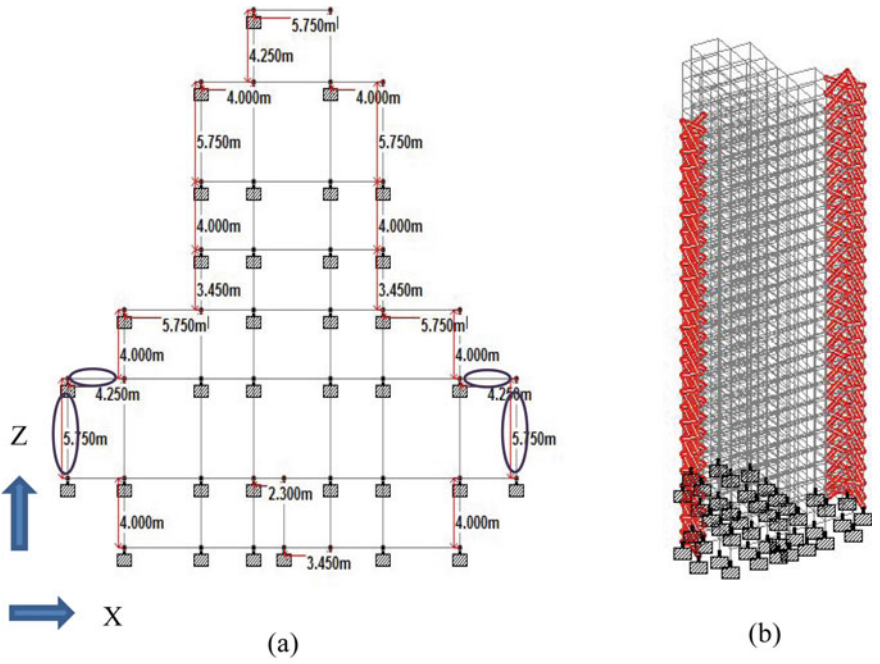

Fig. 3 **a** Top view of the model of B2 with positions indicating shear wall and bracings and **b** isometric view of B2 with shear walls

self-weight of the building, there are different loads such as dead load, live load, seismic load and wind load which are acting on the structure. The load combinations have been assigned as per IS 456-2000 [9].

Seismic Load. Seismic analysis has been performed as per IS 1893 (Part 1)-2002 [10], through STAAD.Pro. For the purpose of the analysis, building location has been considered in Patna, which is categorized under zone IV. The necessary parameters like zone factor as 0.24, response reduction factor as 5, importance factor as 1, rock and soil site factor as 1 and damping ratio as 0.05 have been considered. The natural period for Building 1 has been calculated as 1.72 and 1.55 s along X- and Z-directions, respectively, whereas the same parameter for Building 2 has been obtained as 1.25 and 1.30 s along X- and Z-directions, respectively. The natural period for Building 3 has been calculated as 1.19 and 1.40 s along X- and Z-directions, respectively.

Wind Load. Wind load analysis has been performed through STAAD.Pro. Wind load data has been calculated as per IS 875 (Part 3)-1987 [11]. The zone has been considered as Patna, where the basic wind speed is 47 m/s. The terrain category has been considered as 3 and building class has been considered as C.

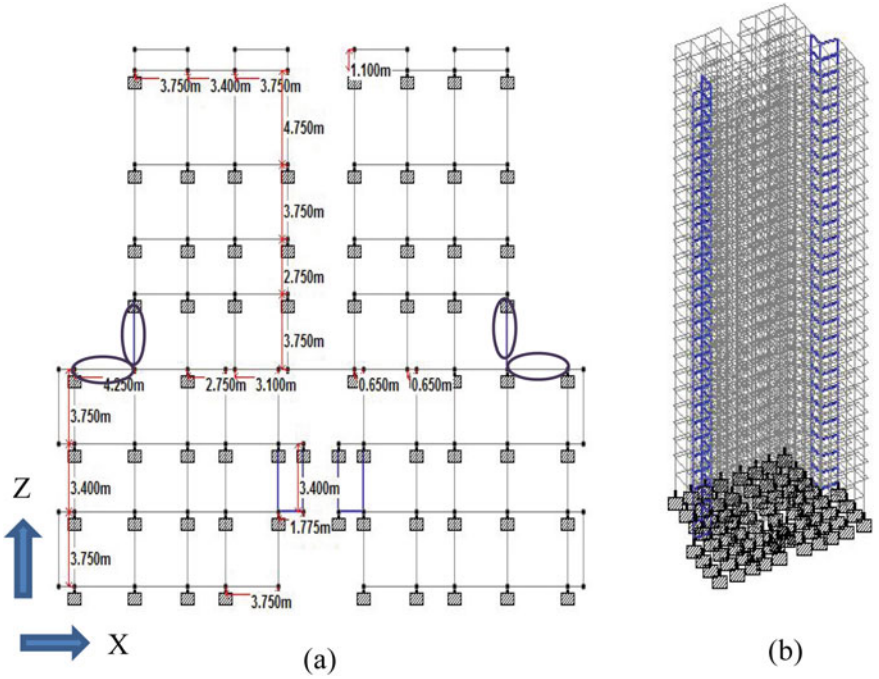

Fig. 4 **a** Top view of the model of B3 with positions indicating shear wall and bracings and **b** isometric view of B3 with shear wall

4 Results and Discussions

The frame structure buildings have been analyzed with shear wall and X-type of RCC bracings provided at suitable locations on the boundary of the buildings. Results have been compared in terms of maximum base shear, storey drift at each floor level and maximum base moment. Assuming Building 1, Building 2 and Building 3 as B1, B2 and B3, respectively.

4.1 Base Shear

The maximum expected lateral force on the base of the structure due to seismic activity is defined as base shear. The buildings have been analyzed to calculate the base shear for shear wall and bracing systems at appropriate locations of the buildings.

From Figs. 5, 6, 7, 8, 9 and 10, this is clear that the base shear will be more for the buildings with shear walls as well as for the buildings having RCC bracings because of the increase in the dead load of the buildings. The addition of new elements to

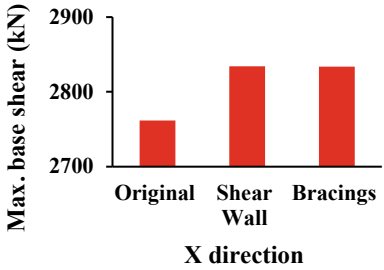

Fig. 5 Maximum base shear of B1 in X-direction

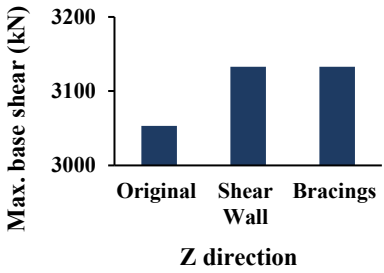

Fig. 6 Maximum base shear of B1 in Z-direction

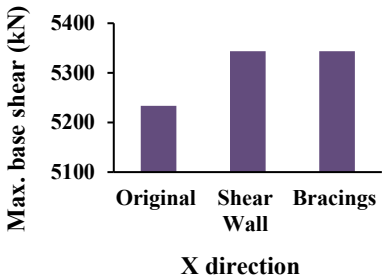

Fig. 7 Maximum base shear of B2 in X-direction

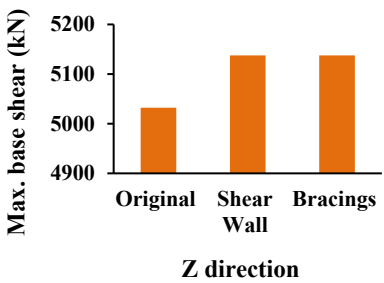

Fig. 8 Maximum base shear of B2 in Z-direction

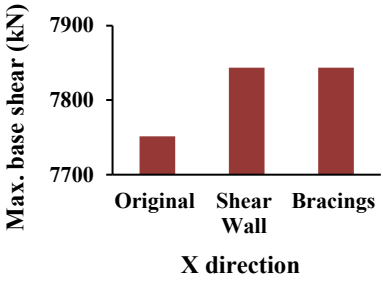

Fig. 9 Maximum base shear of B3 in X-direction

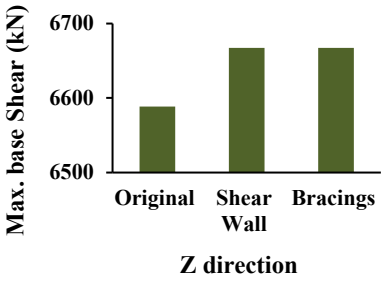

Fig. 10 Maximum base shear of B3 in Z-direction

the original building increases its dead load, which results in an increase in the base shear.

4.2 Storey Drift

Storey drift is defined as the lateral displacement of one storey with respect to the adjacent storey below. Generally, it is caused by lateral loads such as seismic and wind loads. In the figures below storey drift effect on original buildings (ORG), buildings with the shear wall (SW) and buildings with RCC bracings (BR) are shown.

From Figs. 11, 12, 13, 14, 15 and 16, buildings with shear walls show slightly lesser storey drift as compared to the buildings with RCC bracings.

The picture of the storey drift will be clearer, if the drift ratio of the buildings in each direction are observed. The drift ratio of the buildings are shown in Table 2.

From Table 2, it is clearly visible that, the original buildings are under the highest drift, while in the case of the other buildings, the drift is getting lowered with increasing resistance provided by the RCC bracings and shear walls.

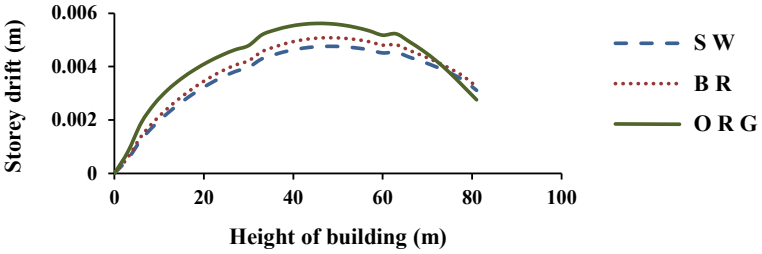

Fig. 11 Storey drift in X-direction for B1

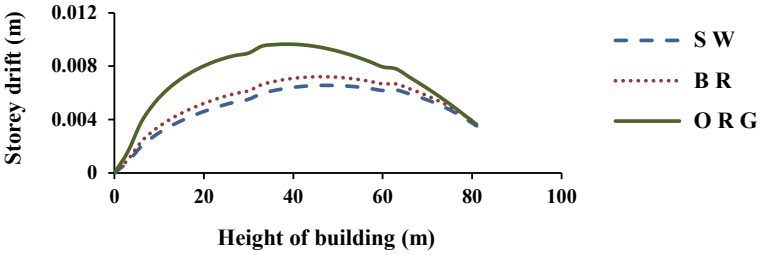

Fig. 12 Storey drift in Z-direction for B1

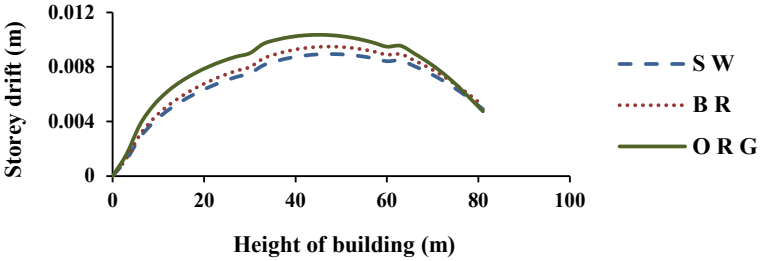

Fig. 13 Storey drift in X-direction for B2

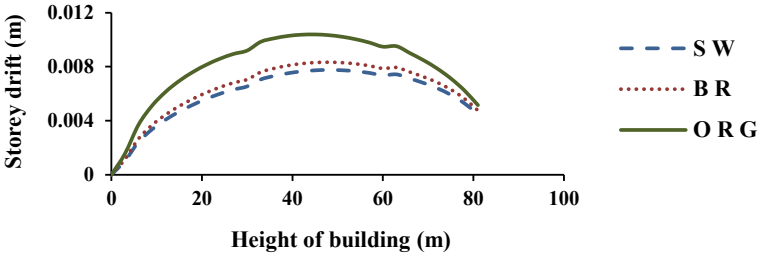

Fig. 14 Storey drift in Z-direction for B2

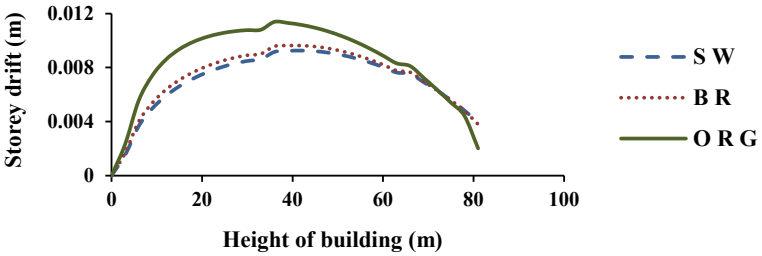

Fig. 15 Storey drift in X-direction for B3

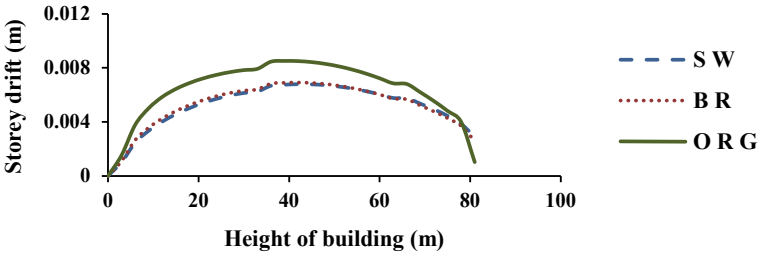

Fig. 16 Storey drift in Z-direction for B3

Table 2 Drift ratio of the buildings

Drift ratio						
Types	Original		Shear wall		Bracing	
	X	Z	X	Z	X	Z
Building 1	0.14460	0.24437	0.12325	0.16890	0.13109	0.18544
Building 2	0.26857	0.27182	0.23124	0.20245	0.24497	0.21760
Building 3	0.28632	0.21712	0.23891	0.17534	0.24801	0.17756

4.3 Base Moment

Base moment is defined as the moment produced at the base of the structure due to different loading conditions that are acting on the structure. The buildings are analysed to calculate the base moment for shear walls and bracings, which are provided at some appropriate locations on the boundary of the buildings.

From Figs. 17, 18, 19, 20, 21 and 22, this is clear that for all of the cases irrespective of direction maximum base moment is highest for the original buildings and lowest for the buildings with shear walls. Also, it is to be noted that, for all of the cases the maximum base moment of the buildings with RCC bracings is higher than the maximum base moment of the buildings with shear walls.

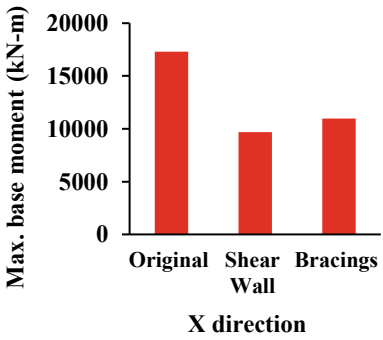

Fig. 17 Maximum base moment of B1 along X-direction

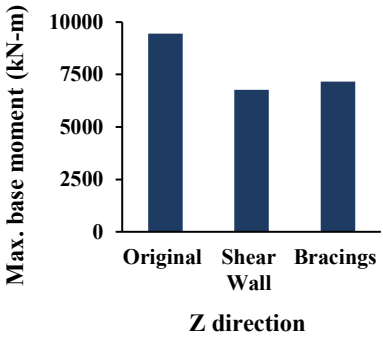

Fig. 18 Maximum base moment of B1 along Z-direction

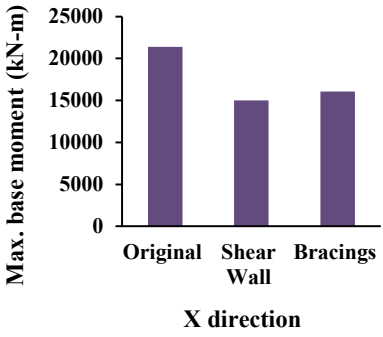

Fig. 19 Maximum base moment of B2 along X-direction

5 Conclusions

In the present work, it can be seen that the weight of the building and the lateral forces generated by seismic and wind loads play an important role to interpret the results.

(a) The buildings with shear wall and RCC bracings show higher value of maximum base shear than the original buildings irrespective of direction. This

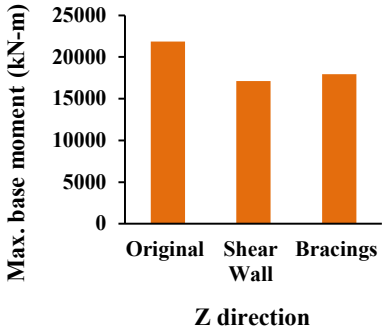

Fig. 20 Maximum base moment of B2 along Z-direction

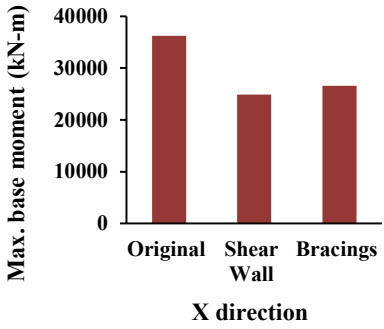

Fig. 21 Maximum base moment of B3 along X-direction

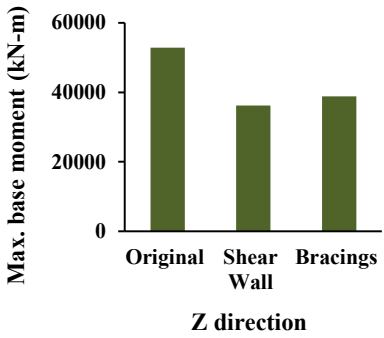

Fig. 22 Maximum base moment of B3 along Z-direction

is because; the addition of new elements to the building increases the weight factor, which in turn increases the base shear also.

(b) The value of maximum base shear is same for both the buildings, i.e. the building with shear wall and the building with bracing for a particular direction. This validates the concept of using the same volume of concrete in the shear wall as well as in the bracings.

(c) The plots of the maximum base shear show the same pattern in the asymmetric plan as well as symmetric plan buildings. So, the maximum base shear does not depend upon the asymmetricity of the plan.
(d) In the case of the storey drift, the buildings with shear walls show slightly lesser drift than the buildings with bracings and significantly lesser drift than the original buildings. The reason may be that, as shear walls connect through the circumference of the panel section, these provide very high stiffness throughout the panel, which resists the drift efficiently, whereas the bracings remain placed diagonally in the panels and are connected at the corners of panels only, due to which, the stiffness remains slightly lesser than the shear wall panels. This is true for the plan in asymmetric as well as for the plan in symmetric buildings.
(e) The maximum base moment is highest for the original buildings and lowest for the buildings with shear walls in each direction of all the cases. This result concludes that the shear walls show high resistance to the base moment.
(f) The maximum base moment of the buildings with RCC bracings are higher than the maximum base moment of the buildings with shear walls. This result accomplishes the fact that the shear walls show higher resistance to the base moment than RCC bracings. The reason may be that, the shear walls in the basement are connected to the ground, due to which, the base moment gets resisted efficiently in those buildings, which is not possible for the buildings with RCC bracings. The bracings are efficient to transfer moment, but as they are not connected to the ground directly, they show lesser efficiency than the shear walls in resisting base moment.

From the above discussion, it can be concluded that the shear walls are quite effective retrofitting elements from the point of resisting storey drift as well as base moment than the bracings. Also, the point to be noted that asymmetricity in the plan of buildings should be reduced to minimize the vulnerability of the structure.

References

1. Bhojkar N, Bagade M (2015) Seismic evaluation of high-rise structure by using steel bracing system. Int J Innov Sci Eng Technol 2(3):264–269
2. Alashkar Y, Nazar S, Ahmed M (2015) A comparative study of seismic strengthening of RC buildings by steel bracings and concrete shear walls. Int J Civ Struct Eng Res 2(2):24–34
3. Azad MS, Gani SHA (2016) Comparative study of seismic analysis of multistory buildings with shear walls and bracing systems. Int J Adv Struct Geotech Eng 5(3):72–77
4. Thapa A, Sarkar S (2017) Comparative study of multi-storied RCC building with and without shear wall. Int J Civ Eng 6(2):11–20
5. Sepehrnia S, Rahami H, Mirhosseini M, Zeighami E (2020) Analysis of shear wall systems using plane stress elements. Iran J Sci Technol Trans Civ Eng 27–34. https://doi.org/10.1007/s40996-019-00314-7
6. Taranath BS (1998) Structural analysis and design of tall buildings, 2nd edn. McGraw-Hill, New York
7. IS 875 (Part 1) (1987) Code of practice for design loads (other than earthquake) for buildings and structures. BIS, New Delhi

8. IS 875 (Part 2) (1987) Code of practice for design loads (other than earthquake) for buildings and structures. BIS, New Delhi
9. IS 456 (2000) Plain and reinforced concrete-code of practice. BIS, New Delhi
10. IS 1893 (Part 1) (2002) Criteria for earthquake resistant design of structures. BIS, New Delhi
11. IS 875 (Part 3) (1987) Code of practice for design loads (other than earthquake) for buildings and structures. BIS, New Delhi